



Defense Nuclear Agency
Alexandria, VA 22310-3398



AD-A273 613



DNA-TR-92-6

X-Ray Simulator Theory Support

James L. Geary, Jr. , et al.
Berkeley Research Associates, Inc.
P.O. Box 241
Berkeley, CA 94701

November 1993

Technical Report

S DTIC ELECTE D
E DEC 9 1993

CONTRACT No. DNA 001-88-C-0006

Approved for public release;
distribution is unlimited.

93-29955



93 12 8 022

Destroy this report when it is no longer needed. Do not return to sender.

PLEASE NOTIFY THE DEFENSE NUCLEAR AGENCY,
ATTN: CSTI, 6801 TELEGRAPH ROAD, ALEXANDRIA, VA
22310-3398, IF YOUR ADDRESS IS INCORRECT, IF YOU
WISH IT DELETED FROM THE DISTRIBUTION LIST, OR
IF THE ADDRESSEE IS NO LONGER EMPLOYED BY YOUR
ORGANIZATION.



REPORT DOCUMENTATION PAGE			Form Approved OMB No. 0704-0188	
Public reporting burden for this collection of information is estimated to average 1 hour per response including the time for reviewing instructions, searching existing data sources, gathering and maintaining the data needed, and completing and reviewing the collection of information. Send comments regarding this burden estimate or any other aspect of this collection of information, including suggestions for reducing this burden, to Washington Headquarters Services, Directorate for Information Operations and Reports, 1215 Jefferson Davis Highway, Suite 1204, Arlington, VA 22202-4302, and to the Office of Management and Budget, Paperwork Reduction Project (0704-0188), Washington, DC 20503				
1. AGENCY USE ONLY (Leave blank)		2. REPORT DATE 931101	3. REPORT TYPE AND DATES COVERED Technical 871020 - 911030	
4. TITLE AND SUBTITLE X-Ray Simulator Theory Support			5. FUNDING NUMBERS C - DNA 001-88-C-0006 PE - 62715H PR - RL TA - RB WU - DH00054	
6. AUTHOR(S) James L. Geary, Jr., Robert J. Kares, Lan-Lan Chen, Nino R. Pereira				
7. PERFORMING ORGANIZATION NAME(S) AND ADDRESS(ES) Berkeley Research Associates, Inc. P.O. Box 241 Berkeley, CA 94701			8. PERFORMING ORGANIZATION REPORT NUMBER BRA-92-WO24R	
9. SPONSORING/MONITORING AGENCY NAME(S) AND ADDRESS(ES) Defense Nuclear Agency 6801 Telegraph Road Alexandria, VA 22310-3398 RAEV/Garcia			10. SPONSORING/MONITORING AGENCY REPORT NUMBER DNA-TR-92-6	
11. SUPPLEMENTARY NOTES This work was sponsored by the Defense Nuclear Agency under RDT&E RMC Code B4662D RL RB 00059 RAEV 3230A 25904D.				
12a. DISTRIBUTION/AVAILABILITY STATEMENT Approved for public release; distribution is unlimited.			12b. DISTRIBUTION CODE	
13. ABSTRACT (Maximum 200 words) This report contains the theory, analyses and computations performed between October 20, 1987 and October 30, 1991 on plasma filled diodes, opening switches, and z-pinch. This includes the first quantitative estimate of plasma blowoff from surfaces in plasma opening switches, the first time-dependent particle-in-cell simulation of a (one-dimensional) plasma opening switch (or plasma-filled diode), the first two-dimensional dynamical model of a plasma diode, and seminal reviews of z-pinch and vacuum spark research.				
14. SUBJECT TERMS Pulse Power Theory Plasma Opening Switch Plasma-Filled Diode			15. NUMBER OF PAGES 246	
			16. PRICE CODE	
PIC Simulations Plasma Radiation Source				
17. SECURITY CLASSIFICATION OF REPORT UNCLASSIFIED	18. SECURITY CLASSIFICATION OF THIS PAGE UNCLASSIFIED	19. SECURITY CLASSIFICATION OF ABSTRACT UNCLASSIFIED	20. LIMITATION OF ABSTRACT SAR	

UNCLASSIFIED

SECURITY CLASSIFICATION OF THIS PAGE

CLASSIFIED BY:

N/A since Unclassified.

DECLASSIFY ON:

N/A since Unclassified.

EXECUTIVE SUMMARY

This report contains the research done by Berkeley Research Associates under contract DNA-001-88-C-0006. The focus of the work is on theory and computation for the pulse power elements in existing and future DNA flash x-ray simulators, in particular DECADE. The pulse power for this machine is based on inductive store technology, which depends on an opening switch. Despite much work over the last 10 years, many details in the operation of the opening switch are known incompletely, preventing extrapolation from the experimental data on existing switches to DECADE. Switch opening improves with a low-impedance load, such as the Plasma Filled Diode or the Plasma Radiation Source.

The following nine sections discuss the Reflex switch, the consequences of dirty electrodes, a zero-dimensional, two one-dimensional, and a two-dimensional treatment of the Plasma Filled Diode, design computations on the Plasma Opening Switch, the Plasma Radiation Source, and a detailed description of a code especially developed for this research. Appendices contain published papers, and some further code details.

Section 1 is the first dynamic study of the Reflex Switch, a device developed by Physics International. Previous Reflex Switch theories were stationary, and therefore missed important dynamical features that were discovered here. Physics International's scientists used these considerations in further experimental work on the Reflex Switch.

Section 2 warns against contamination from electrode material blown off by the plasma injected into the opening switch. The blown-off material modifies the intended plasma density and therefore affects opening switch operation. As expected, in experiments at Physics International the reproducibility and opening speed improve with cleaning of the electrodes.

Sections 3, 4, and 5 discuss different types of theory and modeling of the Plasma Filled Diode, while Section 6 presents fully two-dimensional computations of the switch that contain many features of the simpler theories and computational models. Although it is clear from the essential two-dimensional nature of the plasma dynamics in the diode that one-dimensional approximations can not be accurate, the one dimensional computations show especially clearly the instabilities between fast electrons and the plasma. During the conduction phase the instabilities produce a voltage internal to the plasma that can be many times the applied voltage. The two-dimensional modeling maintains this and other features of the one-dimensional computations.

Section 7 discusses the use of the ANTHEM code for modeling opening switches. This code is intended for the time and density regime associated with the intermediate density plasma opening switches. However, the code has many parameters to be selected by the user, and it is necessary to gain confidence in the code's predictions by careful benchmarking. In addition, the code must be augmented with the experimentally relevant boundary conditions. This work points to the need for another code having many of ANTHEM's features, and the possibility of adding hitherto ignored physics.

Section 8 contains the work on the Plasma Radiation Source, in the form of the papers published over the contract period. These include a review paper summarizing the state of the art of the Plasma Radiation Source, and a review paper on radiative collapse. Other

papers discuss the current outside a z-pinch, and the Pease-Braginskii current. In addition, the Proceedings of the 2nd International Conference on High-Density z-pinches were edited. Section 9 describes the code REFLEX: this code contains many features of general interest to pulse power theory.

In the course of this work we have been in frequent and fruitful interaction with the experimental groups developing opening switches (especially at Physics International), Plasma Filled Diodes (especially at Maxwell Laboratories), and the Plasma Radiation Source (especially at the Naval Research Laboratory).

Accession For	
NTIS CRA&I	<input checked="" type="checkbox"/>
DTIC TAB	<input type="checkbox"/>
U. announced	<input type="checkbox"/>
Justification	
By	
Distribution /	
Availability Codes	
Dist	Avail and/or Special
A-1	

DTIC QUALITY INSPECTED 6

CONVERSION TABLE

Conversion factors for U.S. customary to metric (SI) units of measurement

To Convert From	To	Multiply
angstrom	meters (m)	1.000 000 X E-10
atmosphere (normal)	kilo pascal (kPa)	1.013 25 X E+2
bar	kilo pascal (kPa)	1.000 000 X E+2
barn	meter ² (m ²)	1.000 000 X E-28
British Thermal unit (thermochemical)	joule (J)	1.054 350 X E+3
calorie (thermochemical)	joule (J)	4.184 000
cal (thermochemical)/cm ²	mega joule/m ² (MJ/m ²)	4.184 000 X E-2
curie	giga becquerel (GBq)*	3.700 000 X E+1
degree (angle)	radian (rad)	1.745 329 X E-2
degree Fahrenheit	degree kelvin (K)	$t_K = (t_F + 459.67) / 1.8$
electron volt	joule (J)	1.602 19 X E-19
erg	joule (J)	1.000 000 X E-7
erg/second	watt (W)	1.000 000 X E-7
foot	meter (m)	3.048 000 X E-1
foot-pound-force	joule (J)	1.355 818
gallon (U.S. liquid)	meter ³ (m ³)	3.785 412 X E-3
inch	meter (m)	2.540 000 X E-2
jerk	joule (J)	1.000 000 X E+9
joule/kilogram (J/Kg) (radiation dose absorbed)	Gray (Gy)	1.000 000
kilotons	terajoules	4.183
kip (1000 lbf)	newton (N)	4.448 222 X E+3
kip/inch ² (ksi)	kilo pascal (kPa)	6.894 757 X E+3
ktop	newton-second/m ² (N-s/m ²)	1.000 000 X E+2
micron	meter (m)	1.000 000 X E-6
mil	meter (m)	2.540 000 X E-5
mile (international)	meter (m)	1.609 344 X E+3
ounce	kilogram (kg)	2.834 952 X E-2
pound-force (lbf avoirdupois)	newton (N)	4.448 222
pound-force inch	newton-meter (N-m)	1.129 848 X E-1
pound-force/inch	newton/meter (N/m)	1.751 268 X E+2
pound-force/foot ²	kilo pascal (kPa)	4.788 026 X E-2
pound-force/inch ² (psi)	kilo pascal (kPa)	6.894 757
pound-mass (lbm avoirdupois)	kilogram (kg)	4.535 924 X E-1
pound-mass-foot ² (moment of inertia)	kilogram-meter ² (kg-m ²)	4.214 011 X E-2
pound-mass/foot ³	kilogram/meter ³ (kg/m ³)	1.601 846 X E+1
rad (radiation dose absorbed)	Gray (Gy)**	1.000 000 X E-2
roentgen	coulomb/kilogram (C/kg)	2.579 760 X E-4
shake	second (s)	1.000 000 X E-8
slug	kilogram (kg)	1.459 390 X E+1
torr (mm Hg, 0°C)	kilo pascal (kPa)	1.333 22 X E-1

*The becquerel (Bq) is the SI unit of radioactivity.

**The Gray (Gy) is the SI unit of absorbed radiation.

TABLE OF CONTENTS

Section	Page
EXECUTIVE SUMMARY	iii
CONVERSION TABLE	v
FIGURES	viii
1 REFLEX SWITCH	1
1.1 INTRODUCTION	1
1.2 SIMULATION OF THE CONDUCTION PHASE	3
1.3 REFLEX SWITCH OPENING	15
1.4 DISCUSSION	21
2 ACCUMULATION OF NEUTRALS IN PLASMA OPENING SWITCHES FROM PLASMA BOMBARDMENT OF ELECTRODES	23
2.1 OPENING SWITCHES AND ELECTRODE PLASMAS	23
2.2 MONTE CARLO TRANSPORT IN MATERIALS CODE TRIM	24
2.3 RESULTS AND DISCUSSION	26
2.4 CONCLUSION	31
3 OPENING MECHANISMS OF THE PLASMA FILLED DIODE	32
3.1 INTRODUCTION	32
3.2 EXPERIMENTAL DATA	33
3.3 ANALYSIS OF OPENING MECHANISMS	35
3.3.1 Gap Formation	35
3.3.2 Implosion Model	36
3.3.3 Resistivity	37
3.4 CONCLUSION	38
4 ONE-DIMENSIONAL PARTICLE IN CELL SIMULATIONS OF A PLASMA FILLED DIODE WITH AN EXTERNAL CIRCUIT	39
4.1 INTRODUCTION	39
4.2 COMPUTATIONAL MODEL	41
4.3 CATHODE WITHOUT ELECTRON EMISSION	44
4.4 CATHODE WITH SPACE-CHARGE LIMITED EMISSION	53
4.5 SCALING IN THE SIMULATIONS	60
4.6 CONCLUSIONS	65
5 THEORY OF THE PLASMA FILLED DIODE WITH IMMOBILE IONS	68
5.1 INTRODUCTION	68
5.2 PFD SIMULATION WITH IMMOBILE IONS	68
5.3 ANALYTIC CONSIDERATIONS	75
5.4 COMPARISON WITH SIMULATION	78

TABLE OF CONTENTS (continued)

Section	Page
5.5 TRAPPED ELECTRONS	80
5.6 CONCLUSIONS	88
6 TWO-DIMENSIONAL SIMULATIONS OF PLASMA FILLED DIODES	90
6.1 INTRODUCTION	90
6.2 SIMULATION MODELS	92
6.3 SIMULATION RESULTS	95
6.4 CONCLUSION	109
7 OPENING SWITCH STUDIES WITH ANTHEM	112
7.1 INTRODUCTION	112
7.2 SIMULATION MODEL	113
7.3 ACCURACY OF IMPLEMENTATION	118
7.4 APPLICABILITY OF MODEL	131
7.5 IMPROVEMENTS	138
7.6 CONCLUSIONS	140
8 PLASMA RADIATION SOURCE	143
9 ONE-DIMENSIONAL PIC-CIRCUIT CODE FOR SIMULATING A REFLEX TRIODE	144
9.1 INTRODUCTION	144
9.2 CIRCUIT MODEL	146
9.3 TRIODE MODEL	148
9.3.1 Field Solution	149
9.3.2 Particle Motion	151
9.3.3 Particle Emission and Injection	152
9.3.4 Electron Scattering Model	152
9.4. CONCLUSION	157
10 REFERENCES	158
APPENDIX	163
A REVIEW PAPERS ON PRS	163
B PUBLISHED PAPERS ON PRS	215
C ELECTRON SCATTERING FOR CODE IMPLEMENTATION	227

FIGURES

Figure	Page
1 Configuration of the reflex switch.	1
2 Electron and ion current densities.	2
3 Potential profiles.	4
4 Contour plot of the electric potential.	6
5 Voltage and current for a symmetric triode.	8
6 Time-averaged voltage.	9
7 Expanded view of the fast oscillations.	10
8 Electron phase space (v_x versus x).	12
9 Electric field profiles.	13
10 Ion phase space (v_x versus x).	14
11 Electrical behavior during transition.	16
12 Phase phase space during transition.	17
13 Electrical behavior after plasma injection.	18
14 Electron phase space after plasma injection.	19
15 Ion phase space after plasma injection.	20
16 Total emission coefficient $C_T(\alpha)$.	26
17 $C_T(60^\circ)$ versus incident ion energy.	27
18 Sputtering yield $Y_s(60^\circ)$.	28
19 Normalized velocity distribution of neutrals.	29
20 Density of the desorbed neutrals.	30
21 Cartoons of the PFD in the three models.	33
22 EYESS' voltages and currents.	34
23 Resistance inferred from Figure 22.	35
24 Gap spacing inferred from Figure 22.	36
25 Radius inferred from Figure 22.	37
26 Plasma Filled Diode with circuit.	42
27 Diode parameters without electron emission.	46
28 Electron phase space and electrical quantities.	47
29 Expanded view of cathode region.	52
30 Current and voltage with electron emission.	55
31 Electron phase space and electrical quantities.	56
32 Total charge of electrons and ions with electron emission.	60
33 Conduction current at representative fill densities.	61
34 Conduction time at representative fill densities.	62
35 Conduction current versus fill density.	63
36 Conduction time versus gap width.	64
37 Voltage amplification at representative fill densities.	65
38 Relative electron current J_e/J_i at opening.	66
39 Conduction time t_c versus ion mass.	67
40 Voltage and current with electron emission.	69

FIGURES (continued)

Figure	Page
41 Electron phase space and electric quantities. $\phi(x)$.	70
42 Potential distribution after opening.	73
43 Scaling of the diode current at opening.	74
44 Analytic solution for potential.	77
45 Comparing the potential maximum.	78
46 Comparing potential hump width.	79
47 Comparing the final diode current.	80
48 Amplitude and position of potential maximum.	81
49 Correction factors for position and maximum of potential.	84
50 Potential versus trapped electron strength.	85
51 Electron densities versus trapped electron strength.	86
52 Potential maximum and trapping fraction.	87
53 Analytic value for potential maximum.	89
54 Simulation geometry.	93
55 \vec{J} and \vec{E} at 2.5 ns.	96
56 \vec{J} and \vec{E} at 12 ns.	97
57 Ion configuration and phase space at 12 ns.	98
58 \vec{J} and \vec{E} at 15.5 ns.	99
59 Ion configuration and phase space at 15.5 ns.	100
60 Voltage and current.	101
61 \vec{J} and \vec{E} at 22 ns.	102
62 Ion and electron configuration space.	103
63 Voltage and current for the PFD in REFLEX.	104
64 Electron and ion phase space from REFLEX.	105
65 Voltage and current from FREYA.	106
66 Ion configuration and phase space at 22.5 ns.	107
67 Voltages at 1.9 cm and 7.6 cm, and current.	108
68 ISIS' ion configuration space at various times.	109
69 Voltages at 1.9 cm and 7.6 cm, and current.	110
70 Schematics of circuit, ANTHEM, and load.	119
71 Comparison between FREYA and ANTHEM over 6 ns.	122
72 Comparison between FREYA and ANTHEM over 60 ns.	123
73 Comparing the voltage into ANTHEM.	124
74 Comparing currents beyond the Courant limit.	125
75 Damping of voltage oscillations with time step.	126
76 Effect of ANTHEM's internal time step.	127
77 Radial vacuum transmission line over 60 ns.	128
78 Uniform plasma initialization.	130
79 Electric fields from ANTHEM at 1 ns.	132
80 Coulomb collision time versus plasma parameters.	135
81 Mean free paths versus plasma parameters.	136
82 Generator model for driving ANTHEM.	140
83 Comparing currents computed with ANTHEM.	141

FIGURES (continued)

Figure	Page
84 Schematic of the reflex triode code REFLEX.	145
85 The circuit coupled to REFLEX.	146
86 Finite-difference grid for transmission line.	149
87 Suppressing oscillations with dissipation.	150
88 Geometry of one-dimensional diode simulation.	151
89 Approximate electron paths in solids.	153
90 Coordinate system for particle scattering.	154
91 Comparing TIGER with REFLEX scattering model.	156
92 Comparing widths of Gaussian and Moliere distribution.	229
93 Scattering angles from Moliere's theory.	230

SECTION 1

REFLEX SWITCH

Physics International's Reflex Switch,¹ a viable opening switch candidate at the beginning of this program, is investigated with two different models. The first model uses the two-dimensional particle code ELECTRA. The computations show features that seem qualitatively correct, but they do not exhibit the expected dynamical behavior. The second model employs the one-dimensional particle code REFLEX developed specifically to perform dynamical computations of the reflex switch. REFLEX contains an inductive circuit and an approximate but realistic foil scattering component. This code is able to dynamically attain the expected equilibrium. The time to reach equilibrium is a function of the ionic mass and the anode-cathode gap spacing. Instabilities are evident through all phases of reflex switch operation. The time to opening of the switch depends on removal of ions from the primary gap.

1.1 INTRODUCTION.

The reflex switch¹ is an opening switch concept developed by the Physics International Company (PI) for use with magnetic energy storage. Figure 1 illustrates the geometry of a reflex switch. The device is a triode with a positively charged thin foil anode placed between a primary cathode connected to the pulse power generator and an electrically floating secondary cathode. An externally applied magnetic field maintains axial electron flow.

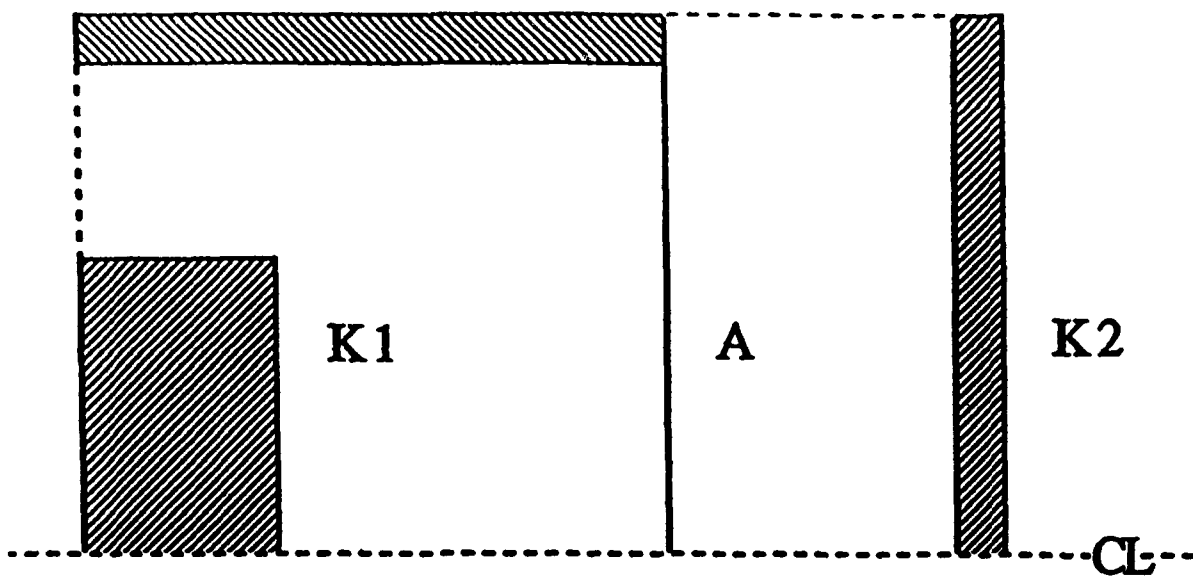


Figure 1. Configuration of the reflex switch. A thin foil anode, A is placed between the primary cathode K1, and a floating secondary cathode K2.

The anode is a thin metallic or plastic foil a fraction of an electron range in thickness. During a high-voltage discharge the foil is covered by a plasma of sufficient density to allow ion emission. The essential feature of the reflex triode is that electrons emitted from both cathodes lose energy traversing the anode foil and are reflected by the opposite cathodes. Electrons continue to "reflex" through the anode until their kinetic energy is small enough for them to be absorbed.

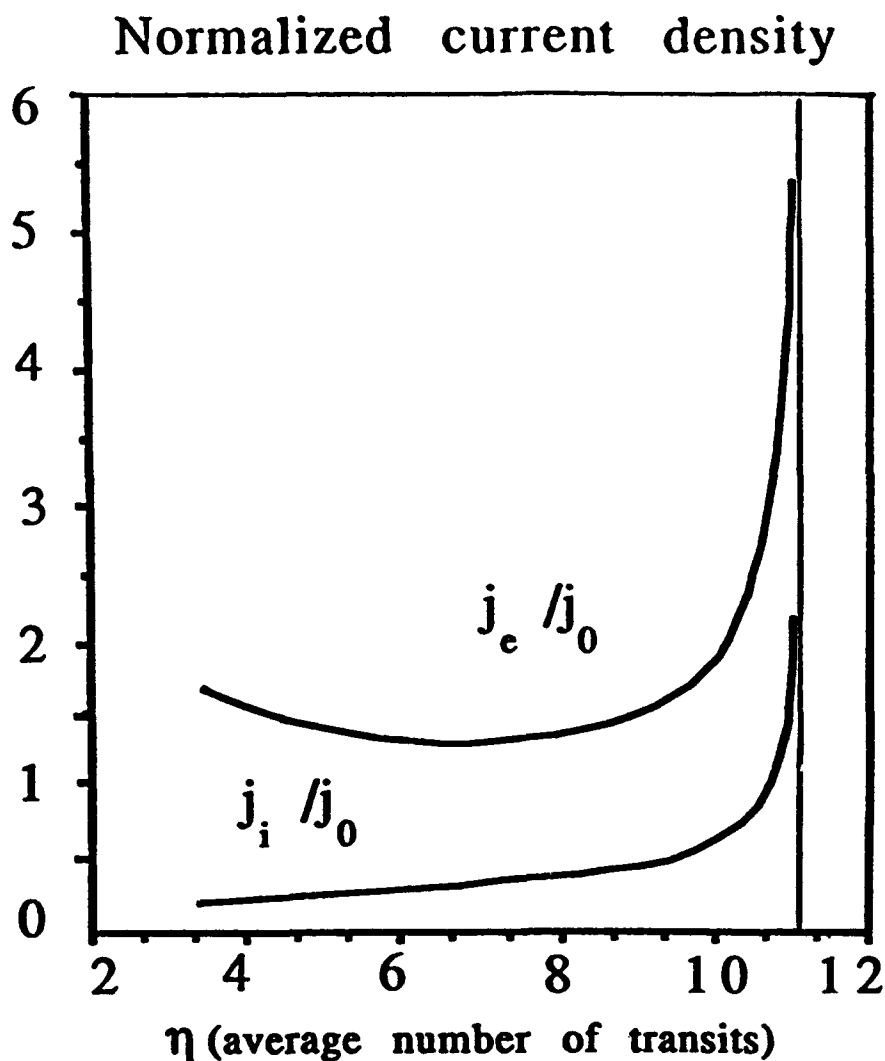


Figure 2. Electron and ion current densities (normalized to the bipolar Child-Langmuir value) versus number of transits η through the reflexing foil anode. Theoretically the current densities become arbitrarily large at a critical value of η (from Ref. 4).

In connection with an experiment involving double diodes, Smith² developed a model showing that multiple reflections of electrons combined with the flow of positive ions from the anode could produce a large increase in current over the usual Child-Langmuir value³ for a given gap voltage. Likewise, the reflex triode would be expected to achieve an impedance much lower than a diode of comparable gap spacing and potential. Prono, et al.⁴ developed a one-dimensional, steady-state theory of reflex triodes demonstrating the existence of such low-impedance equilibrium states. These equilibria depend crucially on the distribution of electrons in the vicinity of the the anode foil and therefore on the average number of transits through the anode, η . Figure 2 shows how the equilibrium current depends on the reflexing parameter η . Theoretically, there is a critical value of η at which the current becomes arbitrarily large, i.e., the dynamic impedance drops to zero, although in a real device the circuit would keep the current finite.

Figure 3 gives examples of the potential profile in one of the gaps at equilibrium and shows how the profile changes with η . Note that as η increases, the potential tends more and more to resemble a sheath. Thus the effective gap becomes narrower consistent with reduced impedance. During this stage, the voltage drop across the anode-cathode gap remains approximately constant. This voltage is determined by the electron energy gain necessary to maintain the reflexing electron population. Generator voltage in excess of the reflexing voltage yields a corresponding increase in switch current flowing through the inductor. The reflex switch operates in a high current, low voltage "closed" mode.

Equilibrium theory has been helpful in understanding the basic characteristics of the reflex triode. However, the steady-state model does not address the dynamics. For example, it is unclear how the triode attains a steady state, and whether the steady state is stable. While experiments indicate that low-impedance states of the reflex triode may be obtained,¹ experimental diagnostics are inadequate to characterize the local electric fields in the switch, let alone the microphysics of the electron and ion distributions. Therefore, dynamical calculations, using particle simulations as a model, can be helpful in understanding the physics of the reflex triode.

Switch opening is thought to begin when a plasma fills the secondary cathode-anode gap. This gap is usually smaller than the primary gap, and therefore it should fill up with plasma first. The plasma effectively shorts the secondary cathode to the anode potential. When this occurs the electrons stop reflexing: they move to the secondary cathode where they are absorbed. The vacuum inductance tries to maintain the current achieved in the reflexing mode, but there are insufficient electrons. As a result, the voltage across the diode must rise sharply.

Once the switch has opened the impedance of the primary gap should correspond to a bipolar Child-Langmuir diode. However, the ion population in the reflexing state is larger than in a bipolar diode. It takes an ion transit time before the excess ions are cleared from the gap. Thus the opening time should scale with the ion transit time.

1.2 SIMULATION OF THE CONDUCTION PHASE.

The first attempts at modeling the reflex switch utilize an existing two-dimensional particle code, ELECTRA.⁵ ELECTRA uses an electrostatic, magnetostatic formulation for the electromagnetic fields in a cylindrical r-z coordinate system. Particles are advanced

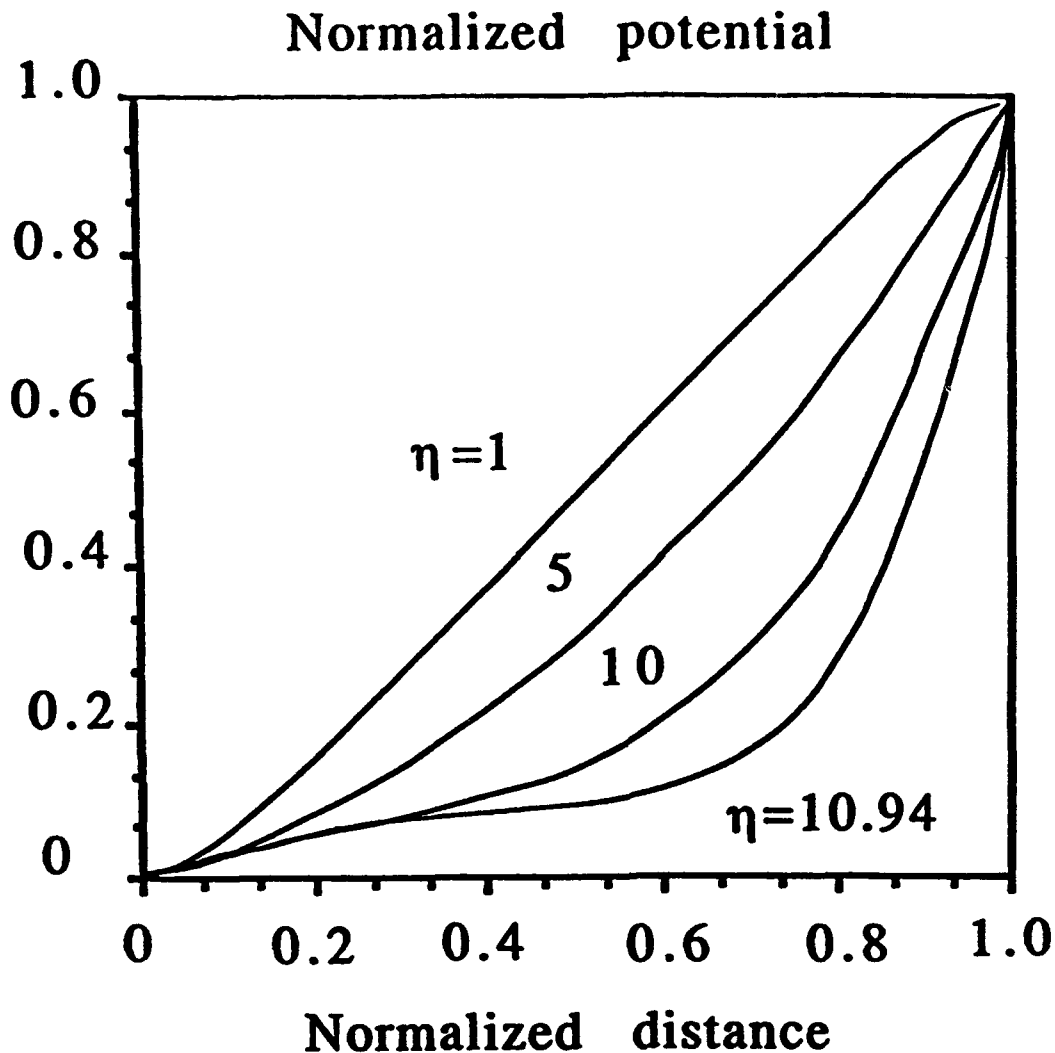


Figure 3. Potential profiles (normalized to the anode potential) as solutions to the steady state reflex triode problem. As η approaches the critical value, the profiles begin to resemble that of a sheath (from Ref. 4).

in time using the relativistic Lorentz force equations. Particle emission based on Gauss's law is allowed from conformal surfaces of internal conductors. Features of ELECTRA relevant to this problem are an ad hoc foil scattering module, external magnetic fields, and a floating conductor. Additional options include a variable spaced mesh and color graphics post-processing.

The simulation parameters are taken from the MOSES I experiment operated by Physics International.⁷ In MOSES I, two Marx banks separately charge the anode and

cathode up to 100 kV for a net 200 kV maximum difference in potential across the electrodes. The anode foil normally used in MOSES I consists of 2 μ m Kimfol whose main component is carbon. Optimal gap spacings are 8 cm for primary gap and 6 cm for secondary gap. The cathode has rollpins or needles on its front face to enhance electron field emission.

During these experiments, the Reflex Switch operated at a conduction phase voltage of 60 kV and current densities hundreds of times higher than bipolar Child-Langmuir. The switch opens to over 500 kV. An electron could be expected to reflex 10-15 times.

Humphries and Xu⁶ investigated the time-dependent behavior of the Reflex Switch using a one-dimensional nonrelativistic particle code. Their study proceeds in two stages. In the first stage, the secondary cathode is placed at the same potential as the primary cathode. The simulation is evolved forward in time until an equilibrium is reached. The secondary cathode is then switched to the anode voltage to observe the opening process. In equilibrium most of the voltage drop occurs near the anode and a smaller drop near the cathode, with an approximately constant voltage in the remainder of the gap. In their computations, the opening time is proportional to the square root of the ion mass, i.e., proportional to the ion transit time.

The simulations here use the same methodology. The voltage difference between the anode and cathode during the conduction phase is given by

$$V(t) = \begin{cases} V_0 \sin(\pi t/2\tau) & 0 < t < \tau, \\ V_0 & t \geq \tau \end{cases} \quad (1-1)$$

After the initial ramp, the voltage is kept constant. This situation would apply if the device were connected to a parallel capacitor.

The simulation comes to an equilibrium with a reflexing electron population when the secondary cathode charges up and reflects subsequent electrons. Ions are then emitted from the anode and after a longer time depending on the ion mass the simulation again comes to an equilibrium. The simulation is stopped at this point in order to set the secondary cathode to the anode potential by external intervention. This procedure is designed to mimic the shorting of the secondary anode-cathode gap by processes taking place in the high-density plasma that are outside the simulation. The simulation is then restarted to observe the opening dynamics.

The configuration of the simulations is similar to Figure 1. Typical values for simulation parameters are: a primary cathode radius of 3 cm, a anode inner radius of 5 cm, a primary gap spacing of 8 cm, and a secondary gap spacing of 6 cm. The voltage risetime is 5 ns with a maximum voltage between the primary electrodes of 60 kV to 200 kV. The foil thickness is varied to allow from 0 to a maximum of 15 reflexes. Either carbon ions, hydrogen ions, or artificial ions with sub-protonic mass are emitted from the foil assuming space-charge limited emission. The external magnetic field strength is 5 kG.

Qualitatively the simulations reproduce what is expected from the stationary theory. For example, Figure 4 shows the voltage for a run with maximum applied voltage of 60 kV and foil thickness of 2 μ m. Hydrogen ions are emitted from the anode. The potential contours are concentrated near the anode as expected. There is very little current carried in the region above the cathode shank. The magnetic field keeps the electron flow well-confined.

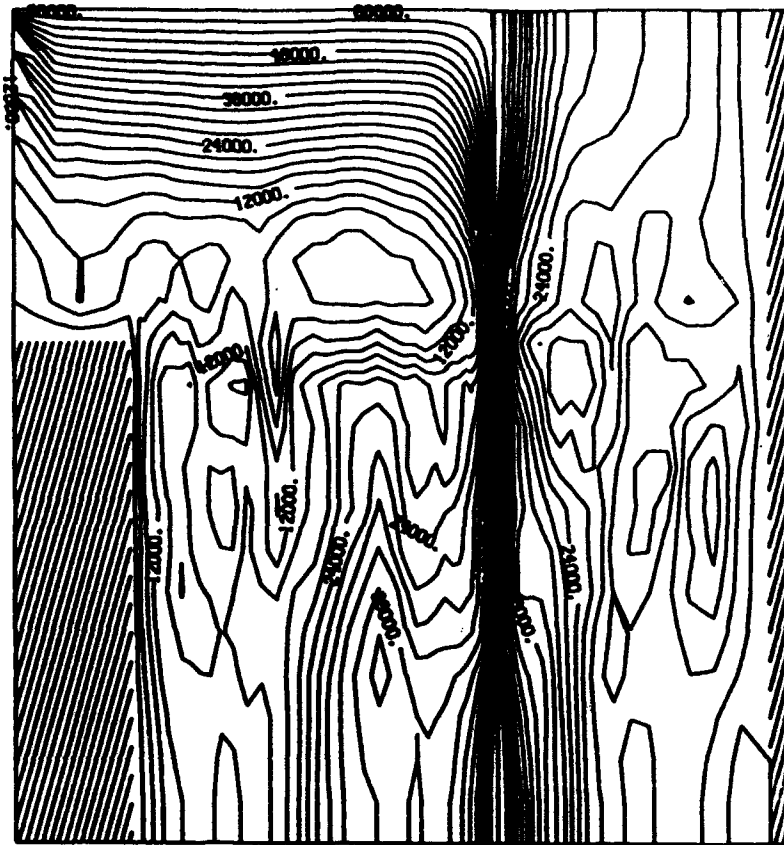


Figure 4. Contour plot of the electric potential in reflexing equilibrium. The labels on the contours are in volts with the values ranging from 0-60 kV. The contours of constant potential are tightly clustered near the anode foil particularly at the cathode radius.

The current found by the simulation in the reflexing state is 2.4 kA. However, this value is an order of magnitude higher than a bipolar Child-Langmuir diode, but twenty times below the currents achieved in the experiment. Moreover, the two-dimensional variations seen in the code make a purely one-dimensional model seem suspect.

Several cases were run varying the scattering model, voltage, and foil thickness. In all cases, the simulation current is more than an order of magnitude below the experimental results. There is a discrepancy between what the theory predicts and the experiments measure and what the simulations are able to achieve. One possibility is that discrete effects in the simulation overwhelm the relevant physics. This is tested by increasing the resolution of the simulation. The number of particles was varied by a factor of three and the grid resolution was also varied by a factor of 2.5 without substantial change in the current or equilibrium profiles. The simulations with ELECTRA are voltage driven. With the voltage drop held fixed, the simulator is unable to adjust itself to find the low-impedance

state. This suggests that the switch must be modeled as part of a circuit.

REFLEX is a one-dimensional electrostatic particle-in-cell (PIC) simulation of a planar triode coupled to a circuit model developed expressly for studying the reflex switch. REFLEX is discussed more thoroughly in Section 9 of this report. The self-consistent coupling of electron and plasma dynamics to a circuit model is an unusual feature of the simulations described in this study. It is nonetheless an essential requirement for following the dynamics of the reflex triode as it seeks an impedance consistent with its interaction within the circuit as a whole. REFLEX extends the PIC-circuit simulations pioneered by Lawson^{8,9} to the complex situation demanded by the reflex switch application. An additional feature is the electron-foil interaction via a Monte Carlo module described in Appendix C which scatters electrons in angle and degrades their energies as they pass through the foil.

The one-dimensional simulation demonstrates how a reflex triode can attain a low-impedance state. The parameters in the simulation match the circuit parameters of the first EYESS experiments at Physics International.¹⁰ Each power supply is charged to 800 kV, discharging into transmission lines with length 1.25 m, inductance 130 nH and a capacitance 130 pF, connected to a circuit with $L=500$ nH, $R=0.2$ Ω and $C=1$ μ F. The impedance of the transmission line is approximately 30 Ω . The area of the plates is 570 cm²: this choice is needed to match the impedance of the diode to the transmission line during the initial high-impedance bipolar Child-Langmuir phase. Both diode gaps are 4, 6, or 8 cm and the anode is assumed to be 2 μ m mylar foil. Each gap is resolved by 80, 120, or 160 cells, hence the simulation grid size $\Delta x = 0.05$ cm, and the timestep is $\Delta t = 1.5$ ps. This ensures that electrons with energies up to 800 keV will move less than a single cell per timestep. Electrons are field-emitted from the primary and secondary cathodes. Ions with an artificial mass ratio of $m_i/m_e = 100$ or with the hydrogen value of $m_i/m_e = 1836$ are emitted from both sides of the foil anode.

Figure 5(a) is the voltage as a function of time, Figure 5(b) is the the current, and Figure 6 is the time-averaged voltage. Initially, the voltage rises rapidly to a value close to the capacitor bank voltage, exhibiting oscillations that are too fast to be seen in an experiment. The voltage then declines as the conduction phase is reached. During this time the current rises steadily as the impedance decreases. After hitting a minimum at 170 ns, the voltage slowly increases again as the current continues to rise.

Figure 7 clearly shows on an expanded scale that the oscillations in the voltage are regular, and on the scale of the electron transit time as expected from a fundamental mode of the triode. Close examination of particle data shows that the mode comes from the collective motion of electrons "sloshing" back and forth across the foil anode, alternately pushing the voltage in the gaps up and down.

Movies of the electron phase space provide fascinating insight in the dynamical behavior of the reflex switch, but this section can only show a few typical snapshots. In the earliest time before the start of the oscillations at 7 ns electrons from both cathodes accelerate toward the foil. They penetrate the foil, and disperse in phase space through directional scattering and energy loss (not shown). The beams remain symmetric until some streaming instability mixes the beams together. The instability creates the space-charge bunch seen in Figure 8(a). The bunch rotates: moving up and down in phase space

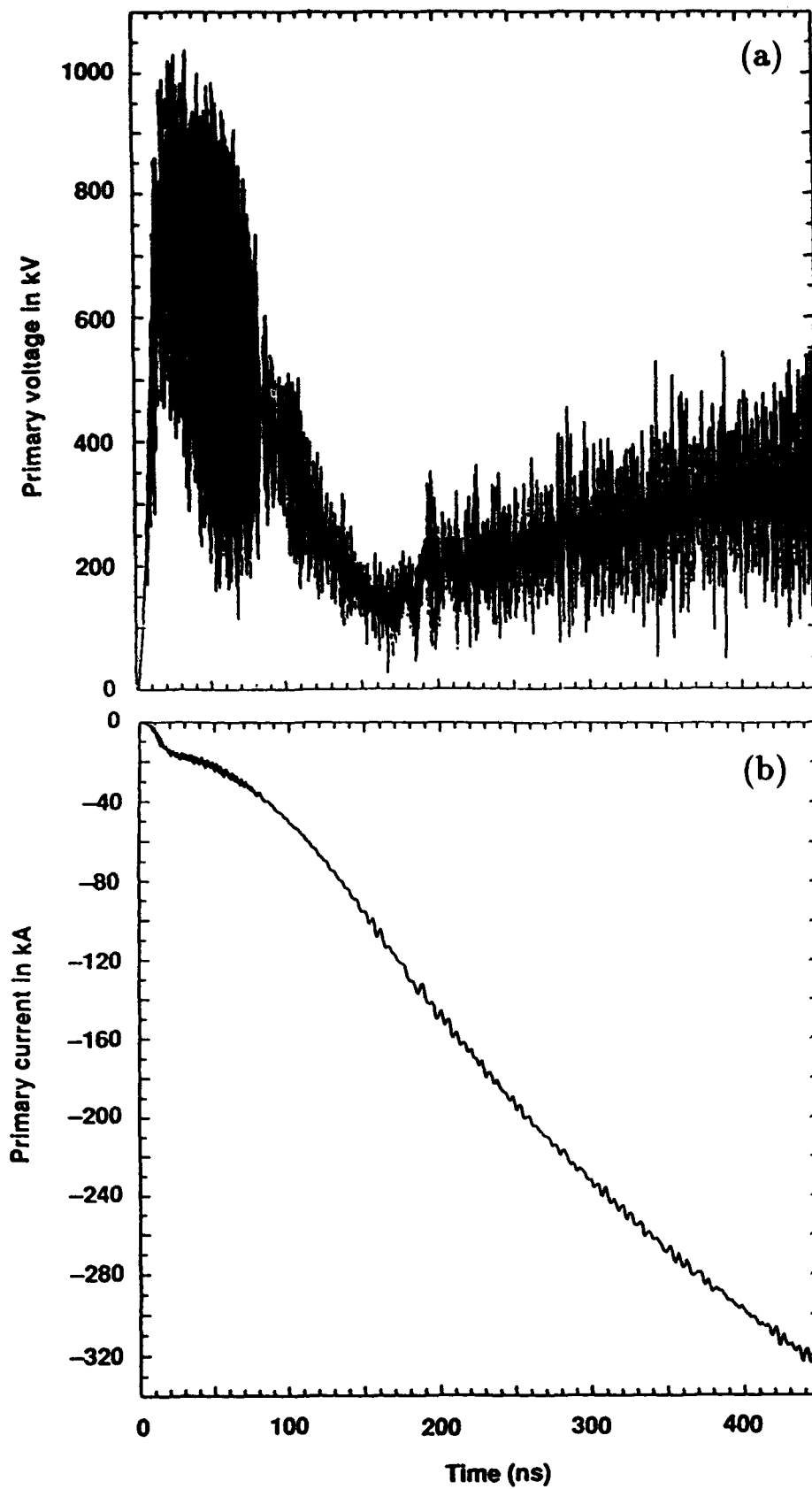


Figure 5. (a) Voltage and (b) current versus time for the simulation of a symmetric triode with 4 cm gaps and with protons as the ionic species.

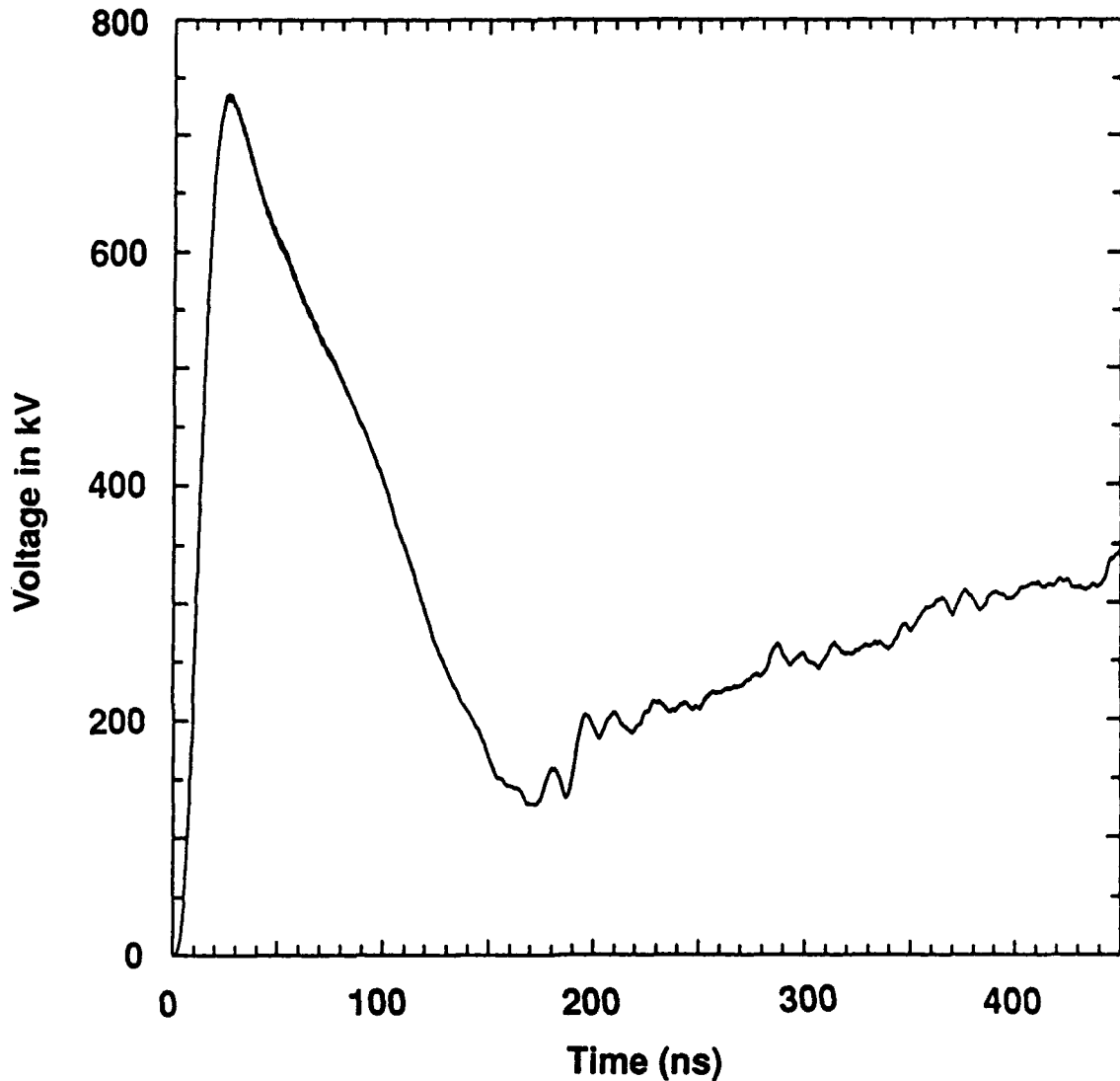


Figure 6. Time-averaged voltage versus time for the simulation of a symmetric triode with 4 cm gaps and with protons as the ionic species.

is directly related to energy oscillations of the electron. Therefore, the rotation of the bunch is correlated with the rapid voltage oscillation in Figures 7 and 5(a). Eventually the system relaxes to the state shown in Figure 8(b) in which electrons are accelerated across a small cathode sheath, drift across the neutral region, and are accelerated in the small effective gaps near the anode.

By 50 ns (not shown) the sloshing mode still continues but causes the entire phase space to oscillate up and down in what appears to be a standing wave pattern. The phase

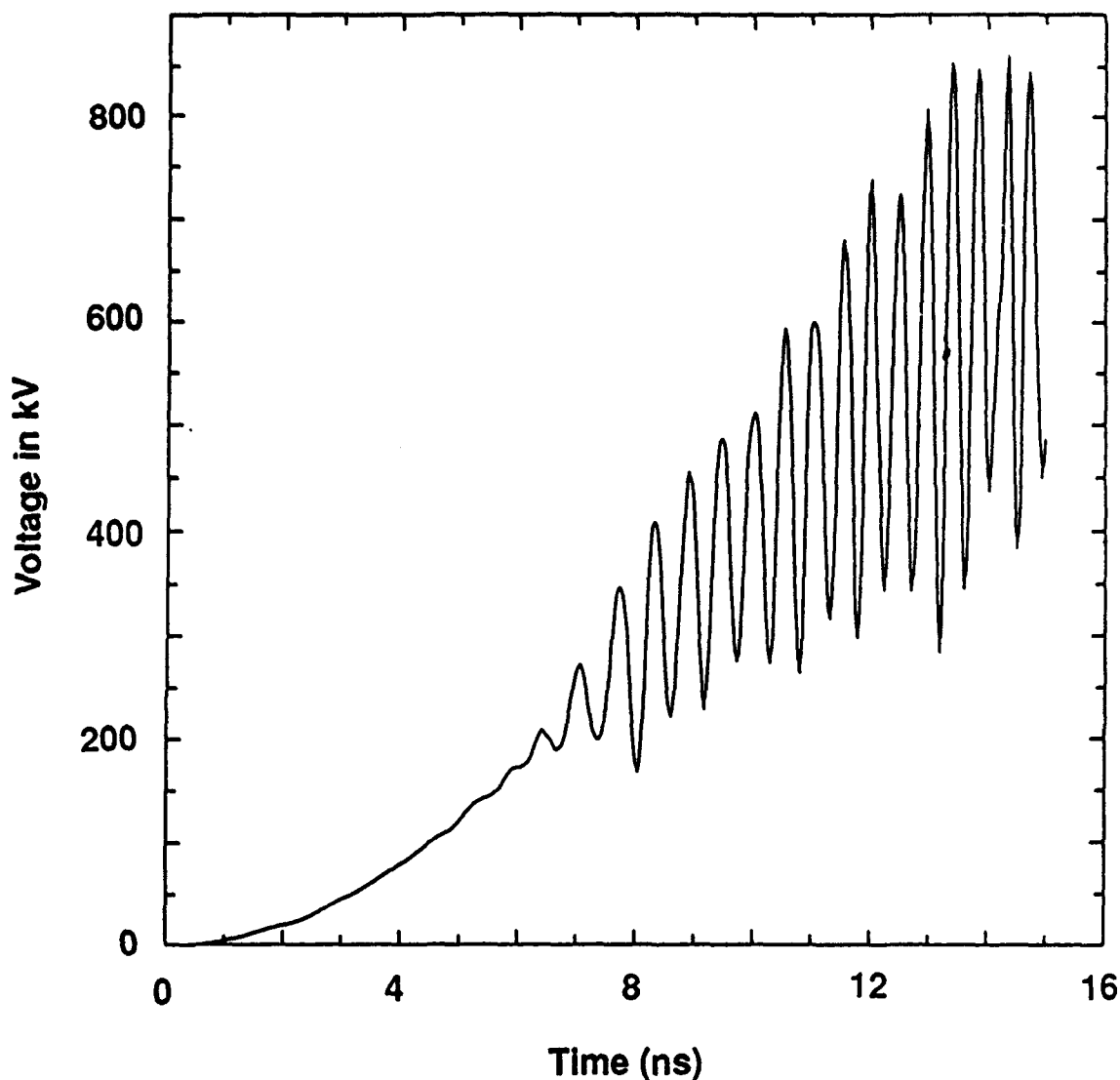


Figure 7. Expanded view of the fast oscillations of Figure 5(a) during the first 15 ns. The oscillation period closely matches the transit time of electrons across the gap.

space in both halves of the triode move together indicating that the oscillation in one gap is 180° out of phase with the other gap. As the voltage decreases and concentrates near the anode, the phase space oscillations begin propagating from the anode to the cathode. The wavelength decreases as the voltage decreases until ~ 150 ns. Figure 8(b) shows the little sprays of electrons that are accelerated by these waves. The oscillations are born in the anode sheath and move towards the cathode opposite in direction to the motion of unscattered electrons. These waves quickly saturate in amplitude in propagating

from the anode to the cathodes. The waves in the first gap and secondary gap start out uncorrelated, but are later on coupled by electron space charge oscillations through the foil.

The transition between high and low-impedance states is evident from the electric field profiles of Figure 9. Figure 9(a) shows a field profile typical of an ordinary diode. However, during the low-impedance state, seen in Figure 9(b), the profile has changed dramatically. Now there is a region essentially free of electric field over most of the diode gap, and a thin sheath with strong electric fields near the anode across which the electron flow is space-charge limited. The narrowing of the space charge region is consistent with the lowered impedance. It should be noted that the accelerating regions near the electrodes do not exhibit bipolar Child-Langmuir flow. Near the anode, the electrons have a much larger space charge than in bipolar Child-Langmuir flow due to their multiple reflections, and this increases the ion current.

The ion phase space in Figure 10(a) shows that early in the simulation the ions are accelerated over most of the diode gap. As the low impedance equilibrium is established, the ions in Figure 10(b) are accelerated by the narrow anode sheath and drift across the remainder of the gaps. Neutral plasma formed by the electron and ion beams now fills most of the gaps. In this region we can see plasma waves with features similar to the well-known two-stream instability.¹² Determination of the relative electron-ion drift in the neutral regions and of the plasma wavelengths seen in the figure are consistent with the dispersion relation for these unstable waves.

The principal characteristics of the various runs done for different parameters are summarized in Table 1. R_m is the ion to electron mass ratio. The time t_{min} is time at which the voltage experiences a minimum when approaching the low impedance state and V_{min} is its value. I_{min} is the value of the current at this time. The last entry in the table is the time at which the voltage decreases to 240 kV after hitting its initial peak. The data indicate that the time to approach the low impedance state is independent of the ion mass in the ranges investigated. The time for the minimum in the 6 cm case is about 1.5 times longer than the 4 cm cases, linear with the gap spacing. For an 8 cm gap, the voltage had not achieved a clearly identifiable minimum during this simulation run. For the artificially light ions and protons, the time to attain 240 kV appears to be ≈ 30 ns/cm times the gap spacing. Thus the time to reach the low impedance state appears to be roughly linear with the gap spacing.

Table 1. Parameters and results from four REFLEX runs.

Gap(cm)	R_m	t_{min} (ns)	V_{min} (kV)	I (kA)@ t_{min}	t (ns)@240 kV
4.	1836.	170.	150.	120.	130.
4.	100.	170.	150.	160.	110.
6.	100.	230.	170.	170.	180.
8.	100.	?	?	?	240.

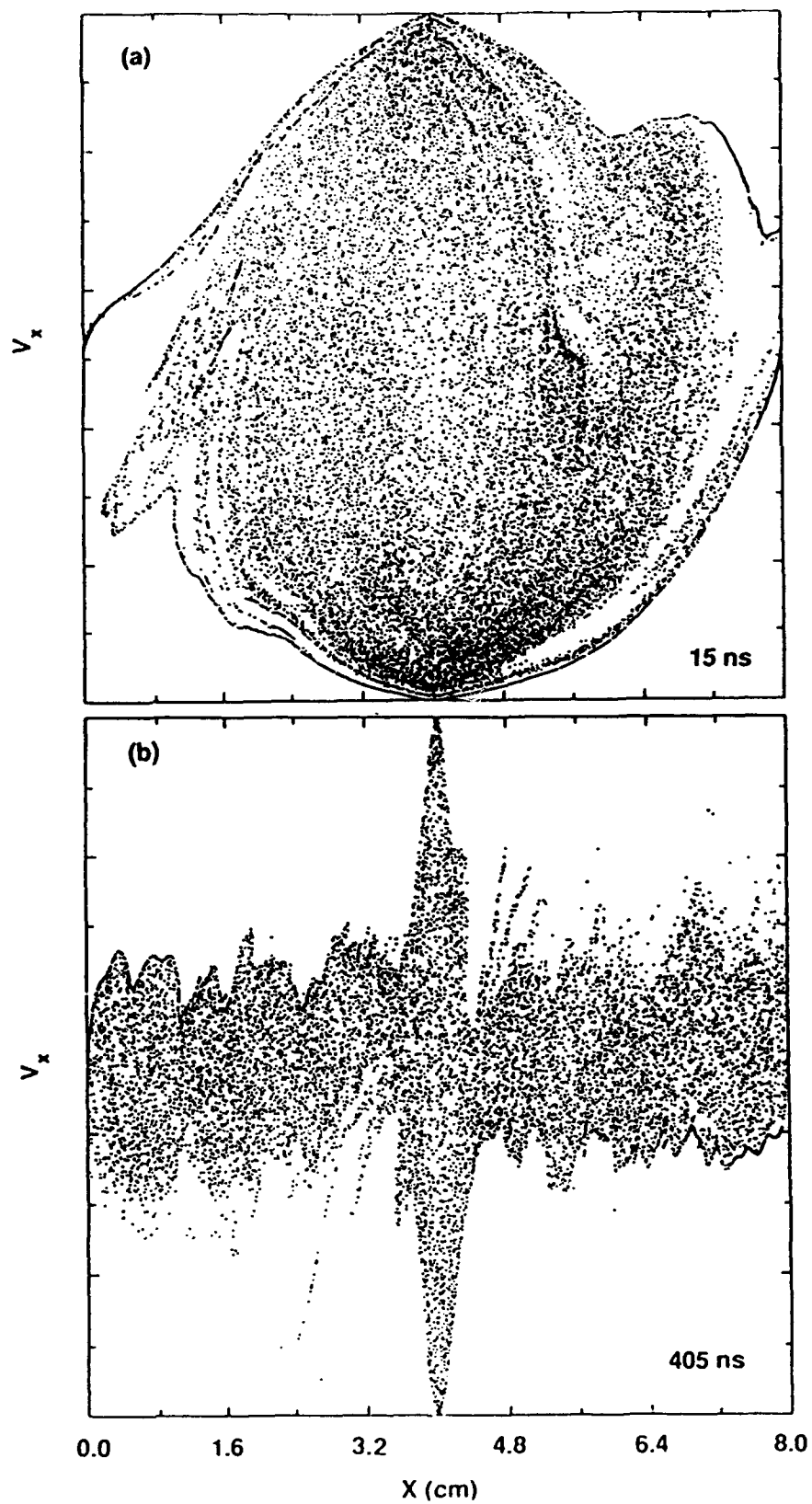


Figure 8. Electron phase space (v_x versus x) (a) at 15 ns during the oscillatory phase, and (b) at 405 ns during the low-impedance phase. The velocity axis is expressed in dimensionless code units.

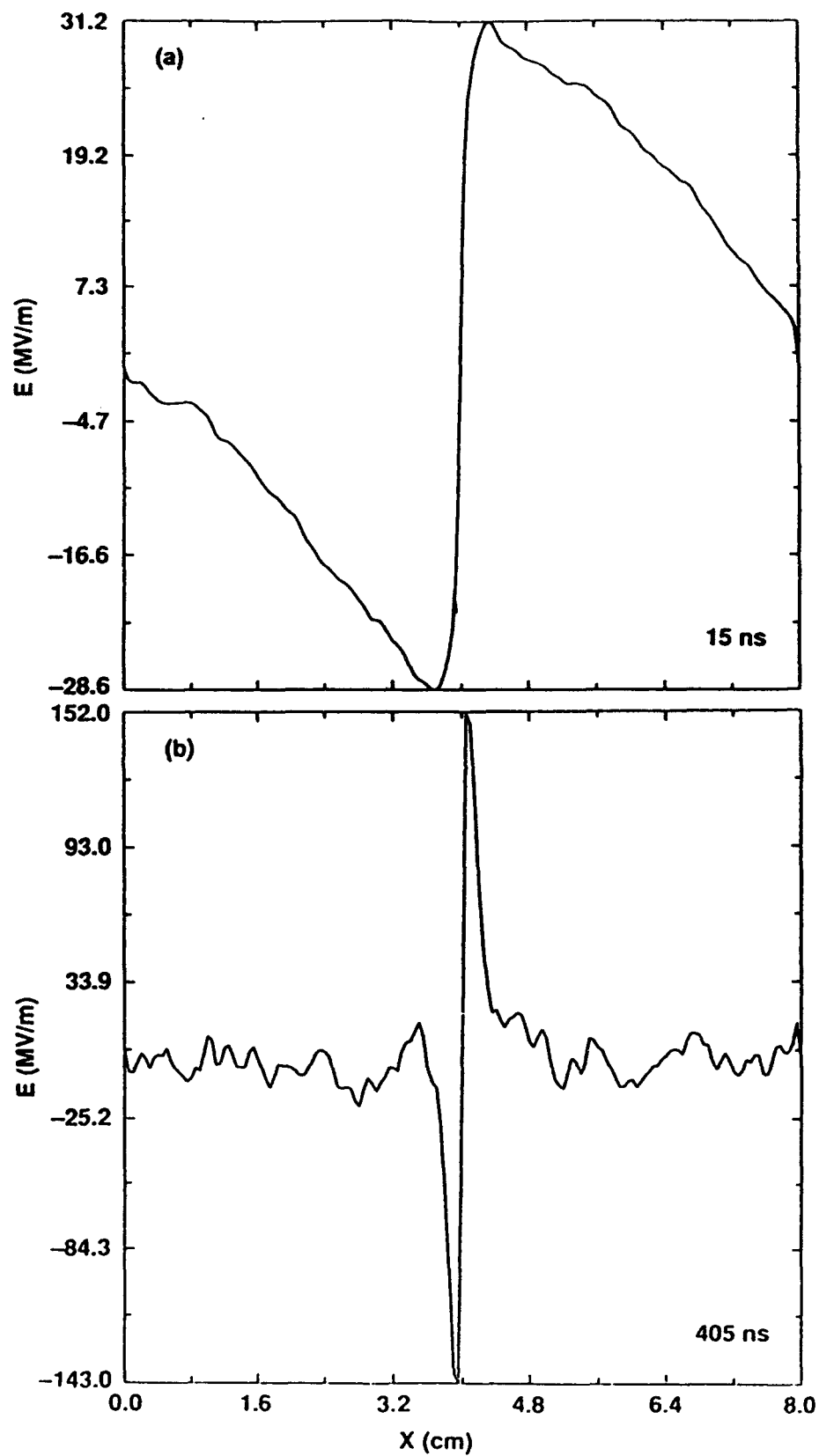


Figure 9. Electric field profiles across the simulated reflex triode (a) at 15 ns, (b) in the low-impedance state at 405 ns. Note the effective shortening of the gaps.

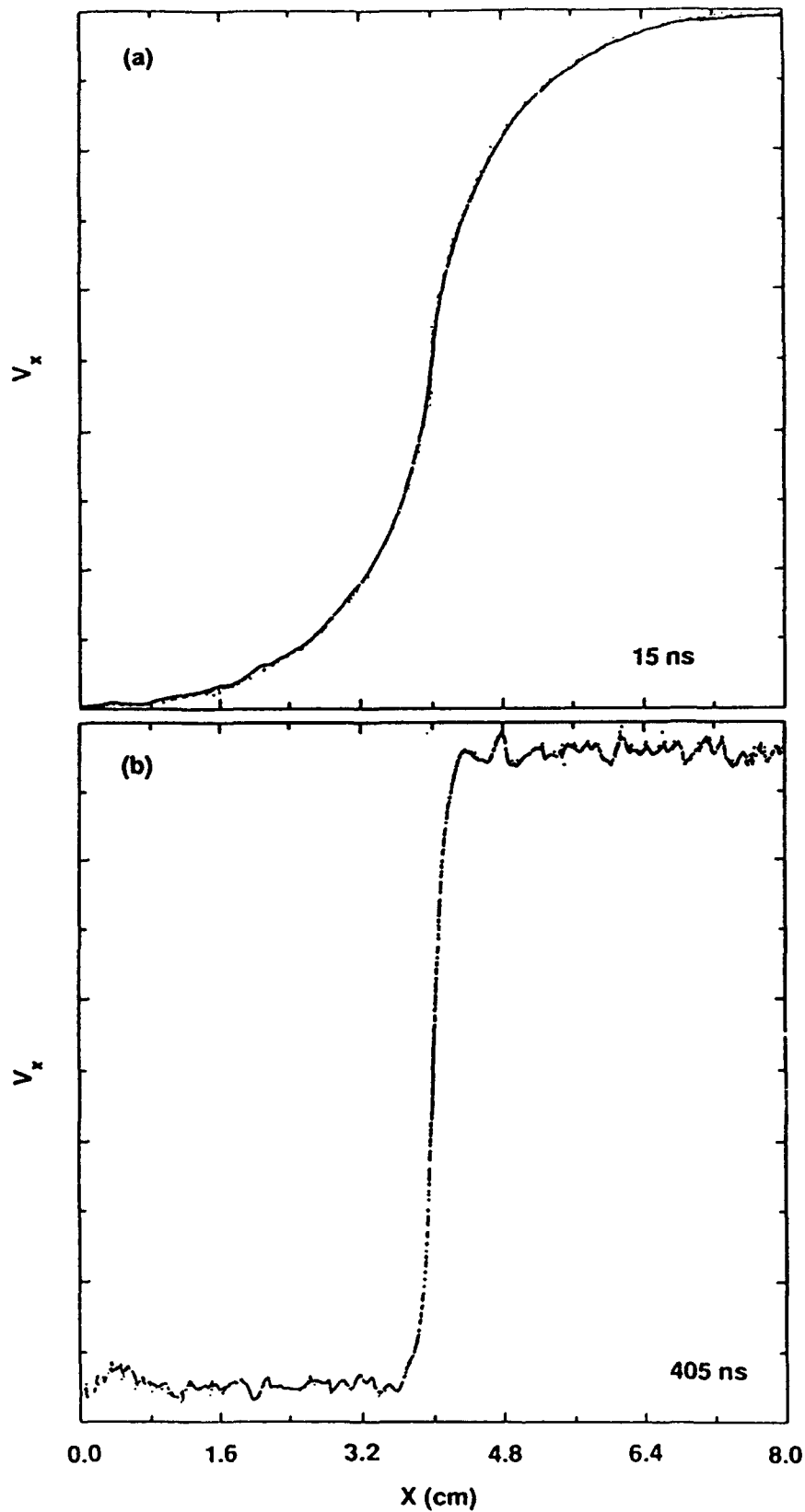


Figure 10. Ion phase space (v_x versus x) at the same times as Figures 8 and 9. The velocity axis is expressed in dimensionless code units.

1.3. REFLEX SWITCH OPENING

In the computations the reflexing state described above would persist, but the experiments contain additional phenomena that trigger switch opening. The opening of the reflex switch is believed to occur when the secondary gap is completely filled with plasma. The secondary gap is shorted by the plasma and upsets the reflexing equilibrium which causes the impedance to rise in the primary gap. The plasma is believed to be created by either expansion of electrode plasmas or by ionization of fast charge-exchange neutrals.^{1,11} Whatever processes create plasma in the secondary gap will also be at work in the primary gap, but the secondary gap is smaller and shorts first. In the simulation the plasma is added to the secondary gap in an ad hoc fashion which is not intended to accurately model plasma closure in the experiments: its sole purpose is to elucidate the opening dynamics of the reflex switch.

In order to save computation time, a run with a floating conductor is not started from scratch. Instead the run is restarted at time 450 ns with a new circuit for the secondary gap. The charge across the secondary circuit capacitor is set to zero and the secondary circuit resistance is increased to $1.0 \times 10^{12} \Omega$, effectively isolating the secondary cathode from ground. This run proceeds for 30 ns. Figures 11(a) and 11(b) show the time averaged current and voltage for the primary gap, and Figure 11(c) shows the time-averaged voltage in the secondary gap. The voltage across each gap increases to ~ 460 kV. The current in the primary gap remains approximately the same: the current through the $1 \text{ T}\Omega$ resistor in the secondary gap drops to virtually zero. An equilibrium is established very similar to the old one as can be seen from the electron and ion phase space plots in Figure 12.

For the next 10 ns after this time, 480 ns, a plasma consisting of protons and electrons with a spatially uniform density increasing at $10^{13} \text{ cm}^{-3}/\text{ns}$, is artificially added into the secondary gap. By 10 ns the plasma in the secondary gap has a density of 10^{14} cm^{-3} . The purpose of this plasma is to electrically short the secondary gap.

Figure 13 gives the current and voltage of the primary gap, and the voltage of the secondary gap, for the next 60 ns. The current in the primary gap during this time drops from 360 kA to 180 kA, while the energy from the vacuum inductance is being transferred to the diodes. During the first nanosecond the voltage in the primary gap decreases to near zero. During the next 12 ns the primary voltage increases sharply to 3 MV after which time it drops more slowly to 2 MV by the end of the run. The voltage in the secondary gap, which also drops to zero during the first nanosecond, starts to rise again, and drops back towards zero where it remains noisily shorted for the remainder of the run.

During the first nanosecond, the reflexing equilibrium is upset by the plasma in the secondary gap. The electron density in the vicinity of the anode foil drops dramatically. The anode sheath collapses to a small size, with a corresponding decrease in the voltage because this is no longer needed to maintain the current across the smaller anode sheath. The decrease in electron space charge near the anode decreases the ion emission from the anode. The evolution of the opening event are highlighted in four electron phase space plots of Figure 14 at 3, 6, 9, and 12 ns after the beginning of plasma creation, and in four ion phase space plots for these same times in Figure 15.

The phase space plots in Figures 14(a) and 14(b) at 3 ns show the anode sheath expanding towards the primary cathode, with neutral plasma filling the bulk of the primary

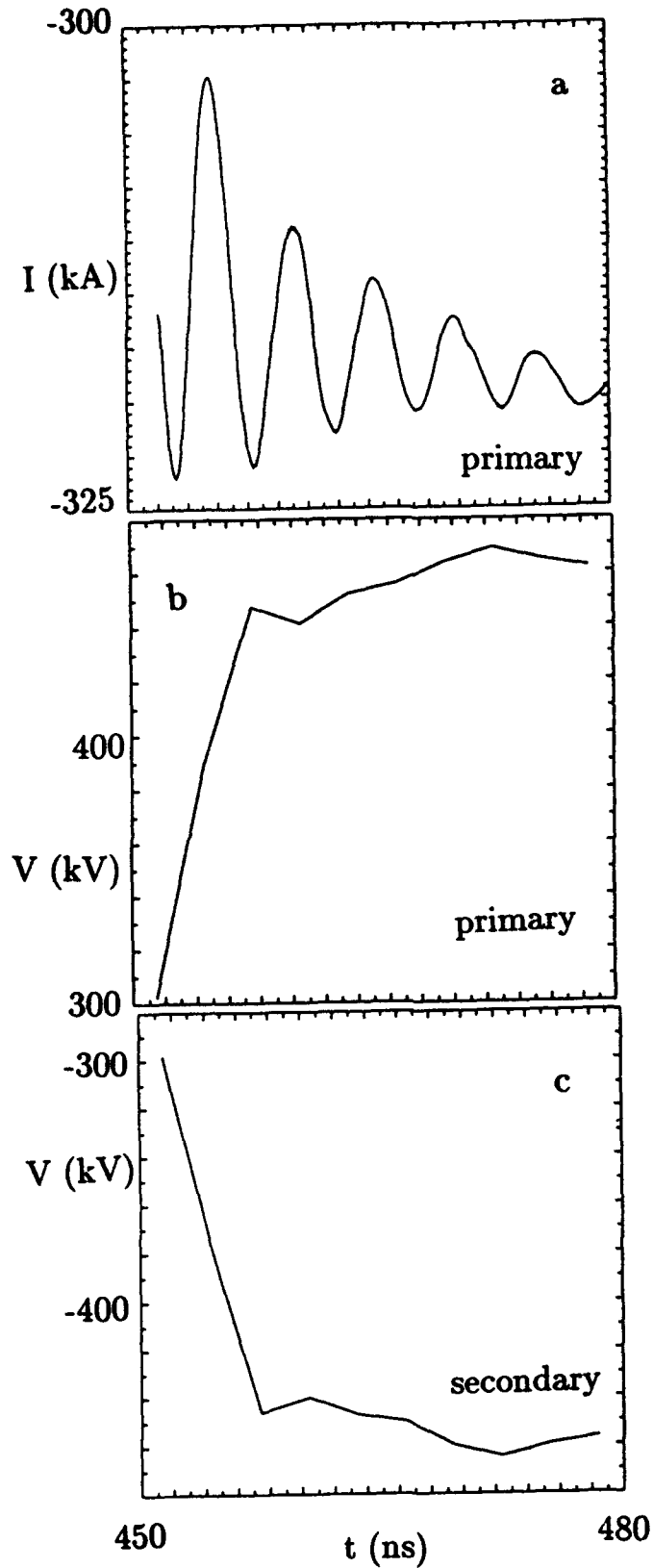


Figure 11. Averaged current and voltage during the transition from a symmetric triode equilibrium to a floating secondary cathode: (a) current in primary gap, (b) voltage in primary gap, and (c) voltage in the secondary gap.

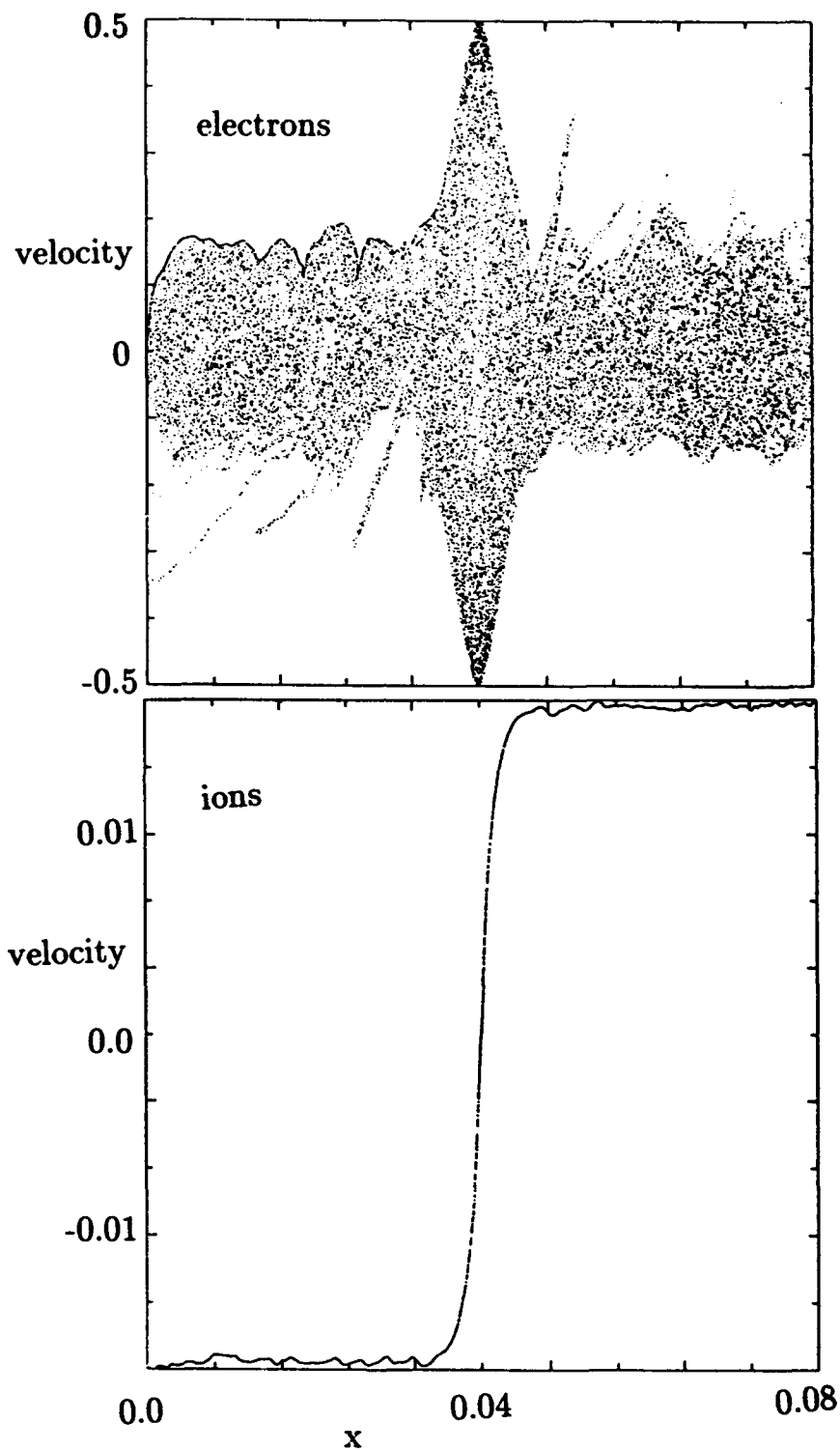


Figure 12. Electron and ion phase space plots for the equilibrium established by the floating secondary cathode at 480 ns. The velocity axis is expressed in dimensionless code units. The equilibrium is very similar to the symmetric triode equilibrium.

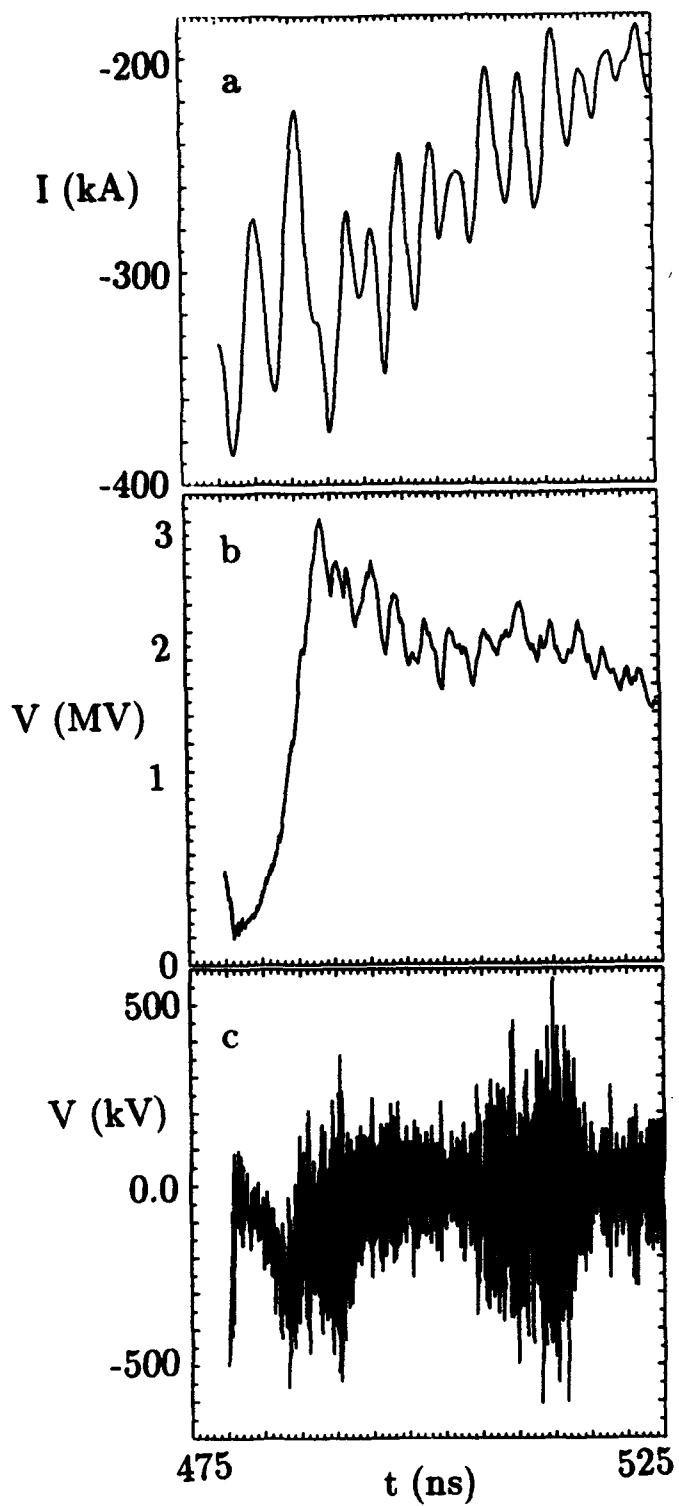


Figure 13. (a) Current in the primary gap, (b) voltage in the primary gap, and (c) voltage in the secondary gap after the introduction of plasma into the secondary gap.

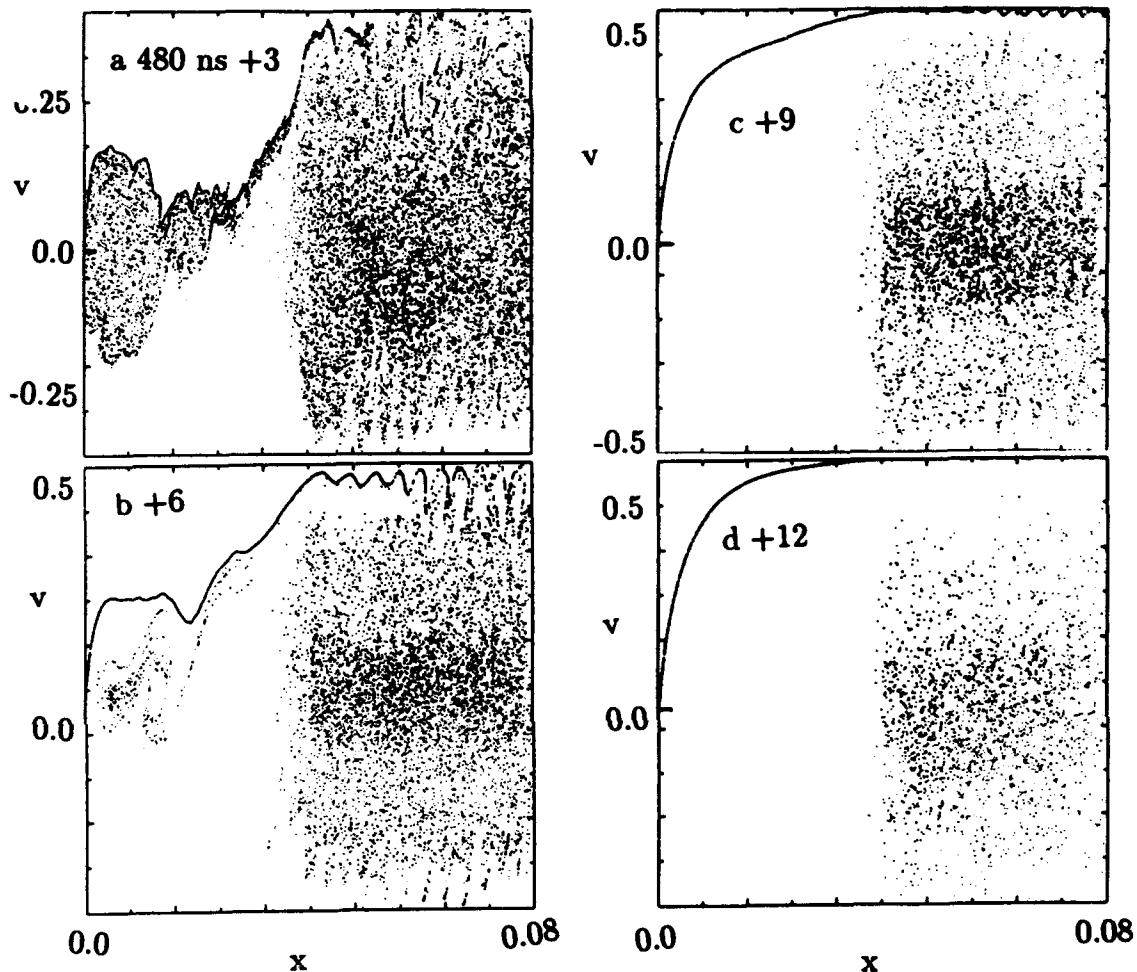


Figure 14. Electron phase space plots at (a) 3 ns, (b) 6 ns, (c) 9 ns, and (d) 12 ns after the introduction of plasma into the secondary gap. The velocity axis is expressed in dimensionless code units. The electrons are accelerated by an expanding anode sheath: oscillations are suppressed.

gap. A larger voltage is seen across the anode sheath while the voltage across the cathode sheath remains about the same. At 6 ns, the ions in the gap are moving at about half of the speed that ions were at the beginning of the opening. Ions accelerated across the anode sheath pile up against flowing plasma, creating the dips at $x=2.5$ cm seen in both the electron and ion phase spaces in Figures 14(b) and 15(b). A larger cathode sheath is forming as the cathode sheath starts expanding at a rate which is still slower than the anode sheath expansion. The ions in the gaps prior to the initiation of the opening event continue to mainly free stream towards the cathodes. The ion emission from the anode is unable to replenish the density of ions that are leaving. In the primary gap, the anode

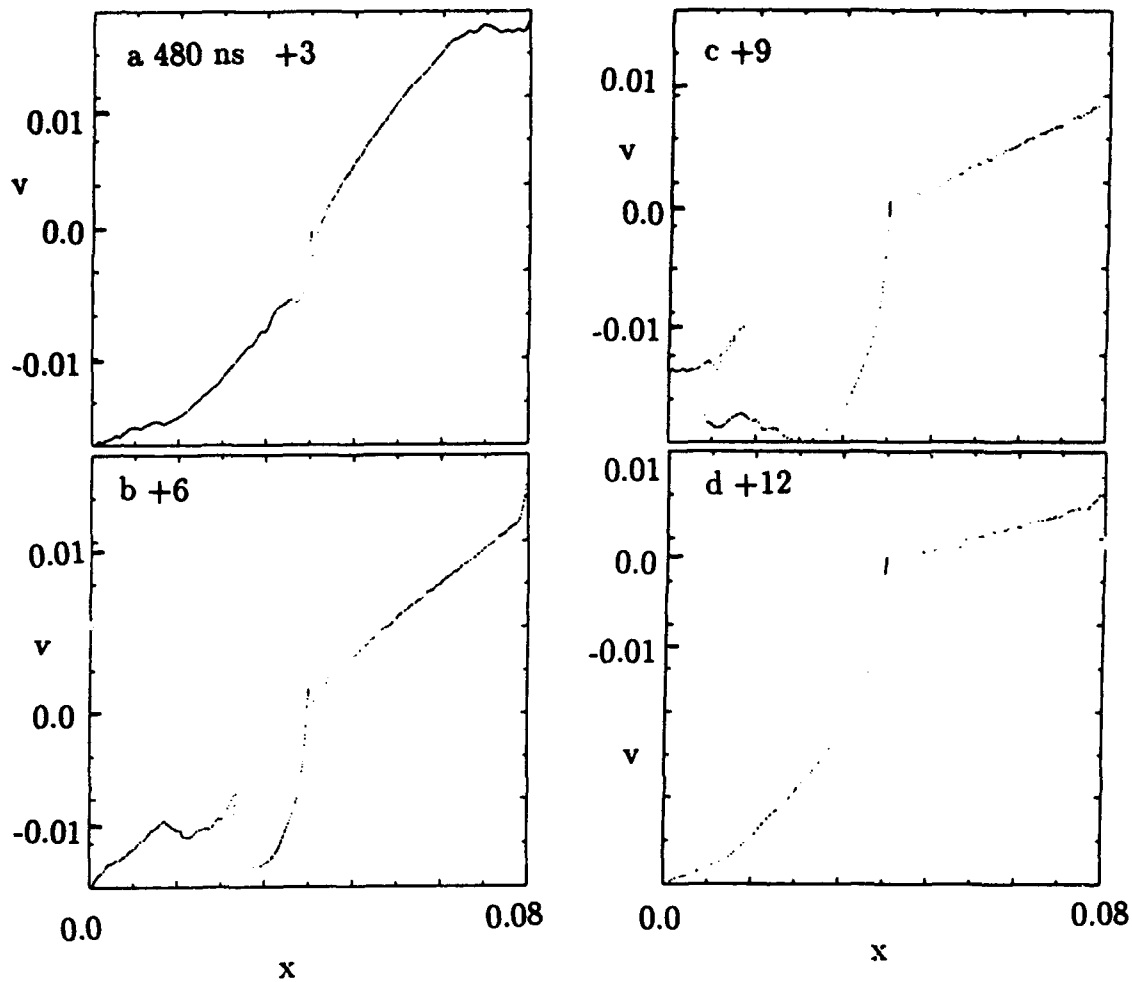


Figure 15. Ion phase space plots at (a) 3 ns, (b) 6 ns, (c) 9 ns, and (d) 12 ns after the introduction of plasma into the secondary gap. The velocity axis is expressed in dimensionless code units. The opening time depends upon sweeping the ions from the gap.

sheath expands towards the cathode following the stream of original ions. The inductance in the circuit tries to maintain the same current. An increased voltage drop is required to maintain the electron current across the widening anode sheath. By 9 ns, most of the original plasma is gone from the gaps. The cathode sheath is accelerating the removal of the ions in the gap. No neutral plasma is left in the primary gap by 12 ns as can be seen from Figures 14d and 15d. The ion and electron phase plots at this time show a bipolar Child-Langmuir flow in the primary gap. The primary gap acts like an ordinary vacuum diode thereafter.

1.4 DISCUSSION.

The early attempts at simulating the reflex switch utilized the existing PIC code ELECTRA. Some of the features of the simulation appeared qualitatively correct. However, it clearly did not achieve the low-impedance state predicted by the theory. This led to the development of the REFLEX code, described in Section 10. REFLEX self-consistently includes the effects of an inductive circuit attached to the simulations necessary for finding the low-impedance phase. REFLEX is able to establish a low-impedance phase, explore its dynamics, and simulate an opening event.

The first feature revealed by the REFLEX simulations is the fast electron transit-time oscillations that pervade all runs. These oscillations only occur when the primary and secondary diodes are coupled by a transparent foil. When the foil is made opaque, the voltage does not oscillate. The simulation diagnostics, including movies of the electron phase-space having good time resolution, show that these oscillations occur after natural perturbations growing out of the interpenetrating electron beams begin to push substantial electron space charge back and forth across the foil. These electrons transit the gaps, impact the cathodes, and increase the voltage. The increased voltage sends electron clouds back across the foil producing steady oscillations.

The interesting plasma/circuit modes discussed above are linked with electron turbulence in the simulations. The turbulence mixes the electron beams and quickly destroys the early symmetric spiral patterns of electrons in phase space. Steady-state models have assumed that the electron distribution in the vicinity of the foil results solely from electron beams repeatedly scattered by the thin foil. Collective interactions among beams are usually neglected. However, according to the simulations the stationary assumption is an oversimplification of the electron distribution. Instead the dynamical behavior has implications for the validity of such models if they are sensitive to the details of the electron energy spectrum near the foil.

Simulations with various ion masses indicate that the time to establish equilibrium does not depend on the ion mass (between the artificial mass ratio 100 and 1836 for hydrogen). Runs with higher mass particles would be needed to extend this result, but these runs are quite expensive computationally. The ion mass could come in when the ion transit time across the gap is larger than the time to establish equilibrium by the relaxation. This time increases linearly with the electrode gap spacing in the computations.

The simulations clearly show the sequence of events during opening. In a previous run stopped at an equilibrium configuration the secondary gap is shorted by artificial loading with plasma. Subsequently, the reflexing electron equilibrium is destroyed very quickly. This leads to the collapse of the anode sheath and drop in the voltage. The ions continue their streaming motion from the anode to the cathode. The subsequent ion emission is insufficient to replace the ions streaming away. The anode sheath expands with the ion motion with the resulting increase in voltage. Most of the opening event involves ions free streaming with some erosion from an expanding cathode sheath later on. The gap is completely open when all vestiges of plasma are gone and the primary gap behaves like a vacuum diode.

The computations suggest that the opening time is controlled by the rate at which ions are removed from the primary gap. Thus it becomes desirable to minimize the amount of

ions in the primary gap just prior to opening. The opening of the reflex switch is believed to be caused by shorting of the secondary gap by plasma which is caused by either electrode plasma expansion or by the ionization of fast charge-exchange neutrals. Whatever process creates plasma in the secondary gap will be at work in the primary gap as well. This issue is not addressed in these simulations. Switch opening should occur mainly by anode sheath expansion, at least when the ion density is largely uniform throughout the primary gap.

The simulations described above are performed in order to probe the dynamical behavior of a reflex switch. Simulations are primarily an intuition building exercise whose aim is to facilitate the development of more complete theories and the design of critical experiments. Compromises with reality are inevitable, e.g., the simulations are purely one-dimensional and electrostatic. It is not known how electromagnetic effects or the additional degrees of freedom available to three-dimensional systems would modify the phenomena. Oscillations tend to be coherent in one-dimensional systems, while in real three-dimensional systems the phase of oscillations at locations transverse to the axial direction could become mixed. It is quite possible that the effects of the instabilities encountered in these simulations are mitigated by the inclusion of electromagnetics as well as by higher dimensionality.

SECTION 2

ACCUMULATION OF NEUTRALS IN PLASMA OPENING SWITCHES FROM PLASMA BOMBARDMENT OF ELECTRODES

Plasma injected into a Plasma Opening Switch hits the electrodes, where it drives off surface contaminants into the vacuum, mostly as neutrals. The spatial and energy distribution of the neutrals is estimated using the Monte Carlo computer code TRIM.SP.¹³ These neutrals can increase the density of the injected plasma twofold (or more), which can significantly affect the behavior of the opening switch. The purpose of this work is to quantify the unintended plasma from electrode blowoff, in order to stimulate measurements and any remedial action that may be fruitful.

2.1 OPENING SWITCHES AND ELECTRODE PLASMAS.

Pulse compression and voltage multiplication in pulsed-power systems can, in principle, be done efficiently by storing electrical energy in a current-carrying inductor followed by an interruption of the current. The crucial component of this inductive energy storage technique is the opening switch. It has proven to be difficult to develop an opening switch with a long conduction time ($\sim 1-10 \mu\text{s}$) that opens rapidly (in $\sim 10-50 \text{ ns}$) at high currents (MA's). Ongoing research aims to increase the conduction time, to increase the conduction current, and to reduce the opening time.

Opening switch concepts such as the Plasma Erosion Opening Switch, the Density Controlled Opening Switch and the Plasma-Filled Diode, conduct the current through a plasma injected between the metal electrodes. Longer conduction times generally require more plasma, which can be provided by leaving the plasma sources on longer. Then the injected plasma interacts longer with the electrodes. Plasma-electrode interaction effects, such as material blowoff, are likely to be greater for long conduction time switches. Obviously, both the conduction and opening phases should be strongly affected by the initial state of the plasma. Here we show that the initial plasma density can be strongly affected by blow-off from the electrodes.

In a Plasma Opening Switch the plasma is usually injected from the anode to the cathode with either a plasma gun or a flashboard. These sources produce a plasma plume that consists mostly of singly and doubly ionized carbon with a density of $10^{13}/\text{cm}^3$ to $10^{15}/\text{cm}^3$, and a drift velocity from 4 to 20 $\text{cm}/\mu\text{s}$. Typically, in a moderate ($10^{-4} - 10^{-5}$ Torr) vacuum an electrode is covered with ~ 100 monolayers of hydrocarbon adsorbates. High-speed ions that hit these weakly bound adsorbates can splatter atoms and molecules out of the monolayers back into the gap. More than 90 % of the particles that leave the surface can be neutrals with energies significantly less than the incident ions. Therefore, the density of blown-off neutrals can be an order of magnitude higher than the density of the incoming plasma. The neutrals can be ionized by collisions with the incoming plasma, substantially modifying the intended plasma density.

Some aspects of plasma-wall interactions have been studied extensively in the nuclear fusion community, especially the effect on single elemental materials in a clean environment from impact by energetic ions (above 1 keV). Computer simulations using Monte

Carlo methods reproduce the experimental data. The data presented below are obtained with such a computer code (the TRansport In Materials code TRIM^{13,14}), which is appropriate for the amorphous surfaces formed by the adsorbates on the electrode surfaces. For crystalline surfaces, a slower computer code MARLOWE¹⁵ is more applicable. The various codes also give insight in the dynamics of sputtering phenomena.¹⁶ However, our purpose is principally to make the DNA community aware of the expected magnitude of the unintended plasma from electrode blowoff in order to stimulate measurements, and possibly remedial action.

Subsection 2.2 contains a brief discussion of TRIM, including reasonable estimates for the (badly characterized) parameters, the composition and binding energies of the dirty surfaces encountered in pulsed-power environments. Subsection 2.3 presents results, such as the number of atoms entering the vacuum per incident ion as function of energy and angle of the incident ions, for different composition and binding energies of the surface. In the absence of quantitative data for surfaces encountered in typical pulse power vacuums, the quantitative numbers generated by this investigation are probably correct in magnitude but not accurate. However the trends and conclusions should be correct.

2.2 MONTE CARLO TRANSPORT IN MATERIALS CODE TRIM.

TRIM.SP^{13,14} is a Monte Carlo computer program that follows the interaction of energetic particles with individual target atoms. With a given atomic density N the atoms are $\ell = N^{-1/3}$ apart, on average. In TRIM the target atoms' positions are related through a randomly generated impact parameter, which ranges from 0 to a maximum value of $\ell/\pi^{1/2}$. Also the impact angle is chosen randomly, as appropriate for an amorphous material. TRIM simulates composite materials by random selection of the target ions, and simulates layered structures by using target ions that depend on the penetration depth of the ion.

For a given incident energy and angle, each ion and the subsequent recoil atoms are followed through their slowing-down processes until their energy falls below a predetermined level or until they have moved back through the surface. In each collision the ion energy is reduced as a result of nuclear and electronic energy losses. Whenever a new recoil atom is created, a certain amount of energy, the binding energy, is subtracted from the ion energy, and whenever the recoil atom leaves the surface, the surface energy is subtracted. These energies are two important parameters in TRIM.

An ion can interact with a surface in three conceptually different ways, viz., backscatter, sputtering, and desorption. An incoming ion that interacts with a material interface is likely to acquire neutralizing electrons. The incident ions that come back from the surface, mostly as energetic neutral atoms, are backscattered. However, most frequently the incoming ion burrows itself into the material, dislodging other atoms in the process. When atoms from the crystalline substrate leave the surface the process is called sputtering, when surface contaminants leave the surface the process is called desorption. Experimentally it is possible to distinguish backscattered atoms from sputtered atoms when the incoming ion is a different species than the target material (although the code tracks the incoming ion and sputtered atom separately even when they are the same species). Sputtering and desorption involve the same physical processes, viz., the loosening of atoms from the

solid. In the absence of good data on electrode surfaces in pulse power systems, we do not distinguish between sputtering and desorption.

Sputtering generally dominates over backscatter. In Plasma Opening Switches the incident ion is the same species as a principal contaminant, carbon. Therefore the sputtering yield, the number of neutral atoms coming back per incident ion, will refer to the total emitted neutral atoms without distinguishing between the sputtered and backscattered atoms. Again, the semi-quantitative information we seek is unaffected by not distinguishing between backscatter, sputtering, and desorption.

TRIM calculates the sputtering yields of each component, i.e., both the total number of reflected ions and the distributions of the sputtered particles in energy and in angles. TRIM also provides detailed information on primary and secondary knock-on atoms, the deposition depth profiles of the incoming ions, and similar quantities useful for ion implantation studies (but not of interest here).

A crucial input parameter in TRIM is the total binding energy, which is the sum of the binding energy of the atoms to the surface, the surface energy, and the binding energy of the atoms inside the material, the bulk binding energy. Theoretically,¹⁶ in an intermediate range of incident energy around 1 keV the sputtering yield should be inversely proportional to the surface binding energy. However, for elemental surfaces the sputtering yield turns out to depend¹⁴ only on the total binding energy. For convenience the bulk binding energy is set to zero, and the sole remaining parameter is the surface binding energy.

For the present study the surface binding energy is chosen in the range of 1 to 5 eV per atom. Values like these are obtained for one or two monolayers on simple surfaces. When the surface is composed of solid compounds whose components are also solids, the surface binding energy is the heat of formation of the compound minus the heat of sublimation of the components. This is typically hundreds of kJ per gram-molecule, or a few eV per atom. For water a similar line of argument gives the total surface binding energies for the hydrogen and oxygen atoms in the water molecule, $\Delta E_{SBE}(H_2O)$, to be equal to the heat of formation of water, $\Delta E_f(H_2O)$, minus the heat of formations of the hydrogen and oxygen molecules from their atomic states, $\Delta E_{SBE}(H_2O) = -\Delta E_f(H_2O) + \Delta E_f(H_2) + \Delta E_f(O_2)$. This gives for the surface binding energy of hydrogen and oxygen atoms in water about 4-5 eV, in the same range.

For more complicated contaminant molecules such as hydrocarbons this way of estimating the surface binding energy is less appropriate, because the component atoms of these large molecules are usually sputtered one atom at a time. Therefore, the binding energy of these atoms to the molecules is more accurately prescribed by the bond strength between the atom and the molecule. Hydrocarbons have bond strengths for the different C-H bonds around 4 eV. For water the bond strength should be an equally good representation of the surface binding energy: the bond strengths of O-HO and O-H bonds are also in the range of 4-5 eV. The different components of a compound have different bond strengths and hence they should have different surface binding energies. Our version of the TRIM.SP code uses only a single binding energy, which we justify by noting that the surface binding energy for all of the carbon, oxygen and hydrogen atoms are close to 4 eV. These considerations suggest a reasonable value for the surface binding energy to be a few

eV. To see what the effect the surface binding energy has on the calculation, the surface binding energy is varied from 1 to 5 eV in the computations.

Another variable is the chemical composition of the surface. Hydrocarbons and water are the most prevalent, i.e., mixtures of hydrogen, carbon, and oxygen. Fortunately, the exact composition of the surface contaminants has a minor influence on the results.

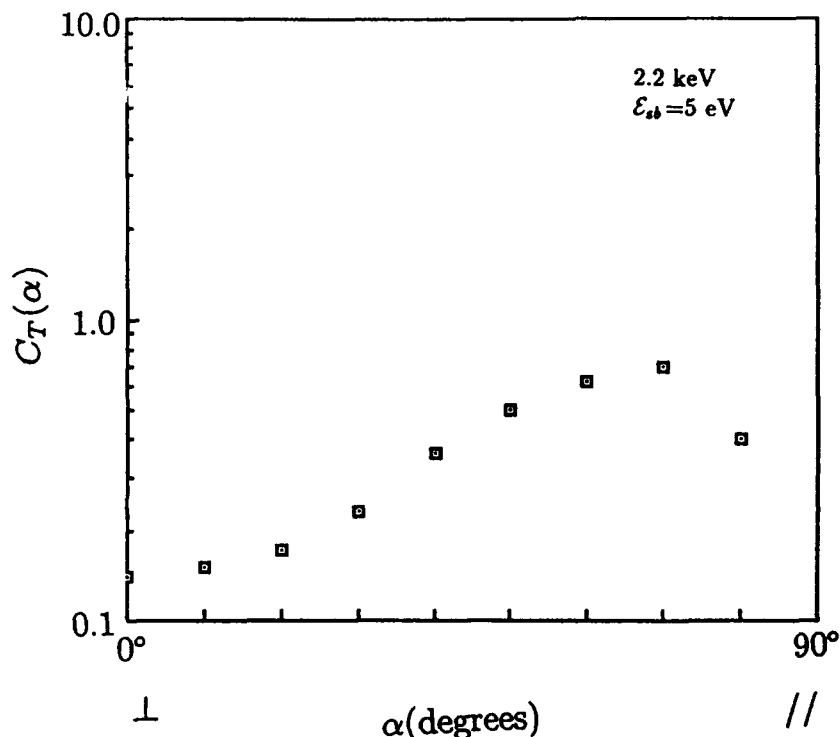


Figure 16. Total emission coefficient $C_T(\alpha)$ as a function of the incident angle α for incident carbon ions with 2.2 keV and an assumed binding energy of 5 eV.

The remaining variables belong to the incoming ion, viz., the energy \mathcal{E} and the angle of incidence α . The drift speed of the plasma is usually greater than the ion thermal speed. Therefore the ions have basically a single energy at a given point. The energy is largest early in the injection pulse, and decreases later. A typical velocity for an injected carbon plasma into a plasma opening switch is measured to be around 10 cm/ μ s, which corresponds to an energy $\mathcal{E} \simeq 650$ eV. The computations are therefore done for \mathcal{E} from a few hundred eV up to a few keV.

2.3 RESULTS AND DISCUSSIONS.

TRIM provides the total number of emitted neutral atoms per incident ion, the sputtering yield Y_s , as functions of the incident energy \mathcal{E} and of the incident angle α . However,

for a given incoming flux the incoming ions are spread over an area inversely proportional to $\cos \alpha$. Therefore, the sputtering yield Y_s must be multiplied by $\cos \alpha$ to normalize to the ion flux. This results in the total emission coefficient, $C_T(\alpha) = Y_s \cos \alpha$.

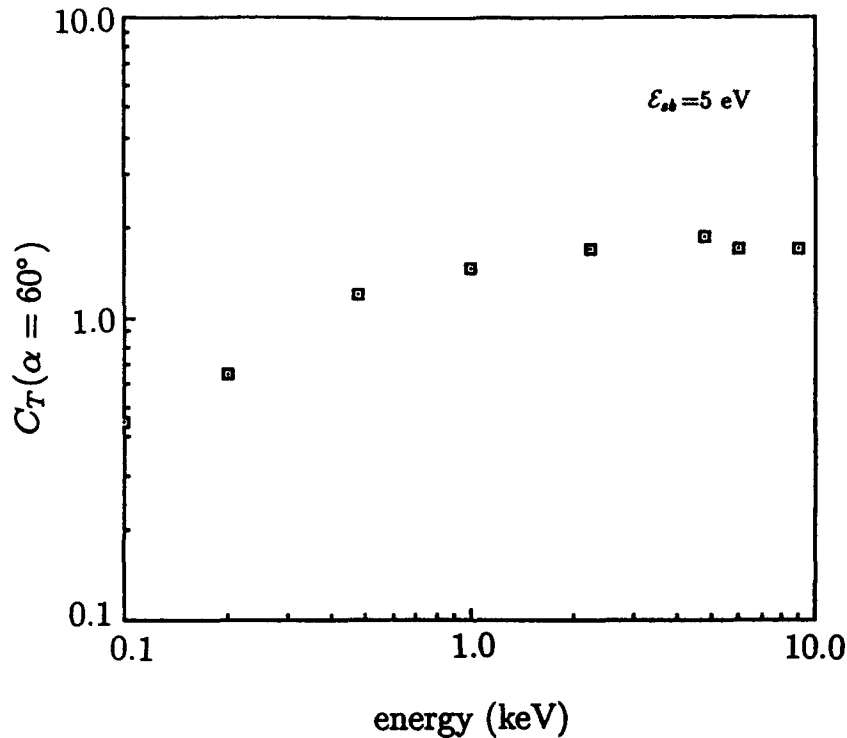


Figure 17. Total emission coefficient $C_T(60^\circ)$ as function of incident ion energy.

Figure 16 shows the total emission coefficient $C_T(\alpha)$ as a function of incoming angle α for carbon ions of 2.2 keV and a surface binding energy of 5 eV. The total emission coefficient $C_T(\alpha)$ increases from about 0.1 at $\alpha = 0^\circ$ to a maximum of about 1.0 at an incoming angle $\alpha \simeq 70^\circ$. Since the plume from a plasma gun or flashboard has an angular spread and since the electrode surfaces are normally curved, the total emission coefficient involves an appropriate average over angles. In a Monte Carlo computation the statistical uncertainty of the results are lowest with the most particles emitted. Computationally, the most convenient angle gives the most particles, therefore $\alpha = 60^\circ$ is chosen as the standard incident angle.

The carbon ions in the plasma opening switch are injected with a velocity in the range of 4×10^6 to 20×10^6 cm/s. A typical velocity of 10^7 cm/s corresponds to a kinetic energy of 0.65 keV. Figure 17 shows the total emission coefficient $C_T(60)$ at $\alpha = 60^\circ$ as function of the incident ion energy \mathcal{E} . The number of particles emitted increases as the incident ion

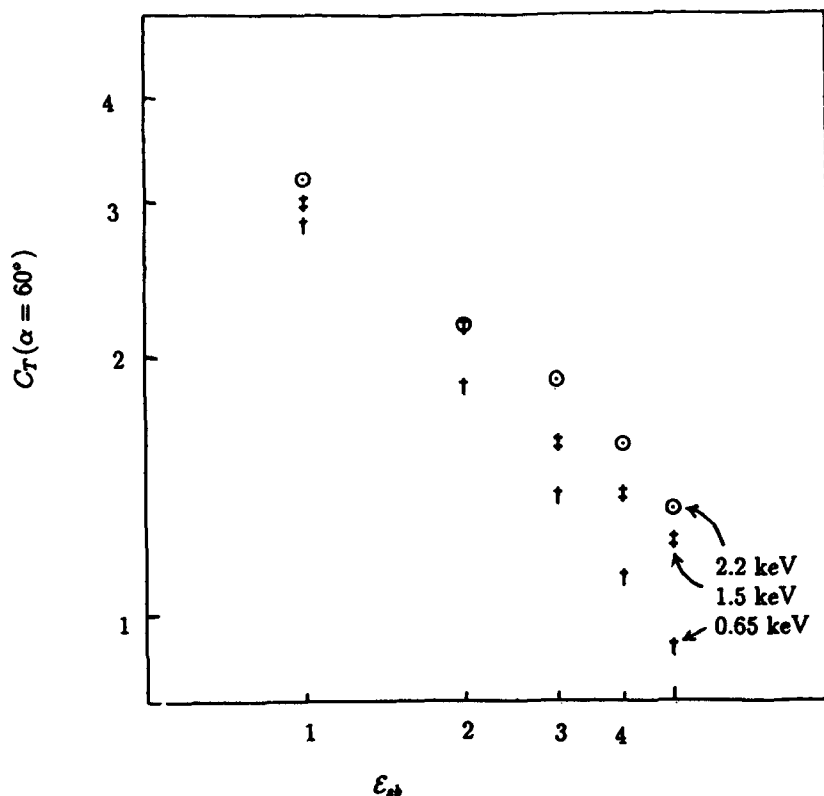


Figure 18. Sputtering yield $Y_s(60^\circ)$ as function of binding energy and incident energy.

energy increases by a factor of three from 0.1 keV to 1 keV and remains approximately constant thereafter.

It seems surprising that C_T depends quite weakly on energy at higher energies. This is due to the deeper penetration of the faster ions, which makes it more difficult for the sputtered ions to escape from deeper inside the material.

Figure 18 shows the sputtering yield $Y_s(\alpha = 60^\circ)$ as function of the surface binding energy E_{bb} , for an incoming carbon ion with impact energy \mathcal{E} of 0.65 keV, 1.5 keV, and 2.2 keV. More than one neutral atom comes back for each impinging ion irrespective of the surface binding energy. The sputtering yield Y_s is approximated reasonably well by $Y_s \simeq 2/\mathcal{E}_{bb}^s$, where the exponent s is between 0.7 for the smaller impact energy, and 0.5 for the higher impact energy. This dependence agrees with expectations.¹⁴

The sputtering yield depends weakly on the exact composition of the surface. For the same surface binding energy, $E_{bb} = 4$ eV, but different concentrations of oxygen, carbon and hydrogen, the sputtering yield is highest around 40% oxygen and no carbon, $Y_s \simeq 1.4$, and lowest with 40% carbon and no oxygen, $Y_s \simeq 0.95$. Thus, sputtering is 40% higher when water is the only surface contaminant than with pure hydrocarbons on the surface.

These and other computations show that the flux of neutrals from the surface is comparable to the flux of ions hitting the electrode in the plasma opening switch, irrespective of the exact parameters of the incoming plasma or the electrode surface. When the neutrals are ionized they become part of the plasma, changing the intended plasma density and affecting opening switch behavior.

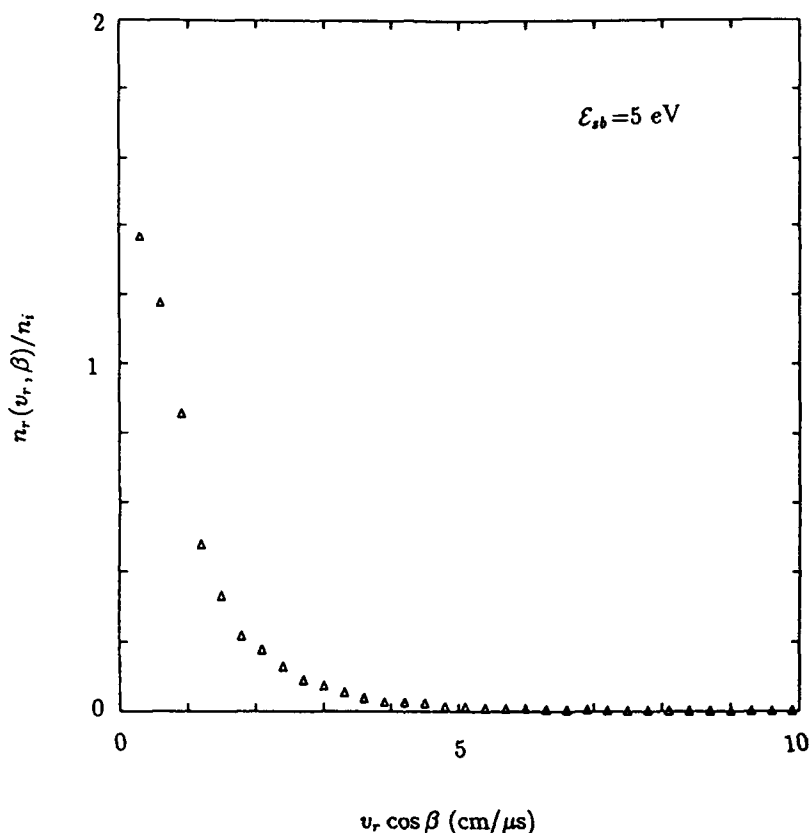


Figure 19. Normalized velocity distribution of the neutral atoms coming off the surface, assuming a binding energy of 5 eV.

Ion impact creates neutral atoms that flow away from the electrode back into the gap with velocity v_r at an angle β . The returned neutral density distribution $n_r(v_r, \beta)$ is given by the differential sputtering coefficient $C(v_r, v_i, \beta, \alpha)$: the total sputtering coefficient shown in Figures 16-18 is $Y, \cos \alpha = C_T(v_i, \alpha) = \int d\beta dv_r C$. In terms of C the incoming and returned ion densities are related by

$$v_r \cos \beta n_r(v_r, \beta) = C(v_r, v_i, \beta, \alpha) n_i v_i.$$

The distribution of the returned ions can be found given the incident ion velocities and angles. Assume that the incident ions come in at 10 cm/ μ s (0.65 keV) with an isotropic angular distribution. Then Figure 19 shows the normalized velocity distribution

function of the emitted neutral atoms, $n_r(v_r, \beta)/n_i$, as a function of the velocity $v_r \cos \beta$ perpendicular to the surface. The velocity distribution of the neutral atoms looks very much like a Maxwellian, with a thermal velocity of around $1 \text{ cm}/\mu\text{s}$, an order of magnitude slower than the incoming ion. The energy of the sputtered ions corresponds to about 9 eV.

These cold neutral atoms can be ionized through direct ionization by the incident plasma, but the dominant process is charge exchange: the cross section of ionization is about 10^{-16} cm^2 while the charge exchange cross section is about 10^{-15} cm^2 .

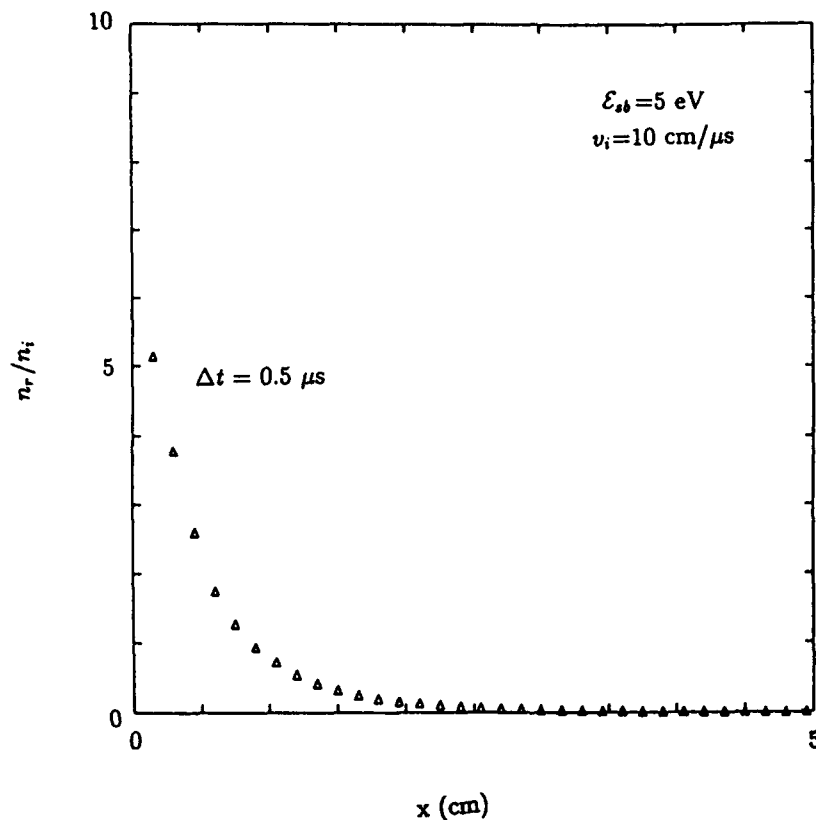


Figure 20. Density of the desorbed plasma as function of distance to the electrode surface after $0.5 \mu\text{s}$ long ion bombardment.

To calculate the density of cold ions formed in the charge exchange process the density profile of the neutral atoms must be known. If the neutrals freely expand, the density of neutral atoms with normal velocity v at a distance x and at time t is the same as the density very near the surface ($x = 0$) at a time $t - x/v$ earlier. Of course, there are no atoms beyond $x = vt$. Therefore, the total density at x and t is

$$n(x, t) = \int_0^\infty f(x, v, t) dv = \int_{x/t}^\infty f(x = 0, v, t - x/v) dv.$$

If the neutral density distribution at the surface remains the same throughout the bombardment, then

$$n(x, t) = \int_{x/t}^{\infty} f(x = 0, v) dv.$$

Figure 20 shows the density as function of distance from the surface after 0.5 μ s ion bombardment. The bulk of the neutral atoms have migrated about 0.5 cm away from the cathode surface. The neutral atom density on the surface is about five times the incident ion density n_i . With $n_i = 10^{14}$ cm^{-3} and using 10^{-15} cm^2 for the cross section of charge exchange processes about 25% of the neutral atoms becomes ionized. This gives a cold ion density of 1.25×10^{14} cm^{-3} , comparable to the density of incident energetic ions.

2.4 CONCLUSION.

The emitted neutral atoms have two orders of magnitude lower energies than the incoming ions, and they build up to a substantial density close to the surface, in roughly a self-similar profile. The neutral atoms are ionized by the incident energetic ions through charge exchange. The density of the resultant cold plasma is a substantial fraction of the incident carbon plasma: in these computations the density increases by a factor of two. The principal conclusion from these computations is that the sputtering affects the density of the plasma, an effect that should be taken into account in theoretical studies of plasma openings switches.

In addition to sputtering, chemical desorption could occur from the heating of the wall surfaces due to bombardment with the energetic ions. Molecules, instead of atoms, may be released and the molecules are capable of transforming into cold ions through the same process of charge exchange. These processes, which have not been considered here, strengthen the conclusion from this work: there could be lots more plasma than you think.

These computations, which were substantially completed in 1989, have been corroborated by experiment. In part inspired by our work researchers at Physics International have cleaned the electrode surfaces in their Plasma Erosion Switch, by using higher vacuums than customary and by applying discharge cleaning. As a result, their opening switch improved its opening characteristics and its reproducibility. More recently, measurements of the plasma density in the Plasma Opening Switch on the HAWK machine at the Naval Research Laboratory have shown a substantial gradient in the plasma density close to the (negative) electrode. The plasma density at the cathode is many times higher than expected from the plasma guns alone.

SECTION 3

OPENING MECHANISMS OF THE PLASMA-FILLED DIODE

In the early days of plasma-filled diode research three different mechanisms were suggested to explain the diode's behavior. These are the formation of a vacuum region filled with space charge, the implosion of the current channel, or an increase in the bulk resistance of the plasma due to turbulence. Simple estimates using electrical and radiation data point to the formation of a space-charge gap as the opening process. This analysis, done early in the performance period, has been borne out by the two-dimensional computations presented in Section 5: it is included here as an example of the considerations that form the background to the computational work.

3.1 INTRODUCTION.

The plasma-filled diode (PFD) is intermediate between a vacuum bremsstrahlung diode and a plasma opening switch (POS). In the PFD plasma sources inject plasma between the electrodes of the vacuum diode. With sufficient plasma the diode becomes almost perfectly conducting in the early part of the current pulse, and the voltage across the PFD is small. However at some point, the diode impedance rises rapidly. When the current is maintained by a large inductance the diode voltage increases. The high voltage accelerates electrons in the diode region for bremsstrahlung x-ray production.

The PFD can be used as a single stage opening switch, or as the last stage switch in tandem with a plasma opening switch. Compared to a plasma opening switch spatially separated from the electron beam diode, which has inductance between switch and load, the PFD has minimal inductance between the opening switch and beam diode since they both occupy the same space. The PFD also helps establish magnetically insulated electron flow to the diode by providing a low-impedance load, yielding better power coupling between a plasma opening switch and the diode.

Physics International tested this device using the EYESS bank. Available measurements include systems parameters like the capacitance, charge and inductance of the bank, the inductance and geometry of the transmission line, the charging circuit and delays of the plasma sources, and the geometry of the diode. Current and voltage monitors recorded the current and the inductively corrected voltage of the diode, and thermoluminescent detectors recorded the x-ray dose. These data and details of the EYESS generator, all graciously provided by Physics International,¹⁷ are discussed in Section 3.2.

Early on it was difficult to evaluate the different models directly because the available diagnostic information does not include detailed plasma measurements such as the location and density of the plasma fill, or on the location and magnitude of the current density. Such data have become available only recently. However, even with limited data it is possible to discriminate between the models. This is done in Section 3.3 for the PFD experiments at Physics International.

In the PFD a plasma column connects the electrodes, except perhaps in a localized gap region. The three opening mechanisms have different features indicated in Figure 21. With gap formation the plasma is presumed to remain a perfectly conducting cylinder,

but the gap has space-charge limited (Child-Langmuir) flow. With implosion there is no gap: instead, magnetic pressure implodes a one-dimensional current sheath on the outside of the plasma. An inductive voltage $V = d(LI)/dt$ then forms across the inductance L , which increases during the implosion at the rate \dot{L} . In the third mechanism the plasma becomes bulk resistive during conduction due to e.g., plasma turbulence. Obviously, in reality the different mechanisms may act simultaneously: here the point is to see which one dominates.

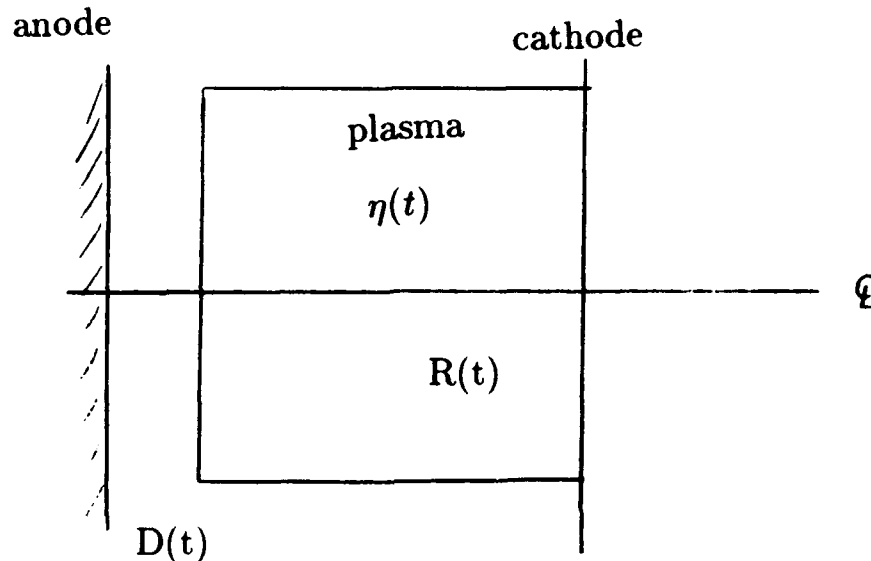


Figure 21. Cartoon of the PFD showing the space-charge gap, the plasma cylinder, and the parameters of the three models.

3.2 EXPERIMENTAL DATA.

The EYESS generator is a $0.96 \mu\text{F}$ Marx capacitor bank with 520 nH inductance connected to a vacuum transmission line and load. The transmission line has a 33 Ohm impedance with 130 nH inductance. The quarter cycle time for a shorted load is $1.25 \mu\text{s}$. The cathode is a cylindrical rod with radius 7.6 cm , with a flat plate facing the anode. The anode is recessed, with an outer radius of 12.8 cm . The gap spacing is typically 10 cm . Four plasma guns inject plasma into the diode. The experiment is easily changed from a single stage PFD into a tandem POS-PFD with an array of flashboards that can inject plasma into a POS region of the transmission line.

Figure 22 shows the current and inductively corrected voltage for two shots provided by Physics International,¹⁷ one for a single stage PFD and the other for a tandem POS-PFD. Each shot exhibited close to optimum performance for its configuration. Both shots show similar features. Early in time the voltage is small while the current is linearly increasing. When the current reaches a maximum the voltage begins to rise, i.e., the

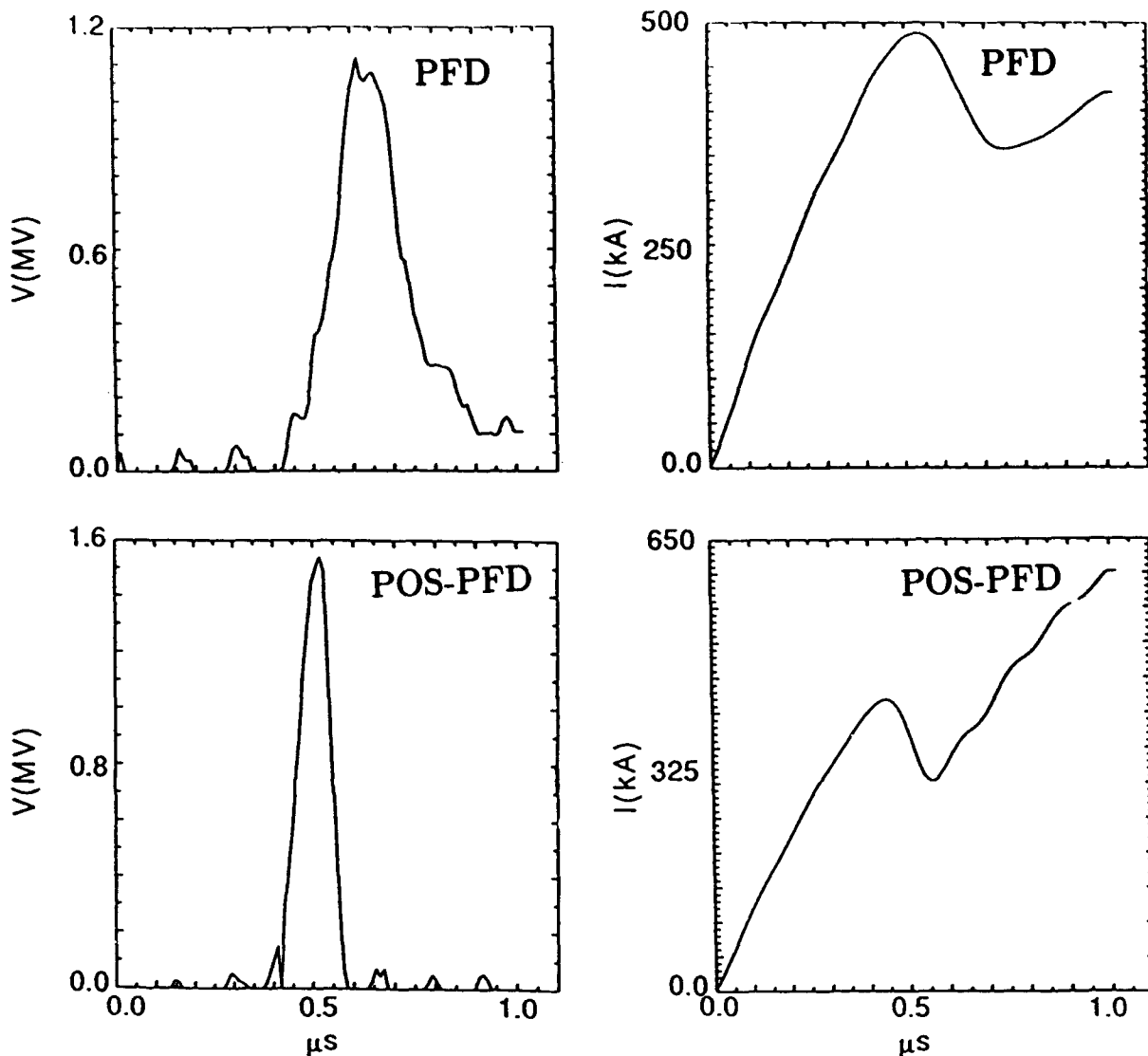


Figure 22. Voltage and current for the PFD and the tandem POS-PFD obtained from the EYESS generator at Physics International.

PFD opens. The current decreases while the voltage increases, reaches a maximum and subsequently decreases. When the voltage is small again, the current resumes a linear rise.

Each shot defines a resistance $R(t) = V(t)/I(t)$, or an inductance by $L(t) = \int_0^t V(t')dt'/I(t)$. Figure 23 shows the resistance $R(t)$ for the two shots. The diode resistance rises, reaching 2-6 Ohms during opening. The POS-PFD tandem gives the shorter opening time and the larger voltage gain. The difference between PFD and POS-PFD tandem may be due to the different plasma densities in these two cases. For the single stage PFD shots, the plasma guns are discharged longer prior to the arrival of the generator pulse than in the tandem experiments, because the single stage PFD needs to conduct the current longer to reach the same current as the POS-PFD tandem. The opening mecha-

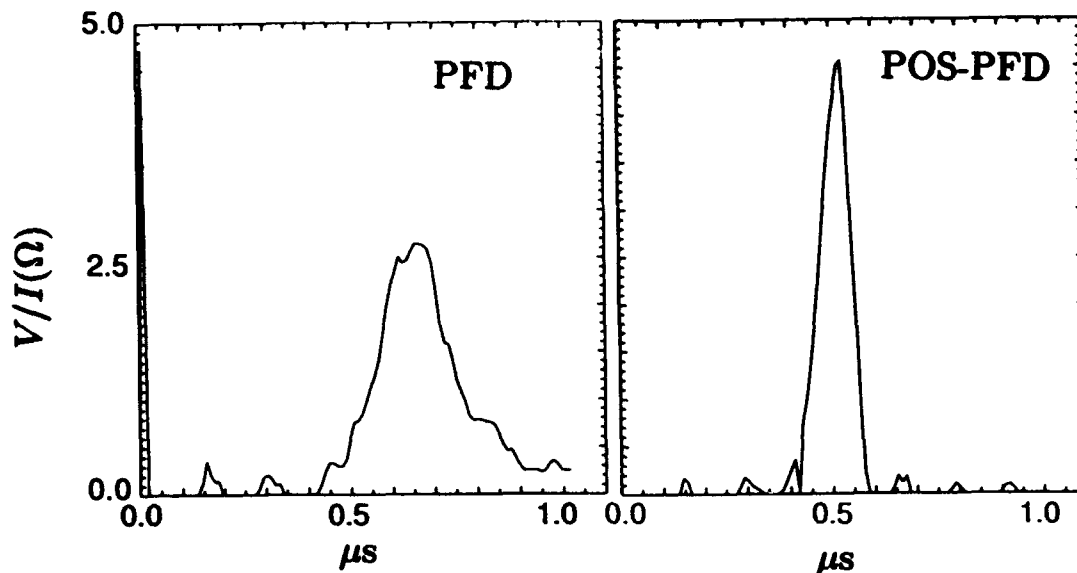


Figure 23. The resistance V/I corresponding to the voltage and current traces of Figure 22.

nism for the PFD apparently slows down with increasing plasma density. As a consequence the voltage gain during the opening event also decreases.

3.3 ANALYSIS OF OPENING MECHANISMS.

3.3.1 Gap Formation.

With this mechanism the plasma is perfectly conducting, and all the voltage is dropped across a gap between an electrode and the plasma surface, or possibly between two plasma surfaces.¹⁸ The current is quasistationary and the current density is constant across the plasma, and the electric fields at both boundaries are zero. In the gap flows the bipolar Child-Langmuir current, given by

$$\frac{I(\text{kA})}{\pi R^2(\text{cm})} = 3.35[1 + \sqrt{M_i/Zm_e}] \frac{V^{3/2}(\text{MV})}{D^2(\text{cm})}, \quad (3-1)$$

where R is the plasma radius, D is the gap spacing, m_e is the electron mass, M_i is the ion mass, and Z is the charge state of the ions. Even though electrons attain relativistic velocities, the nonrelativistic version of bipolar Child-Langmuir flow is adequate for this simple model.

Assuming a constant radius $R=8$ cm, the the voltage and current traces give the gap spacing $D(t)$ shown in Figure 24(a) for the single stage PFD, and in Figure 24(b) for the tandem POS-PFD. The gap spacing goes up to about 1.5 centimeters for the single stage PFD and to about 2.25 centimeters for the tandem PFD. After attaining the maximum the gap spacing and the voltage decrease while the current continues to increase. The standard explanation of this behavior is gap closure by plasmas coming off the electrodes.

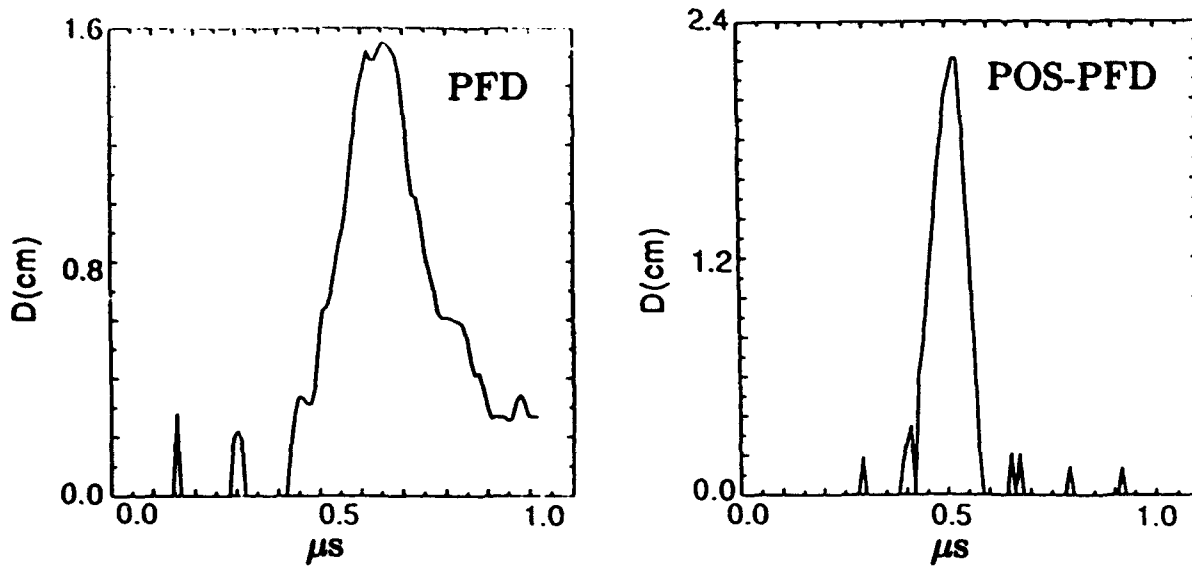


Figure 24. The gap spacing corresponding to bipolar Child-Langmuir flow inferred from the current and voltage traces of Figure 22.

Apparently, gap erosion predicts a reasonable values for the gap spacing, and gap erosion is a viable opening mechanism.

3.3.2 Implosion Model.

The implosion model assumes that the voltage pulse comes exclusively from the increase in inductance due to the contraction of a uniform pinch. The current is restricted to a sheath on the outside of the plasma channel. The magnetic field is

$$B_{\theta} = \mu_0 I / 2\pi r, \quad (3-2)$$

outside the plasma radius r , while inside the magnetic field vanishes.

The inductive voltage is

$$V(t) = -\frac{\mu_0 D}{2\pi} \frac{d}{dt} \left[I(t) \ln\left(\frac{r(t)}{R}\right) \right] \quad (3-3)$$

where D is the electrode gap spacing. Solving Eq. 3-3 for the radius $r(t)$ yields

$$r(t) = R \exp \left[-\frac{2\pi}{\mu_0 D I(t)} \int_0^t V(t') dt' \right]. \quad (3-4)$$

Figure 25 shows $r(t)$ for an electrode gap $D = 10$ cm and an initial radius $R = 8$ cm. Clearly, the current channel is unrealistically small, 3×10^{-10} cm for the PFD tandem and

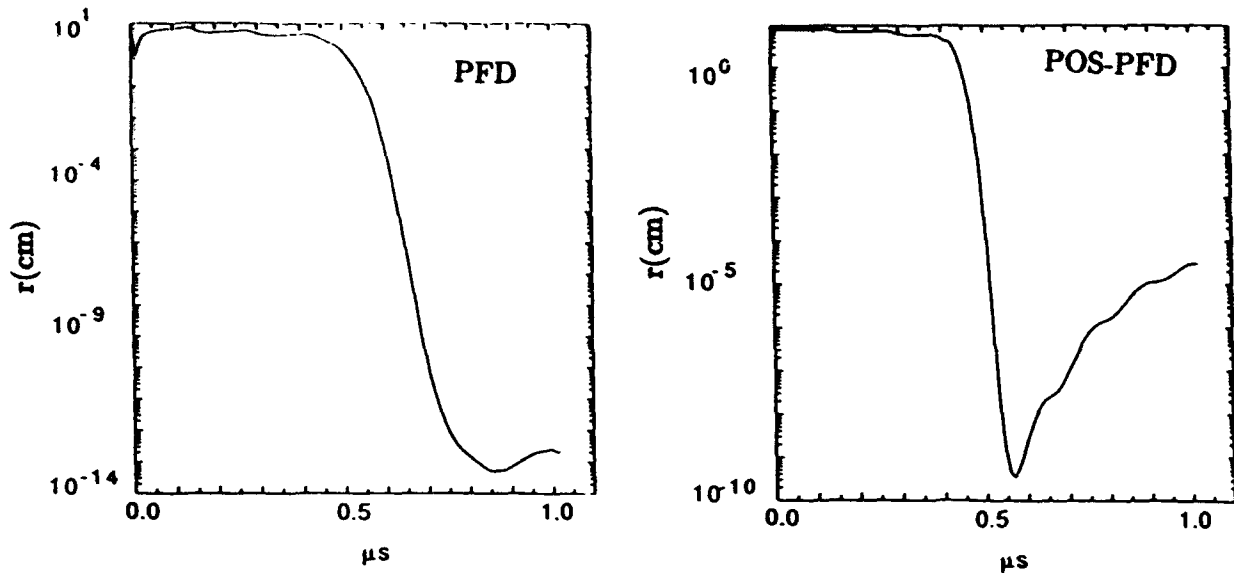


Figure 25. The radius of the current shell computed according to the implosion model from the voltage and current traces of Figure 22.

down to 5×10^{-14} cm for the single stage PFD. Therefore the opening process can not be primarily inductive.

3.3.3 Resistivity.

An increase in bulk resistivity of the plasma has also been advanced as an opening mechanism in the PFD. Turbulent plasmas contain large electric field fluctuations, which perturb the electron trajectories and provide friction to the electron flow. For an estimate, the plasma is assumed to remain a cylinder of constant radius R with homogeneous resistivity η . The resistivity is given by the diode impedance V/I (see Figure 23) multiplied by a geometrical factor,

$$\eta(t) = (\pi R^2/D) V(t)/I(t). \quad (3-5)$$

Again taking $R = 8$ cm and $D = 10$ cm the maximum resistivity in the single stage switch is about 50 Ohm-cm, and the maximum resistivity in the tandem is about 90 Ohm-cm. In contrast, Spitzer resistivity for a plasma with an electron density of 10^{12} cm $^{-3}$ and an electron temperature of 10 eV is 0.054 Ohm-cm. If the electron density is increased to 5×10^{14} cm $^{-3}$, Spitzer resistivity has the value 0.07 Ohm-cm. The resistivity needed for the PFD is about 3 orders of magnitude larger than expected from Coulomb collisions.

Can plasma turbulence change the picture? The PFD has ample sources of free energy to drive various instabilities (two-stream, Buneman, ion-acoustic). All eventually saturate, leading to an order of magnitude estimate for the maximum effective collision frequency

of $\nu \leq 0.4\omega_{pe}$. The resistivity $\eta = m_e/n e^2 \nu$ then becomes

$$\eta(\text{Ohm - cm}) = 8 \times 10^7 / \sqrt{n(\text{cm}^{-3})}. \quad (3 - 6)$$

For a plasma density of 10^{13} cm^{-3} , this expression yields a resistivity of 25 Ohm-cm, consistent with a reasonable values for the pinch resistance.

Although opening by anomalous resistivity agrees with the electrical data, it disagrees with the observed bremsstrahlung.¹⁹ Resistivity prevents electrons from accelerating to high energies, a necessity for bremsstrahlung production. Therefore bulk resistivity can not open the PFD.

3.4 CONCLUSION.

According to these estimates only the appearance of a space-charge filled gap in the diode is consistent with the electrical and radiation data obtained with the PFD on EYESS. However, this conclusion does not imply the absence of the other processes, implosion and anomalous resistivity. Instead, the expected dominance of gap formation gives added confidence in computations that ignore resistivity in favor of space charge phenomena, such as particle in cell codes. The next section discusses some of these computations.

SECTION 4

ONE DIMENSIONAL PARTICLE IN CELL SIMULATIONS OF A PLASMA FILLED DIODE WITH AN EXTERNAL CIRCUIT

The validity of the classical bipolar model for the operation of a planar, plasma filled diode (PFD) is examined using a one dimensional, electrostatic particle in cell simulation of a PFD coupled to an external LC driver circuit. While the high voltage opening phase of operation in the PFD is correctly described by the bipolar model, the low voltage conduction phase is not. In the low voltage conduction phase the unstable interaction between the emitted electron beam and the diode plasma creates internal states of the diode which are far from the bipolar equilibrium state hypothesized by the classical model. As a result the simulation's scaling predictions for the operation of the PFD differ from those of the classical model.

4.1 INTRODUCTION.

In its most frequently encountered form a plasma filled diode (PFD) is a high power cold cathode vacuum diode which consists of a pair of plane parallel electrodes whose anode-cathode gap has been prefilled with a fully ionized low density plasma. Plasma fill densities of the order of 10^{13} cm^{-3} are typically employed in such devices and the fill plasma is often injected into the diode gap with a net drift velocity of several $\text{cm}/\mu\text{s}$ through a semitransparent screen anode. An axial magnetic field may be applied to inhibit pinching of the fill plasma that might occur in the self magnetic field of the diode current. When a high voltage pulse is applied to the diode, explosive electron emission and formation of a cathode plasma rapidly takes place at the surface of the cold cathode so that the cathode quickly becomes a space charge limited (SCL) electron emitter. Plasma filled diodes have frequently been employed in the pulsed power community as high current, relativistic electron beam sources.²⁰

Recently, interest in these devices has focussed on their important application as multimicrosecond conduction time, fast opening switches^{21,22} for use with inductive energy storage systems. Experiments²¹ employed a PFD embedded in a strong externally applied axial magnetic field as a plasma opening switch (POS). In these experiments when current was applied to the magnetized PFD, a low voltage conduction phase up to $2.5 \mu\text{s}$ in duration was observed followed by a rapid opening phase generating a high voltage pulse with risetimes less than 150 ns. These experimental observations have motivated the theoretical work in this section: understanding the plasma processes that control the conduction time and opening rate is essential to opening switch technology.

The generation of high voltages and the acceleration of the electron beam in PFD's have long been thought to result from the rapid expansion of a cathode sheath into the body of the low density fill plasma. A simplified analytic treatment of the problem of ion sheath growth near a negatively biased, non-emitting electrode in contact with a low density plasma was first presented by Sander.²³ This treatment was later extended by Widner and Poukey²⁴ and applied by Miller, Poukey and Wright²⁵ to the problem of sheath growth and electron beam generation in a high power PFD. In the model of Miller²⁵ *et al.* it is

assumed that the impedance of the PFD is controlled by a bipolar sheath at the interface between the cathode and the low density fill plasma across which all of the diode voltage is dropped. The space charge limited electron and ion currents, J_e and J_i , flowing across this sheath are given by the classical bipolar relations,²⁶ viz.,

$$J_i = 1.86 \frac{4}{9} \epsilon_0 \left(\frac{2e}{m_i} \right)^{1/2} \frac{V_D^{3/2}}{x^2}, \quad (4-1)$$

$$J_e/J_i = (m_i/m_e)^{1/2}. \quad (4-2)$$

Here V_D is the diode voltage and x is the sheath thickness. The time evolution of the sheath thickness x is determined by the differential equation

$$en \frac{dx}{dt} = J_i - enu_0, \quad (4-3)$$

where n and u_0 are the density and mean velocity of the ions entering the sheath from the body of the plasma. As long as the ion current J_i is less than enu_0 the sheath remains small and low voltage conduction is obtained. However, when the ion current J_i demanded at the cathode exceeds enu_0 Equation (4-3) shows that the sheath rapidly expands to supply the required ion flux and a high voltage develops across the diode. The onset of this high voltage opening phase will occur when the diode current I increases to the point where,

$$I \simeq I_c = \left(\frac{m_i}{m_e} \right)^{1/2} enu_0 A, \quad (4-4)$$

where A is the area of the diode. This model is a direct generalization of Sander's original treatment of ion sheath growth near a non-emitting cathode to the case in which the cathode is a space charge limited electron emitter. The fundamental assumption is the replacement of the positive ion sheath for the non-emitting case by a bipolar sheath for the SCL case. The explicit numerical calculation to follow shows that this assumption is only partially correct and in fact misses much of the important physics of the PFD.

This section treats a planar PFD self consistently coupled to an external LC driver circuit. The electron flow is explicitly assumed to be one dimensional so that an electrostatic treatment of the problem is adequate. The model presented here might be expected to correctly describe the behavior of the PFD in the case where the B_θ self field of the diode current is much smaller than the external applied B_z field, and the electrons are effectively one-dimensional. Thus, the model describes a magnetized PFD or POS of the type described in reference [2] where the electron flow may be regarded in some approximation as one-dimensional. This approximation is not valid for the plasma erosion opening switch (PEOS)¹⁸ where magnetic insulation of the electron flow and other essentially two-dimensional effects play a significant role. Nevertheless, the results of the one-dimensional electrostatic model may be expected to provide some interesting insights into the processes taking place in the PEOS.

The investigation is done with a version of the computer code PDW1 originally developed by Lawson²⁷ *et al*, a particle in cell (PIC) model of the one-dimensional PFD

coupled to an external LC circuit. Both electrons and ions are treated by the PIC method and phenomena on the time scale of an electron plasma period and Debye length scale are explicitly resolved. The code thus provides a fully self-consistent solution for the simultaneous behavior of the plasma and the external driver circuit. In this section the code is used to solve a simple PFD problem that represents a scale model version of a POS experiment.²¹ The model problem is solved numerically for two different cases, one without electron emission at the cathode, the other with space charge limited (SCL) electron emission.

The case without emission recovers the results of earlier investigators, e.g., the sheath theory of the PFD as discussed by Widner and Poukey. The computation therefore provides a correct description of the impedance evolution of the diode under study. However, turning on SCL emission gives a substantially different result. In this case, the acceleration of the emitted electron beam by the growing cathode sheath leads to the development of a strong beam-plasma instability. This instability rapidly evolves to a non-linear state, which is characterized by a large potential maximum near the center of the diode gap, with a relatively small net voltage drop and significant trapping of electrons out of the emitted beam. This low-voltage conduction phase of the PFD is essentially different than the bipolar equilibrium hypothesized by Miller²⁵ *et al.*

Eventually, this low voltage phase terminates and a high voltage opening phase appears which is characterized by the expansion of a large bipolar sheath at the cathode that sweeps the remaining ions out of the diode gap. Hence, while a bipolar sheath is indeed responsible for the generation of high voltages in the PFD, the details of this process differ substantially from those of the classical sheath theory and lead to a variety of new scaling relationships for the conduction time and conducted current in a 1D POS model.

The remainder of Section 4 is organized as follows. Section 4.2 describes the computational model implemented in the PDW1 code, and the choice of parameters for the model POS problem to be solved. Section 4.3 examines the numerical solution without electron emission from the cathode surface. Section 4.4 describes the general phenomenology of the results for the SCL emission case. Section 4.5 discusses some detailed scaling results for the SCL emission case which illustrate how the conduction time, conducted current and other parameters of interest scale in our simple 1D model POS. Finally, Section 4.6 summarizes the discussion and indicate the direction of future work in this area.

4.2 COMPUTATIONAL MODEL

Figure 26 illustrates the model POS problem solved by the PDW1 code. It consists of a planar diode gap of spacing d and area A coupled to an external driver circuit with inductance L and capacitance C . The diode gap is pre-filled with a thermal Maxwellian plasma of electrons and ions with temperatures T_e and T_i respectively. The initial fill plasma has a spatially uniform density and no net drift motion. Hence, the present discussion treats only the simple case wherein the fill plasma is stationary and is not renewed by continuing injection of plasma into the diode gap. The more complex case of injecting a drifting thermal plasma is treated later. The anode is assumed to be a non-emitting cold wall. Two different cathode emission conditions are considered, no emission and SCL electron emission. For SCL electron emission the emitted electrons are given an initial

thermal spread of velocities corresponding to the flux distribution $vf(v)$ where $f(v)$ is a half Maxwellian whose temperature is the same as that of the fill plasma.

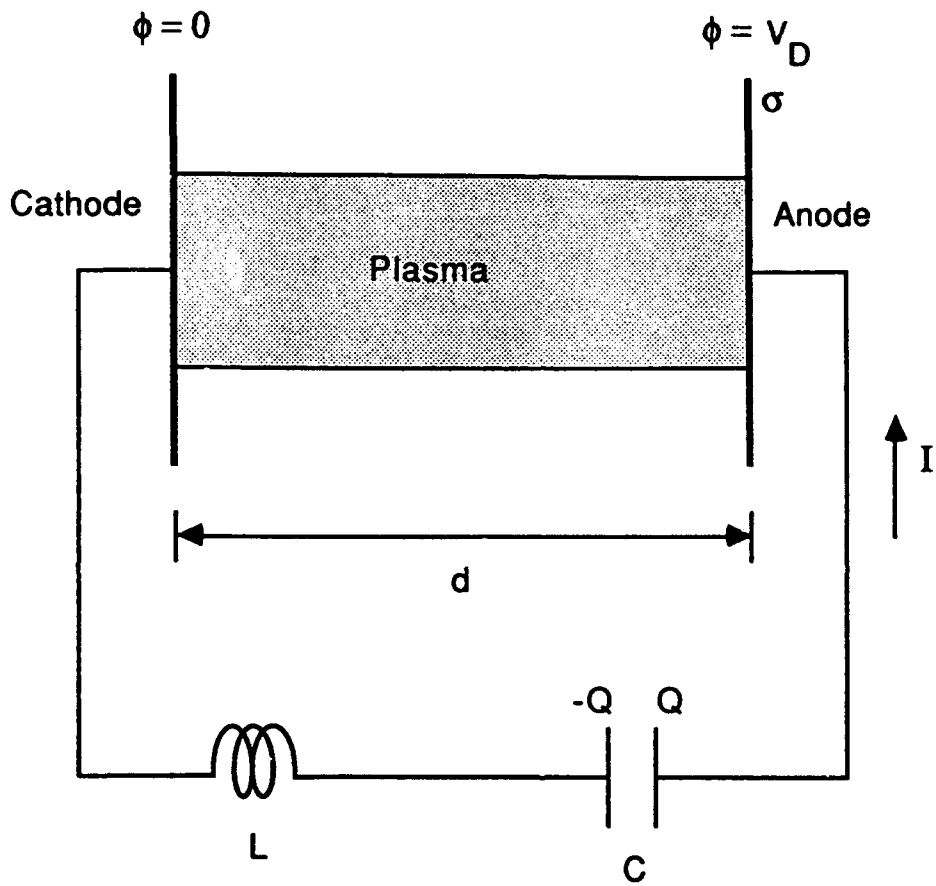


Figure 26. Plasma Filled Diode with circuit.

The calculation is one-dimensional and electrostatic. Hence, all quantities depend only on x , the coordinate across the diode gap, and the electric field is obtained explicitly from the solution of Poisson's equation in the region between the electrodes. Both electrons and ions are treated as one-dimensional macroparticles by the particle in cell method. To self-consistently solve for the simultaneous behavior of the plasma and the external circuit the code must integrate the equations of motion for all the macroparticles, together with the following system of equations for the circuit and the diode:

$$L \frac{d^2 Q}{dt^2} + \frac{Q}{C} = V_D(t), \quad (4 - 5)$$

$$A \frac{d\sigma}{dt} = -\frac{dQ}{dt} + AJ_{plasma}(x=d), \quad (4-6)$$

and

$$\frac{\partial^2 \phi(x,t)}{\partial x^2} = -\frac{\rho(x,t)}{\epsilon_0}, \quad (4-7)$$

subject to the boundary conditions

$$\phi(0,t) = 0, \quad (4-8)$$

$$\left[\frac{\partial \phi}{\partial x} \right]_{x=d} = -\frac{\sigma}{\epsilon_0}, \quad (4-9)$$

and

$$V_D(t) = \phi(x=d,t). \quad (4-10)$$

Here σ is the net surface charge density on the right hand electrode and J_{plasma} is the net current density from the plasma into the right hand electrode boundary. Equation (4-5) above is just the circuit equation for the external driver circuit including the voltage drop V_D across the diode gap. Equation (4-6) simply states that the rate of change of the net charge on the right hand electrode is determined by the balance between the net current supplied by the plasma and the current drawn off by the external circuit. Equation (4-7) is Poisson's equation for the potential distribution in the region between the electrode boundaries subject to the boundary conditions on ϕ given in Equations (4-8) and (4-9). The potential is solved on a finite spatial grid in the x direction, with grid spacing Δx . The spacing is sufficiently small so that a single Debye length of the plasma is explicitly resolved. At any given time step the potential ϕ_j is known at each of the points $j\Delta x$ (from $j = 0$ to $j = N$). By convention, the potential $\phi = 0$ at the left hand boundary, and the initial value of Q is taken to be positive. Then the right hand electrode is always the anode as shown in Figure 26.

The algorithms used in the PDW1 code and their implementation²⁷ are as follows. The calculation typically begins at $t = 0$ with the initial distribution of electron and ion macroparticles in the diode gap, the external capacitor charged to some initial voltage V_0 , zero current in the external circuit and zero voltage drop across the diode gap.

At time step n the potential $\phi(x, t_n)$ is known, together with the positions of all the macroparticles of the plasma. The electric fields are obtained from the potential ϕ by center differencing. The electric field is used to push the particles via the standard leapfrog algorithm. The circuit quantities are simultaneously advanced by this same method. The surface charge value of σ is then adjusted to account for the charge carried by plasma particles that may have been absorbed from the plasma during the timestep, as well as the charge that has been drawn off by the external circuit. The charge density on the spatial grid at step $n + 1$ is then obtained by weighting the particles to the grid using linear weighting. Given σ and ρ at step $n + 1$ Poisson's equation is solved by a simple finite difference method to yield $\phi(x, t_{n+1})$, thus completing the time step. This process is repeated many times to obtain the time evolution of the coupled plasma-circuit system.

Parameters can be chosen to mimic the POS experiment, while at the same time providing an economical computational model for study. The fill plasma is a thermal

hydrogen plasma with density $n_i = 10^{13} \text{ cm}^{-3}$ and $T_e = 5 \text{ eV}$, $T_i = 1 \text{ eV}$. In this case the Debye length $\lambda_D \approx 5.25 \times 10^{-4} \text{ cm}$, and the grid cell must be on this order. To avoid an excessive number of grid cells, the diode gap must be much smaller than the experimental value. It is also desirable to have many tens of macroparticles per grid cell in order to avoid noise. In the model of Figure 26 the A-K gap spacing is $d = 1 \text{ mm}$, with 128 grid cells across the gap. The grid cell is then $\Delta x_D \simeq \lambda_D$, which provides adequate spatial resolution with a reasonable number of grid cells. For most model calculations a plasma pre-fill of 8320 macroparticles of each species is loaded uniformly into the diode gap, giving about 65 particles per cell. The initial charge voltage V_0 on the external capacitor must be scaled down to 1 kV in order to preserve the typical²¹ vacuum electric field in the diode gap of 10 kV/cm. The scaling with gap width is addressed further in Section 5.

The behavior of the PFD as a circuit element can vary between that of a short circuit and that of an open circuit with vacuum capacitance $C_D = \epsilon_0 A/d$, where C_D is typically very much smaller than the capacitance of the external driver C . The timescale of the external circuit is defined by the relatively long \sqrt{LC} time associated with the external inductance L and capacitance C of the driver if the PFD acts as a short. In the opposite limit when the PFD acts as an open circuit the effective capacitance of the series combination of C and C_D is $CC_D/(C + C_D) \approx C_D$, so that the timescale becomes the much shorter $\sqrt{LC_D}$ time defined by the vacuum capacitance C_D of the diode gap. Realistic values for these timescales must be preserved in the modeling, which determines the remaining model parameters L , C and A . Thus, $L = 1 \mu\text{H}$ and $C = 1 \mu\text{F}$, and the quarter cycle time matches the experiment, $1.6 \mu\text{s}$. Similarly, to get $\sqrt{LC_D} \simeq 3.3 \text{ ns}$ the diode area is chosen as $A = 0.314 \text{ cm}^2$ (or $\pi/10$), maintaining the current density of the experiment with a much smaller diode.

Sections 4.3 and 4.4 below use the basic model parameters discussed above and examine the effect of varying the electron emission at the cathode surface on the impedance history of the diode. Section 4.5 focuses on the SCL emission case and examines the effect of model parameters such as fill density on the conducted current and other properties of our model POS.

4.3 CATHODE WITHOUT ELECTRON EMISSION.

Consider first a PFD without electron emission from the cathode. As already discussed the calculation starts at $t = 0$ with a spatially uniform fill of neutral hydrogen plasma with density 10^{13} cm^{-3} , 1 kV on the external capacitor, and zero current. The evolution of the diode impedance in this case is controlled by the rapid growth of a large positive ion sheath at the cathode surface which expands into the fill plasma at several times the ion acoustic speed $C_s = \sqrt{T_e/m_i}$. Sheath growth near a negatively biased non-emitting electrode in contact with a low density plasma is treated in the literature.^{23,24,28} The computations exhibit this process in some detail, and agree with earlier investigations.

Figures 27(a) and (b) show the time history of the diode current and total diode voltage drop during the first 80 ns of time development. Figures 27(c) and (d) show corresponding plots of the cathode sheath thickness and the velocity of the sheath edge as a function of time for the same period. The sheath thickness, defined as the distance from the cathode surface to the sheath edge where $E = 0$, is measured in grid cell units: the

full width of the diode gap $d = 1$ mm corresponds to 128 grid cells.

Almost immediately after the onset of current flow a significant voltage drop begins to develop corresponding to a rapid growth of the cathode sheath. By $t = 4$ ns the sheath edge has reached a peak expansion velocity of $2.2 C_s$, or about 6 cm/ μ s. At this same time the total diode voltage drop V_D exceeds the 1 kV charge voltage on the external capacitor, so that dI/dt must change sign in accordance with the circuit Equation (4-5). Then the diode current begins to drop, together with the velocity of the sheath edge. By $t = 6.8$ ns the velocity of the sheath edge has fallen below C_s . Pre-sheath electric fields now penetrate out ahead of the sheath at velocity C_s , and they begin to accelerate ions back into the sheath from the body of the plasma. As a result the sheath has slowed almost to a halt by $t = 8$ ns. This situation does not persist indefinitely because the supply of plasma is finite. At about $t = 20$ ns the sheath begins to accelerate again, until by $t = 30$ ns it has attained a relatively constant velocity of 1.25 cm/ μ s. This motion is maintained until the sheath has penetrated the full width of the gap and the plasma has been completely eroded away by $t = 75$ ns.

In lieu of the movie, Figure 28 illustrates the detailed evolution of the cathode sheath with a sequence of snapshots at different times of interest. Figure 28 shows from top to bottom the electron phase space, the potential distribution $\phi(x)$ in the diode gap, the ion phase space, and the electron and ion charge density distributions $\rho_e(x)$ and $\rho_i(x)$. In the phase space plots all velocities are in scaled units normalized to $\Delta x/\Delta t$. The position x across the diode gap is measured in grid cell units from $x = 0$ at the cathode on the left to $x = 128$ at the anode on the right. The potential ϕ is given in volts and all charge densities are in Coulombs/ m^3 . Figure 28(a) for $t = 0$ illustrates the initial spatially uniform distribution of Maxwellian electrons and ions with charge density 1.6 C/ m^3 from the plasma density 10^{13} cm^{-3} . The potential distribution is identically zero across the diode gap.

The fast timescale for the external circuit is the LC_D time, which is about 3.3 ns. For shorter times the PFD has not charged up, and the system behaves like a plasma in contact with two cold metal walls. On the scale of a few hundred picoseconds both cathode and anode charge rapidly negative due to the thermal flux of electrons until stable Langmuir sheaths are formed at both electrodes with a floating potential of about¹⁰

$$\phi_f = -\frac{kT}{e} \ln \left[\left(\pi \frac{m_e}{m_i} \right) \left(1 + \frac{T_i}{T_e} \right) \right] \approx 13.7 \text{ V.} \quad (4-11)$$

Figure 28(b) is a snapshot taken at $t = 1$ ns. The potential distribution clearly shows the Langmuir sheaths at cathode and anode with a floating potential of the correct magnitude. The slight asymmetry in the size of the sheath potentials is due to the action of the external circuit which by $t = 1$ ns has just begun to charge up the diode. In the ion phase space plot of Figure 28(b) the flux of ions to both electrodes due to the sheath electric fields can be easily seen at each end of the gap.

Figure 28(c) shows the situation at $t = 4$ ns corresponding to the time of peak sheath velocity. By this time the cathode sheath voltage has grown to about 1 kV, dwarfing the anode sheath potential on the scale of the potential distribution plot in Figure 28(c). On the left hand side of the ion phase space plot, the cathode sheath can be seen rapidly

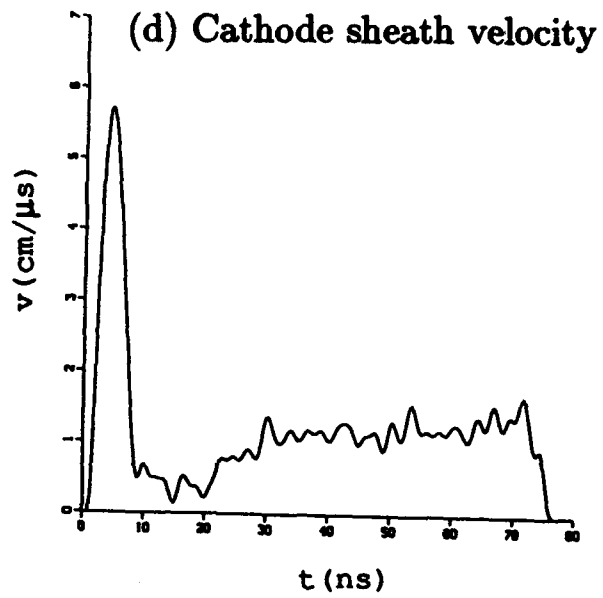
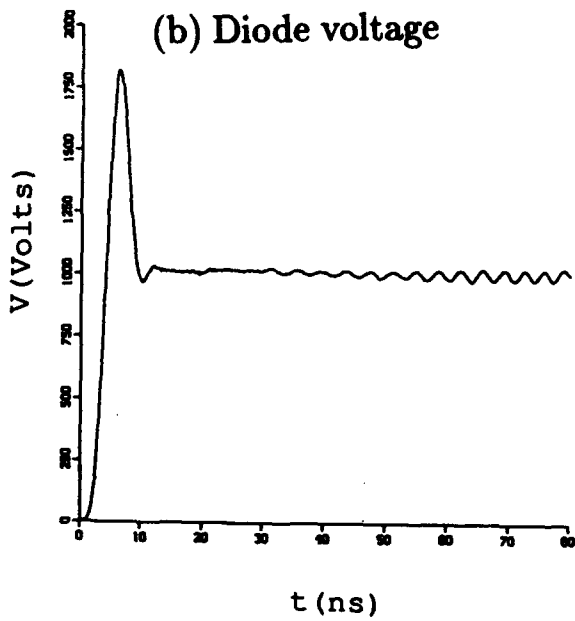
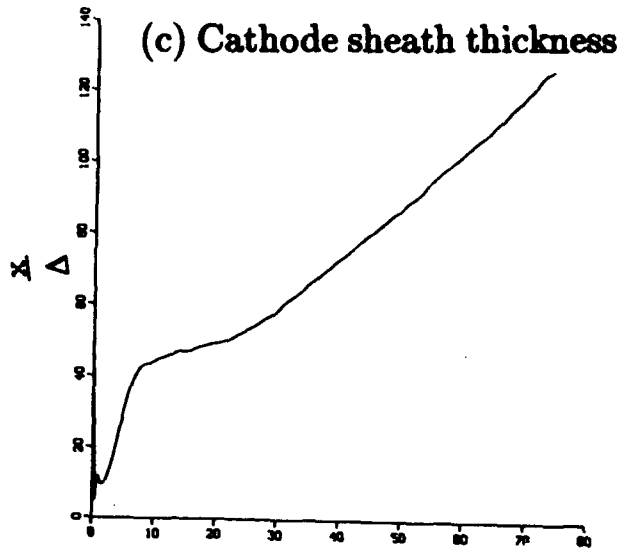
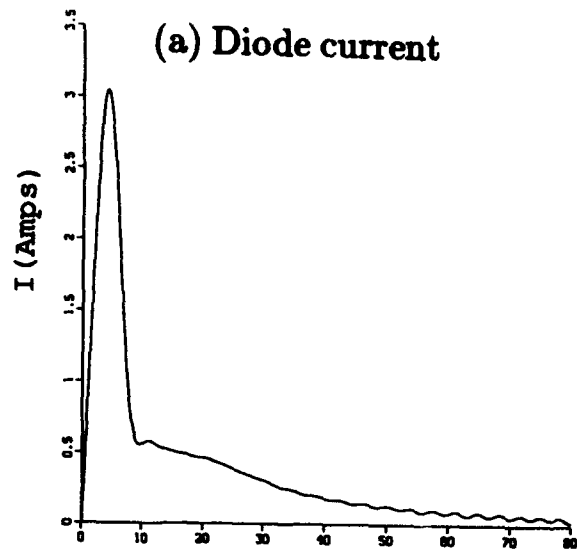


Figure 27. PFD with hydrogen plasma fill $n_i = 10^{13} \text{ cm}^{-3}$ without electron emission from cathode surface.

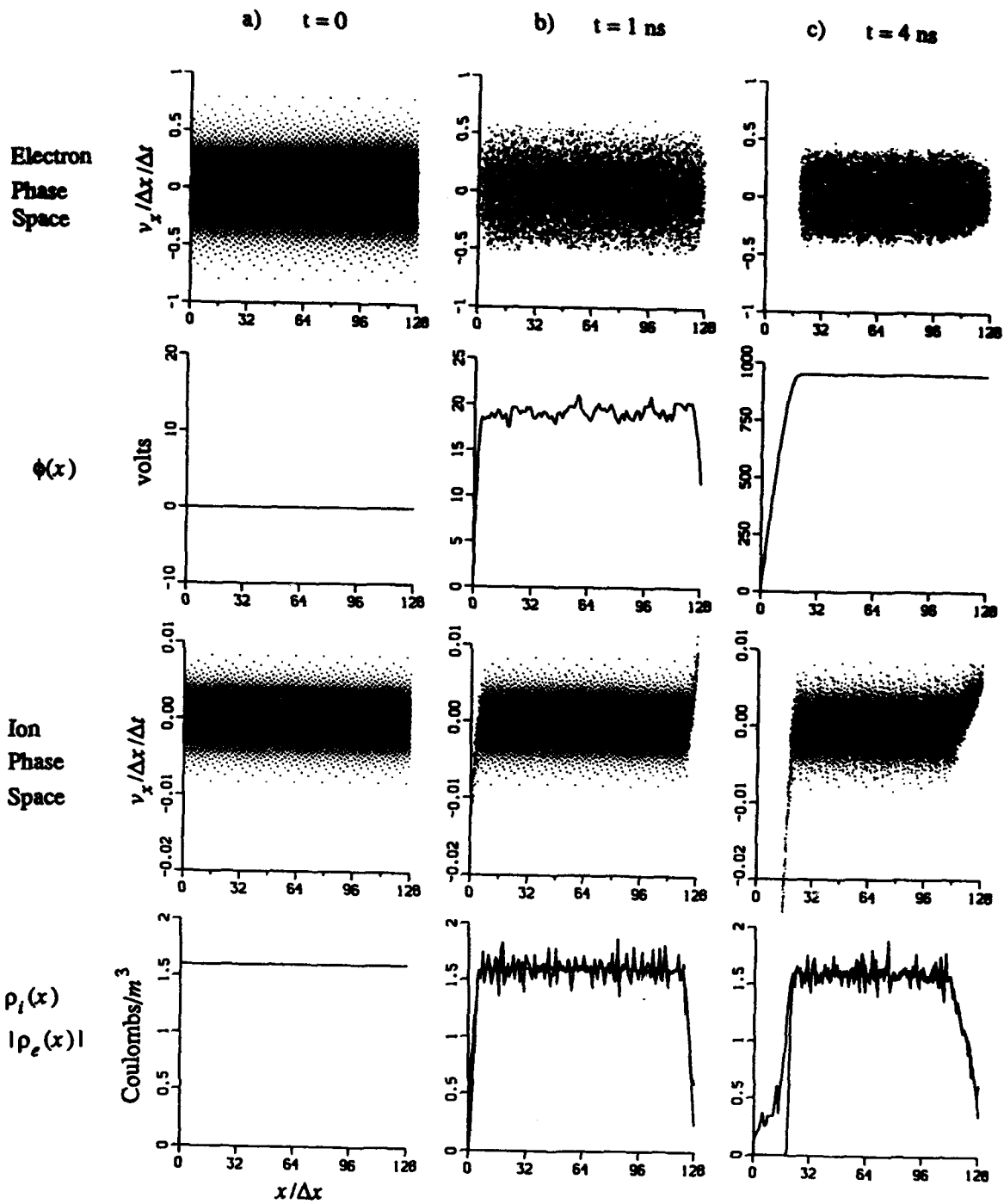


Figure 28. Electron phase space, potential $\phi(x)$, ion phase space, and electron and ion charge densities $\rho_e(x)$ and $\rho_i(x)$ at selected times: no electron emission at cathode.

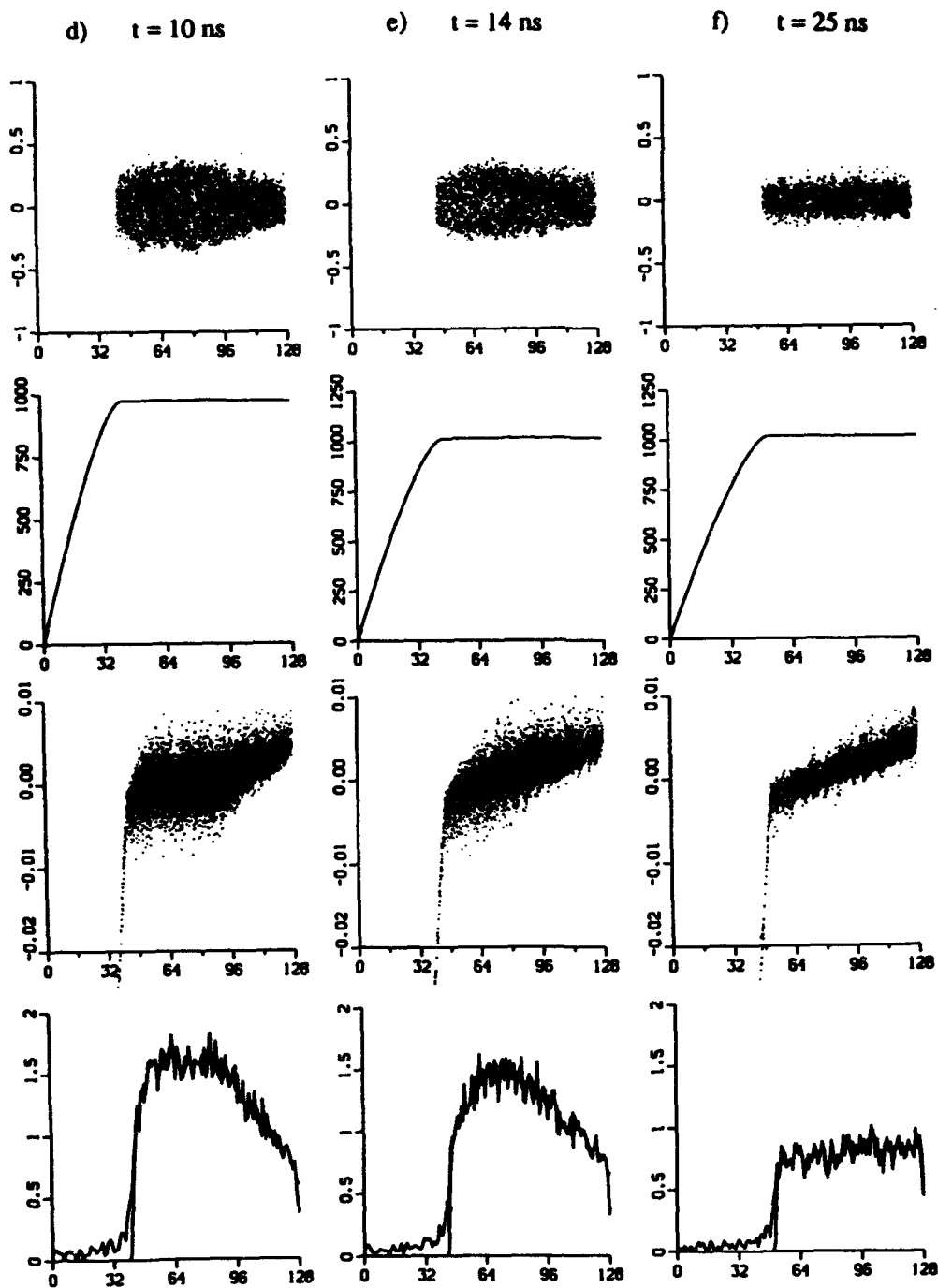


Figure 28. Electron phase space, potential $\phi(x)$, ion phase space, and electron and ion charge densities $\rho_e(x)$ and $\rho_i(x)$ at selected times: no electron emission at cathode (continued).

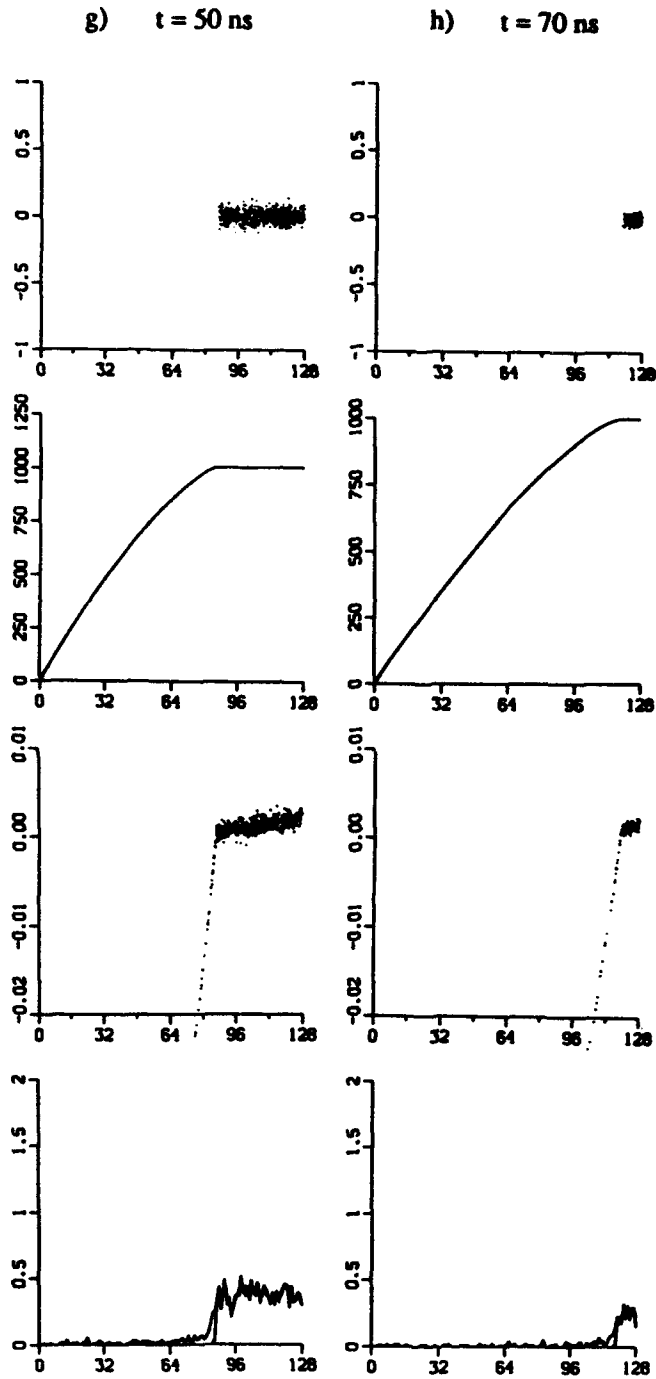


Figure 28. Electron phase space, potential $\phi(x)$, ion phase space, and electron and ion charge densities $\rho_e(x)$ and $\rho_i(x)$ at selected times: no electron emission at cathode (continued).

propagating to the right at several times C_s into the undisturbed plasma. On the right hand side of the ion phase space, the anode side, ions are accelerated toward the anode from the body of the plasma. This is the developing pre-sheath associated with the small Langmuir sheath at the anode. The edge of this pre-sheath region propagates to the left with a measured velocity of C_s . The anode pre-sheath region is also clearly visible on right hand side of the charge density distribution plot as a quasi-neutral region of reduced plasma density.

Figure 28(d) shows the situation at $t = 10$ ns, well after the sheath velocity has dropped below C_s and the sheath edge has come almost to rest. Here the left side of the ion phase space shows a developing pre-sheath region propagating out ahead of the cathode sheath toward the right at a measured velocity of C_s . In this cathode pre-sheath region ions are being accelerated back toward the sheath-plasma interface by the pre-sheath electric fields. The anode pre-sheath is also visible on the right. The charge density distribution plot again shows these developing pre-sheaths as quasi-neutral regions of reduced plasma density. The developing cathode pre-sheath is just the ion acoustic rarefaction wave reported by Widner²⁹ *et al.* in their discussion of sheath motion near a negatively biased electrode.

At $t = 14$ ns shown in Figure 28(e) the edge of the anode pre-sheath propagating to the left and the cathode pre-sheath propagating to the right meet at about $x = 70$. To the left the average ion velocity is toward the cathode while to the right the average ion velocity is toward the anode. Figure 28(f) shows the situation at a later time $t = 25$ ns corresponding to the period during which the cathode sheath again begins to accelerate to the right. The ion phase space clearly shows the cathode sheath on the left and the cathode and anode pre-sheath regions continuously joined together at about $x = 70$. Figure 28(g) shows the situation at $t = 50$ ns as the expanding cathode sheath moving at about 1.25 cm/ μ s slowly erodes away the remaining fill plasma. Finally, Figure 28(h) shows the state of the system at $t = 70$ ns shortly before the fill plasma has been completely eroded away.

Much of the phenomenology observed in the simulation can be understood in terms of an analytic relationship between the sheath velocity, the current in the external circuit and the ion density and mean velocity at the sheath edge first discussed by Sander.²³ This relationship follows from conservation of charge and the assumption of a sharp edge for the sheath. Figure 29 shows the region near the surface of the non-emitting cathode, separated from the neutral plasma region on the right by a positive ion sheath. The sheath-plasma interface is depicted in Figure 29 as a relatively sharp boundary, i.e., the plasma electron density falls off so rapidly at the sheath-plasma interface that the plasma electron contribution to the total charge of the sheath region can be neglected. This becomes a good approximation when the potential drop across the sheath becomes greater than a few times the floating potential ϕ_f , so that even the most energetic thermal electrons from the plasma can no longer penetrate more than a few Debye lengths into the sheath region before being turned back by the sheath potential.

In the theoretical considerations that follow, the density and mean velocity of the ions at the sheath-plasma interface are n_p and u_p respectively, the total positive ion space charge per unit area in the sheath is Q_s , the negative electron surface charge per unit area of the cathode is σ_c , and the magnitude of the current per unit area of electrons delivered

to the cathode by the external circuit is $J_{ext}(t)$. The time rate of change of Q_s can be written as the sum of three contributions,

$$\frac{dQ_s}{dt} = -J_{ic} + en_p \frac{dx}{dt} - en_p u_p. \quad (4-12)$$

The first term on the right hand side is the current of ions lost from the left of the sheath region by absorption at the cathode surface. The second and third terms represent the current of ions which enter the right hand side of the sheath region from the neutral plasma at the moving sheath-plasma interface. Similarly, $d\sigma_c/dt$ is given by

$$\frac{d\sigma_c}{dt} = J_{ic} - J_{ext}. \quad (4-13)$$

The change in surface charge $d\sigma_c/dt$ is a balance between the charge deposited by ions from the sheath and the electrons from the external circuit. Notice that $d\sigma_c/dt$ contains no electron current contribution due to the thermal electron flux from the plasma, under the assumption that the sheath potential is sufficient to turn back any thermal electrons at the sheath-plasma interface. Now applying Gauss's Law to the region indicated in Figure 29 yields

$$\sigma_c = -Q_s. \quad (4-14)$$

Differentiating with respect to time and substituting dQ_s/dt and $d\sigma_c/dt$ from Equations (4-12) and (4-13) gives

$$J_{ext}(t) = en_p \left(\frac{dx}{dt} - u_p \right). \quad (4-15)$$

Equation (4-15) states that the rate at which electrons are delivered to the cathode by the external circuit is equal to the rate at which ions enter the moving sheath from the plasma.

Equation (4-15) is an exact consequence of Gauss's Law and charge conservation when the sheath edge is sufficiently sharp to neglect the contribution of the plasma electrons to the total charge density of the sheath region. An approximate form of Equation (4-15) often discussed in the literature^{23,24} may be obtained by making two additional approximations. First, the so called "displacement current" must be neglected. In other words, $d\sigma_c/dt \ll J_{ext}$ so that from Equation (4-13) $J_{ic} \approx J_{ext}$ in Equation (4-15). If in addition the sheath velocity is sufficiently small so that the sheath does not expand very much during the time required for a plasma ion to transit the sheath, the ion current J_{ic} is given approximately by the stationary Child-Langmuir space charge limited ion current. Hence, the approximate form of Equation (4-15) becomes

$$en_p \left(\frac{dx}{dt} - u_p \right) = \frac{4}{9} \epsilon_0 \left(\frac{2e}{m_i} \right)^{1/2} \frac{V_D^{3/2}}{x^2}, \quad (4-16)$$

as used by Widner and Poukey.²⁴

Equation (4-15) provides a useful consistency check on the simulation results. Dividing both sides of Equation (4-15) by J_{ext} shows that $en_p(\dot{x} - u_p)/J_{ext} \simeq 1$ when the sheath

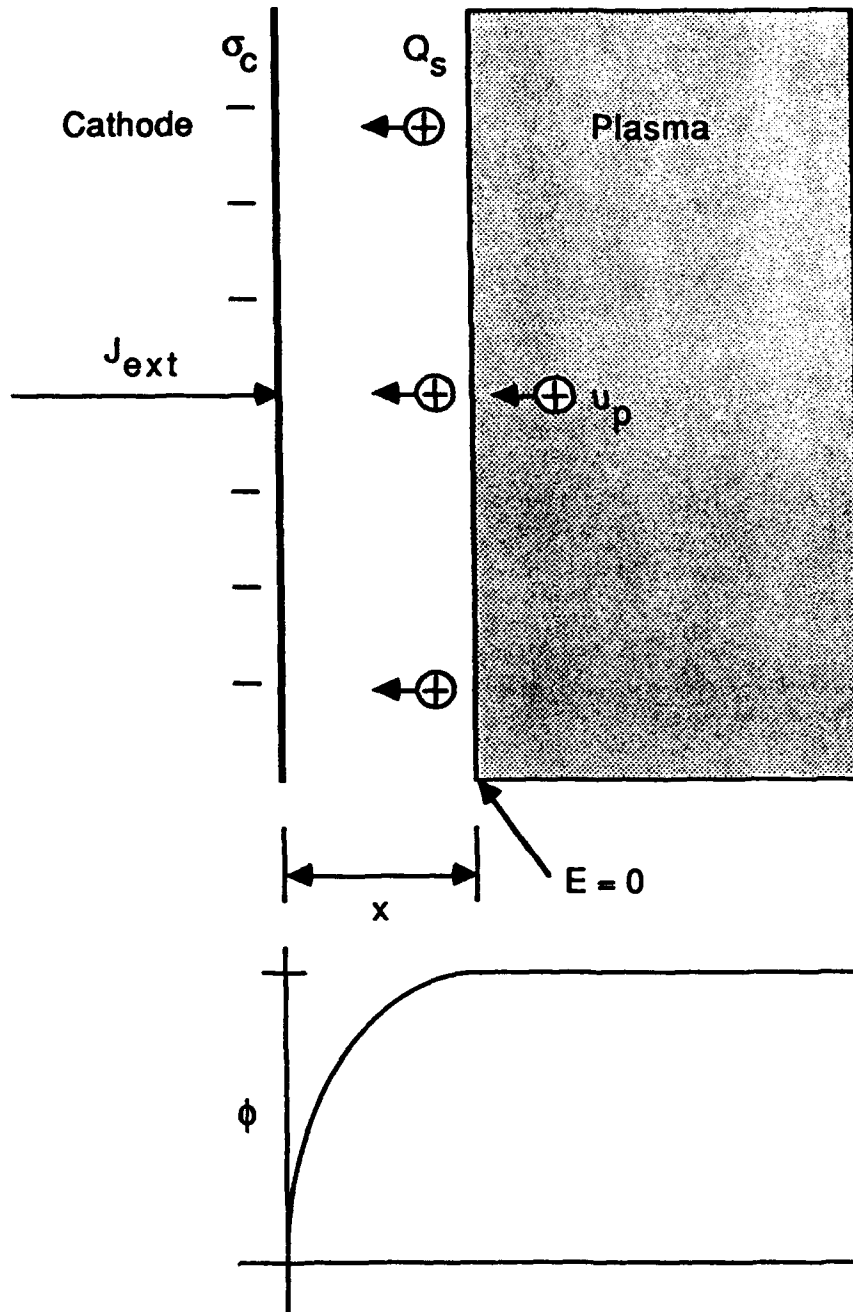


Figure 29. Expanded view of cathode region: no electron emission.

potential becomes greater than a few times ϕ_f . During the computation this ratio is determined using the local values of n_p and u_p at the moving sheath-plasma interface as well as the corresponding simulation values of \dot{x} and J_{ext} . After an initial period before $t = 2$ ns during which the sheath potential grows rapidly to about $7\phi_f$, the ratio drops to 1 and remains at this value out to $t = 75$ ns, the point at which all the plasma has been removed from the gap so that n_p approaches zero.

Equation (4-15) also provides a convenient basis for understanding the general character of the sheath evolution observed in Figure 28. Consider a sheath propagating into an undisturbed plasma of uniform density n_p with a velocity $dx/dt > C_s$. Then $u_p \approx 0$, and Equation (4-15) shows that the velocity of the sheath edge is proportional to the current in the external circuit. Hence, the rising current in the external circuit drives the initial rapid penetration of the sheath observed during the first 8 ns of conduction. Similarly, the limitation of the current in the external circuit by the growing sheath voltage drop is responsible for the sheath velocity falling below C_s at about $t = 6.8$ ns.

4.4 CATHODE WITH SPACE-CHARGE LIMITED EMISSION.

Space-charge limited (SCL) electron emission from the cathode changes PFD behavior due to the additional presence of an electron beam that can interact with the background plasma. In the simulation below all parameters are unchanged except for the emission of electrons from the cathode such that the electric field vanishes. Now a well defined bipolar sheath develops at the cathode. The emitted electrons are accelerated across this sheath and stream through the fill plasma with some mean velocity v_b . A strong beam-plasma instability develops once the sheath potential has grown sufficiently so that v_b exceeds $v_{th} = \sqrt{2kT_e/m_e}$. In the initial stages of the interaction unstable electrostatic waves are launched from the edge of the cathode sheath and propagate toward the anode growing spatially in amplitude until they begin to trap the beam at some distance away from the cathode. The character of the beam-plasma interaction is largely determined by the value of the parameter $\eta = n_b/n_e$, the ratio of the beam electron density to the total electron density $n_e = n_b + n_p$. The weak beam limit $\eta \ll 1$ in spatially infinite systems has been extensively studied since the 1960's and is well described by single wave trapping theory.³⁰ The linear theory of the beam-plasma instability in this limit can easily be obtained from the Bohm-Gross dispersion relation for the one-dimensional beam-plasma system,

$$(\omega_p^2 + \frac{3}{2}k^2 v_{th}^2)/\omega^2 + \omega_b^2/(\omega - kv_b)^2 = 1. \quad (4-17)$$

Applying the expansion technique of O'Neill and Malmberg³¹ to Equation (4-17) with v_{th} in the range $0 \leq v_{th}/v_b \leq 0.2$ yields a maximum spatial growth rate for the unstable waves of

$$k_i = \frac{\sqrt{3}}{2} \left(\frac{\eta}{3}\right)^{1/3} \left(\frac{v_b}{v_{th}}\right)^{2/3} \frac{\omega_p}{v_b}, \quad (4-18)$$

with wavenumber

$$k = \left[1 + \frac{3}{4} \left(\frac{v_{th}}{v_b}\right)^2 + \frac{1}{2} \left(\frac{\eta}{3}\right)^{1/3} \left(\frac{v_b}{v_{th}}\right)^{2/3} \right] \frac{\omega_p}{v_b}. \quad (4-19)$$

The weak beam linear theory illustrates some important trends. As the voltage across the cathode sheath increases so does the beam velocity. The wavelength of the instability then increases according to Equation (4-19) while the spatial growth rate is reduced. Beam trapping then begins further away from the cathode boundary. However, the results from linear theory are only qualitatively relevant for the present investigation. In the PFD simulations η ranges between 0.15 and 0.35 during the conduction phase so that the observed beam-plasma interaction always lies far outside the weak beam regime.

According to Morey and Boswell,³² the beam-plasma interaction in a bounded, one-dimensional system with arbitrary η is classifiable into a linear regime for $0 \leq \eta \leq 0.05$, and into two nonlinear regimes with $0.05 \leq \eta \leq 0.3$ and $0.3 \leq \eta \leq 0.7$. The PFD in our simulation always operates in the nonlinear regimes, which are characterized by strong non-linear heating of the plasma and variety of other non-linear effects. These are clearly seen in the simulations presented below.

Figure 30 shows the diode current and voltage during the first 80 ns in a diode with SCL emission. In contrast to Figure 27 without SCL emission, where the voltage develops immediately, the voltage in Figure 30 has a 34 ns long low-voltage conduction phase, followed by a sudden opening phase that generates a peak diode voltage about 4.8 times that of the charge voltage. Without SCL emission the current reaches an early peak of 3 A (10 A/cm^2), while with SCL the current increases until opening to over 30 A (or 100 A/cm^2)

In lieu of the movie, Figure 31 illustrates the detailed evolution of the phase space, potential and charge density distributions for the PFD with SCL emission. The initial state in Figure 31(a) is identical to Figure 27(a), except that the scales are different to accommodate the subsequent development. Figure 31(b) at $t = 10 \text{ ns}$ shows that the potential distribution within the diode gap is essentially flat and the diode acts as a short circuit. This situation is typical of the internal state of the diode for the first 18 ns of conduction, the period prior to the formation of the bipolar sheath.

As the conduction phase progresses a well defined bipolar sheath begins to develop at the cathode starting at about $t = 18 \text{ ns}$. The voltage across this sheath quickly exceeds the thermal energy $kT_e \simeq 5 \text{ eV}$, and the instability turns on almost immediately thereafter at about $t = 20 \text{ ns}$. Figure 31(c) shows the state of the system at a slightly later time $t = 23 \text{ ns}$. A 20 V bipolar sheath is present on the left hand side of the potential distribution in Figure 31(c) with the unstable waves visible to the right of the sheath. These waves are launched from the sheath edge and propagate toward the anode on the right, growing spatially as they move away from the cathode until they trap the beam. The electron phase space plot in Figure 31(c) shows beam trapping beginning at about $x = 45$. Most of the trapped beam electrons are carried along by the waves. However, some are scattered out of the waves and are left behind to become part of the plasma electron distribution. Conversely, the waves trap not only beam electrons but also plasma electrons leading to the formation of electron holes like the ones visible in the electron phase space of Figure 31(c). These holes can propagate all the way across the gap as coherent structures and may provide an efficient mechanism for rapidly removing plasma electrons from the diode gap. The electric fields of the waves also accelerate the remaining plasma electrons leading to the rapid heating of the plasma electron distribution which is already visible in the electron.

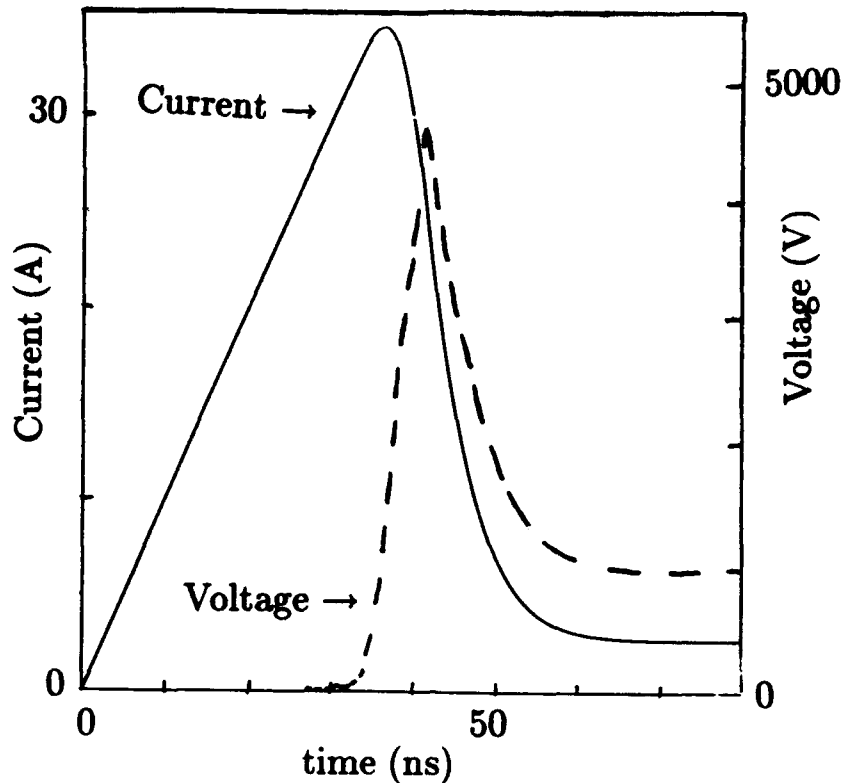


Figure 30. PFD with hydrogen plasma fill $n_i = 10^{13} \text{ cm}^{-3}$ with space-charge limited electron emission from cathode surface.

phase space plot of Figure 31(c). The net voltage drop at the instant of the snapshot in Figure 31(c) happens to be about 31 V, but in fact this value is rather arbitrary because the potential at the anode boundary oscillates at the plasma frequency with a maximum amplitude determined by the beam-plasma interaction. The amplitude is sufficient to cause reflection of some beam electrons at the anode boundary.

As the heating progresses the hot plasma electrons escape from the diode faster than the more massive ions, resulting in an increasing net positive charge for the plasma and the corresponding potential hump in the diode gap. Figure 31(d) shows the state of the system at $t = 28 \text{ ns}$. The construction of this potential hump is well underway and the heating of the plasma electron distribution is readily apparent. The wave behavior of the interaction becomes more chaotic and the time average point in space at which beam trapping begins tends to move toward the right, away from the cathode toward the anode boundary. Correspondingly, the structure of the electron holes becomes less coherent and the holes less prominent.

As the process continues the amplitude of the potential hump grows while trapping tends to occur further and further toward the right. Wave trapping gives way to a state in which much of the trapping occurs due to reflection of the beam by the oscillating potential at the anode boundary. Figure 31(e) shows the situation for $t = 33 \text{ ns}$ at the very end of the conduction phase. Here the potential plot shows a distribution for $\phi(x)$

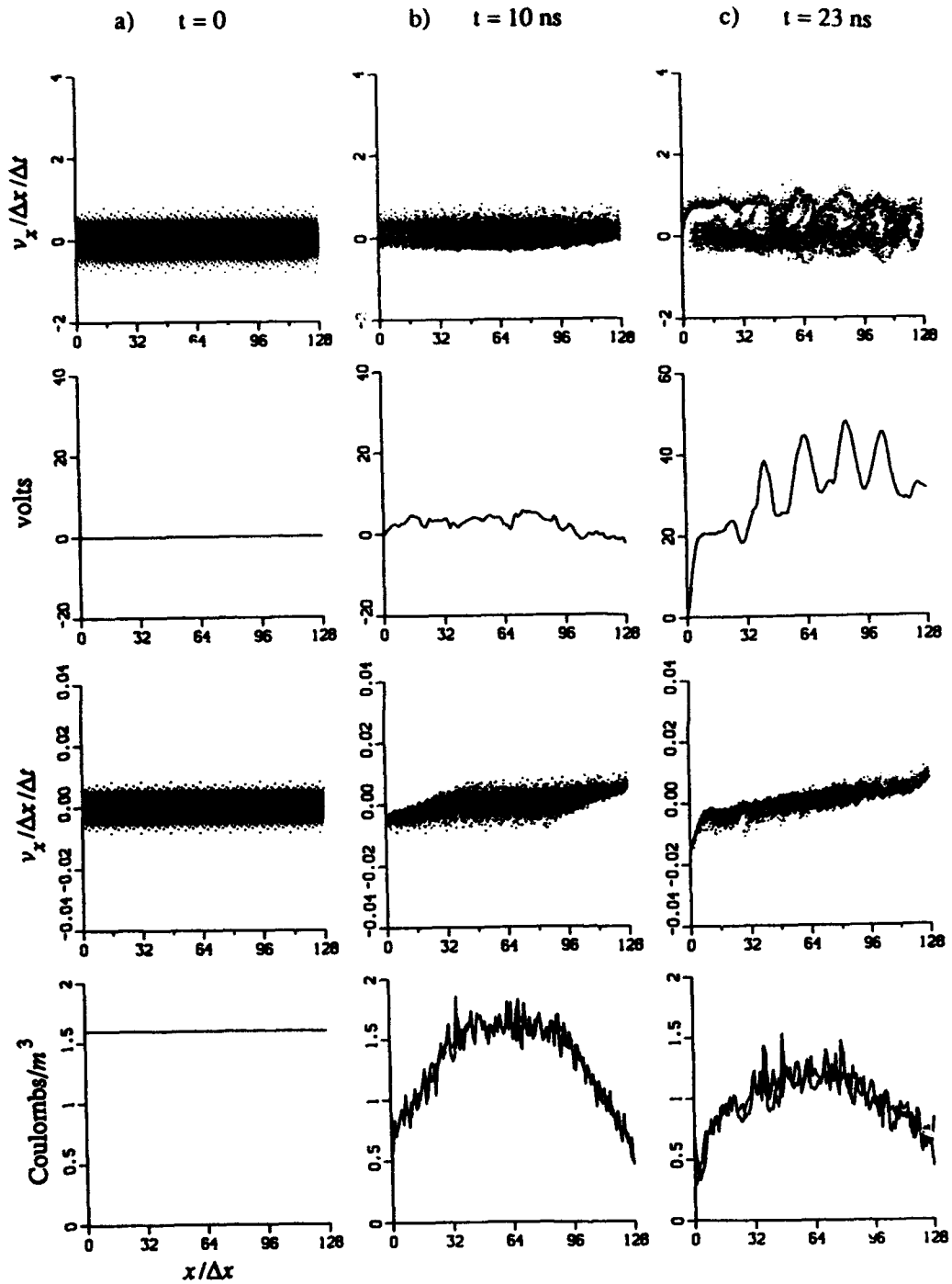


Figure 31. Electron phase space, potential $\phi(x)$, ion phase space, and electron and ion charge densities $\rho_e(x)$ and $\rho_i(x)$ at selected times: space-charge limited electron emission at cathode.

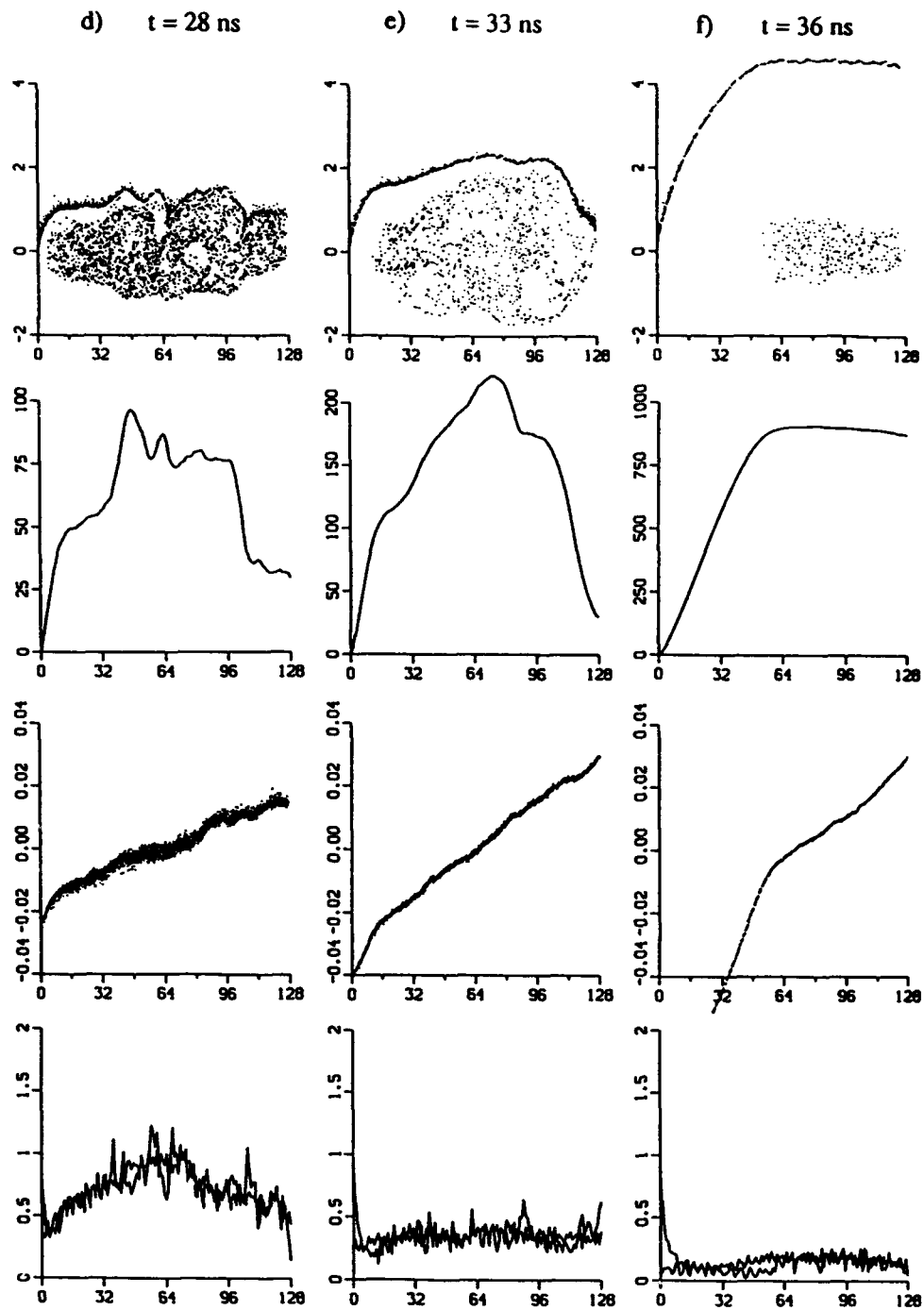


Figure 31. Electron phase space, potential $\phi(x)$, ion phase space, and electron and ion charge densities $\rho_e(x)$ and $\rho_i(x)$ at selected times: space-charge limited electron emission at cathode (continued).

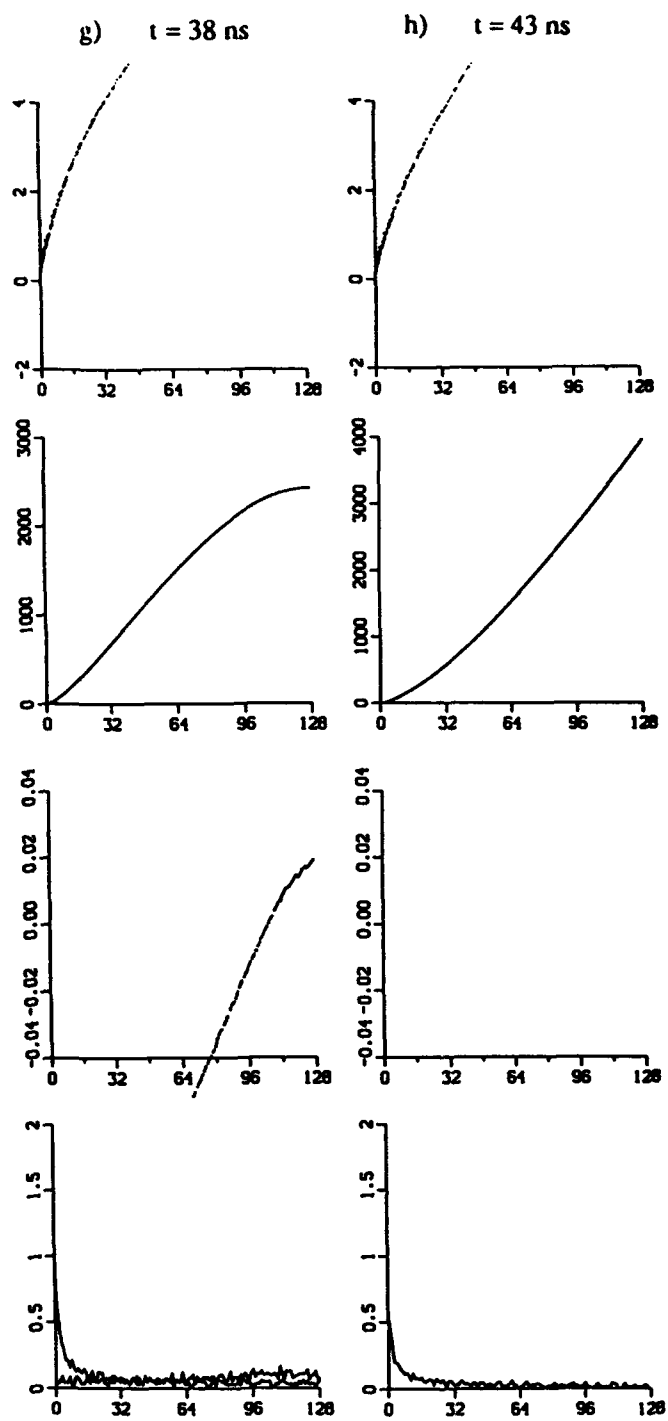


Figure 31. Electron phase space, potential $\phi(x)$, ion phase space, and electron and ion charge densities $\rho_e(x)$ and $\rho_i(x)$ at selected times: space-charge limited electron emission at cathode (continued).

with a maximum of 222 V (or 2.2 kV/cm) near the center of the gap, even though the diode voltage is only about 30 V (or 0.3 kV/cm). At this point all of the beam trapping is taking place at the anode boundary as can be seen in the electron phase space plot. The ion phase space plot in Figure 31(e) shows that the potential hump accelerates the ions, creating a significant enhancement of the ion current to both cathode and anode. As a result the ratio of emitted electron current to ion current at the cathode is substantially lower for this state than the classical value $\sqrt{m_p/m_e} \simeq 43$ for a simple bipolar sheath with hydrogen ions. In Figure 31(e) the ratio of electron to ion current is about 27.

At $t = 34$ ns the conduction phase ends and a rapid transition to a high voltage opening phase begins. This transition is characterized by the termination of electron trapping and the formation of a large bipolar sheath at the cathode. The sheath expands rapidly and sweeps the remaining ions out of the diode gap. Figure 31(f) shows the state of the system at $t = 36$ ns. The conduction phase potential distribution of Figure 31(e) has made an extremely rapid transition to the bipolar distribution shown in Figure 31(f). The total diode voltage in Figure 31(f) has already reached nearly 1 kV as the bipolar sheath expands and grows. The phase space plot shows that electrons accelerated across this sheath no longer interact with the remaining plasma.

The bipolar sheath expands very rapidly to the right reaching a peak sheath velocity of about 23 cm/ μ s. By $t = 38$ ns shown in Figure 31(g) the sheath edge has already reached the anode. All of the plasma electrons have left the diode at the anode side and the remainder of the ions are being removed at the cathode. Finally, Figure 31(h) shows the state of the system at $t = 43$ ns after all of the ions have been swept out of the diode gap. The diode now operates as a simple SCL electron diode with the characteristic Child-Langmuir $x^{4/3}$ potential distribution.

The overall effect of the beam-plasma interaction on the plasma electrons is the result of a balance between two processes. On the one hand the heating of the plasma electrons and the transport of plasma electrons to the anode by propagating electron holes tend to deplete the plasma electrons. On the other hand trapping of electrons out of the emitted beam adds to the plasma electrons. On balance the plasma loss processes dominate. Figure 32 illustrates this point. The lower curve represents the time history of the total charge in the emitted beam. The middle curve is the total charge in the plasma electron distribution. The upper curve is the sum of the two, the total electron charge in the diode. An electron is considered to belong to the beam if it was emitted from the cathode and has not turned around. An electron is considered to belong to the plasma electron distribution if either it was present in the initial fill plasma or it was emitted from the cathode but has turned around once or more. Figure 32 shows that after the instability turns on at $t = 20$ ns, the plasma electron population is rapidly depleted until the total charge in the plasma electron distribution equals the total charge in the beam at about the time that opening begins. Hence, the net effect of the beam-plasma interaction during the conduction phase is that the emitted electrons increasingly provide for the neutralization of the plasma ions.

Comparison of the results for the SCL emission case discussed above with the no emission case of Section 3 clearly illustrates the fundamental difficulty with the classical PFD model.²⁵ With SCL emission the system evolves through a series of states which are far from the bipolar equilibrium state hypothesized by the classical model. As a result,

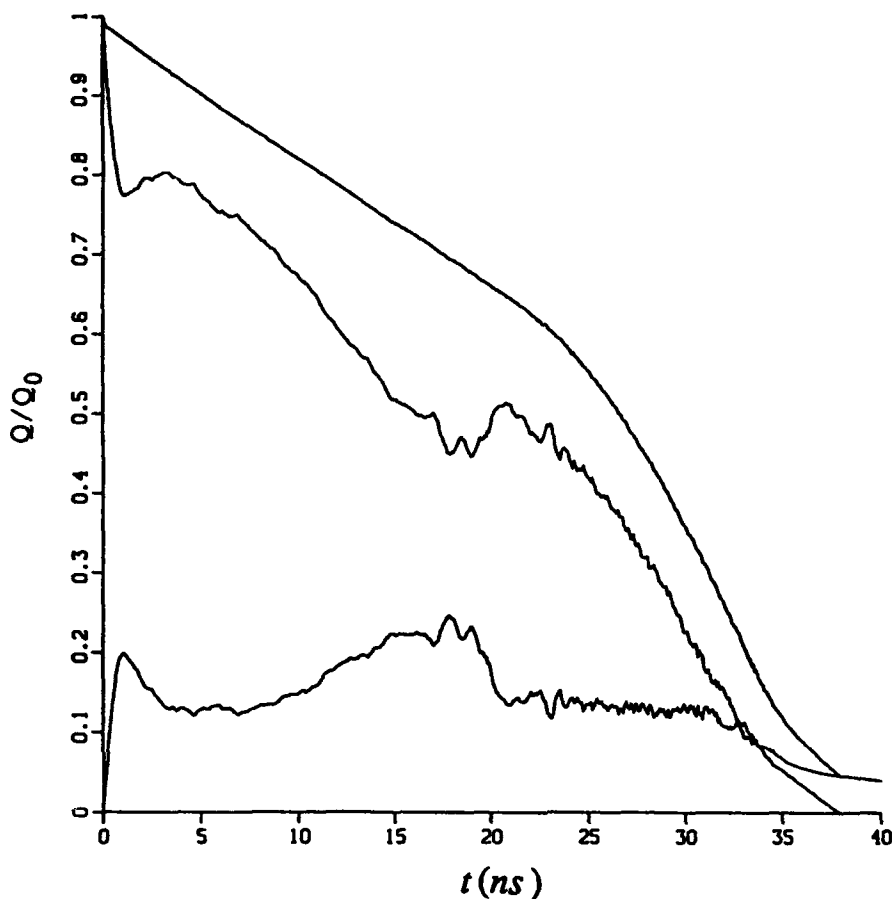


Figure 32. Total beam electron charge (lower), total plasma electron charge (middle) and total (beam + plasma) electron charge (upper) for SCL emission case. Values are normalized to the total electron charge present in the initial fill plasma at $t = 0$.

the scaling predictions for conduction time, conducted current and other quantities must be modified substantially.

4.5 SCALING IN THE SIMULATIONS.

This Section discusses the scaling of conduction time and current in the computations with model parameters such as the initial dI/dt , plasma density, gap width and ion mass. The conduction time, t_c , is defined as the time interval from the onset of current flow at $t = 0$ to the time at which a significant net diode voltage drop begins to develop. The conducted current, I_c , is the corresponding diode current at time t_c . During the conduction phase the diode acts as a short circuit ($V_D \simeq 0$). Then the initial current risetime dI/dt

is V_0/L where V_0 is the initial charge voltage on the external capacitor and $L = 1 \mu\text{H}$ is the circuit inductance. Hence, the scaling of I_c and t_c with initial dI/dt can be found by varying V_0 while keeping L and the other model parameters held fixed.

Figures 33 and 34 show how I_c and the corresponding value of t_c scale with V_0 and hence initial dI/dt for three different initial plasma densities $n_i = 10^{12} \text{ cm}^{-3}$, 10^{13} cm^{-3} and 10^{14} cm^{-3} . The plotted points are simulation results. The simulation results for I_c and t_c versus V_0 lie roughly on a straight line on this log-log plot, suggesting an approximate power law dependence for these quantities. The solid curves are least squares fits to the simulation data for a given density assuming a power law dependence for I_c and t_c on V_0 .

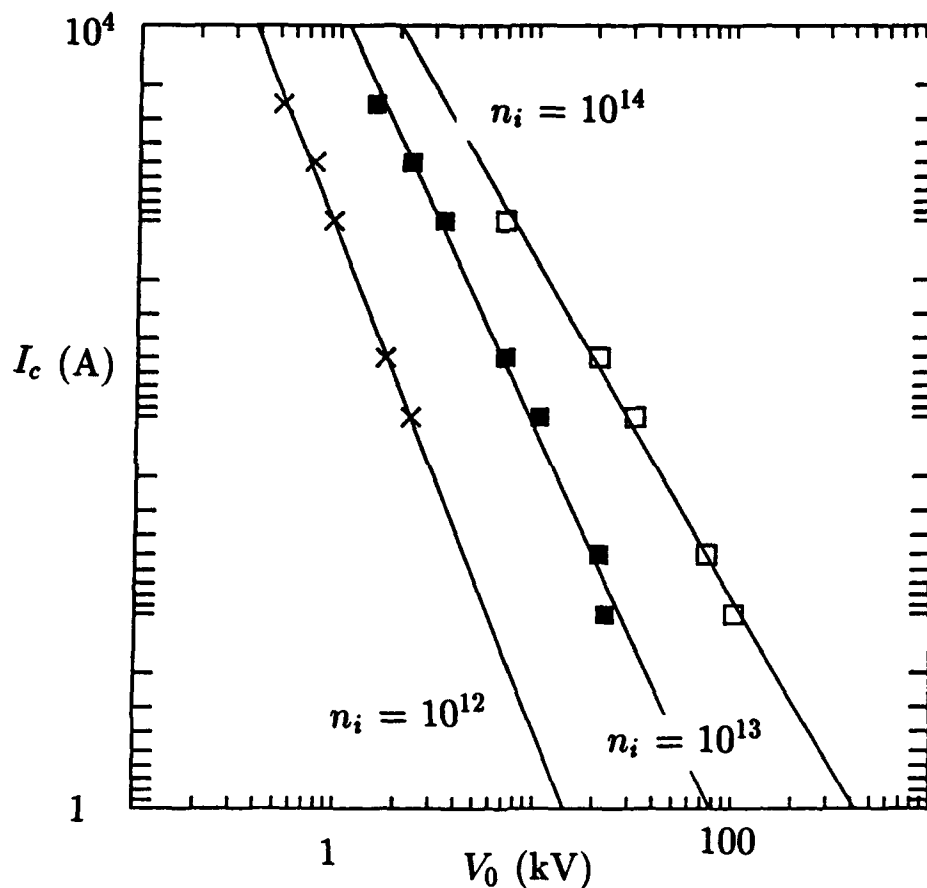


Figure 33. Conduction current I_c versus V_0 for fill densities $n_i = 10^{12} \text{ cm}^{-3}$, $n_i = 10^{13} \text{ cm}^{-3}$, and $n_i = 10^{14} \text{ cm}^{-3}$. Solid curves are least squares fits to a power law V_0^δ .

The scaling from the simulations for I_c with dI/dt is in sharp contrast to the classical PFD model. The classical model predicts that switching occurs at a current threshold that is completely determined by the properties of the fill plasma, but completely independent of the initial dI/dt . Figure 33 shows that the simulation result for I_c increases with increasing dI/dt to a power ~ 0.5 that depends slightly on initial plasma density. For example, at $n_i = 10^{13} \text{ cm}^{-3}$ I_c is fitted well by $(dI/dt)^{0.463}$. The optimum exponent varies slowly

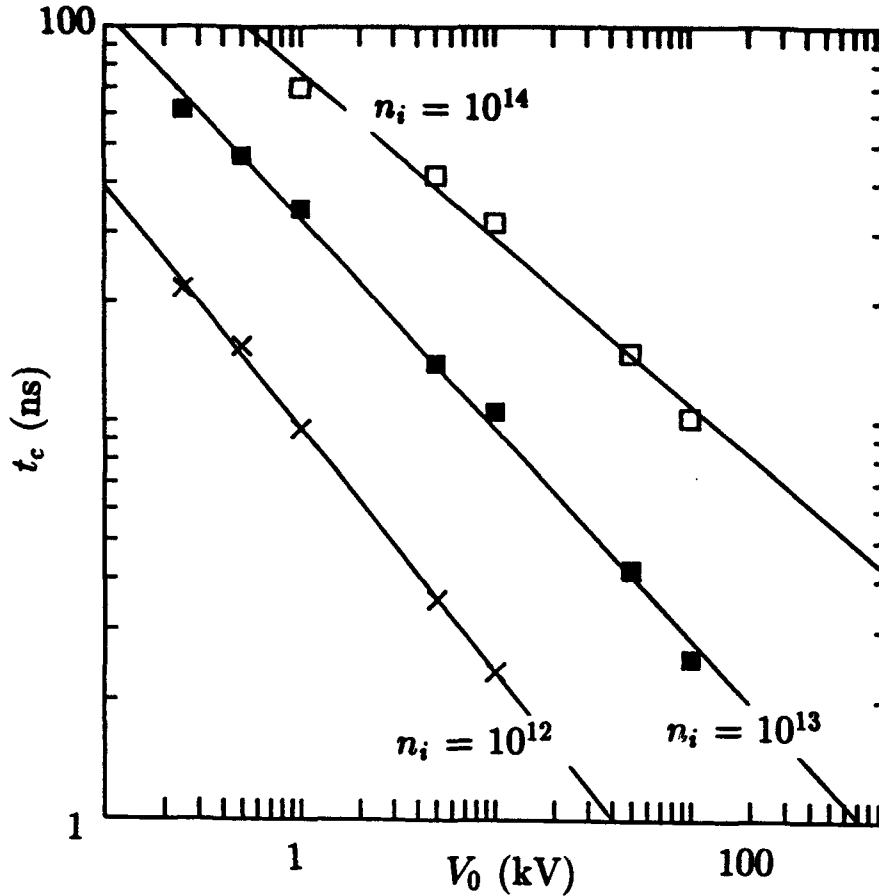


Figure 34. Conduction time t_c versus V_0 for fill densities $n_i = 10^{12} \text{ cm}^{-3}$, $n_i = 10^{13} \text{ cm}^{-3}$, and $n_i = 10^{14} \text{ cm}^{-3}$. Solid curves are least squares fits to a power law V_0^δ .

with density from 0.396 at $n_i = 10^{12} \text{ cm}^{-3}$ to 0.581 for $n_i = 10^{14} \text{ cm}^{-3}$. Correspondingly, t_c scales like dI/dt to about the -0.5 power, again with a slight variation of the exponent with density. The variations in the power law exponent for I_c and t_c with density are, of course, related since the ratio I_c/t_c must always be proportional to dI/dt .

Figure 35 shows how the conduction current I_c scales with initial plasma density n_i for fixed current risetime dI/dt obtained by setting $V_0 = 1 \text{ kV}$ and $V_0 = 10 \text{ kV}$. The solid curve is a power law least squares fit with the initial capacitor voltage $V_0 = 10 \text{ kV}$ (or an initial $dI/dt = 10 \text{ kA}/\mu\text{s}$). The result is that I_c scales as $(n_i)^{0.56}$. For $n_i = 10^{13} \text{ cm}^{-3}$ and below the simulation data for $V_0 = 1 \text{ kV}$ show similar power law dependences, but above $n_i = 10^{13} \text{ cm}^{-3}$ scaling curves flatten out, showing that the power law dependence is only approximate.

In the classical model²⁵ I_c does not vary with gap width d , but the simulations give a different result. Figure 36 shows t_c versus the gap width d from a series of simulation runs with $n_i = 10^{13} \text{ cm}^{-3}$ and V_0 held fixed at $V_0 = 1 \text{ kV}$. The solid curve is least squares fit indicating a scaling of t_c as $d^{0.52}$. This prediction should be easily testable in an experiment.

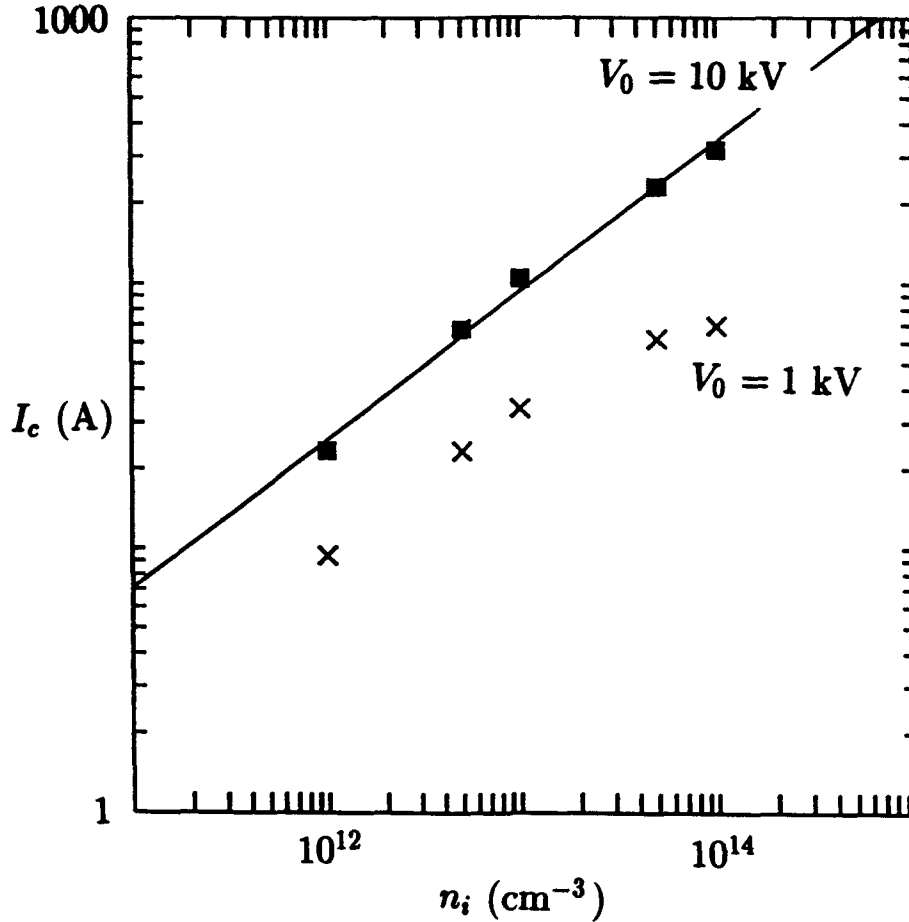


Figure 35. Conduction current I_c versus n_i for $V_0 = 1$ kV and 10 kV. Solid curve is a least squares fit to a power law n_i^δ

Voltage amplification during opening V_p/V_0 is particularly relevant. Figure 37 shows the peak value V_p of the voltage compared to the initial voltage on the capacitor V_0 , as a function of V_0 and hence the initial current risetime dI/dt at three different initial plasma densities $n_i = 10^{12} \text{ cm}^{-3}$, $n_i = 10^{13} \text{ cm}^{-3}$, and $n_i = 10^{14} \text{ cm}^{-3}$. The decrease of V_p/V_0 with increasing dI/dt at fixed density is readily apparent. It should be noted that for each density there is a value of dI/dt (or V_0) above which no net voltage amplification is obtained. Correspondingly, at fixed dI/dt , V_p/V_0 increases with increasing fill density.

All of the scaling results discussed above were obtained using a hydrogen fill plasma. How do these change with mass of the plasma ions? Figure 28 is a log-log plot of the ratio of emitted electron current to ion current into the cathode at the onset of opening, J_e/J_i , as function of the ion mass m_i normalized to the proton mass m_p . The initial voltage V_0 is held fixed at 1 kV, and $n_i = 10^{13} \text{ cm}^{-3}$. The solid curve is a least squares fit to an assumed power law dependence for the simulation data. Apparently J_e/J_i at the onset of opening scales like $(m_i/m_p)^{1/2}$. Hence, even though the value of J_e/J_i is not simply given by $\sqrt{m_i/m_e}$ as would be the case in the classical bipolar model, the simulation result still

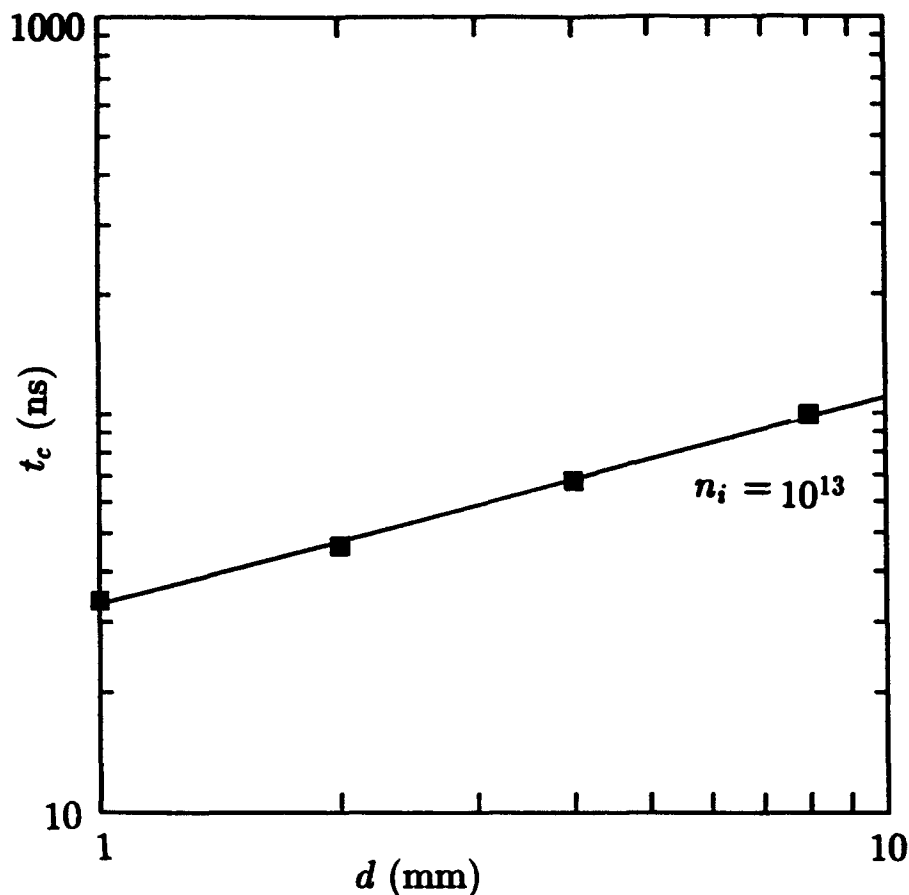


Figure 36. Conduction time t_c versus gap width d for $n_i = 10^{13} \text{ cm}^{-3}$, $V_0 = 1 \text{ kV}$. Solid curve is a least squares fit to a power law $d^0.6$.

shows that,

$$J_c/J_i = \alpha \sqrt{m_i/m_e}, \quad (4-20)$$

where $\alpha \simeq 0.63$ for $n_i = 10^{13} \text{ cm}^{-3}$ as shown. The dashed line in Figure 38 shows the bipolar value $\sqrt{m_i/m_e}$ for comparison. Note that Figure 38 contains physically unrealizable ion masses up to $10^4 m_p$, approaching the limiting case of infinite ion mass to be treated elsewhere.

Figure 39 shows the simulation results for t_c versus m_i/m_p , from runs with V_0 at 1 kV, and densities $n_i = 10^{12} \text{ cm}^{-3}$ and $n_i = 10^{13} \text{ cm}^{-3}$. For both densities t_c scales like $m_i^{0.22}$. However, for $n_i = 10^{12} \text{ cm}^{-3}$ and beyond $m_i/m_p = 100$ the t_c scaling curve flattens out and approaches a constant limiting value $t_c = 40.8 \text{ ns}$ shown by the horizontal dashed line. For the higher density, $n_i = 10^{13} \text{ cm}^{-3}$ the data suggests a much higher limiting value for t_c , and a much larger value of m_i/m_p for the onset of saturation. Theoretical considerations elsewhere suggest that the saturation value of t_c should be about $2.2 \mu\text{s}$.

Saturation of t_c with m_i demonstrates a surprising result, namely, that a low voltage conduction phase exists even for infinitely massive ions. Since the ions can not move the system never relaxes to a bipolar equilibrium state during the opening process. Research

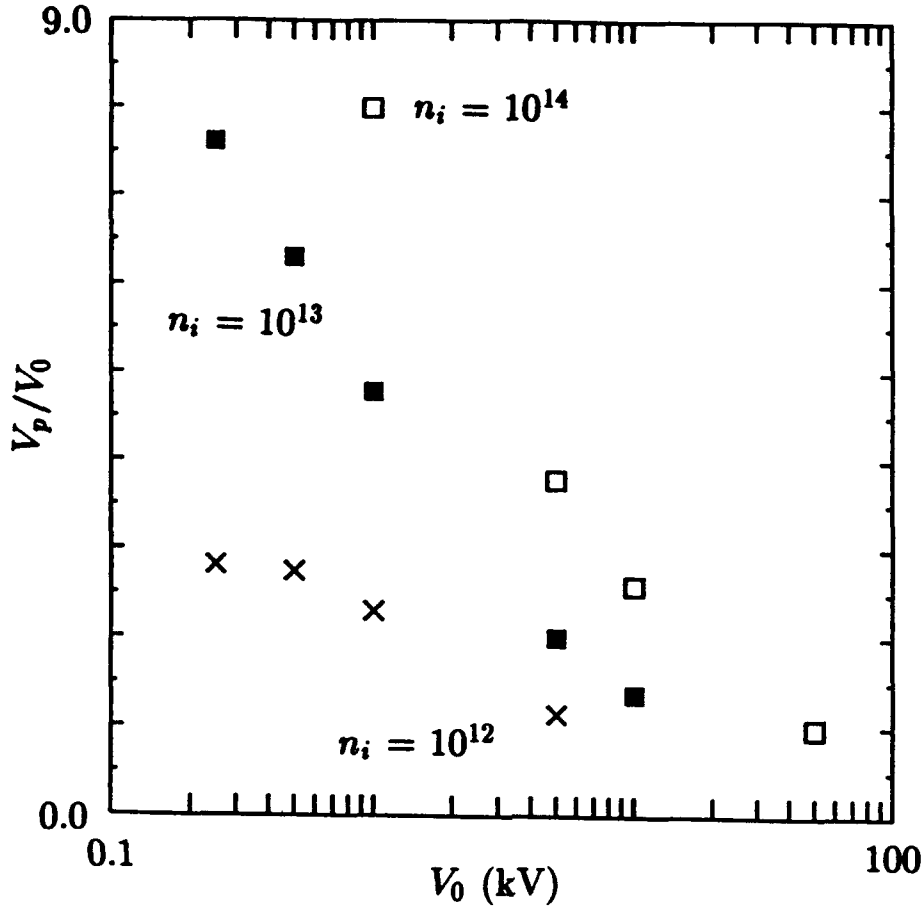


Figure 37. Voltage amplification (V_p/V_0 versus V_0 : $V_0 = LI$) for fill densities $n_i = 10^{12}$ cm^{-3} , $n_i = 10^{13}$ cm^{-3} , and $n_i = 10^{14}$ cm^{-3} .

on the PFD with immobile ions, presented elsewhere, clarifies the conduction process for the PFD studied here.

4.6 CONCLUSIONS.

This section demonstrates by an explicit numerical example why the classical bipolar model²⁵ incorrectly describes the conduction phase of a magnetized PFD or POS. This failure arises from violation of the bipolar equilibrium state assumed to exist during the conduction phase. Instead the low voltage conduction phase is characterized by the growth of a large potential maximum near the center of the diode gap, while the voltage across the diode remains small, and a J_e/J_i ratio that is substantially lower than the bipolar value $\sqrt{m_i/m_e}$. This state is maintained by the nonlinear interaction of the emitted electrons with the plasma fill. The onset of the opening phase is characterized by the termination of electron trapping and the rapid transition to a bipolar equilibrium state. These processes take place even if the ions are infinitely massive. If the particle ions are replaced by a stationary uniform background of positive charge, the system still has a low voltage conduction phase followed by an opening phase in which a significant diode voltage drop

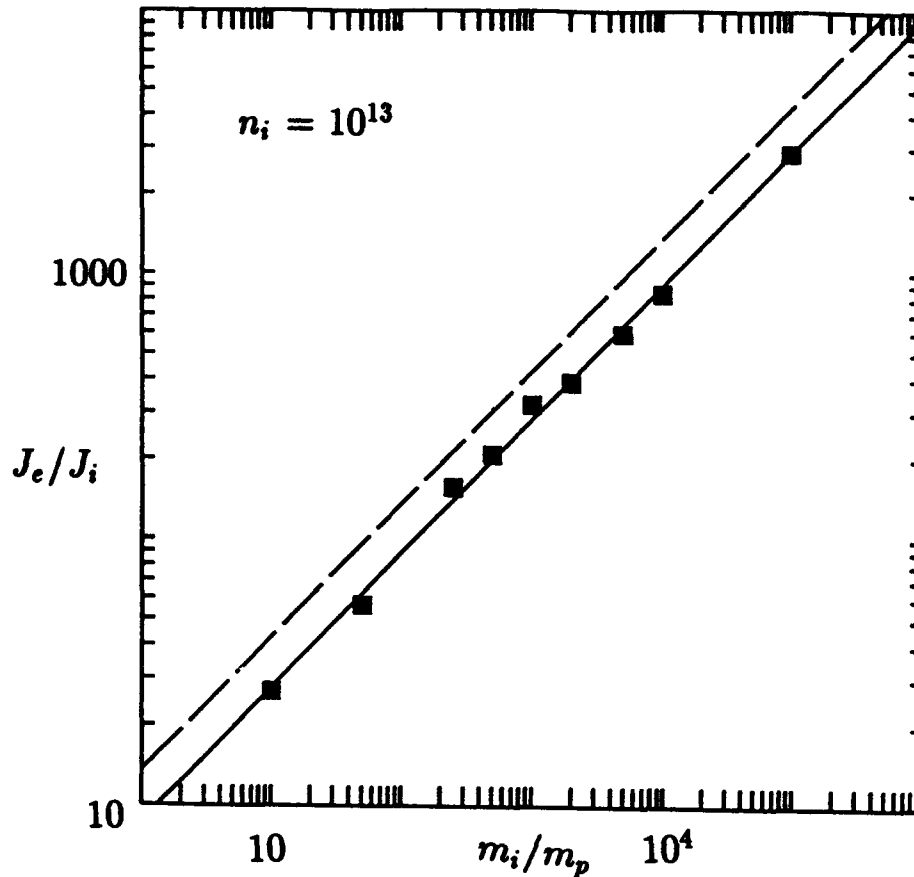


Figure 38. Value of J_e/J_i at the onset of opening versus m_i/m_p $n_i = 10^{13} \text{ cm}^{-3}$, $V_0 = 1$ kV. Solid curve is a least squares fit to a power law m_i^6 . The dashed curve is the bipolar value $\sqrt{m_i/m_e}$.

develops. This infinite mass ion case is smoothly obtained from the case of finite ion mass as m_i increases.

The model for the operation of a magnetized PFD outlined above makes a variety of testable predictions. For example, with fixed plasma fill and increasing V_0 the current conducted before opening increases roughly like $\sqrt{V_0}$, while the classical model²⁵ predicts a constant current. The present model also predicts ions on the anode side of the diode with energies significantly greater than the diode voltage during the conduction phase. These ions betray the presence of the growing potential hump during conduction. Finally, the rapid oscillation of the potential near the anode during the conduction phase might be expected to generate electromagnetic noise near the plasma frequency. Hence, a PFD with plasma fill of $n_i = 10^{13} \text{ cm}^{-3}$ should produce roughly 28 GHz microwave noise during the conduction phase.

Perhaps the simplest and most distinguishing prediction of the simulations is the effect of an initial ion drift. According to the classic model²⁵ the ion drift affects the low-voltage current, while in the present model the ion drift is virtually irrelevant. Recent

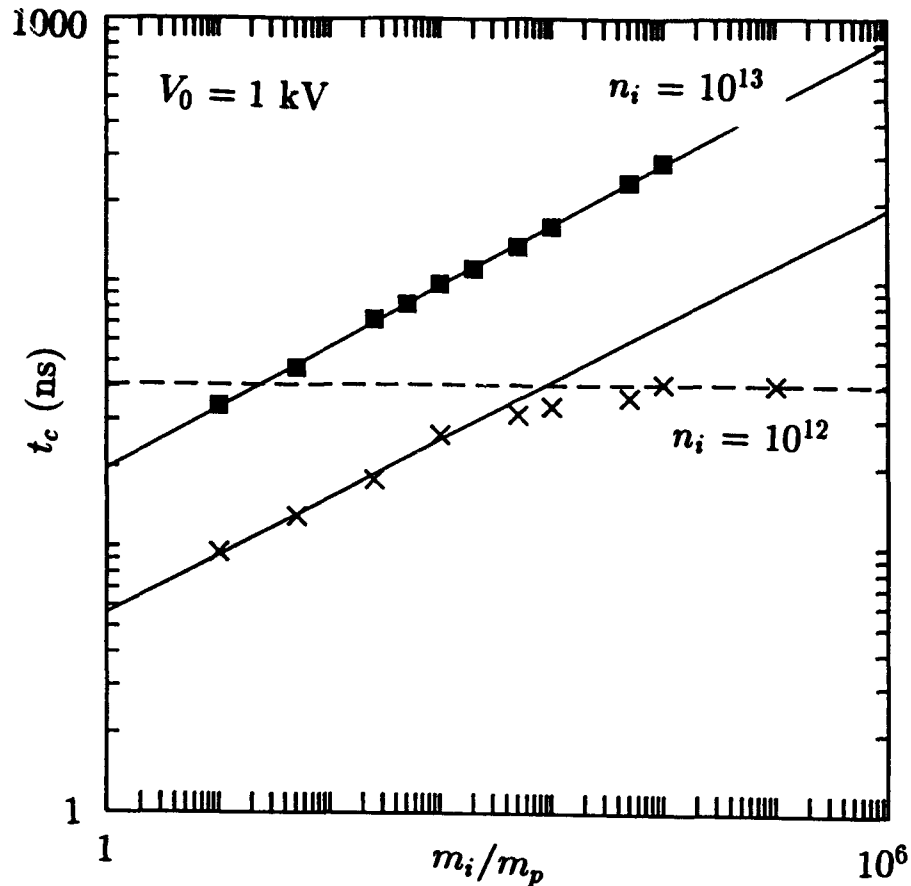


Figure 39. Conduction time t_c versus m_i/m_p for fill densities $n_i = 10^{12}$ cm $^{-3}$ and $n_i = 10^{13}$ cm $^{-3}$ with $V_0 = 1$ kV. Upper solid curve is a least squares fit of the form m_i^6 . The lower solid curve is a least squares fit for $m_i/m_p \leq 100$. The dashed curve is the limit of t_c for $n_i = 10^{12}$ cm $^{-3}$.

experiments³³ seem to support this prediction. In these experiments the fill plasma was created in situ in the diode gap by ionization of a low pressure gas instead of being injected at trans-sonic velocities as happens with plasma guns. In these experiments there is a low voltage conduction phase of about 50 ns followed by a rapid opening. This behavior disagrees with the classical model²⁵ but agrees with the simulations presented here.

SECTION 5

THEORY OF THE PLASMA FILLED DIODE WITH IMMOBILE IONS

This chapter discusses the Plasma Filled Diode (PFD) coupled to an external LC driver circuit in the limit of infinite ion mass.³⁴ In this limit the immobile ions act as a fixed spatially uniform background of positive charge. Although ion motion was thought to be essential to PFD opening, the simulations with immobile ions still show a low voltage conduction phase with a characteristic potential hump, followed by a high voltage opening phase. An analytic theory for the potential hump agrees with the simulation, especially when trapped electrons are included. The considerations are extended to the PFD with mobile ions.

5.1 INTRODUCTION.

The previous section considers a planar Plasma Filled Diode (PFD) coupled to an external LC circuit, as in Figure 26 of Section 4. During the conduction phase the PFD has a bipolar sheath at the cathode, which accelerates electrons to velocities in excess of the electron thermal speed of the background plasma, causing a strong beam-plasma interaction. The effect of this interaction is to drive the plasma electrons out of the diode on a timescale faster than the response time of the ions. As a result, the plasma charges up, and a potential hump develops in the diode gap, with a peak potential much larger than the voltage drop. The surprise in Section 4 was that conduction and opening phase persist even when the plasma ions are infinitely massive.

This section is a detailed investigation of the PFD with infinitely massive ions, which act as a constant uniform background of positive charge. This situation has analytic solutions, which provide a quantitative explanation for the conduction and opening processes observed in simulations, even for the case of mobile ions. Section 5.2 presents a typical simulation of a PFD with space-charge limited emission of electrons and immobile ions. Section 5.3 contains the analytical solution for the space charge flow problem. Section 5.4 shows the agreement of these solutions with the simulations. Section 5.5 adds the effects from trapped electrons, which further improves the agreement with simulations. Section 5.6 discusses how the insight gained from the analytic theory in the immobile ion limit provides a quantitative explanation for the operation of the PFD with mobile ions.

5.2 PFD SIMULATION WITH IMMOBILE IONS.

Figure 40 shows the diode current and voltage obtained from the simulation code PDW1 (see Section 4.2) for a PFD with an initial plasma fill of immobile ions with constant density $n_i = 10^{12} \text{ cm}^{-3}$ and an equal density of plasma electrons. The initial charge voltage on the external capacitor is $V_0 = 1 \text{ kV}$, and the remaining model parameters are as in Section 4. Space-charge limited (SCL) electron emission is allowed from the cathode surface. The diode voltage of Figure 40 has a 41 ns long low voltage conduction phase followed by an opening phase with a significant diode voltage. The voltage increases monotonically to V_0 during the opening phase, in marked contrast to the voltage amplification factor ~ 2.3 observed with mobile hydrogen ions at the same fill density in Section 4.

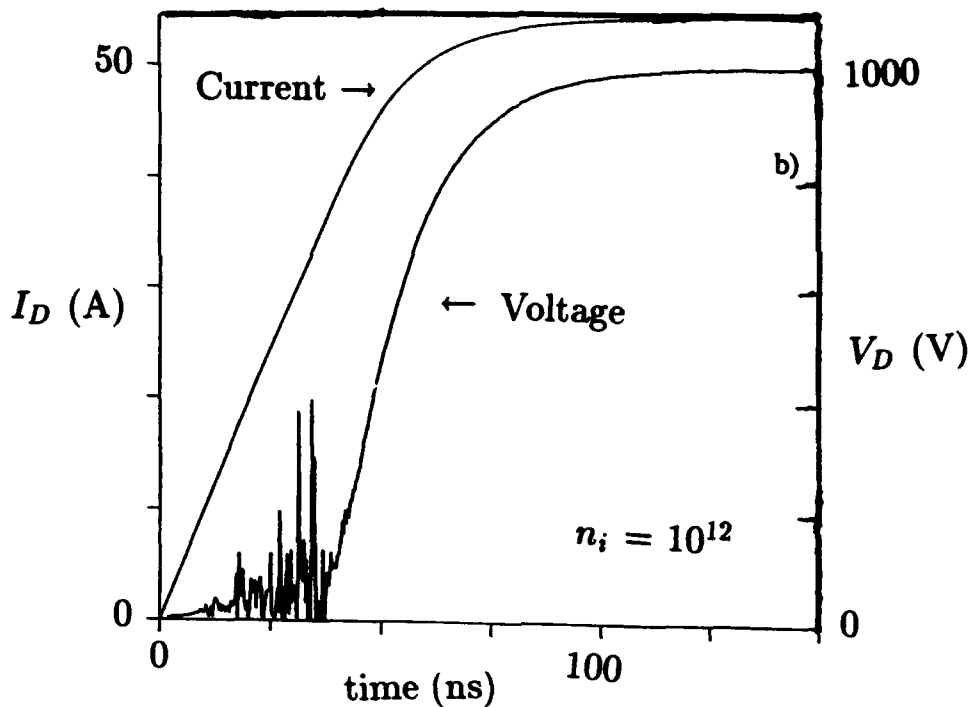


Figure 40. Diode voltage and current with density $n_i = 10^{12} \text{ cm}^{-3}$ of spatially immobile ions, and SCL electron emission from cathode surface.

Figures 41(a) through (h) are a sequence of snapshot plots done at selected times during the first 150 ns of the simulation. At each time indicated the figure shows the electron v_x versus x phase space and the potential distribution $\phi(x)$ in the diode gap. In the phase space plots all velocities are in scaled units normalized to $\Delta x/\Delta t$. The position x across the diode gap is measured in grid cell units from $x = 0$ at the cathode on the left to $x = 128$ at the anode on the right. The potential ϕ is given in Volts.

The initial state is a spatially uniform distribution of Maxwellian electrons with $T_e = 5 \text{ eV}$ and the fixed background of immobile ions with number density $n = 10^{12} \text{ cm}^{-3}$. The potential distribution is initially identically zero across the diode gap. As the current begins to flow in the external circuit the initial plasma electrons are rapidly replaced by beam electrons emitted off the cathode. By $t = 8 \text{ ns}$ this replacement is 95 % complete. Figure 41(c) shows the state of the diode at this time. The potential plot of Figure 41(c) shows a series of potential humps in the diode gap. Initially these humps have a small spatial scale and very small amplitude. Figures 41(c) through (f) are snapshots taken at 2 ns intervals from $t = 8 \text{ ns}$ out to $t = 14 \text{ ns}$ which demonstrate how these potential humps evolve as time progresses. The hump nearest the cathode grows rapidly in both spatial width and amplitude at the expense of the humps to its right until by $t = 14 \text{ ns}$ it spans the full width of the diode gap. The electron phase space plot in Figure 41(c) shows that trapping of electrons out of the emitted beam is taking place due to oscillations of the potential minimum on the right hand side of each of the humps, with most of the trapping taking place at the right hand side of the hump nearest the cathode. By $t = 14 \text{ ns}$ the

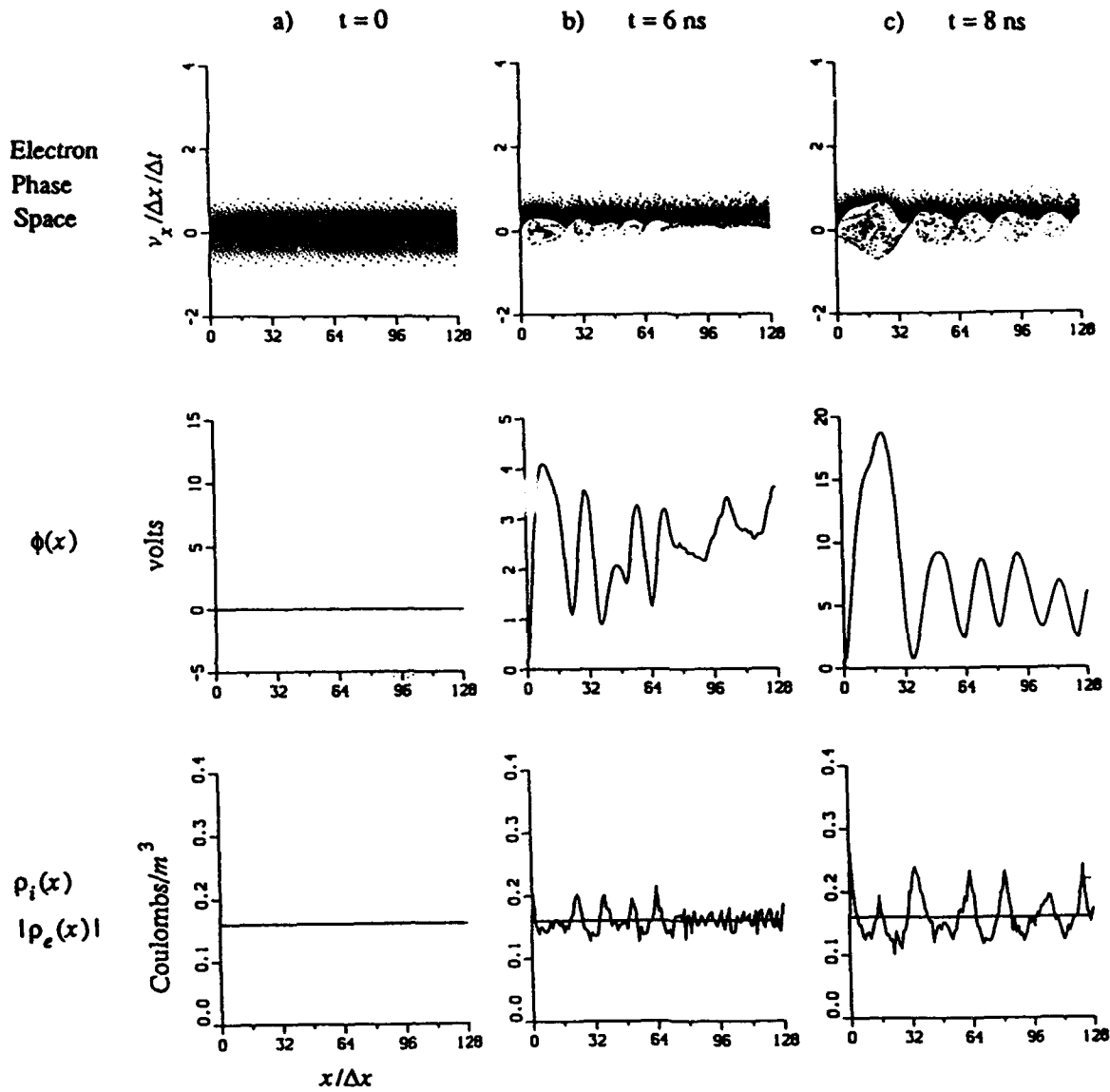


Figure 41. Electron phase space v_x versus x , potential $\phi(x)$, and electron and ion densities $\rho_e(x)$ and $\rho_i(x)$ at selected times for an immobile ion density $n_i = 10^{12} \text{ cm}^{-3}$.

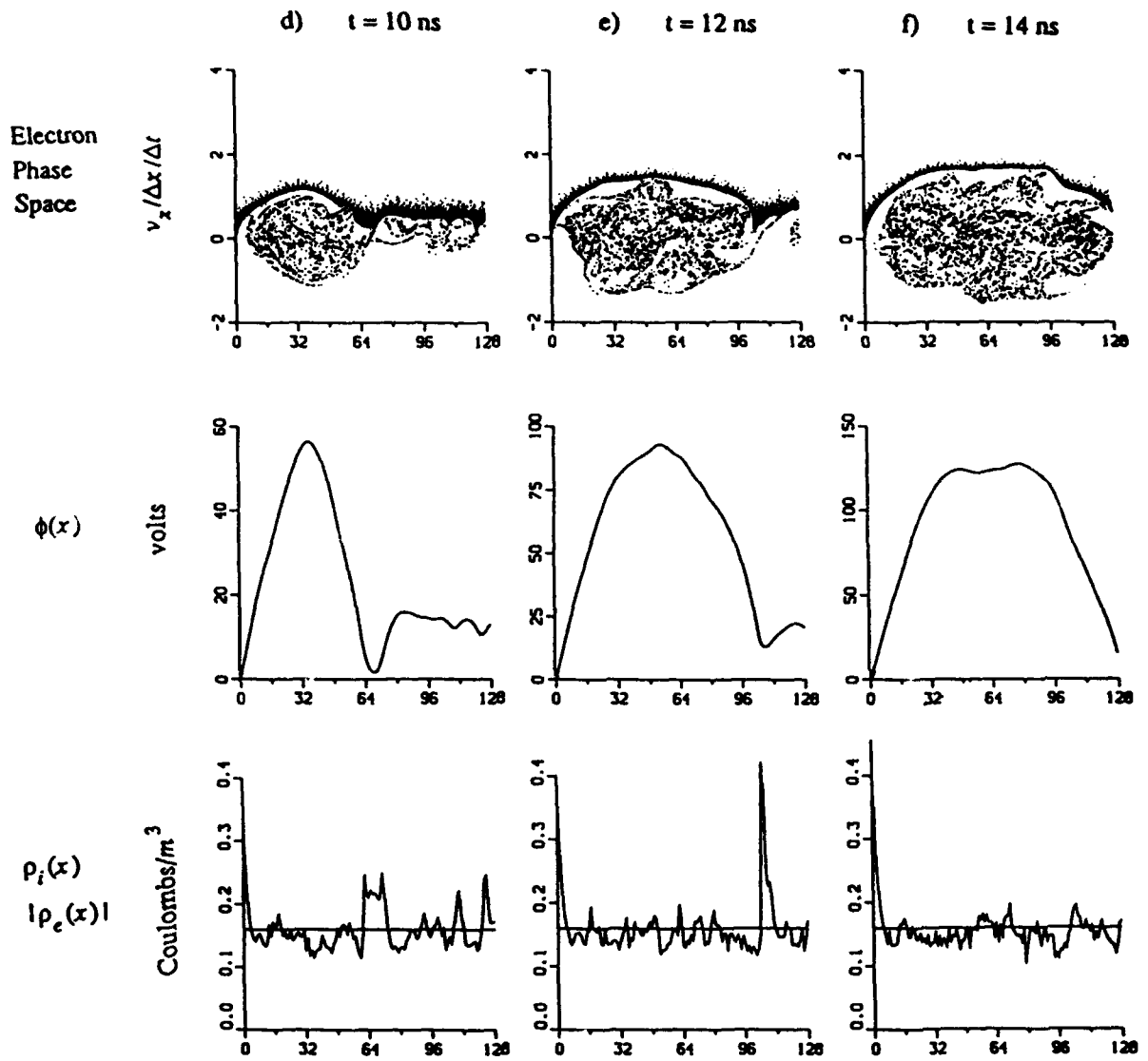


Figure 41. Electron phase space v_x versus x , potential $\phi(x)$, and electron and ion densities $\rho_e(x)$ and $\rho_i(x)$ at selected times for an immobile ion density $n_i = 10^{12} \text{ cm}^{-3}$ (continued).

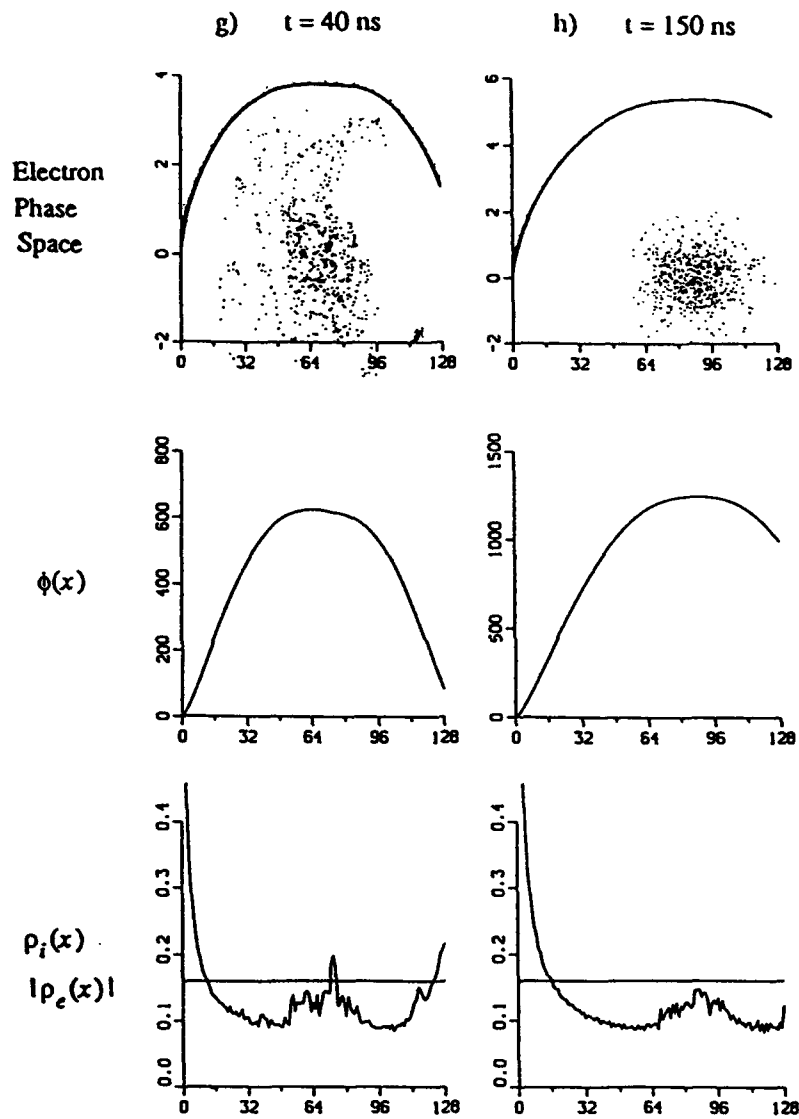


Figure 41. Electron phase space v_x versus x , potential $\phi(x)$, and electron and ion densities $\rho_e(x)$ and $\rho_i(x)$ at selected times for an immobile ion density $n_i = 10^{12} \text{ cm}^{-3}$ (continued).

hump nearest the cathode spans the full width of the gap and all trapping takes place by the oscillation of the potential at the anode.

As the conduction phase proceeds the amplitude of the potential hump continues to grow even though the total diode voltage drop seen by the external circuit remains small. Figure 41(g) shows the state of the diode at the end of the conduction phase at $t = 40$ ns. By this time the potential maximum has grown to 634 V. Most of the trapped electrons are lost and they are no longer being renewed by further trapping of electrons out of the beam.

As the opening phase progresses the total voltage drop slowly grows. Figure 41(h) shows the state of the diode late in the opening phase at $t = 150$ ns. By this time the total voltage drop has reached 994 V while the potential maximum is 1254 V. The maximum is not located at the center of the diode gap but at $x = 87.3 \Delta$ instead. Even in the final open state there still remains a potential hump whose amplitude is significantly greater than the total voltage drop, and a small population of electrons that is permanently trapped inside this hump.

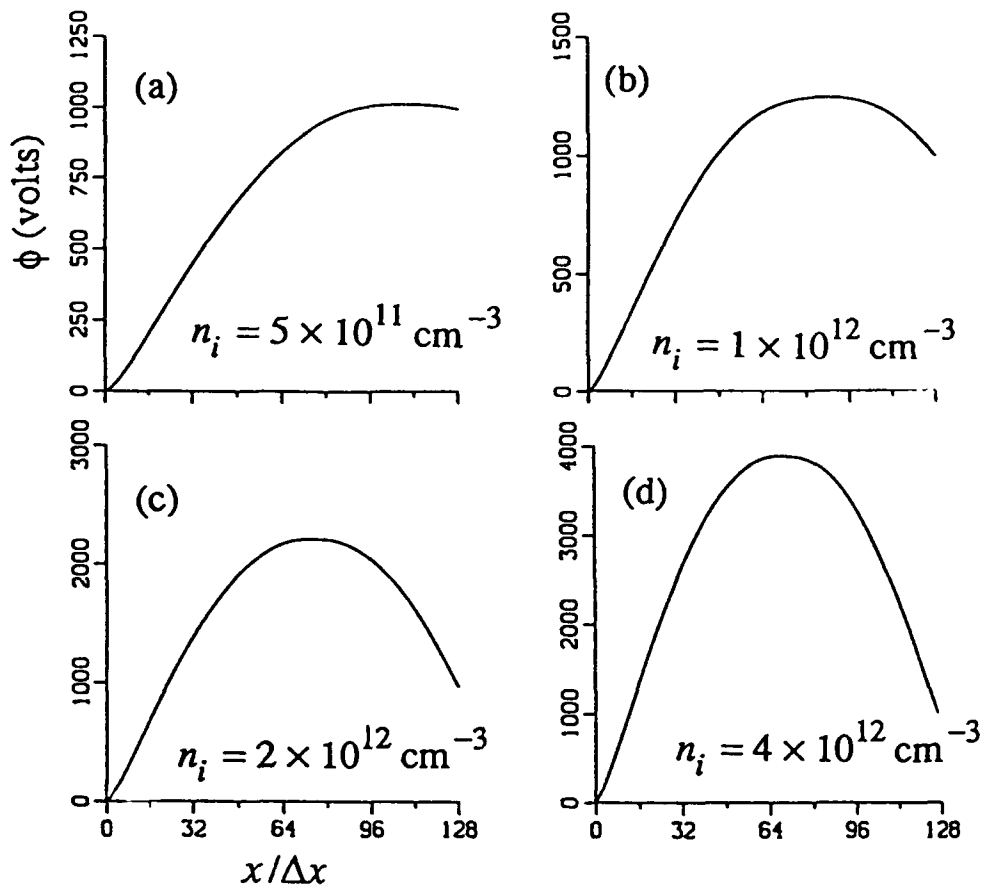


Figure 42. Potential distribution after opening for different ion densities.

The spatial position x_m and amplitude of the potential maximum ϕ_m in the final state are strong functions of the density of the immobile ion background. Figures 42(a)

through (d) show the potential distribution in the diode gap after complete opening, for four ion background densities n_i . Figure 42(d) shows that for $n_i = 4 \times 10^{12} \text{ cm}^{-3}$ the final amplitude of the potential maximum is 3893 V, nearly 4.5 times the total voltage drop, and the position of the maximum is at $x_m = 69$, near the center of the diode gap at $x = 64$. As n_i decreases, ϕ_m decreases while x_m moves toward the anode. Figure 42(a) shows the distribution at $n_i = 5 \times 10^{11} \text{ cm}^{-3}$. Here $\phi_m = 1016 \text{ V}$, only slightly greater than the total voltage drop of 1 kV, and $x_m = 108.7$, near the anode at $x = 128$. For $n_i = 3 \times 10^{11} \text{ cm}^{-3}$, not shown in Figure 42, the potential maximum is at the anode, and for n_i below $3 \times 10^{11} \text{ cm}^{-3}$ no potential maximum is present. As the ion density vanishes the potential distribution $\phi(x)$ in the final state looks increasingly like the $x^{4/3}$ distribution for SCL electron flow in the absence of ion space charge.

Figure 43 shows the simulation results for the conduction time t_c as function of the ion density n_i (points), fitted by a power law $t_c \sim n_i^\delta$, where $\delta \simeq 1.8$. Extrapolating this scaling to ion densities exceeding 10^{13} cm^{-3} gives $t_c = 2.2 \mu\text{s}$, too long for the computations to observe opening.

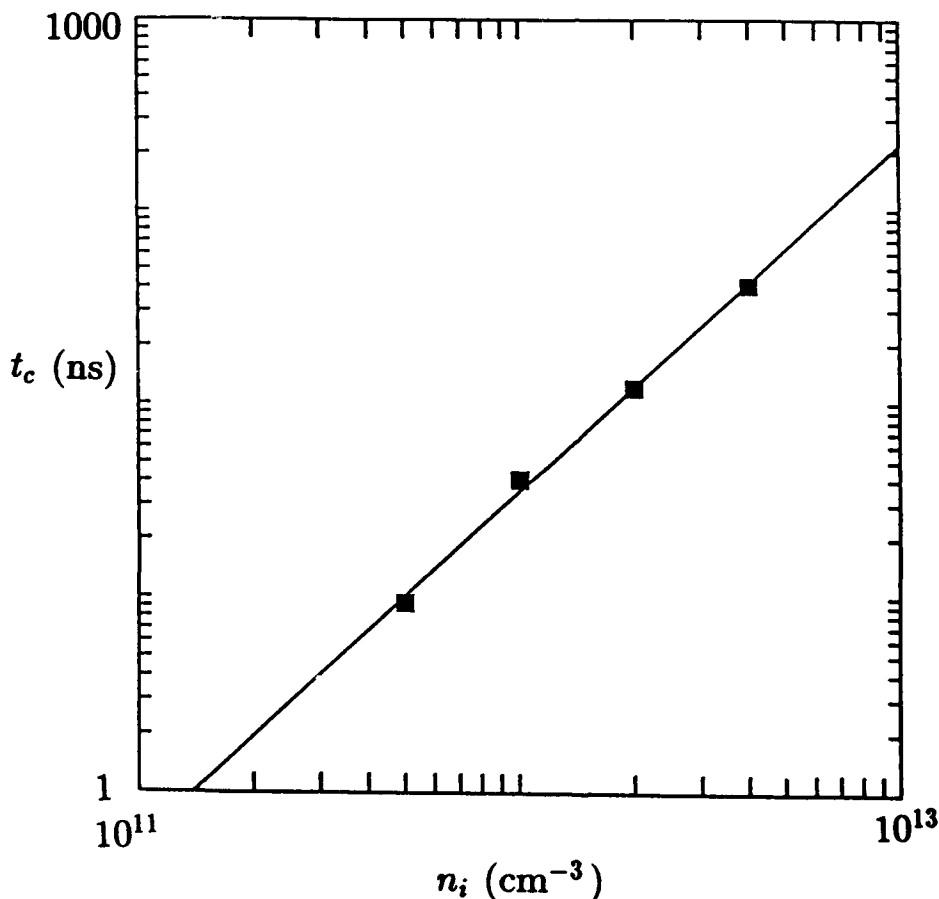


Figure 43. Scaling of the conduction time t_c , which is proportional to the conduction current I_c at opening, with n_i for simulations with immobile ions. The solid curve is a least squares fit of the form n_i^δ , with $\delta \simeq 1.8$.

5.3 ANALYTIC CONSIDERATIONS.

The simulations discussed above find that the propagation of an SCL electron beam in a fixed ion background leads to the formation of quasiperiodic potential humps in the diode gap. This observation suggests that the humps might be computable analytically by considering the time independent flow of a space-charge limited electron beam in a fixed, spatially uniform background of positive charge. In the dynamical simulation the humps are unstable and oscillations in the potential minima between humps lead to trapping of electrons out of the beam. In the first approximation trapped electrons are ignored, as discussed earlier.^{35,36} Neglecting trapped electrons is appropriate for the late conduction and opening phase when the trapped electrons have decreased in importance. Trapped electrons are added below in Section 5.5.

The space charge in the diode has two contributions, the charge density $\rho = en_i$ from the background ions, and the charge density from the electrons emitted at the cathode: the background electrons have disappeared. Electrons are emitted with zero velocity from the cathode, at $x = 0$ with potential $\phi = 0$. Conservation of energy and current for the electrons gives

$$\frac{1}{2}m_e v_b^2 - e\phi = 0, \quad (5-1)$$

$$j_e = en_b(x)v_e(x) = \text{constant}. \quad (5-2)$$

Combining Equations (5-1) and (5-2) with Poisson's equation gives

$$\frac{\partial^2 \phi}{\partial x^2} = \eta_e \phi^{-1/2} - \eta_i, \quad (5-3)$$

where

$$\eta_e = \frac{j_e}{\epsilon_0} \left(\frac{m_e}{2e} \right)^{1/2} \quad (5-4)$$

and $\eta_i = en_i/\epsilon_0$. Multiplying both sides by $\partial\phi/\partial x$, integrating and imposing the SCL boundary condition that $\partial\phi/\partial x = 0$ at the cathode gives

$$\frac{1}{2} \left(\frac{\partial\phi}{\partial x} \right)^2 = 2\eta_e \phi^{1/2} - \eta_i \phi. \quad (5-5)$$

At the potential maximum $\phi = \phi_m$ the derivative $\partial\phi/\partial x = 0$. Combining this with Equation (5-5) above yields

$$\frac{\eta_e}{\eta_i} = \phi_m^{1/2}/2. \quad (5-6)$$

Since $\eta_e \phi_m^{1/2}$ is the electron charge density at the potential maximum Equation (5-6) simply says that the electron charge density is half the background ion density there. Recalling the definition of η_e Equation (5-6) becomes

$$\phi_m = \frac{2m_e}{e} \left(\frac{j_e}{en_i} \right)^2. \quad (5-7)$$

Equation (5-7) gives a relation between the amplitude of the potential maximum, the electron beam current and the background ion density.

Equation (5-5) can be rewritten using the normalized potential $\psi = \phi/\phi_m$ in the region between $x = 0$ to the position of the potential maximum at x_m as

$$\frac{\partial\psi}{\partial x} = + \left[\frac{2\eta_i}{\phi_m} (\psi^{1/2} - \psi) \right]^{1/2}, \quad (5-8)$$

where the positive square root must be taken since $\partial\psi/\partial x \geq 0$. Integrating Equation (5-8) from $x = 0$ to x_m yields

$$\int_0^1 \frac{d\psi}{[\psi^{1/2} - \psi]^{1/2}} = \left[\frac{2\eta_i}{\phi_m} \right]^{1/2} x_m. \quad (5-9)$$

The integral is easily evaluated to yield π so that Equation (5-9) becomes

$$x_m = \pi \left[\frac{\phi_m}{2\eta_i} \right]^{1/2}. \quad (5-10)$$

Combining this result with Equation (5-7) gives

$$x_m = \pi \left(\frac{\epsilon_0 m_e}{e^2 n_i} \right)^{1/2} \frac{j_e}{en_i} = \frac{\pi}{\omega_p} \frac{j_e}{en_i}. \quad (5-11)$$

Equation (5-11) relates the half width of the potential hump to the electron beam current and the ion charge density.

Equation (5-8) becomes when using Equation (5-10)

$$\frac{\partial\psi}{\partial x} = + \frac{\pi}{x_m} [\psi^{1/2} - \psi]^{1/2}. \quad (5-12)$$

This equation describes the solution for the potential in the region $0 \leq x \leq x_m$. Integrating from 0 to ψ gives an implicit equation for $\psi(x)$ of the form,

$$\int_0^\psi \frac{d\psi}{[\psi^{1/2} - \psi]^{1/2}} = \sin^{-1}[2\psi^{1/2} - 1] - 2[\psi^{1/2} - \psi]^{1/2} + \pi/2 = \pi \left(\frac{x}{x_m} \right). \quad (5-13)$$

Similarly, the potential in the region $x_m \leq x \leq 2x_m$ to the right of $x = x_m$ is also described by Equation (5-12) if the plus sign is replaced by a minus, since $\partial\psi/\partial x \leq 0$ in this region. Integrating the resultant equation again leads to an implicit equation for $\psi(x)$ similar to Equation (5-13):

$$\sin^{-1}[2\psi^{1/2} - 1] - 2[\psi^{1/2} - \psi]^{1/2} + \pi/2 = \pi \left(2 - \frac{x}{x_m} \right). \quad (5-14)$$

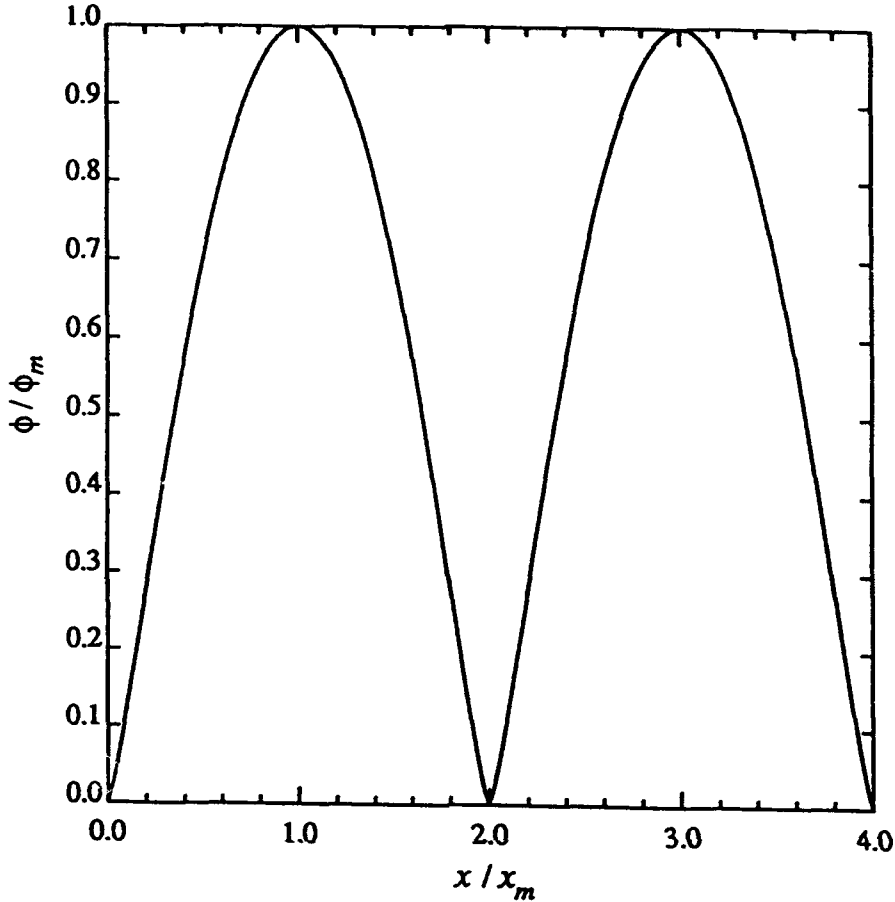


Figure 44. Analytic solution for $\phi(x)$ for a space-charge limited electron beam in a fixed spatially uniform background of positive charge, without trapped electrons.

Equations (5-13) and (5-14) can be solved numerically to yield the complete solution for $\psi(x)$ over the region from the cathode $x = 0$ to the point where ψ again vanishes at $x = 2x_m$. Figure 44 plots the resultant solution. Note that the solution is symmetric about the point $x = x_m$. Further, the point $x = 2x_m$ is completely equivalent to $x = 0$ since $\psi = \partial\psi/\partial x = 0$ there. Hence, the solution for the potential to the right of the point $x = 2x_m$ is a spatially periodic repetition of the solution for $0 \leq x \leq 2x_m$. To emphasize this point Figure 44 contains two repetitions of the solution.

The conclusion is that the time independent solution for a SCL electron beam in a spatially uniform fixed ion background is a series of spatially periodic potential humps. Equations (5-7) and (11) show that the amplitude ϕ_m is proportional to the square of the beam current j_e^2 , while the hump width $2x_m$ is proportional j_e . The current for which a single hump fills the entire diode is a critical value j_{cr} , given by

$$j_{cr} = \frac{1}{2\sqrt{2}\pi} \epsilon_0 \left(\frac{2e}{m_e} \right)^{1/2} \eta_i^{3/2} d. \quad (5-15)$$

Any increase in j_e beyond this critical value will make the width of the hump larger than the physical gap width d and thus will drive up the voltage at the anode. This is precisely

what happens in the simulation late in time during the opening phase when the trapped electron contribution to the potential can be effectively neglected.

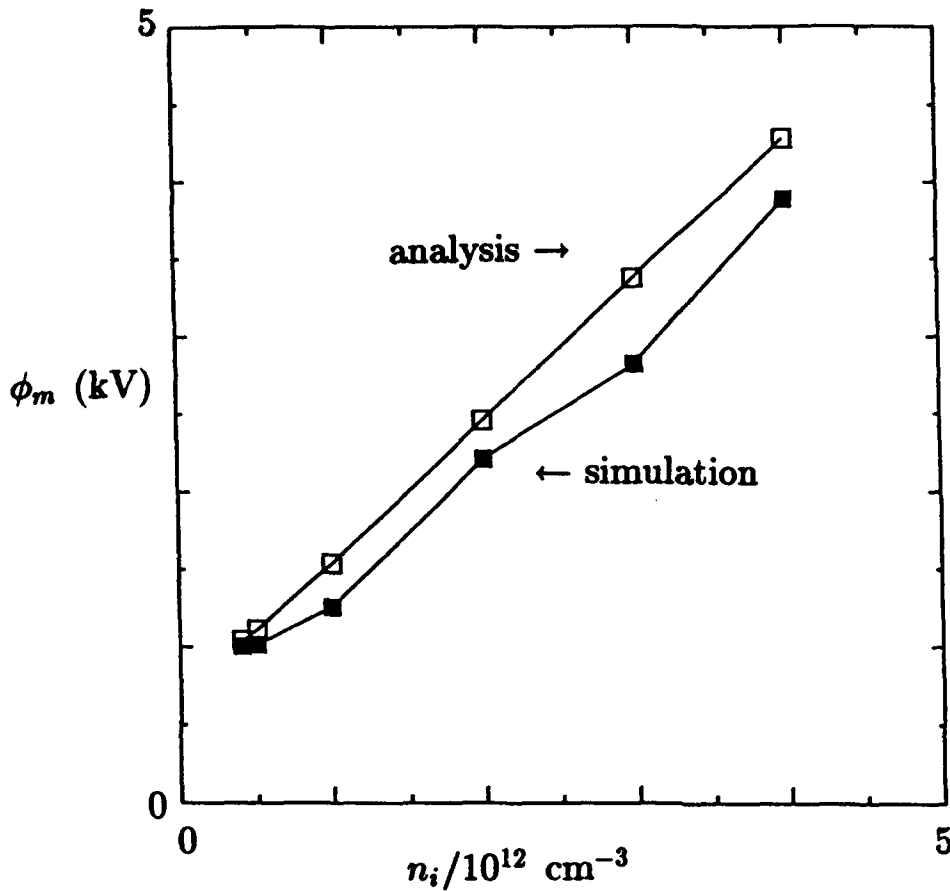


Figure 45. The potential maximum ϕ_m in the analytic theory compared with the value in the simulations.

In these considerations the trapped electrons are ignored. However, during most of the conduction phase the trapped electrons are important. The dynamical simulation suggests that the virtual cathode represented by the potential minimum inside the diode near $x = 2x_m$ is unstable. The virtual cathode oscillates, which causes trapping of electrons out of the beam. Section 5.5 further discusses the trapped electrons and their role in the evolution of the potential during the conduction phase.

5.4 COMPARISON WITH SIMULATION.

The analytic solutions obtained above can be used to predict the position and amplitude of the potential maximum late in the opening phase when the virtual cathode has moved beyond the anode, when $2x_m > d$. Define the normalized diode potential ψ_0 as

$$\psi_0 = \frac{V_D}{\phi_m}. \quad (5-16)$$

Combining Equations (5-10) and (5-14) gives

$$\frac{3\pi/2 - \sin^{-1}[2\psi_0^{1/2} - 1] + 2[\psi_0^{1/2} - \psi_0]^{1/2}}{\psi_0^{1/2}} = \left(\frac{2\eta_i}{\phi_0}\right)^{1/2} d. \quad (5-17)$$

Equation (5-17) determines the I-V characteristic of the diode. Given the total voltage drop V_D , the gap width d and background ion density n_i , Equation (5-17) determines the value of ψ_0 and hence ϕ_m . Inserting ϕ_m into Equation (5-7) then yields the corresponding value of the diode current. Also, ϕ_m determines x_m via Equation (5-10).

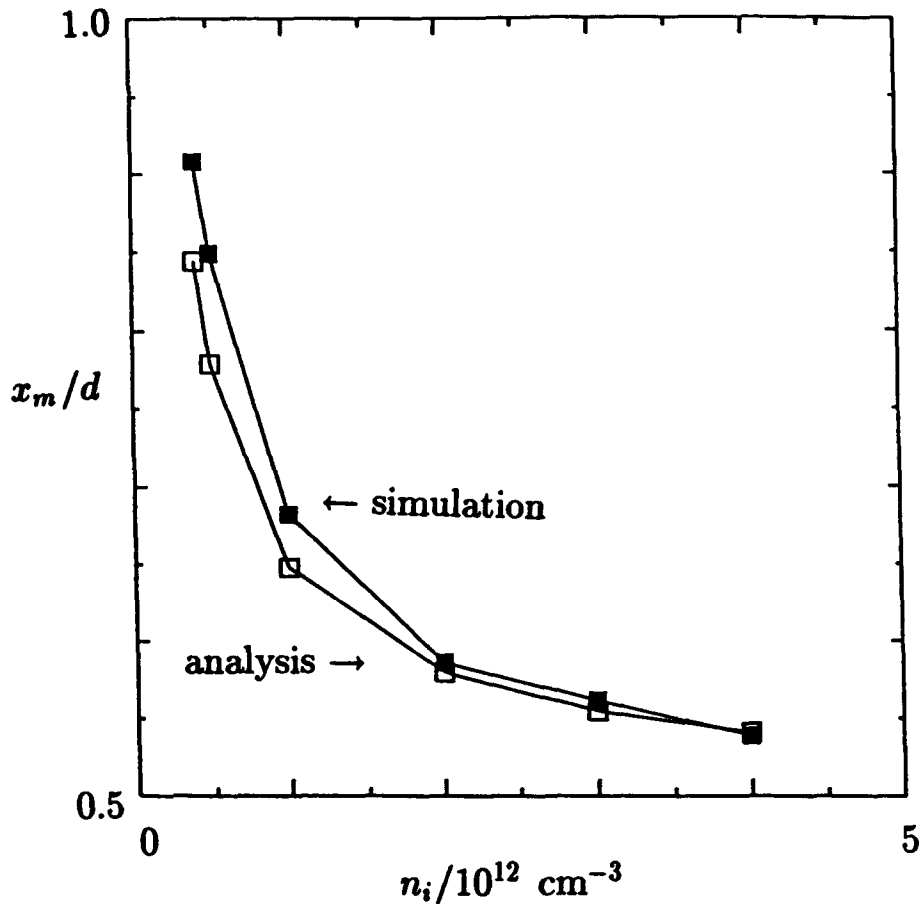


Figure 46. The width of the potential hump x_m in the analytic theory compared to the simulations.

Figure 45 compares the analytic value of ϕ_m predicted by Equation (5-17) with the maximum voltage observed in the simulations (using ϕ_0 measured in the simulation instead of $\phi_0 = 1 \text{ kV}$). Figure 46 compares the (normalized) position x_m of the potential maximum with the simulation, and Figure 47 is the final current. The agreement between analysis and simulation is clearly excellent. The deviations apparent in these figures arise from two effects not included in the above analysis, viz., the trapped electrons already mentioned, and also the finite energy of electron emission as discussed further in Section 5.5.

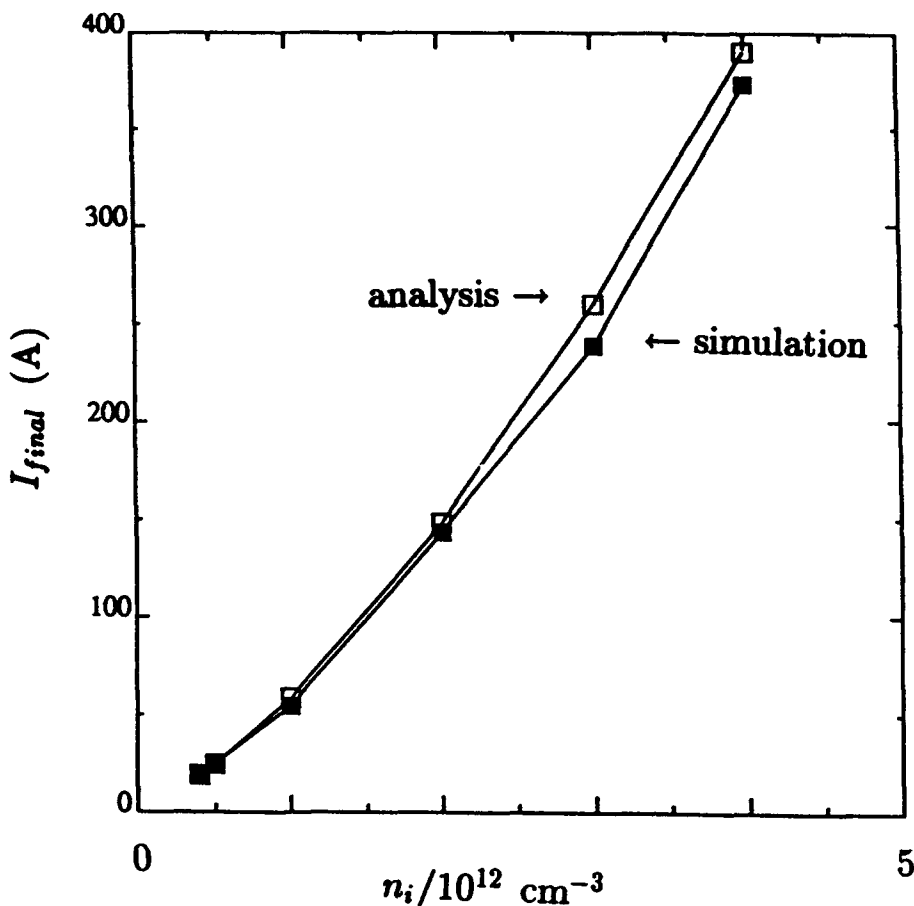


Figure 47. Final diode current I_{final} in the analytic theory compared to the simulations.

5.5 TRAPPED ELECTRONS.

The analytic solution for the potential obtained in Section 5.3 assumes that all the electron space charge in the diode comes from the beam. However, in the simulation the minima between the potential humps become unstable and form oscillating virtual cathodes which trap electrons out of the beam. Figure 48(a) shows the amplitude of the potential minimum on the right hand side of the potential hump nearest the cathode as a function of time early in the conduction phase, corresponding to the snapshot plots of Figure 41(b) through (e) between 6 and 12 ns (for $n_i = 10^{12} \text{ cm}^{-3}$). The amplitude initially executes regular oscillations with a period about equal to the plasma frequency. The oscillations become increasingly chaotic as the time evolution progresses. Figure 48(b) is a plot of the spatial position of this minimum versus time for the same period. This shows an average motion of the minimum toward the anode corresponding to the expansion of the potential hump, with an oscillation on top. This type of behavior is very reminiscent of the oscillations in both position and amplitude of the virtual cathode formed by an electron beam injected into a vacuum region between two grounded parallel conducting planes.³⁷

This section discusses the inclusion of trapped electrons analogous to their treatment in the reflex triode.³⁸ The model assumes that the transit time of a trapped electron across

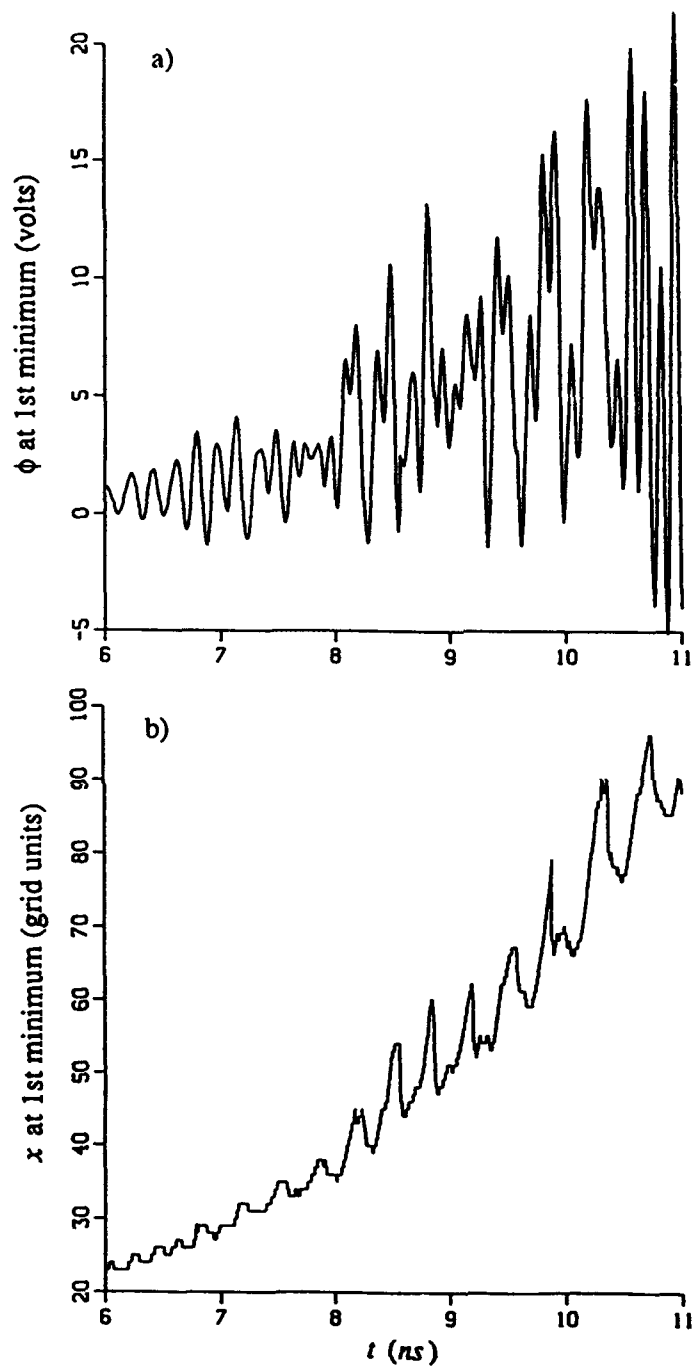


Figure 48. Amplitude (a) and spatial position (b) versus time of the potential minimum nearest to the cathode in a simulation with immobile ion density $n_i = 10^{12} \text{ cm}^{-3}$. The time interval 6 to 11 ns corresponds to Figures 41(b) to near 41(e).

the potential hump is much shorter than the time for a change in the hump's amplitude, so that at each instant the system is approximately in a steady state. Similarly, the energy E of a trapped electron remains constant as it reflexes back and forth inside the potential hump, with a velocity according to $m_e v^2/2 = E + e\phi$. Following Creedon,³⁸

$$\frac{df}{dE} dE \quad (5-18)$$

is the number of trapped electrons per unit area per unit time traveling in the negative x direction at $x = x_m$ with total energy between E and $E + dE$. In a stationary state this number is constant. The density of negative going trapped electrons with total energy between E and $E + dE$ follows by dividing the flux by the local velocity,

$$dn = \frac{df}{dE} dE \left[\frac{2}{m_e} (E + e\phi) \right]^{-1/2}. \quad (5-19)$$

The total electron density then becomes

$$n_e = \frac{j_e}{e} \left(\frac{2e\phi}{m_e} \right)^{-1/2} + 2 \int_{-e\phi}^0 \frac{df}{dE} \left[\frac{2}{m_e} (E + e\phi) \right]^{-1/2} dE. \quad (5-20)$$

The factor of 2 in front of the integral reflects that in steady state the negative going flux of trapped electrons at every point is equal to the flux of positive going trapped electrons.

Equation (5-20) expresses the spatial density of trapped electrons in terms of the energy spectrum df/dE of the trapped electrons at $x = x_m$. This spectrum is determined by the details of the trapping process, which are hard to account for analytically but easily seen in the simulation. Therefore, with some assumptions about the form of df/dE it is possible to use the simulation to approximate the effect of the trapped electrons on the potentials.

Using Equation (5-21) into Poisson's equation, multiplying by $\partial\phi/\partial x$, and integrating with the additional boundary condition $\partial\phi/\partial x = 0$ at $\phi = \phi_m$, gives the generalization of Equation (5-6),

$$2\eta_e \phi_m^{1/2} - \eta_i \phi_m + \frac{4}{\epsilon_0} \left(\frac{m_e}{2} \right)^{1/2} \int_{-e\phi_m}^0 (E + e\phi_m)^{1/2} \frac{df}{dE} dE = 0. \quad (5-21)$$

To proceed further the energy spectrum for the trapped electrons must be defined. The simplest is to assume that the trapped electrons at $x = x_m$ are uniformly distributed throughout the allowed range of total energy, i.e., df/dE is a constant independent of E . This assumption simplifies the analysis because all the integrals involved can be done in closed form. However, a constant energy spectrum is not a very good approximation to the trapped electron distribution observed in the simulation. The actual distribution is strongly peaked at its low energy end (at $E = -e\phi_m$), and falls off rapidly with increasing E . Fortunately, the details of df/dE appear in lower order, and are therefore qualitatively unimportant in computing the correction for the effect of the trapped electrons.

The trapped electron energy distribution is normalized by

$$\int_{-e\phi_m}^0 \frac{df}{dE} dE = \frac{3}{4} \gamma \frac{j_e}{e}, \quad (5-22)$$

where $\gamma = 4f_t/3$ is proportional to the current j_t in trapped electrons compared to the total electron current j_e emitted from the cathode, $f_t = j_t/j_e$. This normalization condition and the assumption of a constant spectrum gives

$$\frac{df}{dE} = \frac{3\gamma}{4e\phi_m} \frac{j_e}{e}. \quad (5-23)$$

Substituting Equation (5-23) into (5-21) and solving for ϕ_m gives

$$\phi_m = \frac{2m_e}{e} \left(\frac{j_e}{en_i} \right)^2 [1 + \gamma]^2. \quad (5-24)$$

Equation (5-24) is the extension of Equation (5-7) including the trapped electron contribution in the case of a constant energy spectrum. Equation (5-24) can be rewritten as

$$\frac{\phi_m^{1/2} n_i}{j_e} = \left(\frac{2m_e}{e^3} \right)^{1/2} (1 + \gamma). \quad (5-25)$$

The potential maximum ϕ_m increases as expected from the addition of the trapped electrons to the total beam current.

In analogy to Section 5.4 the potential for $0 \leq x \leq x_m$ satisfies

$$\frac{\partial \psi}{\partial x} = \left[\frac{2\eta_i}{\phi_m(1 + \gamma)} \right]^{1/2} \left[\psi^{1/2} - (1 + \gamma)\psi + \gamma\psi^{3/2} \right]^{1/2}, \quad (5-26)$$

where $\psi = \phi/\phi_m$. Integrating Equation (5-26) from $x = 0$ to $x = x_m$ gives

$$\int_0^1 \frac{d\psi}{[\psi^{1/2} - (1 + \gamma)\psi + \gamma\psi^{3/2}]^{1/2}} = \left(\frac{2\eta_i}{\phi_m(1 + \gamma)} \right)^{1/2} x_m. \quad (5-27)$$

The integral on the left is a combination of elliptic integrals of the first and second kind,

$$I(\gamma) = \frac{4}{\gamma} \left[F\left(\frac{\pi}{2}, \sqrt{\gamma}\right) - E\left(\frac{\pi}{2}, \sqrt{\gamma}\right) \right]. \quad (5-28)$$

Finally, solving for x_m in Equation (5-27) with Equation (5-24) for ϕ_m gives

$$x_m = \frac{\pi}{\omega_p} \frac{j_e}{en_i} \left[\frac{(1 + \gamma)^{3/2} I(\gamma)}{\pi} \right], \quad (5-29)$$

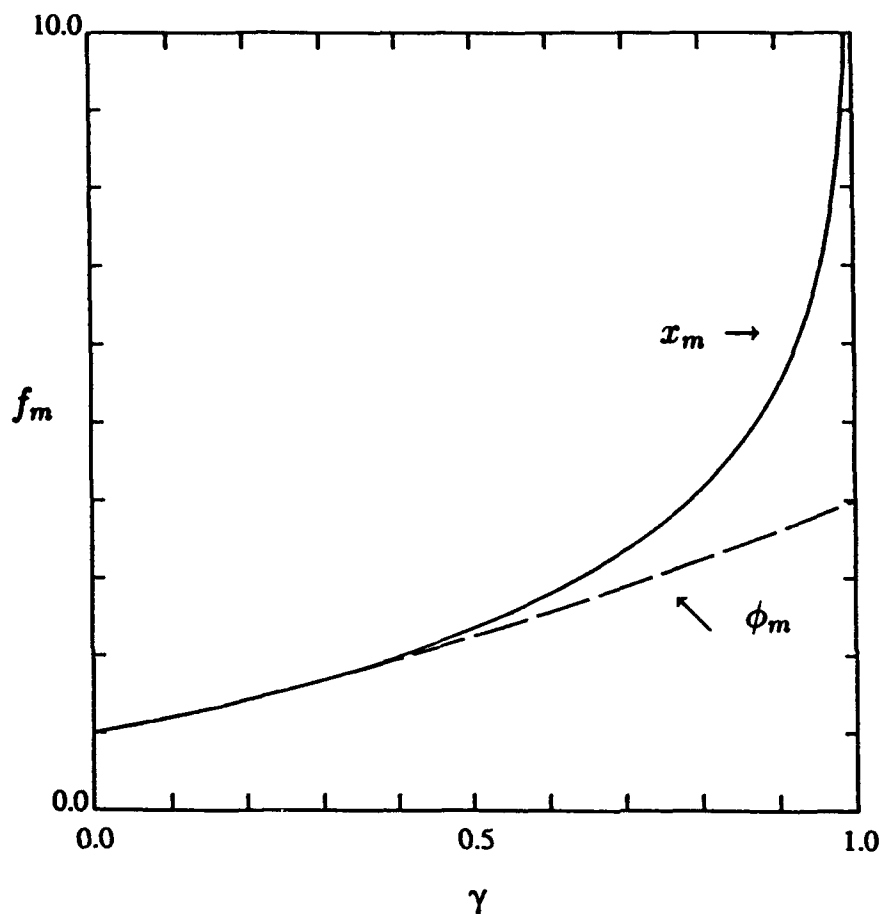


Figure 49. The correction factors for x_m and ϕ_m as function of the trapped electron parameter γ . The trapped electrons have equal energy.

where ω_p is the plasma frequency $\omega_p^2 = e^2 n_i / \epsilon_0 m_e$. Equation (5-27) is the analogue of Equation (5-9) where the expression in square brackets is the multiplicative correction for the trapped electrons.

Integrating Equation (5-26) yields an implicit equation for $\psi(x)$ in terms of elliptic functions that must be solved numerically. With a constant energy spectrum for the trapped electrons, Figure 49 shows that for $\gamma = 1$ the potential maximum ϕ_m approaches $4\phi_m$ in the absence of any trapped electrons ($\gamma = 0$) while the location of the maximum x_m diverges. The meaning of this result is clarified in Figure 50, which illustrates the effect of varying γ on the solution for the potential $\phi(x)$. In Figure 50 ϕ and x are normalized to the values of ϕ_m and x_m for $\gamma = 0$. As γ approaches the critical value $\gamma_{cr} = 1$, the spatial period of the solution increases while ϕ_m approaches 4 times the amplitude of the potential maximum in the absence of any trapping. For γ very close to 1 the location of the maximum x_m approaches infinity. At the same time there appears an extended spatial region around $x = x_m$ in which $\phi \simeq \phi_m$: then the potential distribution looks increasingly like that of a sheath at the edge of a quasi-neutral plasma.

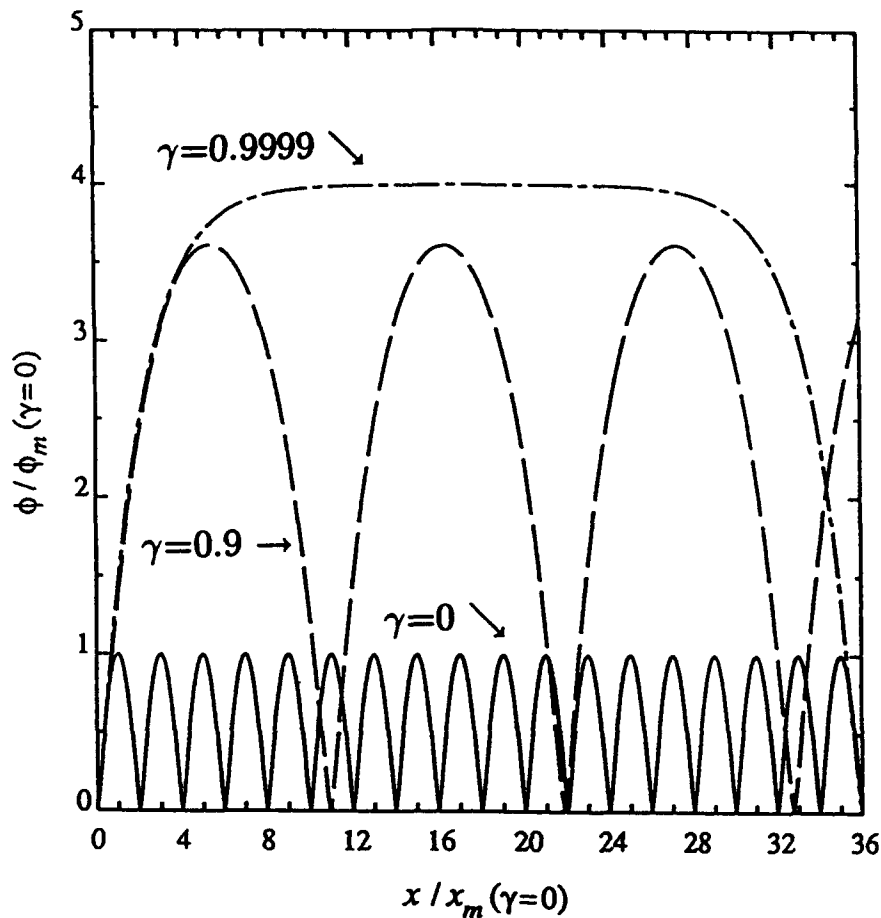


Figure 50. The potential in the diode as function of the trapped electron parameter γ . The potential ϕ and the position of the maximum x are normalized to $\phi_m(\gamma = 0)$ and $x_m(\gamma = 0)$ without trapped electrons.

Figure 51 shows the effect of γ on the density of the beam electrons n_b , the trapped electrons n_t and the total electron density $n_e = n_b + n_t$ at the position $x = x_m$. In the limit $\gamma = 1$ the total electron density $n_e = n_t$ is at $x = x_m$. Note that for $\gamma = 1$ the density of trapped electrons is $3/4$ the total electron density while the beam electrons contribute only $1/4$. In this limit the system does indeed look very much like a beam in a plasma.

Equation (5-29) indicates that the trapped electrons increase the width of the potential hump compared to the potential with the same beam current without trapped electrons given in Equation (5-11). The simulations indeed show this effect. The upper curve in Figure 52(a) shows the position of the potential maximum for the hump nearest the cathode in the simulation of Figure 42, with immobile ions at density $n_i = 10^{12} \text{ cm}^{-3}$. The lower curve is the value of x_m predicted in the absence of trapping using the value of j_e measured in the simulation. Comparison of the two curves shows that the potential hump in the simulation initially expands much more rapidly than it would have without trapping, until the potential hump spans the full width of the gap so that x_m is located near the gap center at $x = 64\Delta$. This situation persists until trapping stops and opening begins at

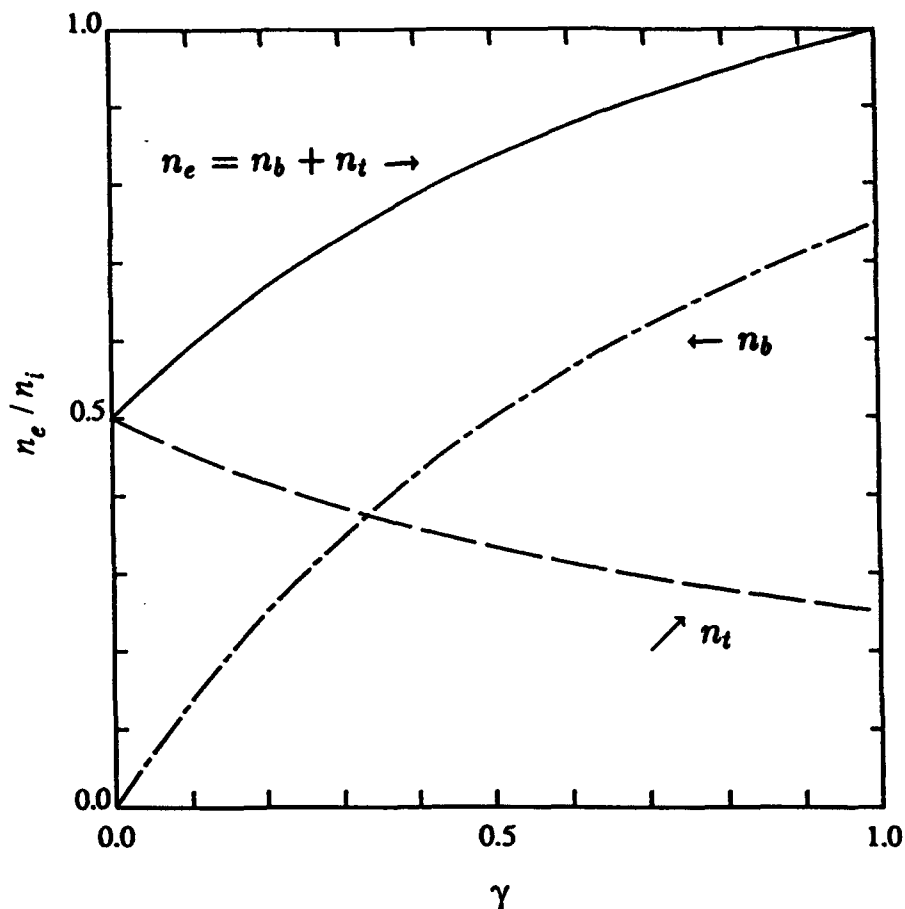


Figure 51. Density of beam electrons n_b , trapped electrons n_t and total electrons $n_e = n_b + n_t$ as function of γ at $x = x_m$. All curves are normalized to n_i .

about $t = 40$ ns. Then x_m increases until it relaxes to a final position slightly greater than that predicted by Equation (5-11) (with j_e from the simulation). The middle curve in Figure 52(a) is the prediction of Equation (5-29) including the approximate effect of the trapped electrons. The value of f_t and hence γ used in Equation (5-29) is measured directly in the simulation and plotted in Figure 52(b). Figure 52 shows that even the relatively crude approximation of a constant energy spectrum for the trapped electrons results in a significant improvement in the agreement between the prediction of the analytic theory and the simulation for the expansion of the potential hump as a function of time.

Equation (5-25) allows some rather general statements concerning the effect of the trapped electrons on ϕ_m for an arbitrary spectrum df/dE . In non-dimensional form

$$\frac{df}{dE} dE = f_t \frac{j_e}{e} F(\xi) d\xi, \quad (5-30)$$

where $\xi = E/e\phi_m$ is the normalized energy and $F(\xi)$ is the normalized distribution function, with $\int_0^1 F(\xi) d\xi = 1$. As before, the influence of the trapped electrons is defined by

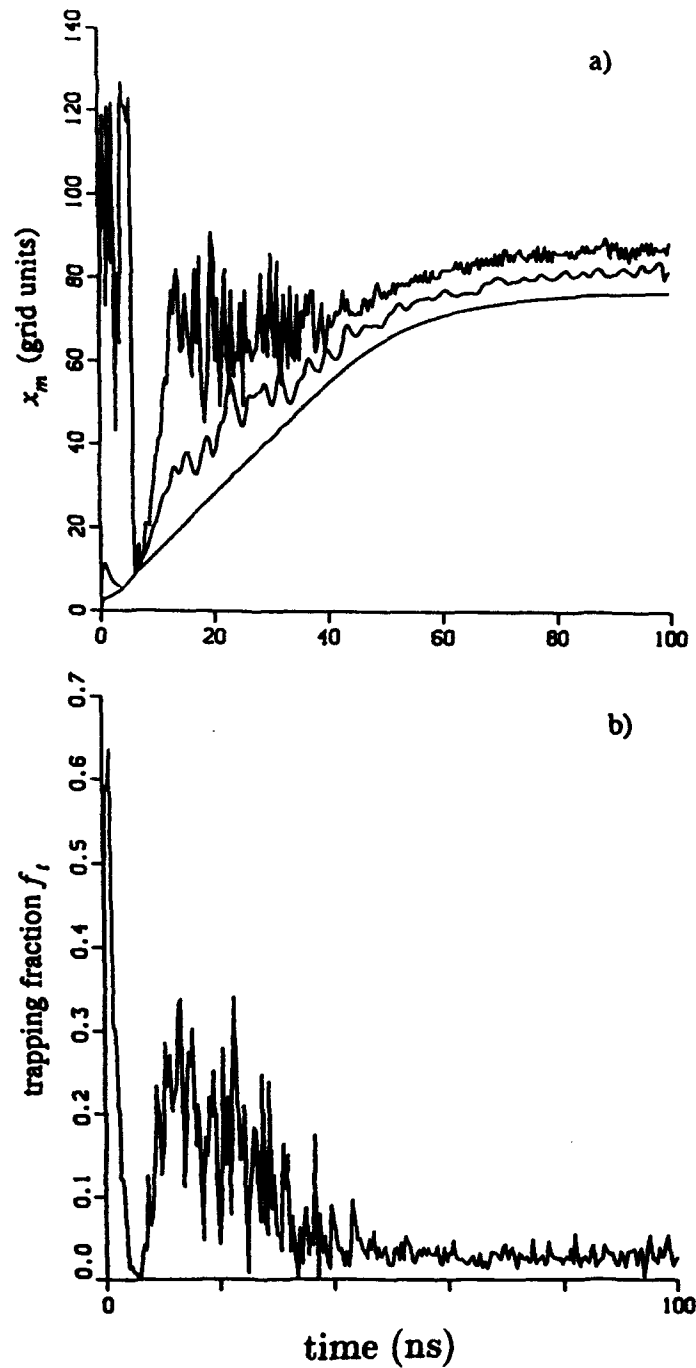


Figure 52. (a) Position of the potential maximum x_m versus time in the simulation with immobile ions of density $n_i = 10^{12} \text{ cm}^{-3}$ (upper curve). Lower curve is the prediction of Equation (5-11). The middle curve includes the trapped electrons according to Equation (5-29), which approximately includes the correction due to the trapped electrons. Figure 51(b) is the trapping fraction f_t used (from the simulation).

the parameter γ , which is for arbitrary $F(\xi)$

$$\gamma = 2f_i \int_{-1}^0 (1 + \xi)^{1/2} F(\xi) d\xi. \quad (5-31)$$

This is always non-negative: therefore the trapped electrons always increase the potential maximum ϕ_m .

The effect of the trapped electrons on ϕ_m is easily seen by comparing the computations with trapped electrons with the analytical theory without trapped electrons. It turns out that the theory in Section 5.3 must be augmented with a finite emission velocity of the electrons. Although the electrons in the simulation are emitted with a distribution of initial velocities, it is sufficient for the theory to consider electrons with a single initial velocity v_0 . Instead of Equation (5-1) energy conservation becomes

$$\frac{1}{2} m_e v_e^2(x) - e\phi(x) = \frac{1}{2} m_e v_0^2 = E_0. \quad (5-32)$$

The equation for the maximum potential ϕ_m becomes

$$\phi_m = \frac{2m_e}{e} \left(\frac{j_e}{en_i} \right)^2 \left[\left(1 + \frac{\phi_i}{\phi_m} \right)^{1/2} - \left(\frac{\phi_i}{\phi_m} \right)^{1/2} \right]^{1/2}. \quad (5-33)$$

This equation differs from its counterpart for $v_0 = 0$, Equation (5-7), in the presence of the square brackets. This factor is less than unity for $0 < \phi_i/\phi_m < 1$, showing that a finite initial velocity $v_0 > 0$ reduces the maximum value of the potential. A similar calculation shows that a non-zero initial velocity does not change the position x_m of the maximum potential.

Figure 53 compares ϕ_m from Equation (5-29) (with the appropriate initial energy $m_e v_0^2/2 = 3.48$ eV) to the actual ϕ_m value observed in the simulation. The simulation's value for ϕ_m is always greater than the analytic value from Equation (5-29) without trapped electrons, because trapped electrons tend to increase ϕ_m over the value without trapping.

5.6 CONCLUSIONS.

This section examines the PFD in the limit wherein the background of mobile ions is replaced by a fixed spatially uniform background of positive charge. This limiting case still exhibits all of the essential features of the conduction and opening process described in Section 4. The potential hump follows the analytic solutions discussed in Section 5.3, especially just before opening when trapped electrons have disappeared. These solutions provide a simple explanation for the high voltage opening phase. To repeat, the spatial width of the potential hump is proportional to the beam current j_e . At first the diode gap accommodates multiple potential humps, but as the external inductor continues to drive the diode current up the potential hump becomes too wide for the diode gap. Then the diode voltage increases, and the diode opens. Section 4 already showed essentially the same scenario for mobile ions. In this case, however, the ion density is continually

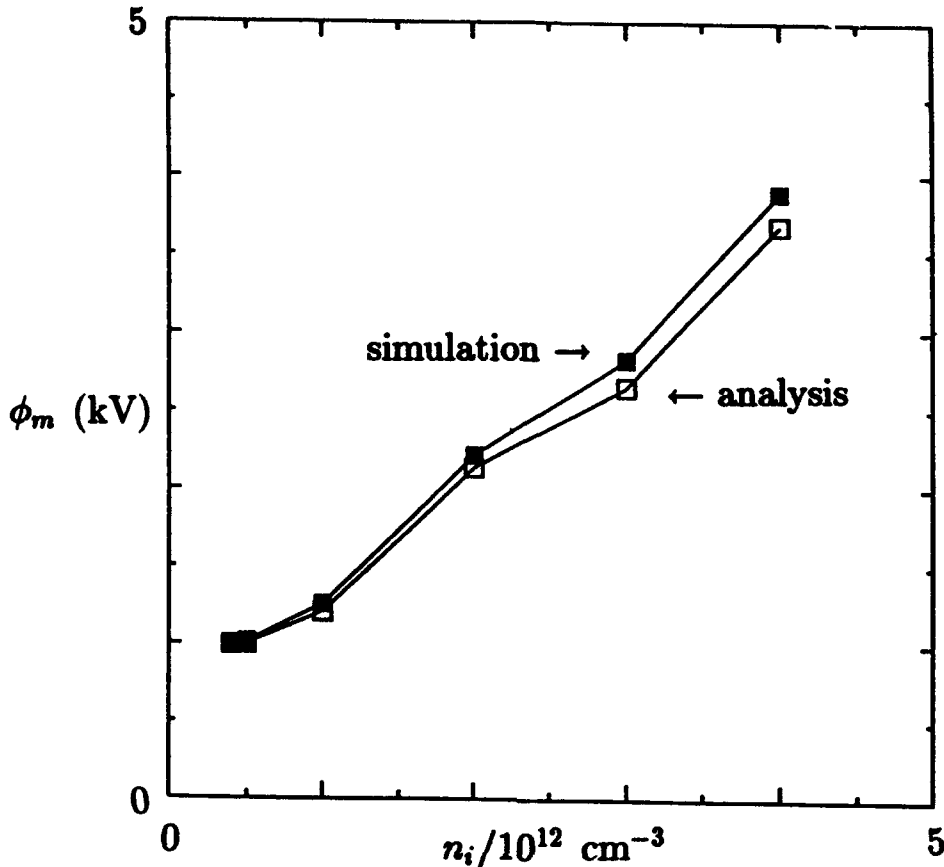


Figure 53. The analytic value for ϕ_m including trapped electrons and initial electron velocity compared with the simulations.

decreasing during the conduction phase and during opening the mobile ions can relax to a bipolar distribution. The role of non-equilibrium ion distributions in the conduction phase of plasma opening switches has been suggested by Grossmann³⁵ *et al.* based upon analysis of two dimensional simulations of the Plasma Erosion Opening Switch using the MASK code.

Section 5.5 demonstrated how to account for trapped electrons in the potential distribution during the conduction phase. This treatment explicitly points out the parallels between the PFD and the reflex triode. It does not, however, provide a complete analytic theory of the simulations since the shape and normalization for the spectral distribution of the trapped electrons is not specified a priori but must be provided as an input to the analysis. These quantities are determined by the trapping process itself, which must be better understood in order to achieve a completely satisfactory analytic theory of PFD operation in the immobile ion limit.

SECTION 6

TWO DIMENSIONAL SIMULATIONS OF PLASMA FILLED DIODES

Electron beam diodes initially filled with a low-density plasma are used for prepulse suppression and as opening switches. In these plasma filled diodes (PFDs), the impedance is initially very low because the initial plasma fill is a good conductor. Subsequently the diode impedance increases somewhat as space-charge limited electron flow is established across a cathode sheath. At some later time the impedance of the diode begins to rise rapidly, i.e., the PFD opens. The voltage across the PFD rises, and the diode produces bremsstrahlung.

During the low impedance phase the self magnetic field of the electron beam bends electrons towards the main body of the plasma. The time over which the plasma filled diode can remain in a low impedance state is controlled by electrostatic gap formation and by hydrodynamic motion of the plasma bulk. Under certain conditions hydrodynamic forces dominate the opening time. In contrast to earlier models, which predict that cathode sheath erosion dominates the opening process, the particle simulations in this section show that sheath formation at the anode also plays an important role.

6.1 INTRODUCTION.

Originally, prepulse suppression^{19,39} motivated prefilling an electron beam diode with plasma. The plasma filled diode (PFD)^{17,22,40} has also been used for inductive energy storage, the primary interest here, by itself or combined with a plasma opening switch. The importance for this application is that the plasma filled diode minimizes the inductance between the switch and the bremsstrahlung load.

One of the earliest experiments on plasma prefilled electron beam diodes¹ used the NEREUS and HYDRA generators. Plasmas with density 10^{13} - 10^{14} cm^{-3} traveling at approximately $1.3 \text{ cm}/\mu\text{s}$ were produced by a vacuum arc across a ceramic surface coated with oil. Two regimes of electron flow were identified, depending on the strength of the self-magnetic field of the electron beam. When the current is low such that the electron gyroradius is substantially larger than the anode-cathode gap spacing, the behavior of the PFD is controlled by a plasma sheath that forms at the cathode. The current across the sheath follows the bipolar Child-Langmuir⁴¹ relations for one-dimensional space-charge limited ion and electron flow. However, higher-dimensional effects become important as current or gap spacing increase, and the electron gyroradius in the self-magnetic field of the beam becomes comparable to the gap spacing. By reversing the polarity on the electrodes, it was determined that the plasma drift motion was inconsequential.

In subsequent experiments³⁹ on PROTO I the PFD is filled with a 10^{12} cm^{-3} carbon plasma traveling at 5 - $7 \text{ cm}/\mu\text{s}$ produced by plasma guns. The plasma fill reduces the prepulse from a 700 ns oscillatory waveform with peak amplitude of $\sim 30 \text{ kV}$ to a 150 ns triangular pulse with 20 kV peak. The prepulse is now sufficiently short to prevent cathode turn-on prior to the main voltage pulse. Other beneficial effects of a plasma prefill are 1) the anode-cathode voltage increases faster than the voltage at the insulator stack, 2) transients at the cathode are suppressed, and 3) prior to cathode turn-on magnetic energy.

is stored between the cathode and wall. This article³⁹ suggests that the PFD could be used as an opening switch for inductive energy storage applications in pulsed power generators.

Widner and Poukey²⁴ examine further the ion sheath motion in the PFD when the ion transit time across the sheath is fast compared to the expansion rate of the sheath. They conclude that the sheath does not expand until the ion current necessary for bipolar Child-Langmuir flow exceeds the flux of ions to the cathode. Subsequently the sheath expands until the sheath velocity drops below the ion acoustic speed, at which point a rarefaction propagates into the plasma. Ions are accelerated into the sheath by the rarefaction wave, and the sheath slows down.

Bailey²⁰ *et al.* study the possible use of a PFD for electron beam injection into a tokamak. The diode is the load of a magnetically insulated transmission line (MITL) coupled to the Pulserad TM 225W generator. The diode is inserted into a chamber prefilled with hydrogen plasma created by titanium washer guns. Plasma densities range from 5×10^{12} - 2×10^{14} cm^{-3} . An external axial magnetic field of 1.5 kG guides the electron beam down the chamber. This PFD couples very well to the MITLs. At the higher densities a cathode sheath erosion model²⁵ shows reasonable agreement with the data. However, at densities below 3×10^{13} cm^{-3} , the diode remained in a low impedance state much longer than predicted.

Subsequent opening switch research^{42,43} emphasizes plasma injection into the vacuum transmission line located between the vacuum interface and the load. However, a PFD combined with an opening switch was successfully tested on the GAMMA accelerator.²² The plasma fill allowed the diode to conduct in a low impedance state for ~ 1 μs . When the switch opens at currents above 200 kA, the voltage increases to ~ 2 MV, 1.7 times the peak voltage delivered to a diode load. Similar results are reported by Goyer¹⁷ *et al.* on the EYESS generator. Using the PFD as the only switching stage, 500 kA is conducted in 0.5 μs , a peak voltage of 1 MV corresponding to a voltage gain of 1.4. The voltage gain increases to 2.2 when the PFD is used as the last stage switch in tandem with a plasma opening switch (POS) located in the vacuum transmission line. In addition, with this tandem POS-PFD the power pulse becomes narrower. Also Bluhm *et al.*⁴⁰ find the shortest pulse width with a POS coupled to a PFD, with almost 100 % current transfer to the diode.

Systematic experiments on long conduction time PFDs are reported by Bugaev⁴⁴ *et al.* using the GIT-4 generator. In related work, Bastrikov⁴⁵ *et al.* show that as much as 30% of the current may be carried by ions (with a spherical cathode).

This section discusses computer modeling of PFDs with two-dimensional particle-in-cell (PIC) codes, and compares the results with analytic approaches, and one-dimensional computations⁴⁶⁻⁴⁸ of PFDs (similar to Sections 4 and 5). The two-dimensional PIC simulations are presently limited to low density plasma fills ($\leq 5 \times 10^{12}$ cm^{-3}) and short conduction times (≤ 40 ns). In the two-dimensional PIC simulations most of the early current is carried by the ambient electrons, and the magnetic field penetrates a few collisionless skin depths into the plasma. A space charge sheath develops that turns on space-charge limited electron emission from the cathode. As the current increases, electron emission from the cathode carries an increasing fraction of the current. In contrast to the 1-D computations, the self magnetic field of the electron beam bends the electrons into the main body of

the plasma. The magnetic field is able to follow the emitted electron stream and chews a path into the plasma towards the anode. During this time the magnetic field continues to accelerate electrons towards the axis. An ambipolar electric field drags the ions along with the electron current channel imploding on axis. The implosion seems to trigger the opening process for the parameter regimes of these simulations.

The 2-D PIC simulations are compared in this section with computations for the same parameters using the one-dimensional code REFLEX. Another model to mimic specifically the opening process through plasma implosion is a hydrodynamic snowplow model connected to an identical driving circuit, in the FREYA circuit code. FREYA agrees reasonably well with the implosion times observed in the 2-D simulations.

Prior two-dimensional plasma opening switch (POS) simulations⁴⁹⁻⁵³ have examined a coaxial geometry where the plasma is injected in the vacuum transmission line rather than in the diode. Although the PFD behavior^{42,43} is similar in many aspects to these simulations there are also significant differences. The principal difference is that the PFD carries all the current, while in a coaxial POS the current can also flow through a downstream load.

Section 6.2 discusses the assumptions and the appropriate parameter regimes for each of the different simulation models. Section 6.3 compares the physical effects and the results from three different simulations. Section 6.4 discusses the results and the implications for PFD design, and suggests further work.

6.2 SIMULATION MODELS.

The primary simulation model is the particle-in-cell (PIC) code ISIS⁵⁴ developed by Mike Jones at LANL. This code solves the full set of Maxwell's equations on a computational grid. An exact charge conserving method⁵⁵ interpolates particle information for the current density \vec{J} , which is used to advance Maxwell's equations forward in time. Particles move according to the relativistic Newton-Lorentz equations of motion. ISIS is operated in a 2 1/2 D (z, r, v_z, v_r, v_θ) mode with explicit differencing of Maxwell's electromagnetic field equations as done in many PIC codes.⁵⁶⁻⁵⁸

ISIS has several features necessary for modelling the PFD; perfectly conducting surfaces, particle injection, space charge limited particle emission, and an electromagnetic power pulse driving the simulation. Limitations on computer time keep a reasonable run below ~ 40 ns.

Figure 54 shows the cylindrical $r - z$ geometry used in the 2-D simulations. The computational grid is uniform with $\Delta z = \Delta r$. The mesh spacings range from 0.125-0.2 cm, or around 50-100 grid points in each direction. Particles are absorbed on the electrodes, assumed to be perfect conductors. The $r=0$ boundary is the symmetry axis: particles crossing $r=0$ are specularly reflected back into the simulation region. The cathode, at the left of the figure, has a radius of 7.6 cm., while the anode, at the right, has a radius of 12.8 cm. The anode-cathode gap spacing is 10 cm. The geometry closely resembles the configuration of the EYESS experiments at Physics International.

A uniform plasma with an average of 4-9 macroparticles per cell is initialized between the electrodes, with subsequent particle injection from the anode. The electron densities range from 1×10^{12} to 5×10^{12} cm^{-3} . Most plasma sources used for PFDs produce

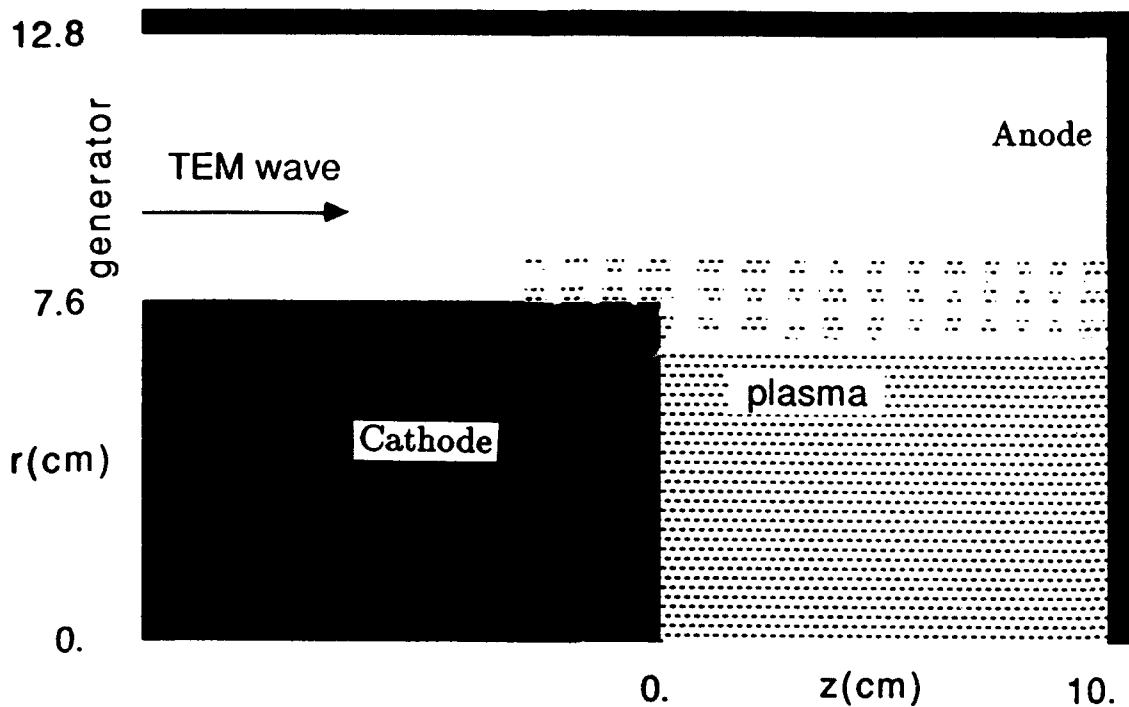


Figure 54. The simulation geometry is cylindrically symmetric around the z -axis. The cathode is the cylinder with radius 7.6 cm in the lower left of the figure, with $z = 0$ at the flat front face of the cathode. The anode is at $z = 10$ cm. The shaded regions indicate the extent of the two plasma fills in the computations.

principally C^{++} . Therefore, the ion charge to mass ratio in the simulations is the electron charge to mass ratio divided by 11,020 ($6 \times m_p/m_e$). The drift velocity has been varied from 0 to 10 cm/ μ s, but the drift speed does not play a significant role in these simulations.

The electron temperature in the diode plasma is typically in the range of 1-10 eV. The minimum spatial scale lengths of plasma phenomena are on the order of the Debye length λ_D . However, the minimum spatial scale that can be resolved in the simulation is the grid spacing Δ . The electrons in the simulation heat up via the grid instability until the Debye length is comparable to the grid spacing. Resolving realistic Debye lengths is prohibitively expensive in 2-D simulations. Since the grid instability saturates when $\lambda_D \simeq 0.3\Delta$, the electron temperature ranges from 6.5 keV to 13 keV for the simulation parameters. Sheaths that develop at the electrodes will establish voltage drops of tens of kilovolts just from the electron temperature. Therefore the simulation does not contain short wavelength instabilities and instabilities requiring low electron temperatures, which is a common problem in 2-D PIC simulations of plasma filled devices. These limitations could have a significant effect on the quantitative features of the simulations, but it is expected that most qualitative features remain unaffected.

When a user-specified electric field criterion is exceeded, electrons are emitted from the cathode using space-charge limited emission. Typically, an electric field $\sim 100\text{-}300$ kV/cm is necessary for the formation of surface plasmas from which the electrons are drawn. In a plasma opening switch, it is likely that a surface plasma is formed in the interaction of the injected plasma with the electrode surfaces. For this reason, a low threshold of 1 kV/cm is used for electron emission in regions where the plasma contacts the cathode. In other regions the simulation uses a threshold electric field of 100 kV/cm. Ion emission from the anode has been allowed, without affecting the results.

The simulation is started with a linearly ramped transverse electromagnetic (TEM) wave traveling forward axially at the speed of light through the gap at the top left of Figure 54. The phase velocity for outgoing waves is set to the speed of light. Thus electromagnetic waves reflected from the plasma opening switch travel back unattenuated as if the gap were attached to a vacuum transmission line extending to infinity. The voltage and current at the inlet gap are the sum of the incoming power pulse and the outward reflected waves. The TEM wave is linearly rising at a rate of 8.2 kA/ns (8.2×10^{12} A/s) into a matched load. The plasma opening switch has a lower impedance load than the transmission line, and part of the TEM wave is reflected. The result is that the current rises as much as a factor of two faster than for a matched load.

As described above, the limitations inherent in 2-D PIC simulations place severe restrictions on the parameters that can be modeled. One restriction is to low density uniform plasmas with high temperatures in a diode that is perfectly axisymmetric, another is that particles are completely absorbed by surfaces rather than possibly reflected. Also, electron emission from the cathode is from an infinitely thin, very dense surface plasma that does not expand from the cathode into the gap. Thus the simulations should not be viewed as a predictive replication of existing experiments. The purpose of the simulations is to gain insight into the behavior of the PFD and to make predictions as to what physical phenomena are most important and what scalings of physical parameters might be expected.

The 2-D PIC computations are compared with two simpler models. One is the code REFLEX⁴⁸, one-dimensional electrostatic particle code described in Section 9. The results from REFLEX should most closely match the ISIS runs when the gap spacing is small relative to the electrode size and when self-magnetic field effects are not important.

Another comparison is with the zero-dimensional circuit code FREYA. FREYA contains an RLC generator circuit attached to a transmission line terminated by a z-pinch plasma. The z-pinch model assumes that the entire current runs in a sheath at the plasma surface, and that the plasma mass gathers into the same sheath as the $\vec{J} \times \vec{B}$ force pushes the plasma radially inward. Then the equation of motion for the sheath radius $R(t)$ is

$$\frac{d}{dt} \left[(R_0^2 - R^2(t)) \frac{dR}{dt} \right] = -\frac{\mu_0 I^2(t)}{4\pi^2 n_0 M_i R(t)}, \quad (6-1)$$

where R_0 is the initial sheath radius, I is the diode current, n_0 is the ion number density, and M_i is the ion mass. For a linearly rising current, the equation can be written with a normalized radius $\chi = R/R_0$ and normalized time $\tau = tv_0/R_0$ as

$$\frac{d}{d\tau} \left[(1 - \chi^2(t)) \frac{d\chi}{d\tau} \right] = -\frac{\tau^2}{\chi}, \quad (6-2a)$$

where

$$v_0 = \left[\frac{\mu_0 \dot{I}^2}{4\pi n_0 M_i} \right]^{1/4}. \quad (6-2b)$$

The normalized time for the plasma to implode on axis is $\tau_i \simeq 1.5$, and the implosion time $t_i = \tau_i R_0 / v_0$ scales as v_0^{-1} . A corresponding scaling relation holds for the opening time of the PFD if opening is triggered by plasma implosion on axis.

6.3 SIMULATION RESULTS.

This section discusses the results of the 2-D computations, and compares them with computations using the 1-D code REFLEX and the 0-D code FREYA. Magnetic field penetration into the plasma is discussed first, followed by a description of the opening characteristics of the plasma filled diode. The first simulation has a plasma radius of 5 cm and electron density of $5.0 \times 10^{12} \text{ cm}^{-3}$. The two other runs shown later have a larger plasma radius of 8.6 cm, one with the same electron density ($5.0 \times 10^{12} \text{ cm}^{-3}$) and the other with a much lower density ($1.0 \times 10^{12} \text{ cm}^{-3}$). These runs give very similar results.

It is impossible to show the detailed dynamics visible in the computer movie. Instead, the few figures that can be shown may be supplemented with a description that is inspired, in part, by the additional information gleaned from the movie.

Figure 55 shows the situation early in time, at 2.5 ns. Starting at $t = 0$, a linearly rising transverse electromagnetic (TEM) wave propagates from the inlet to the plasma at the speed of light, see Figure 55(b). The plasma is conductive, and the plasma bulk is shielded by currents in a thin layer at the plasma surface: Figure 55(a) shows the direction of the current opposite to the electron flow. Equivalently, the electromagnetic fields in Figure 55 show that the radial penetration is over a couple of collisional skin depths, $\delta = c/\omega_{pe}$. When enough current has flowed to remove most of the electron charge from the first cell adjacent to the cathode, a sheath forms at the cathode. The minimum size of the sheaths in these simulations is determined by the grid spacing. Initially the sheath is also a few collisionless skin depths in radial extent but the sheath spreads until it covers the entire cathode surface.

The time τ for the sheath to spread over the whole cathode surface comes from setting the total charge in the sheath $Q \simeq \rho A \Delta z$ equal to the total charge carried by the current during its linear rise with rate \dot{I} , $Q \simeq \dot{I} \tau^2 / 2$. Here ρ is the electron charge density and A is the area of the cathode surface contacting the plasma. Then for this case, $\tau \simeq \sqrt{2\rho A \Delta z / \dot{I}} \sim 1.8 \text{ ns}$, which, when the light transit time is also considered, agrees well with the data from Figure 55.

During the low-impedance phase the current and the magnetic field penetrate into the plasma, which acquires a net negative space charge from the electrons gyrating radially inwards. The same phenomenon is reported in plasma opening switches.^{49,53} As the current increases further a current channel forms that transports the electrons from cathode to anode through their $\vec{E} \times \vec{B}$ drift velocity. The $\vec{E} \times \vec{B}$ drift velocity is parallel to the cathode surface close to the cathode, because the electric field is perpendicular to the cathode surface. Figure 56(a) shows the current vector \vec{J} at 12 ns, over the plasma portion of the diode only, while Figure 56(b) is the electric field at the same time. The current

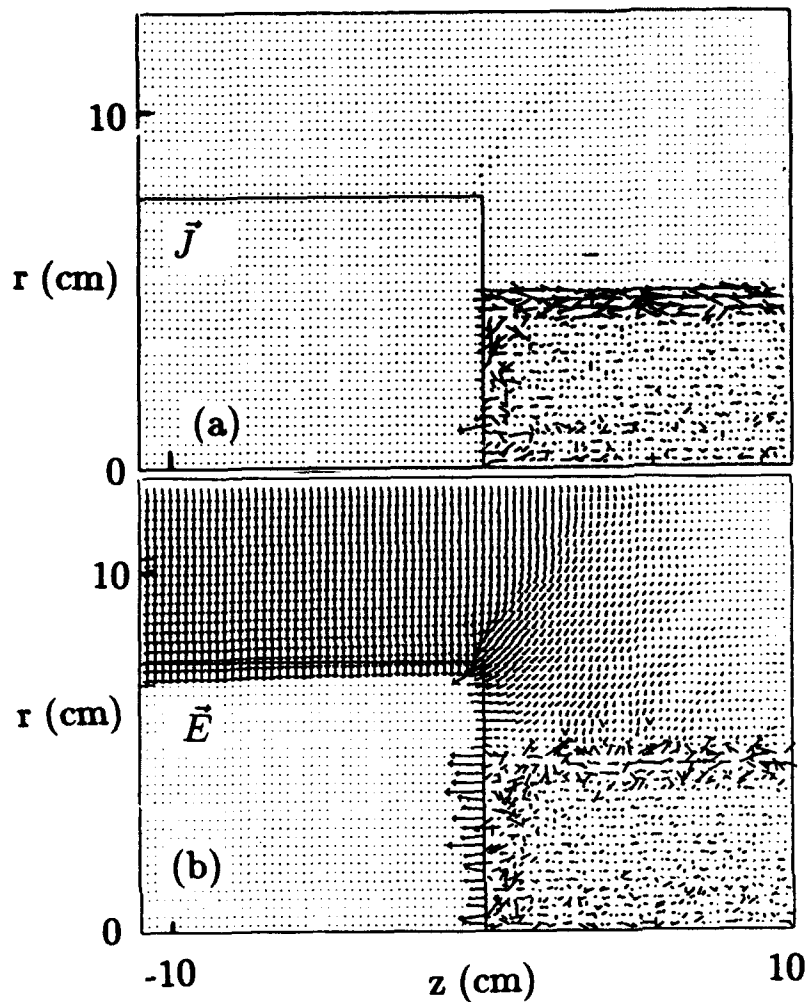


Figure 55. (a) The the current density vector \vec{J} and (b) electric field vector \vec{E} at time 2.5 ns. The electromagnetic wave has penetrated the plasma only over a few skin depths, except for a sheath at the cathode.

$\vec{J} \simeq n_e e \vec{E} \times \vec{B} / B^2$ in the electron flow is largely perpendicular to the electric field in Figure 56(b). The current in Figure 56(a) is mostly from electrons emitted from the upper part of the cathode. These electrons are focussed towards the $\vec{E} \times \vec{B}$ channel that is parallel to the axis below about $r=3$ cm. Upon reaching the anode, the electrons move parallel to the anode towards the $r=0$ axis, again because the electric field is perpendicular to the anode.

Besides the electron flow in the direction opposite to the current flow there is an additional, slower, motion radially downwards towards the axis throughout the full diode gap. Figure 57(a) shows the ion positions at 12 ns, and Figure 57(b) shows the ion phase space $r - p_r$ of radial ion momentum versus radial position. At this time the ions have not yet moved much from their original positions except near the cathode at the outside of the plasma where field-emitted electrons enter the plasma, and away from the anode: no new ions are emitted in this computation. Phase space ([Figure 57(b)]) shows that the ions outside the plasma are accelerated radially away from the plasma due to the plasma's net positive space charge. The strong electric fields in Figure 56(b) accelerate most other

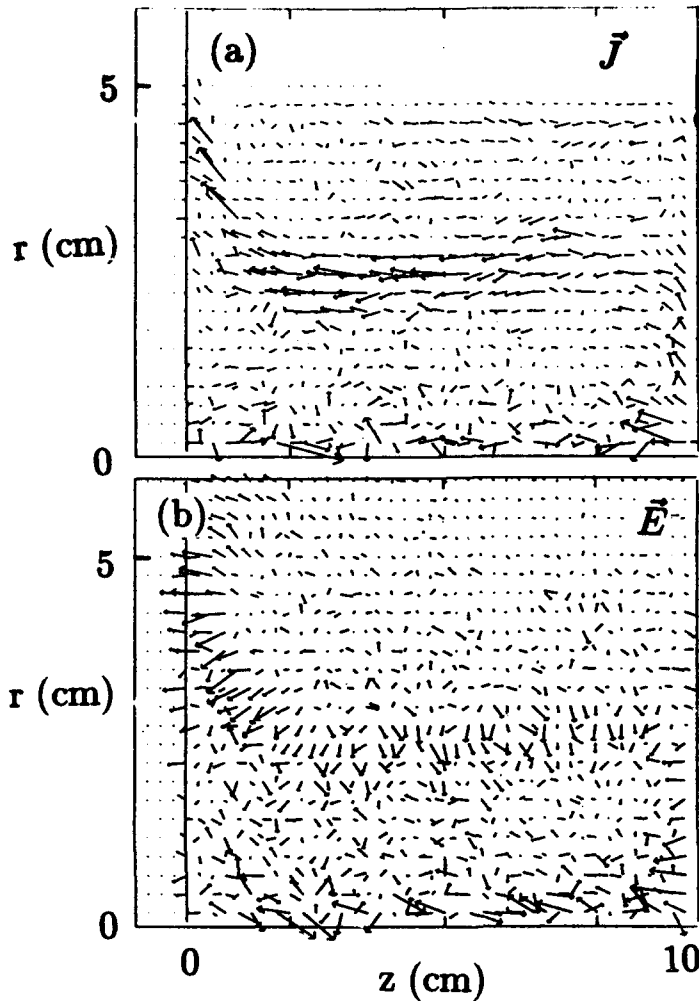


Figure 56. (a) The the current density vector \vec{J} and (b) electric field vector \vec{E} at time 12 ns over the central part of the diode. The current channel between anode and cathode corresponds to the region of non-zero electric field.

ions inward, especially the ions in the current channel at $r \simeq 3$ cm. The plasma is pulled radially inwards similar to the implosion of a z-pinch: some ions initially close to the axis have already crossed the axis and are moving radially outward through other ions that started farther away.

Figure 58(a) is the current vector \vec{J} and Figure 58(b) is the electric field slightly later, at $t = 15.5$ ns. At this time the plasma first hits the axis, approximately 3 cm away from the cathode. Figure 59(a) shows the position of the ions at $t = 15.5$ ns, and Figure 59(b) is the $r - p_r$ radial phase space. The current implodes with the plasma as can be seen in Figures 58 and 59. The current channel is now clearly reflected in the ion density: the outer layer of the ions, with $r \gtrsim 3.5$ cm, has remained relatively stationary, while the innermost ions are swept up by the electric field of the current channel. Other diagnostics show that the implosion point moves forwards axially, hitting the axis 2 ns later near the anode.

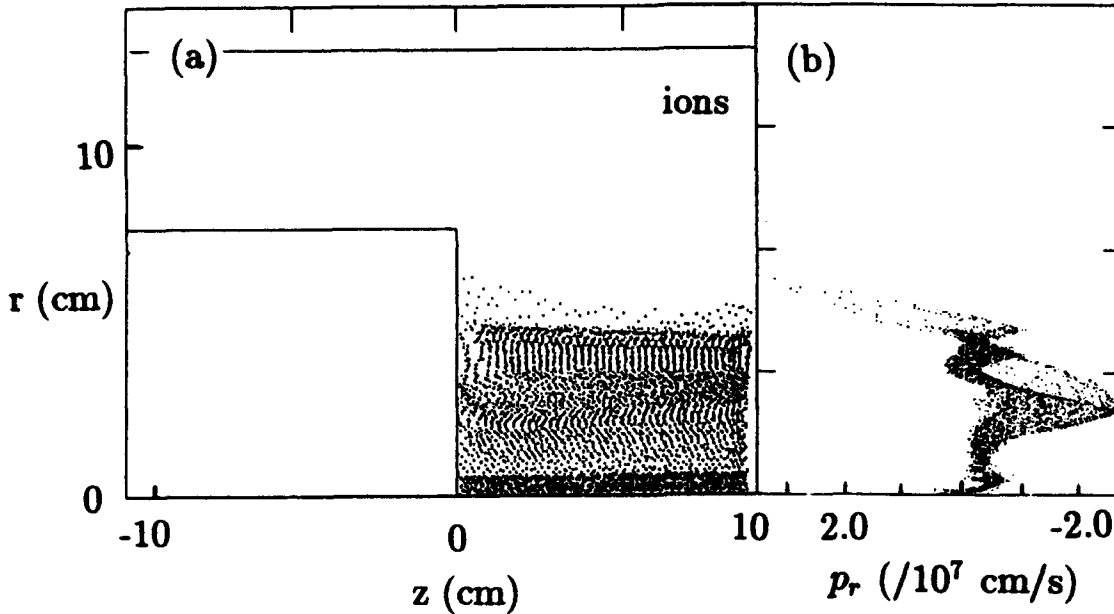


Figure 57. Ion $z - r$ configuration space (a) and ion $r - p_r$ phase space (b) at 12 ns, just before the plasma channel hits the axis.

Voltage and current are shown in Figure 60. In Figure 60 the voltage is the line integral of the axial electric field component $V(t) = -\int E_z(z, r) dz$ along a path parallel to the axis at a given radius r . The solid line is at $r \simeq 0.4$ cm near the axis.

In general the voltage between two points "1" and "0" has two components. The electrostatic component is $\int_0^1 \vec{E} \cdot d\vec{l} = -(\phi_1 - \phi_0)$, which vanishes when the integral is taken around a closed loop, i.e., when point "1" is the same as point "0". The inductive component is the remainder. Around a closed loop of area \vec{S} the electric field satisfies $\int \vec{E} \cdot d\vec{l} = -\partial(\int \vec{B} \cdot d\vec{S})/\partial t$, which is not necessarily zero. The inductive part of the voltage is therefore the difference between the electric field integrated around two different paths between two conductors.

The integral of the electric field at $r \simeq 0.4$ cm is computed close enough to the $r = 0$ axis that the inductive component (proportional to the area $|S|$) can be ignored. This integral approximates the electrostatic voltage. The dash-dot line is the integrated electric field at $r \simeq 5.4$ cm, near the plasma edge: the difference between these curves is the inductive voltage.

Opening of the PFD at $t = 15$ ns is visible in a rapid increase in the electrostatic voltage (at $r = 0.4$) followed by large excursions as the plasma bounces around the axis. At $r = 5.4$ cm outside the plasma the voltage increases more gradually. The two voltages track each other, on average. Therefore the PFD opens electrostatically. The current rises more slowly during PFD opening. The fast wiggles in voltage and current in Figure 60

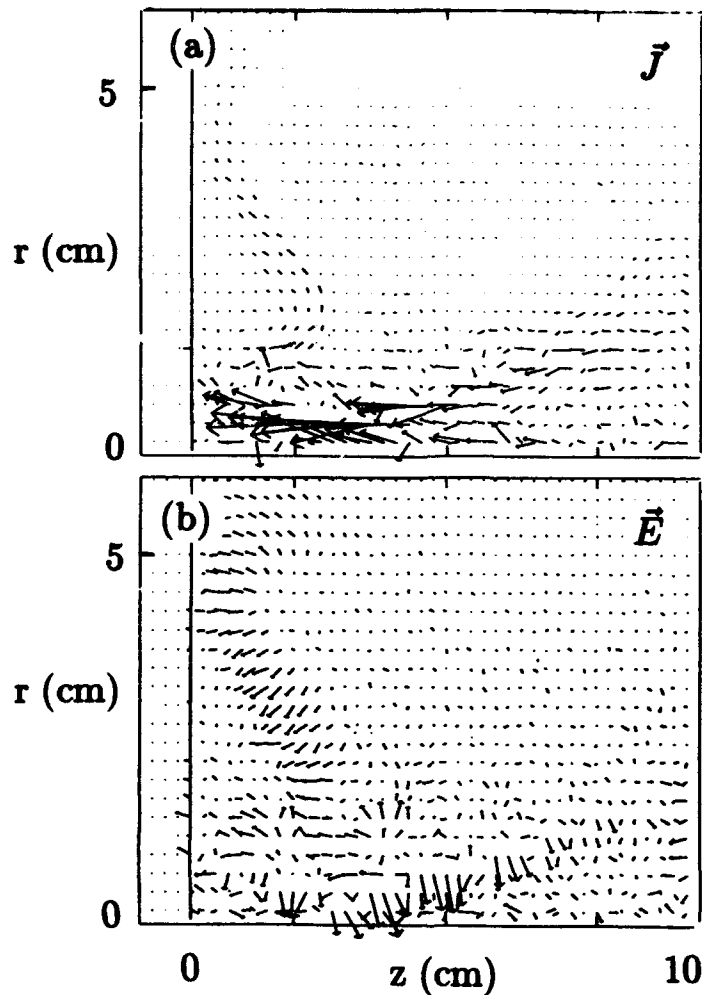


Figure 58. (a) The the current density vector \vec{J} and (b) electric field vector \vec{E} at time 15.5 ns over the central part of the diode, just before the ions hit the axis. The current channel between anode and cathode corresponds to the region of non-zero electric field where $\vec{E} \times \vec{B}$ is substantial.

come from Fourier smoothing of the data. The raw voltage and current vary on the intrinsic time scale of the computation, much faster than can be observed in an experiment.

Figure 61(a) shows the current vector \vec{J} and Figure 61(b) shows the electric field vector \vec{E} at $t = 22.5$ ns, the time of the second rapid increase in the voltage on axis. Most of the current is carried by electrons that come off the cathode shank and the upper portion of the cathode face. These electrons move radially inwards parallel to the cathode until reaching the axis around $z \simeq 3$ cm. Then the electrons flow mostly parallel to the axis through the imploded z -pinch material until they pinch for the last time near the anode. The axial electric field component E_z is largest in the current channel parallel to the cathode: most of the voltage drop occurs across this sheath.

The sheath is also visible in the the position of the ions, Figure 62(a), and the position of the emitted electrons, Figure 62(b), at time $t = 22.5$ ns. The ions form an anode gap near the axis and a gap near the top of the cathode. In the center of the gap, the ions are

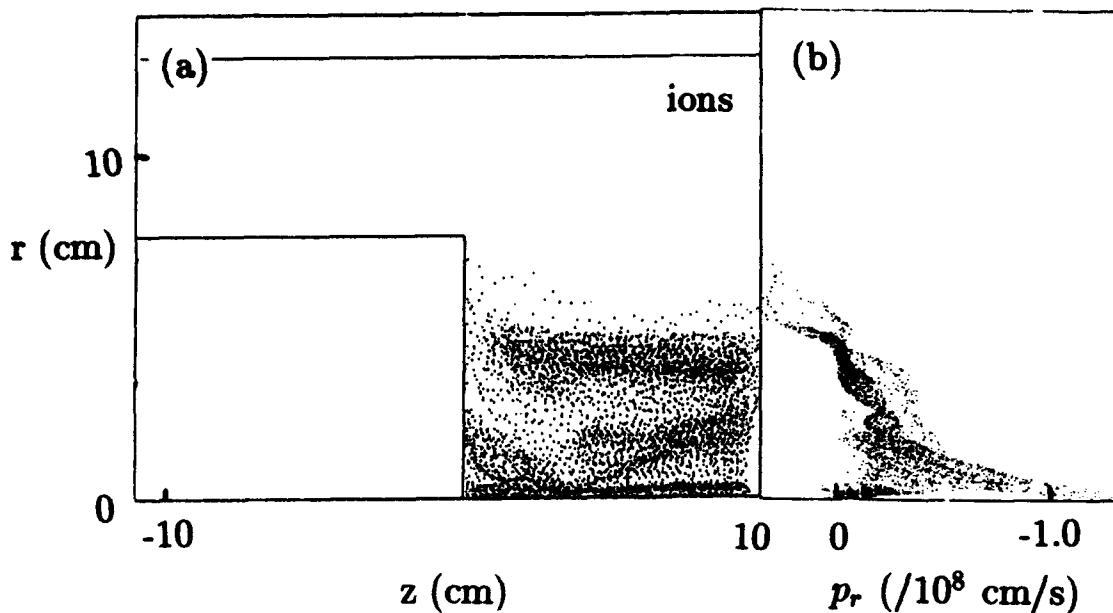


Figure 59. Ion $z - r$ configuration space (a) and ion $r - p_r$ phase space (b) at 15.5 ns, just before the ions hit the axis.

mostly cleared away by the implosion of the plasma. The positively charged plasma at the upper radii funnels the electron beam flow toward the axis after opening.

Which aspects of the full two-dimensional dynamics are captured by the simpler models? Figure 63 gives the voltage and current computed for the same parameters with the one-dimensional code REFLEX, which contains axial dynamics but ignores radial structure. In REFLEX the PFD exhibits a longer conduction time. As discussed more fully in other sections, the voltage drop across the diode begins when the driven current exceeds the thermal current $I \geq 0.5en_0v_tA$. Here v_t is the electron thermal velocity and A is the electrode area. A potential hill develops in the simulation that accelerates ions to both electrodes. The width of the anode and cathode sheaths increases as the current in the diode increases. The anode develops a negative space charge as the plasma in the gap develops a net positive space charge. The sheaths increase as the interaction between the diode electron beam with the plasma gradually decreases the plasma electron population. When the number of plasma electrons pulled out of the plasma decreases dramatically, the diode impedance rises rapidly.

Electron phase space $x - v_x$ in Figure 64(a) at 20 ns shows that the emitted electrons are accelerated by a cathode sheath, interact in a coherent fashion with the trapped plasma, and decelerate somewhat across an anode sheath. The ions in Figure 64(b) accelerate towards the cathode, coast through the central plasma, and accelerate further towards the anode. The start of the opening event, at 22.8 ns in the one-dimensional simulations, is correlated with a decrease in the anode electric field. At this point the difference between the maximum voltage in the simulation and the diode voltage starts decreasing. The

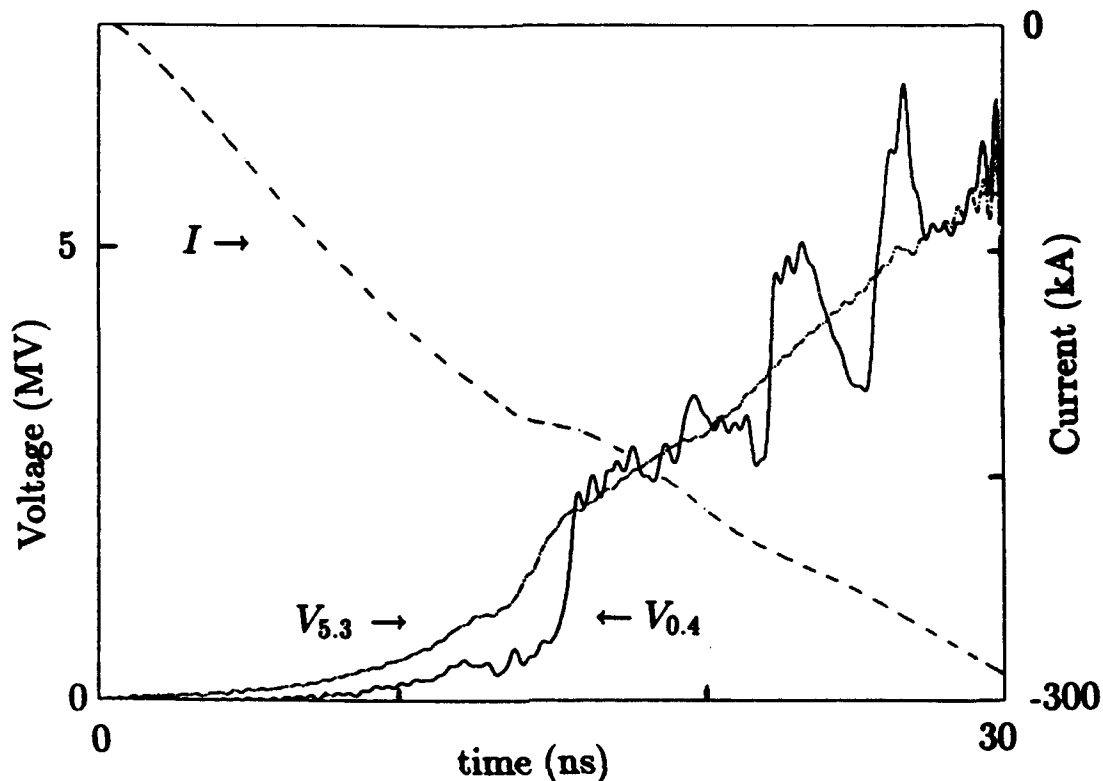


Figure 60. The voltage $V(r) = -\int E_z dz$ at $r = 0.4$ cm (solid line) and at $r=5.3$ cm near the plasma edge (dash-dot), on the left scale. The current (dashed) is on the right scale.

opening in the one-dimensional calculations is driven by expansion of the cathode sheath as can be seen in Figure 64(c) and Figure 64(d) at 30 ns.

There are significant qualitative differences as well as quantitative differences between the one-dimensional and the two-dimensional simulations. Most of the differences can be attributed to bending of the electron flow by the self magnetic field of the electron beam in the two-dimensional computations, which is absent in one dimension, and the streaming instabilities that are enhanced in one dimension but not prominent in two dimensions. For example, only a remnant of the positively charged plasma and potential hill in the one-dimensional simulations is observed in the positively charged plasma above the current after the $\vec{E} \times \vec{B}$ channel is established in the two-dimensional simulations. This potential hill focuses the electron flow below the positively charged plasma as well as shedding ions towards the cathode. The electric field structure responsible for accelerating the electron beam during opening of the two-dimensional PFD computation is located near the cathode for larger radii and near the anode for smaller radii, with a complex shape in between. The electron beam in the REFLEX simulation is accelerated across a cathode sheath.

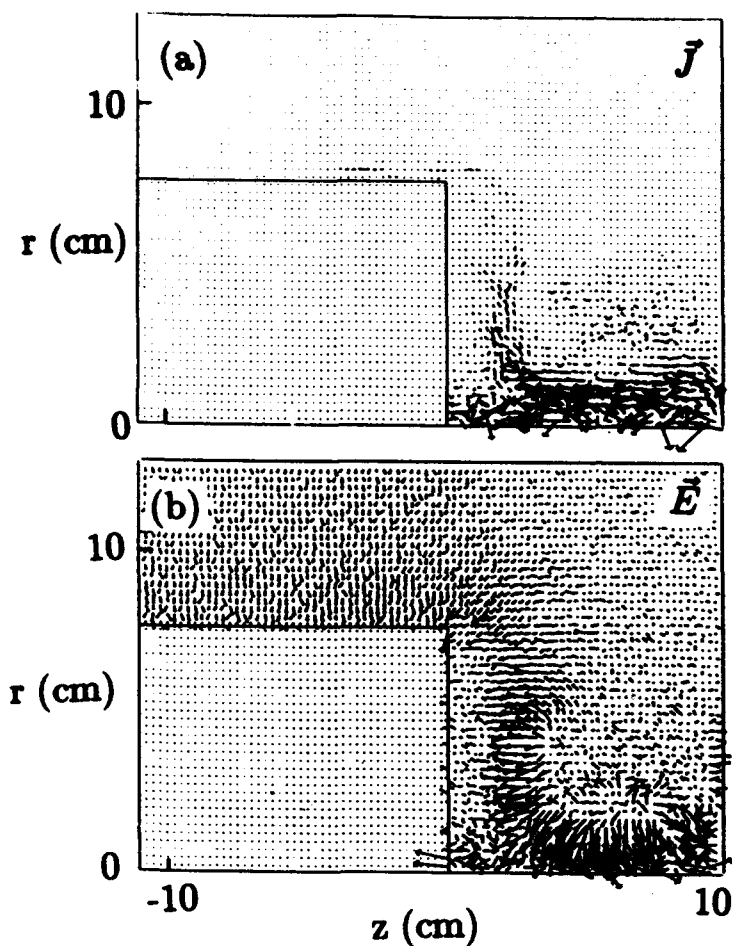


Figure 61. (a) The the current density vector \vec{J} and (b) electric field vector \vec{E} at 22.5 ns. The current moves radially inward at the cathode sheath to 3 cm and then focuses on the axis near the anode.

The hydrodynamic radial motion important in two dimensions is missing in the REFLEX simulations.

The two-dimensional simulations suggest that the opening process is determined by the pinching of the plasma in the central part of the diode. Pinching should be reproducible with a simple zero-dimensional model as implemented in FREYA. The particle plots of Figures 59 and 62 indicate that the plasma above $r=3.5$ cm is not driven towards the axis. Therefore the initial radius R_0 for FREYA is chosen as $R_0 = 3.5$ cm rather than the 5 cm radius of the initial plasma fill. Figure 65 shows the voltage and current generated by FREYA for the same parameters and circuit model as the two-dimensional and one-dimensional computations. The plasma hits the $r=0$ axis at 15.7 ns, in agreement with the two-dimensional simulations. It should be noted that the voltage in Figure 65 is purely inductive, although this computation overestimates the inductive effects by the assumption that the plasma implodes at the same time over the entire axis, in contrast to the two-dimensional simulations that show considerable two-dimensional structure. Despite the

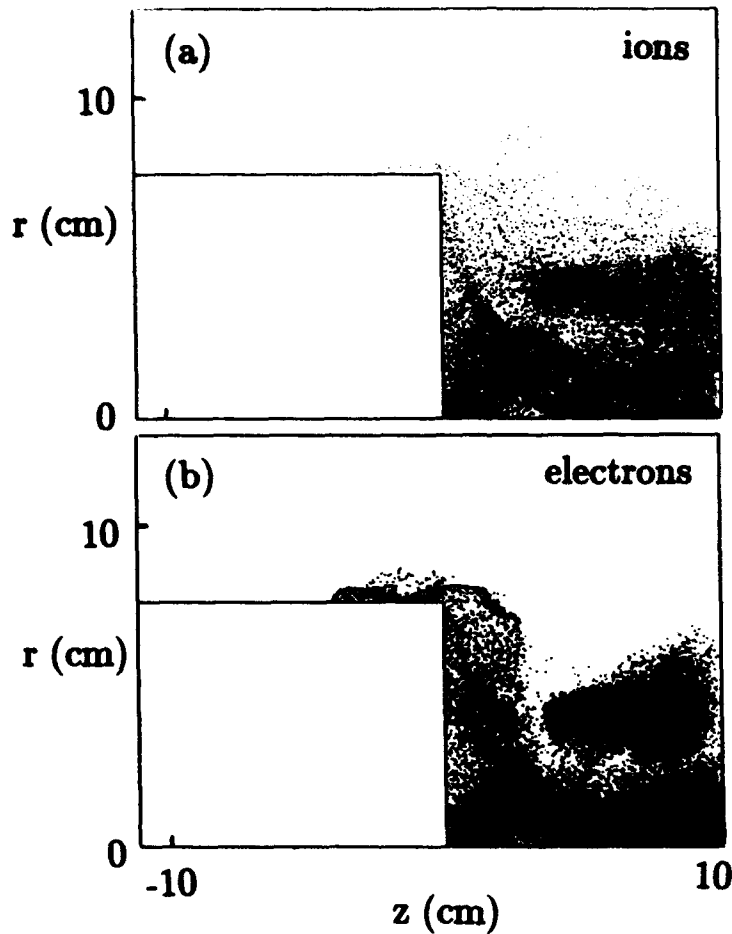


Figure 62. Ion $r-z$ configuration space (a) and electron $r-z$ configuration space (b) at 22.5 ns, just before the ions hit the axis. The plasma at the top right side is positively charged. The electron flow is through the low-density region below this plasma.

agreement in the implosion (opening) time the values of current and voltage generated in FREYA do not agree with the two-dimensional simulations.

Two other 2-D PIC computations serve to illustrate that the 2-D dynamics seen above are fairly typical of a PFD. The first is for electron density $5.0 \times 10^{12} \text{ cm}^{-3}$, as before. However, the initial plasma position in the diode is now out to a radius of 8.6 cm, 3.6 cm beyond the previous plasma limit at $r = 5.0$ cm. In addition, the plasma extends 3 cm to the left of the cathode face as shown by the widely spaced dashes in Figure 54. The total amount of plasma in the diode has increased threefold.

Figure 66 shows the ion position and the radial phase space $r-p_r$ at opening, which is 26.5 ns in this case. The same qualitative features are seen as in the corresponding Figure 59. The principal difference is a second region of higher ion density, at 3.5 cm, when the first ions collide on axis. The electric field (not shown) is again largest in a sheath parallel to the cathode for the larger radii ($r \geq 3$ cm), and therefore the current pinches at the anode starting from a larger radius, $r \simeq 4$ cm.

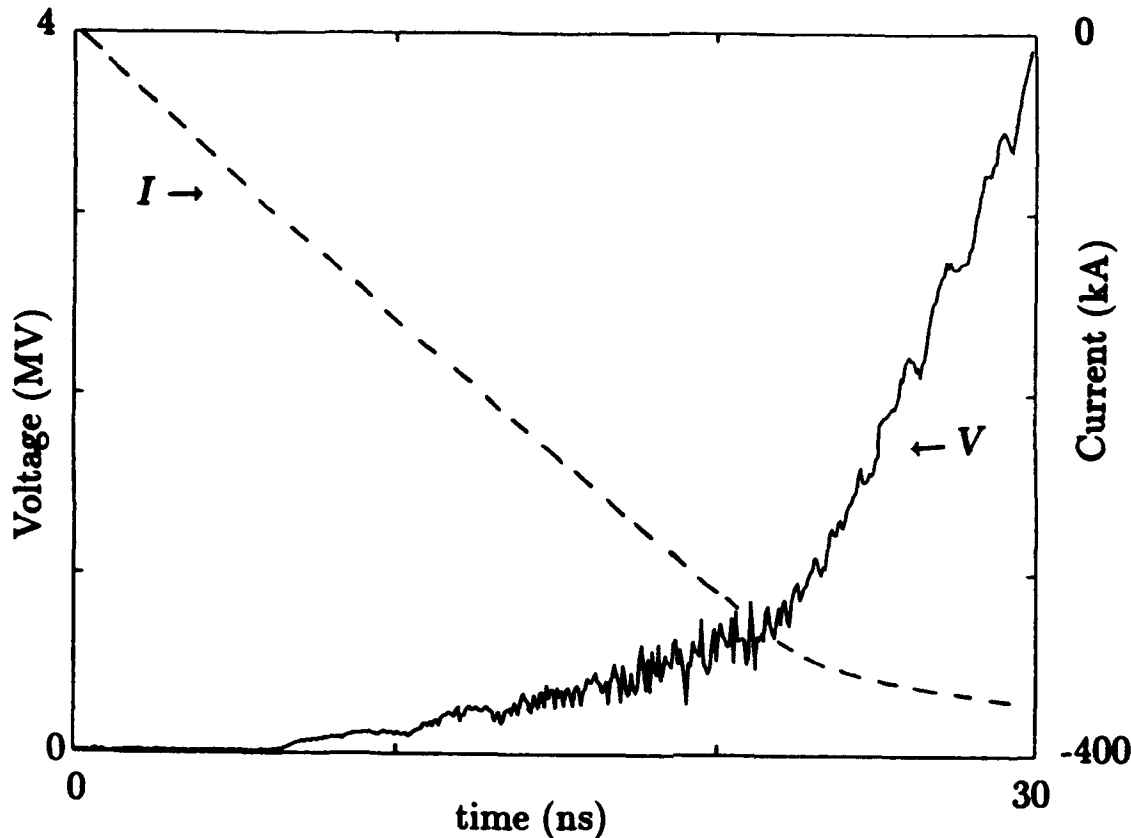


Figure 63. Voltage and current for the PFD modeled with the one-dimensional code RE-FLEX. Opening begins at 22.8 ns, significantly later than the ~ 15 ns opening time for the two-dimensional ISIS run.

The voltages in Figure 67 are the line integrals $-\int E_z dz$ close to the center at $r = 1.9$ cm (dash-dot line) and at the edge of the cathode at $r = 7.6$ cm (solid line). The electrostatic voltage at $r = 1.9$ cm is now always much smaller than the voltage at 7.6 cm. Therefore the PFD opens, between 20 and 30 ns, through an inductive mechanism. The ions close to the anode in Figure 66 show evidence of an electrostatic sheath region close to the axis (for $r \lesssim 1$ cm), but not at larger radii. The current in Figure 67 rises smoothly throughout the run, decreasing in slope as the voltage increases.

The total ion density appears to be a principal parameter that affects the opening mechanism. The final ISIS computation in this section is with the plasma in the larger region (see Figure 54) but at reduced density, $1.0 \times 10^{12} \text{ cm}^{-3}$. Figure 68 shows the ion locations at 12.5 ns, 18 ns, 22 ns (at opening), and 25 ns. At 12.5 ns the current channel is forming toward the outside of the plasma, compare Figure 57. At 18 ns the current channel is established across the diode to the anode and is moving towards the $r=0$ axis. At 22 ns, the ions are just hitting the axis, and the PFD opens as seen from the voltage in Figure 69. The voltages at $r=1.9$ cm (dash-dot) and $r=7.6$ cm (solid line) correlate closely

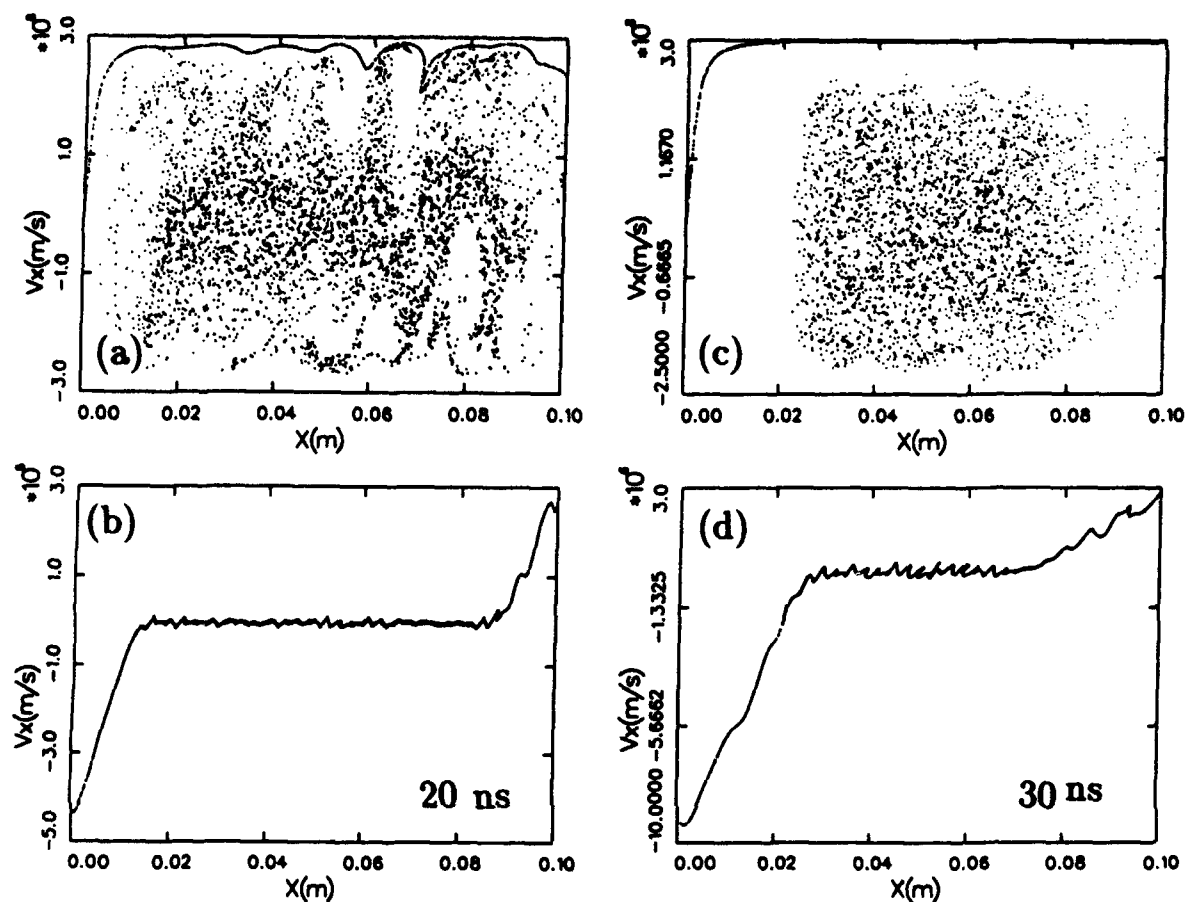


Figure 64. Electron (top) and ion (bottom) $x-v_x$ phase space plots from the one-dimensional code REFLEX, before opening at 20 ns (left) and after opening at 30 ns (right). Before opening, emitted electrons are accelerated by the cathode, interact with the trapped plasma, and are decelerated by the anode. Before opening the ions are accelerated towards both electrodes. After opening the plasma is characterized by a rapid expansion of the cathode sheath.

as the ions approach the $r=0$ axis before opening at $t = 20$ ns, and also for later times. Thus the voltage is largely generated by an electrostatic space charge gap.

Our computations show that the current in the two-dimensional simulations is always smaller than the current in the one-dimensional REFLEX simulations, while the voltage and impedance in the two-dimensional simulations are always larger than the voltage and impedance in the one-dimensional simulations. Thus the one-dimensional simulations suggest a limit on the conduction time and conduction current in a PFD. The self magnetic field of the electron beam increases the impedance of the PFD over the one-dimensional limit, because the self-magnetic field bends the electron trajectories radially inwards, decreasing the area available for conduction.

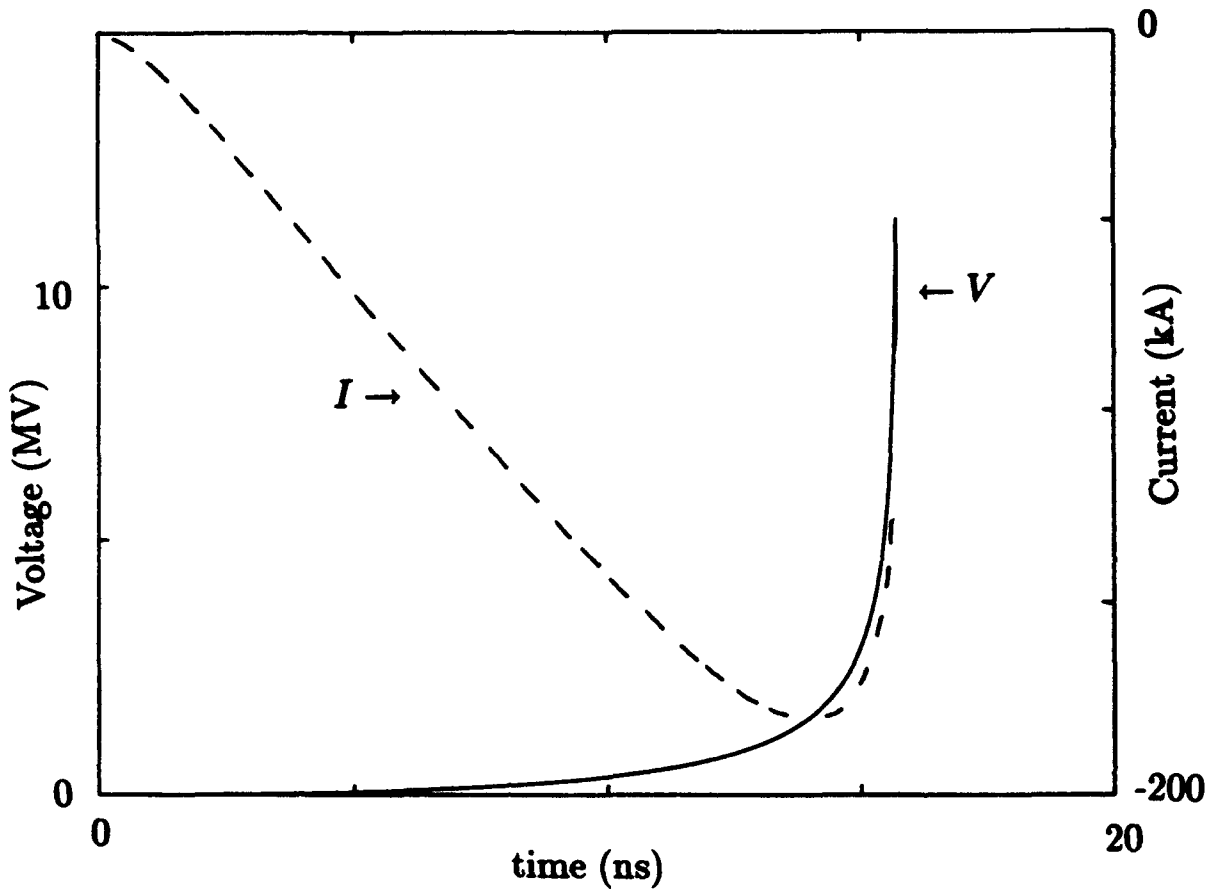


Figure 65. Voltage (solid line) and current (dashed line) computed by FREYA. With an initial radius $R_0 = 3.5$ cm the imploding plasma hits the axis at the same time as in the two-dimensional ISIS calculations.

When the implosion time for the plasma is less than the sheath erosion time for the one-dimensional REFLEX model, the conduction time of the two-dimensional ISIS simulations is similar to the implosion time predicted by a simple zero-dimensional implosion model. The implosion time in this case can be scaled with parameters directly from the analytical expressions used in the computations, Equations (1) and (2). The implosion time is $t \simeq 1.5R_0/v_0$ with

$$v_0 = (\mu_0/4\pi n_0 M_i)^{1/4} \dot{I}^{1/2}. \quad (2b)$$

In a PFD in an inductive circuit the current rises linearly during most of the conduction phase, and \dot{I} is a well-defined parameter. Then conduction time should approximately scale as the initial radius R_0 and the fourth root of the plasma density ($n^{1/4}$), and as the inverse square root of the rate of current rise ($\dot{I}^{-1/2}$). The conduction current I_c would scale as the current rate of rise multiplied by the implosion time, or as the square root of

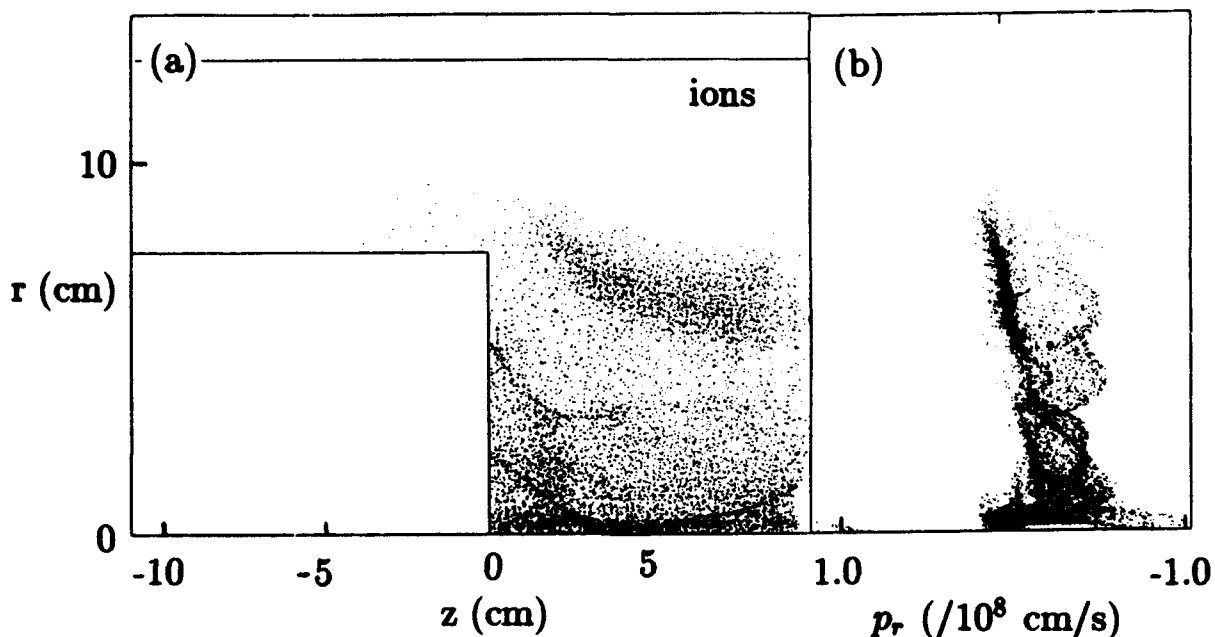


Figure 66. Ion $z - r$ configuration space (a) and ion $r - p_r$ phase (b) at 26.5 ns, just before the ions hit the axis, in a two-dimensional ISIS run with plasma extending out to 8.6 cm and initial density $5.0 \times 10^{12} \text{ cm}^{-3}$.

the rate of current rise ($I_c \propto \dot{I}^{1/2}$). Scaling with density is the same as for the implosion time, $I_c \propto R_0 n^{1/4}$.

For a PFD in the hydrodynamic limit a doubling of the plasma density increases the conduction time and current by only 19%. For the two computations that can be directly compared, the extended plasma fill with $5.0 \times 10^{12} \text{ cm}^{-3}$ and $1.0 \times 10^{12} \text{ cm}^{-3}$, the scaling is even slower than $n^{1/4}$. This is because the electron current channel penetrates deeper into the plasma at the higher density, which decreases the initial radius of the implosion.

Without experimental information about the proper initial conditions for the simulations it is difficult to match the simulations with the experiments. Moreover, the two-dimensional simulations must be run with artificially low plasma densities, because the runs are too expensive for realistic parameters. Instead, extrapolation from the two-dimensional computations must be done with either the simpler zero-dimensional snowplow model or the one-dimensional PIC model.

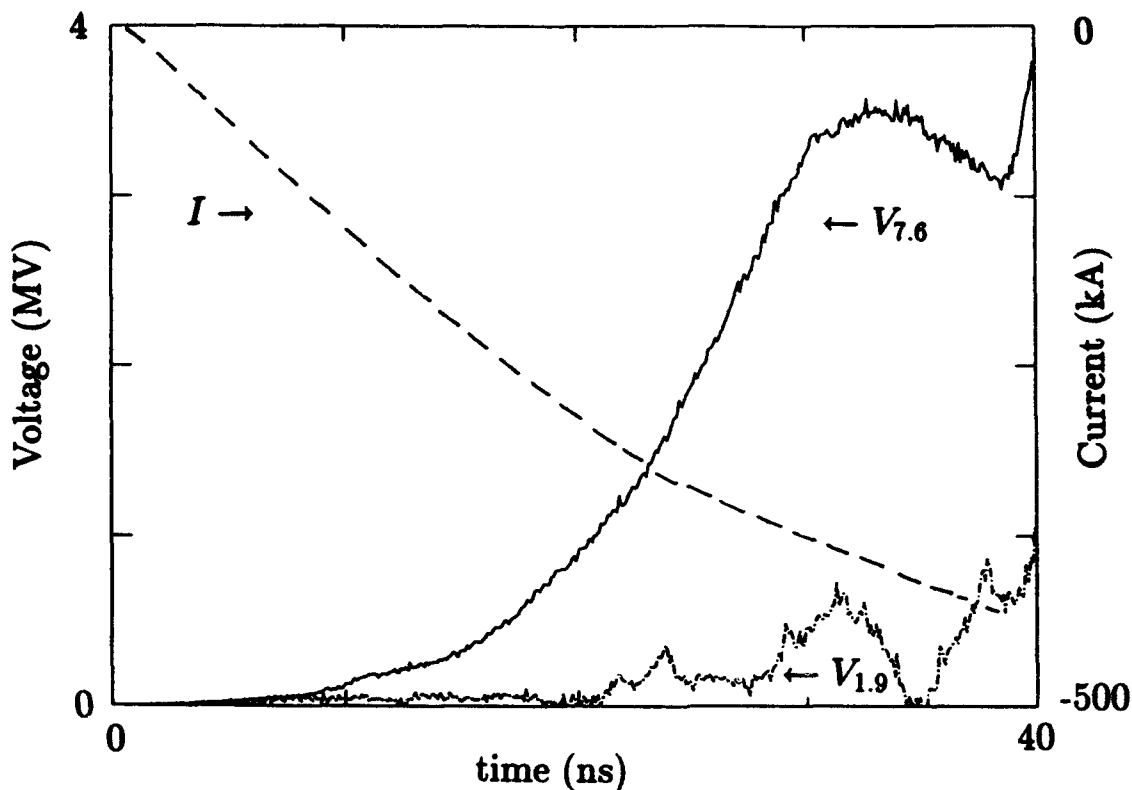


Figure 67. Voltage $V(r) = -\int E_z dz$ at $r = 1.9$ cm (dash-dot line) and at $r=7.6$ cm (solid line) near the plasma edge, on the left scale. The current (dashed line) is on the right scale.

With this approach the agreement with experiment is reasonable. For example, the data from the GIT-4 generator⁴⁴ indicates that the conduction current I_c depends weakly on the rate of current rise, $I_c \propto \dot{I}^{0.2}$, at least for a delay time of $4.5 \mu\text{s}$ between firing the plasma guns and the main generator pulse. For a delay time of $5 \mu\text{s}$, the conduction current depends more strongly on the rate of current rise, $I_c \propto \dot{I}^{0.35}$. These scalings are comparable to the $\dot{I}^{0.25}$ scaling of the one-dimensional simulations. More plasma should be in the PFD when the delay time is increased. Thus the PFD at the delay time of $5 \mu\text{s}$ may be moving into the regime where hydrodynamic effects limit the conduction time.

Scaling with the number of plasma guns indicates that the conduction current depended on the square root of the plasma density $n^{1/2}$. This scaling data agrees more with one-dimensional REFLEX simulations than with a hydrodynamic model. Thus it is likely that the PFD in their experiments are more limited by sheath erosion processes than by hydrodynamic implosion of the plasma. However, the geometrical differences between the experiments and the simulations may influence these results.

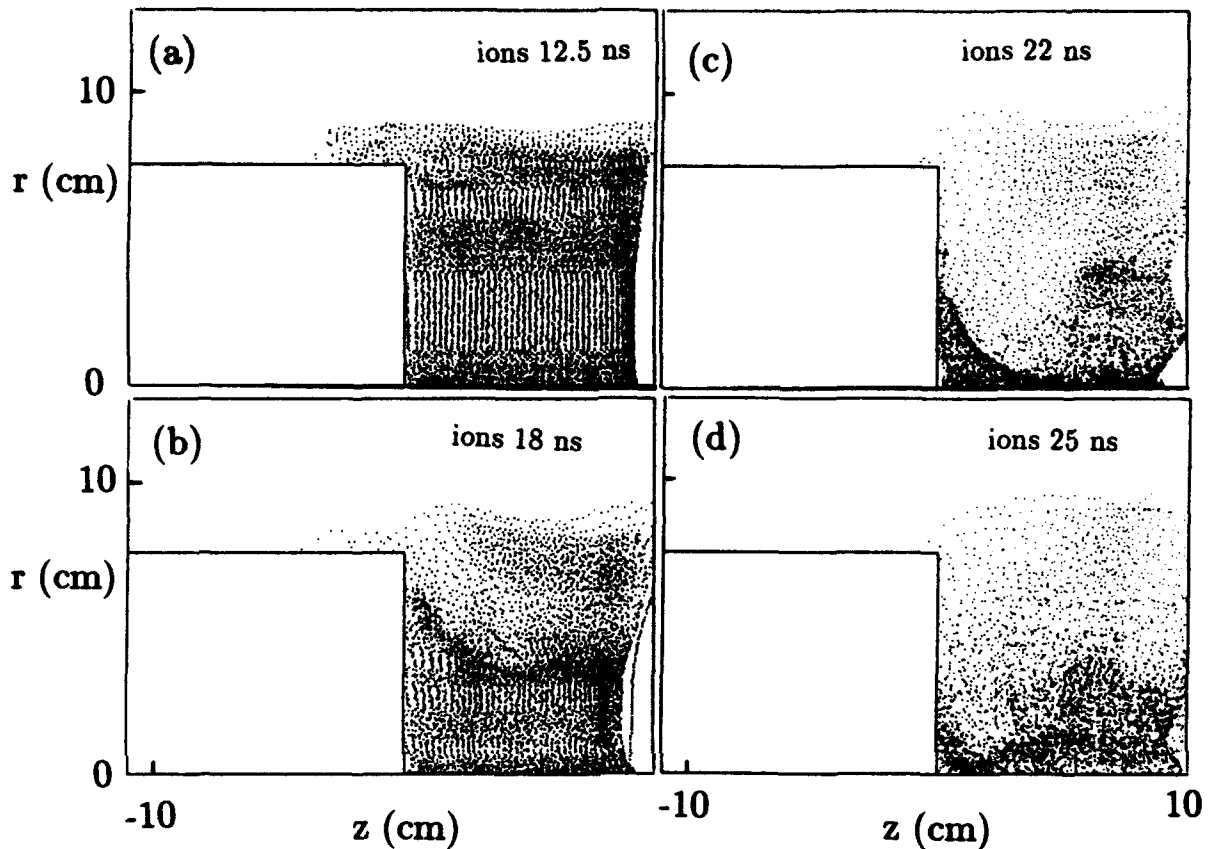


Figure 68. Ion $r - z$ configuration plots at times of (a) 12.5 ns, (b) 18 ns, (c) 22 ns, and (d) 25 ns for an extended plasma fill with density 10^{12} cm^{-3} in a two-dimensional ISIS computation.

6.4 CONCLUSION.

This section presents results from two-dimensional PIC simulations of plasma filled diodes for low plasma densities and short conduction times, and compares these with simpler one- and zero-dimensional models. In the two-dimensional computations the diodes consist of a solid cylindrical cathode inside a hollow cylindrical anode with flat faces for the anode and cathode. The plasma is a single ionic species, C^{++} , initially uniform out to a defined radius. Several phases of PFD behavior are identified. Early in time, the magnetic field and electron current penetrate along the cathode but are shielded from the plasma interior elsewhere. The electrons pinch towards the axis when they are near the anode surface. The ions near the anode are accelerated towards the cathode by the excess electron space charge in the plasma. The self magnetic field of the electron beam eventually bends electrons into the plasma. An $\vec{E} \times \vec{B}$ current channel forms in the plasma. The plasma above the channel is charged positively and the plasma below the channel is

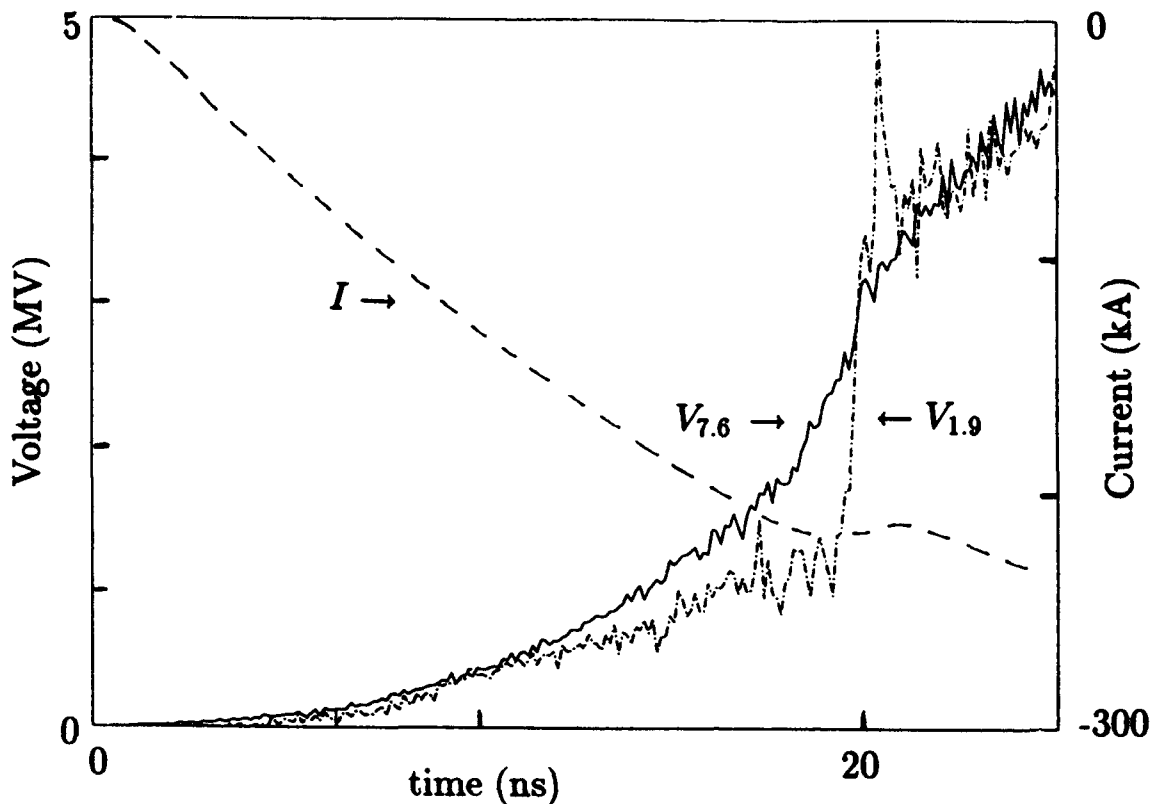


Figure 69. Voltage $V(r) = -\int E_z dz$ at $r = 1.9$ cm (dash-dot line) and at $r=7.6$ cm near the plasma edge (solid line), on the left scale. The current (dashed line) is on the right scale. Opening occurs at about 20 ns.

charged negatively. The channel implodes towards the axis by its own $\vec{J} \times \vec{B}$ force. Most but not all of the ions are swept along with the current channel towards the axis. For the parameters examined here, the implosion of the plasma determines the conduction time of the PFD.

The opening of the PFD is more complicated than the cathode sheath models²⁵ described elsewhere. The opening combines erosion of ions from the plasma near the upper part of the cathode with the acceleration of ions near the lower part of the anode into the plasma to create a gap there with ions swept out by the current channel in between. The voltage generated by the opening event can have a substantial inductive contribution from the implosion of the current channel as well as an electrostatic contribution from gap formation.

The two-dimensional electromagnetic PIC simulations (ISIS) compare reasonably well with the two simpler models, a one-dimensional electrostatic PIC simulation (REFLEX) and a zero-dimensional snowplow model (FREYA). Each of the simpler models is connected to the same circuit as the two-dimensional simulations. These models are far cheaper to

run computationally than the two-dimensional PIC simulations. However, effects such as an initially non-uniform plasma density with several ionic species, or electrode plasmas, can be included in the simpler models relatively quickly to assess their effect on PFD performance.

For the parameters examined in this paper, the implosion time from the snow-plow model is either less than or comparable to the conduction time from the one-dimensional models, and in closer agreement with the conduction time of the two-dimensional PIC simulations. The one-dimensional PIC simulations yield an upper limit to PFD performance. The conduction time and current in the one-dimensional simulations should be larger than the conduction time and current in an actual PFD. Comparisons of the conduction time of the one-dimensional model with the snow-plow model indicate which physical effect dominates the conduction time, sheath erosion or bulk implosion. If the conduction time is hydrodynamically limited, as in the two-dimensional PIC simulations, the scalings for the conduction time are comparable to experimental data.

SECTION 7

OPENING SWITCH STUDIES WITH ANTHEM

ANTHEM⁵⁹, a computer code developed by R. Mason at Los Alamos National Laboratory, is one of the few computational models potentially capable of simulating long conduction time plasma opening switches. At this time the code is still experimental and has not been thoroughly examined with a variety of problems and applications. This section contains some tests with the code to see how well it can simulate the behavior of plasma opening switches. A problem in the way ANTHEM computes current should be fixed with a minor adjustment of the boundary conditions. To date, the ANTHEM simulations have all run in an exclusively fluid mode. However, the particle option of ANTHEM needs to be used to describe the motion of electrons from the cathode.

7.1 INTRODUCTION.

Development of an opening switch is a critical element in the application of inductive energy storage technology to the DECADE simulator. The leading opening switch candidates, such as the plasma erosion opening switch (PEOS), the plasma-filled diode (PFD), and the density-controlled opening switch (DCOS) rely on the behavior of a plasma injected between electrodes in vacuum. Opening switches currently available in the laboratory do not operate at the power levels required for DECADE. Moreover, these devices are not well enough understood to confidently design a plasma opening switch for DECADE.

Several phenomenological models are used for extrapolating experimental data, including simply fitting curves to the data. These models generally fall into three categories, sheath erosion models, hydrodynamic models, and diffusion models. None of the simple models are derived from first principles by a series of approximations. Instead, a reasonable mechanism is postulated to dominate in a highly simplified geometry. Then the consequences of these assumptions are evaluated more or less rigorously, and the results compared to experiment. What survives the comparison is accepted as the working model, at least until further work shows discrepancies, or a more rigorous approach becomes possible.

Alternatives are large computations based on first principles. Particle codes have had success in yielding insight into the behavior of opening switches at low densities (10^{12} - 10^{13} cm^{-3} electron number density) and short conduction times (< 100 ns). One computational model potentially capable of simulating high-density, long conduction time switches is the multi-fluid code ANTHEM, developed by Rod Mason at Los Alamos National Laboratory. ANTHEM employs an advanced implicit formulation of the electromagnetic field equations coupled with a set of fluid equations to describe the electron and plasma behavior. However, this code has not yet acquired the level of confidence and reliability that comes with careful testing and successful application to a range of problems.

At DNA's request, Jim Geary from BRA and John Grossman from NRL's Code 4770 have collaborated in evaluating ANTHEM for its use in long conduction time switch problems. The eventual goal is the development of ANTHEM into a reliable tool for studying, and possibly for designing, plasma opening switches for DECADE and beyond. The evaluation is done in two phases. The first is confirming that the computational model is

implemented correctly, i.e. essentially debugging the code. This involves running ANTHEM on a set of test problems where known solutions exist and comparing ANTHEM's predictions with these solutions. The other phase is examining whether the model, or more specifically, the set of equations that ANTHEM is based upon, is adequate to predict plasma opening switch performance. The second phase is more subtle and difficult.

The remainder of this section is subdivided into the following subsections. The code model is discussed in Section 7.2. The fluid equations are derived, with special attention to the assumptions that go into ANTHEM's equations. Section 7.3 investigates the accuracy of the code model as it currently stands. For the first test, ANTHEM is configured as a shorted vacuum transmission line for examining vacuum electromagnetic wave propagation. In much the same geometry, the next test produces planar Child-Langmuir flow across a vacuum gap. The final test examines the behavior of a plasma in a shorted transmission line. This test reveals a problem near the upper radial conductor in the presence of charged particles. Section 7.4 discusses the adequacy of the model for long conduction time plasma opening switches, in particular the applicability of the present model under various plasma conditions. Some suggestions are made that might improve ANTHEM's performance on this problem. ANTHEM's performance on a short conduction time, low density plasma opening switch is compared with the predictions from the explicit particle code MASK. Section 7.5 describes the RLC generator circuit model attached to a transmission line that has been added to ANTHEM, and the test results. Section 7.6 discusses the results and conclusions of the work, and sets out directions for the future.

7.2 SIMULATION MODEL.

The ANTHEM code utilizes a fluid description of the behavior of the plasma electrons, plasma ions, and electrons emitted from the cathode. A separate set of fluid equations is solved for each of these species. These fluid equations coupled with Maxwell's equations for the electric and magnetic fields comprise the heart of the model. The derivation of the complete fluid equations will be reviewed in this subsection following Braginskii.⁶⁰ ANTHEM uses a simplified set. The approximations employed and their physical implications are also discussed. Throughout the particle motion is assumed to be nonrelativistic.

A plasma can be described by a Boltzmann equation for the distribution function f_α of each particle species (electrons and ions) and of each neutral species,

$$\frac{\partial f_\alpha(\vec{x}, \vec{v})}{\partial t} + \vec{v} \cdot \nabla f_\alpha(\vec{x}, \vec{v}) + \vec{a} \cdot \nabla_v f_\alpha(\vec{x}, \vec{v}) = C_\alpha, \quad (7-1)$$

where C_α is the collision term describing the interaction of species α with all the other species and the boundaries. The distribution function is normalized such that

$$n_\alpha(\vec{x}, t) = \int f_\alpha(\vec{x}, \vec{v}, t) d\vec{v},$$

where n_α is the number density of species α . The acceleration \vec{a} of a charged particle of species α with charge q_α and mass m_α is given by the Lorentz force law,

$$\vec{a}(\vec{x}, t) = \frac{q_\alpha}{m_\alpha} \left[\vec{E}(\vec{x}, t) + \vec{v} \times \vec{B}(\vec{x}, t) \right]. \quad (7-2)$$

The derivation of the Boltzmann equation can be found in many texts on plasma physics.⁶¹ The left hand side of Equation 7-1 describes the conserved motion of the kinetic fluid through an (\vec{x}, \vec{v}) phase space. The right hand side of Equation 7-1 describes changes from particles of species α colliding with particles from all other species. Clearly, the collision term C_α hides a great deal of the physical complexity.

The electric field \vec{E} and the magnetic field \vec{B} are determined by Maxwell's electromagnetic field equations,

$$\frac{\partial \vec{B}}{\partial t} = -\nabla \times \vec{E}, \quad (7-3a)$$

$$\frac{1}{c^2} \frac{\partial \vec{E}}{\partial t} = -\mu_0 \vec{j} + \nabla \times \vec{B}, \quad (7-3b)$$

$$\nabla \cdot \vec{E} = \frac{\rho}{\epsilon_0}, \quad (7-3c)$$

and

$$\nabla \cdot \vec{B} = 0. \quad (7-3d)$$

The charge density ρ is given by the sum of the charge times the number density of the various charged species,

$$\rho(\vec{x}, t) = \sum_{\alpha} q_{\alpha} n_{\alpha}(\vec{x}, t),$$

and the current density \vec{j} is given by the sum of the charge times the flux density of the various charged species,

$$\vec{j}(\vec{x}, t) = \sum_{\alpha} q_{\alpha} \int \vec{v} f_{\alpha}(\vec{x}, \vec{v}, t) d\vec{v}.$$

Maxwell's electromagnetic field equations and the Boltzmann equations for the particle species comprise a complete set of equations for describing the behavior of most plasma systems. This set of equations is too complicated to solve analytically for all but the simplest plasmas: the full Boltzmann equation is six-dimensional, and a numerical solution would require a 6-dimensional grid. With one hundred grid cells in each direction, the six-dimensional grid would consist of one trillion grid points. However, plasma opening switches may have a symmetry that simplifies the problem. Azimuthal symmetry reduces the problem to a four-dimensional phase space, which would require on the order of one hundred million grid points. Thus direct numerical integration of these equations is extremely impractical.

One way to reduce the computational requirements is to use the velocity moments of the Boltzmann equation, at the cost of an increase in the complexity of the formulation. The fluid equations are obtained by multiplying the Boltzmann equation by the velocity to an integer power and integrating over all velocity space. A complete description of plasma phenomena is recovered by an infinite set of these equations. In many cases a good description of plasma behavior can be obtained from only a few of the fluid-moment equations. ANTHEM uses the reduced versions of the first three fluid equations given below.

The lowest moment (integrating $v^0 f = f$) gives number conservation,

$$\frac{\partial n_\alpha}{\partial t} + \nabla \cdot n_\alpha \bar{u}_\alpha = S_\alpha, \quad (7-4)$$

where \bar{u}_α is the bulk streaming velocity of the fluid defined by

$$n_\alpha \bar{u}_\alpha = \int \bar{v} f_\alpha(\bar{x}, \bar{v}, t) d\bar{v}.$$

Here S_α , given by

$$S_\alpha = \int C_\alpha(\bar{x}, \bar{v}) d\bar{v},$$

describes the sources and sinks of particles, i.e., how one species of particles converts into other species. Equation 7-4 says that the change in the number of particles in a given volume over time is equal to the number of particles that enter or leave through the surface plus or minus the number particles that are freed or absorbed. If the collisions leave the number of particles of species α unchanged, then $S_\alpha = 0$. Collision processes such as charge-exchange between different ionic species and ionization would lead to a nonzero S .

The momentum conservation equation is obtained by integrating the momentum $m_\alpha \bar{v}$ times the Boltzmann equation over all velocity space. It is conventional to define a new velocity variable, $\bar{w}(\bar{x}, t) = \bar{v} - \bar{u}(\bar{x}, t)$: $\bar{u}(\bar{x}, t)$ is the streaming velocity of the fluid, while \bar{w} represents the random particle motion. With this definition, the fluid momentum equation becomes

$$\frac{\partial m_\alpha n_\alpha \bar{u}_\alpha}{\partial t} + \nabla \cdot \bar{\mathcal{P}}_\alpha + \nabla \cdot (m_\alpha n_\alpha \bar{u}_\alpha \bar{u}_\alpha) - q_\alpha n_\alpha (\bar{E} + \bar{u}_\alpha \times \bar{B}) = m_\alpha \bar{u}_\alpha S_\alpha + \bar{R}_\alpha. \quad (7-5)$$

where the thermal pressure tensor $\bar{\mathcal{P}}$ is defined as

$$\bar{\mathcal{P}}_\alpha = m_\alpha \int \bar{w}_\alpha \bar{w}_\alpha f_\alpha d\bar{v}.$$

The vector \bar{R} is the rate of momentum gain or loss per unit volume for species alpha due to collisions with all other particles, defined by

$$\bar{R}_\alpha = \int m_\alpha \bar{w}_\alpha C_\alpha d\bar{v}.$$

In the collisionless limit, $\bar{R} = 0$. The continuity Equation 7-4 can be combined with the momentum Equation 7-5 to yield

$$m_\alpha n_\alpha \frac{\partial \bar{u}_\alpha}{\partial t} + m_\alpha n_\alpha \bar{u}_\alpha \cdot \nabla \bar{u}_\alpha + \nabla p_\alpha + \nabla \cdot \bar{\mathcal{P}}_\alpha - q_\alpha n_\alpha (\bar{E} + \bar{u}_\alpha \times \bar{B}) = \bar{R}_\alpha, \quad (7-6)$$

where the scalar pressure p is defined equal to one-third of the sum of the diagonal elements of the pressure tensor,

$$p_\alpha = \frac{1}{3} m_\alpha \int w_\alpha^2 f_\alpha d\vec{v}.$$

In terms of the scalar pressure, the thermal pressure force becomes

$$\nabla \cdot \vec{P} = \nabla p + \nabla \cdot \vec{\Pi},$$

where the stress tensor $\vec{\Pi}$ accounts for the anisotropic part of the pressure tensor. The stress tensor is zero if the thermal velocity distribution has the same functional form in all three velocity directions. The terms proportional to ∇p and $\nabla \cdot \vec{\Pi}$ accelerate or decelerate the fluid depending on the direction of fluid flow compared to the pressure gradient. The terms proportional to the electric and magnetic fields are bulk acceleration from electromagnetic fields.

The third moment equation is formed by integrating $m_\alpha v^2$ times the Boltzmann equation over velocity space to yield

$$\begin{aligned} \frac{3}{2} \frac{\partial p_\alpha}{\partial t} + \frac{\partial m_\alpha n_\alpha u_\alpha^2}{\partial t} + \frac{3}{2} \nabla \cdot (p_\alpha \vec{U}_\alpha) + \nabla \cdot \left(\frac{m_\alpha n_\alpha u_\alpha^2 \vec{u}_\alpha}{2} \right) + \nabla \cdot (\vec{u}_\alpha \cdot \vec{P}_\alpha) \\ + \nabla \cdot \vec{h}_\alpha - q_\alpha n_\alpha \vec{u}_\alpha \cdot \vec{E} = \frac{m_\alpha u_\alpha^2}{2} S_\alpha + \vec{u}_\alpha \cdot \vec{R}_\alpha + Q_\alpha. \end{aligned} \quad (7-7)$$

This equation expresses conservation of energy of species α . Here \vec{h}_α is the flux density of heat carried by thermal motion of particles of species α ,

$$\vec{h}_\alpha = \int \frac{m_\alpha w_\alpha^2}{2} \vec{w}_\alpha f_\alpha d\vec{v},$$

and Q_α is the heat generated or lost due to collisions with all other particles defined by

$$Q_\alpha = \int \frac{m_\alpha w_\alpha^2}{2} C_\alpha d\vec{v}.$$

The temperature is linearly related to the pressure and density by $p_\alpha = n_\alpha k T_\alpha$ where k is Boltzmann's constant.

Using the continuity Equation 7-4 and the momentum Equation 7-5 transforms Equation 7-7 into

$$\frac{3}{2} \frac{\partial p_\alpha}{\partial t} + \frac{3}{2} \nabla \cdot (p_\alpha \vec{u}_\alpha) + p_\alpha \nabla \cdot \vec{u}_\alpha + (\vec{\Pi}_\alpha \cdot \nabla) \cdot \vec{u}_\alpha + \nabla \cdot \vec{h}_\alpha = Q_\alpha. \quad (7-8)$$

This equation describes change of internal energy. The terms proportional to $p \nabla \cdot \vec{u}$ and $(\vec{\Pi} \cdot \nabla) \cdot \vec{u}$ describe how the fluid is heated when it is compressed. The magnetic field does not change the fluid energy, while the electric field only affects the energy in the fluid motion, not the internal energy. The term $\nabla \cdot \vec{h}$ is the heat flow from thermal motion.

Changes in internal energy from diffusion of hot particles to a cooler region is described by this term.

Unfortunately, the time advancement of a fluid variable in a moment equation requires knowledge of a higher order moment, such as \bar{u} for the continuity equation or \bar{P} for the momentum equation. Three moment equations are insufficient: an exact solution requires solving the infinite set of moment equations.

For practical purposes in plasmas (and for good reasons in collisional fluids) the third moment equation is truncated. For a plasma Braginskii⁶⁰ derives the friction force \bar{R} , the anisotropic pressure tensor $\bar{\Pi}$, the heat flux \bar{h} , and the heat exchange term Q in terms of the density n , the drift velocity \bar{u} , and the temperature T for a plasma species in a collision dominated regime when the collisions are elastic using the Chapman-Enskog expansion. This assumes that all macroscopic quantities vary slowly in space and time. If a plasma is collision dominated, the local distribution function is approximately Maxwellian. The total distribution function is linearly expanded into a Maxwellian zero order function and a first order perturbed function $f = f^0 + f^1$. The Maxwellian distribution function f^0 is completely specified by n , T , and \bar{u} . The linearized Boltzmann equation can be solved for the perturbed distribution function f^1 . The quantities \bar{R} , $\bar{\Pi}$, \bar{h} , and Q can be directly computed from f^1 . Braginskii⁶⁰ has calculated approximate expressions for various coefficients for a strong magnetic field $\Omega\tau \gg 1$, and for a weak magnetic field $\Omega\tau \ll 1$ where $\Omega = qB/m$ is the gyrofrequency.

ANTHEM solves the following reduced set of fluid equations:

$$\frac{\partial n_\alpha}{\partial t} + \nabla \cdot n_\alpha \bar{u}_\alpha = 0, \quad (7-9)$$

$$m_\alpha n_\alpha \frac{\partial \bar{u}_\alpha}{\partial t} + m_\alpha n_\alpha \bar{u}_\alpha \cdot \nabla \bar{u}_\alpha + \nabla p_\alpha - q_\alpha n_\alpha (\bar{E} + \bar{u}_\alpha \times \bar{B}) = 0, \quad (7-10)$$

$$\frac{3}{2} \frac{\partial p_\alpha}{\partial t} + \frac{3}{2} \nabla \cdot (p_\alpha \bar{u}_\alpha) + p_\alpha \nabla \cdot \bar{u}_\alpha + \nabla \cdot \bar{h}_\alpha = 0. \quad (7-11)$$

Braginskii's⁶⁰ coefficients are used for the heat flux \bar{h} in Equation 11. These equations are implemented for three particle species, which are: 1) "hot" electrons emitted from the cathode, 2) "cold" electrons initially present in the injected plasma, and 3) a single ionic species of the injected plasma. The use of a single ionic species of course neglects the possibility of multiple ionic species and neutrals.

The anisotropic part of the thermal pressure tensor is neglected in ANTHEM's energy and momentum equations. This makes the assumption that the plasma is collision dominated. It is a consequence of Boltzmann's H-theorem that collisions tend to make the distribution function Maxwellian

$$f_\alpha(\vec{x}, \vec{v}, t) = n_\alpha(\vec{x}, t) \left(\frac{m_\alpha}{2\pi kT_\alpha} \right)^{3/2} \exp \left[-\frac{m_\alpha(\vec{v} - \bar{u}_\alpha)^2}{2kT_\alpha} \right].$$

However, electromagnetic forces and boundary effects can significantly distort the distribution function away from a Maxwellian, especially when the plasma is strongly driven as it is for plasma opening switches. The plasma can have a locally Maxwellian distribution

function when the collisional mean free path is shorter than other spatial scales and when the collision time is much shorter than other time scales. The anisotropic pressure tensor $\bar{\Pi}$ and the heat flux \bar{h} are zero for a symmetric distribution function like a Maxwellian. Thus the adequacy of this approximation depends under what conditions the electromagnetic forces generate a significant pressure tensor $\bar{\Pi}$. This will be discussed in more detail in Section 7.4.

The effects of collisions between species are neglected in ANTHEM's formulation. Any collision process that changes one species particle into another is ignored in the continuity equation. As a consequence the ionization of neutrals is ignored, changes in the charge state of particles are ignored, and charge-exchange effects are ignored. The effects of friction and heat-exchange between different species is also ignored: there is no Joule heating.

7.3 ACCURACY OF IMPLEMENTATION.

This subsection describes three different tests checking the accuracy of the model. The first is checking the accuracy of the implicit electromagnetic field solver by examining vacuum electromagnetic wave propagation for axial and radial transmission lines. The second is verifying Child-Langmuir current flow between the electrodes of a coaxial transmission line. The third category investigates the behavior of an ambient plasma in a transmission line. Most of these tests were performed on the "ANIX" version of ANTHEM.

The boundary condition on the current at the generator side launches a transverse electromagnetic (TEM) wave into the simulation region which is configured as an axial transmission line with a radial gap (as shown in Figure 70), or as a radial transmission line with an axial gap. The accuracy of the implicit electromagnetic field solver will be tested when plasma source terms are not present. The axial transmission line exercises the (E_r, B_θ) mode set and the radial transmission line exercises the (E_z, B_θ) mode set. The linear nature of Maxwell's equations indicates that testing these mode sets separately should be sufficient for the general case where all three field components are present. For these tests the downstream circuit is a shorted load. The results from ANTHEM with different time steps will be compared with a circuit code FREYA designed to solve the relevant transmission line equations. These tests assume that the transmission line walls are perfect conductors.

For a uniform axial vacuum transmission line, the electromagnetic field equations reduce to

$$\frac{\partial B_\theta}{\partial z} = -\frac{1}{c^2} \frac{\partial E_r}{\partial t}, \quad (7-12)$$

and

$$\frac{\partial E_r}{\partial z} = -\frac{\partial B_\theta}{\partial t}. \quad (7-13)$$

The current I in the metal can be related to the magnetic field in the vacuum by

$$B_\theta = \frac{\mu_0 I}{2\pi r}, \quad (7-14)$$

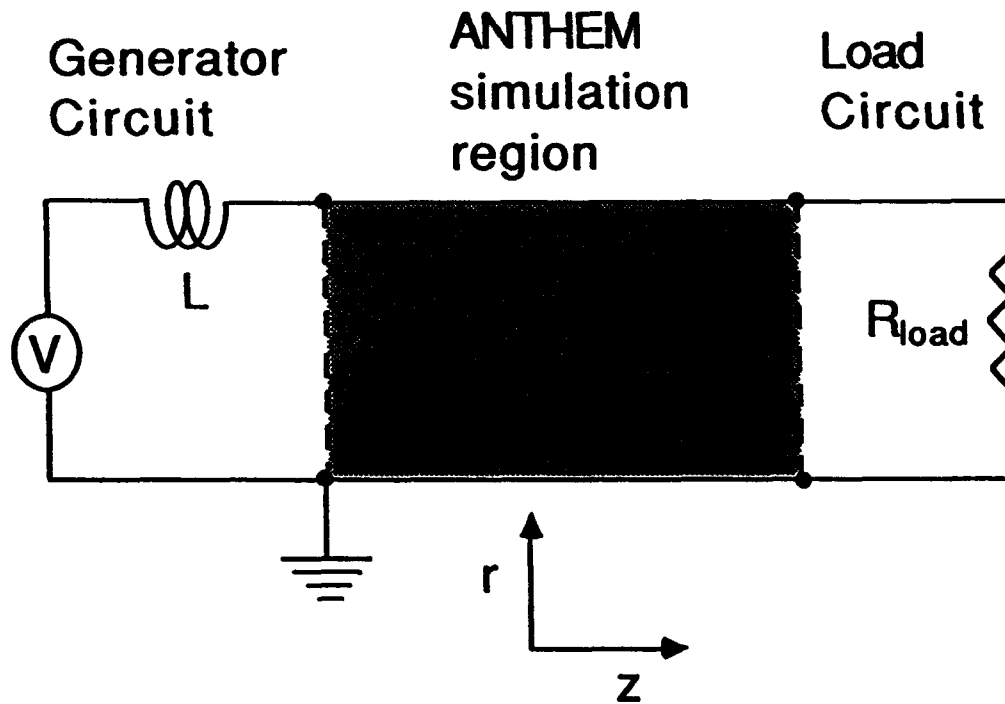


Figure 70. The schematic of the original generator and load circuit models and ANTHEM simulation region in an axial geometry.

where r is the radial position. The voltage drop V at a given axial location between the transmission line surfaces is

$$V(z, t) = - \int_{r_{min}}^{r_{max}} E_r(r, z, t) dr,$$

where r_{min} and r_{max} are the inner and outer radii of the conducting surfaces. Integrating Equations 7-12 and 7-13 over r from r_{max} to r_{min} yields the lossless Telegrapher's equations,

$$\frac{\partial V}{\partial t} = \frac{1}{C} \frac{\partial I}{\partial z}, \quad (7-15)$$

and

$$\frac{\partial I}{\partial t} = \frac{1}{L} \frac{\partial V}{\partial z}, \quad (7-16)$$

where C and L are the capacitance and inductance per unit length given by

$$C = 2\pi\epsilon_0 / \ln(r_{max}/r_{min}),$$

$$L = (\mu_0/2\pi) \ln(r_{max}/r_{min}).$$

The characteristic impedance of the transmission line $Z = \sqrt{L/C}$ is $60 \ln(r_{max}/r_{min})$ Ohms.

A similar analysis can be performed for the radial transmission line. In this case the voltage drop V is defined as

$$V(r, t) = - \int_{z_{\min}}^{z_{\max}} E_z(r, z, t) dz.$$

The equivalent of the lossless Telegrapher's equation for a radial transmission line is

$$\frac{\partial V}{\partial t} = - \frac{D}{2\pi r \epsilon_0} \frac{\partial I}{\partial r}, \quad (7-17)$$

and

$$\frac{\partial I}{\partial t} = - \frac{2\pi r}{\mu_0 D} \frac{\partial V}{\partial r}, \quad (7-18)$$

where D is the axial gap spacing. The characteristic impedance Z changes as a function of radius and is given by $60D/r$ Ohms.

The transmission line modules solve either Equations 7-15 and 7-16, or 7-17 and 7-18 depending on whether the transmission line is axial or radial. These equations are finite-differenced by an explicit leapfrog scheme that is second-order accurate in both space and time (see Section 7.5). The time step is Courant limited $\delta t < c\delta x$ by this scheme. ANTHEM's implicit differencing of the field equations is stable for time steps larger than the Courant limit. The circuit code FREYA can be run with arbitrarily fine resolution in time and space to obtain an accurate benchmark. The benchmark can then be compared with ANTHEM's results, and ANTHEM's time step can be varied to see how the accuracy of the solution is affected.

An axial transmission line is examined first. The external voltage is set at 1.0 MV, and the generator inductance is 100 nH. The inner radius of the transmission line is 10 cm and the outer radius is 20 cm. The axial length is 30 cm. The radial grid spacing is 0.5 cm and the axial grid spacing is 1.0 cm. For these parameters, the inductance per unit length is 13.9 nH/cm, the capacitance per unit length is 97.7 pF/cm, and the characteristic impedance is 41.56 Ohms. The total inductance of the generator and the simulation transmission line is 141.56 nH.

Fluid codes have difficulty resolving regions where the density is zero. As a result, ANTHEM is always operated with some small background density everywhere in the simulation. This background plasma will behave like a vacuum as long as the collisionless skin depth c/ω_{pe} is large compared to the size of the simulation. The background electron density used for the "vacuum" test runs is $1 \times 10^6 \text{ cm}^{-3}$. The collisionless skin depth for this density is 5.3 meters with is much larger than the simulation length of 0.3 m.

The current coming from the inductor will initially be linearly rising at a rate of 10 kA/ns. As the current in the simulation region increases, the voltage seen by the inductance increases due to the characteristic impedance of the transmission line. The voltage rise decreases the rate at which current rises. After one nanosecond, the pulse will propagate down the transmission line and encounter the conducting wall. The radial electric field is shorted at the wall and reflects the pulse back towards the generator section. The pulse continues to bounce back and forth every 2 ns. Over a time which encompasses

many bounces, the current should rise at an average rate of 7 kA/ns, which is the voltage divided by the total inductance of the circuit and the transmission line.

First examine the behavior after 6 ns in which time the wave has made three transits up and down the transmission line. In Figure 71, the current and voltage at the inlet of the transmission line and the current at the shorted end of the transmission line are plotted for three cases, viz., 1) the well resolved circuit code with $dt=0.1$ ps and $dx=0.1$ mm, 2) the circuit code with $dt=10$ ps and $dx=1$ cm and 3) ANTHEM with $dt=10$ ps and $dx=1$ cm. These plots show that the circuit code and ANTHEM with the same spatial and temporal resolution have about the same error. The errors in the generator and load current are quite small. The error in the generator voltage is a little larger. The solutions from ANTHEM are smoother and round discontinuities caused by the reflected wave. The smoothing behavior is expected and is what allows ANTHEM to run at large time steps. The same test for a ten times longer timestep gives the results in Figures 72 and 73. The currents plotted in Figure 72 agree very well for the load and the generator currents. In Figure 73, the voltages in the coarse FREYA run and the ANTHEM run match in phase very well and lag in phase for the voltage for the highly resolved FREYA run. This implies that the propagation speed is just under the speed of light. However as time passes, the oscillation amplitude of the ANTHEM voltage around its mean value decreases as time increases.

When the time step used by ANTHEM increases above the Courant limit of $33 \frac{1}{3}$ ps, the solutions for the load and generator currents remains reasonably accurate as can be seen from Figure 74 for time steps more than 15 times the Courant limit. For the largest time step of 500 ps, the TEM wave would physically travel half of the transmission line length in one time step. All of the ANTHEM runs tend towards a constant voltage at the inlet as time increases as can be seen in Figure 75. The larger the time step, the faster the amplitude of the voltage oscillation is damped. ANTHEM's implicit field solver averages away oscillations. The constant voltage found by ANTHEM is within 0.02 % of the voltage predicted by the ratio of the transmission line inductance to the total inductance times the generator voltage. The agreement degrades if the time step is varied and chosen by ANTHEM as is seen in Figure 76. The average value of the voltage is too small by 12%. The time step increases from 100 ps to 10 ns by the end of the run.

The axial transmission line case is examined next. The external voltage is again set at 1.0 MV and the generator inductance is again 100 nH. The TEM wave is launched at a radius of 40 cm, with the transmission line being terminated into a conductor at 10 cm. The electrode gap spacing is 10 cm in the axial direction. The radial grid spacing is 1.0 cm and the axial grid spacing is 0.5 cm. The capacitance and inductance of the radial transmission line is 40.1 pF and 27.7 nH respectively. The total inductance of the generator and the simulation transmission line is 127.7 nH. With a time step of 10 ps, one short simulation of 6 ns and one longer simulation of 60 ns were performed. The results shown in Figure 77 again demonstrate that the accuracy of the ANTHEM field solver is comparable to an explicit leap-frog scheme for the same grid spacing and time step. The behavior is nearly identical to the axial transmission line runs with the phase lagging as before and the amplitude of the ANTHEM voltage reflections declining as time increases.

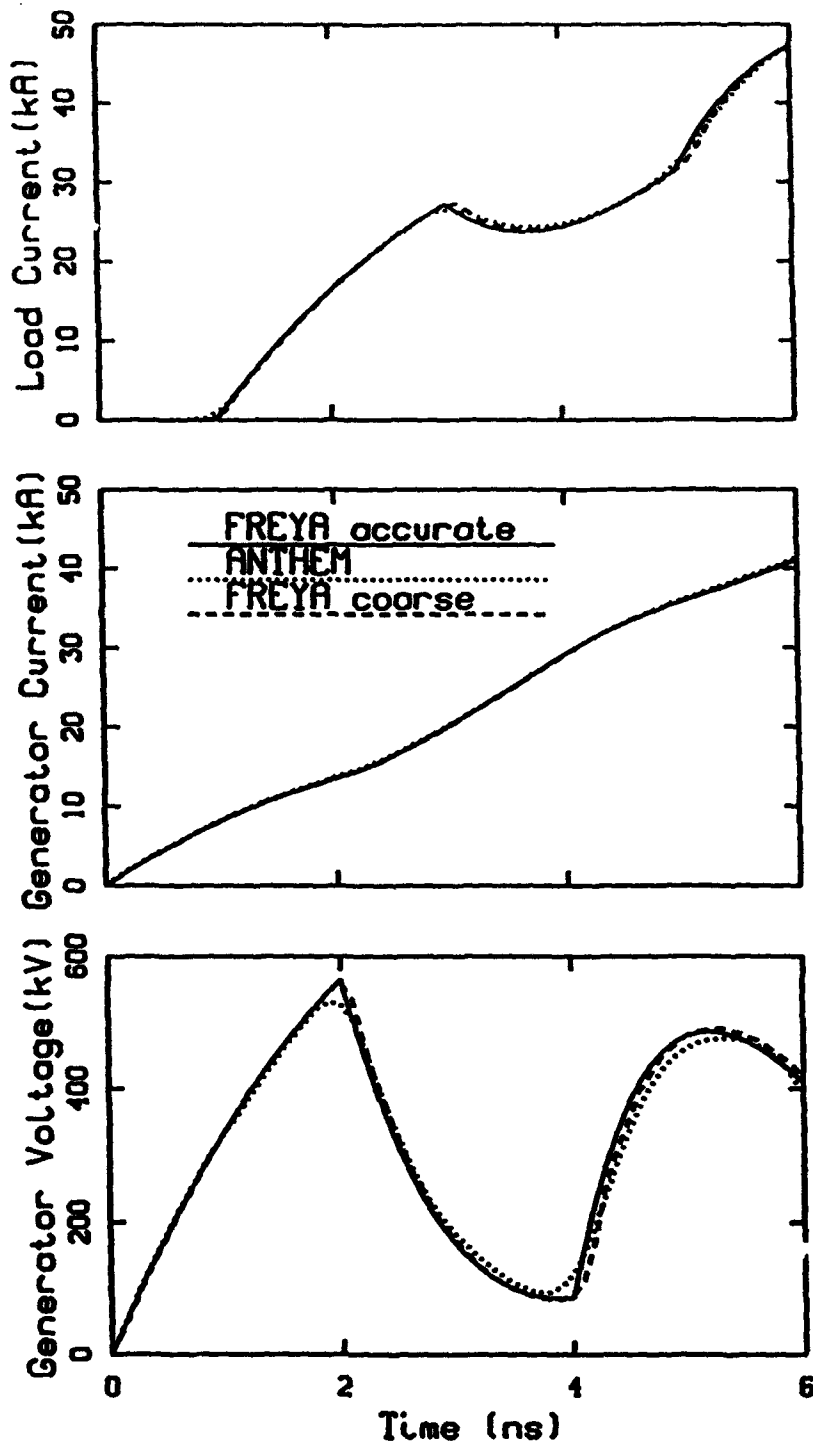


Figure 71. Results for an axial vacuum transmission line for a run time of 6 ns, with a highly resolved run using FREYA (solid lines), ANTHEM (dotted) and FREYA with the same spatial and temporal resolution as ANTHEM (dashed). The top figure is the load current, the middle figure is the generator current and the bottom figure is voltage at ANTHEM's inlet.

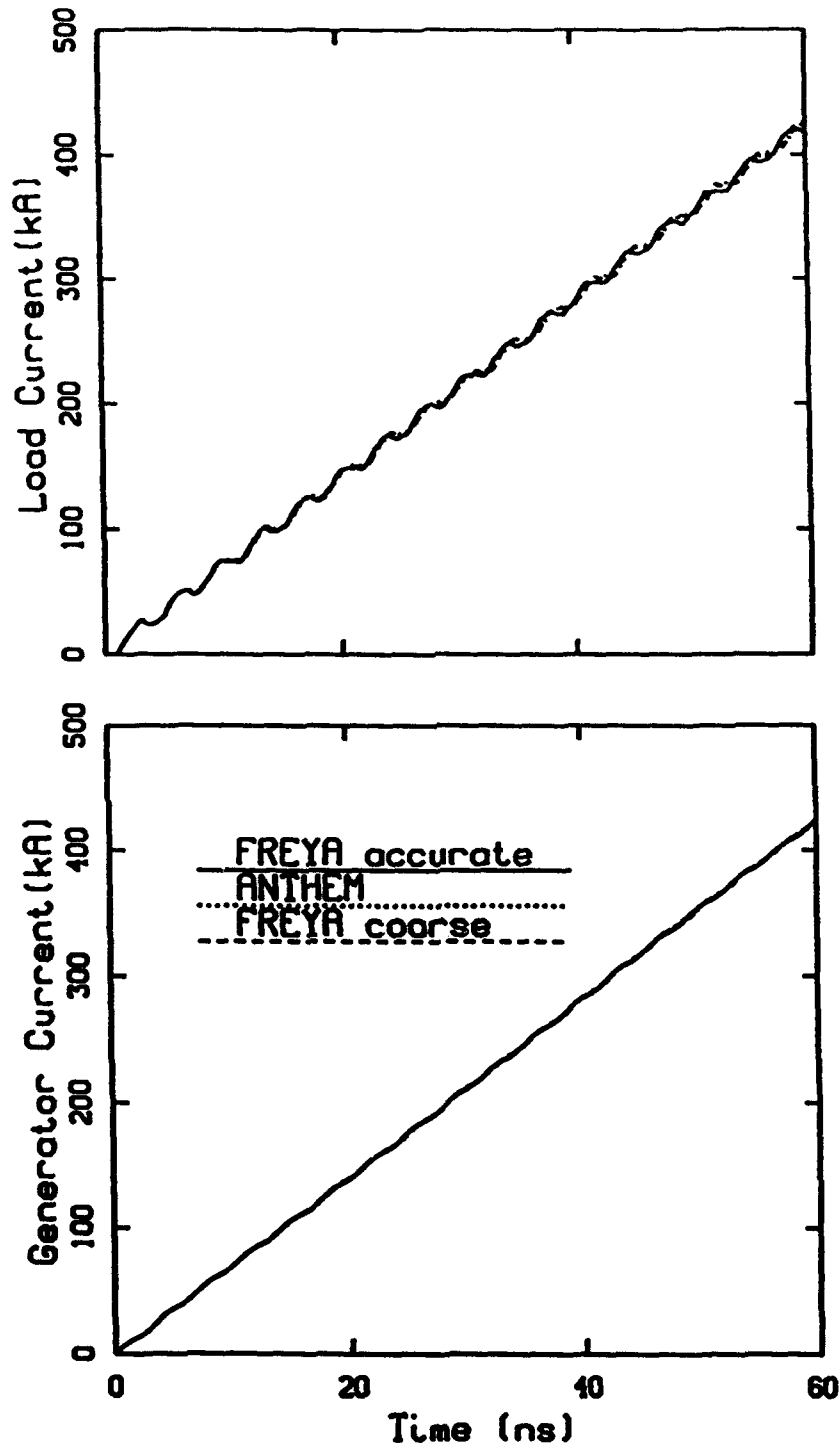


Figure 72. The solutions for an axial vacuum transmission line are shown for a run time of 60 ns, ten times longer than Figure 71. The top figure is the load current and the bottom figure is the generator current. The line types are the same as the previous figure. The solutions for the currents agree very well.

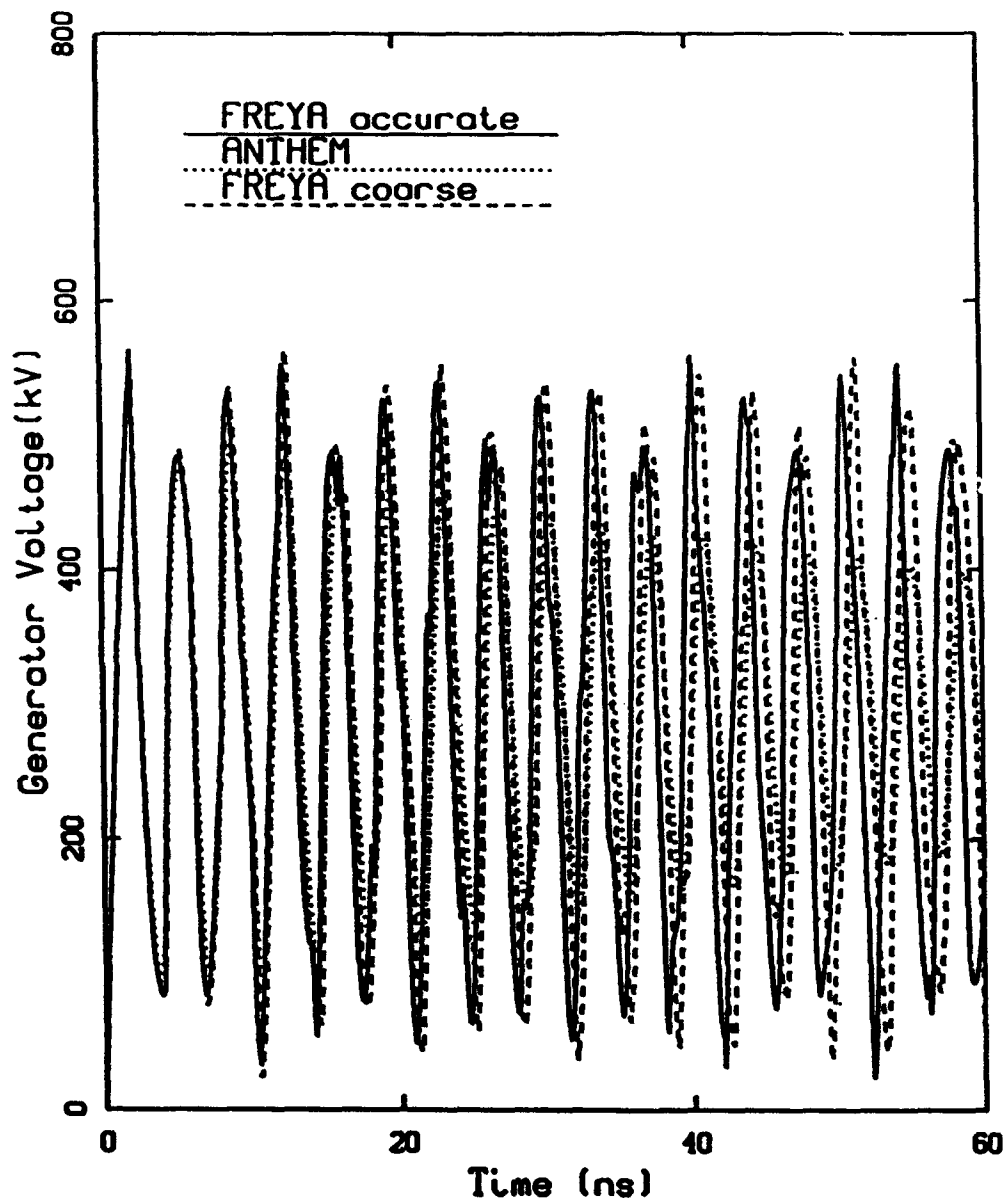


Figure 73. The voltage drop at the inlet to ANTHEM is shown here for the same run as the plots in Figure 72. The solutions agree fairly well. Both runs with the coarser time step and grid lag in phase with the accurate solution implying a vacuum propagation speed just below the speed of light. The oscillation amplitude of the voltage about its mean value decreases for the ANTHEM run.

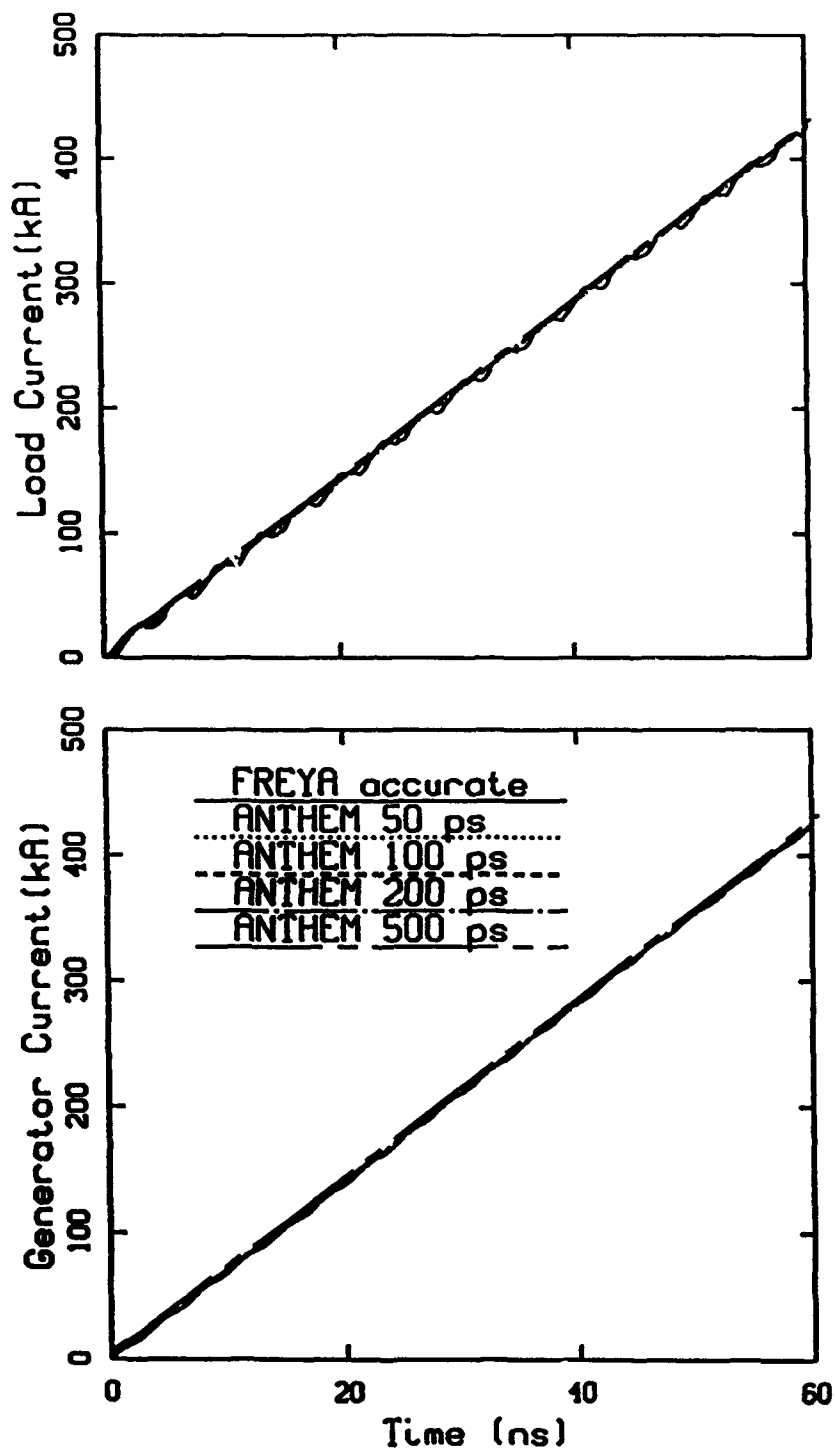


Figure 74. As the time step is increased beyond the Courant limit ($33 \frac{1}{3}$ ps), the solutions for the load and generator currents continue to be accurate.

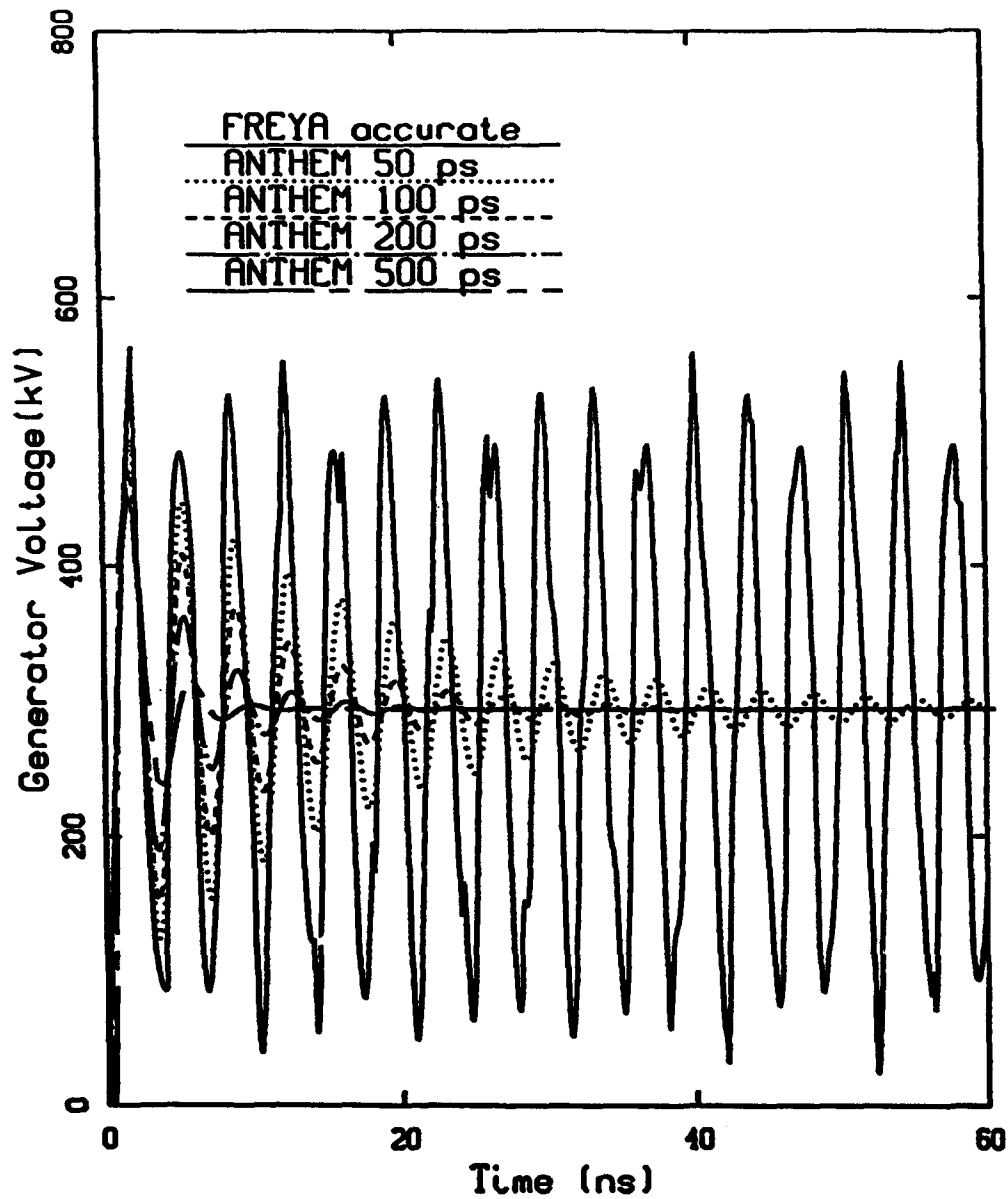


Figure 75. The voltage oscillations produced by reflection from the shorted transmission line are damped more rapidly as the time step increases. The average value of the voltage agrees quite well with treating the transmission line as a lumped inductance.

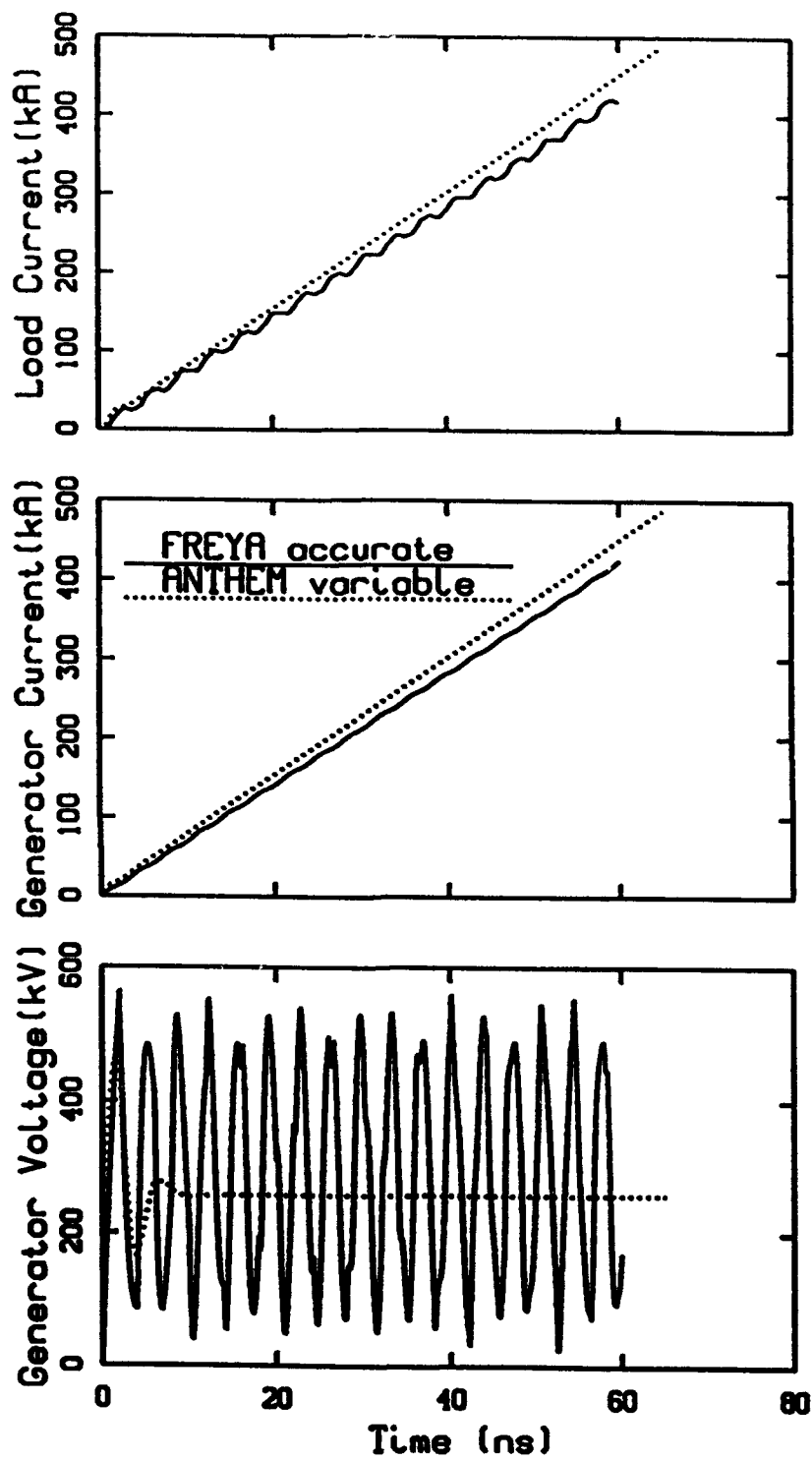


Figure 76. If ANTHEM is allowed to pick its own time step, the accuracy of the solution degrades. The average voltage is too small by 12% which causes the current to rise too rapidly.

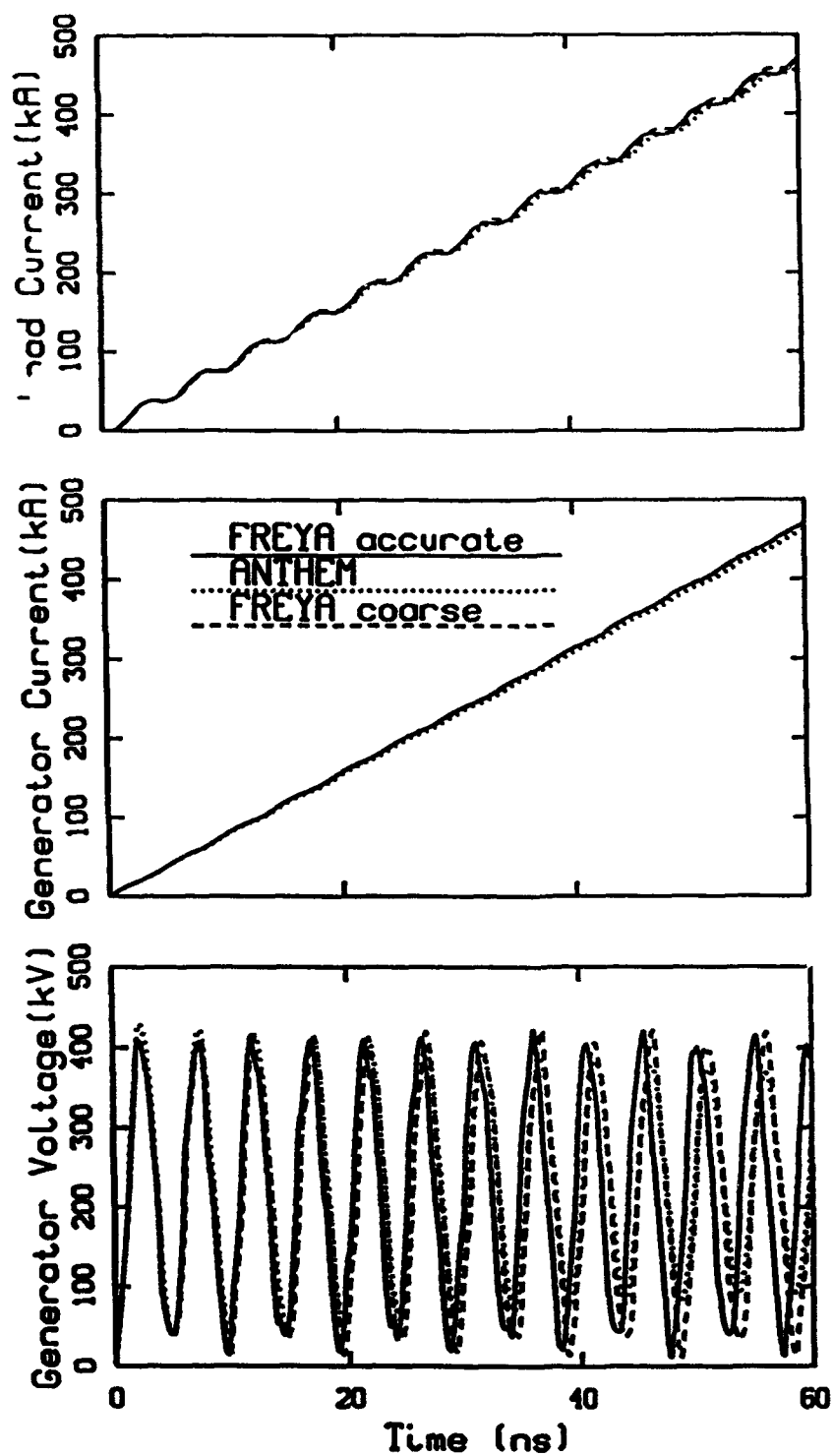


Figure 77. The solutions for a radial vacuum transmission line are shown for a run time of 60 ns. The legends are the same as for Figure 71. The solutions agree very well and resemble the axial transmission line cases.

If the linear current rise is the dominant effect of the circuit model, ANTHEM does an excellent job of predicting the average current rise as long as the time step is not above half of the one way transit time. When the time step gets too large, the accuracy of the solution degrades. For plasma opening switch problems, the time step should probably not exceed one half of the light transit time from the inlet to the plasma. If the details of the reflection in a transmission line are important, the time step will have to remain small enough to resolve the waves.

Several tests have been performed to examine how closely ANTHEM reproduces analytic predictions of space charge limited emission. The tests were run in cylindrical geometry, but the cathode (inner radius) was chosen to be $r_K = 100.0$ cm while the anode-cathode gap spacing was typically less than 0.5 cm, so that the geometry can be treated in analytic comparisons as essentially Cartesian. In the simulations, a fixed voltage source drives current through an inductor and then the radial diode, which are in series. A resistor terminates the transmission line/diode region. For tests of the emission physics, the currents driven in the diode region are small enough that the electrons are unmagnetized. Three different types of tests were run. The first test checks the emission of electron flow into a vacuum anode-cathode gap. The second checks the bipolar emission with an initial plasma fill. The third tests emission physics for the case where ANTHEM uses a high density electrode plasma as a charge emitter rather than the space charge limited boundary conditions used in the first two tests. In this third case, the anode-cathode gap is a vacuum.

The results of these tests were in general very positive. Excellent agreement with analytical predictions were found even when the anode-cathode gaps were poorly resolved with four or even two mesh points in the gap. Certain inconsistencies were found when the top surface was used as the emitter rather than the bottom horizontal surface. Also, when a dense wall plasma is used for the anode conductor, electrons from the anode wall plasma propagated into the interelectrode gap for no obvious reason. These problems should be relatively easy to fix by improving the algorithms at the anode surface.

The last test in this subsection examines certain aspects of plasma behavior near a plasma-wall interface and near a plasma-vacuum interface. A cartoon of the simulation is shown in Figure 78. An ambient hydrogen plasma is placed between the electrodes of a shorted transmission line. The initial ion and electron temperatures are 1.5 keV and the initial density is 10^{12} cm⁻³. The grid spacing in both the radial and axial directions is 0.5 mm, which is twice the Debye length of 0.23 mm. The simulation is 8 cm in length and extends from a radius of 20 cm to a radius of 22 cm. The simulations are connected to a transmission line whose impedance matches the simulation vacuum impedance (5.71 Ω) and whose delay time (20 ns) is equal to the run times of the simulation (20 ns). Two simulation runs were performed. One had a fixed time step of 1 ps and the other run used a variable time step. The results from both simulations exhibited only minor differences.

When a plasma is in contact with a metal wall, some of the electrons and ions will impact the wall and recombine. These particles are lost from the plasma. Since the electrons are lighter and have a higher thermal velocity, more electrons are lost to the walls than ions and the plasma will have a positive potential with respect to the wall. Most of the potential difference between the walls and the plasma is dropped across a thin

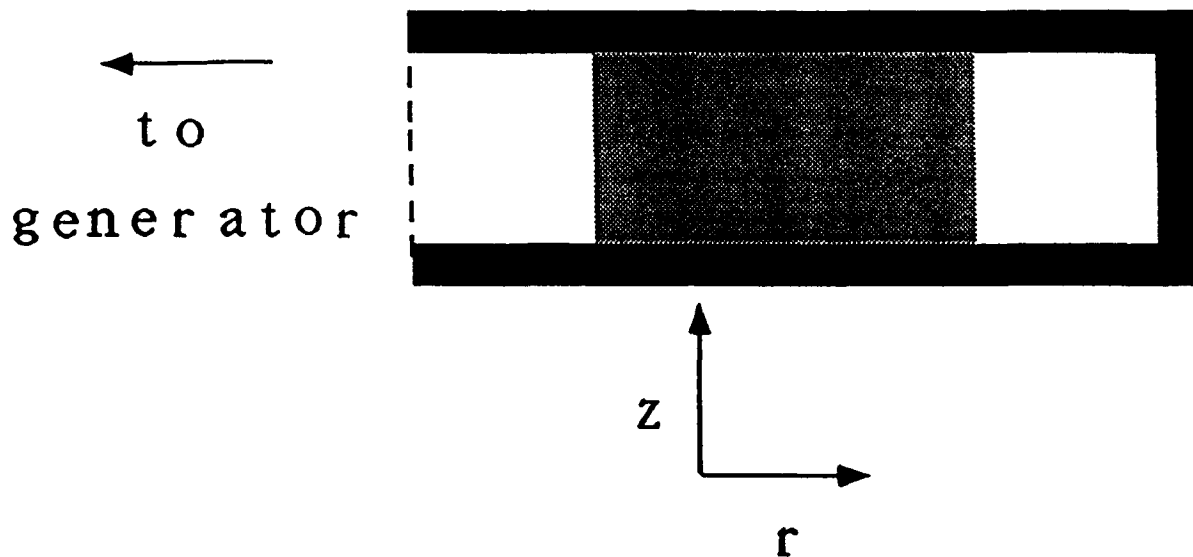


Figure 78. Sketch exhibiting a uniform plasma initialized between the electrodes of a shorted axial transmission line.

layer called a sheath. The sheath electrostatically confines the electrons while accelerating the ions to the wall. The voltage of the sheath adjusts itself such that there are equal fluxes of electrons and ions to the walls. With a constant source of plasma, which is not the case in the present simulation, an equilibrium will be established where there are equal numbers of ions and electrons going to the wall. The equilibrium state of the sheath is sensitive to the details of the electron distribution function. If the plasma is Maxwellian, the voltage drop across the sheath will become 3-4 times the electron temperature.

Similarly for plasma expansion, the lighter electrons will move into the vacuum faster than the ions. The electron space charge will accelerate the ions to a velocity faster than what they would achieve from just thermal expansion. The electrons are slowed down from their thermal expansion by the retarding force of the electric field. The thermal energy of the electrons provides the free energy for the plasma expansion. As the ions move forward, more electrons from the plasma interior move to the edge and continue to accelerate the plasma.

The fluid equations from ANTHEM assume a Maxwellian-like distribution function but do not move individual electrons and ions around. A plasma sheath will only form at the walls if there is a pressure gradient there. The electrons are lighter and will flow into the conducting walls much faster than the ions. The electrostatic retarding fields for both the plasma expansion problem and the sheath problem significantly modify the electron distribution function from a Maxwellian. It is not obvious how much of this distortion can be described by ANTHEM's fluid formulation. At the lower conducting surface (cathode), the differencing at the first cell should create a voltage drop that is twice the electron temperature.

The solutions presented in the literature for both problems take the electrons to be in equilibrium,

$$n_e(x, t) = n_0 \exp(-e\phi(x)/T_e), \quad (7 - 19)$$

assuming that the electrons are described by Maxwell-Boltzmann distribution function. However, it is not obvious that ANTHEM's fluid equations reproduce this density distribution except under restricted conditions. For example, the stationary momentum equation in one dimension reduces to

$$\frac{3}{2} \frac{dp_e}{dx} = \frac{3}{2} T_e \frac{dn_e}{dx} = -en_e(x) \frac{d\phi}{dx} \quad (7 - 20)$$

if the electron flow velocity and temperature are constant. Integration of the above expression yields the Boltzmann distribution. However, the electron temperature does not remain constant in the sheath, because the electrons cool as they enter the sheath and as they expand into the vacuum. At this time it is not known what the analytical solutions to both problems should be. This is a subject for future exploration.

A feature similar to a sheath is seen Figure 79 in near the conducting walls. However, the voltage drop across the sheaths remains approximately equal to the electron temperature, while a kinetic model would predict much higher (3-4 times) temperature. Unfortunately, the grid is too coarse for the sheath. Note also that electrons have expanded into the vacuum region. The features seem qualitatively reasonable within the context of the model but do not match actual sheaths.

In summary, the vacuum field solver used in ANTHEM performs quite well. A time step smaller than one-half the transit time from the simulation inlet to the plasma edge guarantees a good representation of the time-averaged behavior. The tests of Child-Langmuir emission similarly were very good. The simulations show a sheath near the cathode. However, the simulated sheath differs from the Bohm sheath. This should not be a problem when the voltage drop across the sheath is much larger than the electron thermal velocity.

7.4 APPLICABILITY OF MODEL.

How applicable is ANTHEM to the problem of interest here, the plasma opening switch in a coaxial transmission line commonly known as a Plasma Erosion Opening Switch (PEOS)? Ideally, the code contains the three different scenarios (diffusion, hydrodynamics, and erosion) that have been advanced to explain opening switch behavior, but is the plasma collision dominated or collisionless? Under likely operating conditions in long conduction time plasma opening switches the various plasma components may demand different approximations. The weaknesses of ANTHEM's model and possible improvements will be discussed. These include implementing a particle option for electrons emitted from the cathode.

The erosion models^{19,25} are variants of the first theoretical description of the plasma opening switch. Erosion models assume that switch behavior is dominated by a cathode sheath. Ion and electron flow in the sheath is assumed to be quasistationary, i.e., the flow depends solely on the sheath conditions at the present time. The current density across

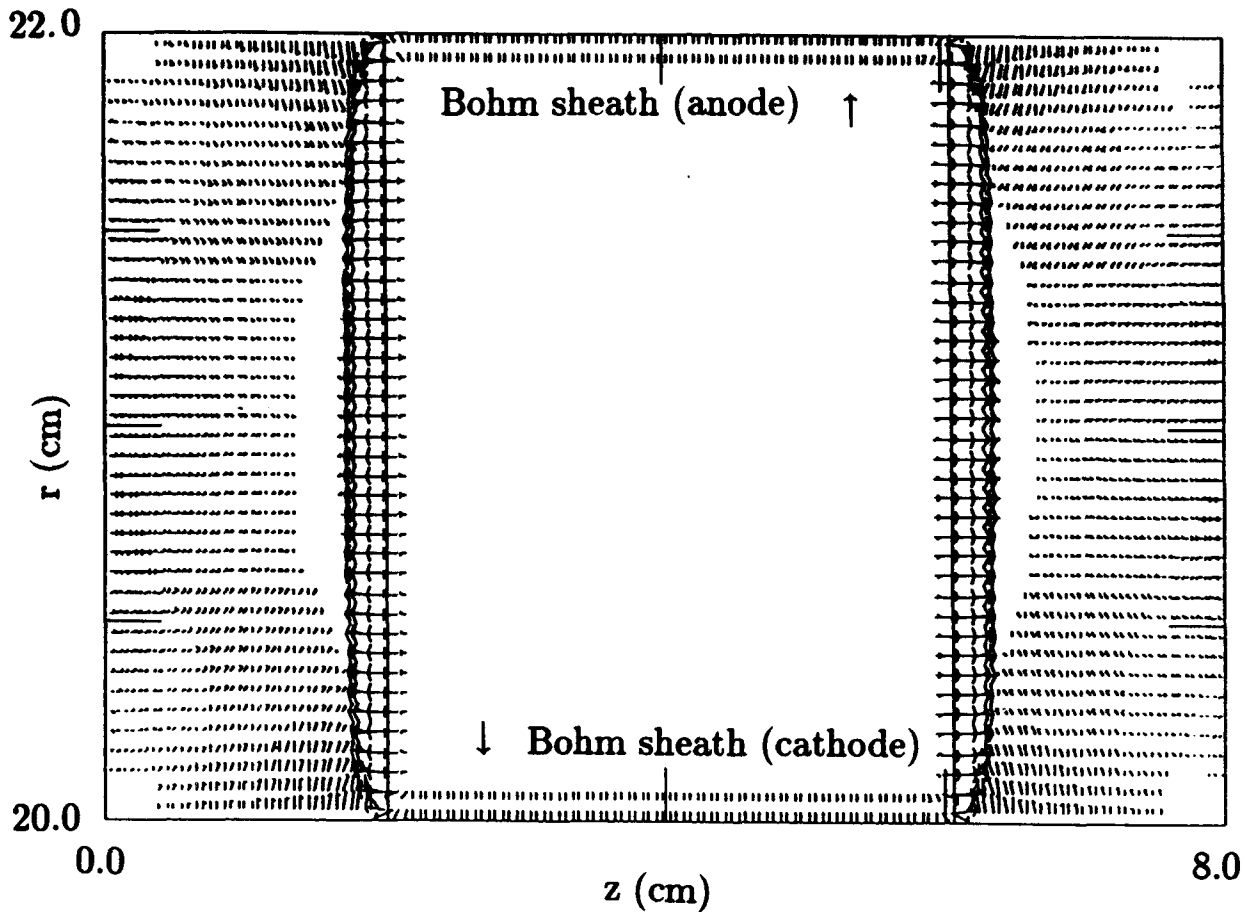


Figure 79. Vector plot of the electric fields produced by ANTHEM at 1 ns when a neutral plasma is placed inside a transmission line. A sheath forms near the lower radial (cathode) surface and near the upper radial (anode) surface. Plasma expands into the vacuum region.

the sheath is then a variant of the Child-Langmuir current density. The opening occurs from the rapid expansion of the cathode sheath. Opening is greatly aided by magnetic insulation of the electron flow. The magnetically insulated electrons are unable to transit the sheath and follow orbits close to the electrode.

Hydrodynamic models^{62,63} assume that magnetic pressure plays an important role during the conduction phase. The $\vec{J} \times \vec{B}$ forces sweep the bulk of the plasma into a front that propagates towards the load. Opening occurs when the plasma reaches the end of the switch. This model's drawback is the lack of an identifiable opening mechanism. There is no reason why the plasma could not keep moving towards the load while continuing to conduct the current. However, hydrodynamic forces may aid in the creation of a voltage sheath, e.g., because the plasma moves more in some radial positions than others from geometrical effects or from plasma inhomogeneities. Then the plasma density in some channel may decrease enough for magnetic insulation of electrons.

Diffusion models⁶⁴ assume that bulk plasma resistivity plays the dominant role during the conduction phase. If the plasma is collisional enough, the current flow can be described by an Ohm's Law $\vec{E} = \eta \vec{J}$ where η is the resistivity. The current penetrates at the rate at which collisions disrupt the electron flow and kick some of the electrons downstream towards the load. The opening process commences when the current has penetrated the full length of the plasma. The load will carry most of the current when the switch resistance is much larger than the load resistance. However, the resistivity from Coulomb collisions is insufficient to explain the observed conduction times, although some other mechanism might provide the required resistivity. As the current rises, the electron drift speed exceeds the thermal velocity, and kinetic microinstabilities become possible. The microinstabilities contain turbulent electric fields that interrupt the motion of particles, or additional (turbulent) resistivity.

In summary, hydrodynamic motion of the plasma bulk, electrode sheath physics, magnetically insulated electron flow, Coulomb collisions, and turbulence from microinstabilities are the physical effects thought to be important in plasma opening switches. Further effects that might be important are neutrals traveling from the plasma source and neutrals coming from the electrodes. The next part of this subsection examines how well ANTHEM describes these various processes.

Discussed earlier are ANTHEM's results for two different kinds of sheaths, the Child-Langmuir sheath (where electron temperature can be neglected), and the Bohm sheath (where the electron energy is about thermal). The Child-Langmuir solution is well represented since kinetic effects are unimportant. A Bohm-like sheath exists in the ANTHEM simulations but its structure is significantly different from the Bohm sheath. The difference is attributed to ANTHEM's inability to represent the non-Maxwellian electron distribution that exists in the Bohm sheath. In plasma opening switches the sheath is probably a mixture between the two types of sheaths. When the voltage drop across the sheath is many times the plasma temperature, ANTHEM should be capable of quantitatively describing the cathode sheath behavior. However, if the sheath width is much smaller than the switch plasma the computational demands of resolving the sheath may be too large for ANTHEM or any other two-dimensional code to resolve. A conservative rule of thumb is that ~ 10 grid points are needed to resolve a sheath, although in practice 4 or even fewer grid points can successfully model the sheath. Additional physics must be added to ANTHEM if details of electrode sheath behavior are important, as a boundary condition or as a sub-grid analytical model for the first cell.

Hydrodynamic motion of the plasma is described by the fluid Equations 7-9 to 7-11 for ANTHEM. As discussed in Section 7.2, ANTHEM assumes that each species is collision dominated, but it neglects the effects of collisions between species. Let us examine more closely what is meant by a collision dominated plasma. It is assumed that the collisions in plasmas are dominated by small angle scattering binary Coulomb collisions. Large angle scattering events are relatively rare. The collision times are a measure of the average time it takes for a particle to change its direction by 90° . For a plasma with just one ionic species where the electron and ion temperatures are approximately equal, the electron and

ion collision times are⁶⁶

$$\tau_e = 3.83 \times 10^5 \frac{T_e^{3/2}}{n_e \ln \Lambda_e} \text{ (s)}, \quad (7-21a)$$

$$\tau_i = 2.09 \times 10^7 \frac{T_i^{3/2}}{Z^2 n_e \ln \Lambda_i} \text{ (s)}, \quad (7-21b)$$

where the density is in units of cm^{-3} and the temperature is in units of eV, where Z is the ionic charge state, and $\ln \Lambda$ is the Coulomb logarithm. Figure 80 shows these collision rates as a function of density for temperatures of 1 eV, 10 eV and 100 eV. Collisional approximations are valid if a characteristic timescale for the electrical fields, τ , is much longer than the ion collision time τ_i ($\tau_e \ll \tau_i$), i.e., $\tau \gg \tau_i$. It is also assumed that the particle mean free path $\lambda = v_i \tau$ is much smaller than gradient scale lengths and electrode dimensions. In Figure 81 the ion and electron mean free paths are plotted as a function of density for three different temperatures.

The estimates and measurements of the background plasma density used in plasma opening switches range from 10^{12} - 10^{15} cm^{-3} and the temperatures range from 2-10 eV. The estimates of plasma density for the long conduction time ($\sim 1 \mu\text{s}$) plasma opening switches are generally between the upper 10^{13} to the low 10^{15} cm^{-3} . The collisional mean free paths and collision frequencies are sensitive to both the density and the temperature. The collision cross-section decreases as particle energy increases. Plasma opening switches can operate in either collisional or collisionless regimes, or in between. As can be seen from Figures 80 and 81, high temperature plasmas ($\geq 100 \text{ eV}$) are mostly collisionless in this density range. The low temperature plasmas ($\leq 1 \text{ eV}$) can be largely collisional for densities ($\lambda > 0.1 \text{ cm}$) greater than $2 \times 10^{13} \text{ cm}^{-3}$ given that the electrode spacings are on the order of a couple of centimeters.

Let us pick a specific electron density of $2 \times 10^{14} \text{ cm}^{-3}$ that might exist in the long conduction time switches and examine the implications. The ion and electron mean free paths are less than 1 mm. when the electron and ion energies are below 3 eV and 7 eV respectively. Similarly the electron and ion mean free paths are greater than 10 cm when the electron and ion energies are above 35 eV and 80 eV respectively. The electrons and the ions in the injected plasma are probably adequately described initially by collisional approximations. However, when the current starts flowing the plasma does not remain collisional. Electrons coming from the cathode get out of the collisional regime when the voltage drop across the cathode sheath exceeds ~ 10 Volts, and when the voltage drop gets above 50 Volts the electrons enter the a collisionless regime. Electrons emitted from the cathode are not adequately described by collisional fluid equations.

The self magnetic field of the current in the switch exerts a force on the particles perpendicular to their flow. In a coaxial geometry the magnetic field at a radius r can be found (ignoring the displacement current) from Equation 7-14. For simplicity, it is assumed that ions are unmagnetized. The nonrelativistic electron gyroradius is given by

$$\rho_e = \frac{v_{\perp}}{\Omega_e} = \frac{m_e v_{\perp}}{eB} = \frac{2\pi r m_e v_{\perp}}{\mu_0 e I} = 2.84 \times 10^{-6} \frac{r v_{\perp}}{I}, \quad (7-22)$$

where ρ and r are measured in cm, v_{\perp} is the velocity perpendicular to the magnetic field measured in cm/sec, and I is measured in kiloAmperes (kA). For a strongly magnetized

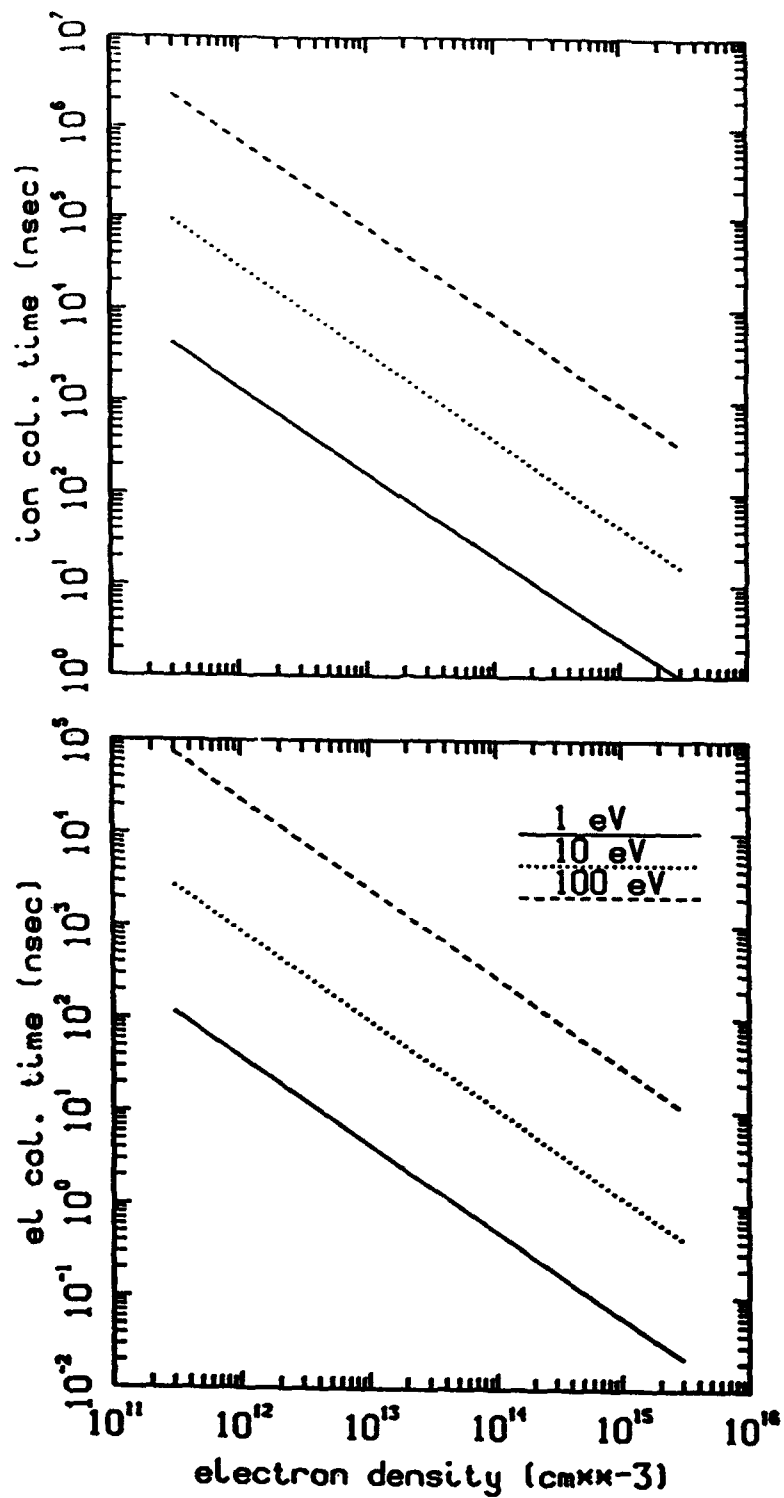


Figure 80. Collision time for small angle Coulomb collisions for a range of plasma densities and three different plasma temperatures, 1 eV, 10 eV, and 100 eV. The top figure is the ion collision time and the bottom figure is the electron collision time.

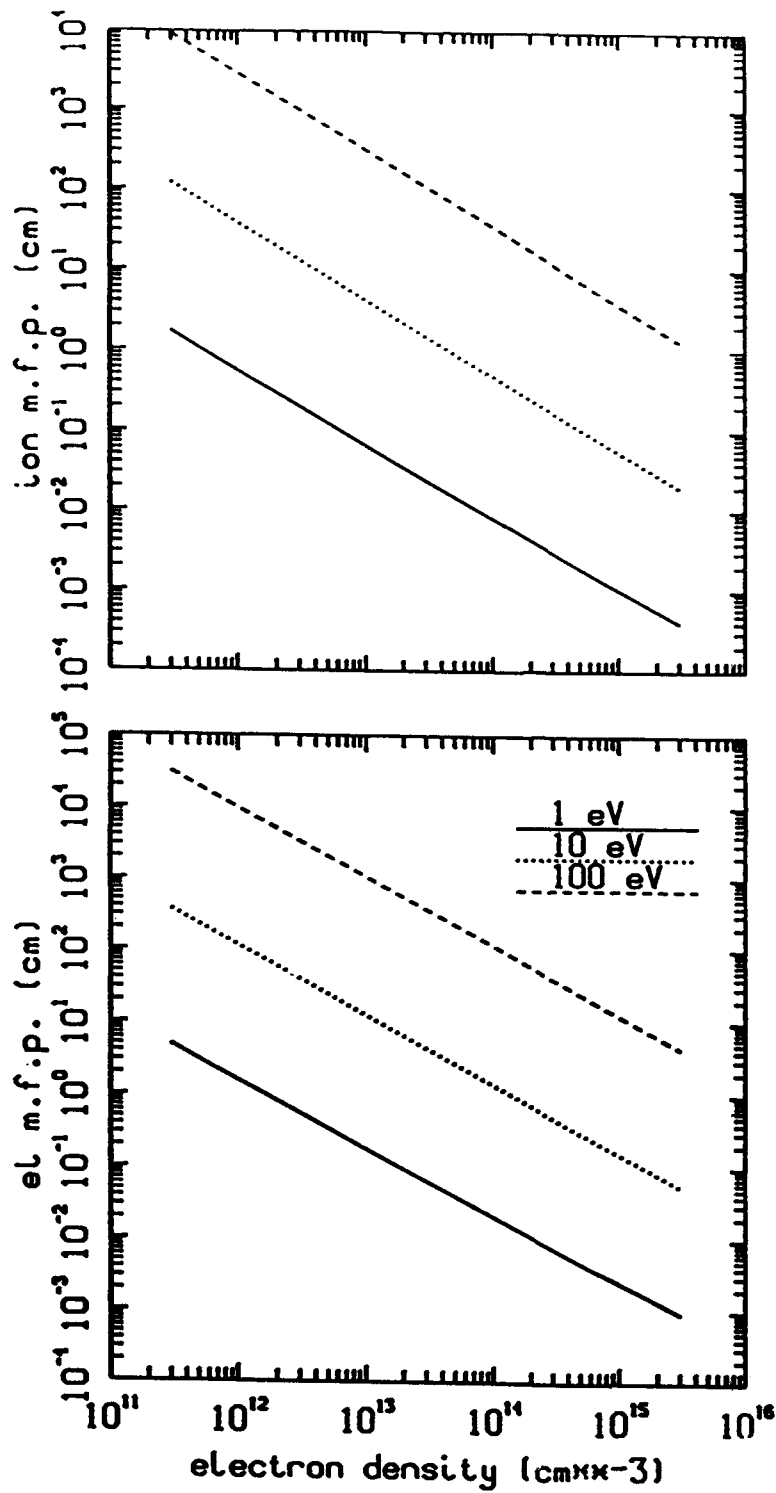


Figure 81. The mean free path for a range of plasma densities and three different plasma temperatures, 1 eV, 10 eV, and 100 eV. The top figure is the ion mean free path and the bottom figure is the electron mean free path.

plasma, the collisional mean free path is greater than the gyroradius $\lambda_e \gg \rho_e$, or equivalently,

$$1.35 \times 10^{15} \frac{I(kA)T_e^{3/2}(eV)}{r(cm) \ln \Lambda_e} \gg 1. \quad (7-23)$$

Thus, the electrons in a plasma with a temperature of 5 eV and with a number density of $2 \times 10^{14} \text{ cm}^{-3}$ at a radius of 20 cm, are strongly magnetized by a current much larger than 2.4 kA.

The approximations of ANTHEM to the full set of fluid equations fall into two categories. One is the neglect of collision terms such as the change in the numbers of particles S_α , the viscous drag \vec{R}_α , and the collisional heat exchange Q_α . Another is the neglect of the anisotropic pressure tensor. Ignoring S , the rate of particle production or loss, is probably adequate except for electrode plasmas. For the injected plasma, there is not enough information to know the densities of the various ionic species and neutrals. More diagnostics are needed to make an informed judgment. For the long conduction time switches, it is quite likely that there is a significant population of neutrals produced near the electrodes from plasma bombardment and from explosive emission. At this time it is probably best not to change the code until more diagnostic information becomes available. Since it might be anticipated that injected plasma ions and electrons are initially close to the same temperature, the heat exchange between the plasma ions and electrons will be small at first. The collision mean free path between the electrons and the ions λ_{ie} is approximately smaller than the electron mean free paths shown in Figure 81 by the square root of the electron to ion mass ratio. The same considerations for the viscous drag \vec{R} indicate that it can also be neglected for the strongly driven opening switch plasmas. It is more likely that the energy exchange and viscous drag between the plasma electrons and the emitted electrons will occur through the action of microinstabilities. The streaming of electrons is expected to generate lots of turbulence. Resistivity caused by microinstabilities has been modeled by supplementing the electron equations of motion with a Krook-like friction term, with a local collision frequency based on the past and present current density.

By the time the power pulse has arrived, the plasma has had time to establish a Maxwellian distribution function for the ions and electrons. Initially the anisotropic piece of the pressure tensor should be quite small. The neglect of the anisotropic pressure may well be justified for low temperature, high density plasmas. If the plasma density is low or if the plasma temperature increases, collisions will not force anisotropies that develop in the distribution function back into a locally Maxwellian. In any case it is probably not a good assumption for the electrons emitted from the cathode. These electrons will be accelerated by a cathode sheath that can easily push them into a collisionless regime. The interaction of the electron motion with the self magnetic field of the beam will create a distribution function that will be anisotropic and not a Maxwellian. This will be especially true during the opening process when it is expected that the electron flow will become magnetically insulated.

Comparisons have been made between MASK and ANTHEM simulations of low density, short conduction switches. Both codes find that a potential hill structure develops at the cathode which in some regimes controls the the conduction and opening of PEOS. The codes disagree on the amount of the magnetic field penetration into the body of the

plasma above the potential hill region. ANTHEM predicts higher levels of magnetic field penetration. While the field penetration is in agreement with certain experimental observations, it is unclear whether the mechanism for the penetration is physical or whether it is due to differences between the numerical models used in ANTHEM and MASK.

Agreement with an experimental observation should be attributable to some physical model. Such models include the nonlinear skin effect theories proposed in the Soviet literature, the Hall resistivity effect proposed by some US and Israeli scientists, and anomalous resistivity effects. Both MASK and ANTHEM resolve the first two effects, and should treat the plasma as effectively collisionless in the short conduction time regime, so it is unclear why they give different results. It is important to rule out the possibility of numerical errors or errors associated with the underlying models employed by the two codes.

To this end, the codes are tested on a problem in which there is a well known analytic solution, viz., magnetically insulated electron flow in a vacuum transmission line. This problem is chosen because the two codes' results differ most obviously in the electron flow patterns. Although the results are preliminary, it appears that magnetically insulated electron flow seen in MASK matches theory significantly better than the flow seen in ANTHEM. One explanation is that ANTHEM takes the pressure tensor to be a scalar, i.e., the diagonal terms of the pressure tensor are equal. However, in magnetically isolated flow it is well-known that the diagonal terms of the pressure tensor are distinctly different. A solution of this problem would be to use particles to represent the emitted electrons species in ANTHEM. Unfortunately, the implementation of this feature is not yet complete.

The most important approximations in ANTHEM are the neglect of collision terms and certain pressure terms. There is not enough diagnostic data to determine whether the collision terms need to be added for opening switch plasmas. The neglect of the pressure terms is not a good approximation for electrons emitted from the cathode and may lead to incorrect behavior for magnetic insulation. One possible way to more accurately represent the largely collisionless behavior of the emitted electrons is to treat them as particles. The background injected plasma ions and electrons should be represented reasonably well by a fluid formulation which also should be computationally cheaper. Some way of incorporating trapped particles into the plasma electron fluid may be needed to maintain computational efficiency in case the injected particles become trapped in the background plasma. It would be necessary to examine the properties of implicit particle moving algorithms, especially for establishing magnetic insulation.

7.5 IMPROVEMENTS.

Some of the designs for DECADE incorporate long transmission lines between the generator and the opening switch and between the opening switch and the load. As was described in Section 7.3, the incoming electromagnetic pulse sees the the plasma and reflects back up the transmission line. If the time for reflection up and down the transmission line is a sizable fraction of the opening time, it is conceivable that these reflections would be a significant effect. While it is possible to increase the simulation volume to include the long transmission lines, a more efficient method is to incorporate a transmission line into the simulation.

One of ANTHEM's original circuit models consists of a fixed voltage into an inductor for the generator circuit and consists of a fixed resistor for the load circuit. An additional option has been added to ANTHEM that substitutes a series RLC generator circuit connected to a transmission line which then would drive the simulation region as shown in Figure 82. The transmission line model solves the Telegrapher's equation described earlier. The transmission line and circuit modules use an explicit, second-order accurate, leapfrog scheme to advance in time. The RLC circuit equation is

$$\frac{Q_{cap}}{C_c} + IR_c + L_c \frac{dI}{dt} = V_{in}, \quad (7-24)$$

where Q_{cap} is the capacitor bank charge, I is the current, V_{in} is the voltage feedback from transmission line, switch, and load regions, and C_c , R_c , and L_c are the capacitance, resistance, and inductance respectively of the generator. It is differenced into the form

$$I^{n+\frac{1}{2}} = \left(1 + \frac{R_c \delta t}{2L_c}\right)^{-1} \left[I^{n-\frac{1}{2}} \left(1 - \frac{R_c \delta t}{2L_c}\right) + \frac{\delta t}{L_c} \left(V_{in}^n - \frac{Q^n}{C_c}\right) \right], \quad (7-25)$$

with the charge updated by

$$Q^{n+1} = Q^n + I^{n+\frac{1}{2}} \delta t. \quad (7-26)$$

Similarly the transmission line equations are finite differenced in the form.

$$I_j^{n+\frac{1}{2}} = I_j^{n-\frac{1}{2}} + \frac{\delta t}{L_t \delta z} (V_{j+\frac{1}{2}}^n - V_{j-\frac{1}{2}}^n), \quad (7-27a)$$

$$V_{j+\frac{1}{2}}^{n+1} = V_{j+\frac{1}{2}}^n + \frac{\delta t}{C_t \delta z} (I_{j+1}^{n+\frac{1}{2}} - I_j^{n+\frac{1}{2}}). \quad (7-27b)$$

This matches the boundary conditions for driving the current into ANTHEM. Voltage feedback from ANTHEM is used to drive the generator circuit models.

The new transmission line and circuit models were tested against the original ANTHEM code on a problem of electromagnetic wave propagation into a shorted transmission line. After the modifications were made, ANTHEM used the original circuit model on this problem and the results agreed to within machine precision with the results from unmodified ANTHEM. Thus if these new modules are not invoked, ANTHEM performs as before. Next the RLC circuit model was first computed separately and compared with the original ANTHEM circuit model. The capacitor of the generator was set to a large enough value such that it remained at a virtually fixed voltage for the run time of the simulation. The voltage on the capacitor and the circuit inductance matched corresponding values in the original ANTHEM generator model. The two cases agree to within four decimal places. The last test compares the behavior of original ANTHEM simulation of a shorted transmission line with a new version where half of the original simulation transmission line is replaced with the transmission line model. As can be seen in Figure 83, the current in the shorted load agrees very well for both cases.

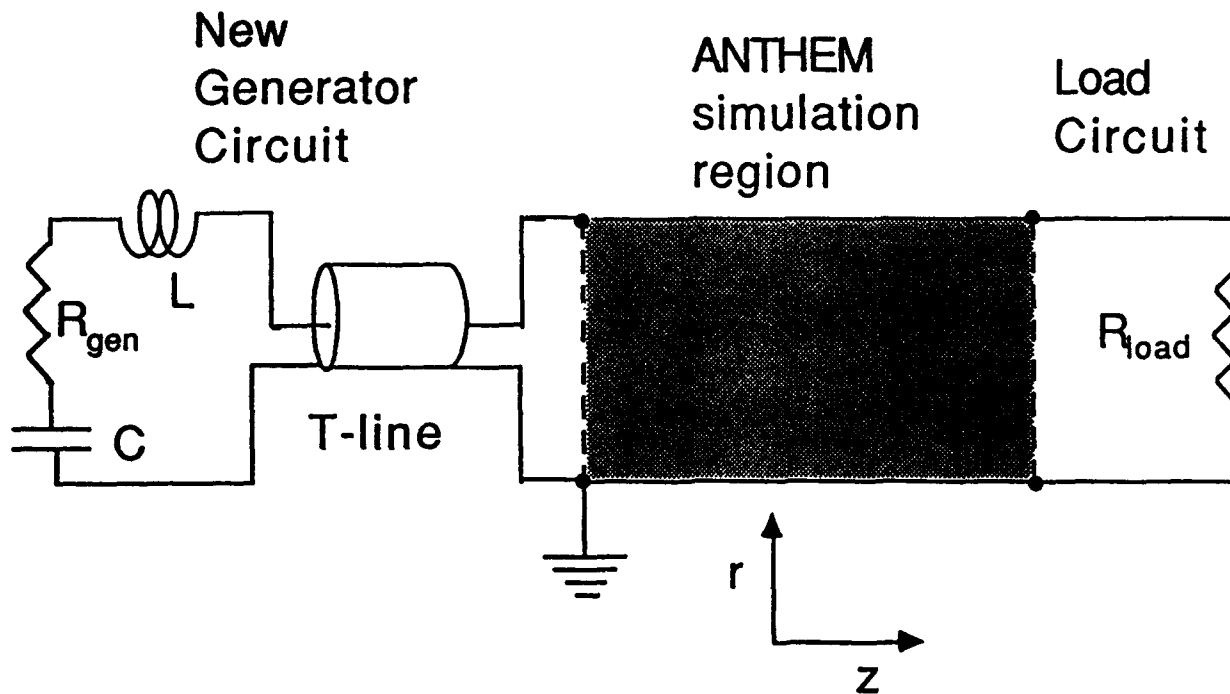


Figure 82. A schematic exhibiting the new generator circuit model consisting of a RLC circuit connected to a transmission line which then drives current into the main ANTHEM simulation region.

7.6 CONCLUSIONS.

This section contains the evaluation of ANTHEM and its applicability for long conduction time switch studies. A principal question is the ability of ANTHEM to model a collisionless fluid in the presence of magnetic fields. The electrons emitted off the cathode are likely to gain enough energy such that their motion will not be significantly affected by collisions. The emitted electrons may require a particle model to adequately represent their motion. The existing fluid model should be adequate for the injected plasma electrons and ions. If the details of a spatially small sheath in the vicinity of an electrode are important, the physics of that interaction will have to be added as a boundary condition or as a subgrid model in the first cell adjacent to the electrode.

Some improvement has already begun with the upgrade of the ANTHEM generator model to include a RLC circuit model attached to a transmission line. A similar upgrade is planned for the load model, which will likely consist of a transmission line attached to a time-varying resistance. However, the first problem to be addressed is the boundary condition near the upper radial conducting surface in the presence of plasma. This problem causes a local violation of Maxwell's equations that could harm the integrity of the simulation.

It will probably be necessary to implement a particle option for electrons emitted from the cathode. Such a capability is supposed to currently exist in ANTHEM but it remains to be tested in opening switch simulations. The particle option should be exercised

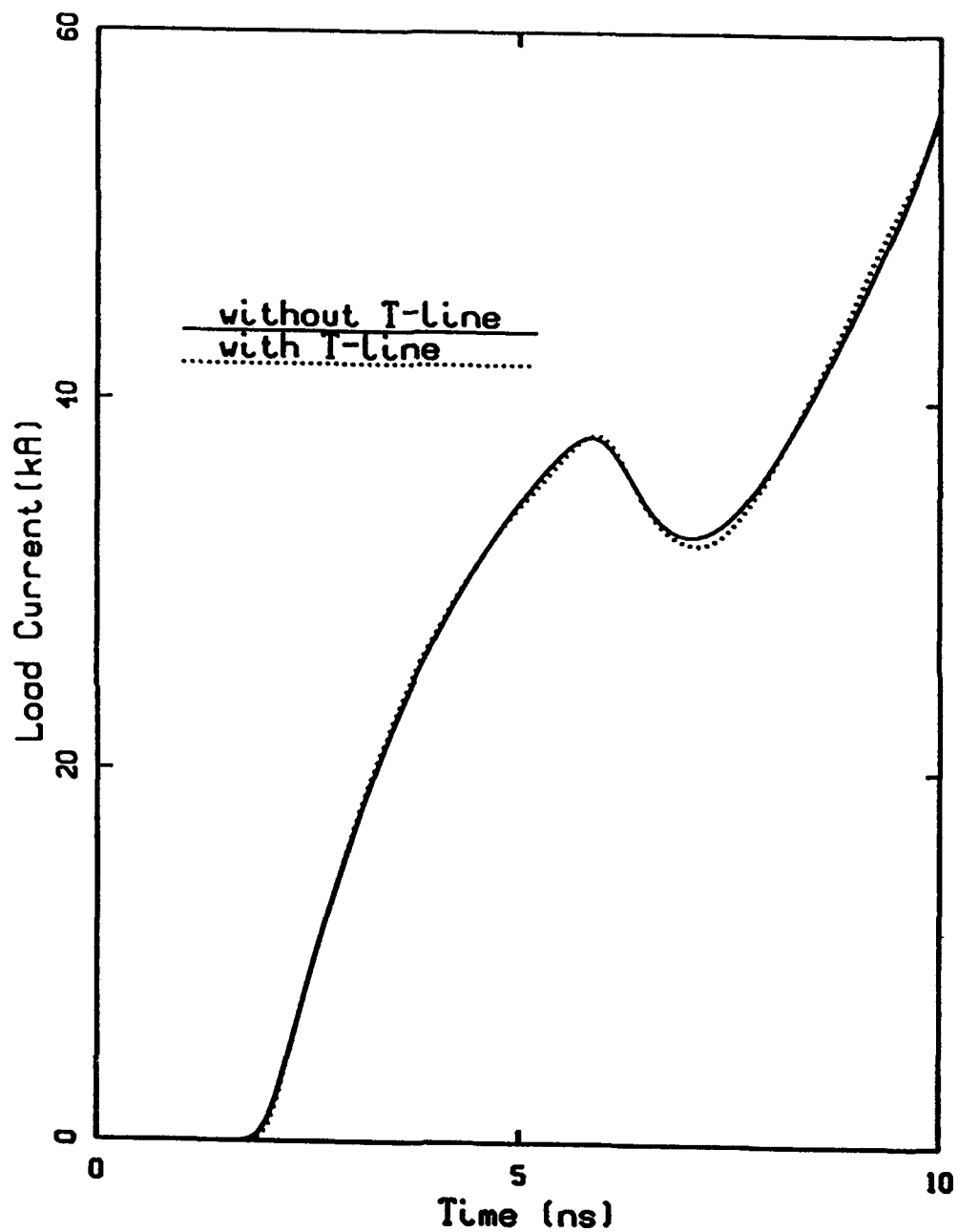


Figure 83. The currents through a shorted load are compared when the one half of an AN-THEM simulation region is replaced by an equivalent transmission line model. The currents agree very well.

in the current version of ANTHEM, tested carefully, and then applied to opening switch problems. It would be much easier to make improvements if the code were streamlined for applications to the opening switch problem. ANTHEM's structure preserves its history of development on different applications such as laser-plasma interactions. Modifications to ANTHEM are best done with the aid of the code's author, Rod Mason.

SECTION 8

PLASMA RADIATION SOURCE

A pulse power generator discharging through an evacuated diode produces photons around 100 keV. These hot x-rays serve to test electronics. Surface effects testing needs cold x-rays, with photon energies around 1 keV. These x-rays can be produced with basically the same pulse power generator by using a small amount of material to connect the electrodes. This is the plasma radiation source (PRS).

In PRS research BRA has cooperated closely with J. Davis of the Radiation Hydrodynamics Branch (Code 4720) of the Naval Research Laboratory. Their charter is detailed modeling of the PRS. Therefore we have done the complementary work of summarizing and reviewing the state of the art in PRS research.

These efforts include a review paper on the PRS,⁶⁶ editing of the Proceedings of the 2nd International Conference on High-density z-pinch⁶⁷ and a review paper on radiation collapse.⁶⁸ As intended, these efforts have provided a common baseline for much of the PRS research sponsored by DNA. The review papers are contained in Appendix A.

Topics treated in more detail relate to the mechanism of current conduction in the PRS. The study of leakage current on the outside of the PRS was started during the preceding contract, but only finalized recently.⁶⁹ Radiative collapse is related to the Pease-Braginskii current, for which Reference 70 gives an expression in terms of the atomic cross sections and the fundamental Alfvén current. Appendix B contains copies of References 69 and 70.

SECTION 9

A ONE-DIMENSIONAL PIC-CIRCUIT CODE FOR SIMULATING A REFLEX TRIODE

This section describes the computer model developed during the contract period to simulate an idealized one-dimensional reflex triode. Charged particle motion and electron scattering by a thin foil are calculated self-consistently with the response of an external circuit. The code has been used for the research reported in some sections of this report: its methods are useful for many other applications in pulse power physics.

9.1 INTRODUCTION.

Charged particle beams or plasmas are integral components of many high-power devices used in pulse power physics for such varied purposes as bremsstrahlung X-ray production,⁷² particle beam injection,⁷³ microwave generation,⁷⁴ and switching.¹

The plasma or beam is usually coupled to an external circuit. Compared to the external circuit by itself, the combined system is much more complicated due to the interaction with the circuit element that represents the nonlinearities and the many degrees of freedom typical of a plasma. The results of this interaction can be surprisingly nonintuitive.⁷⁵ Thus, even though examples of successful analytical descriptions can be found in the literature,^{76,77} simulation and modeling are often essential in order to advance understanding.

Simulations of bounded plasmas have become more commonplace in recent years as the need to handle domains of practical interest has arisen. However, to limit the complexity of the models, most of the boundary conditions assumed have been either constant or given functions of time. For example, in contemporary multidimensional simulations of high-power diodes^{78,79} part of the boundary is used to drive an electromagnetic wave into the simulation region to mock up the effects of a pulse from a capacitor bank. Self-consistent treatments of plasma-circuit systems are rare because of the difficulty in matching the time-integrated equations of the circuit to the simulated plasma at the computational boundaries. These difficulties arise in part from the disparate timescales on which circuits and plasma collective effects evolve as well as from the lack of an established methodology.

Lawson^{8,9} has addressed these issues using a one-dimensional model of a diode coupled to an LRC circuit. His code called PDW1 (PDW is an acronym for the University of California at Berkeley's 1983 Plasma Device Workshop) has become a useful testbed for developing such techniques within a deceptively simple one-dimensional framework. This work has been extended by others to include circuit elements⁸⁰ and atomic processes.⁸¹

This section describes an extension of Lawson's work to DNA-relevant applications in pulse power. The simulation code must match a one-dimensional simulation of a reflex triode to a pair of driving circuits each made up of an LRC-type power supply coupled to the triode through a transmission line. The inclusion of a transmission line model and the addition of electron scattering represent significant advances over the existing PDW1 code. This section describes the model in detail: another section uses the code in a test

case, the evolution to a low-impedance steady state of a reflex triode driven symmetrically by a capacitive discharge.

The code is designed to calculate, from first-principles, charged particle motion and electron scattering by a thin foil together with the response of an external circuit. It has three major components shown in Figure 84: An electrostatic one-dimensional (1-D) particle in cell (PIC) model of a reflex triode, a Monte Carlo model of electron scattering and a module that integrates the differential equations for the circuit. The connection between these modules is illustrated in the figure. Advancement of the complete system is time-split between the particle-field advance and the circuit advance with the output of one providing input for the other. At the beginning of a given cycle, the voltage drops across the primary and secondary diode gaps allow the circuit equations to be integrated forward in time. The charges of particles impinging on the foil and the cathode surfaces are accumulated and, together with the charge flowing in the circuits, specify surface charge densities on the diode and foil. The surface charges provide electric field boundary conditions permitting calculation of the electric field and potential values within the diode. The calculated voltage drops are stored for the next step in the circuit advance and the particles are moved in the fields.

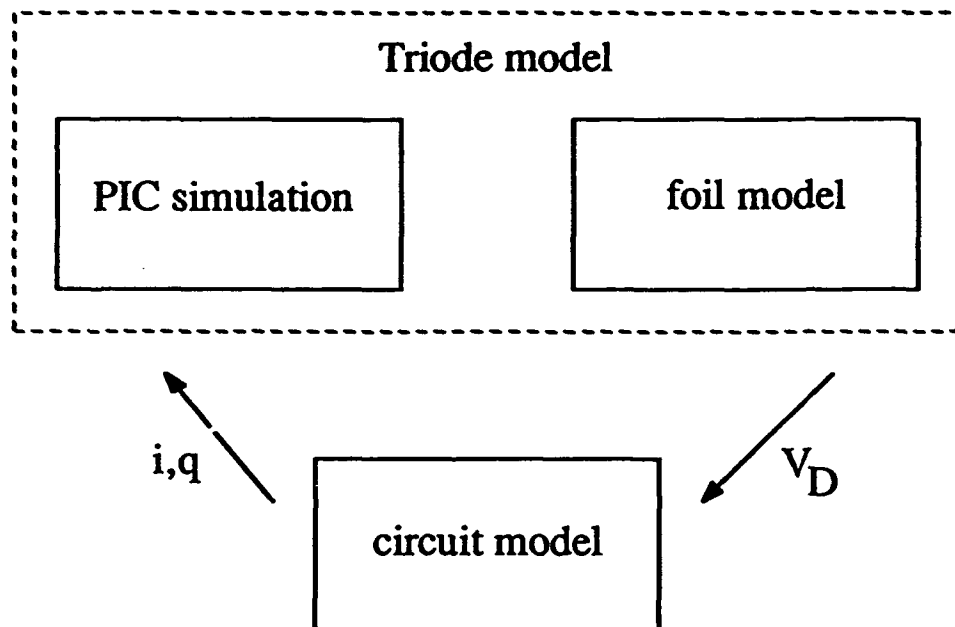


Figure 84. A schematic of the reflex triode code. The code is comprised of a PIC simulation of the diode gaps and a Monte Carlo simulation of electron scattering by a thin foil. These are coupled with modules to advance the circuit model. The arrows indicate the feedback between the modules.

Particles enter the simulation either through a space-charge-limited emission algorithm or by injection. Within the particle push, electrons entering the foil are passed to a

foil-scattering routine which decrements energy and performs momentum scattering as a function of the incident energy. Each of these components is described in detail below.

9.2 CIRCUIT MODEL.

The circuit for the code is shown in Figure 85. It is comprised of twin power supplies, each segment consisting of an LRC-type circuit feeding into a transmission line. The two circuits are linked by the foil and by transiting electrons. This general circuit can emulate many different experimental arrangements by suitable choice of parameters.

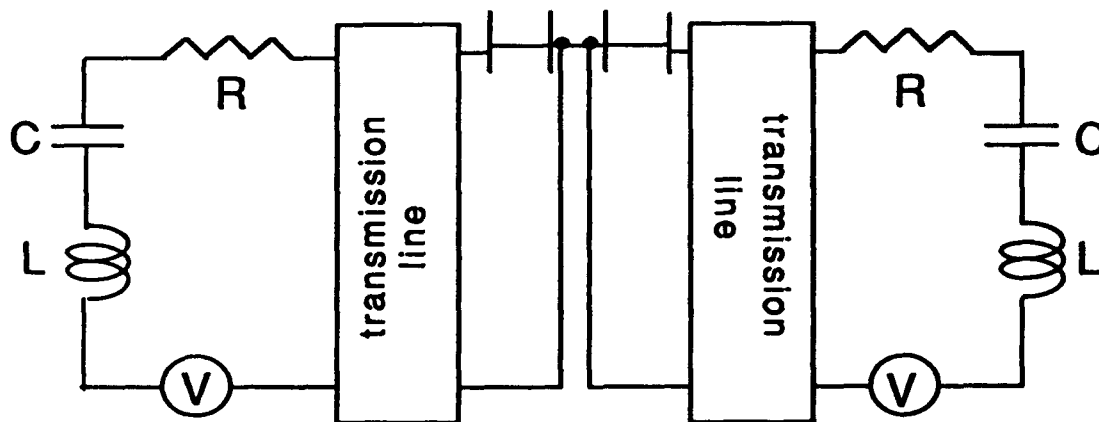


Figure 85. A diagram of the circuit for the reflex triode. Two power supply modules made up of LRC-type circuits with an external voltage supply are fed into transmission lines.

The power supply circuit assumes an inductance L , capacitance C and resistance R connected in series. In addition, an external series voltage source V_{ext} is included. The current I and charge Q flowing through the power supply circuit obey the standard equations.⁸³

$$L \frac{dI}{dt} + RI + \frac{Q}{C} + V_{ext} = V_{ps}, \quad (9-1)$$

$$\frac{dQ}{dt} = I, \quad (9-2)$$

where V_{ps} is the voltage drop across the inlet of the transmission line where it meets the power supply. The above equations can be integrated to second order accuracy using a simple leapfrog scheme in which Q and V_{ps} are given at time level n and I is given at $n + \frac{1}{2}$, i.e.:

$$I^{n+\frac{1}{2}} f_+ = I^{n-\frac{1}{2}} f_- - \frac{\omega_{ps}^2}{\Delta t} Q^n - (V_{ext}^n - V_{ps}^n) \frac{\Delta t}{L}, \quad (9-3)$$

$$Q^{n+1} = Q^n + I^{n+\frac{1}{2}} \Delta t, \quad (9-4)$$

where Δt is the timestep and

$$\omega_{ps}^2 = \frac{\Delta t^2}{LC}, \quad (9-5)$$

$$\tau = \frac{2L}{R\Delta t}, \quad (9-6)$$

$$f_{\pm} = 1 \pm \frac{1}{\tau}. \quad (9-7)$$

One recognizes τ as the decay time and ω_{ps} as the oscillation frequency of the circuit, each normalized to the timestep. Numerical stability of the leapfrog scheme⁸⁴ requires that $\omega_{ps} \leq 2$.

The voltage drop V_{ps} across the power supply is matched to a transmission line model which is constructed as follows: The well-known equations for a lossless transmission line are:⁸¹

$$\frac{\partial I_{TL}}{\partial t} = -\frac{1}{\ell} \frac{\partial V_{TL}}{\partial x}, \quad (9-8)$$

$$\frac{\partial V_{TL}}{\partial t} = -\frac{1}{c} \frac{\partial I_{TL}}{\partial x}, \quad (9-9)$$

where ℓ and c are the inductance and capacitance respectively of the transmission line per unit length. These may be combined to produce equivalent wave equations for the voltage or the current, e.g.:

$$\frac{\partial^2 V_{TL}}{\partial x^2} = \ell c \frac{\partial^2 V_{TL}}{\partial t^2}. \quad (9-10)$$

One must take care in discretizing and integrating these equations to avoid the effects of numerical dispersion. The normal dispersion relation for the wave equation above is $k = \omega\sqrt{\ell c}$ where k is a wavenumber in the transmission line and ω is its frequency. Straightforward discretization of the transmission line into N segments using the leapfrog scheme yields

$$I_{j+\frac{1}{2}}^{n+\frac{1}{2}} = I_{j+\frac{1}{2}}^{n-\frac{1}{2}} - \frac{\Delta t}{\ell\Delta x} (V_{j+1}^n - V_j^n); \quad j \in (1, \dots, N), \quad (9-11)$$

$$V_j^{n+1} = V_j^n - \frac{\Delta t}{c\Delta x} (I_{j+\frac{1}{2}}^{n+\frac{1}{2}} - I_{j-\frac{1}{2}}^{n+\frac{1}{2}}), \quad (9-12)$$

where the current and voltage grids have been interleaved to achieve second-order accuracy in the spatial derivatives (the TL subscript is dropped for simplicity of notation). The dispersion relation for the system 9-11 to 9-12 is

$$\sqrt{\ell c} \sin \frac{\omega\Delta t}{2} = \sin \frac{k\Delta x}{2}. \quad (9-13)$$

Thus the numerical system is highly dispersive although the physical transmission line is nondispersive. The manifestation of this dispersion is the propagation of small wavelength

modes which ring through the system ahead of the main pulse. Note that for a give Δt there is a special value $\Delta x = \Delta t/\sqrt{lc}$ which makes the numerical dispersion relation exact, but it is nice to have the ability to choose Δx and Δt more freely.

To counter the effects of dispersion some artificial dissipation may be added to the equation for the current which then becomes

$$\frac{\partial I}{\partial t} = -\frac{1}{l} \frac{\partial V}{\partial x} + \nu \frac{\partial^2 I}{\partial x^2}, \quad (9-14)$$

where the value of the coefficient ν is chosen ad hoc so as to give the minimum required damping. The dissipative term has a $1/k^2$ dependence on the wavenumber — a desirable feature as it damps high- k modes much more than low- k modes. However, this term produces an additional complication owing to its diffusive nature. The diffusion equation is known to be unstable to explicit time integration, and so the diffusion term is integrated using implicit (Crank-Nicholson type⁸⁵) differencing. The equation for the transmission line current then takes the form

$$I_{j+\frac{1}{2}}^{n+\frac{1}{2}} = I_{j+\frac{1}{2}}^{n-\frac{1}{2}} - \frac{\Delta t}{l\Delta x} (V_{j+1}^n - V_j^n) + \frac{\nu\Delta t}{2\Delta x^2} D^2 (I_{j+\frac{1}{2}}^{n+\frac{1}{2}} + I_{j+\frac{1}{2}}^{n-\frac{1}{2}}). \quad (9-15)$$

Here D^2 is the finite difference approximation to the second derivative defined by

$$(D^2 g)_{j+\frac{1}{2}} \equiv g_{j+\frac{3}{2}} - 2g_{j+\frac{1}{2}} + g_{j-\frac{1}{2}}, \quad (9-16)$$

where g is an arbitrary function defined at half-integer grid points. The update for the current at points on the transmission line therefore requires the inversion of a tridiagonal matrix which is done by the familiar Thomas algorithm.⁸⁶

To complete the algorithm for the transmission line it is necessary to specify the location of sample points for the current and voltage, and match the boundary conditions appropriately to the power supply and the diode. A suitable leapfrog grid is pictured in Figure 86. To center the boundary conditions "ghost" points are added to the current grid on the power supply side and to the voltage grid on the diode side. In the model, the plasma diode simulation determines the voltage across the gap and this feeds back on the circuit equations which respond with a value of current in the power supply for the next cycle. Thus the current grid point at $j = \frac{1}{2}$ is matched to the power supply current while the diode voltage is identified with the voltage grid at $j = N$. V_{N+1} is extrapolated from adjacent values at $j = N$ and $j = N - 1$.

A test of the transmission line is performed by replacing the diode with a small capacitor and discharging the main capacitor in the power supply. Figure 87 shows the voltage oscillation on the output of the transmission line. Figure 87(a) without damping ($\nu = 0$) exhibits high-frequency oscillations caused by numerical dispersion. Figure 87(b) with an appropriately chosen value of ν displays the correct voltage signal without the high-frequency component.

9.3 TRIODE MODEL.

This section describes the triode model which is made up of a PIC simulation and a Monte Carlo simulation of electron scattering by a thin foil.

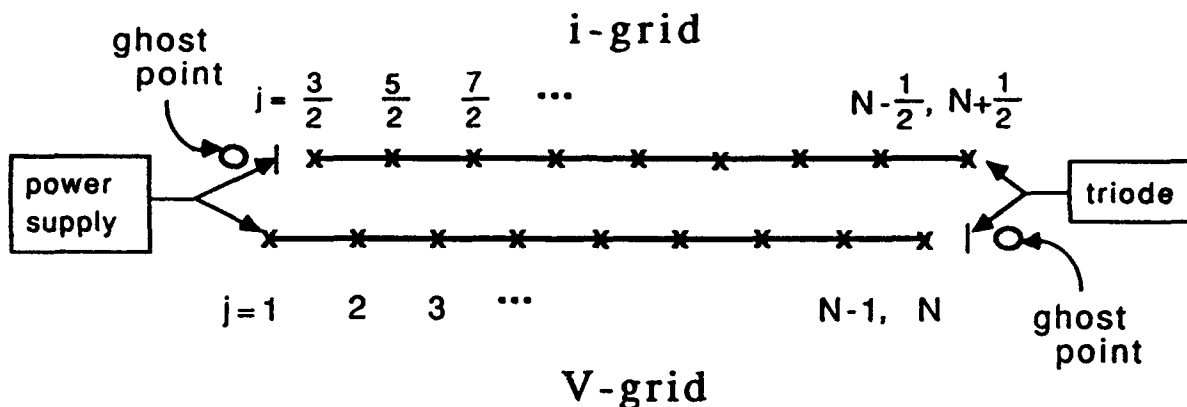


Figure 86. The leapfrog finite-difference grid for a transmission line. The current grid is evaluated at intermediate times and intermediate spatial locations with respect to the charge grid. "Ghost" points are added to center the boundary conditions.

9.3.1 Field Solution.

The fields acting on the simulation particles are the electrostatic field E_x and a constant magnetic field \vec{B}_0 which may be inclined at an arbitrary angle ψ to the x-axis in the x-z plane. Figure 88 illustrates the geometry of the triode simulation region. K1 and K2 are the primary and secondary cathodes respectively while A is the foil anode.

The solution of the potential is obtained from a second-order finite-difference approximation to Poisson's equation:

$$\nabla^2 \phi(x) = -\frac{\rho(x)}{\epsilon_0}. \quad (9-17)$$

The electric field is computed by centered differencing to approximate the gradient of the potential

$$E_x = -\frac{d\phi}{dx}. \quad (9-18)$$

The boundary conditions on the potential are obtained from the flow of charges to the electrodes and to the foil and within the circuit. Because of the presence of the foil, the integration of Poisson's equation is done in two steps: First the net charge deposited on K2 is converted to a surface charge σ_{K2} which determines the boundary value of the electric field $E_{K2} = -\sigma_{K2}/\epsilon_0$. The net charge is the sum of the charges collected by the foil minus the charge carried away or contributed by the circuit. The potential is integrated from K2 to the position of the anode foil assuming an arbitrary value of ϕ_{K2} . Integration from the foil to K1 may proceed once the appropriate boundary values are determined. To obtain the electric field boundary value on the opposite side of the foil, we must first determine the distribution of surface charge on each side of the foil. Because of Gauss's law, the fields E_{K2} and $E_A^{(+)}$ are not independent, but must be consistent with the solution for ϕ on the plus-side of the foil. Thus $E_A^{(+)}$ determines the surface charge $\sigma_A^{(+)}$. Given the net charge

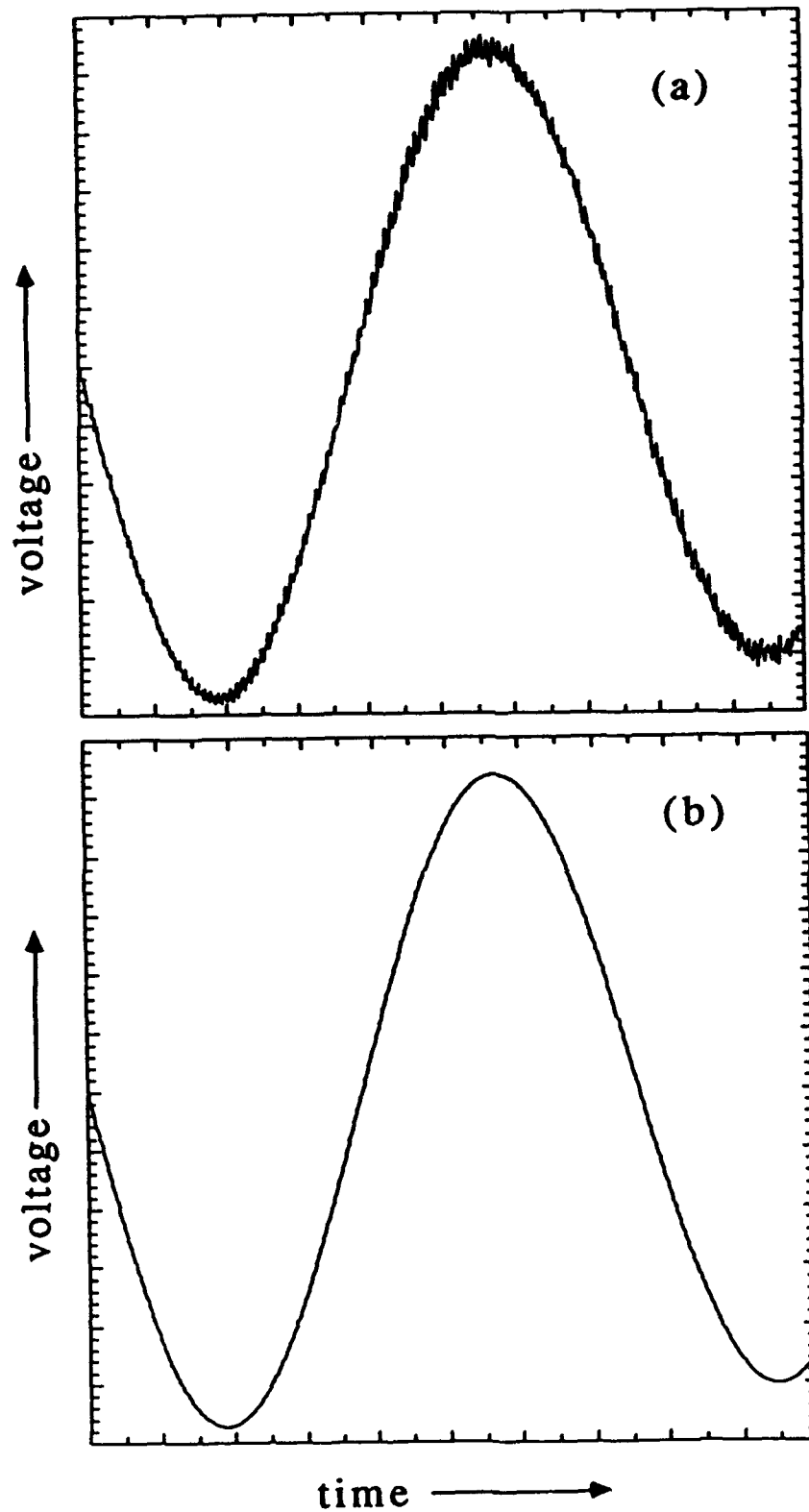


Figure 87. An example showing how dispersive oscillations are suppressed in the transmission line through the addition of a dissipative term with a $1/k^2$ spectral dependence: (a) in the absence of dissipation ($\nu = 0$), a long wavelength mode with dispersive ripples results; (b) appropriate dissipation has eliminated the unwanted mode.

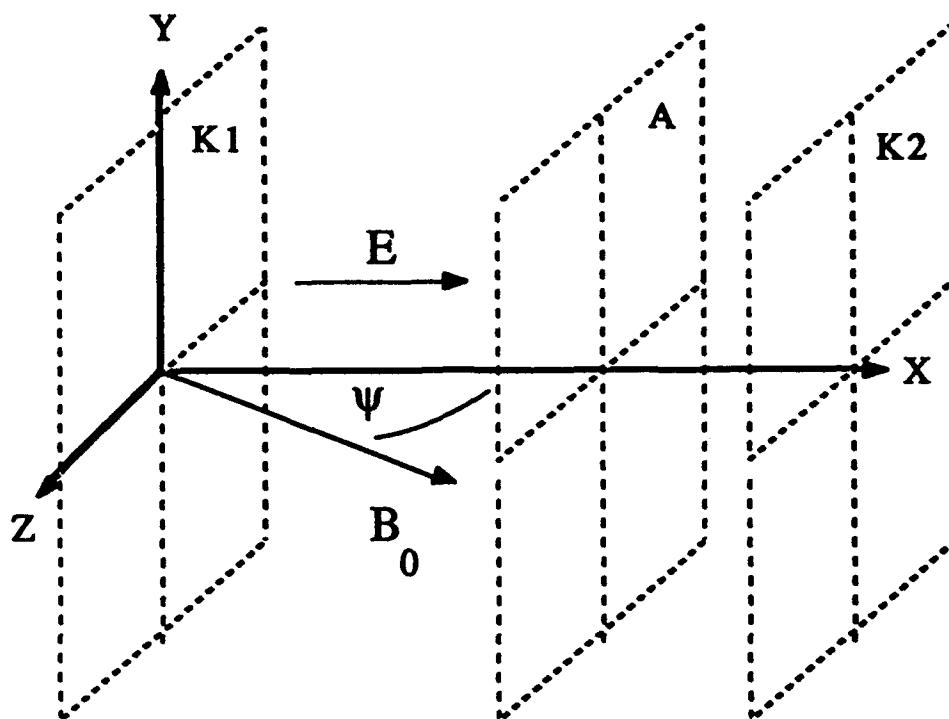


Figure 88. The basic geometry of the one-dimensional diode simulation. K1 and K2 are the primary and secondary cathodes respectively. A is the foil anode. A constant magnetic field \vec{B}_0 may also be specified.

on the foil σ_A , the surface charge on the minus-side of the foil is $\sigma_A^{(-)} = \sigma_A - \sigma_A^{(+)}$. This provides the electric field to the left of the foil and integration of the potential proceeds to the primary cathode. Afterwards the potential is normalized such that $\phi(0) = 0$.

The potentials and fields obtained in the electrostatic solution are used to advance the particles. The solution for the potential also provides the voltage drops V_{D1} and V_{D2} across the primary and secondary gaps which are matched to the ends of the transmission lines.

9.3.2 Particle Motion.

The equation of motion of charged particles in the triode is the familiar relativistic Lorentz force equation:

$$\frac{d\gamma m \vec{v}}{dt} = q[\vec{E} + [\vec{v} \times \vec{B}]], \quad (9-19)$$

with q the charge, m the mass and \vec{v} the velocity of the particle. The relativistic factor γ is

$$\gamma = \sqrt{1 - \frac{v^2}{c^2}}. \quad (9-20)$$

Equation 9-19 is integrated numerically by the standard Boris method.⁸⁷ Rather than integrating the particle velocity \vec{v} , it is more convenient to solve the equation for the normalized momentum $\vec{u} = \gamma\vec{v}$,

$$\frac{d\vec{u}}{dt} = \frac{q}{m}[\vec{E} + \vec{u} \times \vec{B}/\gamma], \quad (9 - 21)$$

with γ related to the momentum by

$$\gamma^2 = 1 + \frac{u^2}{c^2}. \quad (9 - 22)$$

Integration of \vec{u} in Equation 9-22 is accomplished by splitting into acceleration and rotation steps. The method exactly conserves kinetic energy in the absence of accelerating forces and is time-reversible.

It is worthwhile to point out the code follows only a single dimension in space, but all three velocity components. Formulations of this kind are commonly referred to as $1\frac{1}{2}D$.

9.3.3 Particle Emission and Injection.

Particles enter the simulation either by space-charge-limited emission or by injection. Here injection is distinguished from emission in that injected particles are loaded from a given distribution at a fixed rate independent of the surface electric field whereas in emission the particle flux depends directly on the local field.

The algorithm for space-charge-limited emission is based on a common phenomenological model.⁸⁸ At a surface where emission takes place, the normal electric field is checked to see if it exceeds some threshold value. In this case a surface charge is calculated that neutralizes the electric field at the surface. The required charge is obtained by applying Gauss's law to the surface of the half-cell at the boundary:

$$Q = \epsilon_0 E_n S - \frac{1}{2} \rho V_c, \quad (9 - 23)$$

where E_n is the value of the normal component of the electric field, S is the surface area of the electrodes, ρ is the charge density in the boundary cell and V_c is the computational cell volume; i.e. $V_c = S\Delta x$. The charge Q is distributed among a fixed number of particles which are loaded into the simulation just outside the emitting surface. The electric field is subsequently corrected prior to particle advancement to reflect the emitted surface charge.

Injected particles are sampled from some given distribution — usually a Maxwellian of a given temperature T with mean velocity v_0 directed away from the surface, or a half-Maxwellian. The particles are placed at positions consistent with their having been injected at equal subintervals with velocity v_0 during a single timestep.

9.3.4 Electron Scattering Model.

The scattering of real electrons by a thin foil is a complicated atomic process. Electron interactions with material media are usually modeled by Monte Carlo techniques with specialized codes such as ITS.⁸⁹ However, highly detailed calculations such as these are far too expensive to implement in a particle simulation running for thousands of timesteps. Pre-genger and Morel⁹⁰ introduced a simplified approximation that reproduces with reasonable

accuracy the average momentum and energy changes undergone by electrons encountering various materials. The scheme uses data extracted from a data base of particle ranges and values of forward momentum transfer. These data are tabulated as functions of energy and path length using a variety of models. Figure 89 schematically illustrates the nature of the approach. The actual path of a particle through a foil is idealized as a series of small rectilinear path increments. For each path step, interpolated values from the table for a given incident energy are converted into an average energy decrement and scattering angle cosine. The energy is decremented at the end of each path-step and an angle transformation is performed. The algorithm proceeds along the path of the incident particle until it exits the material.

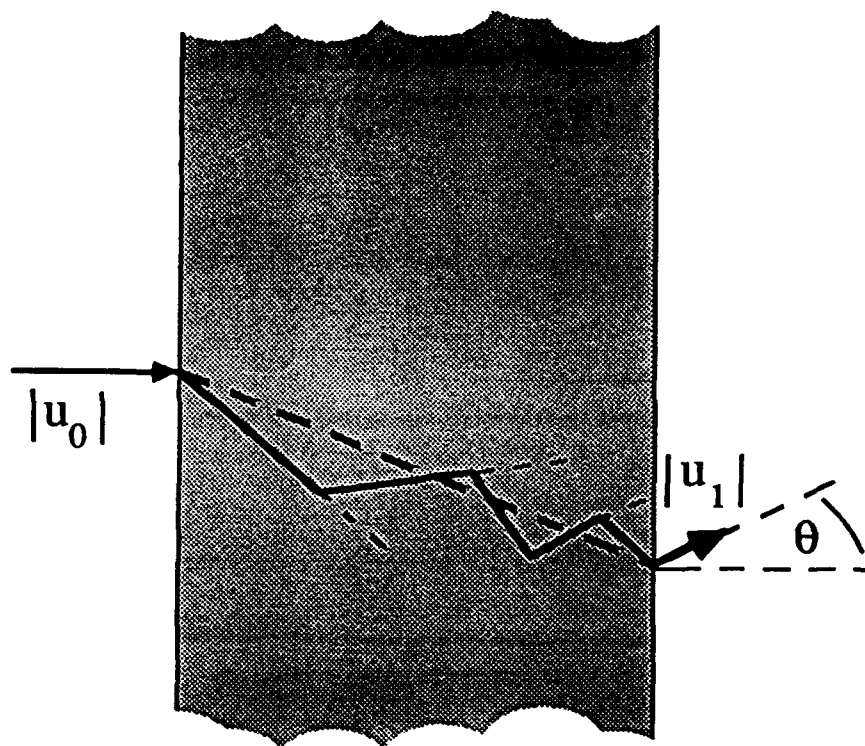


Figure 89. A schematic illustration of the approximate path of electrons (solid lines) assumed in schemes like those of Pregelzer and Morel (ref. 90). In this paper the path through the thin foil is simplified further to become a single straight-line path (dashed line).

The foil scattering module incorporated in our simulations is based on this idea, but is simplified further by additional assumptions. As discussed in Appendix III, the principal approximations are that the energy decrement and the scattering angle may be obtained independently, that incident energies and foil thicknesses are such that the electrons are always in the multiple scattering regime,⁹¹ and that a simple form of the Moliere^{92,93} angular distribution for multiply scattered electrons can be employed.

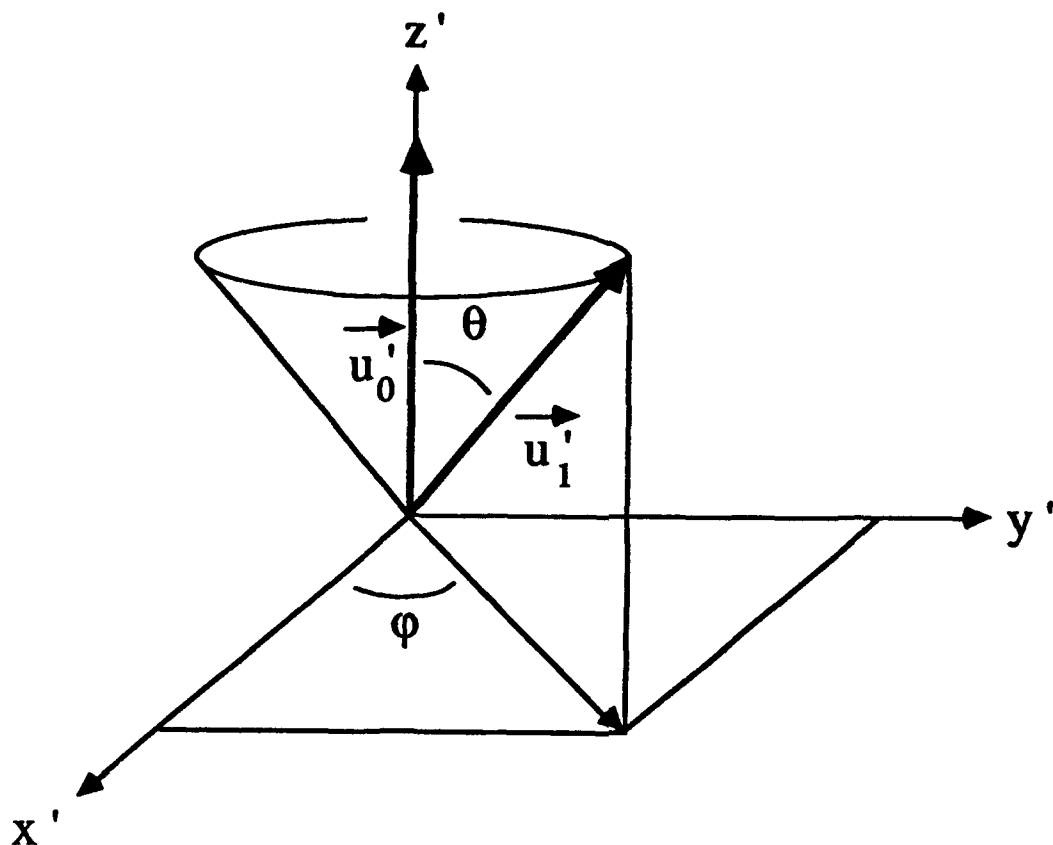


Figure 90. The local spherical coordinate system for an individual particle used in scattering angle transformations.

Using a spherical coordinate system in which the polar axis is aligned with the incident direction as in Figure 90, the distribution expresses the probability of an electron scattering into an angle θ as

$$f(\theta)\theta d\theta = \Theta d\Theta \{2 \exp(-\Theta^2) + B^{-1} f^{(1)}(\Theta) + B^{-2} f^{(2)}(\Theta) + \dots\}, \quad (9-24)$$

Θ is a reduced angle given by

$$\Theta \equiv \theta / (\chi_c B^{\frac{1}{2}}), \quad (9-25)$$

and χ_c and B are parameters that depend on the material and the thickness of the foil. The functions $f^{(n)}$ are given by the theory and may be tabulated numerically from analytical expressions. The distribution given by Equation 9-24 is basically a Gaussian with modifications to extend the tails. The parameter B is always greater than one and often considerably greater, so for most purposes the expansion is terminated after the second term. The Gaussian term reflects that many small-angle scatterings of a single electron tend to produce a normal distribution for the final scattering angle (the central limit theorem), with a half-width that depends on the material, the thickness and the incident energy. Formulas for the parameters and other details of the theory are given in the review paper by Bethe.⁹³

The code employs the simplest form of the distribution, using only the Gaussian term. This approximation is less accurate than the two-term distribution, but more accurate than many other Gaussian scattering models (see references in Ref. 93.)

The scattering angle is often a sensitive function of energy. Therefore it is usually necessary to approximate the scattering process as a sequence of simpler scattering events, as shown in Figure 6, in such a way that the relative changes in energy or angle in any one segment of the path are limited, say to 10 %. However, the thin foils of interest allow the simplifying assumption that only one such segment is needed. This should be good for all particles except those few that barely make it out of the foil. For code operation it is important that particle scattering can now be vectorized easily.

After transiting the foil, the energy of electrons is degraded by reference to a standard table of energy loss versus incident energy (e.g. Berger and Seltzer⁹⁴) for a given material derived from the continuous slowing-down approximation. A polar scattering angle θ is sampled from the Moliere distribution and an azimuthal scattering angle ϕ , uniformly distributed in the interval $0 \leq \phi \leq 2\pi$, is also obtained. The angle scattering is completed when electrons are rotated in the particle frame (Figure 90) and transformed back to the simulation frame. The computational speed of these operations is important. The fastest way to perform the rotations is as follows.

Each electron is referred to a local spherical coordinate system illustrated in Figure 90 where the polar angle θ and azimuthal angle ϕ are the scattering angles. The incident particle momentum in this frame is simply $\vec{u}'_0 = (0, 0, u'_0)$ where the components are those in the local Cartesian coordinate directions (x', y', z') . Clearly the rotated components are given in this frame by

$$\vec{u}'_1 = (u'_0 \sin \theta \sin \phi, u'_0 \sin \theta \cos \phi, u'_0 \cos \theta). \quad (9 - 26)$$

The transformation back to the laboratory frame is constructed by elementary methods of vector analysis.^{95,96} The unit vector \hat{z}' in the particle frame is taken to be the incident direction in the laboratory frame. An orthogonal unit vector is then

$$\hat{x}' = \frac{\vec{A}}{|A|}, \quad (9 - 27)$$

where

$$\vec{A} \equiv \hat{z} - (\hat{z} \cdot \hat{z}')\hat{z}'. \quad (9 - 28)$$

The third unit vector must be orthogonal to the other two, i.e.,

$$\hat{y}' = \hat{z}' \times \hat{x}' = \frac{\hat{z}' \times \hat{z}}{|A|}. \quad (9 - 29)$$

The unit vectors $(\hat{x}', \hat{y}', \hat{z}')$ may be expressed in terms of the direction cosine $(\hat{z} \cdot \hat{z}') \equiv \cos \gamma$, e.g.:

$$|A|^2 = 1 - (\hat{z} \cdot \hat{z}')^2 = 1 - \cos^2 \gamma = \sin^2 \gamma. \quad (9 - 30)$$

Thus

$$\hat{x}' = \frac{\hat{z} - (\hat{z} \cdot \hat{z}')\hat{z}'}{\sin \gamma}; \quad \hat{y}' = \frac{\hat{z} \times \hat{z}'}{\sin \gamma}. \quad (9 - 31)$$

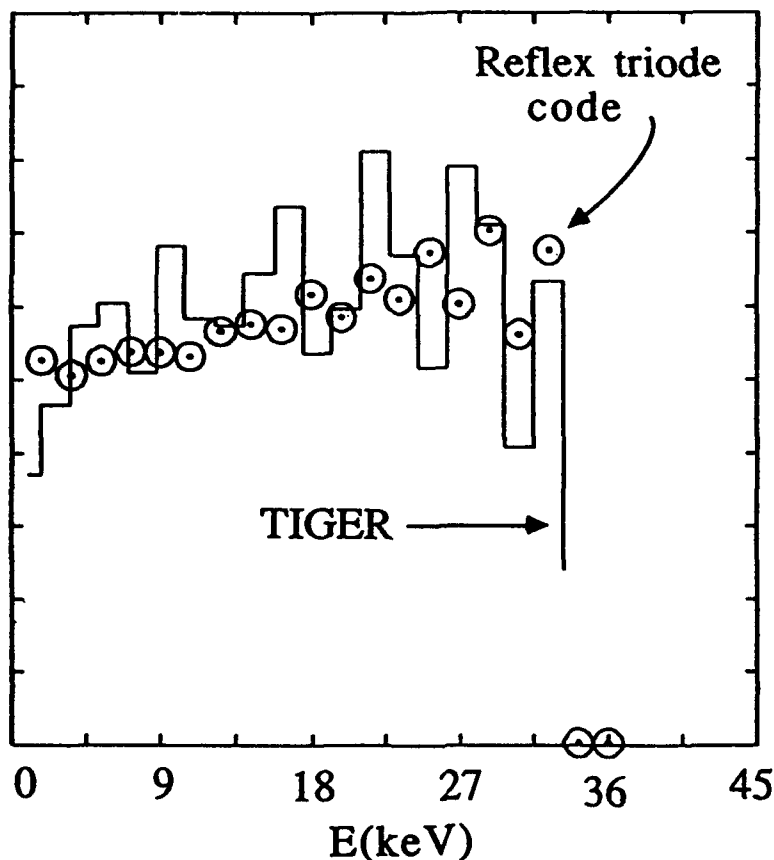


Figure 91. A comparison of TIGER with the simplified foil scattering model using the parallel energy spectra (distribution of kinetic energy normal to the foil surface) for a 35kV electron beam normally incident on a 2μ carbon foil.

The desired transformation matrix is given by

$$\begin{pmatrix} \hat{x} \cdot \hat{x}' & \hat{x} \cdot \hat{y}' & \hat{x} \cdot \hat{z}' \\ \hat{y} \cdot \hat{x}' & \hat{y} \cdot \hat{y}' & \hat{y} \cdot \hat{z}' \\ \hat{z} \cdot \hat{x}' & \hat{z} \cdot \hat{y}' & \hat{z} \cdot \hat{z}' \end{pmatrix}. \quad (9-32)$$

After some algebra this becomes

$$\frac{1}{|u_0||u_{0\perp}|} \begin{pmatrix} -u_{0z}u_{0x} & |u_0|u_{0y} & |u_{0\perp}|u_{0x} \\ -u_{0z}u_{0y} & -|u_0|u_{0x} & |u_{0\perp}|u_{0y} \\ |u_{0\perp}|^2 & 0 & |u_{0\perp}|u_{0z} \end{pmatrix}, \quad (9-33)$$

where

$$|u_{0\perp}| \equiv \sqrt{|u_0|^2 - u_{0z}^2} = |u_0| \sin \gamma. \quad (9-34)$$

Multiplication of the components in 9-26 by the matrix in 9-33 performs a fast scattering angle transformation.

To gauge the accuracy of this simplified procedure, the code was benchmarked against the one-dimensional TIGER member of the ITS code package (version 2.1). The test problem is 35kV electrons that are repeatedly scattered through a 2μ carbon foil until they are absorbed. Figure 91 compares the resultant distributions of parallel kinetic energy (the component normal to the foil or parallel to the incident beam). The comparison is evidently favorable and gives confidence that the model will work for scattering of electrons in the foils encountered in the reflex switch. In addition, timings show that the module is able to process over a million particles in approximately 2 seconds on a Cray XMP. Thus the algorithm can perform well within a PIC simulation.

9.4 CONCLUSION.

Some of the computations in earlier sections have been done with a code that follows the dynamics of a system of coupled one-dimensional diodes separated by a reflexing foil and their driving circuits. This code builds on the previous efforts of Lawson and extends it to a more complex system that is rich in phenomena of interest in pulse power applications. We have used the code in our example to simulate the complex behavior of a reflex triode approaching a low-impedance state.

The computer code described above can be a testbed for developing an understanding of such coupled diode/circuit devices. It is useful for studying basic phenomena in 1D. In principle these techniques may be extended to higher dimensions and more realistic geometries. Self-consistent electromagnetic formulations should also be possible. We hope, with these efforts, to lay the groundwork for more ambitious computations in the future.

10. REFERENCES

1. J. M. Creedon, L. J. Demeter, B. Ecker, C. Eichenberger, S. Glidden, H. Helava, and G. A. Proulx, *J. Appl. Phys.* **57**, 1582 (1985).
2. R. Huff and I. Smith, *Bull. Am. Phys. Soc.*, **19**, 870 (1974).
3. R. B. Miller, *An Introduction to the Physics of Intense Charged Particle Beams*, Plenum Press, New York, 1982, pp. 44.
4. D. S. Prono, J. M. Creedon, I. Smith and N. Bergstrom, *J. Appl. Phys.*, **46**, 3310 (1975).
5. Berkeley Research Associates Technical Report BRA-88-W012R, September 1, 1988.
6. S. Humphries and Xi-Dong Fu, *J. Appl. Phys.* **54**, 4629 (1983).
7. J. Levine and J. Creedon, DNA Pulsed Power Review and SDIO Update held in Las Vegas, Nevada, May 13-15, 1986.
8. Wm. S. Lawson, PDW1 User's Manual, University of California / Electronics Research Laboratory report M84/37 (April, 1984).
9. Wm. S. Lawson, *J. Comput. Phys.* **80**, 253 (1989).
10. J. Goyer, private communication (1987).
11. D. S. Prono, H. Ishizuka, E. P. Lee, B. W. Stallard, and W. C. Turner, *J. Appl. Phys.* **23**, 3004 (1981).
12. F. F. Chen, *Introduction to Plasma Physics*, Plenum Press, New York, 1974, pp. 186-190.
13. J. P. Biersack, and L. G. Haggmark, *Nucl. Instr. and Meth.* **174**, 257 (1980).
14. J. P. Biersack, and W. Eckstein, *Appl. Phys. A* **34**, 73 (1984).
15. E. J. T. Burns, J. R. Woodworth, K. W. Bieg, T. A. Mehlhorn, W. A. Stygar, and M. A. Sweeney, *J. Appl. Phys.* **63**, 1 (1988).
16. J. P. Biersack, *Fusion Technol.* **6**, (1984).
17. J. R. Goyer, G. Barreto, P. S. Sincerny, and M. Krishnan, in *Conference Record of 1988 IEEE International Conference on Plasma Science*, Seattle, Washington (IEEE, New York, 1988), p. 128.
18. P. F. Ottinger, S. A. Goldstein, and R. A. Meger, *J. Appl. Phys.* **53**, 774 (1984).
19. J. Goyer, Private communication (1988).
20. V. L. Bailey, J. M. Creedon, B. M. Ecker and H. I. Helava, *J. Appl. Phys.* **54**, 1656 (1983).
21. J. P. Lidestri, V. L. Bailey, L. J. Demeter, S. D. Putnam, P. Spence and R. J. Kares, *A Plasma Opening Switch Controlled by a Drifting Plasma*, IEEE International Conference on Plasma Science, Oakland CA, May 21-23 1990, IEEE Catalog No. 90CH2857-1, Abstract 5B-9, p 205.
22. E. N. Abdullin, G. P. Bazhenov, A. N. Bostrikov, S. P. Bugaev, A. A. Kim, B. M. Koval'chuk, V. A. Kokshenev, O. B. Ladyzhenskii, G. A. Mesyats and K. N. Sukhushin, *Sov. J. Plasma Phys.* **11**, 66 (1985).
23. K. F. Sander, *J. Plasma Physics* **3**, 353 (1969).
24. M. M. Widner and J. W. Poukey, *Phys. Fluids* **19**, 1838 (1976).

25. P. A. Miller, J. W. Poukey and T. P. Wright, *Phys. Rev. Lett.* **35**, 940 (1975).
26. R. B. Miller, ref. 3, p. 55.
27. W. S. Lawson, *Computer Simulation of Bounded Plasma Systems*, University of California, Berkeley/Electronics Research Laboratory Report M87/14, (1987).
28. P. C. Stangeby, *The Plasma Sheath*, in Proceedings of 1987 NATO Summer Institute on Plasma-Wall Interactions, Plenum Press, New York, 1987, p. 41.
29. M. Widner, I. Alexeff, W. D. Jones and K. E. Lonngren, *Phys. Fluids* **13**, 2532 (1970).
30. W. E. Drummond, J. H. Malmberg, T. M. O'Neill and J. R. Thompson, *Phys. Fluids* **13**, 2422 (1970).
31. T. M. O'Neill and J. H. Malmberg, *Phys. Fluids* **11**, 1754 (1968).
32. I. J. Morey and R. W. Boswell, *Phys. Fluids B* **1**, 1502 (1989).
33. A. E. Blaugrund, G. Cooperstein, W. F. Oliphant, S. J. Stephanakis and B. V. Weber, *Plasma Filled Diode Operation with Plasma Created In Situ by a Low Pressure Hollow Gas Discharge*, Proceedings of the 8th International Conference on High Power Particle Beams, Novosibirsk (1990).
34. R. J. Kares, *J. Appl. Phys.* **71**, 2155 (1992).
35. J. M. Grossmann and P. F. Ottinger, *Potentials Near an Emitting Cathode*, talk given at the Naval Research Laboratory, December (1989).
36. J. M. Creedon, private communication (1990).
37. C. K. Birdsall and W. B. Bridges, *Electron Dynamics of Diode Regions*, Academic Press, New York, 1966, p 68.
38. J. M. Creedon, I. D. Smith and D. S. Prono, *Phys. Rev. Lett.* **35**, 91 (1975); see also ref. 4.
39. C. W. Mendel and S. A. Goldstein, *J. Appl. Phys.* **48**, 1004 (1977).
40. H. Bluhm, K. Böhnel, P. Hoppé, H. U. Karow, and D. Rusch, *IEEE Trans. Plasma Sci.* **PS-15**, 649 (1987).
41. I. Langmuir, *Phys. Rev.* **67**, 238 (1931).
42. R. Stringfield, R. Schneider, R. D. Genuario, I. Roth, K. Childers, C. Stallings, and D. Dakin, *J. Appl. Phys.* **52**, 1278 (1981).
43. R. A. Meger, R. J. Commisso, G. Cooperstein, and S. A. Goldstein, *Appl. Phys. Lett.* **42**, 943 (1983).
44. S. P. Bugaev, A. M. Volkov, A. M. Iskol'dsky, A. A. Kim, B. M. Koval'chuk, V. A. Kokshenev, G. A. Mesyats, A. A. Novikov, and V. P. Yakovlev, *IEEE Trans. Plasma Sci.* **PS-18**, 115 (1990).
45. A. N. Batrikov, S. P. Bugaev, V. M. Bystritskii, S. V. Grigoriev, F. Fursov, B. M. Kovalchuk, A. A. Kim, V. A. Kokshenov, G. A. Mesyats, Y. E. Krasik, and V. P. Yakovlev, *Appl. Phys. Lett.* **46**, 1045 (1985).
46. R. J. Kares, *One Dimensional Particle-In-Cell Simulations of a Plasma Filled Diode with an External Circuit*, Berkeley Research Associates Technical Report BRA-90-360R, October 1990; also Section 4 and ref. 34.
47. R. J. Kares, J. L. Geary, and J. M. Grossmann, *J. Appl. Phys.* **71**, 2168 (1992).
48. J. A. Ambrosiano, and J. L. Geary, *Comp. Phys. Comm.* **67**, 210 (1991).
49. E. M. Waisman, P. G. Steen, D. E. Parks, and A. Wilson, *Appl. Phys. Lett.* **46**, 1045 (1985).

50. J. M. Grossmann, P. F. Ottinger, J. M. Neri, and A. T. Drobot, *Phys. Fluids* **29**, 2724 (1986).
51. R. J. Mason, J. M. Wallace, J. M. Grossmann, and P. F. Ottinger, *IEEE Trans. Plasma Sci.* **PS-15**, 715 (1987).
52. R. J. Mason, M. E. Jones, J. M. Grossmann, and P. F. Ottinger, *Phys. Rev. Lett.* **61**, 1835 (1988).
53. J. M. Grossmann, P. F. Ottinger, R. J. Mason, *J. Appl. Phys.* **66**, 2307 (1989).
54. G. R. Gisler, M. E. Jones, and C. M. Snell, *Bull. A. P. S.* **29**, 1208 (1984).
55. R. L. Morse and C. W. Nielson, *Phys. Fluids* **14**, 2418 (1969).
56. C. K. Birdsall and A. B. Langdon, *Plasma Physics Via Computer Simulation*, McGraw-Hill, New York, 1981.
57. R. W. Hockney and J. W. Eastwood, *Computer Simulation Using Particles*, McGraw-Hill, New York, 1985.
58. T. Tajima, *Computational Plasma Physics: with Applications to Fusion and Astrophysics*, Addison-Wesley, New York, 1989.
59. R. J. Mason, *J. Comp. Phys.* **71**, 429 (1987).
60. S. I. Braginskii, *Reviews of Plasma Physics* **1**, 205 (1965).
61. S. Ichimaru, *Basic Principles of Plasma Physics* W. A. Benjamin Inc., Reading, 1973, p. 16.; N. A. Krall and A. W. Trivelpiece, *Principles of Plasma Physics*, McGraw-Hill, New York, 1973, p. 349.; D. R. Nicholson, *Introduction to Plasma Theory*, Wiley, New York, 1983, p. 37 and p. 45.
62. E. Waisman, D. Parks, P. Steen, and A. Wilson, *PEOS long conduction time theory*, presented at the DNA Pulsed Power Review and SDIO Update held in Las Vegas Nevada, March 31-April 2, 1987.
63. K. V. Chukbar and V. V. Yan'kov, *Sov. Phys. Tech. Phys.* **33**, 1293 (1988).
64. R. J. Kares and S. H. Brecht, DNA Technical Report DNA-TR-87-279.
65. D. L. Book, *NRL Plasma Formulary* (1990).
66. N. R. Pereira and J. Davis, *X-rays from z-pinchs on relativistic electron accelerators*, *Reviews of Applied Physics*, (*J. Appl. Phys.* **64**), R1 (1988).
67. N. R. Pereira, J. Davis, and N. Rostoker, Editors, *AIP Conference Proceedings* **195**, *Dense Z-Pinchs*, Laguna Beach, CA, 1989.
68. K. N. Koshelev and N. R. Pereira, *Plasma points and radiative collapse in vacuum sparks*, *Reviews of Applied Physics* (*J. Appl. Phys.* **69**), R21 (1991).
69. R. E. Terry and N. R. Pereira, *Leakage currents outside an imploding z-pinch*, *Phys. Fluids* **B3**, 195 (1991).
70. N. R. Pereira, *A simple derivation of the Pease-Braginskii current*, *Phys. Fluids* **B2**, 677 (1990).
71. S. Swanekamp, J. Grossman, and J. L. Geary, *Numerical simulations of plasma filled diodes*, accepted for publication in *Phys. Fluids*.
72. T. W. L. Sanford, J. A. Halbleib, J. W. Poukey, C. E. Heath and R. Mock, in: *Proceedings of the IEEE Particle Accelerator Conference* (Washington, D. C., March 1987) p. 931.
73. S. Humphries, Jr., J. J. Lee, and R. N. Sudan, *J. Appl. Phys.*, **46**, 187 (1975).

74. A. Peratt, C. M. Snell and L. E. Thode, *IEEE Trans. on Plasma Science*, **PS-13**, 498 (1985).
75. T. L. Crystal and S. Kuhn, *Phys. Fluids* **28**, 2116 (1985).
76. P. Burger, D. A. Dunn and A. S. Halsted, *Phys Fluids* **8**, 2263 (1965).
77. S. Kuhn, *Phys. Fluids* **27**, 1834 (1984).
78. G. R. Gisler and M. E. Jones, C. M. Snell, *Bull. Amer. Phys. Soc.*, **29**, 1208 (1984).
79. B. Goplen, R. Clark, J. McDonald, G. Warren and R. Worl, *MAGIC User's Manual*, Mission Research Corp. report MRC/WDC-R-126 (1987).
80. I. J. Morey, J. P. Verboncoeur, and V. Vahedi, *Bounded Plasma Device Simulation with PDW1 Including: External RLC Circuit, DC, and RF Drive, and Collisional Processes*, Proc. of the 13th Conf. on the Numerical Sim. of Plasmas, Santa Fe, New Mexico, September 17-20, 1989.
81. V. Vahedi, *A Monte Carlo Collision Model for the Particle-in-Cell (PIC) Method*, Proc. of the U.S.-Japan Workshop on Advances in Simulation Techniques Applied to Plasmas and Fusion, UCLA, Los Angeles, California, September 26-28, 1990.
82. D. Halliday and R. Resnick, *Fundamentals of Physics*, John Wiley-Interscience, New York, 1967, p185-192.
83. E. M. Williams and J. B. Woodford, *Transmission Circuits*, Macmillan, New York, 1957, p. 8.
84. David Potter, *Computational Physics* John Wiley, New York, 1973, p. 33.
85. R. D. Richtmyer and K. W. Morton, *Difference Methods for Initial Value Problems*, John Wiley-Interscience, New York, 1967, pp. 185-192.
86. Hockney and Eastwood (ref. 57), p. 185.
87. Hockney and Eastwood (ref. 57), p. 113.
88. C. K. Birdsall and A. B. Langdon (ref. 56), p. 409.
89. J. A. Halbleib and T. A. Mehlhorn, *ITS: The Integrated TIGER Series of Coupled Electron/Photon Monte Carlo Transport Codes*, Sandia National Laboratory report SAND84-0573 (1984).
90. A. Pregonzer and J. E. Morel, *J. Appl. Phys.*, **57**, 4849 (1985).
91. T. P. Hughes and B. B. Godfrey, *Improved Treatment of Multiple Scattering of Intense Charged Particle Beams*, Mission Research Corp. report AMRC-R-389 (1982).
92. M. J. Berger, in: *Methods in Computational Physics*, Vol. 1, Academic Press, New York, 1963, p. 135.
93. H. A. Bethe, *Phys. Rev.* **89**, 1256 (1952).
94. M. J. Berger and S. M. Seltzer, *Stopping Powers and Ranges of Electrons and Positrons*, National Bureau of Standards report NBSIR 82-2550 (1982).
95. F. F. Chen, *Introduction to Plasma Physics*, Plenum, New York, 1974, pp. 186-190.
96. J. Mathews and R. L. Walker, *Mathematical Methods of Physics*, W. A. Benjamin, New York, 1964, p. 142.
98. W. T. Scott, *Rev. Mod. Phys.* **35**, 231 (1963).
99. S. Goudsmit and J. L. Saunderson, *Phys. Rev.* **57**, 24 (1940).
100. S. Goudsmit and J. L. Saunderson, *Phys. Rev.* **58**, 36 (1940).
101. M. J. Berger, in *Methods in Computational Physics*, Vol. I, Ed. by B. Alder, S. Fernbach, M. Rotenberg, Academic Press, N.Y., 1963, pp. 135-215.

102. T. P. Hughes and B. B. Godfrey, *Mission Research Corporation Report, AMRC-R-389*, July 1982.
103. T. P. Hughes and B. B. Godfrey, *Phys. Fluids* **27**, 1531 (1984).
104. J. D. Jackson, *Classical Electrodynamics*, John Wiley, New York, 1975, p. 649.

APPENDIX A: REVIEW PAPERS ON PRS

X rays from z-pinchs on relativistic electron-beam generators

N. R. Pereira

Berkeley Research Associates, Inc., P. O. Box 852, Springfield, Virginia 22150

J. Davis

Plasma Physics Division, Naval Research Laboratory, Washington, DC 20375-5000

This review summarizes recent experimental data on imploding z-pinchs and their radiation output, and gives an overview of theoretical issues concerning radiation production in the pinch plasma. A z-pinch plasma is created when the current from a fast, powerful electrical generator compresses and heats a small amount of material between the electrodes. The hot, dense plasma emits copious amounts of radiation extending from the visible to the x-ray region. With a 10-TW electrical discharge the radiative power may be a few TW, with an energy per pulse of up to tens of kilojoules. Our interest is mainly in the photons with energy around 1 keV, which are useful in x-ray lithography, microscopy, surface studies, and other applications.

TABLE OF CONTENTS

I. Introduction

- A. Applications of z-pinch x rays
- B. Applications of the z-pinch plasma
- C. Qualitative description of z-pinch radiation sources

II. Experimental Data

- A. Z-pinch creation
- B. A sampling of z-pinch results
 - 1. Implosion dynamics
 - 2. Spatial features
 - 3. XUV radiation
- C. The pinch plasma

III. Theoretical Modeling

- A. Kinematics
 - 1. Snowplow model
 - 2. Kinematic stability
- B. Plasma models
 - 1. Stationary pinch equilibrium
 - 2. Simple pinch dynamics
- C. Radiation
 - 1. Fundamentals
 - 2. One-dimensional radiation hydrodynamics
 - 3. Two-dimensional hydromagnetics

D. Outlook

Acknowledgments

I. INTRODUCTION

The bluish light flash signaling the demise of the filament in a light bulb is produced by about 100 W of household power. X-ray producing z-pinchs are high-power versions of blowing up filaments. The electrical power input reaches 1 TW (10^{12} W) or even higher, with currents measured in megaamperes (MA) and voltages in megavolts (MV). The current's magnetic pressure along the cylindrical axis of symmetry between two electrodes compresses the filament, hence the name z-pinch.

The temperature in a light bulb filament is about 3000 K or ~ 0.3 eV. On increasing the power input the filament temperature should increase: assuming a (temperature)⁴ rela-

tion like that of a blackbody radiator, an increase in power by a factor 10^{10} extrapolates to a temperature on the order of $0.3 \text{ eV} \times (10^{10})^{1/4} \approx 100 \text{ eV}$; temperatures in this range are indeed obtained in z-pinchs. The high power can be sustained only during a short time, perhaps 100 ns.

A hot, dense plasma can be created by exploding a single wire, but multiple parallel wires offer better energy efficiency. The parallel currents in the wires attract each other and the wires accelerate toward the center, storing electrical energy as kinetic energy of implosion. The kinetic energy is thermalized in the collision of the oppositely directed wires, resulting in a hot, dense plasma on axis. The plasma energy from the implosion is augmented by joule heating during implosion, which ionizes wires, and by continued heating during stagnation. The same effect is obtained by smearing out the wire mass in a hollow cylindrical shell.

Imploding z-pinchs are efficient x-ray producers. Typically more than 50% of the plasma energy appears as sub-keV radiation. Perhaps about 10% is radiated in soft x rays between 1 and 10 keV, usually from localized "bright spots." Sometimes minor amounts of high-energy bremsstrahlung are generated, typically less than 1%. The remaining energy goes into magnetic field energy of the vacuum surrounding the pinch and into the thermal energy of the plasma; this energy appears as kinetic energy of the expanding plasma, i.e., the explosion of the pinch after the radiation pulse.

This review discusses the imploding z-pinch for its use as an x-ray source. We emphasize imploding plasmas because in the United States this configuration is the most common. Early examples are the hollow cylinder proposed by Turchi (1973), the multiple wires (Stallings, 1976), and a cylindrical or annular gas shell (Shiloh, 1978). Single exploding wires are mentioned where appropriate. For typical early results on exploding wires see Mosher (1973, 1975). Much work on single wires is continuing in the Soviet Union, see e.g., Zakharov (1983), Baksht (1983, 1987), or Aranchuk (1986).

Not reviewed here is the imploding liner research on the large capacitor bank at AFWL, which is well documented in a series of papers (Baker, 1978; Degnan, 1981; Roderick, 1983). Another summary is the z-pinch work at Imperial

College (Dangor, 1986). Much lower-temperature (~ 1 eV) VUV emitting pinches were extensively reviewed by Finken (1983). Not related to x rays are applications of z-pinches for the generation of large magnetic fields (e.g., Felber, 1985; Wessel, 1986), and as a focusing device in high-energy particle accelerators (e.g., Dothan, 1987). Quite related but still omitted is the use of z-pinches for x-ray laser research (for a review, see Davis, 1988), and the hydrogen z-pinch for thermonuclear fusion. This approach to fusion is discussed by Haines (1982); for recent experimental results see Sethian (1987), and for a review of neutron production mechanisms see Vikhrev (1987) and Trubnikov (1987). A complete bibliography on z-pinch fusion is available from Robson (1987).

Peripheral topics of interest are the pulse power technology needed for driving the pinch (see Camarcat, 1985) and x-ray diagnostic techniques: for quantitative aspects see e.g., Kühne (1985), Eidmann (1986b), and especially Henke (1984a, 1984b).

X-ray sources similar to the z-pinches are vacuum sparks, the plasma focus, and laser-produced plasmas. Although they fall outside this review their x-ray characteristics are sufficiently similar to the z-pinches to merit explicit mention.

In a vacuum spark the current that is passed through an extremely small amount of material that is blown off an electrode, either spontaneously or in a controlled manner with a laser. This gives a hot but perhaps nonthermal plasma with "temperature" of 1–30 keV at various times during the pulse. The x rays come out in multiple bursts (e.g., Burhenn, 1984; Seeley, 1984; Negus, 1979; Cilliers, 1975; Lee, 1975/1974/1971). Vacuum sparks were reviewed by Korop (1979) and by Negus (1979).

In a plasma focus the discharge must find its own path through an initially homogeneous gas fill, leading to a somewhat erratic pinch. The z-pinch configuration, wherein the current can only go where sufficient material is deliberately introduced, makes the discharge more reproducible. Most plasma focus work is directed toward thermonuclear fusion or pulsed neutron production, not to efficient x-ray generation.

Plasmas are created in the focus of optical lasers, with a typical fluence around 100 TW/cm^2 . The plasma may reach a temperature in the neighborhood of 1 keV (e.g., Glibert, 1980; Nicolosi, 1981; Pepin, 1985; Gerritsen, 1986; Mochizuki, 1986; Eidmann, 1986a; Kodama, 1986; Phillion, 1986). The x-ray output per pulse is usually modest, even with a high ($\sim 50\%$) conversion efficiency from optical light to XUV and soft x rays. The world's largest laser, Nova at LLNL (Campbell, 1986), produces up to $\sim 100 \text{ kJ/pulse}$ in the optical, and should yield comparably impressive x-ray pulses. A laser-produced plasma is particularly convenient in many applications because the pulse power is far away from the plasma, while in other applications the potential rep-rate capability of the laser is important (see, e.g., Nagel, 1984; Michette, 1986; also small conventional bremsstrahlung sources can be repetitively pulsed, see, e.g., Davanloo, 1987).

A completely different x-ray source is synchrotron radi-

ation, generated by wiggling GeV electrons. The electrons are accelerated in bunches, and as a consequence the radiation comes out in a continuous train of polarized XUV or soft x-ray bursts with low instantaneous but high average power (see, e.g., Winick, 1980; Koch, 1983; Attwood, 1985; Brown, 1986). The special qualities of these x rays come at a price: a large multiuser facility may cost on the order of \$100M. In contrast, a small z-pinch that produces 10 J/shot of incoherent keV-like x rays costs perhaps $\sim \$100,000$, and the hardware fits in a laboratory corner.

Figure 1 summarizes the parameter regime of the output generated with the various techniques. The z-pinch operates in the 1–10 TW regime with a plasma temperature of 0.1–1 keV. The total energy per pulse depends on the desired photon energy, and obviously on the machine size. Figure 1 suggests a typical power range for neon and argon gas puffs, where $\sim 50\%$ of the photons come out in a single or at most a few narrow lines. Photon energies in between come from elements with intermediate atomic number, or in broadband radiation from higher atomic number elements such as nickel. Laser-produced plasmas (LPP) provide less power at comparable photon energies, and vacuum sparks much less power but in more energetic photons. The x rays are incoherent, and the average power is typically low because most are single-shot devices. Laser-driven x-ray lasers promise a short high-power burst of coherent photons with energy below $\sim 100 \text{ eV}$, but not more energy per pulse (right scale).

The lasers on the left-hand side attain enormous powers in coherent light close to the visible, below at most $h\nu \sim 5 \text{ eV}$; frequency multiplication can give higher photon energies at rapidly decreasing powers. Synchrotron-produced photons are available over a wide energy region, but as always with decreasing power the higher the photon energy.

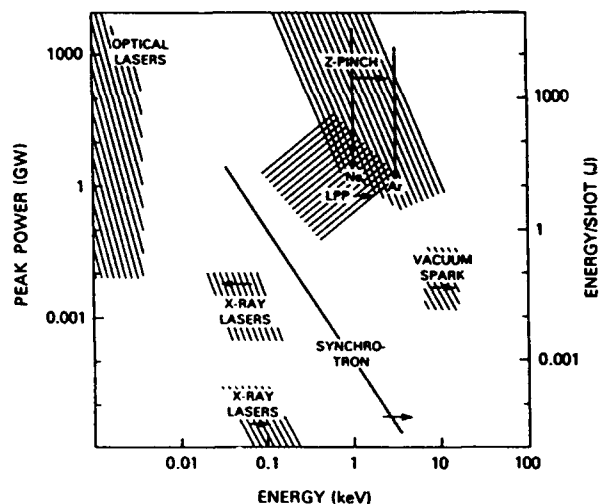


FIG. 1. Typical peak power and energy per shot for the z-pinch, laser-produced plasma (LPP), and vacuum spark x-ray sources as function of a typical photon energy; the vertical lines are the photon energies for the K lines of neon and argon. Sources of coherent x rays are the x-ray lasers, whose very short pulse length is reflected in the relatively high peak power. Synchrotron radiation consists of short pulses at high repetition rates, with average power (in watts) on the right scale. Optical lasers are shown for comparison (upper left).

A final note: our references are almost exclusively limited to the archival literature over the last decade. This choice is most helpful to the reader, while still representative of the available data. We apologize to our colleagues whose work is inadequately highlighted by this admittedly restricted data base. We welcome suggestions for improvements, additions, and especially corrections, for eventual incorporation into an updated version of the review.

A. Applications of z-pinch x rays

A most exciting application of flash x rays is microlithography and x-ray microscopy. In these applications the total energy per pulse is less important than the spectral range of photon energies. Lithography, using x rays with $h\nu$ around 1 keV (and a wavelength around 1 nm), can produce sharply defined features of less than 0.1 μm width on electronic materials, due to the small wavelength and to the strongly localized absorption of the photon energy in the photographic resists. Resist exposure takes only 1–3 shots with a small (~ 50 kJ electrical) z-pinch (Pearlman, 1981/1985a/b; Weinberg, 1986a/b) (or plasma focus; see Kato, 1986). Before z-pinch x rays can be used for routine production of microchips (Pearlman, 1985a/b) it is necessary to resolve difficult problems; these include reducing the size of the x-ray emitting spot, increasing the repetition rate, and protecting the lithographic masks from z-pinch debris.

Contact microscopy with soft x rays (Howells, 1985; Kirz, 1985) produces excellent contrast because their photon energies overlap the K edges of the low atomic number elements that constitute living matter. A photon energy just above the K edge of a given element is attenuated effectively, while a photon with energy just below the K edge is relatively unaffected. Hence, the soft x-ray source can be tuned to look at a particular element, obviating the need to enhance contrast by staining with heavy elements that might kill a cell. A 10-ns long flash of x rays from a z-pinch has caught a bacterium's activities live (e.g., Bailey, 1982a; Feder, 1984; Weinberg, 1985b). Similar results can be obtained with radiation from laser-produced plasmas.

X-ray spectroscopists use the highly charged ions present in copious quantities in the z-pinch for basic atomic physics studies (see, e.g., Striganov, 1983) and, in particular, as a rich source of emission lines (e.g., Burkhalter, 1878, 1979a, 1979b). Highly ionized ions can be made with exploding wires (Dozier, 1977), or vacuum sparks, or by shooting ions through foils; however, the z-pinch is unique in its large x-ray output per shot. At present, much ongoing research is devoted to increasing the z-pinch x-ray output without softening the x-ray spectrum, or to hardening the spectrum without sacrificing x-ray yield.

B. Qualitative description of z-pinch radiation sources

Our z-pinch plasmas are usually driven by a capacitor bank with a total stored energy of 1 kJ–10 MJ. The capacitor bank is discharged either directly or through a pulse-shortening network to produce a current peaking at 100 kA–10 MA: the current rise time is typically between 10 ns and 1 μs .

Table I contains characteristic parameters for a representative selection of machines used in z-pinch work.

A typical z-pinch implosion goes roughly as follows. Initially cold material is located a few centimeters away from the diode axis. In the first few nanoseconds of the current pulse the material heats up and ionizes. The resulting pressure expands the plasma, unhindered toward the axis on the inside but constrained by the magnetic field pressure on the outside. Therefore, the plasma accelerates toward the axis. During the implosion the plasma is heated by ohmic and compressional (shock) heating to perhaps ~ 20 eV. Sometimes the imploding shell is unstable. When the plasma stagnates on axis and the kinetic energy is thermalized the temperature increases steeply, producing a plasma column of ~ 100 eV or higher. This bulk plasma emits a major fraction of the softer x rays.

After stagnation the pinch disassembles. The plasma can expand unhindered if at disassembly time the current is small. However, if the current is appreciable the stagnated plasma is magnetically confined, with additional ohmic heating, and possibly non-ohmic effects such as accelerated electron beams. In addition, a magnetically confined plasma column is hydrodynamically unstable to sausage and kink modes. The sausage mode results in localized "bright spots," which emit the bulk of the harder x rays. Section II contains a selection of the experimental data on which this description is based (bright spots are shown in Fig. 10).

Section III summarizes the theoretical models sometimes used in prediction and interpretation of experiments. The radiative properties of one-dimensional plasma implosions can be computed with some confidence as long as the plasma remains in various kinds of simplifying equilibrium. Under development but still beyond the state of the art are more complicated effects, notably the nonequilibrium plasma physics of the pinch and the pinch's two-dimensional evolution. Unfortunately, these principal problem areas include x-ray production in the bright spots.

II. EXPERIMENTAL DATA

Experiments with plasma radiation sources (PRS) over the last 10 years have produced an abundance of measurements, much of which remains partly analyzed and unpublished. This section contains a selection of experimental data intended to illustrate particular aspects of the behavior of the z-pinch and its radiation output. Abundant data exist in the soft x-ray regime, with photon energy $h\nu$ above ~ 0.8 keV, because many experiments are motivated by increasing the soft x-ray production, and because these photons are easier to analyze and to measure. Quantitative data in the extreme ultraviolet, here defined as $h\nu$ below ~ 0.8 keV, are relatively sparse. The parameter space of the data is very large, with four independent output variables (viz., axial and radial position, time, and photon energy); additional variables are the atomic number Z of the z-pinch material, load parameters (mass per unit length and initial geometry). In addition, the pinches depend on parameters such as current rise time, peak current, and pulse length related to the pulse power generators, mostly large relativistic electron-beam ma-

chines. Qualitative trends in the data are noted where possible: quantitatively, these trends are not necessarily rigorous, proven theoretically, or accepted by all the workers in the field.

Table I summarizes the parameters of the various machines that supply much of the available data on the PRS. The names of some larger facilities express the speculative nature of the pulse power designs. The machines with the largest power levels are water-filled pulse-shortening lines energized by a high-voltage Marx generator (see Camarcat, 1985). Smaller machines may use a less expensive, lower voltage technology, discharging a single stage of 20–50 kV capacitors into a parallel-plate transmission line insulated with a solid dielectric. The various machines are characterized in Table I by their pulse rise time, the maximum electrical power available to a short-circuit load in the diode, and the peak current. The numerical values are illustrative and will change with machine configuration and diode load even for the same charging voltage; moreover, occasional overhauls and upgrades sometimes increase machine parameters. Reliable operation usually requires usage at less than full power.

Energy delivered to the plasma load is converted into optical (vacuum), ultraviolet, x-ray ultraviolet (XUV), and soft x-ray radiation. At a given power, load geometry, and mass, the higher atomic number elements radiate profusely in the VUV and XUV, with much less output of soft x rays. This radiation, generally below ~10 keV, is sometimes accompanied by small amounts of harder x rays.

The XUV radiation pulse is typically much wider than the soft x-ray pulse. For example, the XUV radiation pulse from a krypton gas shell implosion on the Proto II generator

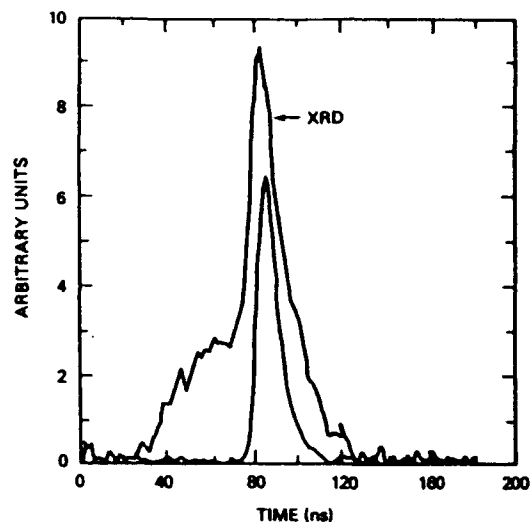


FIG. 2. Pulse shape for XUV radiation measured with a filtered x-ray diode (XRD) and for soft x rays (measured with a filtered *p-i-n* diode) for a krypton implosion on Proto II at SNL (from Spielman, 1985a). The softer the radiation the longer the radiation pulse.

at Sandia National Laboratory (Spielman, 1985a), Fig. 2, has a 30-ns-wide precursor followed by a large 30-ns pulse, compared to the ~10-ns soft x-ray pulse. As usual, the operational definition of XUV is determined by the detector used, here an x-ray diode with an aluminum cathode and a 2- μ m-thick Kimfol filter. This cathode filter combination has a peak response near 270 eV. The soft x-ray signal is measured with a *p-i-n* diode filtered with 25 μ m of aluminum; the

TABLE I. Nominal parameters for some pulse power generators used for imploding z-pinch, and a typical value for the radiative energy per pulse in the x-ray lines specified. The data are indicative of but not necessarily equal to the optimum performance: lower values are often used in z-pinch research. AFWL: Air Force Weapons Laboratory, Albuquerque, NM. CEA: Commission a l'Energie Atomique, France. IColl: Imperial College of Technology, London, England. KI: Kurchatov Insitute, Moscow, USSR. LANL: Los Alamos National Laboratory, Los Alamos, NM. LLNL: Lawrence Livermore National Laboratory, Livermore, CA. MLI: Maxwell Laboratories, San Diego, CA. NRL: Naval Research Laboratory, Washington, DC. PI: Physics International, San Leandro, CA. SNL: Sandia National Laboratory, Albuquerque, NM. UCI: University of California, Irvine, CA.

Machine name	Location	Nominal power (TW)	Nominal I_{max} (MA)	Nominal x-ray yield (kJ)	Reference
Double Eagle	PI	8	3	15 (Ne K)	Dukart, 1983
Blackjack 5	MLI	10	4.6	50 (Ne K)	Gersten, 1986
Pithon	PI	5	3		Stallings, 1979
Proto II	SNL	3	9	2.3 (Kr L)	Spielman, 1986
Supermite	SNL	2	2	(Ne K)	Hsing, 1987
Blackjack 3	MLI	1	1		Riordan, 1981
Gamble II	NRL	1	1.5	4 (Ne K)	Stephanakis, 1986
Owl II	PI	1	1		Stallings, 1976
Sidonix	CEA	0.5		> 0.5 (Al K)	Gazaix, 1984
Shiva	AFWL	1	10	< 4 (Al K)	Roderick, 1983
ZAPP	LLNL	0.2		(Ar K)	Stewart, 1987
	LANL	0.2	0.6		Kania, 1984
	IColl		0.3		Dangor, 1986
Lexis	MLI		0.6	0.02 (Kr L)	Pearlman, 1985
	UCI		0.3		Shiloh, 1979
	KI		1.0		Ivanenkov, 1986

peak response of this detector is near 1.5 keV. Other x-ray ranges can be selected by the proper choice of the cathode combined with filter material and thickness (e.g., Young, 1986).

With a sufficiently powerful generator the soft x-ray emission from low atomic number materials is dominated by line radiation from the *K* shell. For example, Fig. 3 shows three soft x-ray spectra from different axial positions in a neon implosion on Gamble II (Mehlman, 1986). The dominant atomic lines are the Ne IX (He-like) $He\alpha$ $1s^2-1s2p$ at $h\nu = 0.92$ keV and the Ne X (H-like) $H\alpha$ $1s-2p$ resonance line at $h\nu = 1.02$ keV: in the center of the pinch, Fig. 3(b), 42% of the energy is in these lines. Relatively little energy is emitted in the other lines [$\sim 9\%$ for Fig. 3(b)] and in the free-bound continuum with $h\nu > 1.36$ keV. The energy in all continuum radiation between 0.9 and 1.6 keV is about 50% of the total (2.5 kJ for this shot). The relative strength of the lines can be used to estimate the plasma conditions in the pinch. For this pinch the temperature is ~ 100 eV.

How the spectrum looks qualitatively remains unchanged with a larger generator. Figure 4(a) shows a neon spectrum (Rodenburg, 1985a) measured for an implosion on Double Eagle at ~ 10 times the power of Gamble II. Now the pinch reaches a higher temperature, ~ 300 eV, as evidenced by the spectrum. Now the $He\alpha$ line is much weaker than the $H\alpha$ line, which contains over 50% of the soft x-ray energy (total ~ 15 kJ).

In contrast to the neatly separated lines for neon, the implosion of high atomic number elements produces a tangle of overlapping lines. For example, Fig. 4(b) is the spectrum from a nickel wire array on Double Eagle (Rodenburg, 1985b), largely consisting of *L*-shell lines from Ne-like and higher ionization stages of nickel. About 50% of the energy, in total ~ 44 kJ, occurs in a band between 1.0 and 1.12 keV.

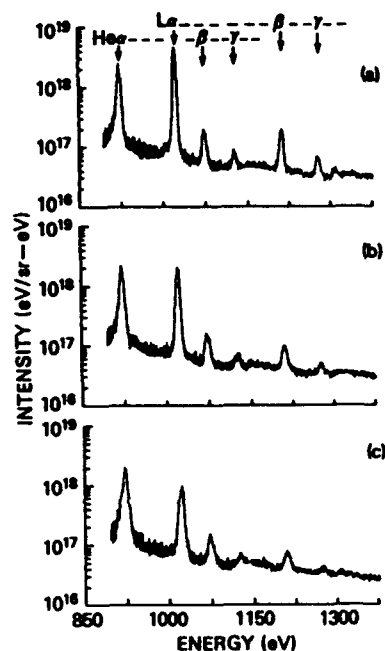


FIG. 3. Experimental soft x-ray spectra at different axial positions in a neon pinch on Gamble II. (a) Near the cathode, (b) midgap between cathode and anode, and (c) near the anode (from Mehlman, 1986).



FIG. 4. (a) Experimental soft x-ray spectrum for neon with dominant *K*-line emission (Double Eagle, from Rodenburg, 1985a). (b) Experimental soft x-ray spectrum for nickel. The individual lines, largely from the *L* shell, are no longer separated but have merged to a quasicontinuum (courtesy of Dr. R. Rodenburg).

The total energy radiated per shot in soft x rays (in a desired energy band) is an important figure of merit. The maximum value of the yield is often preferred over the typical yield. This practice tends to minimize the shot-to-shot variation, which is typically $\sim 5\%$ – 10% for the current, but much larger for the radiation output: similar shots can differ in yield by a factor ~ 2 . The radiation yield data are typically for optimized experimental parameters and include an unspecified spread. The radiation output is usually determined from the fluence over a small detector, and converted to a total yield under the assumption that the photon fluence is isotropic. However, measurement of the yield versus polar angle θ on a small neon and argon pinch shows that the fluence varies approximately as $1 + \epsilon \cos \theta$, with $\epsilon \sim 0.25$ – 0.5 . Consequently, the fluence perpendicular to the pinch ($\theta = 0$) is twice to four times that along the pinch ($\theta = 90^\circ$), although the fluence ratio is not very reproducible from pinch to pinch (Stormberg, 1987).

The yield from various z-pinches is summarized in Fig. 5 (Pearlman, 1985a). The best radiation yield Y_K for *K*-line photons as function of peak current I is reasonably well approximated by $Y_K \propto I^4$. The scaling of yield with current can be understood easily from the implosion dynamics (Wong, 1982).

The *K*-line yield decreases rapidly with increasing atomic number Z or with increasing photon energy $h\nu \sim Z^2$. Approximately, the yield varies as $Y_K = \text{const}(I/h\nu)^4$ or $\sim I^4/Z^8$. The strong scaling with Z can be explained from microscopic physics under reasonable assumptions (Apruseze, 1984b).

Other pulsed plasma devices show comparably strong dependencies on the current. For example, the neutron yield from a plasma focus device could vary even more strongly, as I^6 , and the neutron yield in a solid deuterium z-pinch even goes as I^{10} (Sethian, 1987). Improvements in pulse power, with corresponding increases in peak current, are bound to

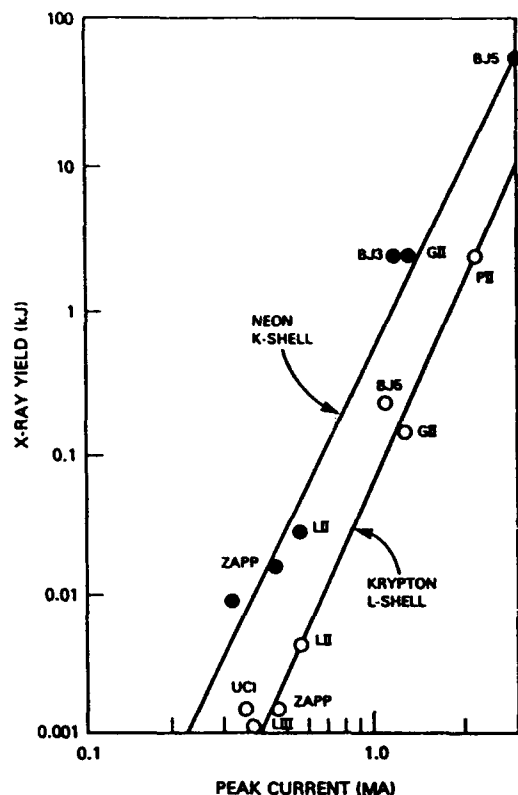


FIG. 5. Optimized radiation yield in neon *K* lines and krypton *L* radiation vs peak current *I* on various pulse power machines (Table I). The yield is proportional to I^4 for both types of radiation (after Pearlman, 1985a).

pay off handsomely in yields from all manner of pulsed power driven plasmas.

Although it is important for x-ray source development to maximize photon output per shot it is equally interesting to pursue alternative goals, e.g., a uniform, linear pinch with controlled plasma conditions for x-ray laser studies (e.g., Dukart, 1983; Wong, 1984; Spielman, 1985b; Stephanakis, 1986). Ease of operation and a moderate price are additional requirements for routine or commercial application (Pearlman, 1985a). Some of the best data on z-pinches has come from innovative diagnostics on smaller machines characterized by high shot rate, ease of modifications, and resources for analysis (e.g., Shiloh, 1978; Marrs, 1983; Kania, 1984; Jones, 1985; Bailey, 1986; Choi, 1986; Stewart, 1987).

A. Z-pinch creation

While PRS diodes differ between machines and applications, the canonical diode for a plasma radiation source consists of a cylindrical rod with a $\sim 1\text{--}5$ cm radius as the cathode, placed a similar distance from the anode. The cathode sticks out of the pulse line plane such that the UV light from the pinch does not reach the insulators that separate the diode vacuum from the pulseline dielectric. Sketches of actual diode geometries usually accompany the experimental papers (e.g., Stephanakis, 1986; Bailey, 1986; Clark, 1982b/c; Kania, 1984b; Pearlman, 1981; Stallings, 1976). The diode is

evacuated to a moderately low pressure, $\sim 10^{-4}$ Torr (0.01 Pa) or less: with appreciably higher diode pressure the gas may break down spontaneously, and becomes more like a plasma focus discharge.

The essential feature of the z-pinch radiation source is the deliberate introduction of the material at the desired location in sufficient quantity to avoid the vacuum spark regime. There is of course a continuous transition between the ultrafast z-pinch and the vacuum spark as the number of electrons per unit length N increases. A value for N may be estimated as follows. In a z-pinch the electrical current I is thought to be collision dominated, while current conduction in a vacuum spark may be dominated by anomalous processes (plasma instabilities leading to high microscopic electric fields, turbulence, etc.). To avoid instabilities the electron thermal velocity v_e should be larger than a typical electron drift speed v_D , with $Ne v_D = I$. In the z-pinch regime, therefore, the number of electrons/length $N > I / e v_{th} \sim I / [ec\sqrt{(T(\text{keV})/500)}]$, which is 6×10^{17} electrons/cm $\times I(\text{MA})$ (for $T \sim 0.5$ keV).

As the number of electrons per unit length decreases, the vacuum spark gradually transforms into an electron diode. The smallest number of pinch electrons per unit length N_{\min} that can carry a current I occurs when all electrons travel with the velocity of light c , i.e., $I = N_{\min} ec$ or $N_{\min} (/cm^3) = 2 \times 10^{16} I(\text{MA})$. If the number of pinch electrons per unit length N is less than N_{\min} the pinch electrons must be supplemented by other electrons, presumably emitted from the cathode. For still smaller N , the bulk of the current is carried by these emitted electrons, as in a pure electron diode. In the process, the character of the discharge changes from a resistive diode to a space-charge-dominated diode.

Whether the discharge material is initially a solid, a gas, or a plasma appears to be unimportant for the radiation output of the pinch provided the electrical breakdown is sufficiently uniform. In all cases the material becomes a plasma early into the discharge. However, the initial mass distribution differs for the various phases, and this may be the most important factor in pinch behavior. Connecting the electrodes with thin wires is convenient. However, this restricts the load material to solids such as plastic, Al, Ti, or Fe. A practical problem with wire loads in their replacement after each shot, which usually involves a time-consuming opening of the diode, although this could be avoided by loading the wires in the vacuum under electrostatic guidance (Kania, 1984a).

Six or more wires are theoretically stable (Felber, 1981) against perturbations that destroy cylindrical symmetry. The symmetry in the implosion is apparently important in the production of radiation. With the same load impedance or initial radius and the same mass per unit length, the output from four wires is indeed smaller than with six wires (Stallings, 1976). Experiments to increase the radiation by using 12 or even 24 wires fail to give a substantial improvement. Therefore, six wires are most common, because this minimizes the difficult handling of fragile wires. When the mass/length can be substantial it is unnecessary to use indi-

vidual wires. Instead, thin cylindrical foils can be used (Baker, 1978).

The dominant alternative to wires is the pulsed injection of gas (Shiloh, 1978), often a noble gas but sometimes a molecular compound or a mixture of gases (Bailey, 1982b), and even a fine powder carried in the gas stream. How much material is injected can be varied by changing the pressure behind the pulsed valve, or the time difference between opening the gas valve and firing of the main pulse. Other ways to provide a load include a discharge through a capillary in an insulator (NaF), which injects a solid plasma plume in the diode (Young, 1986). A hollow cylindrical ring of plasma can be shot into the diode using an auxiliary discharge in a metallic foil (Gazaix, 1984). This technique results in mass distributions with well-defined edges in the radial direction. To obtain a uniform mass density in the azimuthal direction, the auxiliary discharge should be sufficiently well behaved.

For a wire load the cathode and anode can be solid conductors, but for a gas puff load one electrode, typically the cathode, contains the gas nozzle and the puff valve. After opening the puff valve the gas pressure slowly builds up to the proper value, but the tenuous leading edge of the gas, streaming at Mach 4–8 (about 0.1 cm/ μ s) could still be around. To counteract nonuniform gas buildup in the diode the anode should pass this gas into a larger vacuum vessel. Therefore, the anode cannot be a solid plate. Instead, the anode may consist of rods that intercept the gas stream, wires stretched between posts, a conductive mesh, or a honeycomb (e.g., Wessel, 1986).

The amount of gas in the diode is often unknown, although it is sometimes inferred from the implosion time of the pinch material (assuming the material is swept up). Measurements of the gas density after injection, but before the current pulse has arrived, indicate that the initial gas profile is a cone of gas, expanding radially as it moves away from the nozzle (Smith, 1982/1985). The peak density is $\sim 10^{17}$ ions/cm³ (Smith, 1982/1985; Gazaix, 1984). Once the gas is ionized the electron density is measurable with laser interferometry (Shiloh, 1979).

With wires the initial amount of material is known; however, even with wires the mass per unit length participating in the implosion may differ from the initial value. For example (Benjamin, 1981), an outer layer may blow off the wire and implode during the initial part of the pulse, leaving less mass for the main implosion. The mass cannot be determined unambiguously from the acceleration in the implosion and the measured diode current, because an unknown part of the diode current is contained in the blown-off material. Conversely, electrode material can end up in the z-pinch. When wire and electrode material differ, the additional material is visible through its characteristic radiation, but when electrode and pinch are the same element (e.g., aluminum) the increased mass is hardly noticeable, the only indicator being the difference in behavior of the pinch close to the electrodes as compared with that in the center. Then another electrode material may be tried (Choi, 1986). Also, material from the current return posts may get mixed in with the load gas. Finally, instabilities in the pinch cause flow of material along the axis out of the compressed region, modi-

fying the mass/length still further.

If the material connecting cathode and anode is conductive, metal, or plasma, the current starts to flow as soon as the electrical pulse arrives, and the voltage between the electrodes is largely inductive. However, if the material is nonconductive, sometimes plastic wires but commonly a gas, the voltage between the electrodes builds up rapidly until the material breaks down. Self-breakdown tends to give sparks that evolve into random current channels, possibly affecting the implosion symmetry. Preionization of the gas by external means then improves the implosion. Preionization with UV flashboards is common. Initially the flashboard's UV spectrum peaks at 70 eV, decreasing to 30 eV as the pulse proceeds. The UV is readily absorbed in the gas shell. Also, preionization with rf waves is used. Preionization may be superfluous if the pulse power generator has a sizeable prepulse. Then the ionization from the prepulse appears to have time to spread throughout the gas, as evidenced by a sufficiently symmetric behavior of the implosion.

Additional control over the initial condition of the pinch is obtained by injecting low-energy electrons along the diode axis through a ring in the anode. The effect is seen experimentally in a reduced amplitude of instabilities, and an improved implosion (Ruden, 1987).

After the pulse the diode is filled with an exploding plasma no longer contained by the magnetic field from the current. Anything to be exposed to the x rays must be protected from this blast. Thin foils stop the hot gases but transmit a varying fraction of the x rays. Pressure buildup in the diode can be avoided by careful design of the outer conductor. X-ray diagnostics are typically so far away that fast closing valves can be used in addition to the slits needed in the diagnostics. Additional magnets block the electrons.

It is possible to get a radiating region with special properties by providing special load configurations. X-ray laser studies with z-pinches need a linear, homogeneous plasma region that remains moderately hot during a 0.1–1 ns period. A gas column (Sincerny, 1985) or a foam cylinder (Spielman, 1985b) on axis in addition to the standard load improves the homogeneity of the imploding gas shell. The converse effect is reached by connecting the electrodes with crossed wires, the "x-pinch" (Kolomensky, 1983; Faenov, 1985; Ivanenkov, 1986; their data are summarized by Zakharov, 1987). The intent is to concentrate the available power in a single point, and generate on a small (~ 10 -GW electrical) generator the plasma conditions usually seen on terawatt machines.

B. A sampling of z-pinch results

This subsection contains a sampling of diagnostic results available in the literature to illustrate particular aspects of the z-pinch. Table II contains many of the available data. Besides these published results there are many more, but qualitatively similar, data available in internal reports outside the limits of this review.

Usually, soft x rays are the intended product of the PRS, and their energy per pulse is commonly measured on each shot. Also available are the overall electrical parameters of

TABLE II. Some data obtained with z-pinches. In the second column the * indicates quantitative data, a *t* theoretical spectra, a *w* data from wires, and an *x* data from the x-pinch. Spectra are from the given element (SS is stainless steel). The last column indicates a time or spatially resolved spectrum.

Reference		Pinhole	Soft x-ray spectrum	XUV spectrum	Resolved spectrum
Aranchuk, 1985		W			
Baker, 1978		Al			
Benjamin, 1981		SS			
Bleach, 1982		Ar		Ne,Ar,Kr,Xe	
Bruno, 1983		Al			
Burkhalter, 1978	*		Fe	Fe	
Burkhalter, 1979a	*	Al	Al,Si,Ti	Al,SS	
Burkhalter, 1979b	*	Ar,Kr	Ne,Ar,Kr		
Choi, 1986		Ar			
Clark, 1986	<i>t</i>		Ne		
Clark, 1982			Al,Ca,Ti		
Clark, 1983		Ar	Ar	Ar	Ar
Dozier, 1977	<i>w</i>	Pt		Cu,Ag,Au	
Dukart, 1983		Kr	Kr	Kr	
Duston, 1981	<i>t</i>		Ar	Ar	
Duston, 1984	<i>t</i>		Ne,Ar,Kr		
Gersten, 1981	<i>s</i>		Ti		
Gersten, 1985		Al(<i>t</i>)	Al		
Golts, 1986			Kr		
Hammel, 1985			Ar		
Hares, 1985		Ar		Ar	
Ivanenkov, 1986	<i>x</i>	Al,Pd,W		Mo	
Maxon, 1983	<i>t</i>			Ar	
Mehlman, 1986	*	Ne	Ne		Ne
Mosher, 1973	<i>w</i>	Ti,W	Ti		
Pearlman, 1981			Ar,Kr	Kr	
Riordan, 1981		C,Al,SS,W	Al,SS,Kr	C,Al,SS,Kr,W	
Shiloh, 1977		Ar			
Shiloh, 1978		Ar,Kr			
Spielman, 1984		Kr,Xe	Kr,Xe		
Stallings, 1976		Al	Kr,Xe		
Stallings, 1979		Ar			
Stephanakis, 1986		Ne			Ne
Stewart, 1987			Ar	Ar	Ar
Zakharov, 1983		Al,W	Al		Al

the machine, e.g., the current at the entrance to the diode and the voltage at the vacuum insulator. Spatially resolved x-ray pinhole pictures simply show the spatial location of the emission, without being quantitative in the radiation output. The same is true of streak and framing photography, which provide both time and spatial resolution. Optical or x-ray filters are used with these techniques to give rough spectral discrimination.

Complete and detailed measurements so coveted by theorists are very hard to obtain and seldom published. These measurements include time and spatially resolved XUV and soft x-ray spectra on the same shot, the last column in Table II. Even much simpler diagnostics, e.g., time and spatially averaged but quantitative x-ray spectra such as Figs. 3 and 4, are available on relatively few shots. Table II marks these with a star (*). Most often the spectra are given qualitatively in terms of film density versus photon energy.

From the spectrum much can be inferred about the average plasma properties. Most often the spectrum is measured for the whole length of the pinch, and contains information about the bulk plasma mixed with the bright spots. Slits are used to restrict the axial field of view. However, because the spectra contain time-averaged emission along a

line through the pinch, it is still impossible to determine the local plasma state without further data on where and when the plasma emits the radiation of interest. For example, even the single bright spot diagnosed by Hares (1985) is embedded in a blanket of cooler plasma.

The radiation output per pulse increases strongly with generator power and peak current. More power in the generator allows more plasma to be compressed to a higher density and/or a higher temperature, increasing the x-ray output from the bulk of the pinch plasma, but this is not necessarily the reason for the increased yield. Instead, the increased radiation output appears to be primarily related to more and bigger bright spots, or sometimes to a larger density and temperature in each individual bright spot. These statements are anecdotal and will surely need to be modified as more systematic studies are done.

1. Implosion dynamics

Early on in the pulse the z-pinch material is ionized and emits visible light. As the pinch progresses and the material gets hotter the photon energy increases until soft x rays are emitted at stagnation. Visible light is conveniently mea-

sured, and thus is an easy way to follow the implosion. Figure 6 is an optical framing photograph of a hollow gas puff z-pinch imploded on the Lexis capacitor bank (Pearlman, 1985a). Although light cannot be emitted without heated z-pinch material there is no definite relation between light and material, and material and current. For example, the whisks or flares visible in the middle frames do not necessarily indicate that the current flows in the whisks. Also, the fact that the edge of the pinch appears sharp and well defined in frames (a)–(c) does not imply that the current path is thin but results from the emission integrated along the chord. However, visible light, material, and current are often related on the assumption that the pinch material is swept up by the magnetic pressure, as in a snowplow.

In the snowplow model frame (a) suggests a slightly flared gas shell with current running on its outside. The irregularities close to the anode at the bottom appear to result from the gas stream hitting the anode rods. As time goes on, axial perturbations in the pinch edge become more prevalent and the pinch shows deviations from axisymmetry [compare frames (b)–(d)]. Subsequently, the perturbations evolve into the flares of frames (d) and (e). The pinch implodes at all axial locations irrespective of the axial structure, stagnating first close to the cathode and only later close to the anode. This phenomenon is called “zippering.”

Not much radiation is emitted until the pinch stagnates [frames (e) and (f)]. Optical radiation in frame (e) comes from the cathode, where a sheath of leftover gas or plasma seems to participate in the current conduction. A dark gap separates the cathode from the uniformly radiating central part of the pinch. A pair of flares is still present close to the anode, which is also emitting light. The flares have disappeared in frame (f) but the gap is still present: it pops up again during pinch disassembly, shown in frames (g) and (h). This final stage consists of a beadlike helix as could be

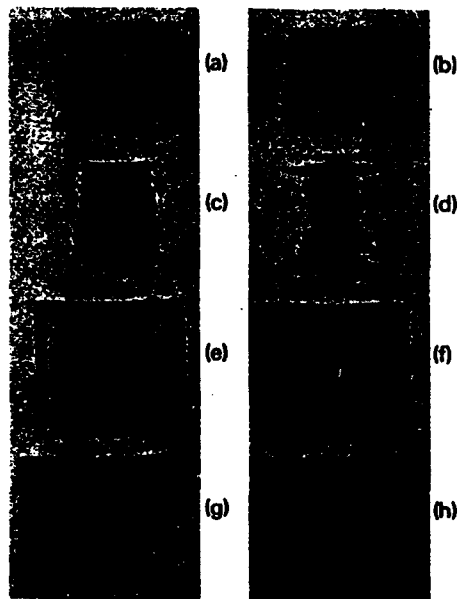


FIG. 6. Implosion sequence of a gas puff z-pinch measured in optical light (from Pearlman, 1985a). The anode-cathode gap is 3 cm, the interframe time is 50 ns.

expected from an advanced stage of hydrodynamic sausage instability superposed on a kink mode (Bateman, 1978).

Is the dynamics of the implosion consistent with all the mass being swept up by the current as if the magnetic pressure were a snowplow (Katzenstein, 1981)? If this were the case, the radial position of the gas sheath as a function of time should be consistent with the acceleration from the $I \times B$ force, and a constant mass per unit length. This can be done by taking an axial slice of the pinch, avoiding axial nonuniformity. For example, Fig. 7 shows the time evolution of a slice perpendicular to the axis in the middle of an argon pinch on a 10-TW pulseline with 100-ns rise time (Clark, 1982c). The “radius of the pinch,” both the plasma edge and the current sheath, is then identified with the light emission.

At the beginning of the main current pulse, 50 ns before stagnation, the plasma already has an inward radial velocity obtained from the prepulse. As the pulse progresses the luminosity sheath (arbitrarily defined by the transition between dark and light blue) implodes and thickens at the same time. Stagnation occurs at $t = 0$ ns as defined by the green curve intersecting the axis, but already 10 ns earlier some precursor plasma (light) has reached the axis. For the purpose of comparison with the implosion model the plasma position is defined as the brightest radius in dark blue until 25 ns before implosion, when it changes to the light blue and the green. The comparison is favorable (see Fig. 8): the measured radius $r(t)$ is in good agreement with the acceleration determined from the force $\mu_0 I(t)^2 / 2\pi r(t)$ and a constant mass per unit length, which is considered as an adjustable parameter. The pinch dynamics has been corroborated in a similar fashion in many other experiments (e.g., Degnan, 1981; Clark, 1982a/b; Bruno, 1983; Bogolubskii, 1986). Use of the mass as an adjustable parameter is almost unavoidable: the mass per unit length of the gas is very hard to measure, and even the mass per unit length of a wire load is uncertain. The value of the current is typically more reliable, even though the current is seldom measured close to the pinch: the magnetic field in a z-pinch can be measured with Faraday rotation (Veretennikov, 1985).

It is important to note that the radiation output cannot be optimized simply by choosing the stagnation time at the peak of the current pulse (Gersten, 1986).

After implosion the pinch at the axial location of the streak radiates strongly for 30 ns in the visible (red in Fig. 7), but the soft x-ray radiation pulse from this particular axial location is much shorter. The soft x-ray pulse from the whole pinch has a full width at half maximum (FWHM) of ~ 20 ns, compare Fig. 2.

2. Spatial features

Some visible light is generated from the start of the current pulse, while XUV radiation is emitted in a fairly wide pulse around the stagnation time. The spatially averaged soft x-ray pulse is still shorter, Fig. 2, but soft x-rays from a given location in the pinch come in an even sharper pulse. For example, Fig. 9 is an x-ray framing photograph of a krypton pinch designed to be linear with minimal zippering (Dukart,



FIG. 7. Optical streak photograph (color plate) showing the radial collapse of argon z-pinch. The picture starts at 170 ns after the beginning of the electrical pulse (see Fig. 8). This initial part of the pulse gives a small initial velocity to the gas; the strongest acceleration occurs just before stagnation. During the contraction the luminosity sheath has a finite width; the final pinch size is about 1 mm. Strong optical emission occurs during about 40 ns (bottom scale) (courtesy of Dr. J. Pearlman: for an uncolored version of this photograph see Clark, 1982c).

1983). A typical axial location strongly radiates soft x rays (blue) during only 2 ns, with the exception of the pinch close to the cathode, where the radiation persists for 10 ns. The total emission from the pinch lasts for about 15 ns. Proper design of the gas nozzle to minimize the zippering can reduce the pulse width from 10 to 4 ns (Hsing, 1987).

Much of the kinetic energy accumulated in the pinch material during run in is converted into optical and XUV photons irrespective of the details of the pinch. In contrast, the soft x radiation is typically emitted by localized bright spots; this radiation is sensitive to the pinch conditions such as current level and atomic number of the load. This point is illustrated in Fig. 10, which compares two sets of pinhole pictures, one in the XUV with photon energy $h\nu$ around a few 100 eV, and the other in soft x rays with $h\nu$ over 1 keV. The left picture is an aluminum pinch ($Z = 13$), and the right is a tungsten pinch ($Z = 74$) (Riordan, 1981). Apart from the atomic number, the pinch conditions were similar, e.g., the same maximum current (~ 1 MA) and an optimum mass per unit length for soft x-ray production ($\sim 150 \mu\text{g}/$

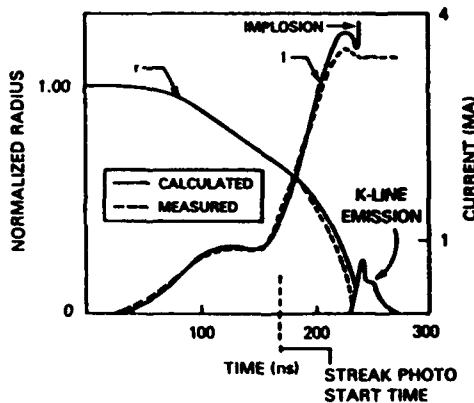
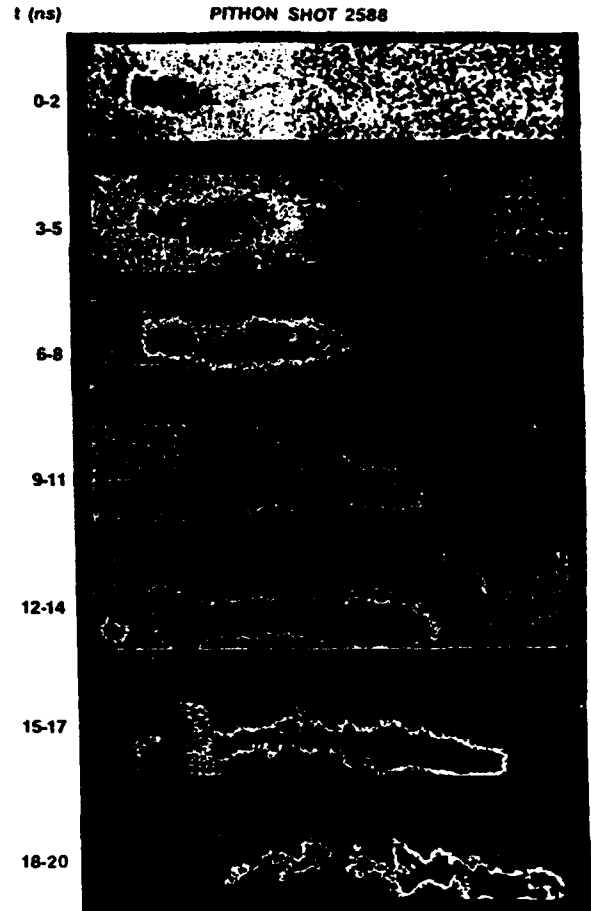


FIG. 8. Measured and calculated load current compared to the measured and calculated radius of the imploding argon pinch in Fig. 7. The K-line x-ray pulse (arbitrary scale) starts 230 ns into the pulse at stagnation (Blackjack 5, after Clark, 1982c).



TIME-RESOLVED X-RAY PINHOLE PHOTOGRAPHS OF A KRYPTON Z-PINCH PLASMA

(2 ns/FRAME EXPOSURE, 3 ns BETWEEN FRAMES)

FIG. 9. Time-resolved pinhole photograph in ~ 1.6 -keV x rays of a krypton gas puff plasma (Pithon; courtesy Dr. S. L. Wong: for an uncolored version of this photograph see Dukart, 1983).

cm). The XUV emission in both shots comes more or less uniformly from a neighborhood of the axis, but the difference in soft x-ray output is striking, with the hot spots much more pronounced for tungsten. For both materials there is also a weak correlation between the bright spots in the soft x-rays and a slight structure in the XUV output.

Similar behavior is seen when the atomic number of the load remains the same but other pinch parameters vary (Riordan, 1981). At the same peak current, increasing the mass per unit length m/l from the optimum for soft x-ray production reduces the number and size of the bright spots, but increases the optical and XUV emission. The pinches still differ even if the implosion time is kept the same by reducing the initial radius r_0 and increasing the mass per unit length to keep $m r_0^2/l$ constant. Figure 11 compares x-ray pinhole pictures under these circumstances for an aluminum pinch (Gersten, 1986). The largest mass per unit length and the smallest initial radius produce a narrow, dense, and strongly radiating pinch, panel (a). Increasing the initial radius by a factor of 2 and decreasing the mass per unit length fourfold gives the wide, tenuous pinch in panel (c). The intermediate case, panel (b), has about half the mass per unit length. The radiation yield decreases from 20 kJ for panel (a) and 4.5 kJ for panel (b), to 0.45 kJ for panel (c). The yields depend somewhat on the pinch temperature, but mostly on the peak density obtained in the pinch. The strong decrease of radiation yield with mass is understandable in part by premature heating of the plasma, which prevents compression to a high density.

The radiation generated by atomic processes in a pinch is sometimes accompanied by detectable amounts of unintended harder radiation, apparently produced by 10–100

keV or even higher energy electrons. These can be generated in the stagnation phase by an (resistive or inductive) electric field along the pinch axis (e.g., Putnam, 1979; Warren, 1987). This bremsstrahlung energy increases with machine power but is never strong enough to dominate the pinch energetics. Moreover, it can be avoided almost completely by increasing the amount of pinch material beyond a critical value. Quantitatively, for a shot with an estimated K-line yield of 20 kJ the bremsstrahlung energy from a thick aluminum anode is estimated at <20 J per pulse (Clark, 1982a). The current in the fast electrons (assumed ~ 1 MeV) is then something like <60 kA, as compared to a ~ 3 MA total current through the pinch.

In addition to bremsstrahlung generated at pinch time, a short burst of bremsstrahlung can appear at the start of the current pulse. This phenomenon may be related to the front edge of the magnetically insulated space-charge sheath that carries power to the diode.

A ~ 20 -keV electron beam in the axial direction has been observed directly with differentially filtered Faraday cups (Kania, 1984 b). These fast electrons carry a small fraction (~ 20 kA) of the total current (~ 600 kA). The atomic radiation excited by these nonthermal electrons could dominate the harder part of the radiation output (Hammel, 1984; Dangor, 1986), but whether this happens in all pinches is an open question at the moment. Spectral diagnostics on a single bright spot shows beam-generated radiation in some cases (Hares, 1985): electron beams accel-

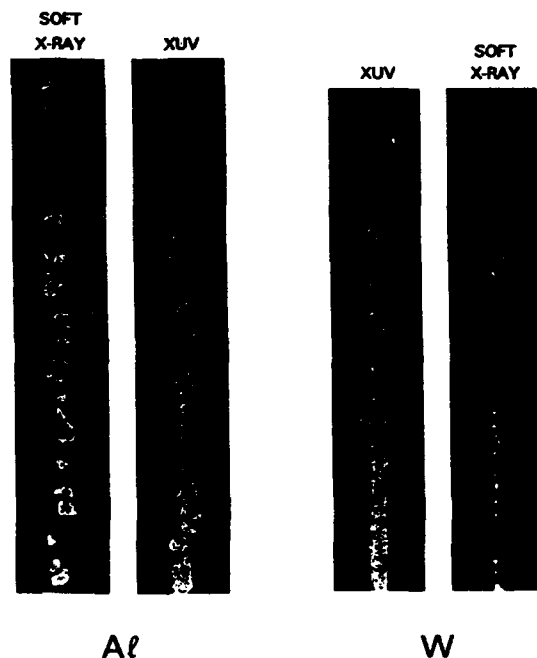


FIG. 10. Time-integrated emission in XUV (inner) and soft x rays (outer) for a $164\text{-}\mu\text{g}/\text{cm}$ aluminum pinch and a $141\text{-}\mu\text{g}/\text{cm}$ tungsten pinch. The anode-cathode gap is 3 cm, and the nominal current is 1 MA (Blackjack 3, from Riordan, 1981).

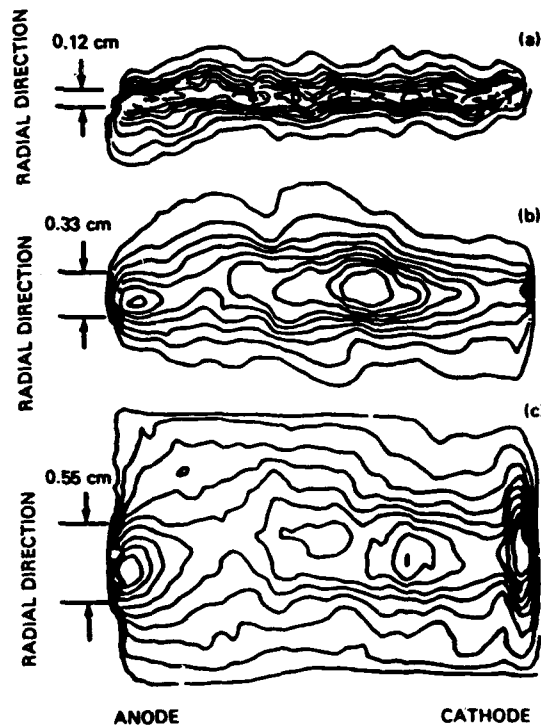


FIG. 11. Contour plots of time-integrated pinhole photographs in soft x rays exceeding 1 keV from aluminum pinches designed to stagnate at the same time during the pulse by changing the initial radius r_0 and the mass per unit length m/l but keeping $m r_0^2/l$ constant. Normalized initial wire array radii r_0 are: (a) 0.5; (b) 0.85; and (c) 1.0 (Blackjack 5, from Gersten, 1986).

erated in the neck of an x-pinch (Zakharov, 1987) produce radiation only in the plasma downstream (between neck and anode). While in z-pinchs most of the radiation is excited by thermal electrons, the converse seems to be true in vacuum sparks where most of the radiation output is apparently generated by nonthermal electrons.

Changes in the shape of the current pulse driving the implosion may influence pinch behavior. An example is the use of a plasma erosion opening switch (PEOS) to provide a faster rising current pulse. Figure 12 compares the x-ray emission from a neon gas puff without a PEOS with a similar puff using a PEOS, increasing the current rise time from 2×10^{13} A/s twofold to 4×10^{13} A/s (Stephanakis, 1986; Mehlman, 1986). With the PEOS the bright region is more uniform, even in the individual spectral lines. Moreover, the pinch radius is smaller and there are fewer flares. Other differences in pinch parameters include a smaller mass per unit length for the PEOS case demanded by the shorter time for acceleration, and by the smaller peak current. (1.2 MA vs 0.8 MA).

In shots where stagnation and peak current coincide, the bright spots seem to dominate the soft x-ray emission. In contrast, the bright spots are much less prevalent when stagnation occurs much after peak current. An extreme example is the lack of bright spots in the PEOS shots. There is no systematic study of this phenomenon, but the observation appears consistent with the suspected origin of the bright spots, viz., a sausage instability in the plasma column.

3. XUV radiation

Unlike soft x rays, XUV radiation (e.g., 50–800 eV) shows little structure in space or energy. Emission is typical-

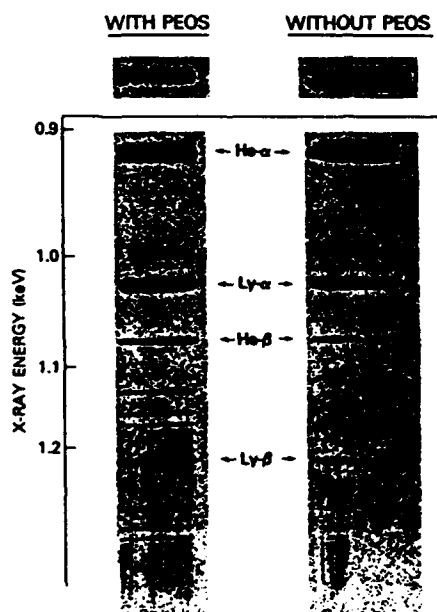


FIG. 12. X-ray pinhole photograph of a neon gas puff implosion without and with the PEOS (Gamble II, from Stephanakis, 1986). The top photograph is spectrally integrated; below these are the spectrally dispersed lines as indicated. Without the PEOS the pinch emits more energetic x rays close to the cathode. The PEOS improves the pinch uniformity.

ly from a relatively homogeneous column of plasma, without bright spots. The spectrum is rich in lines on top of a continuum. Figure 13(a) compares densitometer traces of a neon XUV spectrum with a krypton XUV spectrum, obtained from the center of the pinch with a grazing incidence spectrometer (many features in these spectra were identified by Bleach, 1983). The continuum consists of merged and broadened lines from different diffraction orders superposed on a background of free-bound continuum radiation. The spectrum becomes smoother with increasing atomic number Z , in part because of the larger number of overlapping lines (Riordan, 1981).

Although the details differ from shot to shot, the XUV emission is qualitatively the same for the different regions of the plasma. Even for different load materials on the same machine the XUV emission is quantitatively similar: for example, the XUV output per shot for krypton (~ 30 kJ) is about twice that of neon. Other data on XUV production show comparable features (see Table II).

Quantitative XUV spectra from grazing incidence spectrographs are hard to obtain and therefore rare. Part of the difficulty is the instrument efficiency: in addition, absolute calibration of x-ray film is relatively recent (Henke, 1984a/b; Eidmann, 1986b). However, if only the overall features of

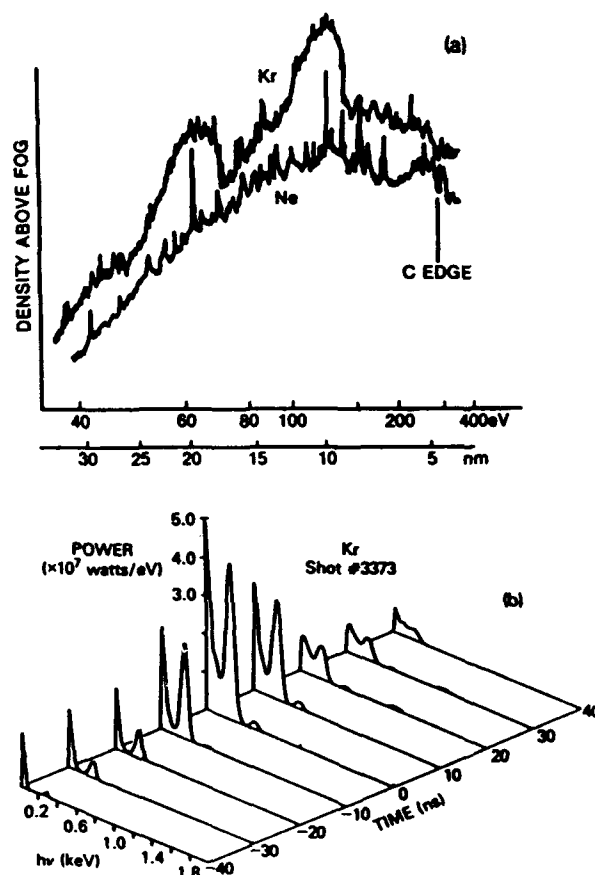


FIG. 13. (a) Densitometer trace of time-integrated XUV spectra at the center of the pinch taken with a grazing incidence spectrometer for neon and krypton (from Bleach, 1983). This reference identifies some of the spectral lines. (b) Time-resolved XUV spectrum from a krypton pinch unfolded from a filtered XRD array (from Bailey, 1986).

the energetics are desired, the spectrum can be determined by the unfolding of differentially filtered x-ray diodes. Figure 13(b) is a time-resolved spectrum of a krypton pinch (output ~ 0.3 kJ) obtained by this method (Bailey, 1983/6). Note that the radiation is dominated by the XUV below 500 eV, with little radiation above 1 keV.

C. The pinch plasma

With suitable theoretical models, the XUV and soft x-ray spectra can be used to infer average values for the density and temperature of the pinch plasma. These averages are not necessarily an accurate characterization of the plasma when the plasma changes rapidly in time and/or when the plasma is nonuniform, as is usually the case. Axial inhomogeneities, in particular the bright spots, can be diagnosed separately from the bulk plasma with axially resolved spectroscopy (Hares, 1985). The short lifetime of the bright spot can afford some time resolution. However, the spectra are always averaged over the line of sight, and their interpretation yields some radial average. Different spectral features may suggest average plasma parameters that are inconsistent: sometimes inconsistencies can be resolved by assuming that a central core is denser than the surrounding plasma (Gersten, 1986). The following highlights some typical determinations of the plasma parameters.

Laser interferometry followed by Abel inversion (Shiloh, 1979; Bailey, 1982b; Smith, 1985) can be used to measure the electron density as a function of radius during the implosion. For example, Fig. 14 shows that the electron density in the midplane of an argon pinch increases with time as the implosion proceeds, while the shell thickness decreases little. The electron line density N remains constant (at $\sim 6 \times 10^{17}$ electrons/cm) until the stagnation point, when N

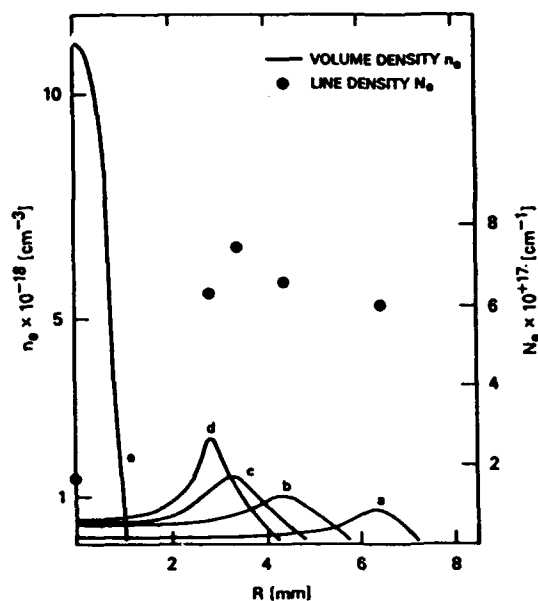


FIG. 14. Time evolution of the radial electron density profile and the electron line density between -100 ns and stagnation at 0 ns, in 20 -ns steps (taken on different shots). The line density remains constant during the pulse. At stagnation the line density decreases, indicating an axial outflow of material consistent with the sausage instability (from Shiloh, 1978a).

decreases to $\sim 2 \times 10^{17}$ /cm: the electron density itself peaks at $\sim 10^{19}$ electrons/cm³. The ion density is not determined by this diagnostic because the ionization fraction is unknown.

The plasma parameters reach their highest value when the material has assembled on axis at and after stagnation. For example, Fig. 15 (Clark, 1983) shows a temporally averaged but axially resolved argon pinch similar to Fig. 6. The radially resolved x-ray emission (lower panel) suggests two bright spots on the anode side of the pinch, and a broader structure on the cathode side. The bright spots, about 2 mm in length and 1 mm radius, appear less pronounced in the radially integrated x-ray emissivity, or in the size of the apparent pinch size in He- and H-like x rays (middle panels). Temperature and density inferred from these data are shown in the top panel: the bright spot is perhaps twice as dense as the adjacent plasma, while the temperature varies relatively little along the pinch. In this case it is reasonable to characterize the plasma by its averaged parameters.

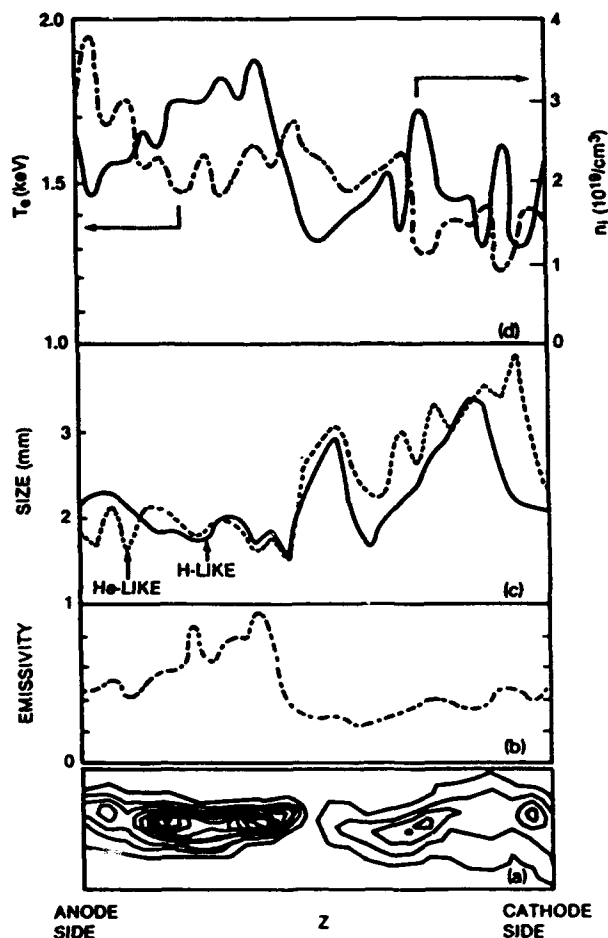


FIG. 15. (a) Contour plot of a pinhole photograph in soft x rays exceeding 1 keV for an argon pinch similar to Fig. 7. (b) Emissivity vs axial distance, (c) time-averaged pinch size for the heliumlike and hydrogenlike argon ions, and (d) axially resolved electron density and temperature from spectral data. The bright spots, at $1/5$ and $2/5$ of the pinch length close to the anode, show the highest density but unexceptional temperatures (after Clark, 1983, courtesy M. Gersten).

Quite often the bright spots differ substantially from their surroundings, and it is important to diagnose them properly in the light of their dominance in the K -line emissivity. The time-integrated K -line spectrum of a single bright spot in an argon pinch given by Hares (1985) allows a local determination of the bright spot parameters. This bright spot, defined by the strong emission of Ar XVII photons, is ~ 0.1 mm in diameter and 0.6 mm long, much smaller than the bright spot in Fig. 15. There may be a similar amount of material in the two bright spots, because the smaller size is compensated by a much higher electron density, $n_e \sim 3 \times 10^{21}/\text{cm}^3$; electron temperatures are comparable, $T_e \sim 1$ keV. Only 2.5% of the initial line density is in the bright spot: the remainder presumably forms a cooler plasma blanket out to some larger radius, or may have flowed out in the axial direction. A cold core surrounded by a hot plasma is found in exploding wire experiments (Aranchuk, 1986), but here the core radiates little.

The Doppler shift of some XUV spectral lines in a similar argon pinch indeed indicates axial plasma flow, with a flow velocity proportional to the ionic charge state (Stewart, 1987): the peak velocity, 2×10^7 cm/s, is comparable to but smaller than the radial velocity before stagnation [also measurable with Doppler broadening or splitting (Perez, 1980)]. Later in time the pinched plasma develops instabilities and bright spots that emit soft x rays.

Sometimes, but not always, the K lines from heliumlike argon are accompanied by radiation from the K shell of neonlike argon. This unlikely mixture of lines implies the presence of a hot region for the generation of the radiation from the stripped ions, and a cooler region for the generation of inner-shell $K\alpha$'s. In the experiment by Hares (1985) part of the $K\alpha$ radiation from neonlike argon comes from plasma ~ 0.3 mm closer to the anode than the bright spot where the He-like argon is located. Another source of $K\alpha$ lines could be radially outside the bright spot but at the same axial location, or at the bright spot location but at a different time. In addition to the plasma parameters Hares (1985) gives a partial energy balance for this bright spot, including an estimate for the energy in the nonthermal electron component. Similar considerations can be found in Jones (1985).

A systematic and comprehensive determination of the dominant physical processes in the bright spot remains to be performed. Challenging questions include: (i) Is the bright spot in energetic equilibrium? (ii) What is the role of axial mass loss? (iii) How important are runaway electrons? (iv) Why are bright spots comparable in size to the bulk of the pinch for low atomic number Z , but become progressively smaller as Z increases (e.g., Fig. 10)? These and other questions continue to make the radiating z-pinch a fascinating subject.

III. THEORETICAL MODELING

The only theoretical consideration commonly used in pinch experiments is the snowplow model, which predicts the time of implosion from the machine parameters, the load mass, and initial radius. In this model the imploding plasma is assumed to remain an infinitely thin cylindrically symmetric shell. The shell's position $r(t)$ is given by integrating in

time the acceleration of a shell element. The magnetic force is the current through this element $dI(t)$ multiplied by the magnetic field $B(r) = \mu_0 I(t)/2\pi r$ divided by the constant mass per unit length dm/l . The current $I(t)$ is determined by a circuit model for the generator coupled to the time-varying inductance of the z-pinch load. One way to avoid the divergence in pinch energy, velocity, and magnetic field at radius $r = 0$ is to cut off the computation when the plasma sheath reaches $\sim 1/10$ of the initial radius (e.g., Katzenstein, 1981). The factor $1/10$ is inspired by experimental data and accounts for the expansion of the shell in an approximate way. The snowplow model is successful in determining the implosion time and the kinetic energy at stagnation, but offers little about the radiation output (Gersten, 1986): obviously, better predictive modeling is mandatory.

Roughly speaking, the two theoretical approaches are (i) global estimates of pinch dynamics, stability, and radiation using simplified models as in the early days of plasma physics, and (ii) radiation production and transport computations with detailed ionization dynamic models characteristic of modern astrophysics. The marriage between these two approaches is progressing nicely, but it will be clear from what follows that much remains to be done.

The more sophisticated radiation models are needed to interpret the radiation spectrum in terms of the plasma density, temperature, presence of (nonthermal) electron beams, and other phenomena. This can be done reasonably well with stationary plasma models without hydrodynamic flows. The ultimate goal, to predict the pinch characteristics in detail from first principles, demands time-dependent hydrodynamic models including the radiation energetics.

When the pinch remains cylindrical, the radiation-hydrodynamic models do a very credible job in predicting the total radiation output, including spectral details (Clark, 1986). In contrast, existing models for the "bright spots" are inadequate for an accurate prediction, although some qualitative features can be explained (Vikhrev, 1982).

A typical z-pinch plasma (see Table IV) may be 10 times ionized at 300-eV electron temperature. The energy stored in a 10-times ionized (H-like) ion is ~ 4000 eV, comparable to the thermal energy of the 10 electrons. Moreover, the power into the plasma, compressional and joule heating, is of the same magnitude as the radiative power output. The ionization balance and the radiative power output for z-pinch plasmas are complicated quantities that oftentimes are inadequately approximated by simple models.

Radiation from z-pinchs may be heavily influenced by opacity effects, i.e., the multiple absorption and subsequent reemission or destruction of photons before they escape the plasma. Therefore, neither an optically thin (no radiation absorption) nor the blackbody model (equilibrium between the radiation and emitters) applies for the plasma's entire history. Then the proper treatment is to account for all relevant ionization states, the detailed configuration of the plasma, by solving the coupled set of appropriate atomic rate equations including the effects due to photons in conjunction with their transport. There is also the issue of the time scales for the various atomic processes (Kononov, 1977). These tend to be shorter than the hydrodynamic time scale ($\sim 1-$

10 ns), suggesting that the plasma should be in collisional-radiative equilibrium (CRE) for much of its history. Therefore, the CRE approximation is a reasonable choice over much of the plasma's evolution. Details of density and opacity effects on the radiation are shown below.

For typical z-pinch parameters the plasma is highly collisional, with a typical electron-electron collision time $\tau_{ee} \sim 0.1$ –1 ps. The collision time is much shorter than the time scale for thermodynamic quantities such as temperature and density, and the bulk of the electron energy distribution is close to a Maxwellian. The plasma transport quantities are moments of the distribution function as given by the standard Braginskii expressions (as corrected by Epperlein, 1986). Likewise, the ionic rates are integrals over cross sections and the Maxwellian electron distribution function that can be determined as functions of temperature.

Deviations from a Maxwellian distribution function are simple to compute, because in the first term expansion of the distribution function a difficult electron-electron collision term can be ignored for a high-Z plasma. This is because the cross section for large-angle Coulomb collisions for electrons with the $Z \sim 10 \times$ charged ions is Z^2 larger than the electron-electron collision cross section, and the collision frequency $\nu\sigma$ is $Z \times$ larger. Hence, most electron collisions are with the almost stationary ions. The distribution function tends to be isotropic and Maxwellian. The transport coefficients for such a Lorentz plasma are available analytically (Epperlein, 1984). However, the radiation from the plasma, connected to the electrons by inelastic collisions, tends to reduce the amount of energetic electrons. For a neon plasma some radiative rates decrease by 50% or more (Pereira, 1988).

The plasma models are not unique to the z-pinch: similar modeling is done wherever strongly radiating plasmas occur. Outstanding examples are laser fusion studies and x-ray laser development. Obviously, each application has its characteristic set of applicable approximations. For example, in laser plasmas the time scales are shorter than in z-pinchs, while spatial gradients and plasma densities are usually larger. Features that are specific to those circumstances, e.g., transport coefficients in high-density plasmas (Lee, 1984), or nonlocal heat conduction in large gradients (e.g., Holstein, 1986), may be relevant in limited domains of the z-pinch.

A. Kinematics

Gross properties of the pinch implosion, such as the implosion time or the kinetic energy at stagnation, can be computed reasonably well in a zero-dimensional approximation. The pinch is approximated as either a sheath or a uniform cylinder. Variables may be the plasma radius, and perhaps average plasma parameters such as temperature, density, and pressure. In this section we mention only the kinematic aspects: issues related to the radiation emission appear in Sec. III C.

1. Snowplow model

The radius $r = r(t)$ of a z-pinch of length l with total mass m carrying a current $I = I(t)$ uniformly distributed

over a cylindrical shell satisfies

$$\frac{m}{l} \frac{d^2 r}{dt^2} = - \frac{\mu_0 I^2}{2\pi(2r)}.$$

The acceleration can be considered as the Lorentz force on a current element $d\theta$, say at azimuthal angle $\theta = 0$, by all other current elements. Only the opposite current element, at $\theta = \pi$ and a distance of $2r$, gives a force through the center. The force from all other elements is not toward the center, but their off-center component vanishes by symmetry; the remaining central force shows an effective distance $2r$ (see also Waisman, 1979).

Typically the current has a maximum I_m , $I = I_m f(\tau)$, where $\tau = t/t_m$, and t_m is a characteristic time. The initial pinch radius is r_m , and $r = r_m R(\tau)$. Then

$$\frac{d^2 R}{d\tau^2} = - \left(\frac{\mu_0 I_m^2 t_m^2}{2\pi m / l r_m^2} \right) \frac{f^2}{R},$$

which contains a single parameter (in parentheses) that can be set to unity, thereby defining the characteristic time t_m . Once $f(\tau)$ is given R can be found, seldom analytically but always numerically. The radius $R(t)$ starts at $R = 1$. $R(\tau_0) = 0$ defines the implosion time τ_0 , which is finite. Time τ_0 can be bounded from above by keeping $R = 1$ in the magnetic force term. Particularly when the implosion velocity and the current are initially zero this upper bound is a good estimate for the implosion time, because in this case the wires spend most of the implosion time getting up to speed.

During the rise time of the pulse the current is often roughly proportional with time, $f(\tau) = \tau$. Then the implosion radius $R(\tau)$ behaves as in Fig. 16 (solid line, left scale): the dashed lines include the second and third term in the analytical approximation $R = 1 - \tau^4/12 - \tau^8/672 + \dots$. Clearly, the approximate radius, and therefore the implosion time, are nearly exact. Unfortunately, the energy per unit length $W/l = (m r_m^2 / 2l) \dot{R}^2$, on the right scale, is not given

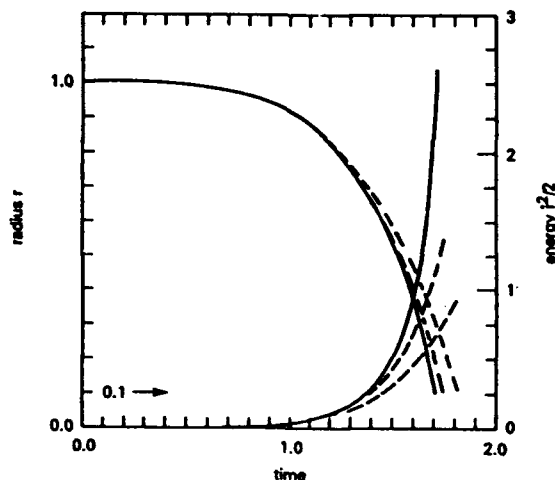


FIG. 16. Pinch radius (left scale) and kinetic energy (right scale) for a snowplow implosion with linear current rise. The solid line is the exact solution, the dashed lines are the two approximations.

accurately by the approximate formulas because much of the pinch energy is acquired toward the end of the implosion. When the current is not given *a priori* but determined with a circuit model it may be advantageous to use circuit parameters in defining the implosion time scale (Katzenstein, 1981). Analytical solutions of the coupled equations are then no longer possible, even though numerical solution is straightforward. However, the moment of inertia per unit length mr_m^2/l always appears in the normalizations, and when this quantity is kept constant the implosions should pick up the energy per unit length, irrespective of the details in the electrical circuit.

The pinch is a time-dependent circuit element with inductance per unit length $L(r,t)/l$. The pinch force per unit length F/l is also the derivative of the inductive energy, $F/l = (\partial L/\partial r)(I^2/2l)$. Integrating over time at constant current leads to an upper bound on the energy transfer, $\Delta L I_m^2/2$, where ΔL is the change in inductance between the initial and final pinch radius. This relation reflects that the power input, $I \times V = I \times dL/dt$, consists of a power with voltage $\partial L/\partial t I$, expressing energy transfer to the pinch, and an inductive power with voltage $L \partial I/\partial t$ corresponding to the increase of magnetic energy in the diode.

The final pinch radius in the snowplow model is zero but here the model obviously breaks down. Instead, one often assumes that the final pinch radius is 1/10 of the initial radius. The inductance change is then on the order of 4.6 nH/cm, and the energy bound for 1-MA peak current is 2.3 kJ/cm. Besides the kinetic energy in the implosion, the pinch acquires energy from joule heating, a term RI in the circuit. Typically $R \ll \partial L/\partial t$.

Snowplow models are not only useful in defining the approximate mass per unit length needed for a good implosion on a given machine, but also for bringing out the scaling with parameters as stated above. A sobering note is the experimental reality (Gersten, 1986): the radiation output depends less on the kinetic energy of implosion than on the average density at stagnation. A simple formula for the stagnation density in a *z*-pinch does not exist. A value for the average density can be obtained from the radially resolved density profile computed with a hydrodynamics code, but once such detailed data are available it is silly to revert to the simpler models.

2. Kinematic stability

In practice the individual wires in a multiple wire implosion are never identical or mounted symmetrically, and this asymmetry could spoil the implosion when the perturbation is unstable. Felber (1981) finds that perturbations in radial displacement are stable for six or more identical wires, with growth rate $\omega < 0$ (or perhaps marginally stable when $\omega = 0$). Perturbations in the axial direction are unstable, but this simply means that the wire parts closer to the center implode faster than those parts of the wire farther away from the center. Introducing an additional current-sharing wire in the center between the wires tends to destabilize the implosion.

The growth rate of perturbations tangential to the (symmetric) reference position is $i\omega$. Consequently, tangential

perturbations are marginally stable, or unstable. Fortunately, tangential displacements of the wires do not affect the magnetic force on the wires, and therefore the implosion toward the center is not affected.

Multiple wires are a discrete version of an infinitely thin current sheath; the instability of a current sheath to sausage and kink modes is familiar from hydromagnetic considerations (e.g., Bateman, 1978). The multiple-wire analog of these instabilities becomes important only when the inter-wire forces are large, i.e., when the wires are close together toward the end of the run-in.

While typical wires remain thin compared to the diode size, the wires expand and contract during the pulse (Bloomberg, 1980). Initially, the resistivity is high enough for the current to penetrate, whence the wire expands. Subsequent heating and ionization of the wire material reduces the resistivity and leads to a skin current: the wire contracts. The interaction between the skin current of one wire with the magnetic field from the other wires may describe the blow-off and separate implosion of material observed with heavy wires (Clark, 1982a; Ivanenkov, 1986).

Each wire can pinch by itself while it is accelerating toward the center. Because the instability of a single wire is fast, each individual wire may have pinched before the wires meet on axis, resulting in an inhomogeneous plasma column. Consequently, wire implosions are often less uniform than gas puff implosions.

Blow-off from wires and instability of a single wire both depend on the magnetic field in the wire's immediate neighborhood. In contrast to the magnetic field around an annular conductor, $B_\theta(r) = \mu_0 I(r)/2\pi r$, the field around multiple wires is far from simple, $B_\theta(r, \theta)$ depending strongly on radius and on θ . For symmetric wires the magnetic field is simply a sum over the field from each individual wire if the current is stationary, and the current density in each wire is constant. The opposite case, a rising current in infinitely conducting wires, is found by Waisman (1979). The most interesting case, where the current penetrates the wire during the current rise, remains to be treated.

B. Plasma models

Plasma conditions in *z*-pinches are often assumed to vary with the radial coordinate in a prescribed way, with one of these a constant. Temperature, density, and radiation output are then, theoretically, functions of time only. This section discusses some of the available models along these lines.

1. Stationary pinch equilibrium

The basic concept is the Bennett pinch, wherein the radial gradient of the (scalar) pressure compensates the Lorentz force $(\nabla p + j \times B)_r = 0$; the Bennett pinch is stationary. Integrating this relation,

$$-\frac{\partial p}{\partial r} = \frac{1}{2\mu_0 r^2} \frac{\partial r^2 B^2}{\partial r},$$

over radius gives an exact relation between the current I , the average electron (ion) temperature $\bar{T}_{e(i)}$, and the number of electrons (ions) per unit length $N_{e(i)}$,

$$\frac{\mu_0 I^2}{4\pi} = 2\pi \int dr r [n_e k(T_e + \bar{Z} T_i)]$$

$$\sim N_e k \bar{T}_e \times \frac{\int dr r n_e k T_e}{N_e k \bar{T}_e},$$

when ignoring the ion pressure $n_i k \bar{T}_i$. Here $n_{e(i)}$ the electron (ion) density, and the line density is $N_e = 2\pi \int dr r n_e$. The average electron temperature is $k \bar{T}_e = \int dr r n_e k T_e / \int dr r n_e$, and $\bar{Z} = \bar{Z}(\bar{T}_e)$ is the number of electrons per ion. The plasma is quasineutral, $N_e = \bar{Z} N_i$. Numerically, $(N_e / 10^{18} \text{cm}^{-1}) \times (\bar{T}_e / \text{keV}) \sim 6 \times (I / \text{MA})^2$. The relation between electron and ion temperature is not always clear, and usually not important. If the electron and ion temperatures are on the same order, the ion pressure is small compared to the electron pressure because typically $\bar{Z} \sim 10$, much larger than unity. Collisions due to ions are unimportant for the ionization equilibrium because the pinch plasma has many more electrons than ions, and moreover the ion velocity vanishes compared to the electron velocity.

An isolated radiating pinch is stationary only on a time scale which is short compared to the cooling down time, i.e., the pinch energy divided by the radiative power. However, the pinch can be rigorously stationary when the energy loss is compensated by energy input from an external source. Power equilibrium was first studied for hydrogen pinches using optically thin bremsstrahlung as the sole radiation loss and joule heating with Spitzer resistivity as the sole energy input. The resulting equilibrium current is known as the Pease-Braginskii current I_{PB} .

For a homogeneous plasma of radius r and average charge state \bar{Z} with a constant current density and total current I , the power gain per unit length is $P/l = I^2 \bar{Z} \ln \Lambda / \sigma_0 (T/eV)^{3/2} \pi r^2$; here the Spitzer conductivity is $\sigma_0 (T/eV)^{3/2} / \bar{Z} \ln \Lambda$, with $\sigma_0 = 100 \Omega^{-1} \text{cm}^{-1}$ and $\ln \Lambda \sim 10$ the Coulomb logarithm. The power density in bremsstrahlung (free-free radiation) is $P_{ff} (\text{W/cm}^3) = X_{ff} n_e n_i$, where $X_{ff} = C_{ff} \bar{Z}^2 (T/eV)^{1/2}$, electron and ion densities in cm^{-3} , and $C = 1.4 \times 10^{-32} \text{W cm}^3$ (e.g., Allen, 1973; Book, 1983). The radiative power/length is $\pi r^2 P_{ff}$.

Balancing these powers in Bennett equilibrium gives

$$I_{PB}^H \sim 1.4 \text{ MA},$$

independent of atomic number, pinch radius, or temperature (except through the Bennett relation). When the electron density $n_e(r)$ and current density $j(r)$ are no longer constant, a correction factor of order unity comes in:

$$I_{PB}^2 \sim (1.4 \text{ MA})^2 \left[\left(\frac{\int dr r j^2}{\int dr r n^2} \right)^{1/2} \frac{\int dr r n}{\int dr r j} \right]$$

(compare Shearer, 1976). In a partly ionized plasma the bremsstrahlung is much weaker than the (free-bound and bound-bound) atomic radiation. The Pease-Braginskii current for a pinch dominated by atomic radiation is therefore much smaller than in a hydrogen pinch, or a hydrogenlike pinch at sufficiently high temperature. In addition, the $T^{1/2}$ temperature dependence of bremsstrahlung no longer combines with the $T^{3/2}$ Spitzer conductivity to give a unique current. For an iron plasma Fig. 17 compares the power coefficients $X = P/n_e n_i$ for bremsstrahlung and total radi-

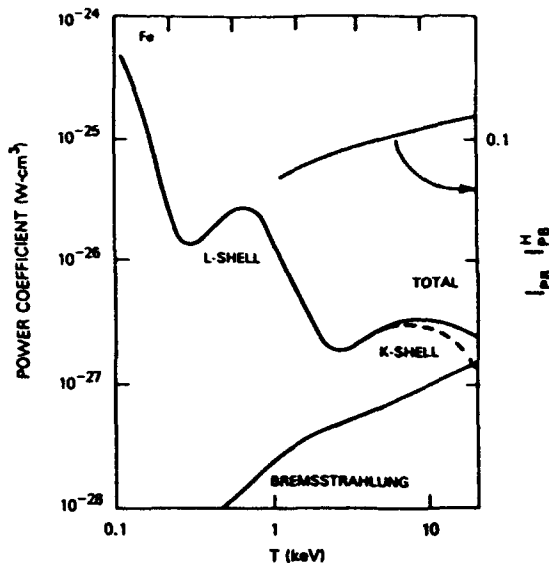


FIG. 17. Bremsstrahlung radiation vs temperature (lower line) compared with atomic radiation (free-bound and bound-bound) for iron in the optically thin limit. Atomic radiation dominates in the temperature region of interest (after Jacobs, 1977). The Pease-Braginskii current I_{PB} for an iron pinch is a weak function of the temperature around 0.1 times the Pease-Braginskii current I_{PB}^H for hydrogen (right scale).

ation as a function of temperature. At 500 eV the atomic radiation is $100 \times$ the bremsstrahlung value; at much higher temperatures > 10 keV bremsstrahlung again becomes appreciable. Radiation emission estimates for many high Z but tenuous plasmas are given by Post (1977) and Jensen (1977).

For comparisons with the Pease-Braginskii current it is convenient to express the total radiation (bound-bound, bound-free, and free-free) by a temperature-dependent function $K(\bar{T})$, which for an optically thin plasma is $K(\bar{T}) = (P_{bb} + P_{bf} + P_{ff}) / P_{ff}$ (Vikhrev, 1977, 1983). Then $I_{PB} = I_{PB}^H / [Z(\bar{T}) K(\bar{T})]^{1/2}$. As an example, the upper line in Fig. 17 is I_{PB} / I_{PB}^H for iron. Obviously, for a radiating pinch the Pease-Braginskii current is much less than 1.4 MA, typically ~ 100 kA.

The Pease-Braginskii current I_{PB} says nothing about the pinch radius because joule heating and optically thin radiation vary with plasma density in the same way. Currents exceeding I_{PB} would not allow power balance and a stationary pinch would not be possible. Instead, the pinch would suffer radiative collapse. The collapse speed depends on the effectiveness of radiative cooling (e.g., Shearer, 1976). In equilibrium the radial profile can be determined from a balance between the heat conductivity, joule heating, and radiative loss [Bobrova, 1987; Scudder, 1983 (for a gas-embedded hydrogen pinch)].

Experimentally the pinches have no problem carrying all the current offered to them by the pulse power, which can exceed $100 \times I_{PB}$. For dense pinches the current could mainly be carried by a small fraction of the mass outside a cool core, i.e., the mass and current density profile gives a large correction factor (as claimed for an exploding wire, Aranchuk, 1986). For less dense pinches it is more likely that

radiative cooling is too slow for the collapse to occur during the pinch lifetime. A contributing factor may be that radiative cooling is less than expected because the plasma is not in ionization equilibrium (Faenov, 1985). Radiative collapse may be modified by other effects also, e.g., the Bennett pinch condition changes due to electrostatic forces from a net space charge in the pinch (Meierovich, 1982/4).

Without violating the Bennett condition or invoking nonstationary effects, the bright spots (or micropinches) are treated by Vikhrev (1983) using plasma parameters inspired by vacuum sparks. His bright spot model includes the effect of opacity on the radiation, and the contribution of some anomalous resistivity model on the ohmic heating. These modifications introduce a dependence of the Pease-Braginskii current on pinch radius; power equilibrium then defines an equilibrium pinch radius for any current. For an iron pinch at 150 kA the equilibrium radius has a minimum of radius $\sim 1 \mu\text{m}$ at an ion line density $N_i \sim 5 \times 10^{15}/\text{cm}$, corresponding to a Bennett temperature $T = 1 \text{ keV}$. Micropinches form only in a limited range of line densities: when the initial line density is outside this range the micropinches may form when the line density enters into the contraction regime. Theoretical work emphasizing the final state of the plasma after radiation collapse is discussed extensively by Meierovich (1982/4/6).

Micropinches are frequently quoted in vacuum sparks and z-pinch experiments in the Soviet Union, but perhaps due to different pinch parameters (Gol'ts, 1986) the z-pinch bright spots are not commonly seen in this light in the US. However, it seems likely that bright spots in z-pinches could be described by Vikhrev's radiative contraction model even though the initial line density may be too large: plasma flowing axially out of the neck of an unstable sausage mode reduces the initial line density.

Another basic model is heating under pressure balance, including joule heating but without radiation loss. For a hydrogen pinch with Spitzer resistivity $\eta_H/T^{3/2}$ this condition determines a specific rise in the current versus time $I = I(t)$ (Haines, 1960): for a pinch with atomic number $Z > 1$ the current rise would differ somewhat because the degree of

ionization $Z(T)$ and the resistivity constant $\eta_Z = Z(T)\eta_H$ increase with temperature. However, for a radiative pinch such a result is less relevant because radiation losses cannot be ignored.

How close are real z-pinches to these theoretical constructs? The Bennett relation is generally believed to be valid, but the experiments with the best spectroscopic measurements generally do not contain data on the electrical part and vice versa. Table III gathers data from some interesting experiments. The Bennett current I_B as computed from the measured density, radius, and temperature is always smaller than the peak current, but they agree to within a factor ~ 3 . The discrepancy is probably due to measurement errors, and to differences between reality and the models. In particular, density and temperature in the pinches vary with radius. Differences remain even when nonuniformity is taken into account by splitting the pinch into a homogeneous core region surrounded by a homogeneous corona, as done by Gersten (1986). None of the pinches satisfy the Pease-Braginskii condition, except the micropinch (Faenov, 1985) with much higher density than the other pinches. For this pinch the parameters in the experiment appear to agree with theory. The bright spot (Hares, 1985) needs additional heating from an electron beam to explain its parameters. In one model (Jones, 1985) this beam consists of runaway electrons.

2. Simple pinch dynamics

Besides being in stationary equilibrium the z-pinch can support self-similar oscillations. In these somewhat artificial but exact solutions to the equations of ideal MHD, the plasma density, temperature, and magnetic field keep their radial dependence, and all time variation is through the plasma radius. When total current and plasma pressure are not in equilibrium initially the pinch radius oscillates in time (e.g., Felber, 1982), but when bremsstrahlung losses are included the oscillations damp until the pinch degenerates into radiative collapse (Meierovich, 1985). Self-similar dynamics of z-pinches are discussed extensively by Liberman (1986).

TABLE III. Measured data for some well-diagnosed z-pinches. Density and temperature estimates are typically uncertain to a factor ~ 2 . Included are the nominal and measured values for one case from Gersten (1986) and the measurements for another. The data from Hares (1985) apply to the bright spot only. Below the line are the same data for a longer pulse micropinch plasma (Faenov, 1985). The Pease-Braginskii current I_{PB} is estimated from the optically thin, low-density plasma emissivity (Jensen, 1977; Post, 1977).

Reference	Atom Z	n_i $10^{18}/\text{cm}^3$	Temperature (keV)	Diameter (mm)	\bar{Z}	N_i $10^{18}/\text{cm}$	I_{max} (MA)	I_B (MA)	I_{PB}
Mehlman (1986)	10	500	0.15	0.9	8.7	1.0	1.4	0.5	0.06
Gersten (1986) (No. 2)	13 (nom)	40	0.65/0.3 0.43	1.2/3.0	11	0.45/2.4 17	3.8 3.8	1.5 4.0	0.07
Gersten (1986) (No. 4)	13	7	1.5/0.75	1.3/3.3	11	0.1/0.5	3.9	1.1	0.08
Hares (1985)	18	3000	beam	0.1	8(?)	1.0	0.25		
Faenov (1985)	13	5000	0.3	0.03	11	0.04	0.15	0.16	0.1

Self-similar oscillations are purely one-dimensional nonequilibrium states representing an axially uniform plasma that contracts and expands in the radial direction only. However, the equilibrium state which supports the oscillations is itself unstable to axial perturbations. In the early days of thermonuclear fusion research with z-pinchs these instabilities destroyed plasma confinement, and much effort has gone into determining pinch stability (Bateman, 1978). For radiative pinches, however, the axial plasma flow due to the $m = 0$ sausage mode seems related to the bright spots, and the sausage model's growth rate becomes interesting: nevertheless, most results in this area are for idealized pinches, certainly without radiation effects.

For an idealized pinch with infinite conductivity the current density cannot penetrate the plasma, and remains in an infinitely thin sheath on the outside. For this case the well-known growth rate is $\gamma = C_A/r_0\Gamma$, where $C_A = (B^2/\mu_0\rho)^{1/2}$ is the Alfvén speed, r_0 is the pinch radius, and the normalized growth rate $\Gamma = \Gamma(k) \sim O(1)$ is a function of the perturbation wave number $k = r_0\lambda$. In a resistive pinch, however, the current diffuses into the plasma and forms a current sheath with finite thickness (Hussey, 1981). Differences between planar and cylindrical geometry are minor when the current sheath thickness is small compared to the pinch radius (Roderick, 1986). Hwang (1987) treats instabilities in the sheath including the effects of acceleration.

With increasing thickness of the current density sheath the normalized growth rate for the sausage mode decreases (Pereira, 1984), and when the current density is constant throughout the pinch the sausage model is neutrally stable. The kink ($m = 1$) perturbation remains unstable. This instability is of minor interest for radiating pinches, largely because it does not change the mass per unit length in the pinch.

In nonideal MHD the growth rate may be modified by other effects, such as resistive diffusion of the current sheath while the instability is growing, a finite Larmor radius of the ions (Coppins, 1984a, 1984b), and by radiation losses. No definite conclusion is known, although it seems reasonable that radiation losses would increase the sausage growth rate by counteracting an increase in the plasma temperature.

C. Radiation

The theoretical considerations above are valuable for their qualitative insight and guidance into the relevant areas of z-pinch physics. Quantitative prediction of z-pinch behavior, however, is much more demanding, and still in progress. One-dimensional pinch models including hydrodynamics and radiation are in reasonably good shape but of limited use. Remember that the most interesting radiation comes from the bright spot, which is at least two-dimensional. Worse, if electron beams are present the bright spot plasma violates the thermodynamic equilibrium assumptions inherent in the hydrodynamic approximation.

Comprehensive modeling of z-pinch hydrodynamics involves a heavy dose of atomic physics and radiation transport, including related effects such as determination of line profiles. Good introductions are Mihalas (1978) or Cannon

(1985). Sobelman (1981) is a relevant research monograph on collisions in plasmas. Recent reviews by DeMichelis (1981, 1984) emphasize radiation from tokamak plasmas but include many references to review articles on specific topics of interest.

The z-pinch plasmas are sufficiently similar to some laser-produced plasmas and x-ray laser media so that many physics issues are the same for both. Much recent literature on the modeling of laser-produced plasma radiation (e.g., Duston, 1980; Apruseze, 1981; Duston, 1983a/b; Duston, 1985b) or x-ray lasers (e.g., Hagelstein, 1983; Apruseze, 1985a; Cochran, 1986; Davis, 1987, 1988) is highly relevant to z-pinchs.

1. Fundamentals

In the corona model, describing a low density, optically thin plasma, the ionization fractions f_a are functions of temperature only. This is because each $f_a = n_a/n_i$ (n_a is the density of ions in a specific ionization state a , n_i is the original ion density) is given by a balance between collisional excitation (including ionization) and radiative decay (including radiative recombination), whose rates depend only on temperature. Consequently, the power lost by the plasma in radiation is simply $P = X(T)n_e n_i$ times the plasma volume, where the power coefficient $X(T)$ depends only on temperature. This is no longer true with increasing density, when the decay rate of the excited states must include collisional processes such as collisional recombination. Ultimately, a reasonably complete model for the radiation should be coupled to the implosion hydrodynamics and the instability development in a self-consistent manner. This section discusses the radiation aspects of z-pinchs in some detail. Radiative processes are particularly relevant to radiating z-pinchs. Typically, the plasma density in a z-pinch (see Table IV) is high enough to modify the ionization fractions from their low density limit. Moreover, the plasma thickness is sufficiently large to make opacity important for the K-shell resonance lines, and certainly for many L-shell lines.

As an example, Fig. 18 shows the power coefficient X_i for line emission from a homogeneous aluminum plasma (Duston, 1981). At $n_i \ll 10^{15}/\text{cm}^3$ the power coefficient peaks around 80 eV (for L-shell radiation); K-shell radiation is maximum around the 1/10 lower second peak around 900 eV. For a typical z-pinch density, $n_i = 10^{19}/\text{cm}^3$, the L-shell peak is comparable to the K-shell peak, which at this density barely changes. At higher densities $> 10^{21}/\text{cm}^3$ relevant to laser-produced plasmas the power coefficient decreases even more, eventually approaching local thermodynamic equilibrium (LTE). Below ~ 0.8 keV the power coefficient X_i varies approximately as $\sim T^{-4}$, reminiscent of a blackbody. However, for a typical z-pinch plasma at $n_i \sim 10^{19}/\text{cm}^3$ the power coefficient X_i estimated in the LTE approximation is unreliable, $30\times$ too large at 0.2 keV and $10\times$ too low at 1.0 keV. Argon shows a similar decrease in power coefficient with increasing density (Duston, 1982).

For a homogeneous plasma cylinder of 0.05-mm radius and 10^{19} ions/cm³, see Fig. 19, the added inclusion of opacity gives a threefold reduction in power density $P_i \bar{Z}(T_e) n_i^2$

TABLE IV. Plasma parameters for a canonical pinch, and estimates for the microscopic length and time scales in this plasma. Parameters for other z-pinches may differ an order of magnitude from the values given, and the ordering of length and time scales may reverse.

	Symbol	Equation (MKS)	Typical value
Mass/length	μ		30 $\mu\text{g}/\text{cm}$
Radius	r		1 mm
Current	I		1 MA
Pulse length	τ_p		20 ns
Ions/length*	N_i	$\mu \times 2N_A$	$10^{18}/\text{cm}$
Ionic charge	Z		10
Charge/length		$eN_e = Z_e N_i$	1.6 C/cm
Electron temperature	T_e		300 eV
Ion temperature	T_i		300 eV(?)
Electron density	n_e		$3 \times 10^{20}/\text{cm}^3$
Ion density	n_i		$3 \times 10^{19}/\text{cm}^3$
Magnetic field (edge)	B	$\mu_0 I / 2\pi r$	200 T
Plasma frequency	ω_{pe}	$(e^2 n_e / \epsilon_0 m)^{1/2}$	$10^{15}/\text{s}$
Gyrofrequency	ω_{ce}	eB / m	$3 \times 10^{14}/\text{s}$
e-e collision time	τ_{ee}		0.5 ps
e-i collision time	τ_{ei}	τ_{ee} / Z	0.05 ps
e-i energy exchange	τ_e	$(M/m)\tau_{ei}$	2 ns
Collisionality		$\omega_{pe} \tau_{ee}$	500
Collisionality (edge)	Ω	$\omega_{ce} \tau_{ei}$	20
Thermal velocity	v_{Te}	$(T_e/m)^{1/2}$	$7 \times 10^8 \text{ cm/s}$
Drift velocity	v_D	I / eN_e	10^8 cm/s

* Avogadro's number $N_A = 6 \times 10^{23}$ electrons/g.

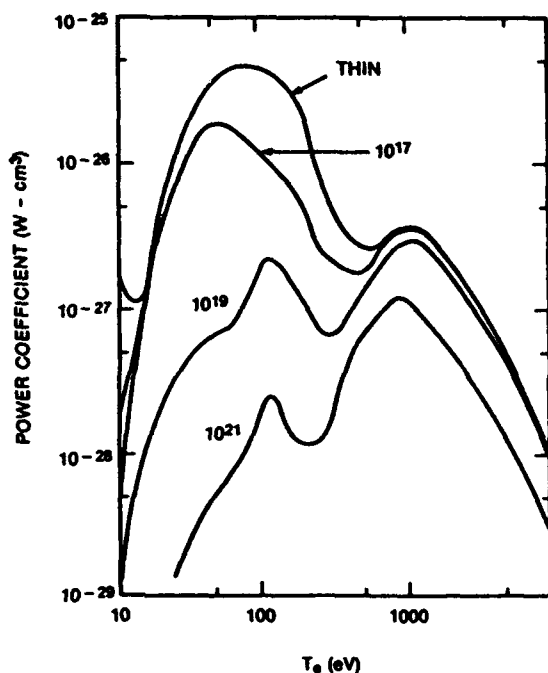


FIG. 18. Line emission power coefficient for aluminum (in the optically thin limit), showing the effect of electron density. Collisional deexcitation reduces the power coefficient around the L-shell peak by an order of magnitude (from Duston, 1981).

at 0.1 keV, but little effect at 1 keV (in contrast to the previous figure this figure includes, besides the lines, the contribution from the continuum). Increasing the cylinder radius to 0.5 mm does not further reduce the power density (the power per unit length would increase 100 \times). The K-line emission power, at ~ 1 keV, is unaffected by opacity, al-

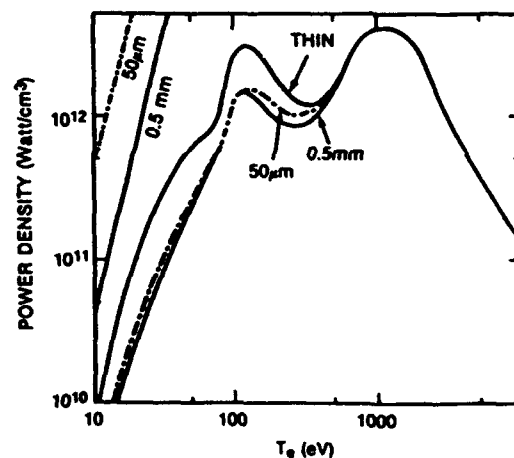


FIG. 19. Radiative power density for a plasma cylinder with 10^{19} aluminum ions/ cm^3 in the optically thin limit, and with inclusion of opacity for 50 μm and 0.5 mm radius. Opacity gives a factor 3 reduction in emission at ~ 200 eV. Blackbody emission would be much stronger, according to the straight lines at left (from Duston, 1981).

though the linewidth increases. The power emitted by this partially transparent plasma is always much less than the equivalent power density for a blackbody, i.e., the power from the blackbody's cylindrical surface divided by the volume $2\sigma_{SB} T_e^4/r$ ($\sigma_{SB} = 10^5 \text{ W/cm}^2 \text{ eV}^4$ is the Stefan-Boltzmann constant). Below the *L*-shell peak a blackbody radiates only one or two orders of magnitude more strongly: at higher temperature the discrepancy is even larger. Opacity effects are invoked to explain the azimuthal dependence of the radiation from a bright spot: the radiation fluence perpendicular to the pinch is perhaps four times larger than the radiation along the pinch, because in the perpendicular direction the photons encounter less plasma (Stormberg, 1987).

Other quantities of interest show corresponding changes from their tenuous and optically thin values, notably the line ratios used as diagnostics of the plasma parameters. Any temperature diagnostic that depends on ionic fractions, such as the $\text{He}\alpha$ to $\text{Ly}\alpha$ line ratio, tends to be affected by density effects. For z-pinch parameters a good temperature diagnostic is provided by the dielectronic satellites on the low-energy side of the strong *K* lines (as in Fig. 3). How this ratio varies for the most prominent satellite line of $\text{Ly}\alpha$ for an aluminum plasma is shown in Fig. 20 (Apruzese, 1986); the density has little influence over this line ratio at typical z-pinch densities. How the plasma opacity affects this diagnostic remains to be studied.

Insight into opacity effects can be used to advantage, as demonstrated by Fig. 21, the *K*-shell power/cm emitted by a uniform plasma cylinder of varying composition but prescribed temperature, radius, and density (Apruzese, 1986). The plasma constituents, neon and sodium, vary such that the total ion density is constant. The neon and sodium *K*-line photons differ in energy (except for a near-coincidence of the He-line $\text{Ne } 1-2$ with He-like $\text{Na } 1-4$ photons essential to a photopumped x-ray laser). Therefore, the neon *K*-line opacity decreases as the sodium fraction increases, and each neon photon escapes more easily. Although the number of photons decreases with the number of neon atoms, the decrease is less than proportional due to the opacity effect. On

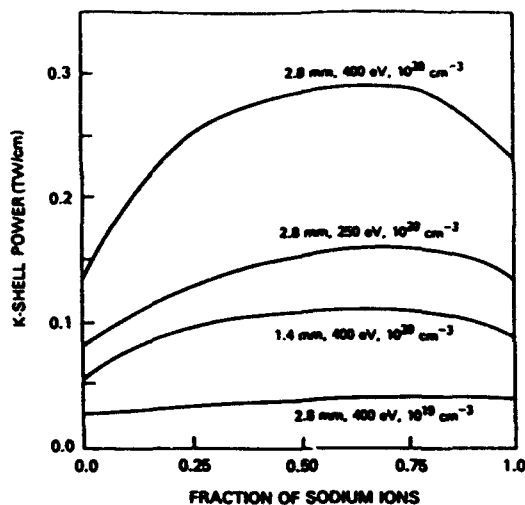


FIG. 21. *K*-shell radiation power from a sodium-neon plasma vs fractional abundance of sodium for 250- and 400-eV temperature, and for two radii, 1.4 and 2.8 mm. Reduction of opacity increases the radiative power (from Apruzese, 1985b).

balance, the power/cm is maximum for an intermediate plasma composition of around 60% sodium. This result suggests that the radiation output of a z-pinch could be increased by using a mixture of similar elements in order to counter the photon trapping effects from opacity. This assumes that the plasma mixture in an actual pinch reaches the same conditions irrespective of composition.

As an example, a calculation (Duston, 1985a) on mixtures such as He/Kr, with disparate atomic numbers, shows that the high-*Z* component dominates the radiation yield already when only 10% of the mass is in krypton. The theoretical suggestions are only partly corroborated in experiment (Bailey, 1983/6); a He/Kr pinch with 25% mass in krypton emits less but harder radiation than a pure krypton pinch. Moreover, in the implosion the helium outruns the krypton and stagnates earlier, as explained by Barak (1982).

Fairly rough radiation models can give reasonable results for gross quantities like yields, but the more accurate

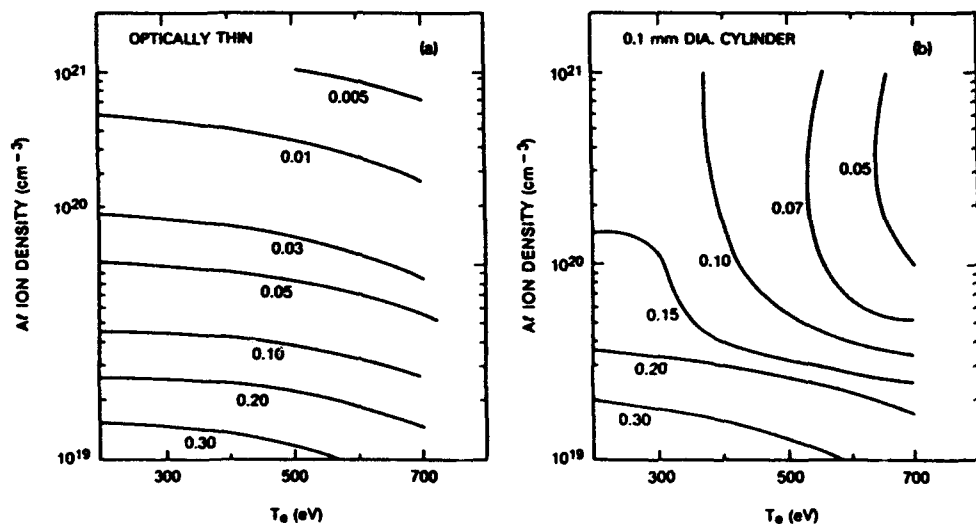


FIG. 20. Contour plots of the intensity ratio between two lines arising from the same ionization state, the $1s^2 \ ^1S_0$ to $1s2p \ ^3P_1$ line, and the $1s^2 \ ^1S_0$ to $1s2p \ ^1P_1$ line in Al XIII. (a) Optically thin plasma; the line ratio is largely independent of temperature. (b) 0.1-mm-diam cylinder with opacity included; the opacity introduces a strong temperature dependence (from Apruzese, 1986).

models are indispensable when comparing the details of computed spectra with those in experiments. Sometimes the theoretical model must be extended to include radial gradients. A temperature measurement using two line ratios and the continuum temperature produced three somewhat different values when assuming the plasma is a homogeneous cylinder; satisfactory matching of the experimental with a computed spectrum is obtained when the plasma consists of a central hot core surrounded by a colder tenuous corona (Gersten, 1986).

2. One-dimensional radiation hydrodynamics

Many of the important effects mentioned above have been combined into models for the dynamic behavior of z-pinch (Maxon, 1984; Spielman, 1984; Clark, 1986). All are based on the standard hydrodynamic equations; major differences between the models exist in the radiation physics, which is continuously being refined by the various groups.

The one-dimensional computations give satisfactory results when the z-pinch implodes uniformly along the axis. This happens when stagnation is late in the current pulse, and current-driven instabilities have no time to grow into bright spots. An example is a recent computation by Clark (1986). In this work the initial state is a 1-cm-long neon gas shell with uniform density 5×10^{-6} g/cm³ between an inner radius of 0.55 cm and an outer radius of 1.95 cm. Instead of imploding the shell with magnetic pressure the gas has an initial velocity around 3×10^7 cm/s. This average velocity might be reached late in the current pulse, although in reality the density will be highly nonuniform.

Figure 22 shows the time history of the plasma kinetic energy and the radiative energy for a neon pinch. Plasma

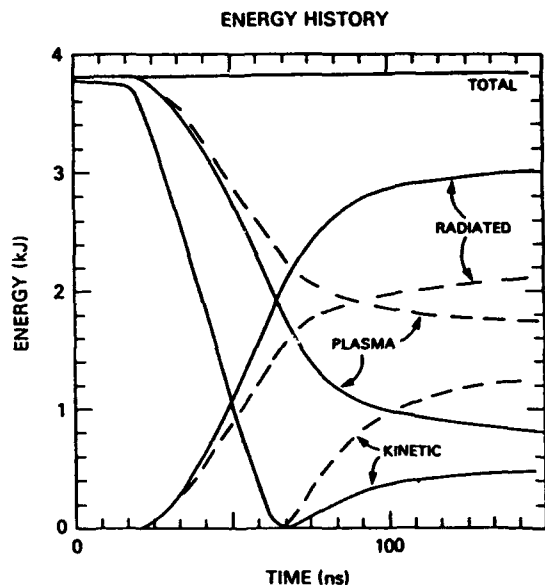


FIG. 22. Temporal development of the kinetic and radiative energy for a 1-cm-long neon shell stagnating on axis according to two different radiation models. The solid lines are from Clark (1986) using a simple model with 27 neon lines, the dashed lines are for a model with over 100 lines (from Clark, 1988). At 70 ns, stagnation, the pinch energy is completely transformed into ionization and thermal energy, or has been radiated. Less than 1/3 of the initial energy is left in pinch disassembly.

ionization and radiation starts already at around 20 ns, when the plasma heats up to ~ 0.3 keV as the inner edges come together on axis. As the plasma continues to arrive on axis the pinch radiates at an increasing rate, until at about 60 ns into the pulse the kinetic energy has almost completely disappeared into radiation and ionization energy, with the remainder in plasma thermal energy. After stagnation the plasma expands and cools. Slightly more than half the initial energy is radiated away; 30% is left for the kinetic energy of the plasma expansion, and about 10% for thermal and ionization energy.

The radiation spectrum during stagnation in Fig. 23 is dominated by the neon *K*-shell lines. The radiation yield in these lines is about 800 J, against ~ 400 J from the *L* shell and the continuum each, for a total of 1600 J. It is satisfying that the relative radiation yields in this computation are similar to those obtained in experiments with neon puffs, even though the parameters differ (e.g., Fig. 3; Mehlman, 1986; Stephanakis, 1986).

Quantitative agreement between experiments and computation is claimed by Spielman (1984) between their rare gas implosions and various computational models available to their group. Instead of mocking up the early stage of the implosion by an inwardly coasting plasma, as in Fig. 22, they follow the implosion in time using the experimental current. Possible difficulties with radiative collapse are avoided when including time dependence in the ionization dynamics (Kononov, 1977). Another computation (Maxon, 1984) employed a general-purpose radiation-hydrodynamics code with atomic models that proved insufficiently specific for direct comparison with experiment.

3. Two-dimensional implosion hydromagnetics

Hydrodynamic instabilities during the run-in can destroy the quality of thin foil implosions, but do not affect the implosion of the thicker gas shells. These instabilities and other features of thin foils have been studied mainly in connection with the relevant experiments that are reviewed elsewhere (e.g., Roderick, 1983). A unique feature of these studies is their two-dimensional hydromagnetic computa-

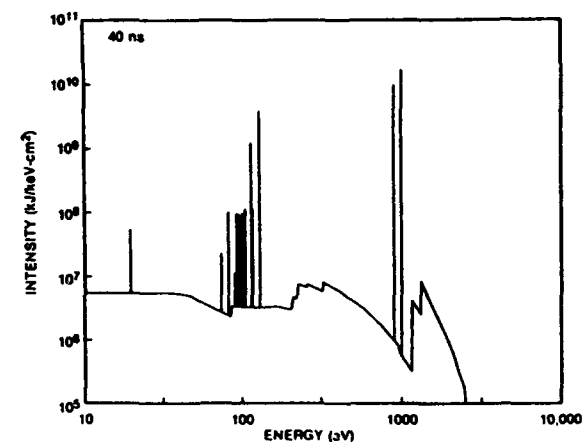


FIG. 23. Neon emission spectrum at 40 ns just before stagnation. Qualitatively the spectrum changes little in time during the implosion, although the power increases with the stagnating volume (from Clark, 1986).

tion of the Raleigh–Taylor instability, its nonlinear saturation, and related problems such as the wall instability (e.g., Hussey, 1980, 1981; Kloc, 1982; Kohn, 1983; Roderick, 1984, 1986b). However, this work omits or underspecifies the radiation physics which is emphasized in this review. Two-dimensional radiation-hydrodynamics models including a satisfactory radiation package are currently being developed, and we look forward to the results.

D. Outlook

This review emphasizes the interplay between the hydrodynamics coupled to the generation and transport of radiation. Certain aspects of radiative z-pinchs are well understood in principle, notably various aspects of the radiation modeling of moderately dense and optically thick homogeneous plasmas in collisional-radiative equilibrium; even the time-dependent problem of approach to equilibrium should pose no unsurmountable problem. The hydrodynamics of imploding plasmas can then be considered, including the important effect of energy loss and redistribution due to the radiation. It is no surprise that reasonably complete computations are difficult because of the vast amount of detail that is required.

Basic to these computations are the ionization dynamics and their atomic rates. These depend heavily on the determination of ionic levels and cross sections in a plasma environment, an active area of research in atomic physics: we mention the effect of plasma density on the ionic energy levels, and the computation of the dielectronic recombination cross section.

Next in importance to the cross sections is the electron distribution function $f(v)$: generally $f(v)$ is thought to be Maxwellian, except perhaps along the pinch axis where a small minority of runaway (or beam) electrons may dominate the production of K-line radiation from the bright spots.

Much is known about plasma hydrodynamics without radiation, including the growth rates of axial instabilities in a pinched or imploding plasma, and the self-similar oscillations around the radial equilibrium. The relevancy of these results to radiating z-pinchs remains to be evaluated by extending the considerations to include radiation. A similar comment applies to the *hydrodynamics* of radiative z-pinchs: how exactly the current penetrates into the plasma is not completely understood.

The major challenge to the theory of radiation z-pinchs is to unravel the physics of the bright spot. Apart from any complications with the distribution function the bright spot is certainly two dimensional. Anomalous resistivity due to plasma turbulence (e.g., Papadopoulos, 1977) is often quoted as important in bright spots, but a satisfactory analysis of anomalous processes in the context of a radiative z-pinch does not yet exist. In this we are not alone: theories attempting to model the production of fusion neutrons struggle with similar problems (Vikhrev, 1985, 1986; Trubnikov, 1986).

ACKNOWLEDGMENTS

It is our pleasure to thank our colleagues at NRL and elsewhere for our use of their data. We are particularly grate-

ful to F. C. Young and A. E. Robson for their helpful comments on the manuscript. We acknowledge useful discussions with J. Z. Farber of the Defense Nuclear Agency, and his continuous efforts in support of radiating pinch research. One of us (N.R.P.) would like to thank N. Rostoker for his introduction to pinching. This work was supported by DNA.

- Allen, C. W. (1973). *Astrophysical Quantities*, 3rd ed. (Athlone, London).
- Alikhanov, S. G., Vasil'ev, V. I., Konov, E. Ya., Koshelev, K. N., Sidelnikov, Yu. V., and Toporkova, D. A. (1984). "Formation of Micropinchs in a High-current Linear Z Pinch with Pulsed Gas Injection," *Fiz. Plazmy* 10, 1051 (Sov. J. Plasma Phys. 10, 605).
- Apruzese, J. P. (1981a). "Direct solution of the equation of transfer using frequency- and angle-averaged photon-escape probabilities for spherical and cylindrical geometries," *J. Quant. Spectrosc. Radiat. Trans.* 25, 419.
- Apruzese, J. P., Kepple, P. C., Whitney, K. G., Davis, J., and Duston, D. (1981b). "Collisional-Radiative-Equilibrium Spectroscopic Diagnosis of a Compressed, Optically Thick Neon Plasma," *Phys. Rev. A* 24, 1001.
- Apruzese, J. P., Davis, J., Duston, D., and Clark, R. W. (1984a). "Influence of Lyman-series Fine-Structure Opacity on the K-shell Spectrum and Level Populations of Low-to-Medium-Z Plasmas," *Phys. Rev. A* 29, 246.
- Apruzese, J. P. and Davis, J. (1984b). "K-Shell Yield Scaling Law for Conventional PRS Loads," NRL Memorandum Report No. 5406 (unpublished).
- Apruzese, J. P. and Davis, J. (1985a). "Kinetics of x-ray lasing by resonant photoexcitation: Fundamentals of pumping power and gain for the Na x-Ne ix system," *Phys. Rev. A* 31, 2976.
- Apruzese, J. P. and Davis, J. (1985b). "Radiative Properties of Puffed-gas Mixtures: The case of Optically Thick Plasmas Composed of Two Elements with Similar Atomic Numbers," *J. Appl. Phys.* 57, 4349.
- Apruzese, J. P., Duston, D., and Davis, J. (1986). "K-shell aluminum resonance line ratios for plasma diagnostics using spot spectroscopy," *J. Quant. Spectrosc. Radiat. Transfer* 36, 339.
- Apruzese, J. P., Mehlman, G., Davis, J., Rogerson, J. E., Scherrer, V. E., Stephanakis, S. J., Ottinger, P. F., and Young, F. C., (1987). "Spectroscopic analysis of sodium-bearing z-pinch plasmas for their x-ray laser pumping efficiency," *Phys. Rev. A* 35, 4896.
- Aranchuk, L. E., Bogolyubskii, S. L., and Tel'kovskaya, O. V. (1985). "Energy balance of a high-current discharge in an exploding-wire plasma," *Zh. Tech. Fiz.* 55, 2222 (Sov. Phys. Tech. Phys. 30, 1312).
- Aranchuk, L. E., Bogolyubskii, G. S., Volkov, G. S., Korolev, V. D., Koba, Yu. V., Liksonov, V. I., Lukin, A. A., Nikandrov, L. B., Tel'kovskaya, O. V., Tulupov, M. V., Chernenko, A. S., Tsarfin, V. Ya. and Yankov, V. V. (1986). "Radiatively cooled z-pinch produced by an exploding copper wire," *Fiz. Plazmy* 12, 1324 (Sov. J. Plasma Phys. 12, 765).
- Attwood, D., Halbach, K., and Kim, K.-J. (1985). "Tunable coherent x-rays," *Science* 228, 1265.
- Bailey, J., Ettinger, Y., Fisher, A., and Feder, R. (1982a). "Evaluation of the gas puff z-pinch as an x-ray lithography and microscopy source," *Appl. Phys. Lett.* 40, 33.
- Bailey, J., Ettinger, Y., Fisher, A., and Rostoker, N. (1982b). "Gas-puff Z Pinches with D₂ and D₂-Ar Mixtures," *Appl. Phys. Lett.* 40, 460.
- Bailey, J., Fisher, A., and Rostoker, N. (1986). "Coupling of radiation and hydrodynamics in a z-pinch plasma," *J. Appl. Phys.* 60, 1939. Also Ph.D. thesis, "Effect of radiation colling and plasma atomic number on z-pinch dynamics," U. C. Irvine (1983).
- Baker, W. L., Clark, M. C., Degnan, J. H., Kiuttu, G. F., McClenahan, C. R., and Reinovsky, R. E. (1978). "Electromagnetic-implosion generation of pulsed high-energy density plasma," *J. Appl. Phys.* 49, 4694.
- Baksh, R. B., Datsko, I. M., Korostelev, A. F., Loskutov, V. V., Luchinskii, A. V., and Chertov, A. A. (1983). "Nanosecond Electrical Explosion of Thin Wires," *Fiz. Plazmy* 9, 1224. (Sov. J. Plasma Phys. 9, 706).
- Baksh, R. B., Datsko, I. M., El'chaninov, A. S., Kovsharov, N. F., Loskutov, V. V., Lushinsky, A. V., Kovalchuk, B. M., Mesyats, G. A., Ratakhin, N. A., Sorokin, S. A., Stasyev, V. P., Sukhov, M. Yu., and Fedushak, V. F. (1987). "Fast Implosion of Liners" in *Megagauss Technology and Pulse Power Applications*, C. M. Fowler, R. S. Caird, and D. J. Erickson, Ed. (Plenum, New York), p.663.
- Barak, G and Rostoker, N. (1982). "Semihydrodynamic model for ion separation in a fast pinch," *Appl. Phys. Lett.* 41, 918.

- Bateman, G. (1978). *MIID Instabilities* (MIT, Cambridge, MA).
- Benford, G. (1978). "Runaway-Electron Model For X-ray Emission in Pinched Discharges," *Appl. Phys. Lett.* 33, 983.
- Benjamin, R. F., Pearlman, J. S., Chu, E. Y., and Riordan, J. C. (1981). "Measurements of the Dynamics of Imploding Wire Arrays," *Appl. Phys. Lett.* 39, 848.
- Bleach, R. D. (1980). "X-UV Spectra from Kr xi-xiv," *J. Opt. Soc. Am.* 70, 861.
- Bleach, R. D., Burkhalter, P. G., Nagel, D. J., and Schneider, R. L. (1983). "Extreme Ultraviolet Emission from Gas Puff Plasmas," *J. Appl. Phys.* 54, 1273.
- Bloomberg, H. W., Lampe, M., and Colombant, D. G. (1980). "Early Expansion in Exploding Multiple Wire Arrays," *J. Appl. Phys.* 51, 5277.
- Bobrova, N. A. and Razinkova, T. L. (1987). "Equilibrium states of a z-pinch with emission and thermal conductivity," *Fiz. Plazmy* 13, 92 (Sov. J. Plasma Phys. 13, 53).
- Bogolyubskii, S. L., Chernenko, A. S., Dan'ko, S. A., Fanchenko, S. D., Gordeev, E. M., Kalinin, Yu. G., Koba, Yu. V., Korolev, V. D., Kuksov, V. P., Liksonov, V. I., Lukin, A. A., Rudakov, L. I., Shashkov, A. Yu., Shestakov, Yu. I., Smirnova, E. A., Tulupov, M. V., Urutskoev, L. I., and Volkovich, A. G. (1986). "Linear Acceleration Experiments at the 'Module' Facility," in *Proceedings of the Eighth International Conference on High Power Particle Beams*, Tokyo, Japan.
- Book, D. L., Ott, E., and Lampe, M. (1976). "Nonlinear Evolution of the Sausage Instability," *Phys. Fluids* 19, 1982.
- Braginskii, S. I. (1957). "The behavior of a completely ionized plasma in a strong magnetic field," *Zh. Eksp. Teor. Fiz.* 33, 645 (Sov. Phys. JETP 6, 494).
- Brown, G. S. and Lindau, E. E. Eds. (1986). *International Conference on Synchrotron Radiation*, Nucl. Instrum. Methods 246 *passim*.
- Bruno, C., Chevaller, J., Delvaux, J., Barbaro, J., Bernard, A., Wolff, G., and David, J. (1983). "X-ray emission efficiency of imploding aluminum wire plasmas," in *Proceedings of Fifth International Conference on High Power Particle Beams*, University of California, San Francisco, CA.
- Burhenn, R., Harm, B. S., Gossling, S., Kunze, H. J. and Mielcarski, D. (1984). "Electron temperature scaling in a vacuum spark discharge," *J. Phys. D* 17, 1665.
- Burkhalter, P. G., Dozier, C. M., Stallings, C., and Cowan, R. D. (1978). "X-ray Line Emission and Plasma conditions in Exploded Fe Wires," *J. Appl. Phys.* 49, 1092.
- Burkhalter, P., Davis, J., Rauch, J., Clark, W., Dahlbacka, G., and Schneider, R. (1979a). "X-ray line spectra from Exploded-Wire Arrays," *J. Appl. Phys.* 50, 705.
- Burkhalter, P. G., Shiloh, J., Fisher, A., and Cowan, R. D., (1979b). "X-ray spectra from a gas-puff z-pinch device," *J. Appl. Phys.* 50, 4532.
- Bykovskii, Yu. A. and Lagoda, V. B. (1982). "Local High-temperature Plasma Formations in a High-current Pinching Discharge," *Zh. Eksp. Teor. Phys.* 83, 114 (Sov. Phys. JETP 56, 61).
- Camarcat, N., Delvaux, J., Etlicher, B., Mosher, D., Raboisson, G., and Perronnet, A. (1985). "Electrical pulsed power generators of the 1 TW class," *Laser and Particle Beams* 3, 415.
- Campbell, E. M., Hunt, J. T., Bliss, E. S., Speck, D. R., and Drake, R. P. (1986). "Nova experimental facility," *Rev. Sci. Instrum.* 57, 2101.
- Cannon, C. J. (1985). *The Transfer of Spectral Line Radiation* (Cambridge University Press, Cambridge, MA).
- Chapin, D. L., Duderstadt, J. J., and Bach, D. R. (1974). "Numerical Studies of Exploding-Wire Plasmas," *J. Appl. Phys.* 45, 1726.
- Choi, P., Dangor, A. E., Deeney, C., and Challis, C. D. (1986). "Temporal development of hard and soft x-ray emission from a gas-puff z pinch," *Rev. Sci. Instrum.* 57, 2162.
- Cilliers, W. A., Datla, R. U., and Griem, H. R. (1975). "Spectroscopic measurements on vacuum-spark plasmas," *Phys. Rev. A* 12, 1408.
- Clark, R. W., Davis, J., and Cochran, F. L. (1986). "Dynamics of imploding neon gas-puff plasmas," *Phys. Fluids* 29, 1971.
- Clark, R. W. and Davis, J. (1988). (unpublished).
- Clark, W., Wilkinson, M., Rauch, J., and LePage, J. (1982a). "X-ray Measurements of Imploding Wire Plasmas," *J. Appl. Phys.* 53, 1426.
- Clark, W., Gersten, M., Katzenstein, J., Rauch, J., Richardson, R., and Wilkinson, M. (1982b). "Aluminum, Calcium, and Titanium Imploding Plasma Experiments on the BLACKJACK 5 Pulse Generator," *J. Appl. Phys.* 53, 4099.
- Clark, W., Richardson, R., Brannon, J., Wilkinson, M., and Katzenstein, J. (1982c). "The Dynamics of Imploding Argon Plasmas," *J. Appl. Phys.* 53, 5552.
- Clark, W., Gersten, M., Tanimoto, D., Kolb, A., Pearlman, J., Rauch, J., Richardson, R., Riordan, J., and Wilkinson, M. (1983). "Imploding Plasma Pinches Driven by High Power Generators," in *Proceedings of Fifth International Conference on High Power Particle Beams 1983*, University of California, San Francisco, CA, 1983.
- Colloque, (1986). *J. Phys. (Paris) Colloq. C6 S-47 passim*.
- Coppins, M., Bond, D. J., and Haines, M. G., (1984a). "On the Vlasov fluid stability of the $m = 0$ mode in a pure z pinch," *J. Plasma Phys.* 32, 1.
- Coppins, M., Bond, D. J., and Haines, M. G. (1984b). "A Study of the Stability of the Z Pinch Under Fusion Conditions Using the Hall Fluid Model," *Phys. Fluids* 27, 2886.
- Dangor, A. E. (1986). "High density z-pinch," *Plasma Physics and Controlled Fusion* 28, 1931.
- Davankoo, F., Bowen, T. S., and Collins, C. B. (1987). "Scaling to high average powers of a flash x-ray source producing nanosecond pulses," *Rev. Sci. Instrum.* 58, 2103.
- Davis, J. and Blaha, M. (1982). "Level Shifts and Inelastic Electron Scattering in Dense Plasmas," *J. Quant. Spectrosc. Radiat. Transfer* 27, 307.
- Davis, J. and Whitney, K. G. (1976). "Line Emission in Al xi as an Optical Diagnostic in Laser-Heated Plasmas," *J. Appl. Phys.* 47, 1426.
- Davis, J., Apruzese, J. P., Agritellis, C., and Kepple, P. (1987). "Argon puff gas soft X-ray laser," in *Radiative properties of hot, dense matter III*, edited by B. Rozsnyai, C. Hooper, R. Cauble, R. Lee, and J. Davis (World Scientific, Singapore).
- Davis, J., editor (1988). *IEEE Plasma Sci., Special issue on x-ray lasers* (to be published).
- DeMichelis, C. and Mattioli, M. (1981). "Soft-x-ray spectroscopic diagnostics of laboratory plasmas," *Nucl. Fusion* 21, 677.
- DeMichelis, C. and Mattioli, M. (1984). "Spectroscopy and impurity behavior in fusion plasmas," *Rep. Prog. Phys.* 47, 1233.
- Degnan, J. H., Reinovsky, R. E., Honea, D. L., and Bengtson, R. D. (1981). "Electromagnetic Implosions of Cylindrical Gas 'Shells,'" *J. Appl. Phys.* 52, 6550.
- Dorokhin, L. A., Smirnov, V. P., Tulupov, M. V., and Tsarfin, V. Ya. (1984). "Laser Studies of Exploding Wires," *Zh. Tekh. Fiz.* 54, 511. (Sov. Phys. Tech. Phys. 29, 304).
- Dothan, F., Riege, H., Boggasch, E., and Frank, K. (1987). "Dynamics of a z pinch for focusing high-energy charged particles," *J. Appl. Phys.* 62, 3585.
- Doucet, H. J., Etlicher, J. P., Furtlehner, and Gazaix, M. (1983). "The 'Needle Plasma,' A soft X-Rays-Initiated, Gas Embedded Z-Pinch Computational and Experimental Approaches," in *Proceedings of the Fifth International Conference on High Power Particle Beams*, University of California, San Francisco, CA.
- Dozier, C. M., Burkhalter, P. G., Nagel, D. J., Stephanakis, S. J., and Mosher, D. (1977). "High Ionization States in Exploded-Wire Plasmas," *J. Phys. B* 10, L73.
- Dukart, R., Wong, S. L., Dietrich, D., Fortner, R., and Stewart, R. (1983). "Studies of an imploding plasma x-ray laser," in *Proceedings of Fifth International Conference on High Power Particle Beams*, University of California, San Francisco, CA.
- Duston, D. and Davis, J. (1980). "Self-Absorption of Heliumlike Satellite Lines in High-density Fusion Plasmas," *Phys. Rev. A* 21, 932.
- Duston, D. and Davis, J. (1981). "Soft-X-ray and X-ray Ultraviolet Radiation from High-Density Aluminum Plasmas," *Phys. Rev. A* 23, 2602.
- Duston, D. and Davis, J. (1982). "Density Effects on the Spatial Emission of a High Temperature Argon Plasma," *J. Quant. Spectrosc. Radiat. Transfer* 27, 267.
- Duston, D., Clark, R. W., Davis, J., and Apruzese, J. P. (1983a). "Radiation Energetics of a Laser-Produced Plasma," *Phys. Rev. A* 27, 1441.
- Duston, D., Rogerson, J.E., Davis, J., and Blaha, M. (1983b). "Dense Plasma Effects on K-shell Dielectronic Satellite Lines," *Phys. Rev. A* 28, 2968.
- Duston, D., Davis, J., and Agritellis, C. (1985a). "Radiative Properties of Puffed-Gas Mixtures," *J. Appl. Phys.* 57, 785.
- Duston, D., Clark, R. W., and Davis, J. (1985b). "Effects of radiation on spectra, gradients, and preheat in laser-produced plasmas," *Phys. Rev. A* 31, 3220.
- Eidmann, K. and Kishimoto, T. (1986a). "Absolutely measured x-ray spectra from laser plasmas with targets of different elements," *Appl. Phys. Lett.* 49, 377.
- Eidmann, K., Kishimoto, T., Herrmann, P., Mizui, J., Pakula, R., Sigel, R., and Witkowski, S. (1986b). "Absolute soft x-ray measurements with a transmission grating spectrometer," *Laser and Particle Beams* 4, 521.
- Epperlein, E. M. (1984). "The accuracy of Braginskii's transport coefficient for a Lorentz plasma," *J. Phys. D* 17, 1823.

- Epperlein, E. M. and Haines, M. (1986). "Plasma transport coefficients in a magnetic field by direct numerical solution of the Fokker-Planck equation," *Phys. Fluids* 29, 1029.
- Faenov, A. Ya., Khakhalin, S. Ya., Kolomensky, A. A., Pikuz, S. A., Samokhin, A. I., and Skobelev, I. Yu. (1985). "Superdense high-temperature exploded-wire plasma observations in a high-current vacuum diode," *J. Phys. D* 18, 1347.
- Feder, R., Pearlman, J. S., Riordan, J. C., and Costa, J. L. (1984). "Flash x-ray microscopy with a gas jet plasma source," *J. Microsc.* 135, 347.
- Felber, F. S. and Rostoker, N. (1981). "Kink and Displacement Instabilities in Imploding Wire Arrays," *Phys. Fluids* 24, 1049.
- Felber, F. S. (1982). "Self-similar oscillations of a z-pinch," *Phys. Fluids* 25, 643.
- Felber, F. S., Liberman, M. A., and Velikovich, A. L. (1985). "Methods for Producing Ultrahigh Magnetic Fields," *Appl. Phys. Lett.* 46, 1042.
- Finken, K. H. (1983). "Untersuchungen an Dichten Z-Pinch-Plasmen (Investigations of dense z-pinch plasmas)," *Dtsch. Phys. Z.* 31, 1.
- Gazaix, M., Doucet, H. J., Etlicher, B., Furtlehner, J. P., Lamain, H., and Rouillé, C. (1984). "A New Method to Produce an Annular Cylindrical Plasma for Impeding Plasma Experiments," *J. Appl. Phys.* 56, 3209.
- Gerritsen, H. C., van Brug, H., Bijkerk, F., and van der Wiel, M. J. (1986). "Laser-generated plasma as soft x-ray source," *J. Appl. Phys.* 59, 2337.
- Gersten, M., Rauch, J. E., Clark, W., Richardson, R. D., and Wilkinson, G. M. (1981). "Plasma Temperature Measurements from Highly Ionized Titanium Imploding Wire Plasmas," *Appl. Phys. Lett.* 39, 148.
- Gersten, M., Clark, W., Rauch, J. E., Wilkinson, G. M., Katzenstein, J., Richardson, R. D., Davis, J., Duston, D., Apruzese, J. P., and Clark, R. (1986). "Scaling of Plasma Temperature, Density, Size, and X-Ray emission above 1 keV with Array Diameter and Mass for Aluminum Imploding-Wire Plasmas," *Phys. Rev. A* 33, 477.
- Gerusov, A. V. and Imshennik, V. S. (1985). "Radiative cooling of a z-pinch discharge in a deuterium-neon mixture during the collapse of the cylindrical plasma," *Fiz. Plazmy* 11, 568 (Sov. J. Plasma Phys. 11, 332).
- Gilbert, K. M., Anthea, J. P., Gusinow, M. A., Palmer, M. A., Whitlock, R. R., and Nagel, D. J. (1980). "X-ray Yields of Plasmas Heated by 8-ns Neodymium Laser Pulses," *J. Appl. Phys.* 51, 1449.
- Gol'ts, E. Ya., Kolosnikov, G. V., Koshelev, K. N., Kramida, A. E., Sidel'nikov, Yu. V., Vikhrev, V. V., Ivanov, V. V., Palkin, A. A., and Prut, V. V. (1986). "A high-temperature micropinch in a discharge with a current of 1 MA," *Phys. Lett. A* 115, 114.
- Hagelstein P. L. (1981). Ph.D. thesis, "Physics of short wavelength laser design," JCR-53100 (unpublished). Also, "Review of Radiation Pumped Soft X-ray Lasers," *Plasma Phys.* 25, 1345 (1983).
- Haines, M. G. (1960). "The Joule heating of a stable pinched plasma," *Proc. R. Soc. London* 76, 250.
- Haines, M. G. (1982). "The Physics of the Dense Z-Pinch in Theory and in Experiment with Application to Fusion Reactor," *Phys. Scr.* T2/2, 380.
- Haines, M. G. (1983). "Ion Beam Formation in an $m = 0$ Unstable Z Pinch," *Nucl. Instrum. Methods* 207, 179.
- Hammel, B. A. and Jones, L. A. (1984). "Effects of the Internally Produced Nonthermal Electrons on the Temperature Diagnostics of a Hollow Gas Shell Z Pinch," *Appl. Phys. Lett.* 44, 667.
- Hares, J. D., Marrs, R. E., and Fortner, R. J. (1985). "An Absolute Measure of Heating by Suprathermal Electrons in a Gas Puff Z-Pinch," *J. Phys. D* 18, 627.
- Henke, B. L., Kwok, S. L., Uejio, J. Y., Yamada, H. T., and Young, G. C. (1984a). "Low-energy x-ray response of photographic films. I. Mathematical models," *J. Opt. Soc. Am. B* 1, 818.
- Henke, B. L., Fujiwara, F. G., Tester, M. A., Dittmore, C. H., and Palmer, M. A. (1984b). "Low-energy x-ray response of photographic films. II. Experimental characterization," *J. Opt. Soc. Am. B* 1, 828.
- Holstein, P. A., Delettrez, J., Skrupsky, S., and Matte, J. P. (1986). "Modeling nonlocal heat flow in laser-produced plasmas," *J. Appl. Phys.* 60, 2296.
- Howells, M., Kirz, J., Sayre, D., and Schmah, G. (1985). "Soft x-ray microscopes," *Phys. Today* (August 22).
- Hsing, W. W. and Porter, J. L. (1987). "Measurements of axial nonuniformities in gas-puff implosions," *Appl. Phys. Lett.* 50, 1572.
- Hussey, T. W., Roderick, N. F., and Kloc, D. A. (1980). "Scaling of magnetohydrodynamic instabilities in imploding plasma liners," *J. Appl. Phys.* 51, 1452.
- Hussey, T. W. and Roderick, N. F. (1981). "Diffusion of Magnetic Field into an Expanding Plasma Shell," *Phys. Fluids* 24, 1384.
- Hussey, T. W., Matzen, M. K., and Roderick, N. F. (1986). "Large-Scale Length Nonuniformities in Gas Puff Implosions," *J. Appl. Phys.* 59, 2677.
- Hwang, C. S. and Roderick, N. F. (1987). "Potential flow model for the hydromagnetic Raleigh-Taylor instability in cylindrical plasmas," *J. Appl. Phys.* 62, 95.
- Ivanenkov, G. V. (1984). "Electron Runaway and Plasma Pinching in a High-current Diode," *Dokl. Akad. Nauk SSSR* 282, 1106. (Sov. J. Plasma Phys. 10, 680).
- Ivanenkov, G. V., Kolomensky, A. A., Pikuz, S. A., Samokhin, A. I., and Zakharov, S. M. (1986). "Z-Pinch in a High-Current Diode," in *Proceedings of the Eighth International Conference on High Power Particle Beams*, Tokyo, Japan.
- Jacobs, V. L., Davis, J., Kepple, P. C., and Blaha, M. (1977). "The influence of autoionization accompanied by excitation on dielectronic recombination and ionization equilibrium," *Ap. J.* 211, 605.
- Jensen, R. V., Post, D. E., Grasberger, W. H., Tarter, C. B., Lokke, W. A. (1977). "Calculations of impurity radiation and its effects on tokamak experiments," *Nucl. Fus.* 17, 1187.
- Jones, L. A., Finken, K. H., Dangor, A., Källne, E., and Singer, S. (1981). "A Laser Initiated, Gas-Embedded Z Pinch: Experiment and Computation," *Appl. Phys. Lett.* 38, 522.
- Jones, L. A. and Kania, D. R. (1985). "Temporally and spatially resolved x-ray emission from a collapsing gas shell z-pinch plasma," *Phys. Rev. Lett.* 55, 1993.
- Kania, D. R. (1984a). "Device for Loading Thin Wires in a Vacuum," *Rev. Sci. Instrum.* 55, 39.
- Kania, D. R. and Jones L. A. (1984b). "Observation of an Electron Beam in an Annular Gas-Puff Z-Pinch Plasma Device," *Phys. Rev. Lett.* 53, 166.
- Kato, Y. and Be, S. H. (1986). "Generation of Soft X rays Using a Rare Gas-Hydrogen Plasma Focus and its Application to X-ray Lithography," *Appl. Phys. Lett.* 48, 686.
- Katzenstein, J. (1981). "Optimum Coupling of Imploding Loads to Pulse Generators," *J. Appl. Phys.* 52, 676.
- Kirz, J. and Rarback, H. (1985). "Soft x-ray microscopes," *Rev. Sci. Instrum.* 56, 1.
- Kloc, D. A., Roderick, N. F., and Hussey, T. W. (1982). "A simple model for plasma temperature in imploded hollow plasma liners," *J. Appl. Phys.* 53, 6706.
- Koch, E. E. Ed. (1983). *International Conference on Synchrotron Radiation*, Nucl. Instrum. Methods 208 *passim*.
- Kodama, R., Okada, K., Ikeda, N., Mineo, M., Tanaka, K. A., Mochizuki, T., and Yamanaka, C. (1986). "Soft x-ray emission from ω_p , $2\omega_p$, and $4\omega_p$ laser-produced plasmas," *J. Appl. Phys.* 59, 3050.
- Kohn, B. J., Roderick, N. F., and Beason, C. W. (1983). "Two-dimensional Numerical Simulation of an Inductively Driven Imploding Foil Plasma," *J. Appl. Phys.* 54, 4348.
- Kolomensky, A. A., Lebedev, A. N., Papadichev, V. A., Pikuz, S. A., and Yablokov, B. N. (1983). "Generation and acceleration of multicharge and negative ions in high-current diodes and by means of collective effects," *Proceedings of the International Conference on High Power Particle Beams*, University of California, San Francisco, CA, pp. 533-539.
- Kononov, É. Ya., Koshelev, K. N., and Sidel'nikov, Yu. V. (1977). "Spectra of multiply ionized iron atoms in a low-inductance vacuum discharge: time-varying ionization model for the 'plasma-point,'" *Fiz. Plazmy* 3, 663 (Sov. J. Plasma Phys. 3, 375).
- Kononov, É. Ya., Koshelev, K. N., and Sidel'nikov, Yu. V. (1985). "X-ray Spectroscopic Study of Micropinches in a Low-Inductance Vacuum Spark," *Fiz. Plazmy* 11, 927 (Sov. J. Plasma Phys. 11, 538).
- Korop, E. D., Meferovich, B. É., Sidel'nikov, Yu. V., and Sukhorukov, S. T. (1979). "Micropinch in a High-Current Diode," *Usp. Fiz. Nauk.* 129, 87 (Sov. Phys. Usp. 22, 727).
- Kühne, M. and Wende, B. (1985). "Vacuum UV and Soft X-ray Radiometry," *J. Phys. E* 18, 637.
- Lee, T. N. and Elton, R. C. (1971). "X Radiation from Optical and Inner-Shell Transitions in a Highly Ionized Dense Plasma," *Phys. Rev. A* 3, 865.
- Lee, T. N. (1974). "Solar-Flare and Laboratory Plasma Phenomena," *Astrophys. J.* 190, 467.
- Lee, T. N. (1975). "High-density Ionization with an Intense Linear Focus Discharge," *Ann. NY Acad. Sci.* 251, 112.
- Lee, Y. T. and More, R. M. (1984). "An electron conductivity model for dense plasmas," *Phys. Fluids* 27, 1273.
- Liberman, M. A. and Velikovich, A. L. (1986). "Self-similar motions in z-

- pinch dynamics," *Nucl. Fusion* **26**, 709.
- Marrs, R. E., Dietrich, D. D., Fortner, R. J., Levine, M. A., Price, D. F., Stewart, R. E., and Young, B. K. F. (1983). "Time and Space Resolved Vacuum-ultraviolet Spectroscopy of an Argon Gas-Puff Z Pinch," *Appl. Phys. Lett.* **42**, 946.
- Maxon, S. and Wainwright, T. (1984). "Radiation spectra from an imploding argon gas puff," *Phys. Fluids* **27**, 2535.
- Mehlman, G., Burkhalter, P. G., Stephanakis, S. J., Young, F. C., and Nagel, D. J. (1986). "Quantitative x-ray spectroscopy of neon z-pinch plasmas," *J. Appl. Phys.* **60**, 3427.
- Meierovich, B. E. (1982). "Electromagnetic Collapse. Equilibrium of a Dense Pinch," *Phys. Rep.* **92**, 83.
- Meierovich, B. E. (1984). "Electromagnetic Collapse. Problems of Stability, Emission of Radiation and Evolution of a Dense Pinch," *Phys. Rep.* **104**, 259.
- Meierovich, B. E. (1985). "Self-similar model of the radiative compression of a z-pinch," *Fiz. Plazmy* **11**, 1446 (*Sov. Phys. Plasma Phys.* **11**, 831).
- Meierovich, B. E. (1986). "Toward the realization of electromagnetic collapse," *Usp. Fiz. Nauk.* **149**, 221 (*Sov. Phys. Usp.* **29**, 506).
- Michette, A. G., Cheng, P. C., Eason, R., Feder, W., O'Neill, R. F., Owadano, Y., Rosser, R. J., Rumsby, P., and Shaw, M. J. (1986). "Soft x-ray contact microscopy using laser plasma sources," *J. Phys. D* **19**, 363.
- Mihalas, D. (1978). *Stellar Atmospheres*, 2nd ed. (Freeman, San Francisco, CA).
- Mochizuki, T., Yabe, T., Okada, K., Hamada, M., Ikeda, N., Kiyokawa, S., and Yamanaka, C. (1986). "Atomic-Number Dependence of Soft-X-Ray Emission from Various Targets Irradiated by a 0.53- μm -wavelength Laser," *Phys. Rev. A* **33**, 525.
- More, R. M. (1982). "Electronic Energy-Levels in Dense Plasmas," *J. Quant. Spectrosc. Radiat. Transfer* **27**, 345.
- Mosher, D., Stephanakis, S. J., Vitkovitsky, I. M., Dozier, C. M., Levine, L. S., and Nagel, D. J. (1973). "X-Radiation From High-Energy-Density Exploded-Wire Discharges," *Appl. Phys. Lett.* **23**, 429.
- Mosher, D., Stephanakis, S. J., Hain, K., Dozier, C. M., and Young, F. C. (1975). "Electrical Characteristics of High Energy-Density Exploded Wire Plasmas," *Ann. NY Acad. Sci.* **251**, 632.
- Nagel, D. J., Brown, C. M., Peckerar, M. C., Ginter, M. L., Robinson, J. A., McIlrath, T. J., and Carroll, P. K. (1984). "Repetitively pulsed-plasma soft x-ray source," *Appl. Opt.* **23**, 1428.
- Nagel, D. J. (1982). "Potential characteristic and applications of x-ray lasers," in *Advances in x-ray spectroscopy: Contributions in honour of Professor Y. Cauchois*, edited by C. Bonnelle and C. Mande (Pergamon, New York).
- Negus, C. R. and Peacock, N. J. (1979). "Local regions of high-pressure plasma in a vacuum spark," *J. Phys. D* **12**, 91.
- Nicolosi, P., Jannitti, E., and Tondello, G. (1981). "Soft X-ray Emission of Continua from Laser Produced Plasmas," *Appl. Phys. B* **26**, 117.
- Papadopoulos, K. (1977). "A review of anomalous resistivity for the ionosphere," *Rev. Geophys. Space Phys.* **15**, 113.
- Pearlman, J. S. and Riordan, J. C. (1981). "X-ray Lithography Using a Pulsed Plasma Source," *J. Vac. Sci. Technol.* **19**, 1190.
- Pearlman, J. S. and Riordan, J. C. (1985a). "Bright discharge plasma sources for x-ray lithography," *Proc. SPIE* **537**, 102.
- Pearlman, J. S., Riordan, J. C., and Kolb, A. C. (1985b). "A bright pulsed x-ray source for soft x-ray research and processing applications," *Radiat. Phys. Chem.* **25**, 709.
- Pease, R. S. (1957). "Equilibrium characteristics of a pinched gas discharge cooled by bremsstrahlung radiation," *Proc. Phys. Soc. London B* **70**, 11.
- Pépin, H., Fabbro, R., Faral, B., Amiranoff, F., Virmont, J., Cottet, F., and Romain, J. P. (1985). "The X-Ray Emission, Ablation Pressure, and Preheating for Foils Irradiated at 0.26 μm Wavelength," *Phys. Fluids* **28**, 3393.
- Pereira, N. R., Rostoker, N., and Pearlman, J. S. (1984). "Z-Pinch Instability with Distributed Current," *J. Appl. Phys.* **55**, 704.
- Pereira, N. R. and Whitney, K. G. (1988). "Non-Maxwellian electron energy distribution due to radiation in a z-pinch," to be published in *Phys. Rev. A*.
- Perez, J. D., Chase, L. F., McDonald, R. E., Tannenwald, L., and Watson, B. A. (1981). "Subkilovolt x-ray radiation from an argon plasma," *J. Appl. Phys.* **52**, 670.
- Phillion, D. W. and Hailey, C. J. (1986). "Brightness and duration of x-ray line sources irradiated with intense 0.53- μm laser light at 60 and 120 ps pulse width," *Phys. Rev. A* **34**, 4886.
- Post, R. S., Johnson, D. J., and Stephanakis, S. J. (1978). "Nonthermal infrared radiation from exploding wire plasmas," *Plasma Phys.* **20**, 1039.
- Post, D. E., Jensen, R. V., Tarter, C. B., Grasberger, W. H., and Lokke, W. A. (1977). "Steady-state radiative cooling rates for low-density, high-temperature plasma," *At. Data Nucl. Data Table* **20**, 397.
- Potter, D. (1978). "The Formation of High-Density Z-Pinches," *Nucl. Fus.* **18**, 813.
- Putnam, S., Stallings, C., Childers, K., Schneider, R., Rothe, I., Creedon, J., Bailey, V., and Young, T. S. T. (1979). "Recent Developments in Fast Z-Pinch Plasma Production Using Superterawatt Generators," in *Proceedings of International Conference on High-Power Particle Beams*, Santa Fe, NM, 1979.
- Riordan, J. C., Pearlman, J. S., Gersten, M., and Rauch, J. E. (1981). *Sub-Kilovolt X-ray Emission from Imploding Wire Plasmas*, AIP Conference proceedings, edited by D. Attwood and B. Henke (APS, New York), Vol. 75.
- Robson, A. E. (1987). "A Bibliography of the linear z-pinch," Naval Research Laboratory document, Washington, DC (unpublished).
- Rodenburg, R., Wong, S., Koppel, L., and Burr, L. (1985a). "Neon Source Optimization on Double-Eagle," in *Proceedings of the 1985 International Conference on Plasma Science*.
- Rodenburg, R., Wong, S., Koppel, L., and Burr, L. (1985b). "Observation of L-Series X-Ray Spectra Radiated by a High Temperature Nickel Plasma," presented at The 27th Annual Meeting, Plasma Physics Division, American Physical Society (unpublished).
- Roderick, N. F., Kohn, B. J., McCullough, W. F., Beason, C. W., Lupo, J. A., Letterio, J. D., Kloc, D. A., and Hussey, T. W. (1983). "Theoretical Modeling of Electromagnetically Imploded Plasma Liners," *Laser and Particle Beams* **1**, 181.
- Roderick, N. F. and Hussey, T. W. (1984). "A model for the saturation of the Raleigh-Taylor instability," *J. Appl. Phys.* **56**, 1387.
- Roderick, N. F. and Hussey, T. W. (1986a). "Magnetic diffusion smoothing with application to the hydromagnetic Raleigh-Taylor instability," *J. Appl. Phys.* **59**, 662.
- Roderick, N. F. (1986b). "Diffusion of azimuthal magnetic fields into a cylindrical plasma," *J. Appl. Phys.* **60**, 1269.
- Rozsnyai, B. F. (1982). "An Overview of the Problems Connected with Theoretical Calculations for Hot Plasmas," *J. Quant. Spectrosc. Radiat. Transfer* **27**, 211.
- Ruden, E., Rahman, H. U., Fisher, A., and Rostoker, N. (1987). "Stability enhancement of a low initial density hollow gas-puff z-pinch by e-beam preionization," *J. Appl. Phys.* **61**, 1311.
- Scudder, D. W. (1983). "Steady-state radial heat conduction in a z-pinch," *Phys. Fluids* **26**, 1330.
- Seeley, J. F. and Lee, T. N. (1984). "Density Measurement in a Vacuum-Spark-Discharge Microplasma from the Inner-Shell Excitation of Satellite Transitions," *Phys. Rev. A* **29**, 411.
- Sethian, J. D., Robson, A. E., Gerber, K. A., and DeSilva, A. W. (1987). "Enhanced stability and neutron production in a dense z-pinch plasma formed from a frozen deuterium fiber," *Phys. Rev. Lett.* **59**, 892. [erratum *Phys. Lett.* **59**, 1790].
- Shearer, J. W. (1976). "Contraction of Z pinches Actuated by Radiation Losses," *Phys. Fluids* **19**, 1426.
- Shiloh, J., Fisher, A., and Rostoker, N. (1978). "Z Pinch of a Gas Jet," *Phys. Rev. Lett.* **40**, 515.
- Shiloh, J., Fisher, A., and Bar-Avraham, E. (1979). "Interferometry of a Gas-Puff Z-Pinch Plasma," *Appl. Phys. Lett.* **35**, 390. Also, Ph.D. thesis, "High density z-pinch," UC Irvine, 1978.
- Sincerny, P., Wong, S., Buck, V., Gilman, C., and Sheridan, T. (1985). "Pulsed Compression with an Imploding Gas Puff," in *Proceedings of IEEE 5th Pulsed Power Conference* (unpublished).
- Skowronek, M. and Romeas, P. (1985). "Experimental Study of the Current Penetration in a Dense Z Pinch," *J. Appl. Phys.* **57**, 2519.
- Smith, R. S., Doggett, W. O., Roth, I., and Stallings, C. (1982). "Supersonic Gas Shell for Puff Pinch Experiments," *Appl. Phys. Lett.* **41**, 572.
- Smith, R. S. and Doggett, W. O. (1985). "Experimental characterization of a puff-gas z-pinch plasma prior to implosion," *Appl. Phys. Lett.* **46**, 1128. Also, Ph.D. thesis, North Carolina State University, Raleigh, 1985.
- Solov'ev, L. S. (1984). "Dynamics of a Cylindrical Z pinch," *Fiz. Plazmy* **10**, 1045 (*Sov. J. Plasma Phys.* **10**, 602).
- Sobelman, I. I., Vainshtein, L. A., and Yukov, E. A. (1981). *Excitation of Atoms and Broadening of Spectral Lines* (Springer, Berlin).
- Spielman, R. B., Hanson, D. L., Palmer, M. A., Matzen, M. K., Hussey, T. W., and Peck, J. M. (1985a). "Efficient X-ray Production from Ultrafast Gas-Puff Z-Pinches," *J. Appl. Phys.* **57**, 830.
- Spielman, R. B., Matzen, M. K., Palmer, M. A., Rand, P. B., Hussey, T. W., and McDaniel, D. H. (1985b). "Z-Pinch Implosions onto Extremely

- Low-Density Foam Cylinders," *Appl. Phys. Lett.* 47, 229.
- Stallings, C., Nielsen, K., and Schneider, R. (1976). "Multiple-Wire Array Load for High-Power Pulsed Generators," *Appl. Phys. Lett.* 29, 404.
- Stallings, C., Childers, K., Roth, I., and Schneider, R. (1979). "Imploding Argon Plasma Experiments," *Appl. Phys. Lett.* 35, 524.
- Stephanakis, S. J., Apruzese, J. P., Burkhalter, P. G., Davis, J., Meger, R. A., McDonald, S. W., Mehlman, G., Ottinger, P. F., and Young, F. C. (1986). "Effect of Pulse Sharpening on Imploding Neon Z-Pinch Plasmas," *Appl. Phys. Lett.* 48, 829.
- Stormberg, H.-P., Murayama, S., and Watanabe, Y. (1987). "Angular distribution of x-ray radiation from optically thick z-pinch plasmas," *J. Appl. Phys.* 62, 4090.
- Striganov, A. R. (1983). "Progress in studying the spectra of atoms and ions and the current level of knowledge about them," *Usp. Fiz. Nauk.* 139, 719 (*Sov. Phys. Usp.* 26, 373).
- Stewart, R. E., Dietrich, D. D., Egan, P. O., Fortner, R. J., and Dukart, R. J. (1987). "Spectroscopic studies of an argon plasma produced in a relativistic electron beam gas puff z-pinch," *J. Appl. Phys.* 61, 126.
- Trubnikov, B. A. (1986). "Particle acceleration and neutron production at the necks of plasma pinches," *Fiz. Plazmy* 12, 468 (*Sov. J. Plasma Phys.* 12, 271).
- Turchi, P. J. and Baker, W. L. (1973). "Generation of high-energy plasmas by electromagnetic implosion," *J. Appl. Phys.* 44, 4936.
- Vertennikov, V. A., Polukhin, S. N., Semenov, O. G., Sidel'nikov, Yu. V. (1981). "Dynamics of a Vacuum-Arc Micropinch," *Fiz. Plazmy* 7, 1199 (*Sov. J. Plasma Phys.* 7, 656).
- Veretennikov, V. A., Dolgov, A. N., Krokhin, O. N., and Semenov, O. G. (1985a). "Micropinch Structure in a High-Current Discharge," *Fiz. Plazmy* 11, 1007 (*Sov. J. Plasma Phys.* 11, 587).
- Veretennikov, V. A., Polukhin, S. N., and Semenov, O. G. (1985b). "Measurement of Faraday rotation in z-pinches," *Fiz. Plazmy* 11, 1411 (*Sov. J. Plasma Phys.* 11, 814).
- Vikhrev, V. V. and Braginskii, S. I. (1980). "Dynamics of the z-pinch," in *Voprozy teorii plazmy*, edited by M. A. Leontovich (Atomizdat, Moscow), Vol. 10. Translated in *Reviews of Plasma Physics* (Consultants Bureau, New York, 1986), Vol. 10.
- Vikhrev, V. V., Ivanov, V. V., and Koshelev, K. N. (1982). "Formation and Evolution of the Micropinch Region in a Vacuum Spark," *Fiz. Plazmy* 8, 1211 (*Sov. J. Plasma Phys.* 8, 688).
- Vikhrev, V. V. and Ivanov, V. V. (1985). "Propagation of a high-temperature plasma along a z-pinch," *Sov. Phys. Dokl.* 30, 492.
- Vikhrev, V. V., Ivanov, V. V., and Prut, V. V. (1986). "Dynamics of a Z-pinch with radiative loss," *Fiz. Plazmy* 12, 328 (*Sov. J. Plasma Phys.* 12, 190).
- Vikhrev, V. V. (1986). "Mechanism for neutron production in z-pinches," *Fiz. Plazmy* 12, 454 (*Sov. J. Plasma Phys.* 12, 262).
- Vinogradov, A. V., Sobelman, I. I., and Yukov, E. A. (1975). "Possibility of constructing a far ultraviolet laser utilizing transitions in multiply charged ions in an inhomogeneous plasma," *Kvant. Electron. (Moscow)* 2, 105 (*Sov. J. Quantum Electron.* 5, 59).
- Waisman, E. M. (1979). "The magnetostatic field of a periodic cylindrical array of perfect conductors of arbitrary x-y cross section," *J. Appl. Phys.* 50, 23.
- Warren, S. W. R., Degnan, J. H., Beason, C. W., Price, D. W., and Snell, M. P. (1987). "High-energy photon spectra from a coaxial gas-puff experiment," *J. Appl. Phys.* 61, 2771.
- Weinberg, I. N. (1985a). "X-ray lithography and microscopy using a small-scale z-pinch device," Ph.D. thesis, UC Irvine, CA.
- Weinberg, I. N. and Fisher, A. (1985b). "Elemental Imaging of Biological Specimens Using a Z Pinch," *Appl. Phys. Lett.* 47, 1116.
- Weinberg, I. N. and Fisher, A. (1986). "A small-scale z-pinch device as an intense soft x-ray source," *Nucl. Instrum. Methods A* 242, 535.
- Wessel, F. J., Felber, F. S., Wild, N. C., Rayman, H. U., Fisher, A., and Ruden, E. (1986). "Generation of High Magnetic Fields Using a Gas-Puff Z Pinch," *Appl. Phys. Lett.* 48, 1119.
- Whitney, K. G. and Kepple, P. C. (1982). "Spectrum Diagnostics. The Necessity for Detailed Non-LTE Modeling of X-ray Emission from Dense Plasmas," *J. Quant. Spectrosc. Radiat. Transfer* 27, 281.
- Winick, I. and Doniach, S., Eds. (1980). *Synchrotron Radiation Research* (Plenum, New York).
- Wong, S., Gilman, C., Sincerny, P., and Young, T. (1982). "A Scaling Law for K-Line Radiation in the Imploding Argon Gas Puff," in *Proceedings of the 1982 IEEE Plasma Science Conference* (unpublished).
- Wong, S., Dukart, R., and Burr, L. (1984). "Imploding Gas Puff on Single Wires," Presented at the 26th Annual Meeting, Plasma Physics Division, American Physical Society (unpublished).
- Young, F. C., Stephanakis, S. J., and Scherrer, V. E. (1986). "Filtered x-ray diodes for imploding plasma experiments," *Rev. Sci. Instrum.* 57, 2174.
- Zakharov, S. M., Ivanenkov, G. V., Kolomenskii, A. A., Pikuz, S. A., and Samokhin, A. I. (1983). "Exploding-Wire Plasma in the Diode of a High Current Accelerator," *Fiz. Plazmy* 9, 469 (*Sov. J. Plasma Phys.* 9, 271).
- Zakharov, S. M., Ivanenkov, G. V., Kolomenskii, A. A., Pikuz, S. A., and Samokhin, A. I. (1984). "Pinch Effect in the Plasma of a Laser Burst in the Diode of a High-Current Accelerator," *Fiz. Plazmy* 10, 522 (*Sov. J. Plasma Phys.* 10, 303).
- Zakharov, S. M., Ivanenkov, G. V., Kolomenskii, A. A., Pikuz, S. A., and Samokhin, A. I. (1987). "Plasma of an exploding multiwire load in the diode of a high-current accelerator," *Fiz. Plazmy* 13, 206 (*Sov. J. Plasma Phys.* 13, 115).

Plasma points and radiative collapse in vacuum sparks

K. N. Koshelev

Institute for Spectroscopy, USSR Academy of Sciences, 142092 Troitsk, USSR

N. R. Pereira

Berkeley Research Associates, P. O. Box 852, Springfield, Virginia 22150

(Received 2 April 1990; accepted for publication 5 February 1991)

This review discusses the intense x-ray emitting regions, called plasma points, that appear in low-inductance vacuum sparks and other high-current discharges. Accurate x-ray spectroscopy indicates the existence of two types of plasma points with different plasma parameters. One type is extremely small (\sim microns), dense ($\sim 10^{23}/\text{cm}^3$), and hot (≥ 1 keV), while the second type is an order of magnitude less extreme. A dynamic model (Vikhrev 1982a) based on radiation cooling with axial outflow of plasma predicts a radiative collapse that is consistent with many features of the plasma points.

I. INTRODUCTION

The high voltage vacuum discharge was proposed more than 70 years ago as a spectroscopic source (Millikan 1918). The original apparatus operated at high voltage with a relatively modest current, typically 100 kV and less than 100 kA. In the mid-sixties (Cohen 1968) the power of the trigger electrode was increased, the inductance was reduced to less than about 100 nH and the voltage to ~ 20 –50 kV, while the capacitance was increased to ~ 10 –20 μF . The resulting apparatus is the "low-inductance vacuum spark."

The peak current in the low-inductance vacuum spark is more than 100 kA, and the trigger injects a significant amount of material in the interelectrode vacuum. Both the higher current and the presence of material between the electrodes are needed to make the low-inductance vacuum spark into an intense source of x-rays from highly ionized ions. The low-inductance vacuum spark is now a widely used research tool and an intensively studied research object. The discharge has many interesting features that are easily observed qualitatively but were unanticipated theoretically, e.g., pulsed x rays, multiply ionized atoms, and electron and ion beams.

It is relatively easy to produce hot, highly ionized plasma despite the low-inductance vacuum spark's modest energy (~ 3 –30 kJ). Already the first experiments (Cohen 1968) measured spectra of He- and H-like ions of titanium and iron (Ti XXI–XXII; Fe XXV–XXVI); somewhat later (Beier 1978) observed the resonance transition of the He-like ion Mo XLI ($\lambda = 0.69$ Å). In pinhole photographs the K-line radiation appears to come from small, pointlike regions in the plasma that are called plasma points, bright spots, or hot spots. The relative simplicity and high shot rate of the low-inductance vacuum spark allow a thorough study of the formation dynamics of the plasma point and the properties of its plasma.

This review describes experimental investigations of the plasma point in low-inductance vacuum sparks. In addition, the review interprets many aspects of the plasma points with the radiative collapse model (Vikhrev 1982a; Koshelev 1985). The literature contains alternate models

that we mention but do not discuss because, in our opinion, they are not far enough developed for comparison to experiment. Likewise, we do not discuss in detail the bright spots that occur in more powerful discharges because their analysis emphasizes bulk x-ray production by implosion (Pereira 1988b). However, plasma points and bright spots appear to be related, and insight in plasma points could become useful in understanding bright spots.

It should be emphasized that the plasma point is by its very nature a dynamic phenomenon with constantly changing parameters. For example, during its development the temperature of the plasma point changes from tens of electron volts to several kilovolts. The size and density of the plasma point also change significantly, e.g., from 1 mm to less than 10 μm and from $10^{19}/\text{cm}^3$ to $10^{23}/\text{cm}^3$. Moreover, the plasma point must have spatial gradients in temperature and density that cannot always be resolved experimentally. Therefore it is necessary to keep in mind that a particular measurement may apply only to a specific phase in the development of the plasma point. This realization may help eliminate disparities between experimental results, resulting in an improved description of the plasma point.

A previous review (Korop 1979) summarizes the first ten years of research on the low-inductance vacuum spark. The devices used in various laboratories (e.g., Cilliers 1975; Turechek 1975; Golts 1975; Kononov 1977; Veretenikov 1981; Negus 1979; Morita 1983) have capacitances of 10–30 μF charged to 10–20 kV, with a circuit inductance of 50–100 nH. The discharge current is typically a damped sinusoid with peak amplitude $I_m \approx 150$ –200 kA and pulse length ≈ 1.5 –2 μs . The discharge is ignited by an electrical trigger in the cathode or by irradiating the anode with a powerful laser (Lee 1974; Koloshnikov 1985).

With an electrical trigger the initial stage of the discharge is characterized by an erratic initial current and an x-ray pulse from the anode, and by the formation of plasma jets from the electrodes (e.g., Epstein 1970). The trigger pulse forms the cathode plasma: the anode plasma is produced by bombardment of the anode surface by a beam of electrons from the cathode plasma accelerated in the electric field between the electrodes. The anode and cathode

plasmas move toward each other with velocities $\approx 10^6$ cm/s. The initial phase is complete when plasma bridges the vacuum gap: the voltage across the gap V_g drops to $V_g = L_g di/dt$ (L_g is the inductance of the current channel).

In the next phase of the discharge the current increases as prescribed by the circuit voltage V and inductance L of the circuit, $di/dt = V/L$. On top of the smoothly rising current there appear short (< 100 ns) single or multiple dips in the current. These current dips are accompanied by intense bursts of x rays. The dips have a random character, although many authors have noted that they depend on discharge initiation, circuit parameters, and the material and shape of the electrodes (e.g., Cilliers 1975; Negus 1979).

The current dips are correlated with the appearance of plasma points. The plasma point principally emits x-ray lines from ions of the anode material; radiation from cathode material is weak. However, the trigger to the cathode must be sufficiently strong for a plasma point to develop (Sidel'nikov 1982a).

Triggering the low-inductance vacuum spark by irradiating the anode with a laser produces the anode jet directly. The erratic initial current is now absent, and the current starts slightly after the laser pulse. After this initial stage the discharge develops as described above (Koloshnikov 1985).

The x-ray pulses correlated with the dips in the current and the formation of plasma points contain photons with a wide range of energies, typically $h\nu \approx 5\text{--}150$ keV (e.g., Cohen 1968; Lee 1974; Cilliers 1975; Veretennikov 1981). The x-ray spectrum contains information about the plasma in the plasma point. The name "plasma point" is particularly apt when looking at photons with $h\nu < 10$ keV, corresponding to resonance transitions in He- and H-like ionization states of moderately heavy ions (nuclear charge $Z_n < 30$); the points are often less than $10\ \mu\text{m}$ in size.

Higher energy photons may appear to be less localized. Typically, the x-ray spectrum below $h\nu \sim 150$ keV is emitted from a plasma with electron temperature $T_e \sim 10$ keV. For the relatively few photons with $h\nu > 150$ keV the spectrum decreases with photon energy according to a power law (Cilliers 1975; Fukai 1975). Some discharges show even more energetic quanta with energies $h\nu > 500$ keV (Lee 1974).

This review is principally concerned with the two types of plasma points (Aglitskii 1986; Antsiferov 1989) that appear in low-inductance vacuum sparks. The first type consists of a minute region of ions stripped to the K -shell, with size around $\sim 10\ \mu\text{m}$ or less as shown below in Fig. 1. According to the radiative collapse theory a type-1 plasma point is a short stage in the radiative collapse of a pinch: the collapse process is called micropinching, and a type-1 plasma point is sometimes called a micropinch. A type-2 plasma point is an order of magnitude larger and radiates few (or no) resonance lines: its radiation is insufficient for a full collapse, and is sometimes referred to as a hot (or bright) spot.

Not all localized regions of intense x-ray emission in

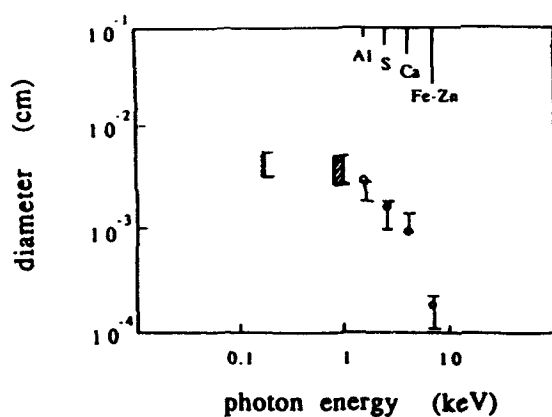


FIG. 1. Plasma point size vs photon energy $1 < h\nu < 10$ keV of the resonance line (the corresponding element is on top). The bracket is the size of an iron plasma point measured with softer photons exceeding 1 keV, the line around 0.1 keV is the size seen with softer photons.

other types of vacuum sparks or other pulse power devices can be classified in these two categories. For example, some generators of short electrical pulses used in exploding wire research have a sizable prepulse. The prepulse could result in a hollow cylinder of plasma surrounding the wire (e.g., Aranchuk 1986), and develop into striations that radiate x rays. These structures fall outside the present review.

Intense soft x-ray emission from small regions is also common in radiative z-pinch discharges on relativistic electron beam generators (Pereira 1988b). These z-pinch differ from vacuum sparks in their higher currents (~ 1 MA) and shorter pulse times (~ 100 ns); moreover, z-pinch have ample material between the electrodes before the start of the electrical pulse. In the context of z-pinch these regions are called "bright spots" (or sometimes hot spots): their diameter is quoted as $50\text{--}100\ \mu\text{m}$ (Stallings 1979; Burkhalter 1979; Riordan 1981). Compared to the extremely high electron densities ($n_e \sim 10^{23}/\text{cm}^3$) in low-inductance vacuum sparks, the x-ray spectra in z-pinch indicate much lower electron densities, even in the bright spots ($n_e \sim 10^{21}$; e.g., Deeney 1989). Perhaps these lower values reflect the spectral features used in the interpretation. However, when a single group looks at both vacuum sparks and z-pinch the bright spots in z-pinch seem identical to plasma points (Alikhanov 1984; Gol'ts 1986; Gol'ts 1987). They document a 1-MA discharge through a gas puff in Kr ($Z_n = 36$) and Xe ($Z_n = 54$), with plasma points of $\approx 5\ \mu\text{m}$ diameter in He-like Kr and Xe. At this time we believe that bright spots in z-pinch are similar to plasma points in vacuum sparks, at least in part (e.g., Sopkin 1990). The same is true for the bright spots seen in the plasma focus, but this device, used mostly for thermonuclear fusion research, falls outside this review.

II. THE PLASMA POINT: EXPERIMENTAL DATA

This section describes the experimental results on the formation of the plasma points, their size, and the plasma parameters temperature and density. In the older literature these parameters have a confusingly large range of values.

One reason is the existence of two types of plasma points. Another reason is that plasma points are dynamic entities, wherein the plasma parameters change rapidly over a large range of values. Plasma thermometry or densitometry applies to a limited range of plasma parameters, and therefore each measurement method gives a value characteristic of the method's range of applicability. Section III below describes the radiative collapse model that gives a coherent description of plasma points.

A. Plasma point size

Already the first investigators of low-inductance vacuum sparks noted that very small regions in the plasma produce the bulk of the x rays. In pinhole pictures these regions show up as bright spots or points, whence their name plasma points. The plasma points are elongated: for example, in discharges of titanium and iron the size of the plasma point perpendicular to the discharge axis was estimated as $<3\text{--}4\ \mu\text{m}$ (Schwob 1972; Klapisch 1977), or $<10\ \mu\text{m}$ (Morita 1983; Veretennikov 1985) to $20\text{--}50\ \mu\text{m}$ (Lee 1975). Along the pinch axis the size is 3–10 times larger. These size measurements are typically carried out with pinhole cameras with filters that pass the resonance and characteristic lines of the respective elements (and the few available higher-energy photons). These measurements will be called "K measurements," because most photons originate in the K-shell of the element.

It became clear later that there are two types of K measurements. The first type of K measurement looks at the resonance lines, and characterizes the plasma point in the stage wherein the plasma consists of ions stripped to the K shell. The second type of K measurements sees characteristic lines of low-multiplicity ions. These lines are probably excited by suprathermal electrons or electron beams in a much cooler plasma.

The two types of K measurements define two types of plasma points: the plasma points of the first type are an order of magnitude smaller than the plasma points of the second type. Much confusion in published measurements was clarified by the recognition of these two types of plasma points (Aglitskii 1986; Antsiferov 1989; and below). For a wide range of elements they measure the K size of the plasma point from its magnified image through a square pinhole. The blurring of the edge determines the length and width of the plasma point even when the pinhole is relatively large.

A pinhole image gives an overestimate of the plasma size. When the pinhole is small compared to the x-ray source the source size is the size of the image divided by the magnification, but when the pinhole is large compared to the source the image reflects the size of the pinhole irrespective of the dimensions of the source: a point source still produces an extended image. However, a point source gives an image with sharp edges, while the image is blurred with an extended source. The width of the blurring is the magnification times the source size if the effects from diffraction and film grain size are suppressed.

Fresnel diffraction smears out the image over a distance $\delta_f \sim \sqrt{\lambda R}$, where λ is the x-ray wavelength and R

is the distance between plasma point and the pinhole. For iron with $\lambda \sim 0.2\ \text{nm}$ and a typical distance $R \approx 2\ \text{cm}$ the Fresnel diffraction gives a contribution of $\approx 2\ \mu\text{m}$. The contribution from film grain size can be suppressed by using sufficient magnification: the grains are $\sim 10\ \mu\text{m}$, and their influence is reduced to below $2\ \mu\text{m}$ when the magnification exceeds ~ 5 . The total effect from Fresnel diffraction and grain size is therefore less than $\sim 2\ \mu\text{m}$. In addition, any motion of the source smears out the image and adds to the blurring of the edge, but this does not seem to be a problem (see below).

The plasma point size was measured carefully (Antsiferov 1989) in the resonance lines of He- and H-like iron, with $5\times$ magnification. Fresnel diffraction is eliminated by putting the pinhole close to the source, $1 < R < 5$. Parallel and perpendicular sizes are measured simultaneously by orienting the square pinhole along the axis of the discharge. The plasma point blurred the edge of the image less than $15\text{--}20\ \mu\text{m}$ perpendicular to the axis and $25\text{--}50\ \mu\text{m}$ along the axis. Thus, the perpendicular size d of the plasma point for this iron plasma is $d < 2\ \mu\text{m}$, and the aspect ratio $\alpha \sim 3\text{--}5$. Analogous measurements carried out for plasmas of aluminum ($Z_n = 13$) give $d \sim 20\text{--}30\ \mu\text{m}$, for a plasma of sulfur ($Z_n = 16$) and calcium ($Z_n = 20$) $d \sim 10\text{--}15\ \mu\text{m}$, and $d < 2\ \mu\text{m}$ for all heavier elements (Fe, $Z_n = 26$; Cu, $Z_n = 29$; Zn, $Z_n = 30$). The four right-most points in Fig. 1 give these K measurements for the size of the plasma point with the different elements as indicated.

The filter in front of the pinhole can be chosen to transmit the x rays from the L shell of moderately heavy elements, i.e., photons with $h\nu \sim 1\ \text{keV}$. The plasma point seen in this light is larger than indicated by the K measurements. For example, the perpendicular size of the plasma point in the L shell light for an iron pinch (Veretennikov 1985) is $\sim 30\ \mu\text{m}$, and the aspect ratio is $\sim 3\text{--}5$. Figure 1 gives this point by the rectangle around $h\nu \sim 1\ \text{keV}$.

Churilov *et al.* (1990) measured the plasma points size for iron in a broad range of the VUV spectrum, from $5\ \text{nm}$ ($0.25\ \text{keV}$) to $20\ \text{nm}$ ($0.08\ \text{keV}$), using a spatially resolved VUV spectrum from a grazing incidence spectrograph. Spatial resolution in the direction perpendicular to the discharge axis is possible with an additional slit. The blur in the edge of the spectrum allows the determination of the effective size of the source of emission for each of the wavelengths separately, similar to the size measurement with a square pinhole. The left-top line in Fig. 1 gives the results. The size of the iron plasma point decreases with wavelength, from $420\text{--}450\ \mu\text{m}$ for $\lambda = 20\ \text{nm}$ to about $300\ \mu\text{m}$ for $\lambda = 5\ \text{nm}$.

The existence of certain x-ray lines gives a rough indication of the plasma temperature. Therefore it is possible to correlate plasma point size with plasma temperature. How to determine the plasma point temperature is discussed in the next subsection.

B. Plasma point temperature

A stationary blob of plasma with uniform temperature, density, and size emits a complicated spectrum that is fully

characterized by these three parameters. In principle, only three spectral features suffice to determine the three parameters. The remainder of the spectrum can serve as a consistency check. However, determining the parameters for a real plasma point from a measured spectrum gives different values depending on which part of the spectrum is used.

Obvious reasons for this discrepancy are spatial gradients and time dependence. Spatial gradients are unavoidable when hot plasma is sitting in colder surroundings. Unfolding gradients from spectra measured along a line of sight is difficult, and therefore rarely done (Gersten 1986) despite the importance of gradients in virtually all plasma points.

In a plasma point the temperature changes over one or two orders of magnitude in such a short time (~ 30 ps) that only time-integrated spectra have been taken up to now. The time-integrated spectrum contains the signature of the various stages in the plasma point evolution. Each stage contributes principally to a specific spectral region, but with substantial overlap between the regions. Measurements of the plasma parameters could differ substantially, depending on the spectral region used for the measurement.

Additional problems arise if the plasma is not in ionization equilibrium as it heats up or cools down. Ionization equilibrium can only be obtained if the plasma goes through each ionization stage slowly, staying longer than a time τ that depends on the electron density, the element, and its ionization state (Kononov 1977, and below). For example, for a Ne-like iron plasma to reach the He-like ionization state $n_e \tau$ must exceed 10^{11} cm³/s. Sometimes a beam of electrons creates additional radiation. Given these complexities extreme caution is needed in unfolding experimentally measured spectra from plasma points (or any plasma). Much confusion in the published values of plasma parameters is due to insufficient appreciation of the complicated nature of plasma point spectra.

Consider the plasma point temperature. In the first experiments an electron temperature $T_e > 1-2$ keV was inferred from the K-line spectra of iron and titanium. On the other hand, measurement of the spectral distribution of more energetic photons in the continuous spectrum by differential filters (Lee 1974) (for photon energies $h\nu < 150$ keV) indicated electron temperatures $T_e \approx 10$ keV in the same plasma. That the inferred temperature increases with hardness of radiation is to be expected, but these measurements do not lead to a reasonable temperature for the plasma point. Spectral methods should be sufficient to distinguish plasmas with thermal, Maxwellian electron distributions from those with nonthermal but isotropic distributions (Pereira 1988a), or from thermal plasmas with an admixture of directional electron beams.

1. Temperature diagnostics with satellites of resonance lines

The plasma temperature can be found from the x-ray spectrum in various ways. Some methods use the continuous part of the spectrum, others employ line intensities of

highly stripped ions. For a transient plasma, such as the plasma point, one should select a method that is unaffected by time variation in plasma properties. The relative intensities of resonance lines and their dielectronic satellites (Gabriel 1972a) depend on temperature but not on ionization equilibrium in the plasma. Thermometry with this method, often used for the H- and He-like lines, is therefore ideal for transient plasmas, provided that the electron distribution is still Maxwellian.

For a "coronal" plasma the radiative decay of the resonant levels dominates over all types of collisional deexcitation. The intensity of the resonant line I_r in a coronal plasma is then proportional to the collisional excitation rate of the process $1s^2 + e \rightarrow 1s2p + e'$. Often the principal channel for excitation of the satellite is dielectronic capture of a free electron by a He-like ion in the ground state, $1s^2 + e \rightarrow 1s2e2e'$. Then both the resonant line and the satellites are excited from the same ground state, $1s^2$, and the relative intensity I_{sat}/I_r of the satellite line does not depend on the ionization state of the plasma. In addition, this ratio does not depend on the electron density (in the coronal case), and is most suitable to determine the electron temperature of the plasma.

Another excitation mechanism for doubly excited He-like ions is collisional excitation of the inner-shell of a Li-like ground state, $1s^22l + e \rightarrow 1s2l2l' + e'$. When this mechanism dominates the intensity ratio of satellites to the resonance line gives information on the ionization state of the plasma, more specifically about the relative population of Li- and He-like ions. The temperature of the plasma obtained in this case is called the "ionization temperature" T_z (Gabriel 1972b). In stationary equilibrium $T_e = T_z$. For most real sources the values T_e and T_z differ, which suggests that plasmas are typically not in equilibrium. The inequality $T_e > T_z$ indicates that the plasma is ionizing, while $T_e < T_z$ indicates a recombining plasma (Bhalla 1975).

In general the satellites are excited through both excitation channels, and it requires special effort to separate the contribution of each channel to the line intensity. When the lines strongly overlap, as usual for spectra from plasma points, it is still more difficult to determine the weight of each channel. Figure 2 contains two samples of realistic spectra to be analyzed later.

An elaborate fitting procedure (Kononov 1983; Kononov 1985) is necessary to obtain diagnostic information from strongly broadened and superposed spectra of a group of satellite transitions. This procedure constructs the spectrum from theoretical data for each of the excitation channels, taking into account the superpositions of the lines. The relative contributions needed to match the experimental spectrum then determines T_e and T_z . In high-density plasmas the collisional transfer between autoionized states $1s2l2l'$ causes further distortions of the spectral profile (see below). In turn these distortions can be used to determine the electron density.

The spectra from plasma points in sulphur, in Fig. 2(a), and from nickel in Fig. 2(b), are used as examples of this procedure in the next section.

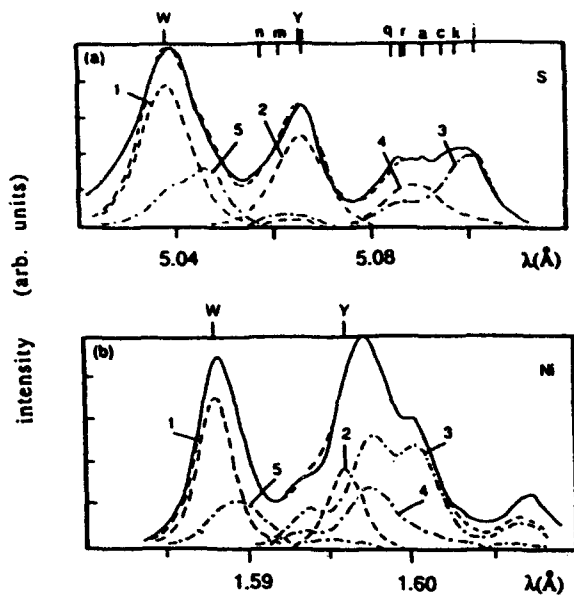


FIG. 2. Spectrum around the resonance line of (a) sulphur; and (b) nickel.

2. Measurements of T_e and T_z for elements from Mg to Cu

Kononov *et al.* (1985) used a fitting procedure to find the electron temperature for different compositions of the plasma points in a low-inductance vacuum spark with peak current ~ 200 kA. Spectra of the He- and H-like ions of Mg ($Z_n = 12$), Al ($Z_n = 13$), and S ($Z_n = 16$) were obtained using the 001 plane of a mica crystal ($2d = 19.9$ Å); for elements from Ca ($Z_n = 20$) to Cu ($Z_n = 29$) the crystal was the quartz 1011 plane, with $2d = 6.68$ Å. The instrumental line width was 3×10^{-3} Å around 5–9 Å (for Al, Mg, and S), and 8×10^{-4} Å in the region 1–3 Å (for Ca to Cu). These spectra are from up to 100 shots using a focusing crystal spectrograph in Johann geometry.

Figure 2(a) shows the spectrum (solid line) close to the resonance line of He-like S, and Fig. 2(b) gives the spectrum around the He-like resonance line of Ni. The unmarked dashed line gives the best fit; also shown are the contributions of some of the individual transitions in the marked dashed lines: "1" indicates the resonance line $1s^2(^1S_0) - 1s2p(^1P_1)$, and "2" the intercombination line $1s^2(^1S_0) - 1s2p(^3P_1)$. The broad structure "3" is the superposition of different satellite lines excited by dielectronic recombination, of which the "j" satellite is the strongest. The dashed line "4" is the intensity of the satellites due to collisional excitation of the K shell of the Li-like ground state, while "5" is the dielectronic satellite with principal quantum number n of the spectator electron $n > 3$, ($1s^2nl - 1s2pnl$). Their intensities are needed because these transitions form a strong long-wavelength wing to the resonance line, and may contribute significantly to its intensity. The calculated position (Vainshtein 1978) of the most intense satellites on the long-wavelength side of the resonance line (at 5.037 Å) for S, and 1.587 Å for Ni are

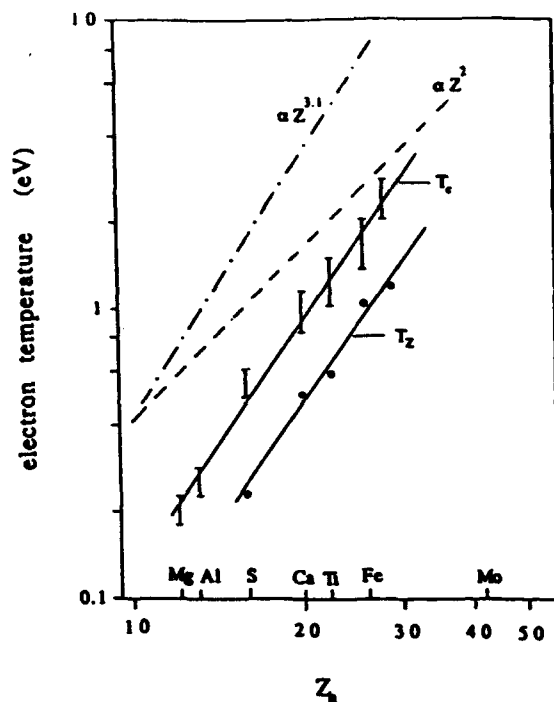


FIG. 3. Plasma point temperatures vs atomic number (or element). The bars come from the fitting procedure, the circles from the Li/He-like line ratio, and the dashed lines from the continuum (see text).

shown above the figure in the designation of Gabriel (1972b).

The spectra of Fig. 2 illustrate the complexity that can be treated. For other atoms, such as magnesium and aluminum, the satellite and resonance lines overlap little, and the electron temperature T_e can be obtained immediately from the relative intensity of the "j" satellite.

The bars in Fig. 3 give the electron temperature T_e as measured for many different elements (Kononov 1985). Within experimental error (about 10% due to densitometry and 20% from uncertainties in atomic modeling), the dependence of T_e on the nuclear charge Z_n is well described by

$$Z_n \approx 4.5 \times T_e \text{ (eV)}. \quad (\text{II.1})$$

The circles in Fig. 3 give the ionization temperature T_z determined by the relative abundance of Li- and He-like ions, $T_z(\text{Li/He})$. For all elements T_z turns out to be considerably smaller than the electron temperature inferred from the satellites to the resonance line of the He-like ion $T_e(\text{He})$. As already noted, $T_e > T_z$ suggests that the plasma point is being heated and ionized.

The electron temperature can also be determined from the relative intensity of satellites to the resonance line of the H-like ion. The electron temperature $T_e(\text{H})$ for iron turns out to be $T_e(\text{H}) \approx 4.5$ keV (Kononov 1977), much larger than the value $T_e(\text{H}) \approx 1.7$ keV measured with satellites to the helium-like resonance line. The relative intensities of the resonance transitions for H- and He-like ions, $I_{\text{H}}/I_{\text{He}}$, also gives an ionization temperature for the ioniza-

tion equilibrium between these two ionization states, $T_e(\text{He}/\text{H})$. However, in these experiments the electron temperature $T_e(\text{H}) \approx 4.5$ keV agrees with the ionization temperature $T_e(\text{He}/\text{H}) \approx 4$ keV (Kononov 1977), and with values from other investigators, $T_e(\text{He}/\text{H}) \approx 4.3$ keV (Negus 1979), and $T_e(\text{He}/\text{H}) \approx 4$ keV (Schwob 1972).

The older results are generally obtained using multiple overlapping spectra from many (typically 100) different shots. However, when comparing different single shots it turns out that $I_{\text{H}}/I_{\text{He}}$ varies much more from discharge to discharge than other intensity ratios used for diagnostics (Schultz 1989). The disparity between the results obtained by use of various methods will be considered below in discussing theoretical ideas on the nature of plasma points.

3. Measurement of the electron temperature with differential filters

We already noted that an iron plasma point gives a continuous spectrum up to photon energy $h\nu \approx 150$ keV. The continuous spectrum, often measured through differential filters, can also be used to define an electron temperature $T_e(f)$. For the iron pinch mentioned the continuous spectrum corresponds to an electron temperature $T_e(f) \approx 10$ keV (Lee 1974; Lee 1975). More recently, Burhenn (1984) measured the electron temperature in the plasma point as function of plasma composition. For iron the measurements give two different temperatures $T_e(f) \approx 2.7$ keV and $T_e(f) \approx 8.5$ keV, depending on the type of discharge. The dashed line in Fig. 3 displays the cooler temperature as function of the element in the plasma: it is given quite well by $T_e(f) \approx 4Z_n^2$ (eV). The hotter temperature, the dot-dashed line in Fig. 3, is approximately given by $T_e(f) \approx 0.32Z_n^{3.1}$ (eV).

The separate dependence of the temperature on atomic number suggests that there exist two types of discharges, each with its own dependence on atomic number. Other data (Antsiferov 1989) to be discussed later lead to the identification of two classes of plasma points, small and large. It turns out that $T_e \sim Z_n^2$ corresponds to the small plasma points while the $T_e \sim Z_n^{3.1}$ dependence reflects the radiation generated by an electron beam that occurs in a large plasma point.

C. The electron density of the plasma point

It has proven difficult to determine the electron density in the plasma point, let alone its spatial and temporal dependence. The first estimates, based on Bennett equilibrium for the plasma (Lee 1974), suggested $n_e \sim 10^{21}/\text{cm}^3$ for an iron plasma. Comparing the x-ray emission of the plasma point with theoretical calculations of radiation loss (Negus 1979) gives somewhat higher values, $n_e \sim 3 \times 10^{21} - 2 \times 10^{22}/\text{cm}^3$. Further experimental study led to a reexamination of these estimates. Lee's 1974 estimate was based on a plasma point radius $r \sim 15 \mu\text{m}$ and a plasma temperature $T_e \sim 8$ keV, but later it became clear that the radius of a plasma point in a "normal" regime of pinching is less than $2 \mu\text{m}$ for iron, and that the electron temperature T_e is about 2 keV (from dielectronic satellites). Using

these data increases Lee's estimate for n_e by two orders of magnitude, to $n_e \sim 10^{23}/\text{cm}^3$. The electron density estimate by Negus (1979) is also based on too large a value of the plasma point volume, $\Delta V \approx 4 \times 10^{-10} \text{cm}^3$, and on too high a temperature ($T_e \sim 4.3-7$ keV). The improved values for the plasma point volume and temperature used with the original radiated power (Negus 1979) now suggests $n_e > 10^{23}/\text{cm}^3$ for iron, in agreement with the more recent data discussed in this review.

An interesting observation is a peak in optical radiation at $\lambda \sim 760$ nm (Cilliers 1975). Interpreting this peak as collective bremsstrahlung radiation at twice the plasma frequency suggests an electron density $n_e \approx 5 \times 10^{20}/\text{cm}^3$. However, the optical light need not come from the high-density stage of the plasma point, but may reflect other stages of the discharge.

Until recently the only spectroscopic measurements of the electron density of the plasma point were done by Datla (1978/9), who used Stark broadening of the Rydberg lines in H-like and He-like magnesium and aluminum. Using He-like and H-like ions ensures that the information comes from the high-temperature stages of the evolution of the plasma point, when their emission is maximum. The result was $n_e \approx 5-10 \times 10^{21}/\text{cm}^3$. However, it was realized later that a significant part of the line broadening is due to the radial size of the plasma: the corrected value turns out to be around $n_e \approx 2-3 \times 10^{21}/\text{cm}^3$.

1. The electron density from collisional redistribution of satellite transitions

As already noted, some spectral methods give the temperature of a specific phase in the development of the plasma point. Likewise, the electron density should be measured only while the plasma is hot. The satellite spectrum changes with electron density by collisional transfer between the autoionizing states $1s2l2l'$. This effect in Li-like calcium and titanium was used to determine the electron density for a plasma point (Kononov 1980). A density effect was already observed in the satellite spectra of H-like Al and Mg in a laser-generated plasma (Bayanov 1976; Vinogradov 1977).

In the limit of small densities the population of the autoionized levels n_{ai} is determined by

$$n_{ai} = n_{ai}^* \times \frac{\Gamma_i}{\Gamma_i + A_i} \quad (\text{II.2})$$

Here n_{ai}^* is the Saha-Boltzmann equilibrium population of the autoionizing state with respect to the ground state: for Li-like ions this is the He-like $1s^2$. Also Γ_i is the autoionization rate, and $A_i = \sum_j A_{ij}$ is the total radiative decay rate, the sum of all possible decay rates A_{ij} from level i to level j . For a metastable level ($i=1$) the radiative decay rate is small, $A_1 \ll \Gamma_1$, and the population is close to equilibrium, $n_1 \approx n_1^*$. At the same time, for a level ($i=2$) with fast radiative decay, $\Gamma_2 \ll A_2$, the population can be much less than the equilibrium, $n_2 \sim n_2^* \times (\Gamma_2/A_2) \ll n_2^*$.

In a plasma with sufficiently high electron density one must include the transfer of excitation between levels as a result of electron-ion collisions. In a two-level approxima-

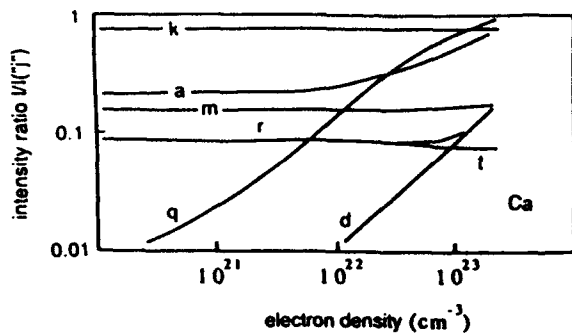


FIG. 4. Intensity of various satellites of calcium with respect to the resonance line, as function of electron density.

tion this effect leads to (collisional) transfer of an excited level from a metastable level (1) to a radiating level (2), which appears as an increased intensity of the corresponding (2) satellite. Calculations show that the "q" satellite is particularly sensitive to collisional transfer effects, and thus to the electron density.

Kononov *et al.* (1980) determine the effect of electron density on the relative population of the satellites using all possible collisional transfers between the levels $1s2s^2$, $1s2s2p$, and $1s2p^2$ of calcium. In stationary state this leads to a system of linear algebraic equations:

$$n_{ai} \times \left(\sum_j A_{ij} + \Gamma_i + n_e \times \sum_j C_{ij} \right) - n_e \times \left(\sum_j n_{aj} C_{ji} \right) = \omega_i \Gamma_i \quad (\text{II.3})$$

Here C_{ij} is the rate of collisional transfer from state i to j , and ω_i is the statistical weight of the i th state. The summations are over the number of levels of the $1s2l2l'$ configuration.

The results in Fig. 4 come from calculations with 16 levels of calcium, at about 1 keV where He-like calcium is abundant. The figure shows the intensities of calcium's satellite lines "a," "d," "k," "m," "q," "r," and "t" relative to the intensity of the "j" satellite as function of electron density. In the region of interest, $n_e \sim 10^{22} - 10^{23}/\text{cm}^3$, only the "q" and the "d" satellite depend strongly on electron density, with a smaller density effect on the "a" satellite. The "q" satellite is most useful as a density diagnostic because the dependence is relatively strong, changing from 1% to about 100% of the intensity of the "j" satellite in the density region of interest. For higher densities the "a" satellite may also become useful.

The solid line in Fig. 5 gives an experimental spectrum in the region of the resonance line Ca XIX. The solid line at the top of the figure around 3.199 Å (marked 5) is the difference between the experimental spectrum and the computed spectrum without the density effect. The difference curve is located at the theoretical wavelength for the "q" satellite. The shape of the difference is reminiscent of the computed single line profile, which suggests that the observed difference can be accounted for by increasing the intensity of the "q" satellite by increasing the electron den-

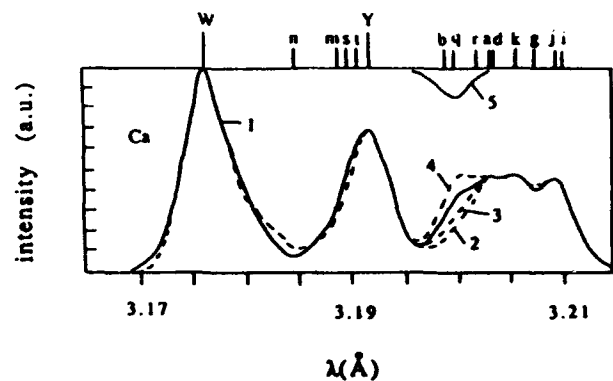


FIG. 5. Calcium spectrum (solid line) around the resonance line (W), the intercombination line (Y), and the satellite lines, with various fits for different densities (dashed lines): 1: $n_e < 10^{20}/\text{cm}^3$; 2: $n_e = 10^{22}/\text{cm}^3$; 3: $n_e = 3 \times 10^{22}/\text{cm}^3$; 4: $n_e = 10^{23}/\text{cm}^3$; Solid line 5 (on top) is the difference between the measured spectrum and the spectrum computed without the density effect.

sity. The dashed lines in Fig. 5 are the theoretical spectra computed for electron densities $10^{22}/\text{cm}^3$ (curve 2), $3 \times 10^{22}/\text{cm}^3$ (curve 3), and $10^{23}/\text{cm}^3$ (curve 4). The best fit to the experimental spectrum is obtained for $n_e \approx 5 \times 10^{22}/\text{cm}^3$. Analogous measurements of electron density were made for a titanium plasma, with similar results. The density determination using the "q" satellite (Kononov 1980) was apparently the first direct evidence for an extremely high electron density in the plasma point, on the order of $10^{23}/\text{cm}^3$.

For plasma points with heavier elements such as iron ($Z_n = 26$), nickel ($Z_n = 28$) or copper ($Z_n = 29$) the density can, unfortunately, not be found from the "q" satellite, because for these elements this line overlaps with the intercombination line "y" of the He-like ion, the $1s^2(^1S_0) - 1s2p(^3P_1)$ transition.

The procedure has been used with other K lines. For example, the density dependence of the satellites to the resonance line of the H-like ion Ti XXII (Seely 1984) gives $n_e \sim 1.5 \times 10^{23}/\text{cm}^3$, in good agreement with the above-described measurements. Other measurements show that the density increases with nuclear charge, from about $3 \times 10^{21}/\text{cm}^3$ for Al, to $10^{23}/\text{cm}^3$ for Ca and Ti, and $> 10^{23}/\text{cm}^3$ for Fe.

Like the other parameters of the plasma point the density changes in time. However, each spectral line occurs only during a specific state in the evolution of the plasma. Determining both temperature and density from the same spectral data preserves the proper relation between T_e and n_e during the collapse process.

D. Investigation of pinch dynamics

The first space-time study of the plasma point in the low-inductance vacuum spark was done with high-speed photography in visible light (Lee 1971; Lee 1974). These experiments showed the beginning stage of the pinching of the discharge channel after filling the inner electrode space by high-conductivity plasma. It was shown that the pinch-

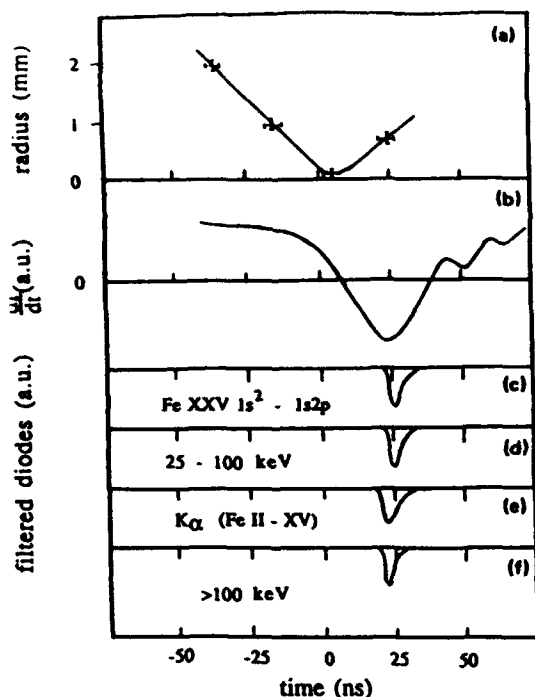


FIG. 6. Temporal characteristics of the low-inductance vacuum spark discharge: (a) r t diagram of the pinching of the plasma in the region of the pinch and characteristic oscillograms; (b) derivative of the discharge current; (c)–(f) x-ray pulses of the low-inductance vacuum spark in various energy bands. The time $t=0$ corresponds to the beginning of emission of the resonance line Fe XXV, i.e., to the moment of formation of the micropinch.

ing was local, producing a constriction. However, the space-time resolution of this method is insufficient to observe compression of the plasma to less than 1 mm. Laser shadowgraphy with five frames, together with time-correlated observation of the current and x-ray pulses in various photon energy bands (Veretennikov 1981a; 1981b), gives a quite complete picture of the compression of the plasma column up to the formation time of the plasma point and its breakup.

The shadowgrams typically show an $m=0$ Raleigh-Taylor instability. In the early stage of the discharge the radial velocity v_r is approximately $v_r \approx 10^6$ cm/s, increasing to $\approx 5 \times 10^6$ cm/s close to the time of minimum radius when the neck is formed.

Figure 6(a) shows a composite r t diagram, obtained from many different shadowgrams of an iron pinch, with error bars indicating the temporal and spatial resolution of 1.5 ns and 100 μ m: note that this measurement does not resolve the minimum size of the pinch in K light (see Fig. 1). Figure 6(b) is a typical trace of the current derivative dI/dt . The current reaches its maximum ($dI/dt=0$) around the time of the minimum radius, while dI/dt is minimum about 25 ns thereafter.

Figures 6(c)–6(f) contain the x-ray pulses from this pinch correlated to within 0.5 ns resolution with the current trace of Fig. 6(b). The x-ray is resolved in four rough energy bands, viz., Fig. 6(c) resonance lines of he-

lium-like Fe XXV and their satellites (1.84–1.87 \AA); Fig. 6(d): hard x rays with photon energies $h\nu = 25$ –100 keV; Fig. 6(e): K_{α} radiation of ions of low ionization multiplicity (1.93–1.96 \AA); and Fig. 6(f): hard x rays with $h\nu > 100$ keV.

The harder x rays appear from 15 to 25 ns after the occurrence of the minimum radius as seen in the shadowgram, and the current maximum. This timing indicates that the plasma point forms about 20 ns after maximum compression. A separate x-ray pinhole photograph shows that the plasma point sits in the neck of the pinch.

The beginning of the characteristic K_{α} radiation from the partly stripped ions Fe II to Fe XVII, Fig. 6(e), coincides with the emission of x rays in the hard x-ray band $h\nu > 100$ keV, Fig. 6(f). However, this pulse starts typically 3 ns before the beginning of the x-ray pulse in He-like resonance lines of Fe XXV stripped to the K shell, Fig. 6(c): this last pulse coincides with the x-ray pulse in the photon energy range 25–100 keV, Fig. 6(d). These data are similar but more precise than earlier observations on a copper pinch (Lee 1974).

The electron temperature and density inferred from the data in Fig. 6 do not match the spectroscopic measurements. The pinch region in the shadowgram is opaque because the light frequency ω_0 is less than the plasma frequency $\omega_e = \sqrt{n_e e^2 / \epsilon_0 m}$ (Veretennikov 1981a,b). This leads to a lower limit for the electron density on axis, $n_e > 10^{20}/\text{cm}^3$. Another estimate is obtained from the pinch size in VUV light as displayed in Fig. 1. A ~ 100 μ m radius corresponds to 0.5-keV photon energy and 0.2-keV temperature. The Bennett relation (with $I \approx 200$ kA) then gives $n_e \approx 2 \times 10^{21}/\text{cm}^3$. A similar upper limit to the density, $n_e < 10^{21}/\text{cm}^3$, has been obtained by conservation of line density during compression of an initially tenuous plasma (Negus 1979). In contrast, spectroscopic measurements using the resonance lines of high-Z (Z_n 20–30) elements give densities of $n_e \sim 10^{23}/\text{cm}^3$ and temperatures $T_e \sim 2$ keV (see Fig. 1).

The different data can be reconciled by a model with two compression stages. The first stage, the relatively slow hydrodynamic compression seen by the shadowgraphy, creates a neck of warm plasma and the conditions for a second compression. This second compression is consistent with the radiative collapse model of Vikhrev (1982a) as described in Sec. III below. Radiative collapse creates the plasma point.

In the hydrodynamic compression stage the plasma heats up to a moderate temperature consistent with the occurrence of partly stripped ions like Fe II to Fe XVII: K_{α} radiation from these ions and hard x rays with $h\nu > 100$ keV indicates that nonthermal processes occur in addition. Subsequently, the plasma point develops. This second stage takes place on a fast, nanosecond-like timescale inside the plasma neck. Its hot, dense plasma is consistent with the emission of resonance lines of He-like Fe XXV, and with x rays in the 25–100 keV energy range.

The second compression stage leading to the plasma point is faster (< 100 ps) than the response time of the diagnostics for Fig. 6. A soft x-ray emission time of 60–100

ps was estimated with a fast x-ray streak camera, indicating that the hot phase of the plasma point is comparably short (Peacock 1968). Aglitski *et al.* (1985) used high-resolution spectroscopic equipment for a precise measurement of the line shape and position of the resonance line of He-like iron. The shape of the lines indicates Doppler broadening from radial expansion (or contraction) with velocity $v_r \sim 2-3 \times 10^7$ cm/s, while the Doppler shift suggests a velocity for the total plasma point of less than $v_p \sim 10^7$ cm/s. From the apparent size of the plasma point, about $r_p \sim 2 \mu\text{m}$, they conclude that the radiation lasts about $r_p/v_p \sim 20$ ps.

The remainder of this review describes the radiative collapse of the plasma into a plasma point in more detail, principally from the theoretical side but with reference to experimental data where appropriate.

III. RADIATIVE COMPRESSION MODEL FOR THE PLASMA POINT

A successful model for the plasma point must explain its high (~ 2 keV) temperature, high ($\sim 10^{23}/\text{cm}^3$) electron density, small ($\lesssim 10 \mu\text{m}$) size, and short (~ 30 ps) lifetime. Presently the most developed model for the plasma point is a radiative collapse theory in the form proposed by Vikhrev *et al.* (1982a). In an approximate way this theory reproduces the scaling of the plasma point parameters with the atomic number of the pinch material. In a radiative collapse the plasma point is heated by compression and Joule heating. Beams of high-energy electrons are considered a minor influence for the energetics, and they are not part of the model. Below we discuss the radiative compression model in some detail.

Over the years certain aspects of plasma points have been explained in different ways. An early theory assumed that the plasma points are electrode dust ejected and heated by an electron beam (Negus 1979). A plasma point-sized microparticle with a 0.01 mm diameter is easily heated by a 100 kA beam of 10 keV electrons, or a fluence of 10^{15} W/cm². Getting to keV-like temperatures demands no more than $\sim 10^{16}$ W/cm³, allowing for a deposition length of 1 mm along the pinch axis in agreement with the elongated shape of the plasma point.

However, other observations contradict this model. Beam heating predicts pancake-shaped plasma points, because 10 keV electrons penetrate only a fraction of a micron into a solid. Also, a plasma point heated by fast electrons would be the source of the hard x rays, while in experiments the hard x-ray emission comes from between the plasma point and the anode. And in gas-puff z pinches electrode-generated microparticles should not appear, but the gas-puff pinches do show plasma points.

Other explanations of the plasma point emphasize the radiation produced by electron beams, i.e., plasmas with non-Maxwellian and anisotropic electron energy distributions. There is no doubt that electron beams exist in low-inductance vacuum spark discharges (Welch 1974; Choi 1987). In other discharges electron beams have been measured directly (Kania 1984) and inferred from spectroscopic data (Hammel 1984; Hares 1985). In the theoretic

cal approach we favor, the radiative collapse model, the electron beams do not cause the plasma point, but the plasma point could create an electron beam. Electron beams are mentioned in this review solely for their effect on the radiation.

In our opinion the radiative collapse model is the only reasonably complete approach that accounts for the formation of plasma points. For this reason we spent the bulk of this review on an account of this model, and a discussion of the relevant experimental data.

A. Historical development of plasma point theory

Various aspects of plasma point formation with compression and Joule heating were first formulated in connection with research on nuclear fusion with deuterium pinches. In these experiments the dense plasma located on the axis of the discharge produces soft x rays, accompanied by neutrons and high-energy ion and electron beams (Filippov 1983; Trubnikov 1976).

A uniform hydrogen pinch in radial force equilibrium (Bennett 1934) has a critical current determined by power between Joule heating and optically thin bremsstrahlung (Pease 1957; Braginskii 1957). The Pease-Braginskii current for hydrogen, $I_{PB}^H \approx 1.6$ MA, applies to fusion-like parameters with a Coulomb logarithm $\sqrt{\ln \Lambda} \approx 10$. For other plasma parameters I_{PB}^H changes weakly with the Coulomb logarithm. Apart from the weak dependence on plasma parameters through the Coulomb logarithm the Pease-Braginskii current does not depend on the temperature T because Joule heating and bremsstrahlung both increase with temperature as $T^{1/2}$, at least when line density, current, and temperature are connected by the Bennett relation $NT \propto I^2$. Likewise, with decreasing radius r both Joule heating and optically thin radiation increases as $1/r^2$, and the pinch radius drops out of the power balance. Joule heating and optically thin radiation do not determine an equilibrium radius.

For atoms other than hydrogen I_{PB}^Z is a function of the nuclear charge of the ions Z through a factor $1 + 1/Z$. For ions with $Z_n \gg 1$ the top lines in Fig. 7(a) show $I_{PB} \approx 0.8$ MA, for $\ln \Lambda = 10$. In what follows the weak dependence on the Coulomb logarithm is neglected because its influence is on the same order as the many other approximations.

For fusion plasmas bremsstrahlung dominates the radiation loss, but this is not the sole radiation process. In extremely hot and dense plasmas synchrotron radiation can be balanced against Joule heating (Korop 1979). The resulting equilibrium, with $I \sim 100$ kA, is unstable. At sufficiently small plasma radius (~ 1 nm) electron degeneracy effects appear, synchrotron radiation loss begins to exceed Joule heating power, and the plasma cools. Cooler plasma implies reduced pressure, and further contraction of the plasma: the plasma collapses. In this theory, the average energy of the particles before the collapse is already several hundreds of keV, at a plasma density of $10^{30}/\text{cm}^3$, and synchrotron radiation emitted during the collapse is in the hard x-ray regime as observed in x-ray bursts from plasma points. These considerations and related ideas

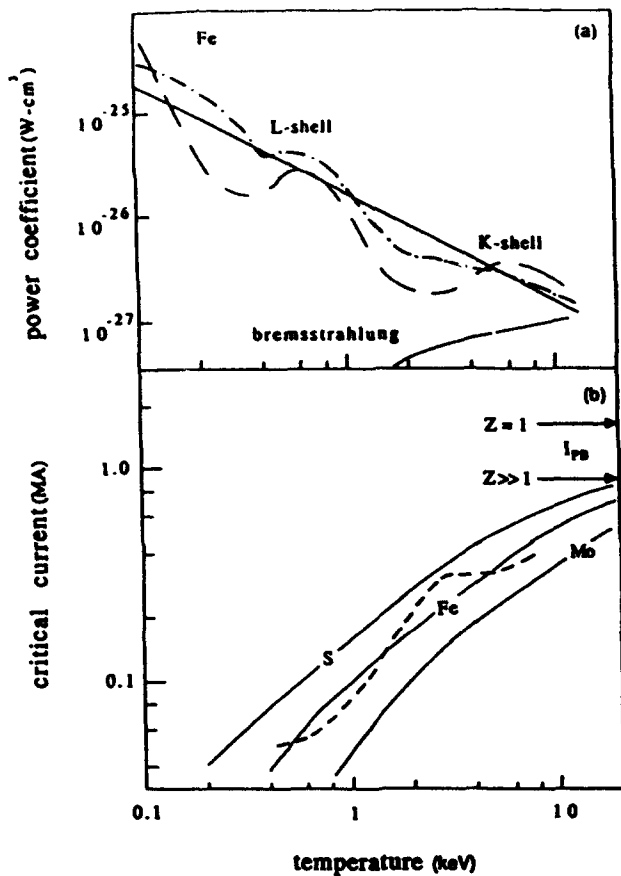


FIG. 7. (a) Power coefficient in iron line radiation vs plasma temperature. The dashed line are computations by Jacobs, the dash-dot line by Breton. The solid line is the approximation used later. Bremsstrahlung (at bottom) can be ignored. (b) the Pease-Braginskii current based on Jacobs' power coefficient for iron (dashed line), and for the approximate model (solid). Approximate values for sulphur and molybdenum are also given. The arrows at left give I_{PB} for hydrogen, and I_{PB} for $Z \gg 1$ in the limit of complete ionization.

(Meierovich 1984; Meierovich 1986) were important in clarifying the phenomenon of radiative collapse, although we now know that plasma turbulence and the associated anomalous heating prevents the supercompressed state to be reached from normal physical parameters (e.g., $n_e \sim 10^{23}/\text{cm}^3$ and $T \sim 1 \text{ keV}$). Radiative collapse in hydrogen pinches continues to be investigated including these additional effects (e.g., Chittenden 1989; Giuliani 1989; Robson 1989a).

In plasmas with atoms of higher atomic number $Z_n \geq 10$ and thermodynamic parameters relevant to vacuum sparks the power loss from bound-bound and free-bound transitions exceeds the bremsstrahlung power by a large factor, $K(T; Z_n)$. As a result the Pease-Braginskii current I_{PB} is less than I_{PB}^H for hydrogen: $I_{PB}(T; Z_n) = I_{PB}^H / \sqrt{K}$. The function K , which depends on detailed atomic physics considerations, is available in the literature (e.g., Post 1977): $I_{PB}(T; Z_n)$ has been computed for some elements with these data (Shearer 1976; Negus 1979; Vikhrev 1982a). Figure 7(a) shows $I_{PB}(T; Z_n)$ as function of temperature for sulphur, iron, and molybdenum

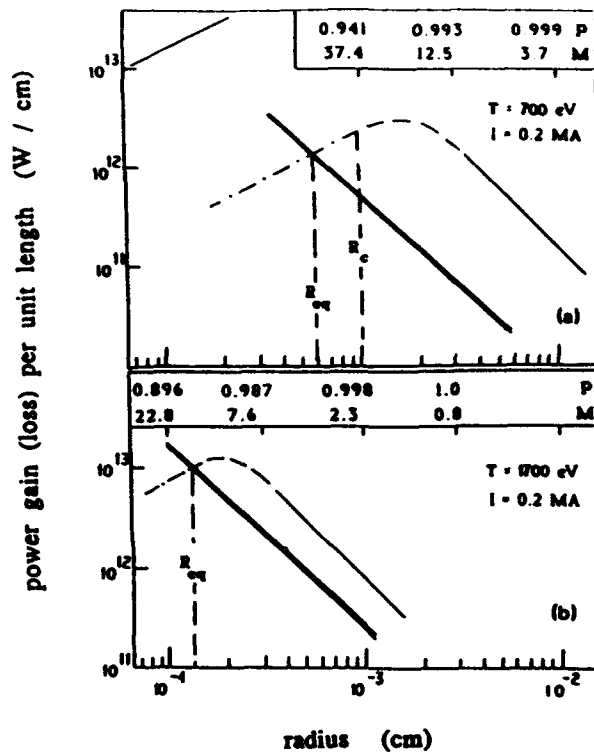


FIG. 8. Power per unit length as function of radius for an iron pinch with 0.2 MA in equilibrium at two line densities and two corresponding temperatures, (a) 700 eV; and (b) 1700 eV. The double line is Joule heating, the solid-dashed line is the radiative power loss. The equilibrium radius is given by the intersection of the two curves. See text for numbers on top.

($Z_n = 16, 26,$ and 42).

Reabsorption of radiation turns out to be important in the vacuum spark plasma: the plasma is optically thick for the relevant parameters $T_e \sim 1-10 \text{ keV}$ and $n_e \sim 10^{23}/\text{cm}^3$ or $n_i \sim 10^{22}/\text{cm}^3$. A cylinder of tenuous plasma emits optically thin volume radiation, which varies with radius as $1/r^2$. In the opposite extreme, blackbody radiation, the radiation depends only on the emitting area. Then the radiation per unit length increases linearly with radius, $P_{BB}/l = 2\pi r \sigma_{BB} T^4$ (the Stefan-Boltzmann constant $\sigma_{BB} \approx 10^5 \text{ W/cm}^2 \text{ eV}^4$). In reality, the total energy loss by radiation for intermediate plasma radii varies smoothly, from $1/r^2$ for large r to a linear increase with radius for small r . However, for our relatively small plasmas the surface radiation loss is still one or two orders of magnitude less than for an ideal blackbody. Figure 8, to be discussed later, illustrates the energy loss as function of radius for two temperatures in iron: the blackbody radiation loss is visible in the upper left corner (for 700 eV). Unlike optically thin radiation, the equilibrium between optically thick radiation with Joule heating does give an equilibrium radius for the pinch, r_{eq} in Fig. 8.

These equilibrium estimates assume that the plasma is radially uniform in current density, particle density, and temperature. Of course, none of these is necessarily true in reality, in part because these conditions are inconsistent with pressure and energy balance. As an example, radial

structure changes the radiation output, and affects the resistivity (Robson 1989b). Despite these inconsistencies a uniform plasma is a frequent approximation that should be reasonable in many cases (except for plasmas with a dense, cold core and a tenuous, hot periphery when the opposite approximation would be more reasonable).

A typical pinch is hydromagnetically unstable to axial perturbations. The sausage mode creates the conditions for radiative collapse. The basic idea is that the neck of a hydromagnetic sausage instability forms a plasma column of smaller size (Book 1976). Collapse can proceed when the energy loss from radiation in a characteristic instability time, $\tau \sim r/v_A$ (v_A is the Alfvén speed at the edge of the pinch), exceeds the heat content of the plasma (Shearer 1976; Winterberg 1978); equivalently, the radiation power per unit length of the plasma must be larger than the energy loss due to expulsion of plasma from the pinch (Vikhrev 1978a; Vikhrev 1978b). It is important to realize that the plasma increases the value of $n_e \tau$ during compression (Vikhrev 1977; Vikhrev 1978a). This guarantees that the radiative power continues to exceed the energy lost by plasma expulsion, and the plasma column can continue its radiative collapse.

These concepts, atomic radiation with opacity and axial outflow of plasma, are the core of a simplified, zero-dimensional model for the plasma point (Vikhrev 1982a), the radiative collapse model. The simplifications make it possible to follow the entire process of radiation collapse in time, in an approximate way. Although more accurate modeling can be done for 2D hydrodynamics, opacity, and ion kinetics in isolation, it is barely possible to integrate all these aspects into one single computation. The most detailed computations to date either have little radiation (Lindemuth 1990) or contain a conceptually complete radiation package (but without radiation transport) that is constrained by computation considerations (Cochran 1990). Eventually, as resources increase these and similar computations will supersede the abridged models discussed here.

Vikhrev's model appears to contain the phenomena that dominate the life of the plasma point: it successfully predicts plasma temperature, density, and plasma point lifetime. In addition there are experimental indications that plasma outflow is related to the plasma point (Hares 1984; Stewart 1987).

B. Model for radiation compression of a high-Z plasma

This section introduces the general ideas of the radiative compression model as well as some quantitative results from a simple analytical model (Koshelev 1985). This analytical approximation seems to provide a good qualitative (and for many cases quantitative) description of the process. The next section presents results for a more complete model that includes the hydrodynamics of the plasma and a more exact form for the radiative energy loss.

1. Critical current

Force balance in the radial direction (Bennett 1934) gives a simple relation between the line density for electrons, $N_e = \pi r^2 n_e$, the electron temperature T_e , and the total current I . The Bennett relation is

$$\frac{\mu_0 I^2}{4\pi} = (Z_{\text{eff}} + 1) N_e k T. \quad (\text{III.1})$$

The left-hand side is the linear energy density of the magnetic field for a total current I , and the right hand side is the linear kinetic energy of the plasma, with N_i the number of ions per unit length, and T the plasma temperature (assumed equal for ions and electrons): the electron line density $N_e = Z_{\text{eff}} N_i$. In numerical form,

$$(Z_{\text{eff}} + 1) N_i T = 3.12 \times 10^{21} I^2, \quad (\text{III.2})$$

where T is the plasma temperature (in eV), N_i is the number of ions per unit length (in cm) and I is the pinch current (in MA). The Bennett relation applies when kinetic and magnetic pressure are the only relevant forces, and when the radial velocity of the plasma column is small compared to the sound speed.

Bennett equilibrium deals only with the averaged particle density, temperature, and current density, and says nothing about the value of the radius where the plasma edge is located. Once in equilibrium the external forces on the plasma are balanced, and the plasma edge would remain at the same radial position while the radial profiles of the thermodynamic quantities continue to evolve.

In a hydrogen plasma column in Bennett equilibrium the energy loss by bremsstrahlung balances Joule heating with Spitzer conductivity at the Pease-Braginskii current I_{PB} (Pease 1957; Braginskii 1957). A current I with constant current density produces in a homogeneous plasma of radius r and average charge state Z_{eff} a power Q_{Joule} per unit length l of $Q_{\text{Joule}}/l = I^2/\sigma A$. The conductivity $\sigma = \sigma_0 T^{3/2}/Z_{\text{eff}}$ in Λ is the Spitzer conductivity, $\ln \Lambda$ is the Coulomb logarithm, and the pinch area $A = \pi r^2$. The constant $\sigma_0 = 100 \Omega^{-1} \text{cm}^{-1} \text{eV}^{-3/2}$. Then

$$Q_{\text{Joule}}/l = 3.3 \times 10^9 \frac{Z_{\text{eff}} \ln \Lambda I^2}{T^{3/2} r^2}, \quad (\text{III.3})$$

where Q_{Joule}/l is in W/cm, and I in MA.

As the radius decreases and the density goes up to the assumptions that lead to Spitzer resistivity are no longer true. With more realistic models I_{PB} may change a factor ~ 2 (Giuliani 1989; Robson 1989b), on the same order as possible dependences on the Coulomb logarithm. Anomalous heating related to current-driven instabilities is more difficult to estimate, and also more important [see below Eq. (III.29)]. For the moment Eq. (III.3) is sufficient, and convenient in future use.

The radiative power density in bremsstrahlung (or free-free radiation) $P_{\text{ff}} = X_{\text{ff}} n_e n_p$, where the free-free power coefficient $X_{\text{ff}} = 1.4 \times 10^{-32} Z_{\text{eff}}^2 T^{1/2} \text{W cm}^3$. In Bennett equilibrium the bremsstrahlung power loss per unit length is

$$Q_{ff} = 4.3 \times 10^{10} \frac{Z_{\text{eff}} I^4}{T^{3/2} \Lambda^2} \quad (\text{III.4})$$

for $Z_{\text{eff}} \gg 1$ (Q_{ff} is in W/cm). This leads to the well-known value for $I_{\text{PB}}^2 = 0.27 (\ln \Lambda)^{1/2}$ MA, for a fully ionized high-Z plasma. I_{PB} can also be expressed as the Alfvén current $I_A = 17$ kA multiplied by a factor that compares the cross sections for collisional energy transfer ($\propto \ln \Lambda$) and bremsstrahlung (Pereira 1990).

In reality the current is never constant. Typically, $I(t)$ has a pulse shape determined largely by the pulse power machinery, with some details reflecting the dynamics of the pinch. Assume for the moment that the pinch has reached equilibrium at a certain current. If the current increases above I_{PB} without a corresponding change in temperature the magnetic pressure exceeds the thermal pressure: the plasma contracts. However, Bennett equilibrium can be reestablished due to compressional heating, i.e., the conversion of magnetic field energy to thermal energy. In fact, it is possible to heat the pinch while remaining in Pease-Braginskii equilibrium if the current increases in time as $I \propto t^{1/3}$ (Haines 1960; Hammel 1976). The hydrogen pinch in variants of these zero-dimensional approximations was discussed recently by Chittenden (1989), Giuliani (1989), and Robson (1989a,b).

In a plasma of heavy ions it is possible to maintain Bennett equilibrium during contraction of the pinch. As the plasma contracts the radiative losses decrease due to opacity and density effects, and the small difference between the radiative losses and Joule heating is easily compensated by magnetic field work.

Energy balance based on bremsstrahlung radiation is relevant to hydrogen plasmas, and to fully ionized high-Z plasmas. However, the majority of ions is fully stripped only at exceedingly high temperatures $T \gtrsim 3Z^2 Ry$ (e.g., Huddleston 1965: $Ry = 13.6$ eV is the Rydberg constant). Usually a pinch with high-Z plasma is only partly ionized, line radiation dominates over bremsstrahlung, and I_{PB}^2 no longer defines power balance. Instead, power balance occurs at a critical current $I_{\text{cr}} < I_{\text{PB}}^2$: I_{cr} depends on the thermodynamic variables of the plasma but not on the plasma size, because the plasma is still assumed to be optically thin.

The critical current I_{cr} for a plasma of heavy ions is obtained easily from the total radiation loss of a plasma in the form $P_{\text{tot}} = P_{ff} \times K(T, Z_n)$. The factor $K(T, Z_n)$ is a complicated function of temperature T , and of nuclear charge Z_n . Its computation involves detailed atomic physics considerations that fall outside this review. Here $K(T, Z_n)$ is considered given by the literature (e.g., Post 1977).

In Bennett equilibrium, and assuming uniform current density over the pinch,

$$\frac{I_{\text{cr}}^2}{I_{\text{PB}}^2} = \frac{P_{\text{tot}}}{P_{ff}} \quad (\text{III.5})$$

which gives the critical current $I_{\text{cr}} = 0.27 (\ln \Lambda / K)^{1/2}$.

Figure 7(b) compares the temperature dependence of the power coefficient X_{ff} for bremsstrahlung (lower solid line) with the power coefficient for line radiation X_{line}

$= P_{\text{line}} / n_e n_i$, for iron ($Z_n = 26$), in three approximations. The dashed line comes from the computation by Jacobs (1977), and the dot-dashed line from Breton (1978). The two computations are similar in the onset of L-shell radiation (around 0.6 keV) and K-shell radiation (around 4 keV), but the power coefficients differ by a factor on the same order as the already neglected influence from the Coulomb logarithm (~ 2). Bremsstrahlung becomes important beyond about 5 keV. The solid line is an analytical approximation to X_{line} (Koshelev 1985):

$$X_{\text{line}} \approx 4 \times 10^{-29} \frac{Z_n^4}{T} \quad (\text{III.6})$$

(where X_{line} is in W cm^3). This approximation agrees with the more accurate computations to within their differences in the relevant temperature regime (0.3–10 keV). The power loss per unit length in line radiation for a plasma in Bennett equilibrium then becomes:

$$Q_{\text{line}} \approx 1.24 \times 10^{14} \frac{Z_n^4 I^4}{Z_{\text{eff}} T^3} \times \frac{1}{\Lambda^2} \quad (\text{III.7})$$

Balancing radiative power with Joule heating, $Q_{\text{line}} + Q_{ff} = Q_{\text{Joule}}$ gives the critical current I_{cr} . The dashed line in Fig. 7(a) is the critical current for iron (Fe, $Z_n = 26$): it reflects the variations with temperature seen in Jacobs' power coefficient (dashed line in Fig. 7b).

Bremsstrahlung can safely be ignored up to moderately high temperatures, when $Q_{\text{line}} > Q_{ff}$. This approximation gives I_{cr} for sulphur (S, $Z_n = 16$), iron and molybdenum (Mo, $Z_n = 42$). Analytically

$$I_{\text{cr}} \approx 5 \times 10^{-3} \sqrt{\ln \Lambda} T^{3/4} \frac{Z_{\text{eff}}}{Z_n} \quad (\text{III.8})$$

which is for $\ln \Lambda \sim 10$

$$I_{\text{cr}} \approx 0.016 \times T^{3/4} \frac{Z_{\text{eff}}}{Z_n} \quad (\text{III.9})$$

(where I is in MA). The deviation from the $T^{3/4}$ line in Figure 7(a) comes principally from the inclusion of bremsstrahlung at high temperatures, and to a minor degree from the (weak) temperature dependence of the effective atomic number Z_{eff} . The Pease-Braginskii current estimated analytically differs by about 50% from the more accurate approximations.

In the following we continue to illustrate the basic physics behind the different pinch phenomena with simple analytical approximations rather than with more precise numerical results. This is partly for clarity, and partly because the broad atomic and radiation physics background falls outside this review. The various estimates that follow are intended to be semiquantitative. Quantitatively correct results must await computations that include all the complications inherent in radiation transport computations: an accurate computation of optically thick radiation has only recently been applied to radiation collapse (Apruzese 1889/1990).

2. Equilibrium radius

In an equilibrium pinch optically thin radiation losses vary with radius as $1/r^2$ only in the low density, "coronal," type of plasma. In the coronal approximation the ions are excited exclusively by collisions with electrons, and all excited ions de-excite only by radiating a photon which leaves the plasma. In contrast, for higher densities collisional de-excitation can be significant. Then the excitation energy is given back to the plasma instead of being radiated out, and the plasma radiates less. Moreover, the radiation varies with radius in a different way because collisional de-excitation depends on density, and therefore on radius.

Consider a plasma wherein the ions have only two energy levels. The spontaneous radiation rate is W_n and the collisional de-excitation rate by collisions with electrons is $n_e W_e$. The total de-excitation rate is then $W_n + n_e W_e$ compared to W_n in the coronal plasma. The radiation coefficient decreases by the factor $W_n / (W_n + n_e W_e)$ to

$$X'_{\text{line}} = X_{\text{line}} \times \frac{1}{1 + n_e W_e / W_n} \quad (\text{III.10})$$

In a low-density plasma, $n_e W_e \ll W_n$ the radiation coefficient does not change with density. Then the radiated power $P \propto n_e n_i \propto n^2$, and the radiated power per unit length is $Q = \pi^2 P$. For a pinch in Bennett equilibrium, with current I and temperature T and a line density $N = \pi r^2 n$ that remains constant with radius the radiated power per unit length is $Q \propto I^4 / r^2$, inversely proportional to the cross-sectional area r^2 . However, in a denser plasma when $n_e W_e \gg W_n$ the radiation coefficient $X' \sim W_n / n_e \times W_n / W_e$ is inversely proportional to the electron density n_e . Then the radiated power P is no longer $P \propto n^2$, but one of the density factors cancels, and $P \propto n_e$. Although the plasma is still optically thin, i.e., the photons are not reabsorbed by the plasma, the radiated power is no longer inversely proportional to $1/r^2$. Instead, for a denser but still optically thin plasma the power loss per unit length of a Bennett pinch with given line density becomes $Q \propto I^2$, independent of pinch radius r .

The coefficient for radiative de-excitation W_n scales with excitation energy, or photon energy $h\nu$, as $W_n \propto (h\nu)^2$ (e.g., Vainshtein 1979). The collisional de-excitation rate $W_e \sim \nu \sigma_e$ is proportional to some average electron velocity ν and the de-excitation cross section σ_e which scales inversely with average electron energy T as $\sigma_e \sim T^{-2}$. Therefore, $W_e \propto T^{-3/2}$. Often the average energy of the photons responsible for most of the plasma radiation is proportional to the temperature, $h\nu \sim 2kT$, and $W_n / W_e \sim (h\nu)^{-1/2} \sim T^{-1/2}$. The numerical factor in front of these scaling estimates is approximately constant along the isoelectronic sequence but differs for different types of ions (K ions, L ions, ...). For analytical modeling below we use $W_n / W_e \approx 10^{-14} / T^{1/2} \text{ cm}^3$ for both L shell and K shell, with T in eV.

A photon escapes from the plasma (and the plasma radiates) if its mean free path l_ν is much larger than the plasma radius r . Otherwise, when the optical depth $r/l_\nu \gg 1$, the photon excites a large number M of ions before it

reaches the plasma edge: $M \approx r/l_\nu$. When the radius r decreases the density of ions in the ground state n_i increases (assuming constant line density $N = n_i \pi r^2$). The mean free path $l_\nu \sim 1/n_i$ decreases as r^2 . Thus the number of photon-ion collisions M increases as $M \sim 1/r$.

Without collisional de-excitation each of these ions re-emits the photon in an arbitrary direction. The energy of the re-emitted photon is random with a probability distribution given by the lineshape. All the radiation escapes, but in a broader line. Multiple scattering together with collisional de-excitation deposits the photon energy back into the plasma, and reduces the radiation loss.

The decrease in the radiation rate due to opacity is estimated as follows. The probability p that a photon is re-emitted in one absorption-emission cycle is $p = 1 / (1 + n_e W_e / W_n)$. The probability that the photon escapes the plasma without being redeposited is then $\beta = p^M$, where M is the average number of scatterings per photon. For the case of total frequency redistribution inside a Doppler line contour an acceptable approximation is $M = \alpha r / l_\nu$ where the parameter α depends on geometry, optical depth (as $\ln r / l_\nu$) and line profile: typically $\alpha \sim 5$ (e.g., Holstein 1951).

The mean free path $l_\nu = 1 / n_i \sigma_\nu$ where σ_ν is the cross section for absorption of the line photon. This cross section depends strongly on the line width and on the photon energy, and is proportional to the statistical weight ω_g of the ground states of the ions that are likely to be present in the plasma, e.g., $\omega_g \sim 10$. Again assuming that $T \approx 2h\nu$ and using $n_e = Z_{\text{eff}} n_i$, the mean free path becomes

$$l_\nu \approx 3 \times 10^{13} \frac{Z_{\text{eff}}^{3/2} T^{3/2}}{Z_n^{1/2} n_e} \quad (\text{III.11})$$

with l_ν in cm. For a plasma in Bennett equilibrium this becomes

$$l_\nu \approx 3 \times 10^{-8} \frac{Z_{\text{eff}}^{3/2} T^{3/2}}{Z_n^{1/2}} I^2 \quad (\text{III.12})$$

(with current I in MA and r in cm).

Figure 8 shows the radiation per unit length for an iron pinch as function of radius. Figure 8(a) is a warm pinch with temperature $T = 700$ eV and electron line density $N_e = 18 \times 10^{16} / \text{cm}$ corresponding to Bennett equilibrium for a current $I = 0.2$ MA. Figure 8(b) is for a hot pinch with $T = 1700$ eV and reduced mass per unit length $N_e = 7.3 \times 10^{16} / \text{cm}$, but approximately the same current (assuming no change in $\ln \Lambda$ with temperature and density). For the warm pinch the effective atomic number is $Z_{\text{eff}} = 17$, and the linear ion density is $N_i = 10^{16} / \text{cm}$; for the hot pinch $Z_{\text{eff}} = 25$ and the ion density is $3 \times$ smaller, $N_i = 0.3 \times 10^{16} / \text{cm}$. Note that the warm pinch could evolve into the hot pinch by axial outflow of material, but not by compression without outflow.

The solid line is the radiation per unit length for coronal and optically thin radiation, decreasing as $1/r^2$ with increasing radius. The dashed line shows the reduction in radiation per unit length due to optical thickness, according to the formula $Q' = Q p^{1+M}$. The upper number in the

box at the top of the figure is the probability for collisional de-excitation $p = 1/(1 + n_e W_e/W_r)$, which decreases with radius through the density $n_e \propto 1/r^2$. The probability p is close to unity and the coronal approximation is well justified up to rather small radius of compression.

The lower number in the box is the number of scatterings M . The large number of scatterings $M \gg 1$ combined with small deviations from the coronal approximation, $p \lesssim 1$, strongly reduces the radiation per unit length as the pinch contracts.

The critical radius r_c indicates where the plasma radiation goes over from volume-like to surface-like. This transition should occur approximately when a sizeable fraction of the photons is reabsorbed, e.g., when

$$p^{1+M} \approx 1/e \approx 0.37.$$

Assuming $n_e W_e/W_r \ll 1$ in $p = 1/(1 + n_e W_e/W_r)$ gives $p^{1+M} \sim M n_e W_e/W_r$ (using $M \gg 1$), and this gives a critical radius

$$r_c \approx 1.2 \times 10^5 \frac{I^{1/3} Z_n^{1/6}}{Z_{\text{eff}}^{1/2} T^{1/3}}, \quad (\text{III.13})$$

with r_c in cm.

The radiative losses are assumed to be surfacelike for plasma smaller than the critical radius. Then $Q_s \approx Br$. The coefficient B can be obtained by setting $Q_s = Br$ equal to the estimate $Q = Qp^{1+M}$ at the critical radius:

$$Q_s \approx 0.027 \times r \times Z_n^{1/2} Z_{\text{eff}}^{1/2} T^4, \quad (\text{III.14})$$

with Q_s in W/cm. This procedure gives the dash-dot line in Fig. 8.

Surfacelike radiation from this plasma is much weaker than blackbody emission. A blackbody cylinder of radius r radiates $Q_{\text{BB}} = 2\pi r \sigma_{\text{SB}} T^4$ per unit length, where the Stefan-Boltzmann constant $\sigma_{\text{SB}} = 10^5 \text{ W/cm}^2 \text{ eV}^4$. This is the solid line in the left-top corner of Fig. 8(a), but off-scale in Fig. 8(b). The emissivity $Q_s/Q_{\text{BB}} \approx 4 \times 10^{-7} Z^{1/2}$ is about 1/30 for iron.

Estimating the opacity effects with a simple two-level model is highly approximate but still semiquantitatively correct. For example, a detailed radiation transport model with 162 levels and 511 radiation lines (Apruzese 1989/90) finds an emissivity below ~ 0.1 for a krypton ($Z_n = 36$) cylinder (with relevant plasma parameters $n_e \sim 5 \times 10^{22}/\text{cm}^3$ and $T = 1 \text{ keV}$). Figure 9 shows the x-ray spectrum for this computation. Many individual lines have merged together in two broad bands that approach the blackbody spectrum and account for most of the radiated energy. In this regime, around the transition from volume to surface radiation, the spectrum exceeds the blackbody limit for certain photon energies, reflecting the approximations even in this relatively comprehensive computation.

The different radial dependencies of radiation with the opacity effects and with Joule heating allow the determination of an equilibrium radius r_{eq} . Figure 8 shows the radial dependence of Joule heating in the double solid line, and the intersection with $Q(r)$ that gives the equilibrium radius R_{eq} . The equilibrium radius decreases with increas-

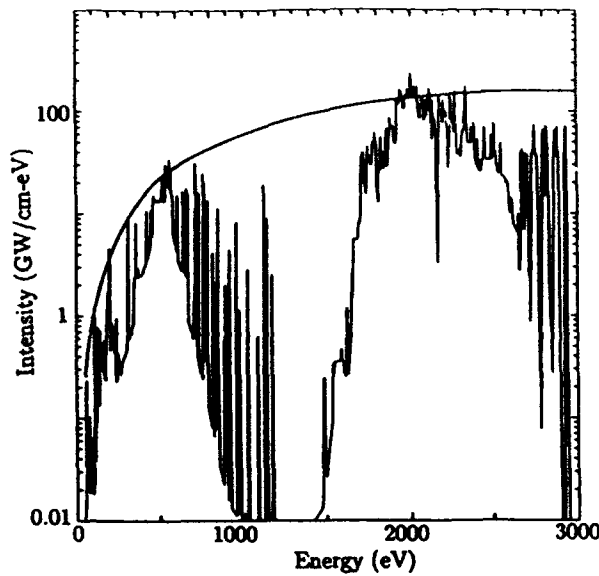


FIG. 9. Computed spectrum from a cylindrical krypton plasma of 0.01 cm radius, ion density $4.9 \times 10^{22}/\text{cm}^3$, and temperature 1 keV. Spectrum exceeding Planck limit in two regions indicates breakdown of approximation technique (from Apruzese 1989).

ing temperature, from about $6 \mu\text{m}$ for 700 eV iron to about $1 \mu\text{m}$ for 1700 eV iron. Such behavior has a clear physical reason. The higher temperature plasma is more coronal, and at the same time the radiated photons are more energetic and the absorption coefficients are lower. Therefore a higher compression is needed to reach the surfacelike radiation regime.

Using the analytical approximation for surfacelike radiation Q_s [Eq. (III.14)], and for Joule heating [Eq. (III.3)] gives an analytical estimate for the equilibrium radius,

$$r_{\text{eq}} \approx 10^4 \left(\frac{I^2 Z_{\text{eff}}^{1/2}}{T^{11/2} Z_n^{1/2}} \right)^{1/3}, \quad (\text{III.15})$$

where r_{eq} is in cm.

These considerations are valid only if the current is larger than the critical current I_{cr} for which Joule heating would be balanced by volumelike radiation without opacity effects. As shown below III.10 the Joule heating increases with current as $Q/I \propto I^2$, but radiation increases faster, as $Q_{\text{rad}} \propto I^4$. Then Joule heating is less than volumelike radiation [as in Figs. 8(a) and 8(b)], and equilibrium is obtained with opacity-reduced radiation. In the opposite case $I < I_{\text{cr}}$ Joule heating always exceeds radiation losses, and an equilibrium radius does not exist. The critical current $I_{\text{cr}} \approx 0.016 T^{3/4} Z_{\text{eff}}/Z_n^2$ increases with temperature: for an iron pinch $I_{\text{cr}} \approx 0.2 \text{ MA}$ for $T = 3 \text{ keV}$.

The solid line in Fig. 10 shows the equilibrium radius for an iron plasma with current 0.2 MA, calculated according to Eq. (III.15), as a function of electron temperature. The lower scale is the ion density corresponding to Dennett equilibrium with a fixed current. The dashed curve shows the equilibrium radius r_{eq} calculated with an improved representation of W_e/W_r , that takes into account the transition

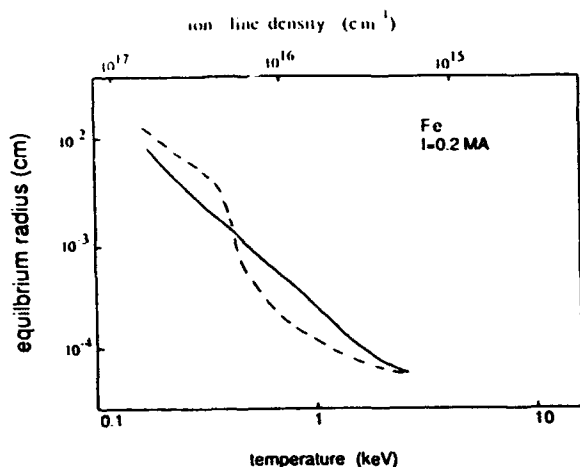


FIG. 10. Equilibrium radius for an iron at 0.2 MA vs temperature or linear ion density. The approximate power coefficient gives the solid line. Jacobs' power coefficient gives the dashed line.

from M shell (Ar-like) to L shell (Ne-like). This transition is responsible for the relatively rapid change in equilibrium radius $r_{\text{eq}} \approx 10 \mu\text{m}$ around 0.4 keV. Nevertheless, the more elaborate result does not differ much from the rough analytical approximation, because the equilibrium radius is weakly dependent on the details of the radiation physics (about as the 1/3 power of the various coefficients). The equilibrium radius curve ends at the cross, at $T = 3 \text{ keV}$, where $I_{\text{cr}} = 0.2 \text{ MA}$ and power equilibrium is no longer possible.

The analytical formula for r_{eq} combined with Bennett equilibrium gives an estimate for the electron density in the plasma, viz.,

$$n_{e,\text{eq}} \approx 10^{13} I^{2/3} Z_n^2 T^{6/3}, \quad (\text{III.16})$$

where $n_{e,\text{eq}}$ is in $/\text{cm}^3$.

All these formulas were obtained considering only radiative losses and Joule heating with Spitzer conductivity with $\ln \Lambda \sim 10$. Other energy gain or loss mechanisms, such as anomalous resistivity or plasma outflow, give another value for the equilibrium radius, which is still defined by $Q_{\text{Joule}} = Q_r$. Vikhrev (1982a) considered r_{eq} including a model for anomalous resistivity from current-driven instabilities (see below).

3. Formation of a micropinch in a vacuum spark

The zero-dimensional equilibrium of the pinch estimated above is hydrodynamically unstable to the sausage instability ($m = 0$). The radiative collapse model (Vikhrev 1982a) assumes that the hot spot in a low-inductance vacuum spark is caused by a local contraction due to the plasma outflow from the neck of the sausage, aided by large radiative energy losses. Such a development is visible in the experimental data of e.g., Veretennikov (1985), which shows a sausage-type instability in an iron pinch with current 0.15 MA, with a plasma radius in the neck around 0.01 cm and temperature of about 100–150 eV. These measurements agree with the estimates for the equi-

librium radius, which is also $r_{\text{eq}} \sim 0.01 \text{ cm}$. Other measurements support the existence of plasma outflow: an argon pinch shows a fourfold reduction of the initial line density, from $6 \times 10^{16}/\text{cm}$ to $\sim 1.5 \times 10^{16}/\text{cm}$ (Hares 1985); the axial velocity of the plasma increases with ionization states (Stewart 1987), and therefore with temperature.

In the radiative collapse model the outflow of particles along the pinch axis decreases the line density in the pinch region. However, during the outflow the pinch plasma remains in quasi-equilibrium, and the equilibrium radius and associated quantities change along the curve $r_{\text{eq}}(N_i)$ shown in Fig. 10. An earlier model (Vikhrev 1977) assumed that the outflow of particles is the sole energy loss mechanism.

The decrease in the line density due to axial plasma loss is approximated by the equation:

$$\frac{dN_i}{dt} = -\frac{N_i}{\tau}, \quad (\text{III.17})$$

where τ is a characteristic escape time. A reasonable value is $\tau \approx h/c_s$, where h is the height of the sausageing part of the pinch and c_s is the sound speed, or $\tau \approx r/c_s \times \alpha$, where α is the aspect ratio of the sausage, $\alpha = h/r$. Typically, α is in the range $1 < \alpha < 10$, or about 3.

Using the equilibrium values of radius [Eq. (III.15)] and density [Eq. (III.16)] with initial values for current I_0 gives for the temperature

$$T(t) = \frac{T_0}{(1 - t/\tau_0)^{2/3}}. \quad (\text{III.18})$$

Here T_0 is the initial temperature, and the characteristic timescale τ_0 is

$$\tau_0 \approx 0.006 \frac{\alpha I_0^{2/3}}{Z_n^{2/3} T_0^{5/3}}, \quad (\text{III.19})$$

with τ_0 in seconds. Equation (III.18) indicates that the temperature could increase rapidly after a time on the order of τ_0 . Radius and density will behave similarly, because these are directly coupled to the temperature $T(t)$ by Eqs. (III.15) and (III.16).

The time constant τ_0 can be taken as the characteristic lifetime of the micropinch with initial parameters T_0 and r_{eq} . For a low-inductance vacuum spark in iron with current $I_0 = 0.2 \text{ MA}$ the lifetime of the plasma with aspect ratio $\alpha = 3$ is $\tau_0 \approx 14 \text{ ns}$ at temperature $T \approx 100 \text{ eV}$. This delay agrees reasonably well with the delay time between the initial compression to the equilibrium radius $r = 0.01 \text{ cm}$ and the high-temperature micropinch stage with K-line radiation emission (Veretennikov 1981a,b). The calculated characteristic time for a plasma with temperature $T \approx 1500 \text{ eV}$ when K ions radiate is about 20 ps, which also agrees with experimental measurements described above.

The radiative collapse model envisions a pinch in radiative equilibrium that produces a high temperature during a radiation-assisted compression with axial outflow of material. The high temperature ionizes the pinch ions to the K shell, and the pinch radiates K lines. During the compression the pinch remains in radiative equilibrium.

Radiative equilibrium demands that the current I_0 remain less than the critical current I_{cr} , Eq. (III.9). However, I_{cr} increases with temperature as $T^{3/4}$. Eventually I_{cr} exceeds the pinch current I_0 , which remains constant during the radiative collapse. At this point the pinch can no longer remain in radiative equilibrium. Once out of equilibrium the plasma expands, the density decreases, and the radiation stops.

K line radiation starts at a temperature $T_K(Z_n)$ that depends on the nuclear charge Z_n . This happens approximately when $T_K \approx 3 \times 10^{-3} Z_n^4$ eV (Breton 1978). The plasma point can radiate K lines if the critical current $I_{cr}(T, Z_n)$ at $T_K(Z_n)$ exceeds the pinch current I_0 . Taking $Z \approx Z_n \approx Z_{eff}$ gives the maximum atomic number for which the K shell can be reached:

$$Z_{max} \approx 70 \times I^{1/2}, \quad (III.20)$$

with I in MA. According to this formula He-like ions with $Z_n \lesssim 30$ or so can be excited in a micropinch with $I_0 = 0.2$ MA. This agrees with experiment: iron ($Z_n = 26$) is stripped to the K shell in a micropinch with $I_{max} = 0.2$ MA, while in a molybdenum ($Z_n = 42$) pinch the K lines are very weak.

A similar estimate can be made for Ne-like ions. These appear when $T_{Ne} \approx 5 \times 10^{-4} Z_n^4$: therefore, ions with nuclear charge $Z_{max} \lesssim 135 \times I^{1/2}$ can be expected to radiate L lines. For a pinch with $I_0 = 0.2$ MA the estimate, $Z_{max}^N \lesssim 55$, is in good agreement with experimental observations (Aglitskii 1986).

Another quantity of interest is the radial size of the plasma point seen in K line light, and the point's electron density. Equation (III.15) gives an equilibrium radius $r_{eq} = 1 \mu\text{m}$ for an iron plasma at $I = 0.15$ MA with temperature $T = 1700\text{--}2000$ eV, $r_{eq} = 5 \mu\text{m}$ for calcium ($Z_n = 20$) at $T = 100$ eV, and $r_{eq} = 15 \mu\text{m}$ for sulphur ($Z_n = 16$). These numbers compare favorably with the experimental observations in Fig. 1. There is also good agreement for the electron densities: for calcium $n_e = 10^{23}/\text{cm}^3$ under the circumstances given, and for aluminum ($Z_n = 13$) $n_e = 4 \times 10^{21}/\text{cm}^3$ at $T = 400$ eV.

The radiation power of the plasma point is obtained by multiplying the surfacelike radiation power per unit length (III.14) by the micropinch length ($\alpha \times r_{eq}$). This gives for the radiation power of the plasma point the expression

$$Q_{tot} = 2.7\alpha \times I^{3/4} Z_n^{7/6} Z_{eff}^{5/6} T^{1/3}, \quad (III.21a)$$

with Q_{tot} in MW. With the usual approximations $h\nu \approx 2kT$ and $Z_n \approx Z_{eff}$ this becomes

$$Q_{tot} \approx 2.1\alpha I^{3/4} Z_n^2 (h\nu)^{1/3}, \quad (III.21b)$$

which shows a weak ($1/3$ power) dependence on photon energy $h\nu$. For an iron plasma with $\alpha = 6$ and $I = 0.15$ MA the power radiated by the plasma point varies from $Q_{tot} = 3$ GW for a choice of $h\nu = 0.2$ keV, to 10 GW for $h\nu = 6$ keV.

The total energy ϵ radiated by the point in the region between $h\nu$ and $1.5 h\nu$ can be estimated multiplying the power Q_{tot} by the lifetime τ :

$$\epsilon \approx 7 \times 10^4 \alpha^2 I^2 Z_n^{4/3} / (h\nu)^{13/6}. \quad (III.22)$$

This estimate gives $\epsilon \approx 0.02$ J for the K-radiation from a plasma point in an iron plasma. The experimental value is also 0.02 J. Obviously, this exact coincidence is accidental: both theory and experiment are only accurate to within a factor of 2.

Below we discuss the results for a more accurate numerical model of micropinching. However, the simple physical investigation above already suggests that the model of radiative compression correctly describes qualitatively and quantitatively many aspects of the physical scaling of plasma points.

C. Zero-dimensional dynamic model of micropinching

The zero-dimensional dynamic model of micropinching (Vikhrev 1982a) discussed below is the first qualitatively and quantitatively correct description of many of the characteristics of plasma points. This model grew out of the so-called simple model of the plasma focus by adding radiative energy losses due to line radiation of multiply charged ions. It gives good results for an iron pinch, which has been studied in detail.

In the final stage of the hydromagnetic sausage instability the pinch evolves into a neck with an elongated shape, with height h and radius a (Book 1976). The aspect ratio $\alpha = h/a$, and $\alpha \sim 3\text{--}10$. The center of the neck is at $z = 0$, and the neck edges are at $\pm h/2$. Density and temperature are taken to be uniform throughout the neck. During compression the uniformity is maintained when the radial speed $v_r(r) = (r/a)v$ is linear with radius: $v = v_r(a)$ is the radial velocity at the column edge.

What is the compression dynamics of the neck? Radial motion follows the equation:

$$\frac{2}{3} m n \frac{dv}{dt} = -2\pi a \left(p - \frac{2nT}{\pi a^2} \right). \quad (III.23)$$

Here m is the ion mass and $p = B^2/2\mu_0$ is the magnetic pressure at the plasma edge. The change in the line density $N = \pi a^2 n$ is given by

$$\frac{dN}{dt} = -\frac{N}{\tau}. \quad (III.24)$$

The constant τ is the characteristic escape time of the plasma:

$$\frac{1}{\tau} = \frac{1}{\tau_z} + \frac{1}{\tau_r}, \quad (III.25)$$

where τ_z is the escape time of the plasma through the ends of the plasma column, and τ_r is the radial compression time. It is given by the growth rate of the hydromagnetic instability corrected with the aspect ratio α , viz., $\tau_r = \alpha(a/c_s)$, where c_s is the Alfvén speed (and the ion thermal speed in Bennett equilibrium, v_{T1}).

The velocity of the plasma along the z axis at the edge of the neck determines the axial escape time $\tau_z = h/2v_z$, where the axial velocity v_z is given by

$$\frac{dv_z}{dt} = \frac{2}{hnm} \frac{(nT - n_0T_0)}{h/2} - \frac{v_z^2 h}{h/2} \quad (\text{III.26})$$

Here n_0 and T_0 are the density and temperature of the plasma escaping from the pinch. The first term on the right hand side contains the pressure gradient along the z axis. The second term describes the decrease of v_z due to the escape of plasma through the ends, under the assumption that the axial velocity increases linearly with axial distance z .

The energy per unit length of the plasma column is ϵN_p , with ϵ the average energy per ion. The energy per unit length develops according to the equation:

$$\frac{d(\epsilon N_p)}{dt} = -2\pi a p \frac{da}{dt} - \frac{\epsilon N_p + \pi a^2 p}{\tau} - Q. \quad (\text{III.27})$$

The first term on the right hand side is the power input by adiabatic compression, and the second describes the outflow of energy associated with the escape of material from the neck. The last term is the radiation loss.

The pinch current is given by the circuit equation:

$$\frac{d}{dt}[(L_0 + L_p)I] + R_p I = 0, \quad (\text{III.28})$$

where L_0 and L_p are the inductances of the circuit and the discharge channel, respectively, and R_p is the resistance of the neck region in the plasma.

The resistance $R_p = h/\sigma\pi a^2$, with σ the plasma conductivity. To mock up anomalous resistivity the conductivity σ is taken to be $\sigma = nev/mv_{eff}$, with $v_{eff} = v_{cl} + v_{anom}$ the effective collision frequency. Spitzer conductivity comes from elastic collisions between electrons and ions, with collision frequency v_{cl} . The collision frequency v_{anom} takes into account an anomalous resistivity related to plasma instabilities that may be excited by current flow in the pinch. In the absence of a good model the anomalous collision frequency is taken as

$$v_{anom} = (v_D/v_{Ti})^2 (\omega_c/\omega_{ce})^{1/2}. \quad (\text{III.29})$$

Here v_D is the drift velocity of the electrons, and the ω_c 's are the ion and electron Larmor frequencies. The formula primarily serves to define a reasonable timescale for a typical but unspecified current-driven instability in a strong magnetic field. The important point here is to include an anomalous resistivity effect: further research is needed to pin down the appropriate instability, and to replace Eq. (III.29) with an updated formula. At this time it is sufficient that an instability threshold is reached (at constant current) when the plasma escapes from the neck, the line density N decreases, and the drift velocity $v_D \sim I_0/N$ exceeds the thermal velocity.

The computation shown below (Ivanov 1986) includes the anomalous resistivity, and a slightly more elaborate way of computing radiative loss than described here, viz., various line broadening effects for calculating the optical depths of individual lines. These added features allow the study of fine detail in the compression of micropinches, but the simple approach for calculating radiative losses is quantitatively correct for the basic properties.

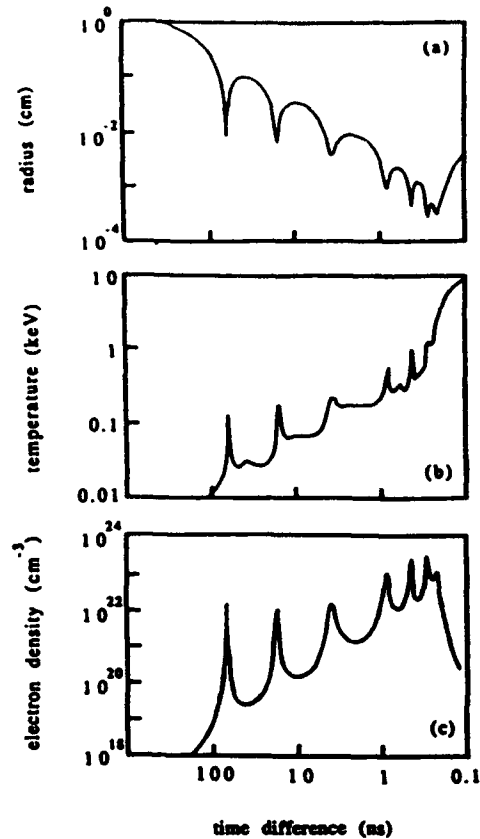


FIG. 11. Zero-dimensional numerical modeling of micropinching in an iron plasma with peak current ~ 150 kA: (a) plasma radius; (b) electron temperature; (c) electron density.

Figure 11 shows the temporal evolution of the plasma parameters during the process of micropinching. A special logarithmic time difference scale is used to represent all stages in a single graph. Zero time is the end of the final compression, usually when the temperature exceeds some high, but arbitrary value (20–50 keV). The duration of any stage corresponds to the difference between the ordinates.

The initial conditions for this computation are given on top of the figure. The distance between the iron electrodes is equal to the initial radius of the plasma, 1 cm, and an initial line density is $N_l = 3 \times 10^{17}/\text{cm}$. The first regime is a slow compression during the first 920 ns or so, followed by an hydrodynamic series of compressions and expansions (similar to Felber 1982) topped off by a fast radiative collapse in the final 1 ns.

At first the plasma compresses hydrodynamically to a radius 70–80 μm , at ~ 90 ns before the end of the computation, expands, and compresses again to a radius that decreases with each subsequent compression due to radiative energy loss (Meierovich 1985). These compressions end with a very small plasma region reminiscent of a plasma point, with radius around 3 μm . The temperature in Fig. 11(b) gets into the region 1–10 keV at this stage. The electron density in Fig. 11(c) goes up to $n_e \approx 10^{23}/\text{cm}^3$.

In this computation the plasma is initially uniform over radius. In this case the formation time of the plasma

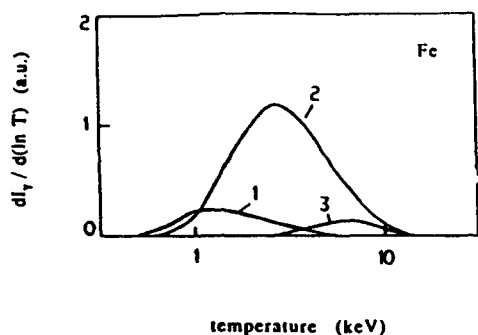


FIG. 12. Intensities of radiation versus temperature for iron: (1) dielectronic satellites of Li-like ions; (2) resonance lines of He-like ions; (3) resonance lines of H-like ions.

point, taken from the second compression to the end of the run, is about 20 ns. In other runs, where different radial distributions are assumed, the formation time varies from 50 to 20 ns. These values agree well with observations of the dynamics of micropinching.

The stagnation phase, between 20 and 1 ns, is characterized by a plasma radius $r \approx 0.1-0.2$ mm, electron temperature $T \approx 100$ eV, and an electron density oscillating around $n_e \sim 10^{21}/\text{cm}^3$. These parameters agree reasonably well with observations of the plasma during hydromagnetic compression.

In the plasma point region [denoted by "K" in the Fig. 12(a)], the plasma contracts to a radius of order $3 \mu\text{m}$. The electron density in this compression stage varies from $n_e \sim 3 \times 10^{23}/\text{cm}^3$ to $n_e \sim (1-2) \times 10^{24}/\text{cm}^3$; the electron temperature increases from 1.3 to 5 keV. The lifetime of the plasma point with radius $r < 2 \mu\text{m}$ is shorter than 100 ps. The calculated lifetime of the hot phase of the micropinch agrees well with the measured values (Aglitskii 1985) of 20 ps.

After the final compression the plasma column expands rapidly due to the fast loss of plasma from the pinch and the simultaneous appearance of anomalous resistance. During the expansion the plasma temperature continues to increase rapidly, reaching tens and more of keV. However, the expansion phase does not contribute significantly to K-line radiation due to its short lifetime and the rapidly decreasing plasma density.

Figure 11 appears to contain the basic phenomena observed in micropinching, including quantitatively correct results for the plasma parameters of the plasma point. The model also gives a quantitatively reasonable account of the plasma point's disassembly. We conclude that the radiation compression model captures the principal physics of radiation collapse. In the next section we discuss the scaling of plasma point parameters with initial parameters such as nuclear charge Z_n , peak current, and initial line density.

IV. EXPERIMENTAL RESULTS ON PLASMA POINTS INTERPRETED WITH THE RADIATION COLLAPSE MODEL

Section II presented the experimental results on plasma points, and Sec. III gave a computation for radia-

tion collapse of an iron pinch. This section uses the radiation collapse computation to interpret the experimental results. An important insight is that in a radiative collapse the plasma goes through a wide range of temperatures. As a result, the different measurement techniques for the electron temperature all give values within their range of validity. Electron temperature measurements for plasmas of various compositions corroborate the radiation collapse scenario. Radiative collapse can evolve in two different types of plasma points.

A. Electron temperature of plasma points

Computations of radiative collapse suggest that the plasma point goes through two orders of magnitude in density and temperature in a sub-ns time. In contrast, the x-ray spectral measurements are time-integrated, while their interpretation in terms of density and temperature usually assumes a stationary plasma. The plasma parameters obtained this way are always somewhere in the sensitivity range of the particular measurement technique. Measurements valid in widely different regimes then give widely different results corresponding to the regimes of validity.

Consider first the procedure for measuring the electron temperature T_e by the relative intensities of dielectronic satellites to the H- and He-like resonance lines. Figure 12 gives the relative intensity I_v for the resonance lines of H- and He-like iron ions, and for the dielectronic satellite lines, as function of temperature T . The intensities are given as $dI_v/d(\log T)$ to compensate for the logarithmic temperature scale, so that the total radiation in a specific line is proportional to the area under the corresponding curve. The intensities come from the iron pinch computations of Ivanov (1986), and take into account the changes in radius and density of the plasma point during its evolution over the last 200 ps of its life (see Fig. 11). Although the intensities vary with time it is possible to plot them as function of temperature, because the temperature increases monotonically with time.

Singly excited He-like iron is most abundant at a temperature of $T_e \approx 2.5$ keV, and therefore the resonance line of He-like iron is strongest at this temperature. For the same reason the resonance line of H-like iron peaks at a higher temperature $T_e \approx 6$ keV. Excitation of Li-like iron accounts for the satellites of the He-like resonance line, through dielectronic recombination, which therefore peaks at the lowest temperature $T_e \approx 1$ keV.

A spectrometer does not see the intensity ratios at each particular temperature if it is slow compared to the 20 ps timescale of plasma point formation. Instead, it registers the time-integrated intensity. The ratio between the time-integrated intensities corresponds to some intensity ratio for instantaneous intensities. The intensities of the H- and He-like resonance lines can be used to measure the temperature between 2.5 and 8 keV. Therefore, the effective temperature inferred from a time-integrated measurement with these lines, $T_{\text{He/H}}^{\text{eff}}$ is some average value, here $T_{\text{He/H}}^{\text{eff}} \approx 3.8$ keV, which depends somewhat on the detailed time history of the plasma point. Likewise, the effective

temperature $T_{He-DS}^{eff} = 1.9$ keV obtained from the ratio of dielectronic satellites to the He-like resonance line lies in the region where this temperature measurement is applicable. When the plasma point's temperature traverses a wide range of temperatures the measurement technique gives some arbitrary temperature in the regime of validity.

Similar arguments apply for temperature measurements with bremsstrahlung. In an optically thin plasma with temperature T_e the spectral intensity $I(h\nu)$ in harder photons with $h\nu \gg kT_e$ varies exponentially with photon energy $h\nu$. The temperature defined by this continuous spectrum is then $kT_e = -d(h\nu)/d[\ln I(h\nu)]$, which depends on the length of time that the plasma point spends in the photon energy regime used for the measurement. Therefore this approach produces temperatures that increase with the hardness of the radiation used for the measurement (Lee 1974; Burhenn 1984), and that are higher than the temperatures deduced from the line ratios. The computation of radiation collapse shows that the effective temperature in the micropinch would be $T_{30}^{eff} \approx 7$ keV when measured in the energy band around $h\nu \approx 30$ keV, but would increase to $T_{100}^{eff} \approx 11$ keV for the energy band $h\nu \approx 100$ keV.

Other computations show that the temperature inferred from bremsstrahlung varies with pinch current in a qualitatively correct manner. Changing the current from 100 to 150 kA increases the temperature in the computations from 9 to 11 keV (measured with radiation around $h\nu \approx 50$ keV). Under similar circumstances in an experiment the temperature of the plasma point increases from 5 to 7 keV (Bykovskii 1982).

B. Experiments with compound plasmas: Fe/Mo, Ti/Mo, Ti/Nb

The radiative collapse model predicts that density and temperature of plasma points increase with the atomic number of the element used in the pinch. Unfortunately, time-integrated measurements on the same line for the different elements also give results that increase with increasing atomic number. This problem is resolved by using a single element selected for diagnostic purposes intermixed with heavier elements.

Plasma parameters were inferred from the spectra of He-like iron Fe XXV in a pure iron pinch and a mixed iron-molybdenum pinch (Vikhrev 1982b; Sidel'nikov 1982b). Figure 13(a) is the spectrum from 100 discharges with pure iron, Fig. 13(b) from an iron-molybdenum pinch, with 50% Mo ($Z_n = 42$).

The spectra can be fully interpreted with the spectrum fitting procedure discussed earlier, but some qualitative features are obvious. The shape of the long-wavelength wing of the "j" satellite is equally broad in both spectra, and not through accidental overlap with other lines. Thus individual lines in both spectra have the same intrinsic broadening. However, the measured width of the resonance line is due to the overlap with the dielectronic satellites with principal quantum number $n > 3$. This width is 4.2×10^{-3} Å for Fe, but decreases to 3.4×10^{-3} Å for (Fe + Mo), reflecting a smaller contribution of the satel-

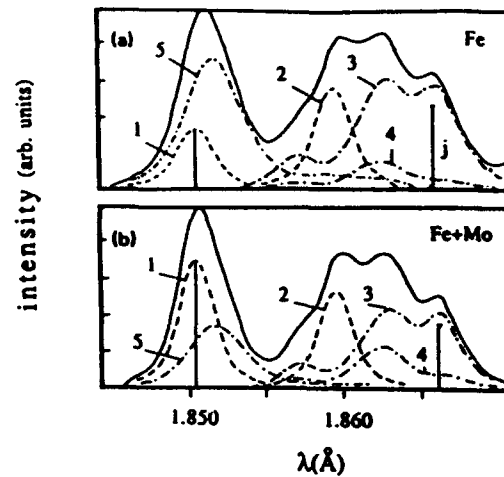


FIG. 13. Spectrum of a plasma point (a) with an anode of pure iron; (b) with a 50% iron, 50% molybdenum anode.

lites to the long-wavelength wing of the total lineshape due to the increased temperature of the emitting plasma.

The full fitting procedure shows that the relative intensity of dielectronic satellites in the (Fe + Mo) plasma is 3–3.5 times smaller than the pure iron plasma. The intensity decrease corresponds to an increase in the electron temperature from 1.4 keV for pure iron to 2.0–2.4 keV for the compound (Fe + Mo) plasma.

The spectrum around the resonance line of Fe XXV can not be used to measure the plasma's electron density using the collisional mixing of autoionized states, but this can be done with spectra of Ti XX–XXI. Therefore, titanium plasmas with various admixtures were diagnosed by using the resonance line Ti XXI and its satellites (Sidel'nikov 1982b). The electrodes in these experiments varied from pure titanium to a blend of titanium with 20%–50% of molybdenum and niobium ($Z_n = 41$).

The measurements are not precise enough to see a difference in the spectrum with a 20% admixture of Mo and Nb to the titanium, but a 50% admixture of heavy impurities (Mo or Nb) gives a ~20% narrower resonance line due to a smaller contribution from the intercombination and dielectronic satellite lines. Full analysis of the spectra shows that the temperature increases T_e from 1.2–1.3 keV for a pure Ti pinch to $T_e \approx 1.4$ –1.5 keV for Ti with a 50% admixture of heavy impurities. The increase in the density-sensitive satellite "q" corresponds to an increase in the electron density by a factor of about 1.5. These careful estimates of density and temperature for plasma points with different atomic numbers confirm the expectations from the radiative collapse model: time-averaged diagnostics give values for density and temperature that increase with atomic number.

C. Two regimes of micropinching

Many experiments integrate x-ray spectra over many shots under the assumption that all plasma points are similar in character. However, plasma points do not develop

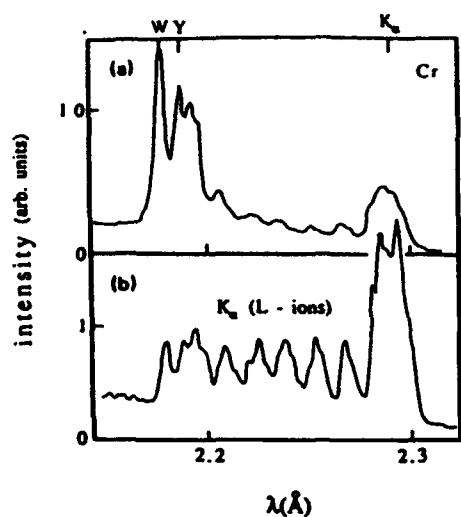


FIG. 14. Spectrum in chromium ($Z_n = 24$): (a) from a small plasma point ($d < 3 \mu\text{m}$); (b) from a large plasma point ($d \approx 100 \mu\text{m}$).

on some shots, and when a plasma point appears it can have quite irreproducible size and position. What happens in individual plasma points?

Single-shot spectra must be studied with a highly sensitive spectrometer (e.g., Schultz 1989; Aglitskii 1984). The measurement technique (Antsiferov 1989) uses a curved quartz crystal spectrograph with different crystals ($2d = 2.26, 4.91, \text{ and } 6.68 \text{ \AA}$) and radii of curvature $R = 300\text{--}800 \text{ mm}$. The spectra are amplified by a micro-channel plate covered by a layer of ZnS doped with Ag (Aglitskii 1984), and registered photographically. Plasma size can be correlated with the spectrum on each shot by using the blurring of the x-ray image's edge.

These measurements, done with a maximum current $I_m \sim 150\text{--}200 \text{ kA}$ and plasmas of Cr, Mn, and Fe, give two types of plasma points, large and small. The small plasma points are a few μm across, the large plasma points are $\sim 0.1 \text{ mm}$ in diameter. Both types, large and small, emit spectra with resonance lines ($1s^2-1s2p^1P_1$) and intercombination lines ($1s^2-1s2p^3P_1$), and also satellite transitions in ions of low multiplicity, but obvious differences in the spectra suggest that the plasma points have quite different parameters.

The chromium (Cr, $Z_n = 24$) spectra in Fig. 14 are good examples. Figure 14(a) is a spectrum for a small plasma point, and Fig. 14(b) for a large plasma point. The spectra contain the same lines, but in quite different proportions: the small plasma point radiates $\sim 10\times$ more in the resonance line (line "W" at 2.19 \AA), and the satellite transitions are relatively less important. In the large plasma point [Fig. 14(b)] the dominant radiation consists of K_α lines, between 2.1 and 2.9 \AA , probably excited by nonthermal electrons of a colder plasma in the L-shell ionization state. The nonthermal electrons could be isotropic, but they are more likely in the form of a directed beam: the spectrum is consistent with both possibilities.

Plasma of lighter elements, such as sulphur

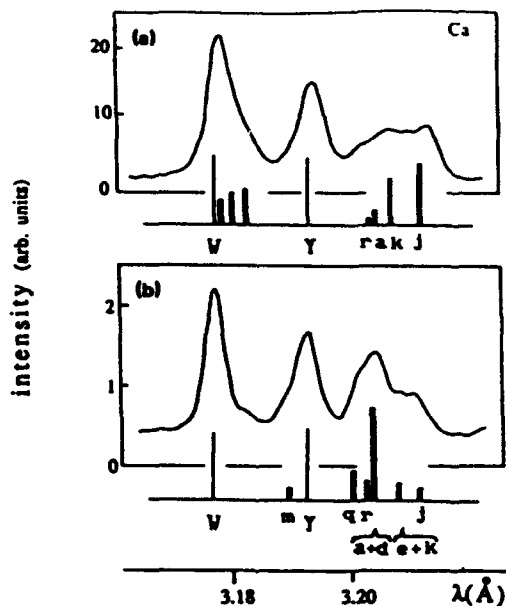


FIG. 15. Spectrum in a calcium ($Z_n = 20$) plasma: (a) from a small plasma point; (b) from a large plasma point. The bars give the positions and relative magnitudes of the brightest dielectronic satellites.

($Z_n = 16$) and calcium (Ca, $Z_n = 20$), show analogous results, but now the diameter of the small plasma point is about $10\text{--}15 \mu\text{m}$, while the large plasma point is $0.2\text{--}0.3 \text{ mm}$ across. Both regimes of micropinching were also found (Aglitskii 1986) for heavier elements, Cu at $Z_n = 29$ and Zn at $Z_n = 30$. In this case the small points were smaller than the experimental resolution ($< 3 \mu\text{m}$), while the large plasma points have diameters $\sim 30\text{--}50 \mu\text{m}$. The x-ray spectra of these elements show the same tendencies as in Fig. 14, so that for the large plasma points the resonance lines are practically absent.

A characteristic feature of the x-ray spectra from the large plasma points are dielectronic satellites excited from Li-like ions by electron-ion collisions, while the satellite lines in the x-ray spectra of the small plasma points come from dielectronic recombination. An example is the spectrum for a small plasma point in calcium, Fig. 15(a), compared to Fig. 15(b) for a large plasma point. The resonance line "W" for the small plasma point is visibly wider than the same line for the large plasma point, indicating dielectronic recombination due to the high density (compare the discussion of Fig. 13). The bars in Fig. 15 are the (relative) strengths of the different lines needed to fit the spectrum. These agree with predictions from dielectronic capture. The resonance line in the large plasma point is not broadened by satellites, and the relative strength corresponds to collisional excitation.

Why are there two kinds of plasma points? In the radiative collapse model the plasma point disassembles due to anomalous Joule heating connected with the development of microturbulence. If the plasma remains in the Joule heating regime during compression a small plasma point emerges, while a large plasma point is formed if

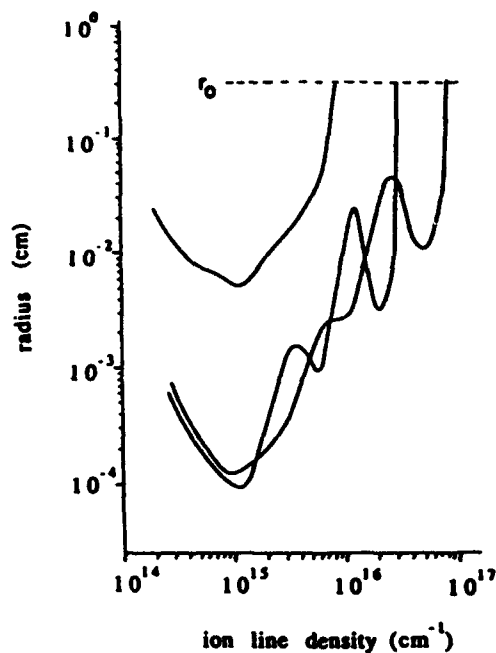


FIG. 16. Micropinching in iron for three linear ion densities $N_l(r_0)$ and the same initial radius $r_0 = 3$ mm.

anomalous heating exceeds the radiative losses early on in the compression process. Anomalous heating starts when the drift velocity $v_D = I/eN_e$ is on the order of a characteristic thermal velocity in the plasma such as the ion sound velocity $v_s = \sqrt{kT/M}$. For a Bennett pinch $v_D = v_s$ implies $N_e r_e = M/m$, where $r_e = (e^2/mc^2)[1/4\pi\epsilon_0]$ is the classical radius of the electron. The critical line density would then be $N_c \approx 3M/m \times 10^{12}/\text{cm}$, corresponding to an initial line density $N_0 \sim 10^{16}/\text{cm}$, weakly dependent on the other pinch parameters such as temperature or the effective atomic number Z_{eff} .

According to these considerations the dynamics of micropinching may depend significantly on the initial line density in the discharge. The initial line density in a vacuum spark arises primarily as a result of evaporation of the anode by electrons pulled out of the pre-cathode plasma by the initial voltage. This complicated process is likely to give different initial line densities from shot to shot. Moreover, the line density of this plasma decreases with increasing distance from the anode, creating different initial conditions for the development of the pinch along the axis of the discharge.

The radiative collapse model is sensitive to the initial line density N_0 . Figure 16 contains results from three computations on an iron plasma with 150 kA peak current and initial radius $r_0 = 3$ mm, and different line densities given in the figure (Antsiferov 1989). Shown is the compression dynamics by plotting the radius $r(t)$ and ion line density $N_l(t)$ in the (r, N_l) plane.

In the initial stage of the compression the line density remains constant for all three cases, indicating no outflow of plasma. After this initial stage the tenuous case with $N_l(0) = 10^{16}/\text{cm}$ loses mass while contracting radially un-

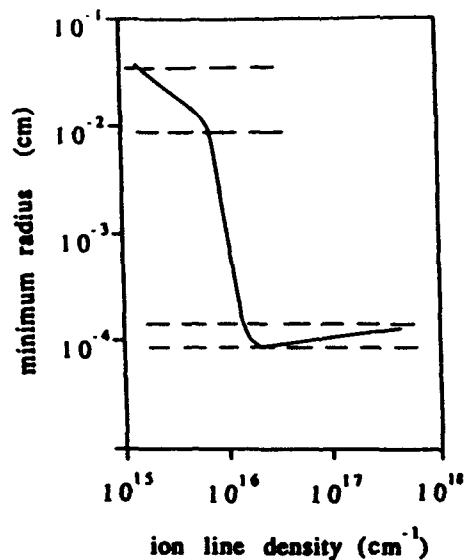


FIG. 17. The minimum radius of an iron plasma during micropinching as function of the initial linear ion density N_l .

til it reaches a minimum of 0.1 mm at $N_l \approx 10^{15}/\text{cm}$. In contrast, the pinches with initial line density $\geq 2.5 \times 10^{16}/\text{cm}$ contract in an oscillatory fashion also seen in Fig. 11 (for different initial conditions). The final size is now much smaller, $r_{min} \sim 1 \mu\text{m}$. Expansion starts at about the same line density for all three cases, namely when the drift speed for the 150 kA current exceeds a thermal velocity.

Figure 17 shows the minimum radius r_{min} obtained during the compression as function of the initial line density. For initial line density $N_l(0) > 10^{16}/\text{cm}$ the pinch reaches a minimum radius of 1–2 μm , while for an initial line density $N_l(0) < 10^{16}/\text{cm}$ the final pinch size exceeds ~ 0.1 mm. The plot suggests two radiative collapse regimes, one with large final radius for pinches with small line density, and one with small final radius for more massive pinches, with a small transition region in between. A collapse with large final radius is reminiscent of the large plasma point, while the collapse with small final radius looks like a small plasma point. This phenomenology is corroborated by experimental data (Koloshnikov 1985): for aluminum the transition occurs around $3 \times 10^{15}/\text{cm}$ (Ivanenkov 1989).

Other computations, for calcium ($Z_n = 20$) and zinc ($Z_n = 30$), show the same well-defined transition between the two micropinch regimes. Moreover, in these computations the minimum radius decreases with increasing nuclear charge Z_n , in agreement with experimental results.

The computed radiation output per plasma point agrees with the experimental value. In the computations the energy K lines from a small plasma point is about 0.04 J per shot, while the experimental value is about 0.02 J (Veretennikov 1985). For the large plasma point the computed K-line energy per shot is more than an order of

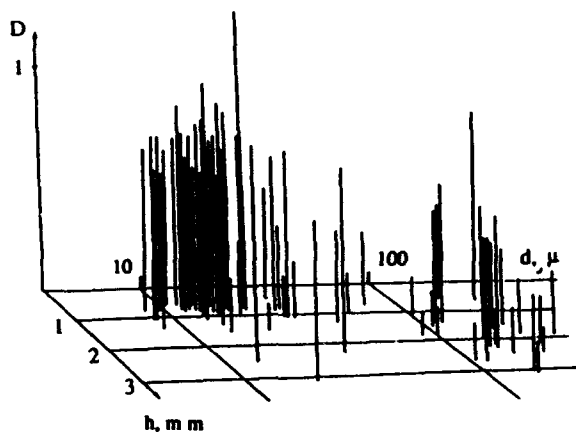


FIG. 18. Correlation between the size of d of the plasma point (horizontal axis), the distance between the anode and the point's h in the discharge gap (forward axis), and the intensity of radiation D (vertical axis). The plasma is titanium ($Z_a = 22$), and the current is 100 kA.

magnitude less, in agreement with experimental data of Figs. 14 and 15.

The size of the plasma point is correlated with its position in the discharge gap (Antsiferov 1989) in a manner that is consistent with the two regimes of radiative collapse. The measurements were made at 100 kA in a Ti plasma ($Z_a = 22$), with an experimental resolution of the pinch size of $5 \mu\text{m}$. Figure 18 shows the results. The forward pointing axis is the distance to the anode, the horizontal axis is the size of the plasma point, and the vertical axis is the intensity of the K -line output as gauged by the film density.

The data show two groups of plasma points. The small plasma points, with radius $r \sim 10 \mu\text{m}$, are located mainly close to the anode, while the large plasma points, with radius $r \sim 0.2 \text{ mm}$, are typically farther away. Moreover, the film density of the small plasma points is several times larger than for the large plasma points. These experimental data are consistent with the results in Figs. 16 and 17 obtained from computations on simple theoretical models.

V. CONCLUSION

The experimental results appear to show a radiative collapse phenomenon in low-inductance vacuum sparks. Two types of plasma points have been documented, small plasma points around a few microns in size, with extreme values for density $n \sim 10^{23}/\text{cm}^3$ and temperature $T_e \gtrsim \text{keV}$, and large plasma points with one order of magnitude larger size and two orders of magnitude smaller density. Discrepancies between the values given in the literature over the years are explained in part by the two different regimes, and in part by the fact that a plasma point is dynamic: the plasma's density and temperature can change drastically during collapse. In this case the plasma parameters inferred from time-averaged x-ray spectroscopy depend on the range of validity of the measurement technique.

Many characteristics of the plasma points are successfully reproduced by a radiative collapse model (Vikhrev

1982a). The model's principal ingredients are the strong radiative power from the ions as modified by opacity effects, and the reduction of line density due to axial outflow. Radiative collapse ends by the onset of anomalous heating.

Other types of discharges with axial symmetry often show small, bright regions of x-ray emission that appear to be similar to the plasma points discussed here. For example, plasma points appear in experiments with exploding wires (Burkhalter 1977; Zakharov 1983). For currents up to 200 kA the parameters of the plasma point are close to the ones measured in low-inductance vacuum sparks.

Gas puff z-pinches also show plasma points, generally called bright spots in the z-pinch literature, whose size, temperature, and density of plasma appear to vary considerably depending on the type of the apparatus, the current in the discharge, and the initial conditions. However, it is possible to have a regime that produces small plasma points with sizes of several μm in a $\sim 1 \text{ MA}$ current discharge (Gol'ts 1986/7; Sopkin 1990). The x-ray spectrum of the He-like krypton and xenon in these experiments shows plasma points with temperatures of tens of keV, and $n_e \tau \gtrsim 10^{12} \text{ cm}^3/\text{s}$.

Similar observations come from plasma focus experiments. Plasma points with size $\sim 10 \mu\text{m}$ arise in the second compression of the focus, when the hydrogen plasma increases its radiation loss through additional anode material (copper) (Fillipov 1983). Similar phenomena are seen in experiments on a plasma focus discharge in a mixture of deuterium and heavy noble gases (Peacock 1969; Volobuev 1988; Koshelev 1988). The x-ray spectra of the heavy impurities indicate that the electron temperature reaches about 700–1000 eV in plasma points of about $20 \mu\text{m}$.

The addition of several percent impurities produces a significant change in the character of the final pinch in these and other experiments. In the explosion of CD_2 wires (Young 1977) the radiation from carbon ions apparently leads to small plasma points (Decker 1990). Also the compression of z pinches in deuterium changes drastically with the admixture of high atomic number elements (Bailey 1986). These experiments again demonstrate the essential role of radiation loss on the dynamics of many types of discharges, and especially on plasma point formation.

Micropinches are primarily used as radiation sources for spectra of multiply charged ions, but in the future micropinches may become sources of XUV and soft x rays for technological applications (e.g., Veretennikov 1982), and for pumping of x-ray lasers (e.g., Finkenthal 1986; Oravskii 1987). For this application it is important that the short lifetime of a micropinch corresponds to a high radiation power despite the small total energy.

- E. V. Aglitskii, E. Ya. Gol'ts, Yu. A. Levykin, and A. M. Livshits (1984). *Opt. Spectrosc.* 56, 33 (*Opt. Spectrosc.* 56, 20).
- E. V. Aglitskii, P. S. Antsiferov, and A. M. Panin (1985). *Fiz. Plazmy* 11, 1266 [*Sov. J. Plasma Phys.* 10, 726].
- E. V. Aglitskii, P. S. Antsiferov, K. N. Koshelev, and A. M. Panin (1986). *Fiz. Plazmy* 12, 1189 (*Sov. J. Plasma Phys.* 12, 683).
- S. G. Alikhanov, V. I. Vasilev, E. Ya. Kononov, K. N. Koshelev, Yu. V. Sidel'nikov, and D. A. Toporkov (1984). *Fiz. Plazmy* 10, 1051. (*Sov. J. Plasma Phys.* 10, 605).

- P. S. Antsiferov, K. N. Koshelev, A. E. Kramida, and A. M. Panin (1989). *J. Phys. D* 22, 1073.
- J. P. Apruzese and P. C. Kepple (1989). *AIP Conf. Proc.* 195, 108.
- J. P. Apruzese and P. C. Kepple (1990). *J. Quant. Spectrosc. Radiat. Trans.* 44, 529.
- L. E. Aranchuk, G. S. Bogolyubskii, G. S. Volkov, V. D. Korolev, Yu. V. Koba, V. I. Liksonov, A. A. Lukin, L. B. Nikandrov, O. V. Tel'kovskaya, M. V. Tupolov, A. S. Chernenko, Ya. V. Tsarfin, and V. V. Yankov (1986). *Fiz. Plazmy* 12, 1324 (*Sov. J. Plasma Phys.* 12, 765).
- J. Bailey, A. Fisher, and N. Rostoker (1986). *J. Appl. Phys.* 60, 1939.
- V. I. Bayanov, V. A. Boiko, A. V. Vinogradov, S. S. Gulidov, A. A. Ilyukin, V. A. Katulin, A. A. Mak, V. Yu. Nosach, A. L. Petrov, G. V. Peregodov, S. A. Pikuz, I. Yu. Skobelev, A. D. Starikov, A. Ya. Faenov, V. A. Chirikov, and E. A. Yukov (1976). *Pis'ma Zh. Eksp. Teor. Fiz.* 24, 352 (*JETP Lett.* 24, 319).
- R. Beier and H. -J. Kunze (1978). *Zeits. Phys. A* 285, 347.
- W. H. Bennett (1934). *Phys. Rev.* 45, 89.
- C. P. Bhalla, A. H. Gabriel, and L. P. Presnyakov (1975). *Mon. Not. R. Astron. Soc.* 172, 359.
- D. Book, E. Ott, and M. Lampe (1976). *Phys. Fluids* 19, 1982.
- S. I. Braginskii (1957). *Zh. Eksp. Teor. Fiz.* 33, 645. (*Sov. Phys. JETP* 6, 494).
- C. Breton, C. DeMichelis, and M. Mattiolo (1978). *JQRST* 19, 367.
- R. Burhenn, B. S. Harn, S. Gossling, H. -J. Kunze, and D. Mielczarski (1984). *J. Phys. D* 17, 1665.
- P. J. Burkhalter, J. Shiloh, A. Fisher, and R. D. Cowan (1979). *Appl. Phys.* 50, 4532.
- P. G. Burkhalter, C. M. Dozier, and D. J. Nagel (1977). *Phys. Rev. A* 15, 700.
- Yu. A. Bykovskii and V. V. Lagoda (1982). *Zh. Eksp. Teor. Fiz.* 56, 114 (*Sov. Phys. JETP* 56, 61).
- J. P. Chittenden (1989). *AIP Conf. Proc.* 195, 118.
- J. P. Chittenden and M. G. Haines (1990). *Phys. Fluids B* 2, 1889.
- P. Choi, A. E. Dangor, C. Deeney, H. Herold, and C. S. Wong (1987). "Experimental Investigation of Hotspot and Electron Beam Formation in a Gas Puff *z*-pinch and a Plasma Focus," presented at the IEEE International Conference on Plasma Science, Arlington, VA.
- S. S. Churikov, L. A. Dorokhin, K. N. Koshelev, and Yu. V. Sidel'nikov, *JQSRT* 44, 567 (1990).
- W. A. Cilliers, R. U. Datla, and H. R. Griem (1975). *Phys. Rev. A* 12, 1408.
- F. L. Cochran and J. Davis (1990). *Phys. Fluids B* 2, 1238.
- L. Cohen, U. Feldman, M. Swartz, and J. H. Underwood (1968). *J. Opt. Soc. Am.* 58, 843.
- R. U. Datla and H. R. Griem (1978). *Phys. Fluids* 21, 505.
- R. U. Datla and H. R. Griem (1979). *Phys. Fluids* 22, 1415.
- G. Decker, W. Kies, M. Malzig, Yu. V. Sidel'nikov, C. van Calcar, G. Zieton, H. Bluhm, D. Rusch, and W. Ratajczak (1990). *Nucl. Fusion* (in press).
- C. Deeney, T. Nash, P. D. LePell, K. Childers, and M. Krishnan (1989). *AIP Conf. Proc.* 195, 62.
- H. M. Epstein, W. J. Callagher, P. J. Mallozzi, and T. F. Stratton (1970). *Phys. Rev. A* 2, 146.
- F. S. Felber (1982). *Phys. Fluids* 25, 643.
- N. V. Filipov (1983). *Fiz. Plazmy* 9, 25. (*Sov. J. Plasma Phys.* 9, 14).
- M. Finkenthal, J. L. Schwob, and P. Mandelbaum (1986). *J. de Physique* 47, C6-129.
- J. Fukai and E. J. Clothiaux (1975). *Phys. Rev. Lett.* 34, 863.
- A. H. Gabriel and C. Jordan (1972a). *Case Studies in Atomic Collision Physics*, edited by McDaniell and McDowell (Amsterdam, North-Holland, 1972, v. 2, p. 209).
- A. H. Gabriel (1972b). *Mon. Not. R. Astron. Soc.* 160, 99.
- M. Gersten, W. Clark, J. Rauch, G. M. Wilkinson, J. Katzenstein, R. D. Richardson, J. Davis, D. Duston, J. P. Apruzese, and R. Clark (1986). *Phys. Rev. A* 33, 477.
- J. L. Giuliani (1989). *AIP Conf. Proc.* 195, 124.
- E. Ya. Gol'ts, I. A. Zhitnik, E. Ya. Kononov, S. L. Mandel'shtam, and Yu. V. Sidel'nikov (1975). *Dok. Akad. Nauk SSSR* 220, 560 (*Sov. Phys. Dokl.* 20, 49).
- E. Ya. Gol'ts, G. V. Koloshnikov, K. N. Koshelev, A. E. Kramida, Yu. V. Sidel'nikov, V. V. Vikhrev, V. V. Ivanov, A. A. Palkin, and V. V. Prut (1986). *Phys. Lett. A* 115, 114.
- E. Ya. Gol'ts, L. A. Dorokhin, K. N. Koshelev, A. E. Kramida, A. A. Palkin, and Yu. V. Sidel'nikov (1987). *Phys. Lett. A* 119, 359.
- M. G. Haines (1960). *Proc. R. Soc. London* 76, 250.
- J. E. Hammel (1976). "The Joule heating of a stable pinched plasma," LANL Report LA-6023-MS.
- B. A. Hammel and L. A. Jones (1984). *Appl. Phys. Lett.* 44, 667.
- J. D. Hares, R. E. Marrs, and R. J. Fortner (1985). *J. Phys. D* 18, 627.
- T. Holstein (1951). *Phys. Rev.* 83, 1159.
- R. H. Huddleston and S. L. Leonard (1965). *Plasma Diagnostic Techniques* (Academic, New York).
- G. V. Ivanenkov, A. N. Lebedev, S. A. Pikuz (1989). "Spectral investigations of a *z*-pinch," Preprint No. 210, P. N. Lebedev Institute, Moscow.
- V. V. Ivanov (1986). Dissertation, Kurchatov Institute, Moscow.
- V. L. Jacobs, J. Davis, P. C. Kepple, and M. Blaha (1977). *Astrophys. J.* 211, 605.
- M. Klapisch, J. L. Schwob, B. S. Frankel, and J. Ored (1977). *J. Opt. Soc. Am.* 67, 148.
- D. R. Kanis and L. A. Jones (1984). *Phys. Rev. Lett.* 53, 166.
- G. V. Koloshnikov, K. N. Koshelev, Yu. V. Sidel'nikov, and S. S. Churikov (1985). *Fiz. Plazmy* 11, 259 (*Sov. J. Plasma Phys.* 11, 150).
- E. Ya. Kononov, K. N. Koshelev, and Yu. V. Sidel'nikov (1977). *Fiz. Plazmy* 3, 663 (*Sov. J. Plasma Phys.* 3, 375).
- E. Y. Kononov, K. N. Koshelev, V. I. Safronova, Yu. V. Sidel'nikov, and S. S. Churikov (1980). *Pis'ma Zh. Eksp. Teor. Fiz.* 31, 720 (*JETP Lett.* 31, 679).
- E. Ya. Kononov (1983). *Physica Scripta* 27, 117.
- E. Ya. Kononov, K. N. Koshelev, and Yu. V. Sidel'nikov (1985). *Fiz. Plazmy* 11, 927 (*Sov. J. Plasma Phys.* 11, 538).
- E. D. Korop, B. E. Meierovich, Yu. V. Sidel'nikov, and S. T. Sukhorukov (1979). *Usp. Fiz. Nauk* 129, 87 (*Sov. Phys. Usp.* 22, 727).
- K. N. Koshelev, Y. V. Sidel'nikov, and V. V. Vikhrev (1985). *Nucl. Instrum. Methods B* 9, 704.
- K. N. Koshelev, V. I. Krauz, N. G. Reshetniak, R. G. Salukvadze, Yu. V. Sidel'nikov, and E. Ya. Khautiev (1988). *J. Phys. D* 21, 1827.
- T. N. Lee and R. C. Elton (1971). *Phys. Rev. A* 3, 865.
- T. N. Lee (1974). *Astrophys. J.* 190, 467.
- T. N. Lee (1975). *Ann. N.Y. Acad. Sci.* 251, 112.
- L. R. Lindemuth (1990). *Phys. Rev. Lett.* 65, 179.
- B. E. Meierovich (1984). *Phys. Rep.* 104, 259.
- B. E. Meierovich (1985). *Fiz. Plazmy* 11, 1446 (*Sov. J. Plasma Phys.* 11, 831).
- B. E. Meierovich (1986). *Usp. Fiz. Nauk* 149, 221 (*Sov. Phys. Usp.* 29, 506).
- R. A. Millikan and R. A. Sawyer (1918). *Phys. Rev.* 12, 167.
- S. Morita and J. Fujita (1983). *Appl. Phys. Lett.* 43, 443.
- C. R. Negus and N. J. Peacock (1979). *J. Phys. D* 12, 91.
- A. N. Oraevskii, O. G. Semenov, and B. N. Chichkov (1987). *Kvan. Elektron* 14, 1998 [*Sov. J. Quant. Electr.* 17, 1274].
- N. J. Peacock (1968). Private communication.
- N. J. Peacock, R. J. Speer, and M. G. Hobby (1969). *J. Phys. B* 2, 798.
- R. S. Pease (1957). *Proc. R. Soc. B* 70, 445.
- N. R. Pereira and K. G. Whitney (1988a). *Phys. Rev. A* 38, 319.
- N. R. Pereira and J. Davis (1988b). *J. Appl. Phys.* 64, R1.
- N. R. Pereira (1990). *Phys. Fluids B* 2, 677.
- D. E. Post, R. V. Jensen, C. B. Tarter, W. H. Grasberger, and W. A. Lokke (1977). *At. Data Nucl. Data Tables* 20, 397.
- J. C. Riordan, J. S. Pearlman, M. Gersten, and J. E. Rauch, "Sub-kilovolt x-ray emission from imploding wire plasmas," in *AIP Conference Proceedings*, Vol. 75, edited by D. Attwood and B. Henke.
- A. E. Robson (1989a). *Phys. Fluids B* 1, 1834.
- A. E. Robson (1989b). *Phys. Rev. Lett.* 63, 2816.
- A. Schultz, R. Burhenn, F. B. Rosmej, and H. J. Kunze (1989). *J. Phys. D* 22, 659.
- J. J. Schwob and B. S. Frankel (1972). *Phys. Lett.* 40A, 81.
- J. F. Seely and T. N. Lee (1984). *Phys. Rev. A* 29, 411.
- J. W. Shearer (1976). *Phys. Fluids* 19, 1426.
- Yu. V. Sidel'nikov (1982a). Dissertation, Institute of Spectroscopy, USSR Academy of Sciences, Troitsk.
- Yu. V. Sidel'nikov (1982b). *Zh. Tekh. Fiz.* 52, 2283. (*Sov. Phys. Tech. Phys.* 27, 1402).
- Yu. V. Sopkin, L. A. Dorokhin, K. N. Koshelev, and Yu. V. Sidel'nikov (1991). *Phys. Lett. A* (submitted).
- C. Stallings, K. Childers, I. Roth, and R. Schneider (1979). *Appl. Phys. Lett.* 35, 524.

- R. E. Stewart, D. D. Dietrich, P. O. Egan, R. J. Fortner, and R. J. Dukart (1987). *J. Appl. Phys.* **61**, 126.
- B. A. Trubnikov and S. K. Zhdanov (1976). *Zh. Eksp. Teor. Fiz.* **70**, 92. (*Sov. Phys. JETP* **43**, 48).
- J. J. Turechek and H. -J. Kunze (1975). *Zeits. Phys. A* **273**, 111.
- L. A. Vainshtein and U. I. Safronova (1978). *Atomic Data and Nuclear Data Tables* **21**, 49.
- L. A. Vainshtein, I. I. Sobelman, and E. A. Yukov (1979). *Excitation of Atoms and Broadening of Spectral Lines*, Nauka, Moscow; also Springer Verlag, Berlin and New York (1981).
- V. A. Veretennikov, V. A. Gribkov, E. Ya. Kononov, O. G. Semenov, and Yu. V. Sidel'nikov (1981a). *Fiz. Plazmy* **7**, 455. (*Sov. J. Plasma Phys.* **7**, 249).
- V. A. Veretennikov, S. N. Polukhin, O. G. Semenov, and Yu. V. Sidel'nikov (1981b). *Fiz. Plazmy* **7**, 1199. (*Sov. J. Plasma Phys.* **7**, 656).
- V. A. Veretennikov, A. N. Dolgov, A. I. Isakov, V. L. Kotsyrev, O. N. Krokhin, A. P. Nekunde, O. V. Sagalovskaya, O. G. Semenov, Yu. V. Sidel'nikov, V. V. Ulyanov (1982). *Pisma Zh. Eksp. Teor. Fiz.* **8**, 1041 (*Sov. Tech. Phys. Lett.* **8**, 448).
- V. A. Veretennikov, A. N. Dolgov, O. N. Krokhin, and O. G. Semenov (1985). *Fiz. Plazmy* **11**, 1007. (*Sov. J. Plasma Phys.* **11**, 587).
- V. V. Vikhrev (1977). *Fiz. Plazmy* **3**, 98 (*Sov. J. Plasma Phys.* **3**, 539).
- V. V. Vikhrev (1978a). *Pis'ma Zh. Eksp. Teor. Fiz.* **27**, 104 (*JETP Lett.* **27**, 95).
- V. V. Vikhrev and K. G. Gureev (1978b). *Zh. Tekh. Fiz.* **48**, 2264. (*Sov. Phys.-Tech. Phys.* **23**, 1295).
- V. V. Vikhrev, V. V. Ivanov, and K. N. Koshelev (1982a). *Fiz. Plazmy* **8**, 1211. (*Sov. J. Plasma Phys.* **8**, 688).
- V. V. Vikhrev, V. V. Ivanov, K. N. Koshelev, and Yu. V. Sidel'nikov (1982b). *Dokl. Akad. Nauk SSSR* **262**, 1361 (*Sov. Phys. Dokl.* **27**, 153).
- A. V. Vinogradov, I. Yu. Skobelev, and E. A. Yukov (1977). *Zh. Eksp. Teor. Fiz.* **72**, 1762. (*Sov. Phys. JETP* **45**, 925).
- I. V. Volobuev, V. A. Gribkov, D. Denus, N. V. Kalachev, T. A. Kozlove, O. N. Krokhin, S. Sledzinski, S. A. Startsev, and S. Cackaj (1988). *Fiz. Plazmy* **14**, 682. (*Sov. J. Plasma Phys.* **14**, 401).
- T. J. Welch and E. J. Clothiaux (1974). *J. Appl. Phys.* **45**, 3825.
- F. Winterberg (1978). *Zeits. Phys. Z* **284**, 43.
- F. C. Young, S. J. Stephanakis, and D. Mosher (1977). *J. Appl. Phys.* **48**, 3642.
- S. M. Zakharov, G. V. Ivanenkov, A. A. Kolomenskii, S. A. Pikuz, and A. I. Samokhin (1983). *Fiz. Plazmy* **9**, 469. (*Sov. J. Plasma Phys.* **9**, 271).

APPENDIX B: PUBLISHED PAPERS ON PRS

A simple derivation of the Pease-Braginskii current

Nino R. Pereira

Berkeley Research Associates, P.O. Box 852, Springfield, Virginia 22150

(Received 7 September 1989; accepted 29 November 1989)

The Pease-Braginskii current is rederived for a uniform single species Z pinch. The result contains the Alfvén current and the ratio between the collisional and bremsstrahlung cross sections.

The Pease-Braginskii current I_{PB} is a unique value of the current for a fully ionized hydrogen pinch.^{1,2} This current corresponds to force equilibrium, expressed by the Bennett relation,³ and, in addition, the power equilibrium between bremsstrahlung loss and Joule heating. The literature^{3,4} typically contains various numerical formulas for I_{PB} , e.g., I_{PB} (MA) = 0.433 (ln Λ)^{1/2}, where ln Λ is the Coulomb logarithm; often ln Λ is implicitly taken as ~ 10 and I_{PB} is given as ~ 1.4 MA.

It should be expected that this unique value of the current is related in some transparent way to nature's current scale, the Alfvén(-Lawson) current I_A . This current scale is defined by the fundamental constants of nature (c, e, μ_0 , and the like) as $I_A = ec/r_e$, where the classical radius of the electron $r_e = (e^2/mc^2)[1/4\pi\epsilon_0]$. Here we rederive the Pease-Braginskii current as the natural current scale I_A , multiplied by a ratio between the cross sections for multiple collisions ($\sim 8 \ln \Lambda$) and bremsstrahlung ($\sim \alpha F$) [Eq. (6)].

The model pinch consists of a stationary plasma cylinder with uniform temperature T , electron density n_e , ion density $n_i = n_e/Z$, and single charge state Z . Irrespective of any radial gradients the total current I is related to the total line density and temperature by the Bennett relation⁵

$$\mu_0 I^2 / 4\pi = 2N_e (1 + 1/Z) kT, \quad (1a)$$

where the electron line density $N_e = \pi r_0^2 n_e$ and r_0 is the pinch radius. In terms of the Alfvén current, which can be written as $\mu_0 I_A^2 / 4\pi = mc^2/r_e$, the Bennett relation becomes

$$\left(\frac{I}{I_A}\right)^2 = 2\left(1 + \frac{1}{Z}\right) \left(\frac{kT}{mc^2}\right) (N_e r_e). \quad (1b)$$

The Pease-Braginskii current I_{PB} in this stationary pinch is defined by a balance between resistive (or Joule) heating and bremsstrahlung radiative loss. In the absence of heat conduction, opacity, and the like (as we shall assume), both Joule heating and bremsstrahlung loss are local, collisional processes. It is therefore tempting to express these losses as a local power density of the form $P = n_e n_i v \sigma (\Delta\epsilon)$, where v is some average velocity, σ a typical cross section, and $\Delta\epsilon$ a typical energy transfer per collision.

In the simplest model of Joule heating an electron is accelerated by the electric field until a time $1/\nu_{ei}$, when it suffers a collision and the energy gain is randomized. The power deposition from Joule heating is $P_j = \eta j^2$, where η is the resistivity and j is the current density. Explicitly, $\eta = m\nu_{ei}/n_e e^2$, with $\nu_{ei} = 8 \ln \Lambda (u_0 a_0^2) Z n_e (2\mathcal{R}/kT)^{3/2}$. This useful but nonstandard form is written in atomic units,⁶ viz., the Bohr radius $a_0 = \hbar^2/mc^2[4\pi\epsilon_0]$, the atomic veloc-

ity $u_0 = \alpha c$, where $\alpha = (e^2/c\hbar)[1/4\pi\epsilon_0]$ is the fine structure constant, and the Rydberg energy $2\mathcal{R} = m u_0^2 = \alpha^2 mc^2$.

The Joule power density $P_j = \eta j^2$ is then

$$P_j = n_e n_i v \left[8 \ln \Lambda a_0^2 Z^2 \left(\frac{2\mathcal{R}}{kT}\right)^2 \right] \left(\frac{mj^2}{n_e^2 e^2}\right), \quad (2)$$

where the characteristic velocity v is defined by $mv^2 = kT$. The energy loss per collision can be identified with the last term, $\Delta\epsilon_j = mj^2/n_e^2 e^2 = mv_d^2$, where the drift velocity $v_d = j/n_e e$. Then a collision cross section for Joule heating is given by the term in square brackets.

The energy loss per collision can be expressed in terms of the total current I and the electron line density N_e . For a uniform pinch $I = \pi r_0^2 j$ and $N_e = \pi n_e r_0^2$, and $\Delta\epsilon_j = mI^2/N_e^2 e^2$, which is also

$$\Delta\epsilon_j = (mc^2/r_e^2 N_e^2) (I/I_A)^2. \quad (3)$$

The power density for bremsstrahlung can be written in a form reminiscent of Eq. (3),

$$P_b = n_e n_i v a_0^2 Z^2 \alpha F_b (2\mathcal{R}) (2\mathcal{R}/mc^2), \quad (4)$$

where the factor $F_b = (2\pi/27)^{1/2}$ in the most accessible derivation,⁷ and slightly different for more complete calculations. Although bremsstrahlung is emitted with a continuous spectrum the energy of a typical bremsstrahlung quantum is $\hbar\omega \sim kT$. Therefore kT can be identified with the energy loss per collision $\Delta\epsilon_b = kT$. Then the bremsstrahlung cross section is $\sigma_b = a_0^2 Z^2 \alpha F_b (2\mathcal{R}/kT)^2 (kT/mc^2)$.

Pease-Braginskii equilibrium adds to the Bennett relation the condition $P_b = P_j$, which corresponds to local energy balance in the microscopic processes, viz., $\sigma_b \Delta\epsilon_b = \sigma_j \times \Delta\epsilon_j$. This becomes

$$a_0^2 Z^2 \alpha F_b (2\mathcal{R})^2 / mc^2 = a_0^2 Z^2 8 \ln \Lambda \left[\left(\frac{2\mathcal{R}}{kT}\right)^2 \left(\frac{mc^2}{r_e^2 N_e^2}\right)^2 \left(\frac{I}{I_A}\right)^2 \right]. \quad (5)$$

The plasma parameters are grouped in the square brackets. The atomic cross section a_0^2 can be divided out, and the plasma parameters disappear on using Eq. (1b). The result is the transparent formula

$$\frac{I_{PB}}{I_A} = \left(\frac{8 \ln \Lambda}{\alpha F_b}\right)^{1/2} 2\left(1 + \frac{1}{Z}\right). \quad (6)$$

The Pease-Braginskii current is the natural current scale I_A , multiplied by the square root of the ratio between the cross sections for the collisions that are responsible for heating, $\sigma_j \propto 8 \ln \Lambda$, and energy loss from bremsstrahlung, $\sigma_b \propto \alpha F_b$.

Multiple collisions and bremsstrahlung are completely classical processes, but Eq. (6) still contains an essentially quantum mechanical quantity, the fine structure constant $\alpha = (e^2/c\hbar)[1/4\pi\epsilon_0]$. This α comes from a lower limit to the impact parameter in the integration of the bremsstrahlung from an electron passing a fixed charge. This cutoff, which keeps bremsstrahlung finite, was an early triumph of quantum theory. Interestingly enough, the factor $\ln A$ also results from a cutoff, this time from Debye screening at the upper limit to the impact parameter.

Bremsstrahlung is the only energy loss mechanism in the Pease-Braginskii current I_{PB} . However, bremsstrahlung is usually swamped by line radiation and power balance between line radiation and Joule heating gives rise to a much smaller equilibrium current. Knowing the ratio $K = \sigma_l \Delta\epsilon_l / \sigma_b \Delta\epsilon_b$ between the cross sections and energy losses for line radiation and bremsstrahlung gives an estimate for the Pease-Braginskii current for line radiation, viz., $I'_{PB} = I_{PB} / K^{1/2}$. This same result is obtained by comparing the power densities.⁸ Likewise, I_{PB} increases with the decrease in radiation as a result of opacity,⁹ and changes by introducing radial nonuniformities^{1,2,10} and anomalous resistivity.¹¹

ACKNOWLEDGMENT

This work was supported by the Defense Nuclear Agency.

¹R. S. Pease, Proc. Phys. Soc. London Sect. B 70, 11 (1957).

²S. I. Braginskii, Zh. Eksp. Teor. Fiz. 33, 645 (1957) [Sov. Phys. JETP 6, 494 (1958)].

³A. E. Robson, Nucl. Fusion 28, 2171 (1988).

⁴A. E. Robson, Phys. Fluids B 1, 1834 (1989).

⁵W. H. Bennett, Phys. Rev. 45, 890 (1934); see also J. D. Lawson, *The Physics of Charged-Particle Beams* (Clarendon, Oxford, 1977), Chap. 4.4.

⁶A useful table of atomic units is given, e.g., by G. K. Woodgate, *Elementary Atomic Structure* (Oxford U.P., London, 1980), 2nd ed.

⁷S. Glasstone and R. H. Lovberg, *Controlled Thermonuclear Reactions* (Van Nostrand, New York, 1960), Chap. II.

⁸V. V. Vikhrev, Fiz. Plazmy 3, 981 (1977) [Sov. J. Plasma Phys. 3, 539 (1977)]; V. V. Vikhrev, V. V. Ivanov, and K. N. Koshelev, Fiz. Plazmy 8, 1211 (1982) [Sov. J. Plasma Phys. 8, 688 (1982)].

⁹J. P. Apruzese and P. C. Kepple, in *Proceedings of the 2nd International Conference on Dense Pinches*, edited by W. R. Percira, J. Davis, and N. Rostoker (AIP Conf. Proc. 195, New York, 1989), p. 108.

¹⁰J. W. Shearer, Phys. Fluids 19, 1426 (1976).

¹¹A. E. Robson, Phys. Rev. Lett. 63, 2816 (1989).

Leakage currents outside an imploding Z pinch

R. E. Terry

Naval Research Laboratory, Washington, DC 20375

N. R. Pereira

Berkeley Research Associates, Springfield, Virginia 22150

(Received 7 June 1989; accepted 24 August 1990)

Leakage currents outside a pulse-line-driven Z pinch are considered in two circumstances. In the initial stage of the pinch a non-neutral electron flow can arise before magnetic insulation is established. The relative importance of such currents is estimated in terms of diode impedance and pulse-line dimensions. In the later stages of the pinch a neutralized current flow can arise in any tenuous plasma that may be present in the pinch periphery. The effects of the neutral current are estimated through self-similar solutions to a gyrokinetic equation. The collisionless plasma corona can contain an important fraction of the implosion energy.

1. INTRODUCTION

An imploding Z pinch can be used to generate large amounts of kilovolt x rays.¹ In the region of interest the yield in kilovolt x rays is roughly proportional to the fourth power of the peak current into the diode,² in agreement with theory.³ The models assume that the current density in the pinch is constant, and that all the current that goes into the diode flows through the pinch. It is very difficult to confirm experimentally that no current flows outside the Z pinch. However, the strong dependence of x-ray yield on the current implies that a small current leakage through the pinch periphery could reduce the pinch's x-radiation efficiency substantially.

In this paper we consider the leakage current outside a Z pinch in two circumstances. One is a non-neutral electron flow in the initial stage of the pinch; the other is a neutralized current flow in a tenuous plasma that may be present in the pinch periphery.

The non-neutral electron flow at the start of the pulse comes from the onset of magnetic insulation. For relevant parameters (e.g., $I \approx 1$ MA and pinch radius $r \approx 1$ cm) the magnetic field in the vacuum outside the pinch is approximately 20 T (200 kG), sufficiently strong to provide magnetic insulation. However, magnetic insulation needs some time to become established. In high-impedance vacuum transmission lines a small current pulse⁴ is seen at the front end of the pulse, and a similar transient may have been observed in a low-impedance Z pinch.⁵ Subsequently the current becomes sufficiently large to cut off this transient. According to our computer simulations the transient current is composed of an electron sheath that is captured by the magnetic field. When magnetic insulation sets in the electron sheath rolls up into relatively stable vortices.

The neutralized current flow in the pinch periphery would take place at a later time, during pinch compression. In the initial stage of the pulse the material in the diode is rapidly ionized, a complicated process outside the scope of this work. The current compresses the bulk of the material, which becomes a dense collisional plasma that is accelerated toward the axis. The behavior of this plasma is described by the resistive radiation-hydrodynamic equations.⁶ However,

in computations with these equations⁷ the exterior of the plasma sometimes becomes too conductive in an unphysical way—the plasma temperature T as computed can exceed 100 keV. In this case the standard Spitzer formula for the conductivity σ in a collisional plasma, $\sigma \propto T^{3/2}$, predicts a highly conductive plasma in the pinch periphery that prevents the current from entering the Z pinch. The problem disappears when the currents in the plasma periphery are computed by keeping account of the transition from a plasma dominated by collisions to a collisionless plasma. For practical purposes the plasma becomes collisionless when the electron-electron collision time exceeds a typical hydrodynamic time scale.

In the strongly magnetized collisionless exterior plasma the standard equations of resistive hydrodynamics are not valid. Instead, the plasma electrons drift in the confining magnetic field $B_\theta(r)$ and the combined applied and space-charge electric field $\mathbf{E} = [E_z(z,r), E_r(z,r)]$. The $E_z \times B_\theta$ drift inward generally dominates. The current density J_z no longer satisfies Ohm's law, but can be derived by setting the power density $J_z \cdot E_z$ equal to the change in kinetic energy density.

The collisional core of the Z pinch implodes differently than the plasma periphery. In the core the collisions guarantee an isotropic velocity distribution, and an isotropic pressure, but in the periphery the electrons conserve their angular momentum p_θ as they travel along the magnetic field lines around the pinch axis. As the radius r decreases the electron velocity v_θ increases as $1/r$, and the parallel pressure $P_\parallel \propto v_\theta^2$ increases as $1/r^2$. Also, the magnetic moment around the magnetic field, $\mu \propto mv_\theta^2/B_\theta$, is conserved. Therefore the perpendicular pressure $P_\perp \propto v_\theta^2$ increases linearly with the magnetic field $B_\theta(r)$, which is proportional to $1/r$. The ratio of parallel to perpendicular components of the pressure, $P_\parallel/P_\perp \propto r^{-1}$, can become important.

A simple estimate for any peripheral current can be obtained from the Bennett relation applied separately to the core and the periphery. One has $I^2 \sim NT$, with I the current, N the line density of the particles, and T the temperature. Therefore, in order of magnitude $I_{\text{per}}/I_{\text{core}} \sim (N_{\text{per}} T_{\text{per}}/N_{\text{core}} T_{\text{core}})^{1/2}$, where $N_{\text{core(per)}}$ is the number

of particles in the core (periphery) of the pinch, $T_{core(per)}$ is the applicable temperature, and $I_{total} = I_{pinch} + I_{core}$.

A reasonable mass per unit length for the core of the Z pinch is perhaps $100 \mu\text{g}/\text{cm}$. The initial particle density in the Z-pinch periphery is on the order of $n \approx 10^{13}/\text{cm}^3$ (for 0.1 Pa or 1 mTorr), spread over, perhaps, 100cm^2 . The mass per unit length on the outside of the pinch is thus $\sim 0.01 \mu\text{g}/\text{cm}$. Setting the typical temperatures about equal suggests a relative current loss of $\sim 1\%$ in such an equilibrium, which is negligible. However, when $T_{per} > T_{core}$ after compression of the periphery, and/or when pressure balance is not applicable, the current loss through the periphery may become larger.

In Sec. III of this paper we treat current conduction through the periphery with the gyrokinetic formulation of Bernstein and Catto.⁸ This model is obtained from the single-particle kinetic equation by introducing higher-order accurate invariants in the velocity space and then averaging over the gyrophase. We employ a current density obtained from the velocity moment equation of this gyrokinetic formulation, which expresses the momentum balance between particles and fields. The current density then involves a pressure tensor.

Analogous to self-similar hydromagnetic flows⁹ with scalar pressure, the gyrokinetic momentum equation also admits self-similar distribution function solutions that exhibit tensor pressure. If $P_{\parallel} \neq P_{\perp}$ these special solutions remain separable but exhibit three characteristic frequencies instead of two, and, when we retain displacement current, a fourth frequency is added. A particular example from the self-similar theory is used here to illustrate the effects of peripheral gyrokinetic plasma, future work will discuss these solutions in more depth.

The retention of displacement current is required for the energy transport from an external circuit through the vacuum region to the plasma load. The principal consequence is that the well-known plasma dielectric constant $\epsilon \sim (1 + c^2/c_A^2)^{1/2}$ becomes significant (c_A is the Alfvén speed). The plasma dielectric, the radial acceleration of plasma mass, and the two tensor pressure components provide a four-fold energy sink between the core plasma load and the external driver circuit.

II. ESTABLISHMENT OF MAGNETIC INSULATION AROUND A Z PINCH

In the initial stage of the pinch all material is contained in the conductor, and outside of the conductor is vacuum. Free electron current in the diode can be computed with a particle in cell code. One computation uses the geometry of Fig. 1, which is typical for Z pinches. The cathode is a cylinder with radius 3.4 cm, inside an anode with radius 5 cm, and a 3 cm wide anode-cathode gap forming the diode. The diode is bridged by an ideal conductor that mimics the Z pinch. The Z pinch radius, 0.6 cm, is representative of multiple wire loads but substantially smaller than the initial radius of a gas puff. Electrons can be emitted from the cathode surfaces as indicated. The emission assumes space-charge limited flow, i.e., electron emission continues until the normal electric field vanishes. Ions are ignored in our computations.

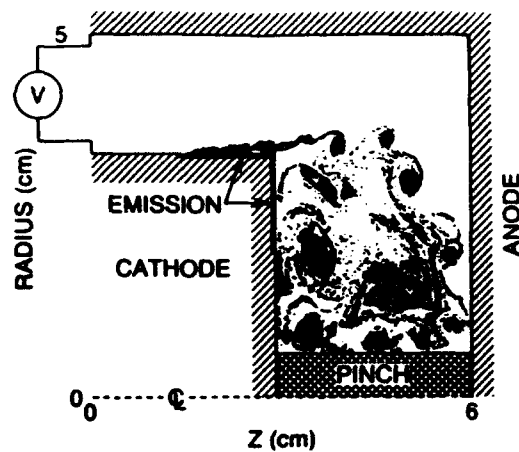


FIG. 1. Geometry of the Z-pinch diode as used in the computation. The cathode is a cylinder of radius 3.4 cm at 3 cm away from an anode with radius 5 cm. The Z pinch is mocked up as a 0.6 cm radius conductor that connects cathode and anode. The electron emission surfaces are indicated on the cathode. The voltage source is connected at the entrance of the diode, 6 cm away from the anode plane. Initially the diode vacuum contains no electrons. The figure shows the electron positions at 4.4 nsec into the simulation.

Figure 2 is the assumed electrical pulse at the diode. The voltage rises linearly on a 5 nsec time scale to over 1 MV. The current is quadratic in time in agreement with $I = V/L$. At the end of the simulation the current exceeds 100 kA, for a magnetic field at the Z-pinch edge up to about 4 T (40 kG). The current in free electrons is the lowest line in Fig. 2. The current starts once the electric field in the diode feed exceeds the field emission threshold, taken to be 200 kV/cm in the code. This occurs at about 1.5 nsec.

When the first electrons are emitted the current through the Z pinch is only 15 kA, insufficient for magnetic insulation. Therefore the free electrons simply cross the diode gap. Later in time these electrons become trapped by the magnetic field from the Z-pinch current. These intermediate stages are not shown, but they can be inferred from Fig. 1, which

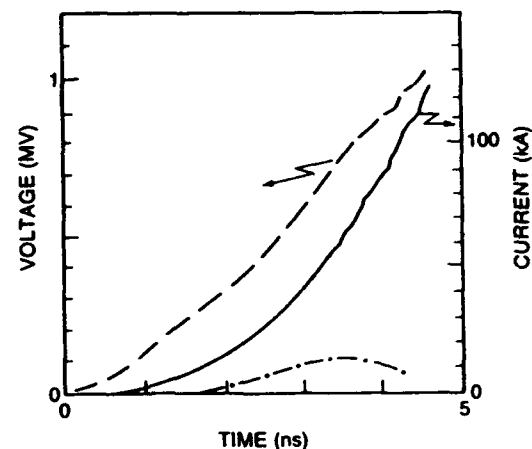


FIG. 2. The voltage V and the current I of the electrical pulse at the diode entrance. The dashed line at the bottom gives the leakage current in free electrons coming off the cathode shank.

shows the distribution of free electrons at the end of the run. The magnetically insulated space-charge sheath in the current feed appears to stream off the cathode into the diode already filled with electrons emitted previously. The sheath is clearly unstable, rolling up into vortex-like structures that persist as they move toward the center conductor.

There is an exact analogy between strongly magnetized non-neutral electron beams and inviscid fluid flow.¹⁰⁻¹³ In two-dimensional Cartesian geometry with constant magnetic field B_z , the combination of charge density, permittivity, and magnetic field in the form $\rho/\epsilon_0 B_z$ corresponds to the vorticity $\zeta_z = \nabla \times U_D$, where U_D is the two-dimensional drift velocity. This drift velocity U_D can be derived from the streamfunction ψ as $U_D = (-\partial\psi/\partial y, \partial\psi/\partial x)$, where $\nabla^2\psi = \zeta_z$.

The exact correspondence breaks down in cylindrical geometry because the magnetic field varies with radius, $B_\theta = \mu_0 I / 2\pi r$, now

$$\nabla \times U_D = \frac{-\rho}{\epsilon_0 B_\theta} - E_r \frac{\partial(1/B_\theta)}{\partial r}. \quad (1)$$

The last term is small compared to the first, except perhaps near the central conductor, where the blob size is comparable to the geometrical scale. Hence in our diode the analogy with inviscid shear flow is largely valid.

The magnetically insulated space-charge sheath coming off the cathode is then analogous to a vortex sheath. It is well known that such a sheath is unstable, and that the instability develops into coherent vortex regions reminiscent of the space-charge blobs seen in our simulation. It is also known that the vortex regions are relatively stable, similar to the persistence of our blobs. Furthermore, interaction between the blobs can be treated as the motion of two-dimensional vortex lines.

The electron blobs appear to be self-contained entities, consistent with $E \times B$ drift motion for the strongly magnetized electrons in the blob's space-charge field. In this case the blob electrons remain on equipotential lines, since the drift is perpendicular to the potential gradient, $(E \times B) \cdot E = 0$. In a cylindrically symmetric blob the charge convected by the drifting electrons is then invariant, and the blob is a stationary entity. Qualitatively similar results are found in simulations with other parameters, e.g., a slower voltage rise time, or a smaller Z-pinch inductance more representative of a gas puff.

The leakage current in free electrons for the run in Fig. 2 peaks at 15 kA around 3.5 nsec, and decreases thereafter. At these later times the current is magnetically insulated, and its magnitude can be estimated by considering the drift current in the thin space-charge sheath parallel to the cathode shank (see Fig. 1). The current in the detached blobs can be considered equal to that flowing along the cathode shank since there are no sources or sinks in the detachment region.

In an insulating magnetic field B_θ the sheath electrons drift in the axial direction along the cathode shank with drift velocity $U_z \approx E_r \times B_\theta / B_\theta^2$. The electric field varies throughout the electron sheath from zero at the metal surface of the cathode to E_r at the top of the sheath, but the magnetic field is mainly from the central current; hence $B_\theta \approx \mu_0 I / 2\pi r$.

The current in the electron sheath I_c is then approximately $I_c \approx 2\pi r \sigma U_z$. The surface charge density σ of the cathode sheath is $\sigma = \epsilon_0 E_r$, where E_r is the normal electric field at the outside of the electron sheath. Since the sheath is thin compared to the width d of the pulse line, and d is less than the inner radius r_i , the electric field can be approximated by $E_r \approx V/d$. Usually the rise time τ is so fast that the voltage can be approximated by the inductive voltage $V \approx LI/\tau$, with L the diode inductance and I the total diode current.

The relative importance of early free electron leakage current to the total pulse line current then becomes

$$\frac{I_c}{I} \approx \left(\frac{E_r}{cB}\right)^2 \approx \left(\frac{r_i}{d}\right)^2 \left(\frac{Z_D}{Z_0/2\pi}\right)^2, \quad (2)$$

where $Z_0 = (\mu_0/\epsilon_0)^{1/2} = \mu_0 c = 377 \Omega$, and $Z_D = V/I \approx L/\tau$ is the total diode impedance. After magnetic insulation is established in the pulse line this leakage current decays away.

The literature on magnetic insulation¹⁴⁻¹⁷ contains estimates along the same lines as the above. In addition, it is shown in detail that the single-particle considerations used here correspond well to a treatment that includes the self-electric and self-magnetic fields.

A typical Z-pinch diode is about 3 cm wide, and the inductance $L \approx 6$ nH. A typical pulse rise time may be ≈ 12 nsec, for a diode impedance of about 0.5 Ω . In contrast, the vacuum impedance $Z_0/2\pi = 60 \Omega$, and the impedance ratio is $\frac{1}{10}$. The leakage electron current I_c is thus always a small fraction of the total current I , whence I_c can be ignored.

However, for single exploding wires the vacuum current may become comparable to the conduction current. As an example, the inductance of a single 25 μm radius wire load in a 3 cm wide diode is about 45 nH. For a fast (10 nsec) rise time pulse the factor $Z_D/Z_0 \approx 0.1$, but a relatively small gap size partly compensates. When $r_i/d \approx 3$, for example, I_c/I is of the order $\frac{1}{10}$. In this case there should be a sizable leakage current in free electrons, potentially generating a measurable bremsstrahlung x-ray signal. If corroborated by further work the bremsstrahlung x-ray signal may be an excellent indicator for the arrival time of the electrical pulse at the Z pinch.

III. COLLISIONLESS PLASMA PERIPHERY

Once magnetic insulation has been established, as discussed in Sec. II, the current flows principally through the pinch, and the pinch accelerates inward. Eventually the pinch stagnates on axis, forming a dense, current-carrying cylinder of plasma. However, this pinch core could be surrounded by a periphery of collisionless plasma, from Z-pinch material that did not fully implode or from background gas that was swept in from the outer regions of the diode. In this section we consider the current that might be carried by such a plasma.

The peripheral plasma might be different in Z pinches that start from an injected gas on one hand, and multiple wires on the other. The injected gas forms a plume with the highest density opposite the nozzle opening, and wide wings of decreasing density. The initial breakdown and current conduction should occur along the spatial contour in the

diode, which (given the electric field and material profiles) is at the minimum of the Paschen curve, and thus should leave some gas outside the initial current channel. This gas may be ionized later to form the periphery. With wires the exterior plasma would come from the early blowoff as the wire load is heated, or it might not exist at all. The ambient gas in the diode can be another source of tenuous plasma, perhaps resulting in ion densities as high as $10^{12}/\text{cm}^3$ (and electron densities $< 10^{13}/\text{cm}^3$).

Ironically, sometimes¹⁸ there is current leakage through a tenuous plasma on axis inside the wires: when the wires are heavy the outer part of the wire is shed continuously throughout the current pulse. This plasma implodes on axis before the original wires have moved, and diverts part of the current.

More recent wire load implosions¹⁹⁻²¹ involving Ni arrays indicate a fairly weak inductive current notch and radiation emission peaking after the plasma starts to expand. When the diode energy flow is examined the energy input to the load from classical Ohmic heating and inductance change is apparently insufficient to account for the total energy radiated. Some energy must be removed from the vacuum magnetic field in order to account for the discrepancy. Now such an analysis is not supported by an independent measure of the current distribution in the pinch; indeed, the location of the current path is simply taken as the boundary of luminosity in pinhole photos. Should the current flow deeper in the plasma so that the peak compression is greater, then some improvement in the energy discrepancy would be realized insofar as the effective inductance change would be larger. Yet it is difficult to account for the energy by this effect alone because the current path would have to be very deep (≈ 0.01 mm). Such a current filament would be much thinner, in fact, than the observed (Ni) *L*-shell emission filament. If, however, the outer load regions are in a gyrokinetic coronal limit, as described below, then the work done on the gyrokinetic plasma would be absorbed from the vacuum magnetic field and at least partially transferred to the interior pinch after stagnation. In consonance with observation, such motion would not provide much of an inductive current notch, because of the ability of this coronal plasma to hold a more constant current while a load stagnation occurs.

Moreover, comparing theoretical and experimental energy coupling to Ar gas puffs provides further indirect evidence of exterior energy sinks, which could be tenuous peripheral plasma. The work of Thornhill²² suggests that lower mass puff loads exhibit radiative *K*-shell yields lower than expected if all the energy transferred to the load cavity was, in fact, coupled to the central plasma load. The experimental yields were more heavily weighted to the *L* shell, suggesting a lower load temperature at stagnation—even though the puff gas load accepted more generator energy than the hydromagnetic calculations could predict. This is again precisely what would be expected should an intervening energy sink arise in the load periphery and “soften” the implosion.

In contrast, more recent gas puff implosions²³ show a fairly pronounced inductive current notches as little as 5 cm from the load. The design changes to the gas puff load were quite substantial in comparison to the experiment studied by

Thornhill. In Spielman's experiment the puff mass was much larger, the front end inductance was reduced, the neutral flow speed was increased to Mach 8 (rather than Mach 4), and the return current anode plane was both a somewhat thinner wire mesh and closer to the cathode. It would appear that the energy transfer was quite efficient, perhaps indicating that coronal plasma was either absent or if present not behaving as a strong energy sink. The best data presently available cannot resolve these possibilities.

Hence there is a good reason to believe that only a detailed examination of the differences in behavior between gas puffs and imploding wires would contain some direct evidence for current leakage throughout a peripheral plasma. The differences to be examined must rest upon clear measures of the load mass in a gas puff, which is not generally available, and good measures of energy flow in the diode region. If corona plasma is produced mostly from background gas, then no major wire/puff differences would be expected. If the corona plasma in gas puffs is due to an incomplete sweep-up of the load gas, then wire/puff differences would depend on the actual puff load mass (and its distribution) as compared to the extent (and distribution) of any early wire blowoff.

The remainder of this paper assumes that the *Z*-pinch periphery contains a collisionless plasma, with density and temperature fixed to values within the known experimental and theoretical limits. For the number and energy densities one could reasonably associate with such a “test” plasma, a simple calculation will show how the peripheral plasma can become important for *Z*-pinch implosions.

What is the current density in the collisionless periphery surrounding the current carrying *Z* pinch? In a dense plasma the collisions are the dominant influence balancing the motion of the plasma electrons against the acceleration by the electric field. The resulting collisional electron drift, and thus the current density *J* is proportional to the electric field E , $J = \sigma E$. The electrical power input into the plasma ends up in increased random velocities of the plasma particles, viz., Ohmic heating.

In the absence of collisions the magnetized plasma in the *Z*-pinch periphery can absorb energy from the electrical pulse. In this case the energy does not go into random motion of the plasma particles, but instead is put into organized motion. A strongly magnetized plasma in an electric field is not accelerated along the field, but drifts perpendicular to the electric and magnetic fields with a velocity $W = cU = -(E/B)$. For constant *E* the drift speed remains constant, but when the electric field increases in time the plasma accelerates. The kinetic energy density $\mathcal{E} = \rho W^2/2$ increases (ρ denotes the plasma mass density) and electrical power is absorbed. Likewise, electrons that $E \times B$ drift into a region of increased magnetic field spin up, increasing their perpendicular energy w_\perp , while the magnetic moment $\mu \sim w_\perp/B$ stays constant. The increase in w_\perp , or the increased magnetization, is another power sink. In a cylindrically symmetric geometry with $B \sim 1/r$ the particle's angular momentum about the axis, $p_\theta = mrv_\theta$, is conserved; therefore a drift toward the axis increases the parallel energy w_\parallel as $1/r^2$. Further details of the description are developed

in the Appendix, where it is shown how special solutions of the gyrokinetic equation can be used to model the coronal plasma.

In particular, the limit of homogeneous compression and special initial conditions allows the solutions to simplify. The dependent variables and their derivatives are then functions of the single self-similar invariant $\xi = r/r_0 \alpha(\tau)$. Here $r_0 = r_0/l_0$ is a dimensionless scale length that arises naturally in the theory with $cl_0 = l_0$ and $\tau = t/l_0$. The time scale l_0 is tied to a particular implosion time scale. The variable $\alpha(\tau)$ contains the sole time dependence, e.g., $U = \dot{\alpha} r_0$, $DU/D\tau = \ddot{\alpha} r_0$. Four primary frequencies arise. The oscillatory frequency is related to the magnetic field pressure; $\tau_A = \omega_A^{-1}$ is the transit time of an Alfvén wave with velocity c_A through the pinch scale length. Two new frequencies, expressed as ratios of thermal velocities to light speed, are related to the anisotropy. The parallel pressure frequency is $\omega_{\parallel}^2 \equiv c_{\parallel}^2/c^2$, and the perpendicular pressure frequency, $\omega_{\perp}^2 \equiv c_{\perp}^2/c^2$. The displacement current frequency, $\tau_K = \omega_K^{-1}$ is a measure of the overall dielectric strength characterizing any particular flow.

To assess the role of this sort of collisionless current channel in the evolution of a Z pinch, we select a set of self-similar profile functions, which is compatible with the (rather sparse) information available on the coronal plasma and examine the evolution of the special solution. In particular, what fraction of "new" current is absorbed into such a corona after it is formed under the magnetizing influence of early interior currents flowing only in the dense pinch? What fraction of the incoming energy flow from the driving circuit is diverted into this corona, and what circuit waveform behavior is characteristic of such an external plasma layer?

We can formulate these questions in a realistic context by specializing the self-similar equation of motion derived in the Appendix to portray a coronal rundown in a Z-pinch diode. Each of the four independent frequencies appearing in

$$\ddot{\alpha} = \frac{\omega_{\parallel}^2}{\alpha^3} + \frac{\omega_{\perp}^2}{\alpha^2} - \frac{\omega_A^2}{\alpha} + \frac{\omega_K^2}{\alpha} \dot{\alpha}^2$$

can be set to produce a desired result in the solution. In the example developed here ω_{\parallel}^2 and ω_{\perp}^2 are selected to correspond to 1(||) temperatures of 75(60) eV, which is consistent with ionization at a few electron volts and subsequent Ohmic heating by about a factor 10 before a "collisionless" state is obtained.²⁴ This leaves ω_K^2 , ω_A^2 , a radial extent $[\xi_-, \xi_+]$, and an initial velocity $U(\xi_-)$ to be developed. Since $r_0 = \omega_K/\omega_A = U(\xi_-)/\dot{\alpha}$, the selection of either α_0 or $U(\xi_-)$ ($\approx 7.33 \times 10^7$ cm/sec) is, for fixed r_0 , guided by the typical collapse time of pinch loads, taken here to be about 30 nsec over a radial extent of 1.5 cm. In keeping with common pinch diode dimensions, the radial extent of the corona is taken to be ≈ 4 cm. Hence the values for ξ_+ and ξ_- will correspond to $\xi_+ = 1.5 \text{ cm}/l_0 r_0$, $\xi_- = 5.5 \text{ cm}/l_0 r_0$; $l_0 = 30$ cm, since the collapse time is in the nanosecond range.

The value inferred for r_0 must be guided by the densities implied for the profile. With an upper limit of 10^{15} ions/cm³, suggested by the lower limit of schlieren measurements, values of r_0 on the order of [0.25, 0.312] keep the

density bounded above by this constraint when the density scale $n_0 = (2.366 \times 10^9/\Lambda) [\dot{\alpha}_0/U(\xi_-)]^2 (I_{\text{core}}/1 \text{ MA})^2$ (cm⁻³), and the density profile

$$n(\xi) = \frac{n_0}{\xi^2} \left(\frac{\tau_K^2}{1-\xi^2} - 1 \right) \times \left(\frac{1}{\sqrt{1-\xi^2}} - \frac{1}{\sqrt{1-\xi_-^2}} + 1 \right), \quad (3a)$$

are evaluated for an enclosed current $I(\xi) = I_{\text{core}} (1/\sqrt{1-\xi^2} - 1/\sqrt{1-\xi_-^2} + 1)$ of a few mega-amperes.

The selection of r_0 to set the density leaves arbitrary the choice of either ω_K or ω_A . For this example the selection of a moderately strong dielectric coefficient,

$$\epsilon(\xi)/\epsilon_0 = \tau_K/\sqrt{1-\xi^2} \quad (3b)$$

(peaking at about 150 ϵ_0) implies, together with r_0 , a value for ω_A . Similar expressions for the temperature profiles are easily derived from Eqs. (A9b) and (A9c).

Such a group of solutions is shown in Fig. 3. To summarize, initially the interior boundary of the solution domain is given a velocity of 2.0×10^7 (cm/sec), which corresponds to a typical peak implosion velocity of Z-pinch loads in machines of moderate energy. The interior coronal (H^+) ion density is about 1.04×10^{15} cm⁻³ per MA² of interior current; it extends for 4 cm outside the interior radius of 1.5 cm. [The factor MA² is obtained from Eq. (3a), in analogy to the Bennett pinch relation.] The initial coronal conduction current is 34% of the core current. The density $n(\xi)$ decays nearly $\propto 1/\xi^2$, while the perpendicular nearly h_{\perp} is nearly $\propto \xi$; Eq. (A9b) produces a parallel energy profile h_{\parallel} also nearly $\propto \xi^2$. Since c_{\perp} is an azimuthal thermal speed at the scale radius, and since the thermal speed profile is proportional to the scale radius, the average angular momentum profile is $p_{\theta} \sim r_0 v_{\theta} \sim c_{\perp} \xi^2 r_0$, so that $L_{\parallel}^2 \sim \xi^4 (l_0 r_0)^2 c_{\perp}^2$ as demanded by the self-similarity constraints. The net result is that the azimuthal component $P_{\parallel} = \rho L_{\parallel}^2/r^2 \propto n_0 v_{\theta}^2$ is nearly independent of radius. The perpendicular component $\xi P_{\perp} \propto \xi n_0 v_{\perp}^2$ is also weakly dependent on radius.

The initialization conditions required to produce this sort of energy profile are not precisely known, but the fact

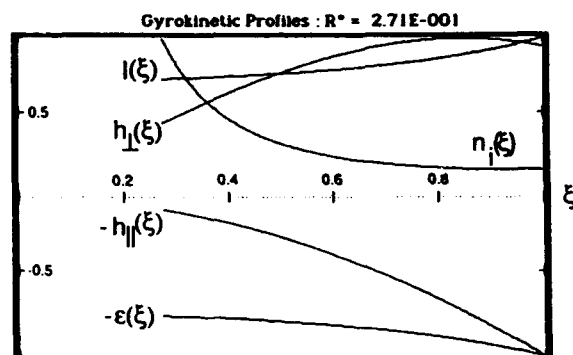


FIG. 3. Examples of initial self-similar profiles are shown. As labeled the curves are normalized to $n_0 = 1.04 \times 10^{15}$ cm⁻³ MA⁻², $I = 1.34 I_{\text{core}}$, $\epsilon = 150$, $h_{\perp} = 60$ eV, and $h_{\parallel} = 75$ eV.

that $r_{\parallel} \sim \xi r_{\perp}$ is consistent with a simple model for the early phase. If thin peripheral gas is photoionized and Ohmically heated while in an azimuthally directed magnetic field, then it will evolve to a collisionless state principally through electron-neutral collisions. The conductivity will smoothly evolve to a small value as runaway electrons separate in energy from the bulk electrons that interact readily with the neutrals and ions. Since the runaway electrons are captured in a radial $\mathbf{E} \times \mathbf{B}$ drift they are confined to the r - z components of the velocity space unless scattered into the θ component. The energy dumped into the r - z motion depends on the time history of the conductivity and local E_r field, but the rate of scattering into the θ direction depends on the number of scattering neutrals and ions available at any radial location. Since the number of such scattering centers in any azimuthal flux tube is linear in the radial coordinate, the power diverted to the azimuthal direction increases $\propto r$. Hence, for any particular time history of r - z heating, the final energy dumped in the θ direction will be proportionately greater at larger radius. The energy density in the r - z component is deposited in each volume independently, but at a fixed radius scattering in the whole volume swept out by a gyrating electron diverts energy to the azimuthal component.

Insofar as these self-similar flows fix the (conduction) current partition between the core and the periphery, they are only useful as approximate models of the load as it enters the final rundown and stagnation phase. At this time the interior load is expected to be hot enough to curtail further magnetic diffusion, while the peripheral plasma is forced to conserve flux unless it becomes turbulent as a result of microinstabilities. Since much of the energy transfer to a Z pinch is due to the load's inductance change, a fair fraction of this energy is transferred in the last phase of the rundown. The self-similar models can therefore offer a simple treatment of this important phase of the motion by initializing their parameters to pinch load conditions after the implosion is well underway.

The dynamic consequences for an imploding load surrounded by a coronal plasma of this sort are shown in Fig. 4. The final 30 nsec of the rundown are strongly modified by

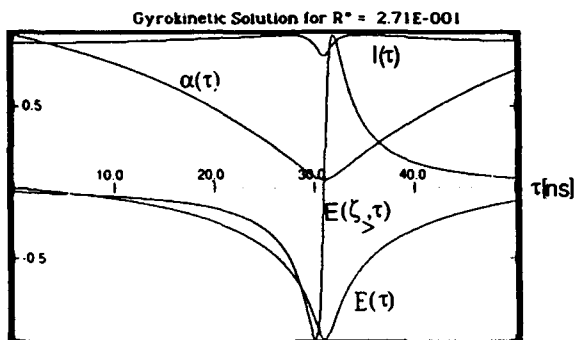


FIG. 4. Time histories of the current $I_{\text{core}}/I_{\text{core}}$, exterior electric field $E(\xi)$, radius (α) , and absorbed energy $E_r(\tau)$ over a 50 nsec rundown. As labeled the curves are normalized to $I = 1.45 \times I_{\text{core}}$, $E_r = 1.45$ MV/cm MA², $E_r = 143$ kJ/cm MA², and $\alpha = 1$.

the collisionless magnetoplasma corona. As the radial compression ($\sim \alpha^{-2}$) reaches its maximum, the exterior electric field reverses and the peak in the absorbed energy is obtained. While the conduction current is constant over the interval, the total current rises slightly and exhibits a very mild inductive notch. All this time dependence, about a $\pm 11\%$ current variation, is due to the displacement current, which alternately charges and discharges the plasma dielectric while a fixed conduction current leaks across the diode.

If the load were a bare slug, its motional impedance would become more important in the rundown. Further power absorption by the Z pinch would be strongly curtailed and one might expect a 30%–40% "inductive notch" to develop in the current waveform. The gyrokinetic corona has changed this picture substantially. Now further power absorption can occur, but most of the energy goes no further than the corona. The implosion and stagnation occur on a normal time scale but the interior load current is fixed. Whereas the coronal conduction current is fixed as well, the displacement current component can vary in strength from 5%–20% of the core current, depending on the strength of the plasma dielectric that has been trapped in the periphery. At fixed interior current the stronger dielectric cases tend to implode less sharply as a result of the larger mass and slower Alfvén speeds. The slower time scale implies less displacement current because the accelerations are weak. In contrast, the weaker dielectric cases provide a more prominent displacement current component because the accelerations are stronger. During the stagnation, energy is deposited in the coronal fields and matter. The energy given the coronal plasma is released when the motion reverses, as a result of the recoil of the gyrokinetic plasma from the angular momentum and magnetization stresses, which build up as the radius gets smaller and finally cannot be overcome.

In the case illustrated previously (at the time of peak compression) this diverted energy $E_r(\tau)$ has risen to 143 kJ/cm MA² of interior current. In the absence of any dissipative mechanisms this energy would be released back to the driving circuit as the plasma expands—it is never coupled to the dense portions of the load! If we evaluate the peak coronal energy for the currents and load lengths discussed in the Gamble II analysis by Thornhill, the absorption of this coronal energy into the load region would result in much more additional energy removed from the pulseline, which more than removes the energy coupling discrepancy between theory and experiment at lower load masses. If anomalous dissipative mechanisms are, in fact, active in these coronal plasmas, then this is also the rough magnitude of energy available to the load as additional heating. Such a channel would provide a path for conversion of energy in the vacuum magnetic field to the load without compression of the current filament to very small dimensions, as required to explain the observations of Ref. 19.

IV. SUMMARY AND CONCLUSIONS

Current can be lost in the periphery of a Z pinch by various mechanisms. Initially the Z pinch carries no current, and the inductive voltage at the edge of the cathode away

from the pinch material can drive a current in free electrons. The free electrons can be the bulk of the current at the very start, but this current is cut off rapidly once the current starts flowing through the Z pinch.

The tenuous plasma outside the Z pinch can also carry current. How much current is shunted through this plasma depends on the plasma density, and also on parameters such as the temperature and the magnetic field in the periphery, i.e., the current in the main Z pinch. The pressure of the collisionless plasma in the periphery becomes anisotropic as the plasma contracts toward the axis, as a result of the separate conservation of the electron's magnetic moment, and the electron's angular momentum about the axis. Under these conditions the plasma can still oscillate in a self-similar manner for a constant interior Z-pinch current. The constraint of constant interior current is also consistent with the ideal hydromagnetic self-similar flows useful in modeling the dense interior plasma. Both interior and peripheral plasma are thus modeled in a mutually consistent way. While the apportioning of current between the interior and the corona is an important issue, it is beyond the scope of this work. Here the model is built to describe the motion after the interior plasma is hot enough to curtail further magnetic diffusion, and thus a fixed interior current is the proper boundary condition.

In contrast to self-similar hydromagnetic oscillator solutions, the present gyrokinetic oscillators continue to absorb generator power as they collapse. The coronal plasma may thus be a common modifying influence on the current waveform, reducing or removing the "inductive notch" expected from simpler treatments. Because of this extra energy sink, the comparison of theory and experiment is modified in the right direction and magnitude.

While there are many potential caveats to the development presented here as we consider the early time development of the corona, the detailed role of transit time effects and the microstability of the evolving distribution functions, the collisionless magnetoplasma corona treated here may be an important ingredient in many plasma radiation sources, one that deserves close experimental attention.

ACKNOWLEDGMENTS

We acknowledge many helpful discussions with Ira Bernstein.

Support by the Defense Nuclear Agency for this work is gratefully acknowledged, and in particular the use of the PIC code MAGIC.

APPENDIX: DEVELOPMENT OF SELF-SIMILAR SOLUTIONS

Because the electrical properties of collisionless plasma are generally determined by a few moments of the distribution function, a convenient path to developing the constitutive relation $\mathbf{j}(\mathbf{E})$ is to examine the moment relations of the gyrokinetic equation. Only four parameters are, in fact, required to determine the response of the system. Each of these is based on a particular moment of the distribution function. For example, using the variables of the main text, energy conservation is expressed by the statement

$$\mathbf{j} \cdot \mathbf{E} = \frac{d\gamma}{dt} + \mathbf{v} \cdot \mathbf{F}, \quad (\text{A1})$$

where the pressure force is $\mathbf{F} = -\nabla \cdot \mathbf{P}$, and \mathbf{P} is the pressure tensor. Two of the basic parameters are already obvious in the two independent pressure tensor components, the others arise as shown below.

The macroscopic quantities that enter into the fluid (moment) equations are averages over the particle distribution function. The distribution functions that solve the gyrokinetic equations contain a class of separable functions of the form $g(r, t)F(\mu, p_\perp, r_0)$. Here, instead of writing the distribution in terms of the velocity components in cylindrical geometry, it is better to use the dynamical invariants, the magnetic moment μ , and the angular momentum p_\perp . The two equivalent representations of the gyroaveraged distribution function are connected by

$$f(r, \mathbf{v}, t) = [m^2 r / 2\pi B(r, t)] n(r, t) F(\mu, p_\perp, r_0). \quad (\text{A2})$$

The factor in [...] is the Jacobian of the transformation from \mathbf{v} to μ , p_\perp , and ϕ the gyrophase. Without collisions the invariants for each particle do not change, and the velocity function F is constant in time along a guiding center trajectory, $r(r_0, t)$. The particle density $n(r, t)$ is no longer part of F , which is normalized as

$$\left(\frac{m^2 r_0}{2\pi B_0(r_0)} \right) \int d\mu dp_\perp F(\mu, p_\perp, r_0) = 1, \quad (\text{A3})$$

for both electrons and ions. With the assumption of quasineutrality the mass density ρ is $\rho = (Zm_{\text{ion}} + m_{\text{elec}})n(r, t)$.

Without collisions the distribution function is not necessarily Maxwellian. Instead, the distribution function should be computed by modeling the transition between the collisional and the collisionless plasma. While this is a complicated problem, outside the limited scope of this paper, the general result²⁴ is a tenfold increase in mean kinetic energy before the electrons become collisionless. Here the distribution function is viewed as an input to the problem.

The parallel pressure is defined through the average value of p_\parallel ,

$$r^2 P_\parallel = \rho L_\parallel^2 = \rho \int d\mu dp_\perp F \frac{p_\parallel^2}{m^2}, \quad (\text{A4a})$$

and the perpendicular pressure becomes

$$P_\perp = \rho B M_\perp = \rho B \int d\mu dp_\perp \frac{F p_\perp^2}{m}. \quad (\text{A4b})$$

Here, and in other moments, the summation over species is implicit.

The axial current density, defined by averaging of the axial drift velocity of the guiding center

$$nev_\parallel = \left(\frac{nc}{B} \right) \left(\frac{mv_\parallel^2}{r} + mc \frac{D(E/B)}{Dt} - w_\perp \frac{\partial \ln B}{\partial r} \right),$$

is then readily calculated by momentum balance to be

$$J_z = \frac{\rho c^2}{B} \frac{D(E/B)}{Dt} + \frac{c}{B} \left(\frac{\rho L_\parallel^2}{r^2} - \frac{1}{r} \frac{\partial(r\rho B M_\perp)}{\partial r} \right). \quad (\text{A5})$$

The first term is related to the acceleration of the $\mathbf{E} \times \mathbf{B}$ drift motion, the second comes from angular momentum conser-

vation, or P_{\perp} , and the third is the magnetization contribution, from P_{\parallel} . In the acceleration term the ions dominate; the electrons are more important for the two pressure-related terms, without thermal equilibrium between electrons and ions.

The fluid equation of motion in the radial direction, for an anisotropic pressure, includes a centrifugal force L_{\perp}^2/r^3 that reflects the conservation of angular momentum,

$$\rho \frac{DU}{Dt} = \frac{\rho L_{\perp}^2}{r^3} - \frac{1}{r} \frac{\partial(r\rho B M_{\parallel})}{\partial r} - J_{\perp} B. \quad (\text{A6})$$

An isotropic pressure implies that the collisions are sufficiently frequent to keep the velocity components randomized. The frequent collisions imply a finite conductivity, in contrast to the assumption of infinite conductivity, in ideal hydromagnetic theory, which demands a collisionless plasma. One might argue that pressure isotropy has been reached on time scales longer than those of interest, or as an initial condition. However, in a cylindrical geometry, as the plasma gets closer to the axis the pressure P_{\parallel} parallel to the magnetic field $B = B_{\theta}(r)$ increases as $1/r^2$, while the perpendicular pressure P_{\perp} increases as $1/r$. Thus the anisotropy is intimately connected to the time scale of interest in a collisionless cylindrical plasma.

In this gyrokinetic description the Maxwell-Vlasov system, as completed by the momentum balance including the anisotropic pressure P , can be summarized in the following equations:

$$\frac{\partial n}{\partial t} + \nabla \cdot (n\mathbf{W}) = 0, \quad (\text{A7a})$$

$$\frac{\partial \mathbf{B}}{\partial t} = \nabla \times (\mathbf{W} \times \mathbf{B}), \quad (\text{A7b})$$

$$\nabla \times \mathbf{B} = \frac{4\pi \mathbf{J}}{c} + \frac{1}{c} \frac{\partial \mathbf{E}}{\partial t}. \quad (\text{A7c})$$

The displacement current is retained in the analysis in order to make connection with external power sources or sinks. For a cylindrically symmetric geometry the nonvanishing dependent variables are the fluid density ρ , the radial component of the fluid velocity $W_r = cU$, the axial component of the current density $J_z = J$, the azimuthal component of the magnetic field $B_{\theta} = B$, and the parallel and perpendicular moments L_{\parallel} and M_{\perp} .

In the limit of homogeneous compression ($U \propto r$), special initial conditions in these variables allow the equations to simplify. The dependent variables and their derivatives are then functions of the single self-similar invariant $\xi = r/r_0 \alpha(\tau)$. Here r_0 is a dimensionless scale length that arises directly in the transformation, viz., $r_0 \equiv \omega_E/\omega_A = r_0/l_0$ with $cl_0 = l_0$ and $\tau = t/t_0$. The time scale t_0 is a free parameter only to the extent that a particular implosion time scale for the core plasma remains arbitrary. The variable $\alpha(\tau)$ contains the sole time dependence, e.g., $U = \dot{\alpha} r_0$, $DU/D\tau = \ddot{\alpha} r_0$.

A self-similar oscillation is possible only when the accelerations are proportional to the pinch radius. For an isotropic pressure the proportionality of $J_z B_{\theta}/n$ to radius implies that the magnetic field is proportional to $\sqrt{\rho}$. In the anisotropic case additional profiles must be defined self-con-

sistently. Using Eq. (A/c) to eliminate J , and separating the four distinct spatial dependencies that arise, Eq. (A6) becomes

$$\ddot{\alpha} = \frac{\omega_{\parallel}^2}{\alpha^3} + \frac{\omega_{\perp}^2}{\alpha^2} - \frac{\omega_A^2}{\alpha} + \frac{\omega_E^2}{\alpha} \dot{\alpha}^2. \quad (\text{A8})$$

The oscillatory term related to the magnetic field pressure is $-\omega_A^2/\alpha$, where $\tau_A = \omega_A^{-1}$ is the transit time of an Alfvén wave with velocity c_A through the pinch scale length r_0 , viz., $\omega_A^2 \equiv c_A^2/c^2 = B^2/4\pi\rho c^2$. As expected this term also occurs in the corresponding equation for the isotropic ideal hydromagnetic case. The two new terms related to the anisotropy are the parallel pressure term, with $\omega_{\parallel}^2 \equiv c_{\parallel}^2/c^2$, and the perpendicular pressure term, with $\omega_{\perp}^2 \equiv c_{\perp}^2/c^2$. The velocities c_A , c_{\parallel} , and c_{\perp} are thus alternate measures of the strengths of the fundamental moments in the theory, serving to parametrize the corresponding separation constants. Each dimensionless frequency ($\omega_k \equiv \tau_k^{-1}$) derives from a separate term in the momentum equation, and the velocity ratios obtain from the normalization of the moments to the light speed and the required dimensionality, viz., $L_{\perp}^2 \sim l_0^2 c_{\perp}^2 h_{\perp}(\xi)$ and $BM_{\parallel} \sim c_{\parallel}^2 h_{\parallel}(\xi)$. The final term, proportional to $\dot{\alpha}^2$, arises here only when we keep the full effects of displacement current; $\tau_E = \omega_E^{-1}$ is a measure of the overall dielectric strength characterizing any particular flow.

The four frequencies appearing in Eq. (A8) are connected to four constraint relations that define the required plasma profiles for enclosed current $I(\xi) = (cl_0 r_0/2)\xi B_{\theta}(\xi)$, number density $n_0(\xi)$, perpendicular (kinetic) temperature $h_{\perp}(\xi)$, and parallel (kinetic) temperature $h_{\parallel}(\xi)$. With the dielectric coefficient $\epsilon(\xi)$ given by

$$\epsilon(\xi) = \sqrt{1 + (4\pi m_i c^2) n_0(\xi)/B_0^2(\xi)}, \quad (\text{A9a})$$

the constraints are given by

$$\omega_{\parallel}^2 = (c_{\parallel}^2/c^2) h_{\parallel}(\xi) [1 - 1/\epsilon^2(\xi)], \quad (\text{A9b})$$

$$\omega_{\perp}^2 = -(c_{\perp}^2/c^2) \{ [1 - 1/\epsilon^2(\xi)] /$$

$$r^2 \xi^2 n_0(\xi) \} \partial_{\xi} [\xi n_0(\xi) h_{\perp}(\xi)], \quad (\text{A9c})$$

$$r^2 = [1 + \xi \partial_{\xi} \ln B_0(\xi) / \epsilon^2 \xi^2], \quad (\text{A9d})$$

$$1 = [2 + \xi \partial_{\xi} \ln B_0(\xi) / \epsilon^2]. \quad (\text{A9e})$$

These equations require $\omega_E < 1$ to obtain positive definite number density profiles and offer bounded solutions for each of the variables, usually over a finite range $[\xi_-, \xi_+]$. The spatial range used can be chosen to fit whatever physical dimensions are imposed because these solutions are simply following the motion of the single particle gyrokinetic trajectories. In other words, clipping these solutions in radius is admissible as long as the profile values and derivatives on the interior of any such domain limit to the proper values as one approaches the boundary.

¹ N. R. Pereira and J. Davis, *J. Appl. Phys.* **64**, R1 (1988).

² J. Pearlman and J. C. Riordan, *Proc. SPIE* **537**, 102 (1985); also see Fig. 5 in Ref. 1.

³ J. W. Thornhill, K. G. Whitney, and J. Davis, *J. Quant. Spectrosc. Radiat. Transfer* **44**, 251 (1990).

⁴ G. Merkel and D. A. Whittaker (private communication).

- ⁶ F. C. Young (private communication).
- ⁷ R. W. Clark, J. Davis, and F. L. Cochran, *Phys. Fluids* **29**, 1971 (1986).
- ⁸ F. L. Cochran (private communication).
- ⁹ I. B. Bernstein and P. J. Catto, *Phys. Fluids* **28**, 1342 (1985).
- ¹⁰ F. S. Felber, *Phys. Fluids* **25**, 643 (1982).
- ¹¹ R. C. Davidson, *Phys. Fluids* **27**, 1804 (1984).
- ¹² R. C. Davidson, *The Theory of Non-Neutral Plasmas* (Benjamin, Reading, MA, 1974).
- ¹³ R. J. Briggs, J. D. Daugherty, and R. H. Levy, *Phys. Fluids* **13**, 421 (1970).
- ¹⁴ R. H. Levy, *Phys. Fluids* **8**, 1288 (1965).
- ¹⁵ M. S. di Capua, *IEEE Trans. Plasma Sci.* **PS-11**, 205 (1983).
- ¹⁶ A. Ron, A. Mondelli, and N. Rostoker, *IEEE Trans. Plasma Sci.* **PS-1**, 85 (1973).
- ¹⁷ R. V. Lovelace and E. Ott, *Phys. Fluids* **17**, 1263 (1974).
- ¹⁸ J. M. Creedon, *J. Appl. Phys.* **48**, 1070 (1977).
- ¹⁹ R. F. Benjamin, J. S. Pearlman, E. Y. Chu, and J. C. Riordan, *Appl. Phys. Lett.* **39**, 848 (1981).
- ²⁰ M. Krishnan, C. Deeney, T. Nash, P. D. LePell, and K. Childers, in *Dense Z Pinches*, AIP Conf. Proc. 195 (AIP, New York, 1989), p. 17.
- ²¹ C. Deeney, T. Nash, P. D. LePell, M. Krishnan, and K. Childers, in *Dense Z Pinches*, AIP Conf. Proc. 195 (AIP, New York, 1989), p. 55.
- ²² C. Deeney, T. Nash, P. D. LePell, K. Childers, and M. Krishnan, in *Dense Z Pinches*, AIP Conf. Proc. 195 (AIP, New York, 1989), p. 62.
- ²³ J. W. Thornhill (private communication); and F. C. Young, S. J. Stephanakis, and V. E. Scherrer, *Rev. Sci. Instrum.* **57**, 2174 (1986).
- ²⁴ R. B. Spielman, R. J. Dukart, D. L. Hanson, B. A. Hammel, W. W. Hsing, M. K. Matzen, and J. L. Porter, in *Dense Z Pinches*, AIP Conf. Proc. 195 (AIP, New York, 1989), p. 3.
- ²⁵ R. E. Terry, in NRL Memorandum Report 6051, 1987, p. 49 ff. See AIP Document No. PAPS PFBPE-03-0195-101 for 101 pages of Naval Research Laboratory Memorandum Report 6051, "Advanced Concepts Annual Report 1986" from the NRL Plasma Radiation Branch to the Defense Nuclear Agency. Order by PAPS number and journal reference from American Institute of Physics, Physics Auxiliary Publication Service, 335 East 35th St., New York, NY 10017. The price is \$1.50 for each microfiche (98 pages) or \$5.00 for photo copies of up to 30 pages, \$0.15 for each additional page over 30 pages. Airmail additional. Make checks payable to the American Institute of Physics.

APPENDIX C

ELECTRON SCATTERING FOR CODE IMPLEMENTATION

As discussed in Sections 1 and 9, theories and models of the reflex switch depend crucially on the electron distribution in the vicinity of the anode foil. Thus, electron scattering formulas are summarized in this appendix for reference, and for later use in extensions of the different codes.

The literature contains three basic scattering regimes, depending on the number of scatterings per electron N . Multiple scattering is roughly characterized by $N > 20$, for $1 < N < 20$, one has the so called plural scattering regime while $N < 1$ defines the single scattering regime. This appendix is concerned specifically with the multiple scattering regime and its associated theories. For a more complete discussion see the review article by Scott⁹⁸.

C.1 The distribution of Goudsmit and Saunderson.

One of the first multiple scattering theories is that of Goudsmit and Saunderson.^{99,100} This theory is exact for electrons with the same path length, and is valid for all scattering angles — unlike Moliere's theory (see below) which assumes small angle multiple scattering. The essential result of the theory of Goudsmit and Saunderson is the expression of the scattered electron distribution $f(\theta)$ in terms of a series of Legendre polynomials. Note that here the angle θ is the total deflection from the incident direction.

The general form of f is given by

$$f(\theta) \sin \theta d\theta = \frac{1}{4\pi} \sum_{\ell} (2\ell + 1) G_{\ell} P_{\ell}(\cos \theta) \sin \theta d\theta, \quad (C - 1)$$

where the G_{ℓ} 's are expansion coefficients and the P_{ℓ} 's are the Legendre polynomials. Although the Goudsmit-Saunderson theory is considered well suited to numerical evaluation,¹⁰¹ it is nevertheless too computationally intensive for the repetitive calculations required in a particle-in-cell simulation. Theories that result in Gaussian or quasi-Gaussian distributions are easier to sample from.

C.2 Moliere's theory.

A frequently used approximation is given by Moliere's theory: a simpler derivation leads directly to the Gaussian approximation. Following the derivation by Hughes and Godfrey,^{102,103} the distribution function of the electrons changes due to collisions according to:

$$\left(\frac{\partial f}{\partial t} \right)_{coll} = -2\pi n v f \int \sigma(\chi) \chi d\chi + 2\pi n v \int f(\vec{\theta} - \vec{\chi}) \sigma(\chi) d\vec{\chi}. \quad (C - 2)$$

The subscript *coll* denotes the collision term and $f(\theta, t)$ is the electron distribution function. Here n is the density of scattering centers, v is the incident speed of the scattering electron, $\sigma(\chi)$ is the scattering cross section as function of angle χ , and $\vec{\theta} - \vec{\chi}$ is the direction of the electron before the last scattering event. In Equation C-2 all scattering angles are assumed to be small, thus $\sin \theta \sim \theta$. The first term on the right hand side of Equation C-2 denotes scattering out of the angular interval $d\theta$, while the second term denotes scattering into $d\theta$.

Expanding to second order in χ gives:

$$\left(\frac{\partial f}{\partial t}\right) = \frac{1}{4}\langle\dot{\chi}^2\rangle\left[\frac{\partial^2 f}{\partial\theta^2} + \frac{1}{\theta}\frac{\partial f}{\partial\theta}\right], \quad (C-3)$$

where

$$\langle\dot{\chi}^2\rangle = 2\pi n v \int_0^\infty \chi^3 \sigma(\chi) d\chi, \quad (C-3a)$$

and the integration is extended to ∞ assuming that the cross section falls off sufficiently fast. For a relativistic electron,

$$2\pi\sigma(\chi)\chi d\chi = \frac{2\alpha^2\chi d\chi}{\chi^4}, \quad (C-3b)$$

$$\alpha^2 = \frac{4\pi Z(Z+1)r_e^2}{\beta^4\gamma^2} = \frac{4\pi Z(Z+1)e^4}{(pv)^2}. \quad (C-3c)$$

Here r_e is the classical electron radius, $\beta = v/c$ (and c is the light speed), Z is the atomic number of scattering atoms. The factor $(Z+1)$ takes into account the scattering of atomic electrons.

The solution to Equation C-3 for perpendicular incidence ($f = \delta(v_\perp)$) is:

$$f(\theta, \ell) = \exp(-\theta^2/\langle\dot{\chi}^2\rangle\ell), \quad (C-4)$$

where

$$\langle\dot{\chi}^2\rangle = 2n\alpha^2 \ln\left(\frac{\theta_{max}}{\theta_{min}}\right).$$

The length $\ell = vt$ is the axial path length traveled by the electron. Thus, for an electron scattered by a foil, ℓ is the foil thickness. The cutoff angles θ_{max} and θ_{min} , both functions of Z , are needed to keep the the integral in Equation C-3a finite. Equation C-4 is the standard Gaussian distribution for electron scattering, indicating that the electron acquires a Maxwellian distribution perpendicular to the incident direction. Equation C-4 can also be obtained by purely statistical arguments¹⁰⁴.

Moliere's treatment of small angle scattering is more accurate. The following gives the simpler derivation due to Bethe⁹³ and also by Hughes and Godfrey. Again we begin with the Fokker-Planck Equation, C-2. Expanding the distribution function f by a Fourier Bessel transform,

$$f(\theta, \ell) = \int_0^\infty \eta d\eta J_0(\eta\theta)g(\eta, \ell), \quad (C-5)$$

where

$$g(\eta, \ell) = \int_0^\infty \theta d\theta J_0(\eta\theta) f(\theta, \ell). \quad (C-5a)$$

Using Equations C-5, C-5a and C-2 one can show that

$$f(\theta, \ell) = \int_0^\infty \eta d\eta J_0(\eta\theta) \exp\{-n\ell \int_0^\infty \sigma(x) x dx [1 - J_0(\eta x)]\}. \quad (C-6)$$

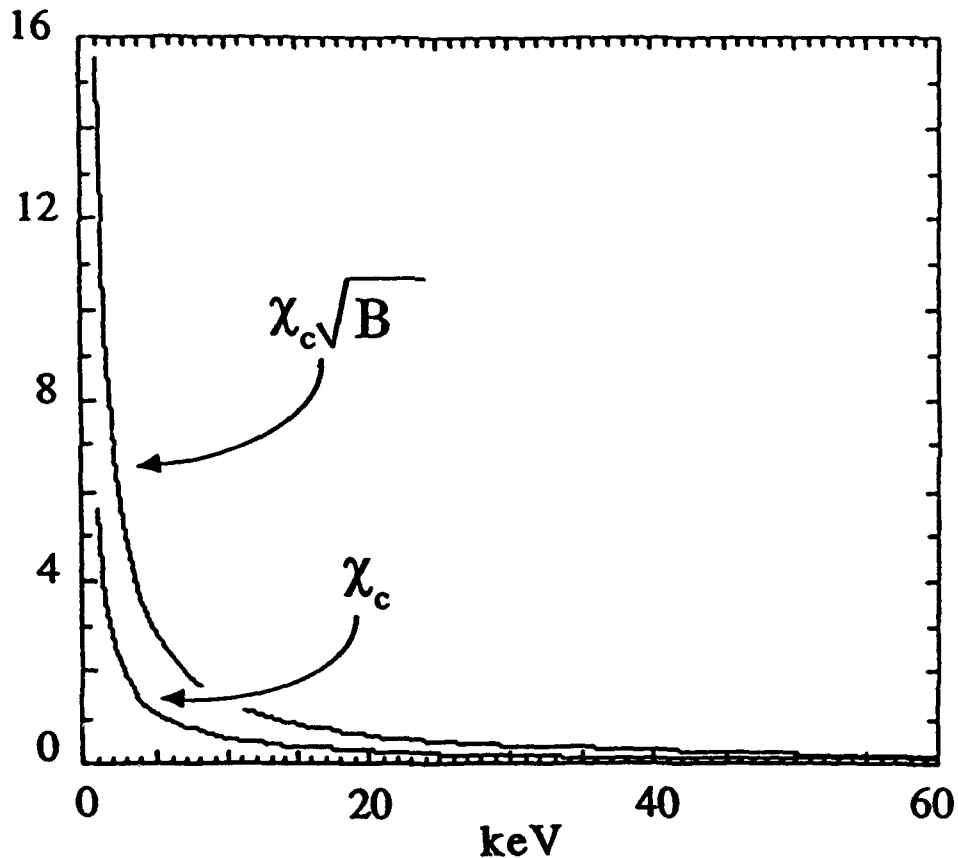


Figure 92. The standard width of the Gaussian distribution for the scattering angle in multiple scattering (Equation C-4) compared to the width according to Moliere (Equation C-9), as function of incoming electron energy.

According to Bethe, Equation C-6 is valid for any scattering law (i.e., cross section) assuming the angles are small. Next, assuming the number of collisions is large, one can make approximations that make Equation C-6 more tractable. In particular, Moliere found that f can be written as a series of the form:

$$f(\theta)\theta d\theta = \theta d\theta [f^{(0)}(\theta) + B^{-1} f^{(1)}(\theta) + B^{-2} f^{(2)}(\theta) + \dots], \quad (C-7)$$

where

$$f^{(0)} = 2 \exp(-\Theta^2),$$

and $f^{(i)}, i > 0$ are derived functions. The angle Θ is a reduced angle given by

$$\Theta = \theta / \chi_c B^{1/2},$$

where $\chi_c^2 = n\ell\alpha^2$ (see Equation C-3b) and B is a parameter given by the transcendental equation

$$\exp B/B = \chi_c^2 / 1.167 \chi_\alpha^2, \quad (C-8)$$

with

$$\chi_\alpha^2 = \chi_0^2 (1.13 + 3.76 \alpha_f^2).$$

The parameter $\alpha_f = Z\alpha/\beta$, where α is the fine structure constant. Obviously, for $v \simeq c$ (or $\beta \simeq 1$), $\alpha_f \ll 1$ for reasonable Z . The angle χ_0 is the minimum cut off angle given by $\chi_0 = \lambda/2\pi a$, where λ is the DeBroglie wavelength of the electron and a is the Fermi radius of the atom. Thus, $a = 0.885 a_0 Z^{-1/3}$ with $a_0 = 5.3 \times 10^{-9}$ cm being the Bohr radius.

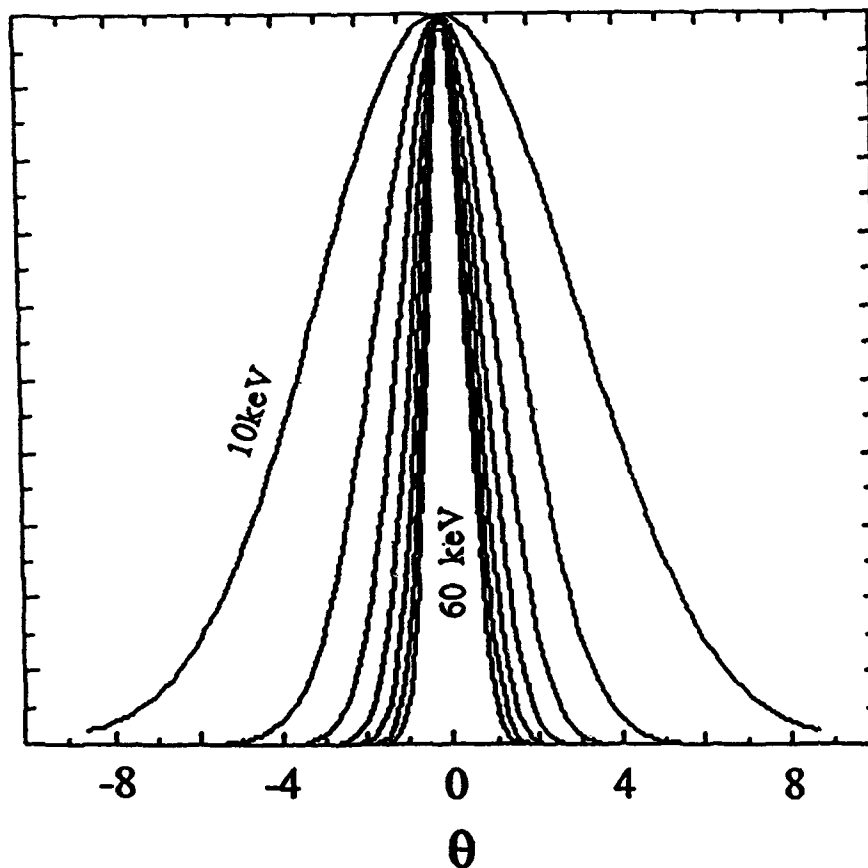


Figure 93. Distribution of scattering angles from Moliere's theory for different electron energies.

It is clear from the definition of χ_c and χ_a that B depends on the type of scattering foil as well as the incident electron energy. Most importantly, B also depends on ℓ , the foil thickness, or the (axial) path length of the electron. Comparing the Gaussian term from Moliere's expansion,

$$f^{(0)}(\theta) = 2 \exp[-\theta^2 / (\chi_c^2 B)] = \exp(-\theta^2 / n \ell \alpha^2 B), \quad (C-9)$$

with Equation C-4, the the Gaussian approximation shows a linear dependence of width on ℓ compared to the Moliere formula C-9. Moliere's theory is valid for $N \gg 1$, where N is again the average number of scatterings. For large N , B will be large, so from C-8 $B \sim \ln(\ell)$ and thus the width of the Gaussian $f^{(0)}(\theta)$ goes like $\ell \ln(\ell)$, rather than ℓ as in C-4.

Figure 92 compares the width of the scattering angle according to the standard Gaussian approximation, Equation C-4, with the width from Moliere's theory, Equation C-9, as function of electron energy. The comparisons at very large energies are not strictly valid since the scattering cross sections become small enough that $N \ll 1$ and neither theory is strictly valid. However, the width according to Moliere should remain larger than the standard Gaussian width. Figure 93 gives the distribution of scattering angles for different energies computed with Moliere's formulas. For larger energies the width of the Gaussian decreases, again because the scattering cross section decreases with energy.

Moliere's theory is more accurate than the standard gaussian approximation (see Scott⁹⁸ or Hughes and Godfrey^{102,103}) and hence a better choice. Calculations with Moliere's theory may be simplified by keeping only the $f^{(0)}$ term in the scattering model (i.e. only the gaussian term). Implicit in this assumption is that $B \gg 1$. This is the model presently implemented in the code. However, for some cases a single term is insufficient. Therefore, later versions of the code will include more terms.

DISTRIBUTION LIST

DNA-TR-92-6

DEPARTMENT OF DEFENSE

ASSISTANT TO THE SECRETARY OF DEFENSE
ATTN: EXECUTIVE ASSISTANT

DEFENSE ADVANCED RSCH PROJ AGENCY
ATTN: ASST DIR ELECTRONIC SCIENCES DIV
ATTN: R REYNOLDS

DEFENSE ELECTRONIC SUPPLY CENTER
ATTN: DESC-E

DEFENSE INTELLIGENCE AGENCY
ATTN: DIW-4
ATTN: DT-1B

DEFENSE NUCLEAR AGENCY
ATTN: RAE E TREE
2 CY ATTN: TITL

DEFENSE SYSTEMS SUPPORT ORGANIZATION
ATTN: JNGO

DEFENSE TECHNICAL INFORMATION CENTER
2 CY ATTN: DTIC/OC

DNA PACOM LIAISON OFFICE
ATTN: DNALO

FIELD COMMAND DEFENSE NUCLEAR AGENCY
ATTN: FCPF R ROBINSON

FIELD COMMAND DEFENSE NUCLEAR AGENCY
ATTN: FCNM

STRATEGIC & SPACE SYSTEMS
ATTN: DR E SEVIN

DEPARTMENT OF THE ARMY

ARMY RESEARCH LABORATORIES
ATTN: AMSRL-WT-NJ
ATTN: SLCHD-NW-RP
ATTN: SLCHD-NW-TN

U S ARMY MISSILE COMMAND
ATTN: AMCPM-HA-SE-MS

U S ARMY NUCLEAR & CHEMICAL AGENCY
ATTN: MONA-NU DR D BASH

U S ARMY RESEARCH OFFICE
ATTN: R GRIFFITH

U S ARMY SPACE & STRATEGIC DEFENSE CMD
ATTN: CSSD-SL

U S ARMY STRATEGIC SPACE & DEFENSE CMD
ATTN: CSSD-SA-E
ATTN: CSSD-SD-A

U S MILITARY ACADEMY
ATTN: LTC AL COSTANTINE

USAISC
ATTN: ASOP-DO-TL

DEPARTMENT OF THE NAVY

NAVAL AIR SYSTEMS COMMAND
ATTN: AIR-536T

NAVAL CMD CONTROL & OCEAN SURVEILLANCE CTR
ATTN: CODE 250

NAVAL POSTGRADUATE SCHOOL
ATTN: CODE 1424 LIBRARY

NAVAL RESEARCH LABORATORY
ATTN: CODE 4600 D NAGEL
ATTN: CODE 4653 A NAMENSON
ATTN: CODE 6613 A B CAMPBELL
ATTN: CODE 6813 N SAKS
ATTN: CODE 6816 H HUGHES

NAVAL SEA SYSTEMS COMMAND
ATTN: NAVSEA-081 A NEWHOUSE

NAVAL SURFACE WARFARE CENTER
ATTN: CODE H21 F WARNOCK
ATTN: CODE H23 R SMITH

NAVAL SURFACE WARFARE CENTER
ATTN: CODE H-21

NAVAL TECHNICAL INTELLIGENCE CTR
ATTN: LIBRARY

NAVAL WEAPONS EVALUATION FACILITY
ATTN: CLASSIFIED LIBRARY

NAVAL WEAPONS SUPPORT CENTER
ATTN: CODE 6054 D PLATTETER

STRATEGIC SYSTEMS PROGRAM
ATTN: JIM HOWARD

DEPARTMENT OF THE AIR FORCE

AERONAUTICAL SYSTEMS CENTER
ATTN: ASD/ENSS

AIR FORCE CTR FOR STUDIES & ANALYSIS
ATTN: AFSAA/SAKI

AIR UNIVERSITY LIBRARY
ATTN: AUL-LSE

PHILLIPS LABORATORY
ATTN: PL/VTE
ATTN: PL/VTEE S SAMPSON

ROME LABORATORY
ATTN: ESR

ROME LABORATORY/SUL
ATTN: RBR

WRIGHT LABORATORY
ATTN: AFWAL/ELE.
ATTN: WRDC/MTE

3416TH TECHNICAL TRAINING SQUADRON (ATC)
ATTN: TTV

DEPARTMENT OF ENERGY

DEPARTMENT OF ENERGY
ALBUQUERQUE OPERATIONS OFFICE
ATTN: NESD

LAWRENCE LIVERMORE NATIONAL LAB
ATTN: L-156 J YEE
ATTN: L-84 G POMYKAL
ATTN: W ORVIS

LOS ALAMOS NATIONAL LABORATORY
ATTN: E LEONARD

SANDIA NATIONAL LABORATORIES
ATTN: DEPT 1332 F SEXTON
ATTN: DR T F WROBEL DIV 9341
ATTN: L D POSEY DIV 9351
ATTN: ORG 2146 T A DELLIN
ATTN: P WINKUR, DIV 1332
ATTN: 2140 J WOODARD

OTHER GOVERNMENT

CENTRAL INTELLIGENCE AGENCY
ATTN: OSWR/NED
ATTN: OSWR/STD/MTB

DEPARTMENT OF TRANSPORTATION
ATTN: ARD-350

NASA

ATTN: CODE 100.0 DR J TRAINOR
ATTN: CODE 313 V DANCHENKO
ATTN: CODE 724.0 M JHABVALA
ATTN: CODE 900 E STASSINOPOULOS

NATIONAL INSTITUTE OF STANDARDS & TECHNOLOGY
ATTN: P ROITMAN

DEPARTMENT OF DEFENSE CONTRACTORS

ADVANCED RESEARCH & APPLICATIONS CORP
ATTN: R ARMISTEAD

AEROSPACE CORP
ATTN: A AMFRAM
ATTN: C RICE
ATTN: D SCHMUNK
ATTN: K G HOLDEN
ATTN: LEE MENDOSA
ATTN: M HOPKINS
ATTN: N SRAMEK
ATTN: P BUCHMAN
ATTN: R KOGA

ALLIED-SIGNAL, INC
ATTN: DOCUMENT CONTROL

ANALYTIC SERVICES, INC (ANSER)
ATTN: A HERNDON
ATTN: A SHOSTAK

BDM FEDERAL INC
ATTN: D WUNSCH

BERKLEY RESEARCH ASSOCIATES, INC
2 CY ATTN: J GEARY JR
2 CY ATTN: L CHEN
2 CY ATTN: N PERIERA
2 CY ATTN: R KARES

BOEING CO
ATTN: D EGELKROUT
ATTN: ROS WOOD
ATTN: O MULKEY

BOOZ ALLEN & HAMILTON INC
ATTN: D VINCENT
ATTN: L ALBRIGHT

CALIFORNIA INSTITUTE OF TECHNOLOGY
ATTN: C BARNES

CHARLES STARK DRAPER LAB, INC
ATTN: J BOYLE
ATTN: N TIBBETTS

CLEMSON UNIVERSITY
ATTN: P J MCNULTY

COMPUTER PRODUCTS A DIVISION OF AMPEX
ATTN: B RICKARD
ATTN: K WRIGHT

COMPUTER SCIENCES CORP
ATTN: A SCHIFF

DAVID SARNOFF RESEARCH CENTER, INC
ATTN: R SMELTZER

E-SYSTEMS, INC
ATTN: MAIN LIBRARY

EATON CORP
ATTN: R BRYANT

ELECTRONIC INDUSTRIES ASSOCIATION
ATTN: J KINN

GENERAL ELECTRIC CO (ASD)
ATTN: D SWANT
ATTN: D TASCA
ATTN: H O'DONNELL
ATTN: J ANDREWS
ATTN: J LINNEN
ATTN: J LOMAN

GENERAL ELECTRIC CO
ATTN: B FLAHERTY
ATTN: G BENDER
ATTN: L HAUGE

GENERAL ELECTRIC CO
ATTN: DAREN NERAD

GENERAL ELECTRIC CO
ATTN: J MILLER

GENERAL RESEARCH CORP
ATTN: A HUNT

GEORGE WASHINGTON UNIVERSITY ATTN: A FRIEDMAN	LOCKHEED MISSILES & SPACE CO, INC ATTN: E HESSEE ATTN: G LUM ORG 81-63 ATTN: J CAYOT DEPT 81-63 ATTN: L ROSSI ATTN: P BENE
H M WEIL CONSULTANTS, INC ATTN: H WEIL	LOCKHEED SANDERS, INC ATTN: BRIAN G CARRIGG
HARRIS CORP ATTN: J C LEE ATTN: J W SWONGER	LOGICON R & D ASSOCIATES ATTN: D CARLSON
HARRIS CORPORATION ATTN: E YOST ATTN: W ABARE	LORAL AERONUTRONIC ATTN: TECHNICAL LIBRARY
HONEYWELL INC ATTN: R JULKOWSKI	LTV AEROSPACE & DEFENSE COMPANY 2 CY ATTN: LIBRARY EM-08
HONEYWELL, INC ATTN: MS 725-5	MARTIN MARIETTA DENVER AEROSPACE ATTN: P KASE ATTN: RESEARCH LIBRARY
HUGHES AIRCRAFT COMPANY ATTN: E KUBO ATTN: L DARDA	MARTIN MARIETTA TECHNOLOGIES INC ATTN: J TANKE ATTN: TIC/MP-30
IBM CORP ATTN: DEPT L75	MARTIN MARIETTA TECHNOLOGIES, INC ATTN: H SCHISLER
IBM CORP ATTN: J ZIEGLER	MARYLAND, UNIVERSITY OF ATTN: H C LIN
IBM CORP ATTN: N HADDAD	MCDONNELL DOUGLAS CORP ATTN: R L KLOSTER
INSTITUTE FOR DEFENSE ANALYSES ATTN: TECH INFO SERVICES	MCDONNELL DOUGLAS CORPORATION ATTN: P ALBRECHT
JAYCOR ATTN: D WALTERS	MESSINGER, GEORGE C ATTN: G MESSENGER
JAYCOR ATTN: CYRUS P KNOWLES ATTN: R SULLIVAN	MISSION RESEARCH CORP ATTN: R PEASE
JAYCOR ATTN: R POLL	MISSION RESEARCH CORP ATTN: J LUBELL ATTN: W WARE
JOHNS HOPKINS UNIVERSITY ATTN: R MAURER	MITRE CORPORATION ATTN: J R SPURRIER ATTN: M FITZGERALD
KAMAN SCIENCES CORP ATTN: DASIAC ATTN: E CONRAD	NATIONAL SEMICONDUCTOR CORP ATTN: F C JONES
KAMAN SCIENCES CORPORATION ATTN: DASIAC ATTN: R RUTHERFORD	NORDEN SYSTEMS, INC ATTN: N RIEDERMAN ATTN: TECHNICAL LIBRARY
KEARFOTT GUIDANCE & NAVIGATION CORP ATTN: J D BRINKMAN	NORTHROP CORPORATION ATTN: J R SROUR
LITTON SYSTEMS INC ATTN: F MOTTER	PACIFIC-SIERRA RESEARCH CORP ATTN: H BRODE
LOCKHEED MISSILES & SPACE CO, INC ATTN: F JUNGA ATTN: TECHNICAL INFO CENTER	

DNA-TR-82-6 (DL CONTINUED)

PHYSITRON INC
ATTN: MARK CHRISTOPHER

PHYSITRON INC
ATTN: MARION ROSE

RAND CORP
ATTN: C CRAIN

RAYTHEON CO
ATTN: D D LEE
ATTN: JOSEPH SURRO

RENSELAER POLYTECHNIC INSTITUTE
ATTN: J HOWARD

RESEARCH TRIANGLE INSTITUTE
ATTN: M SIMONS

ROCKWELL INTERNATIONAL CORP
ATTN: V DE MARTINO

S-CUBED
ATTN: J M WILKENFELD

SCIENCE APPLICATIONS INTL CORP
ATTN: D MILLWARD
ATTN: DAVID LONG

SCIENCE APPLICATIONS INTL CORP
ATTN: J RETZLER

SCIENCE APPLICATIONS INTL CORP
ATTN: W CHADSEY

SCIENCE APPLICATIONS INTL CORP
ATTN: P ZIELIE

SCIENTIFIC RESEARCH ASSOC, INC
ATTN: H GRUBIN

SUNDSTRAND CORP
ATTN: C WHITE

SYSTRON-DONNER,
ATTN: SECURITY OFFICER

TECHNOLOGY DEVELOPMENT ASSOCIATES
ATTN: R V BENEDICT

TELEDYNE BROWN ENGINEERING
ATTN: G R EZELL
ATTN: LEWIS T SMITH

TEXAS INSTRUMENTS, INC
ATTN: J SALZMAN
ATTN: T CHEEK

TRW
ATTN: M J TAYLOR

TRW S I G
ATTN: C BLASNEK
ATTN: DR D R GIBSON

TRW SPACE & DEFENSE SECTOR
ATTN: D M LAYTON

UNISYS CORPORATION-DEFENSE SYSTEMS
ATTN: P MARROFFINO

VISIDYNE, INC
ATTN: C H HUMPHREY
ATTN: W P REIDY